Transactions of the ASME®

FLUIDS ENGINEERING DIVISION
Technical Editor
DEMETRI P. TELIONIS (1999)
Executive Secretary
PAT WHITE (1999)
Assistant to the Editor
N. W. SCHAEFFLER
Calendar Editor
M. F. ACKERSON

Associate Technical Editors
P. R. BANDYOPADHYAY (1998)
S. BANERJEE (1999)
P. W. BEARMAN (1998)
P. BRADSHAW (2000)
M. S. CRAMER (1998)
M. N. DHAUBHADEL (1999)
J. K. EATON (1998)
G. ERLEBACHER (2000)
J. A. C. HUMPHREY (1998)
F. HUSSAIN (1998)
J. KATZ (1998)
C. L. MERKLE (2000)
B. SCHIAVELLO (1999)
P. M. SOCKOL (1998)
M. SOMMERFELD (1999)
M. S. TRIANTAFYLLOU (1998)
F. K. WASDEN (2000)
D. R. WILLIAMS (2000)

BOARD ON COMMUNICATIONS
Chairman and Vice-President
R. K. SHAH

OFFICERS OF THE ASME
President, **W. M. PHILLIPS**
Exec. Director
D. L. BELDEN
Treasurer
J. A. MASON

PUBLISHING STAFF
Managing Director, Engineering
CHARLES W. BEARDSLEY
Director, Technical Publishing
PHILIP DI VIETRO
Managing Editor, Technical Publishing
CYNTHIA B. CLARK
Managing Editor, Transactions
CORNELIA MONAHAN
Production Assistant
MARISOL ANDINO

Transactions of the ASME, Journal of Fluids Engineering (ISSN 0098-2202) is published quarterly (Mar., June, Sept., Dec.) for $205.00 per year by The American Society of Mechanical Engineers, Three Park Avenue, New York, NY 10016. Periodicals postage paid at New York, NY and additional mailing offices. POSTMASTER: Send address changes to Transactions of the ASME, Journal of Fluids Engineering, c/o THE AMERICAN SOCIETY OF MECHANICAL ENGINEERS, 22 Law Drive, Box 2300, Fairfield, NJ 07007-2300.

CHANGES OF ADDRESS must be received at Society headquarters seven weeks before they are to be effective. Please send old label and new address.

PRICES: To members, $40.00, annually; to nonmembers, $205.00. Add $40.00 for postage to countries outside the United States and Canada.

STATEMENT from By-Laws. The Society shall not be responsible for statements or opinions advanced in papers or . . . printed in its publications (B7.1, Par. 3).

INDEXED by Applied Mechanics Reviews and Engineering Information, Inc. Canadian Goods & Services Tax Registration #126148048.

Journal of Fluids Engineering

Published Quarterly by The American Society of Mechanical Engineers

VOLUME 120 • NUMBER 4 • DECEMBER 1998

(Contents continued on p. 675)

This journal is printed on acid-free paper, which exceeds the ANSI Z39.48-1992 specification for permanence of paper and library materials. ♾™

♻ 85% recycled content, including 10% post-consumer fibers.

(Contents continued)

Technical Brief

Announcements and Special Notices

Journal of Fluids Engineering

Editorials

Rotating Flows

The first nine papers in this issue of the *Journal of Fluids Engineering* are on the important topic of rotating flows. Some of these papers were submitted directly to the Technical Editor but most of them were selected from the *Symposium on the Dynamics of Rotating and Buoyancy-Driven Flows.* This symposium was held at the 97th International Mechanical Engineering Congress and Exposition. The papers presented at the symposium were included in the Proceedings of the Ocean Engineering Division technical program, ASME publication OED-Vol. 14, 1997. Rotating flows in containers that are induced by rotating boundaries are important to the designer of fluid mixing devices. These papers are important in that the problems described provide insight into the dynamics of vortices and the generation of secondary flows. There are numerous problems in fluids engineering that involve rotating boundary-driven and buoyancy-driven flows, e.g., centrifugal materials processing (like the growing of crystals in rotating containers), fluid mixing in containers with rotating disks, pumping of fluids with rotating blades, to name a few. Albeit important, the dynamics of rotating fluids is a topic that has not been, in general, covered in undergraduate engineering studies. Over the past twenty years there has been significant advances in our knowledge of rotating flows.

All of the papers selected for this issue of JFE describe new and unique features that occur in confined swirling flows. The authors provide insights into the dynamics of flows induced by the relative rotation between confined fluids and their boundaries. Mullin, Tavener and Cliffe investigate the generation of stagnation points in steady rotating flows induced by co-rotating end walls. Their main contributions are new results for low-aspect ratio containers and the effect of a small-radius inner rod that rotates with the end walls on the predicted occurrence of toroidal vortices. Lopez and Chen examine the rotating flow induced by the rotation of the bottom of a cylinder with a free surface. They show that surfactants can play a major role on the secondary motions induced in the cylinder by the rotating end wall. The paper by Hewitt, Duck, Foster, and Davis extends a previously published theory that describes the onset of spin-up in circular-cylinder containers to containers of more general shape. Depending upon the structure of the density stratification and the rotation-rate change, they show that the flow field evolves to one of three possible states. They also present evidence of a new, finite-time breakdown associated with high Prandtl or Schmidt numbers. Hewitt, Davis, Duck, Foster, and Smith describe the experimental part of this study. In their papers, they examine the spin-up of stratified fluids in conical containers. Comparisons with the theory show good agreement. In addition to these findings, a unique filling method is described to create linear density stratification in containers with sloping boundaries. This is an excellent example of a clever solution to a design problem in fluid mechanics. The paper by Vorobieff and Ecke describes experiments on impulsive spin-up in a cylindrical, Rayleigh-Bénard cell. They discovered a prominent feature of the flow morphology during spin-up; it is the generation of axisymmetric ring-shaped regions of downwelling flow characterized by a local drop in temperature and azimuthal velocity. Mang, Minkov, Schaflinger, and Ungarish examine the problem of particle entrainment in a flow induced by a drain. They discuss the influence of centrifugal separation and viscous resuspension caused by the "bathtub" vortex on the influence of gravity separation of solid impurities lighter than the embedding fluid. The paper by Jahnke and Valentine examines rotating flows in a cylinder induced by the rotation of both end walls that rotate at different rates. Regions in parameter space where multiple vortex rings are formed within the cylinder were discovered. The paper by Birk and DeSpirito describes the interaction between a spinning liquid film with a swirling gas in a cylindrical vessel that models the flow in a combustion device. Rotation of the flow is induced by introducing the liquid and gas into the combustion chamber at an angle tangent to the cylindrical wall. The rotating flow induced in the combustion chamber is designed to maintain the necessary retention time of the liquid in the chamber at any tilt angle with respect to Earth's gravity. D'Agostino, d'Auria and Brennen examine the dynamic forces experienced by the rotor of a whirling and cavitating helical inducer. They show that the large reduction in sonic speed in the bubbly mixtures used to model the cavitating flows in high power density turbopumps significantly modifies the whirl-induced disturbances and, hence, the rotor dynamic forces. All of the papers are intended to introduce the reader to some of the recent findings in rotating flows and, via the references cited by the authors, help the reader get into the details of this area of fluids engineering.

Daniel T. Valentine
Department of Mechanical and Aeronautical Engineering
Clarkson University
Potsdam, New York 13699-5725

and

Craig C. Jahnke
Visiting Assistant Professor
Department of Mechanical, Aerospace, Industrial and Manufacturing Engineering
Polytechnic University
Brooklyn, New York 11201

Modeling of Cavitation and Multiphase Flows in Complex Environments

The present issue of JFE contains several papers dealing with cavitation and its adverse effect on the flow structure, stability, performance and erosion in hydraulic machines. They address a variety of issues that are representative of the difficulties encountered while attempting to determine the occurrence and extent of cavitation. Included are predictions of scale effects on the rates of cavitation events, the effect of the bubble cloud on the stability of inducers as well as the size and shape of attached cavitation, particularly in the closure region, where the physics is only partially understood. Modeling and measurements of cavitation erosion, including an attempt to relate between bubble dynamics and the extent of damage are also addressed.

Two papers deal with the effect of cavitation and bubble clouds on the performance of hydraulic machines, a complex problem with very few available analysis tools. Both papers represent pioneering efforts to include the effect of cavitation in flows that are difficult to compute, even in single-phase flows. D'Agostino et al. study numerically the impact of bubble clouds on rotor dynamic forces in whirling helical inducers. They show that the presence of bubbles significantly alters the relationship between the forces and the whirl speed, resulting in complex behavior that depends on excitation frequency, void fraction, characteristic size of the bubbles and pump operating conditions. Their linearized dynamics model reproduces the experimental trends and provides a previously unavailable insight on an extremely complex phenomenon. The second paper, by Hirschi et al., is an attempt to compute the extent of attached cavitation and its effect on the performance of centrifugal pumps. Their analysis starts with a model for the shape of the sheet cavitation on the impeller blade that is based on the growth and collapse of semi-spherical bubbles. Then, the authors determine the shape of the cavity by bending the stream lines to create a free surface with constant pressure. These models are combined with RANS calculation of the flow within the impeller and the diffuser. In some cases the results agree with experimental data and in others, there are discrepancies. Nevertheless, this approach seems promising.

Cavitation erosion, a major problem in hydraulic machines and propellers is dealt with in two papers. Soyama et al. describe and calibrate a transducer for measuring the high intensity dynamic loading generated by collapsing cavitation bubbles on a surface. The device is based on PVDF and has excellent mechanical properties, high resonant frequency, small size, but high piezo-electric stress constant. They determine the impact area by measuring the size of the erosion pits on the surface of the transducer. Together with the amplitude of the signal they can calculate the impact pressure. Pereira et al. develop an energy approach to prediction of cavitation erosion which is based on the transfer of energy from the cavitation to the material. They determine the energy spectrum of leading edge cavitation by measuring the rate of bubble production and the volume of vapor cavities, using stereo photography. After determining the effect of various flow parameters on the cavitation energy spectrum, it is compared to the material deformation energy spectrum. The result is a remarkable proportionality relationship, which then leads to an estimate for the erosive "efficiency" coefficient of collapsing bubbles. Interestingly, the efficiency is very low, in the 10^{-5}–10^{-4} range. This unique approach, which is based on an idea introduced originally by Hammitt, provides a quantitative method relating the occurrence of cavitation and the resulting damage.

Liu and Brennen estimate the rate of "traveling bubble" cavitation events based on the flow structure and measured population of free-stream nuclei. Their model includes the potential flow and boundary layer around an axisymmetric body, the relative motion between the bubble and the liquid due to pressure gradients near the stagnation point (commonly termed as screening effect), residence time of the bubble in the region with local pressure below the vapor pressure, the observed bubble size and the impact of bubble growth on neighboring nuclei. Their model reproduces some of the measured trends, but overpredicts the rate of cavitation event. Also, the measured increase in rate of cavitation events with decreasing velocity is not reproduced and remains unexplained. This latter disagreement highlights that some fundamental components of the puzzling scaling trends of cavitation remain unexplained.

Still in the area of multiphase flows, two additional papers focus on mixing and entrainment in liquid—gas interfaces. A paper by Brattberg et al. provides data on the entrainment of air bubbles by two dimensional jets discharging into the atmosphere. Using conductivity probes they show that air diffusion starts rapidly downstream of the nozzle. The dimensionless bubble flux is independent of the jet velocity but strongly depends on the dissolved air content. A simple diffusion model, with empirically-determined diffusion coefficient, reproduces the observed trends. The second paper by Birk and DeSpirito deals with the interaction of a spinning liquid film with a swirling gas in a cylindrical vessel. It is included in this issue ahead of the paper by d'Agostino et al. because it is also grouped with the rotating flow papers. Their experimental and computational efforts attempt to simulate the flow conditions in the ignition chamber of a liquid-propellant gun. Both the liquid and the gas are injected tangentially into the chamber. Liquid entrainment and atomization occurs, creating a swirling, transonic two-phase flow. The observations and simulations show that the liquid is sheared unevenly by the gas and forms twisting cellular structures. Part of the sheared liquid is entrained by the swirling gas and is deposited in other locations. The numerical results show only qualitative agreement with the experimental data.

Joseph Katz
Department of Mechanical Engineering
Johns Hopkins University
122 Latrobe Hall
3400 N. Charles Street
Baltimore, MD 21218-2686

Coupling Between a Viscoelastic Gas/Liquid Interface and a Swirling Vortex Flow

J. M. Lopez
Associate Professor,
Department of Mathematics,
Arizona State University,
Tempe, AZ 85287

J. Chen
Staff Scientist,
COMSAT Laboratories,
22300 COMSAT Drive,
Clarksburg, MD 20871

While the structure and dynamics of boundary layers on rigid no-slip walls in rotation dominated enclosed flows are still an area of active research, the interactions between rotating or swirling flows with a free surface have received comparatively less attention. For the most part, investigations in this area have been focused on clean free surfaces, which may be treated as stress-free. However, in most practical situations the surface is rarely clean, and even under laboratory conditions, it is quite difficult to achieve a clean free surface. Most impurities in liquids are surface active, and hence the name surface active agent or surfactant. These surfactants tend to establish an equilibrium surface concentration which alters the interfacial tension and interfacial viscoelastic properties of the gas/liquid interface. The coupling between the bulk swirling flow and the interface is provided via the tangential stress balances, and these stresses on the interface are dependent upon the surface concentration of surfactant, which in turn is altered by the interfacial flow. Forces acting on the interface include surface tension gradients (elastic) and the viscous resistance to shear and dilatation. These viscoelastic properties vary with the surfactant concentration on the surface. Here, we present numerical studies of flow in a cylinder driven by the constant rotation of the bottom endwall with the top free surface being contaminated by a Newtonian surfactant. Comparisons with a clean free surface and a no-slip stationary top endwall provide added insight into the altered dynamics that result from the presence of a small amount of surfactant.

1 Introduction

Many geophysical and industrial flows are dominated by gas/liquid interfaces. Gas/liquid interfaces in general, and the ocean surface in particular, are rarely free of surfactants. The amount of surfactant required to have a significant effect on the hydrodynamic behavior of the interface can be as low as a fraction of a kg km^{-2}, and the surface tension may be halved with 1 kg km^{-2} of many surfactants. At these concentrations, surfactants form an expanded monomolecular surface film or monolayer. Surfactants make the interface not only elastic (surface tension variations as a result of variations in the surfactant surface concentration), but also give it surface (or excess) viscosity, which can be many orders of magnitude larger than the viscosity in the bulk multiplied by an appropriate bulk flow length scale (Hirsa et al., 1997a). In many fluid dynamic systems which have a gas/liquid interface (even when the ratio of inertial to surface tension forces is large), the transport of mass, momentum, and energy is strongly influenced by the viscoelastic nature of the interface; for high Reynolds number flows see Hunt (1984), Asher and Pankow (1991), Hirsa et al. (1995), and for low Reynolds number flows see Grotberg (1994).

In recent years it has been demonstrated that at any instant, the bulk flow near an air/water interface with surfactant is described by interfacial boundary conditions ranging from a clean free surface to a state with characteristics similar to that of a solid wall (Tryggvason et al., 1992; Tsai and Yue, 1995). The variations in the interfacial boundary conditions are dependent on the concentration levels and viscoelastic properties of the surfactant. Furthermore, not only does the presence of a surfactant alter the subsurface flow, but also the subsurface flow alters the conditions on the surface, primarily by redistributing the surfactant on the interface and to/from the bulk. This leads to a coupled nonlinear system rich in dynamical behavior.

We address not only the influence that the interfacial stress imparts upon the hydrodynamics in the bulk, but also the influence of the bulk flow on the dynamics of the interface. When the interface is covered by surfactants, a boundary layer (comparable to the boundary layer on a solid wall) can form at the interface with both elastic and viscous properties. The formation of the free surface boundary layer significantly increases wave damping; it also alters gas transfer rates, reduces turbulence by shedding surface parallel vortices, and tilts surface-normal vorticity, among other effects. It is essential to understand this dynamic nonlinear coupling between the interior flow and the surface processes in order to be able to interpret observations of surface flows and to develop predictive capabilities for both the surface and the subsurface flows.

Studies incorporating the hydrodynamic coupling with the interface have typically included the elastic effects due to surface tension variations (e.g., Foda and Cox 1980; Wang and Leighton 1990; Tryggvason et al., 1992; Ananthakrishnan and Yeung, 1994; Grotberg, 1994). These studies considered the interface itself as being inviscid. The experiments of Hirsa et al. (1995) showed that in flows where the surface velocity field is solenoidal, the surface shear viscosity has a significant influence on the subsurface velocity field. The surface shear viscosity is a relatively easy property to measure, however experiments (Maru and Wasan, 1979) have shown that the surface dilatational viscosity may be several orders of magnitude larger and is a difficult property to quantify (Edwards et al., 1991). The recent study by Tsai and Yue (1995) included for the first time both surface viscosities in hydrodynamic computations of the interactions of surface-parallel vorticity with a contaminated air/water interface in planar two-dimensional flows. However, they treated these as constant coefficients whereas it is known (Maru and Wasan, 1979; Tsai and Yue, 1995) that these quantities vary with, amongst other things, the surface concentration

Contributed by the Fluids Engineering Division for publication in the JOURNAL OF FLUIDS ENGINEERING. Manuscript received by the Fluids Engineering Division November 5, 1997; revised manuscript received July 13, 1998. Guest Editor: D. T. Valentine.

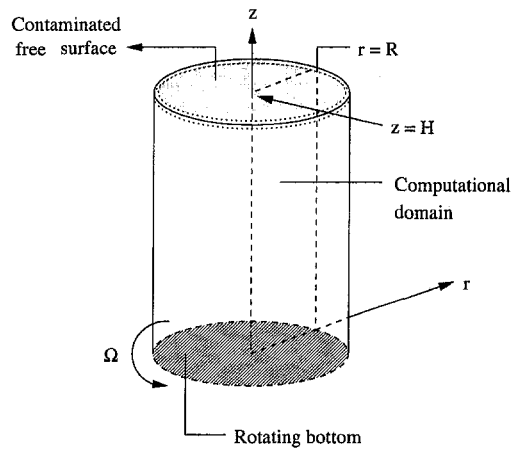

Fig. 1 Schematic of the model flow

of the surfactant. Further, in the flows they considered the surface velocity is everywhere normal to the surface vorticity and both are tangent to the surface. Here, we consider flows where the inner product of surface velocity and surface vorticity is not identically zero, and also the surface viscosities are functions of surface concentration. We derive the appropriate interfacial conditions by balancing the tangential stresses at the interface, written in terms of the surface vorticity, and couple these to a Navier-Stokes solver for the whole flow. The formulation is applied to a model problem that is chosen to isolate and highlight individual processes. The model problem is that of flow in an open cylinder driven by the constant rotation of the bottom endwall with the top free surface covered by a monolayer of insoluble surfactant. A schematic is given in Fig. 1.

It is often seen that the elastic effects, due to surface tension gradients, lead to flow instability (Sternling and Scriven, 1959), and that interfacial viscosity effects tend to damp these instabilities. This is generally true when the vorticity in the bulk flow is predominantly surface-parallel. However, when the vorticity near the interface is predominantly surface-normal, the interfacial viscous effects dominate the dynamics. The interfacial viscous effects provide a mechanism for the tilting of surface-normal vorticity, in an analogous manner that molecular viscosity does at a rigid wall, and leads to secondary motions, boundary layer formation, boundary layer separation, internal shear layers, etc. Once the surface-normal vorticity is tilted into surface-parallel vorticity, the elastic effects at the interface also come into play, and there is a dynamic interaction between the elasticity and the viscosity on the surface and the vortical flow in the bulk.

2 Interfacial Rheology and the Development of Boundary Conditions for Vorticity at a Contaminated Interface

We shall be concerned here with non-deforming surfaces, i.e., negligible Froude number flow. The physical flows that this formulation is primarily being derived for involve very little free surface deformation regardless of the amount of surfactant (Spohn et al., 1993). Also, we consider here axisymmetric flow as it contains the hydrodynamics of interest (both surface-normal and surface-parallel vorticity, and the turning and stretching of vorticity).

The governing equations are the axisymmetric Navier-Stokes equations, together with the continuity equation and appropriate boundary and initial conditions. Using a cylindrical polar coordinate system (r, θ, z) and the Stokes streamfunction ψ, the nondimensional velocity vector is $\mathbf{u} = (u, v, w) = (-1/r\partial\psi/\partial z, \Gamma/r, 1/r\partial\psi/\partial r)$ and the associated vorticity vector is $\boldsymbol{\omega} = (-1/r\partial\Gamma/\partial z, \eta, 1/r\partial\Gamma/\partial r)$. The nondimensional axisymmetric Navier-Stokes equations are:

$$\frac{D\Gamma}{Dt} = \frac{1}{\mathrm{Re}}\nabla_*^2\Gamma, \tag{2.1}$$

$$\frac{D\eta}{Dt} + \frac{\eta}{r^2}\frac{\partial\psi}{\partial z} - \frac{1}{r^3}\frac{\partial\Gamma^2}{\partial z} = \frac{1}{\mathrm{Re}}\left(\nabla^2\eta - \frac{\eta}{r^2}\right), \tag{2.2}$$

where

$$\nabla_*^2\psi = -r\eta,$$

$$\mathrm{Re} = \Omega R^2/\nu,$$

$$\frac{D}{Dt} = \frac{\partial}{\partial t} - \frac{1}{r}\frac{\partial\psi}{\partial z}\frac{\partial}{\partial r} + \frac{1}{r}\frac{\partial\psi}{\partial r}\frac{\partial}{\partial z},$$

$$\nabla^2 = \frac{\partial^2}{\partial z^2} + \frac{\partial^2}{\partial r^2} + \frac{1}{r}\frac{\partial}{\partial r},$$

$$\nabla_*^2 = \frac{\partial^2}{\partial z^2} + \frac{\partial^2}{\partial r^2} - \frac{1}{r}\frac{\partial}{\partial r},$$

ν is the kinematic viscosity, $1/\Omega$ is the time scale and R is the length scale, where Ω rad s^{-1} is the rate of rotation of the bottom endwall and R is the radius of the cylinder, which is filled to a depth H.

We begin our treatment of the interface by considering the Boussinesq-Scriven surface fluid model (Boussinesq, 1913; Scriven, 1960; Slattery, 1990):

$$\mathbf{T}^s = (\sigma^* + (\kappa^s - \mu^s)\mathrm{div}_s\,\tilde{\mathbf{u}}^s)\mathbf{I}_s + 2\mu^s\mathbf{D}^s, \tag{2.3}$$

where the surface stress tensor $\mathbf{T}^s$ is described as a linear function of the surface rate of deformation tensor

$$2\mathbf{D}^s = (\nabla_s\tilde{\mathbf{u}}^s\cdot\mathbf{I}_s + \mathbf{I}_s\cdot(\nabla_s\tilde{\mathbf{u}}^s)^T).$$

In this constitutive equation, κ^s is the surface dilatational viscosity, μ^s is the surface shear viscosity, σ^* is the thermodynamic interfacial tension, $\tilde{\mathbf{u}}^s$ is the surface velocity, div_s is the surface divergence operator, ∇_s is the surface gradient operator, and $\mathbf{I}_s$ is the tensor that projects any vector onto the interface. The surface stress $\boldsymbol{\tau}$ can then be expressed as (Slattery 1990):

$$\boldsymbol{\tau} = \nabla_s\sigma^* + \nabla_s((\kappa^s - \mu^s)\mathrm{div}_s\,\tilde{\mathbf{u}}^s) + 2(\nabla_s\mu^s)\cdot\mathbf{D}^s + 2\mu^s\,\mathrm{div}_s\,\mathbf{D}^s.$$

Noting that there is no slip at the interface, so the tangential component of fluid velocity is continuous across the interface, we balance the above surface stresses with the corresponding components from the bulk flow, using cylindrical polars and nondimensionalizing σ^* with σ_i, a characteristic value of the surface tension, so that $\sigma = \sigma^*/\sigma_i$, and putting $\lambda_\mu = \mu^s/\mu R$, $\lambda_\kappa = \kappa^s/\mu R$, and $\lambda_{\kappa+\mu} = \lambda_\kappa + \lambda_\mu$, where μ is the shear viscosity of the bulk fluid, the nondimensional stress balance in the azimuthal direction is

$$\frac{\partial\Gamma}{\partial z} = \lambda_\mu\left(\frac{\partial^2\Gamma}{\partial r^2} - \frac{1}{r}\frac{\partial\Gamma}{\partial r}\right) + \frac{\partial\lambda_\mu}{\partial r}\left(\frac{\partial\Gamma}{\partial r} - \frac{2\Gamma}{r}\right), \tag{2.4}$$

and in the radial direction

$$\eta = C_a\frac{\partial\sigma}{\partial r} + \lambda_{\kappa+\mu}\left(\frac{1}{r^2}\frac{\partial^2\psi}{\partial r\partial z} - \frac{1}{r}\frac{\partial^3\psi}{\partial r^2\partial z}\right) - \frac{1}{r}\frac{\partial^2\psi}{\partial r\partial z}\frac{\partial\lambda_{\kappa+\mu}}{\partial r} + \frac{2}{r^2}\frac{\partial\psi}{\partial z}\frac{\partial\lambda_\mu}{\partial r}, \tag{2.5}$$

where $C_a = \sigma_i/\mu\Omega R$ is the capillary number.

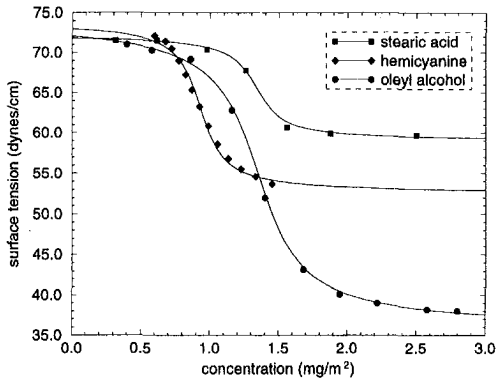

Fig. 2 Nonlinear equations of state for various surfactant/water systems; symbols are experimental measurements of Kim (1996) and solid lines correspond to model Eq. (2.6)

Equations (2.4) and (2.5) represent the balance of forces on a surface element resulting from viscous traction or shearing stress from the bulk, surface tension (or surface pressure) gradients, and surface viscosity effects. Their solution for Γ and η on the interface provide the boundary conditions for the bulk flow Eqs. (2.1) and (2.2). Note that Eqs. (2.4) and (2.5) are also coupled to the bulk flow through normal derivative terms in Γ and ψ, respectively, at the interface. It is clear that the stress balance in the azimuthal direction does not include any elastic term, only surface shear viscosity terms. If the flow near the interface is purely azimuthal, i.e. $\psi = \eta = 0$, $\Gamma \neq 0$, and the vorticity in the bulk is initially normal to the interface, then if the surfactant system has a very small surface shear viscosity, the flow behaves as if the surface is clean, regardless of the elastic properties of the surfactant. This was dramatically demonstrated in recent experiments (Hirsa et al., 1995).

The surface tension, σ^*, and the surface shear and dilatational viscosities, μ^s and κ^s, depend on the thermodynamic state of the interface and thus are functions of the surface concentration of the surfactant, c^*. Most previous theoretical considerations have used a linear equation of state, i.e. $\sigma^* \propto c^*$, and have either set μ^s and κ^s to zero, or by linearizing about an equilibrium state have taken them to be constant coefficients. These linearizations are strictly only valid about an equilibrium concentration level. In problems where there is significant surface velocity, the concentration can be locally far from equilibrium and the nonlinearity of the equation of state and variations in μ^s and κ^s with surfactant concentration need to be taken into account.

Experiments (Gains, 1966; Poskanzer and Goodrich, 1975; Kim, 1996; Hirsa et al., 1997b) have measured the equation of state for a variety of surfactant/water systems (stearic acid, hemicyanine, and oleyl alcohol), and they can be modeled by an equation

$$\sigma^* - \sigma_i = -\frac{\delta}{\pi} \tan^{-1} \beta\left(\frac{c^* - c_i}{c_i}\right), \qquad (2.6)$$

where the dimensional surfactant concentration, c^*, and surface tension, σ^*, are to be nondimensionalized by c_i and σ_i, the concentration and surface tension at the inflection point of the equation of state, respectively; δ is the saturation surface pressure, i.e. the range in surface tension between that of a clean air/water interface and that of the surfactant-saturated interface. It should be noted that the extrapolation of this model to large c^*, as suggested in Fig. 2, is dangerous as many surfactant systems, and in particular stearic acid/water and hemicyanine/water, may undergo molecular reorientation or phase changes for increasing c^*. We characterize a surfactant system by two parameters, a Marangoni number $M = -(c_i/\sigma_i)(\partial\sigma^*/\partial c^*)$ evaluated at $c^* = c_i$ and $\beta = M\pi\sigma_i/\delta$.

For the surface dilatational viscosity κ^s, there is no generally accepted measurement over a range of surfactant concentration (Edwards et al., 1991). For now, we will model both μ^s and κ^s with $\mu^s(c^*)$ and $\kappa^s(c^*) \to 0$ as $c^* \to 0$, and both $\mu^s(c^*)$ and $\kappa^s(c^*) \to$ constant as $c^* \to \infty$. A simple ad hoc function for the dimensionless surface viscosities $\lambda_\mu(c)$ and $\lambda_\kappa(c)$ will be used in this initial study:

$$\lambda_\mu = \Lambda_\mu \frac{c}{c+1}, \quad \text{and} \quad \lambda_\kappa = \Lambda_\kappa \frac{c}{c+1}, \qquad (2.7)$$

where $\lambda_\kappa(c) \to \Lambda_\kappa$ and $\lambda_\mu(c) \to \Lambda_\mu$ as $c \to \infty$.

For insoluble surfactants on a nondeforming interface, the transport equation of c is given by

$$\frac{\partial c}{\partial t} + \nabla_s \cdot (c\mathbf{u}^s) = \frac{1}{\mathrm{Pe}^s} \nabla_s^2 c, \qquad (2.8)$$

where $\mathrm{Pe}^s = \Omega R/D^s$ is the surface Peclet number and D^s is the coefficient of interfacial diffusivity, and $\mathbf{u}^s$ is the dimensionless surface velocity, using ΩR as the velocity scale. Equation (2.8) is solved, along with the evolution equations for Γ and η in the interior, with $\partial c/\partial r = 0$ at $r = 0$ and 1, to give $c(r)$ at each time level, from which $\partial c/\partial r$ is obtained. The boundary conditions on c, together with $u = 0$ at $r = 0$ and 1, ensure that the insoluble surfactant is conserved on the enclosed domain $r \in [0, 1]$. The term $\partial\sigma/\partial r$ in (2.5) can be obtained from $\partial\sigma/\partial r = d\sigma/dc\,\partial c/\partial r$, where $d\sigma/dc$ is determined from the appropriate equation of state and $\partial c/\partial r$ from (2.8). The gradients $\partial\lambda_\kappa/\partial r$ and $\partial\lambda_\mu/\partial r$ in (2.4) and (2.5) are obtained in the same fashion using the model Eqs. (2.7).

3 Coupling of the Interface Dynamics to the Bulk Flow

The axisymmetric Navier-Stokes Eqs. (2.1) and (2.2) are solved using a second-order accurate in both time and space finite-difference scheme. Second-order central differences are used for all terms except the time derivatives. The advection-diffusion equation for c is also discretized in space using central differences in r and second-order one-sided differences in z at the interface. A two-stage second-order predictor-corrector scheme is used for temporal evolution; the scheme is essentially the same as that previously used in related problems (e.g., Lopez, 1990, 1995; Lopez and Weidman, 1996; Lopez and Shen, 1998), with the distinction being the implementation of the interfacial conditions.

The gas/liquid interface is treated as nondeforming, so that it is a flat stream-surface. The surface boundary condition on ψ is that ψ is constant and continuous with the flow on the axis. We can take $\psi = 0$ on the surface. That leaves η and Γ, and their boundary conditions are given by the solutions to (2.4) and (2.5). In the explicit scheme used, η and Γ on the interior grid points are updated to the new time-level first. Then the left-hand side of (2.4) can be written as a second order one-sided difference approximation to the normal derivative. This approximation is in terms of the just updated values of Γ one and two grid points in from the surface and the yet unknown value of Γ on the surface. Equation (2.4) then becomes a second-order ordinary differential equation for Γ on the surface, with $\Gamma = 0$ at $r = 0$ and 1. Using second-order central differences, this results in a tridiagonal system and is readily solved by standard techniques (e.g., LAPACK routines).

The boundary condition on η is a little more involved. The viscous terms couple the surface condition with the recently updated interior flow (as in the case for Γ above). Here, we first compute $\partial\psi/\partial z$ on the surface using second-order one-sided differences of the solution to $\nabla_*^2\psi = -r\eta$ with the updated η on the right-hand side. Then, $\partial(\partial\psi/\partial z)/\partial r$ and $\partial^2(\partial\psi/\partial z)/\partial r^2$ are formed using center-differences and one-sided differences at $r = 0$ and 1. In this way, the viscous contribution to

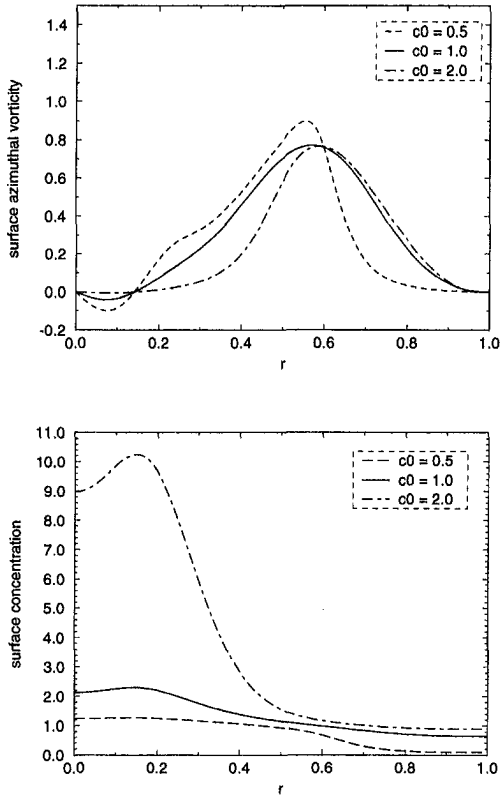

Fig. 3 Influence of different initial uniform concentrations on (*a*) the elastic production of surface azimuthal vorticity and (*b*) the redistribution of surfactant for a surfactant system with the hemicyanine/water equation of state, neglecting surface viscosity effects, at steady state for Re = 2126, H/R = 2.5

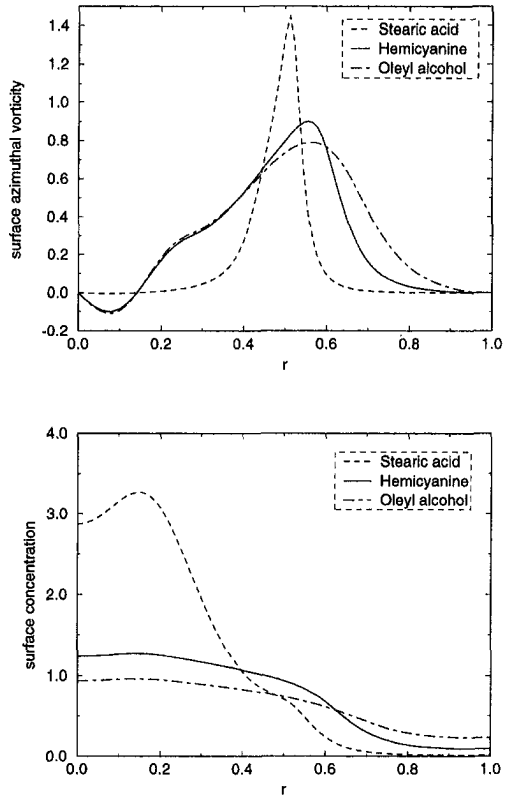

Fig. 4 Influence of different equations of state on (*a*) the elastic production of surface azimuthal vorticity and (*b*) redistribution of surfactant (c_0 = 0.5), at steady state for Re = 2126, H/R = 2.5

η on the surface is calculated. The elastic contribution (both the viscous and the elastic contributions are imposed simultaneously) requires information concerning the surface tension gradients $\partial\sigma/\partial r$.

4 Results

In our model problem, the fluid in the open cylinder is initially at rest. Before any fluid motion, the surfactant is uniformly distributed on the free surface. The initial concentration of surfactant, c_0, is low enough to be considered as a monomolecular layer (monolayer). Note that in general $c_0 \neq 1$. At $t = 0$, the bottom endwall is impulsively set to rotate at constant angular speed Ω. An Ekman boundary layer develops on the rotating disk with thickness of $O(\mathrm{Re}^{-1/2})$. This rotating boundary layer sends fluid radially outwards in a spiraling motion while drawing fluid into it from above. A sidewall boundary layer is also established. In time, fluid with angular momentum reaches the vicinity of the surface covered by the surfactant monolayer, where it is turned and advected towards the center. This flow results in a nonuniform distribution of the surfactant, with an accumulation of the surfactant near the center.

4.1 Nonlinear Equation of State Effects and Elastic Interfaces. Herein, we use three different insoluble surfactant groups, stearic acid, hemicyanine, and oleyl alcohol with water as the bulk fluid. Molecules within a monolayer at a gas/liquid interface can exist in different states, analogous to three-dimensional liquid, solid, or gas states (Adamson, 1982). Stearic acid is a solid-like surfactant (Gains, 1966) with relatively large viscosities, hemicyanine is known (Hirsa et al., 1995) to change from liquid-like to solid-like behavior at large concentration, and oleyl alcohol is a liquid-like surfactant with low viscosities but strong elastic behavior. For stearic acid/water $M = 0.43$ and $\beta = 5.62$, for hemicyanine/water $M = 0.51$ and $\beta = 3.90$, and for oleyl alcohol/water $M = 0.72$ and $\beta = 3.27$.

We first investigate the elastic effects of surfactants caused solely by surface tension gradients. In general, the elasticity of the surface depends strongly on both the composition of the surfactant, as well as the surfactant concentration. The influence of the initial surfactant concentration on a system with an equation of state corresponding to hemicyanine is shown in Fig. 3 (note that here we only consider surface tension gradient effects and are setting the interface to be inviscid, i.e., elastic; Section 4.2 treats the viscoelastic case incorporating the surface viscosities). The presence of surfactants generally lowers the local interfacial tension, and the variation in surfactant concentration gives rise to surface tension gradients and establishes a closed-loop interaction among the hydrodynamic motion, surfactant

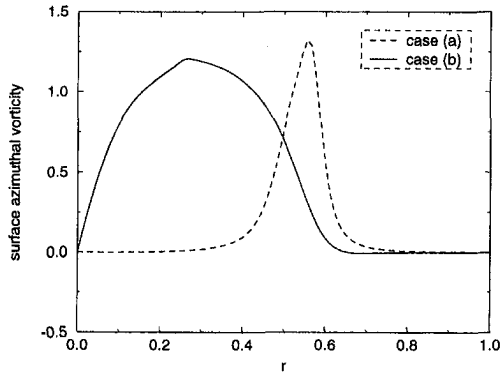

Fig. 5 Influence of surface shear and dilatational viscosities on the production of surface azimuthal vorticity for Re = 2126, H/R = 2.5, M = 0.43, β = 5.62, Pe^s = 500, and c_0 = 0.5: (*a*) elastic interface, $\Lambda_\mu = \Lambda_\kappa$ = 0.0; (*b*) viscoelastic interface Λ_μ = 1.0 and Λ_κ = 5.0

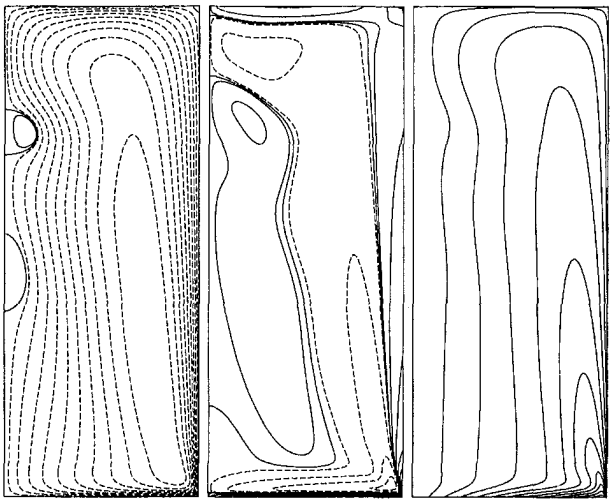

Fig. 6(*a*) Contours at steady state of ψ, η, and Γ for Re = 2126 and H/R = 2.5 for a no-slip stationary top

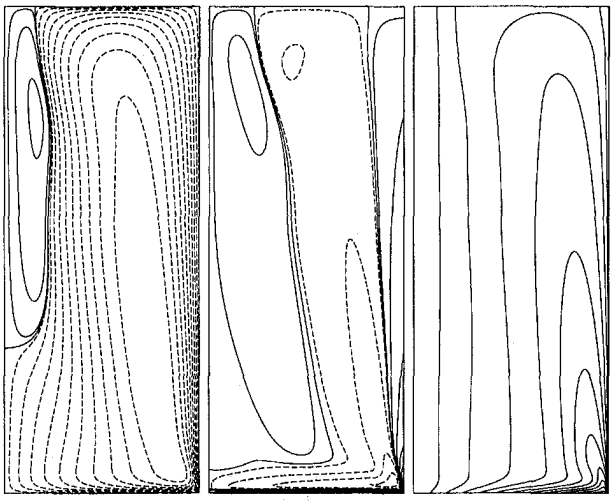

Fig. 6(*b*) Contours at steady state of ψ, η, and Γ for Re = 2126 and H/R = 2.5 for a clean stress-free top surface

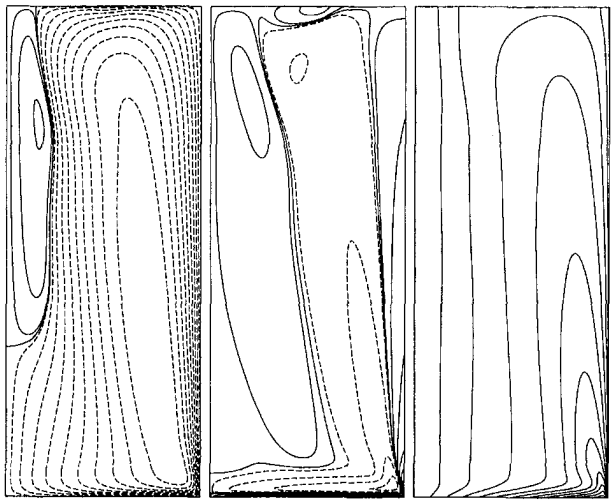

Fig. 6(*c*) Contours at steady state of ψ, η, and Γ for Re = 2126 and H/R = 2.5 for surfactant contaminated top with M = 0.43, β = 5.62, Λ_κ = 0, and Λ_μ = 0 (elastic)

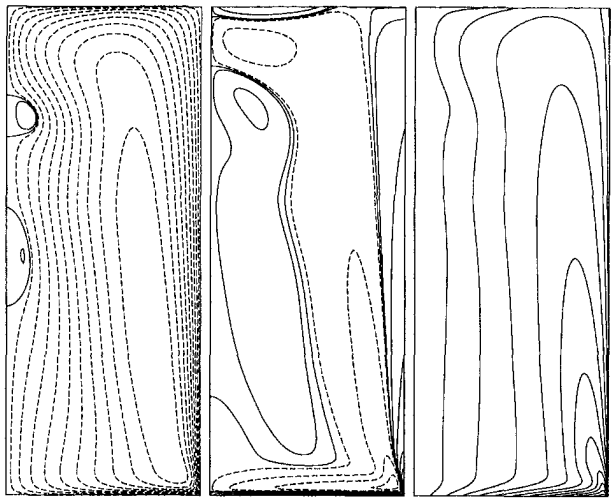

Fig. 6(*d*) Contours at steady state of ψ, η, and Γ for Re = 2126 and H/R = 2.5 for surfactant contaminated top with M = 0.43, β = 5.62, Λ_κ = 5, and Λ_μ = 1 (viscoelastic)

concentration, and surface tension. This is referred to as a Marangoni effect. We observe in Fig. 3(*a*) that an azimuthal component of vorticity is produced on the surface. At larger initial concentration (c_0 = 2.0) the surface tension gradient tends to zero (see Fig. 2) which diminishes the elastic production of surface azimuthal vorticity.

Of the three surfactant systems considered, oleyl alcohol/water has the strongest elastic behavior and stearic acid the weakest (see Fig. 2). For Re = 2126, H/R = 2.5 flows with all three systems, as well as flows with a clean interface and with a stationary no-slip top, reach steady state within one or two hundred rotations of the bottom endwall. All the cases shown in this paper were computed using a uniform grid with 91 radial and 226 axial nodes and a time increment of 10^{-2}. These spatial and temporal resolutions were previously found (e.g., Lopez, 1990, 1995) for the rigid top and stress-free surface cases to give grid independent results. Tests with the elastic and viscoelastic surfaces also indicate that these resolutions are adequate. The steady-state distribution of the surface azimuthal vorticity for the three surfactant systems (due only to elastic interfacial processes) is given in Fig. 4(*a*), along with the corresponding distribution of surface concentration of the surfactants in Fig. 4(*b*). The initial uniform concentration was c_0 = 0.5. In considering elastic interfaces, the presence of surfactants has no direct influence on Γ at the interface and η is only affected through the surface tension gradients. The bulk motions near the interface redistribute the surfactant. The flow near the interface consists primarily of a swirling flow spiraling radially inwards. For a clean interface, conservation of angular momentum (see discussions in Spohn et al., 1993 and Lopez, 1995) leads to a recirculation cell attached to the interface near the axis, where the radial flow on the interface is outwards. With elastic interfaces, similar behavior is found. The redistribution of surfactant by advection is resisted by diffusive processes (all cases in Fig. 4 had a surface Peclet number of 500) and the elastic force due to surface tension gradients. We see that the least elastic system (stearic acid) suffers the most redistribution, with the outer part of the interface ($r > 0.8$) being virtually clean and there is a corresponding large build up of surfactant for $r < 0.1$ where the level is well beyond saturation, i.e. surface tension gradients vanish. So, even though there are strong variations in concentration throughout $0 \leq r \leq 1$ for stearic acid, the elastic production of surface azimuthal vorticity is restricted to $0.35 < r < 0.65$ due to the nonlinearity of the equation of state.

For the more elastic cases, the redistribution of surfactant is far less and is everywhere below saturation levels. The outer parts of the interface are still cleaned somewhat, but the production of surface azimuthal vorticity is more wide spread, although at a lower peak intensity, than with stearic acid. The recircula-

tion near the axis leads to a reversal in the concentration gradient there and the production of negative surface azimuthal vorticity. The same would have occurred with stearic acid if the concentration there had not been at saturation levels. This suggests, that in these type of flows, a build up of a boundary layer type flow near the axis would be more pronounced for lower initial concentration levels c_0.

4.2 Viscoelastic Interfaces. The discussion so far has concerned elastic interfaces, where we have artificially set the surface shear and dilatational viscosities to zero. Now, we include their dynamic effects via the model Eq. (2.7). In this study, we use this ad hoc model as the available rheological information needed is lacking. Incorporating surface shear and dilatational viscosities according to (2.7) with $\Lambda_\mu = 1.0$ and $\Lambda_\kappa = 5.0$, we first investigate how this influences the production of surface azimuthal vorticity for a surfactant system with the equation of state corresponding to stearic acid.

The inclusion of surface viscosities results not only in a quantitative change, but also a qualitative change in the characteristics of the flow. The production of surface azimuthal vorticity is shifted and extended over a much broader central area (see Fig. 5). A number of factors are at play here, all interacting nonlinearly. Whereas for the elastic case the only contribution to η on the surface comes from surface tension gradients, in the viscoelastic situation the right-hand side of (2.5) includes a viscous contribution due to the surface flow and the bulk flow near the surface. Also, the right-hand side of (2.4) is no longer zero, and this leads to vortex line bending at the surface ($\partial\Gamma/\partial z \neq 0$) which contributes to the production of η via the $-1/r^3\partial\Gamma^2/\partial z$ term in (2.2). Note that this vortex line bending at the interface, i.e. vortex lines not meeting the interface normally, is only possible for viscous interfaces, regardless of the concentration level. These surface viscosity-influenced productions of surface vorticity alter the surface flow and result in a different distribution of surfactant concentration, which in turn alters the distribution of surface tension gradients. All of these processes are coupled nonlinearly; they affect not only the surface flow and the bulk flow immediately adjacent to the interface, but also produce large scale global changes in the bulk flow.

In order to gain an impression of the global effects of a viscoelastic interface, we compare the steady state flow when the top is stationary no-slip, a clean free surface, surfactant contaminated with $M = 0.43$, $\beta = 5.62$, $\mathrm{Pe}^s = 500$, $\Lambda_\kappa = 5.0$, and $\Lambda_\mu = 1.0$ (viscoelastic), and $\Lambda_\kappa = \Lambda_\mu = 0.0$ (elastic). The corresponding contours of ψ, η, and Γ are presented in Fig. 6.

On the no-slip stationary endwall the fluid separates at $r = 0$ and a central vortex is formed whose core size depends on the thickness of the boundary layer from which it emerged (Fig. 6(a)). For a clean stress-free top surface there is a large recirculation zone on the axis attached to the free surface, producing a reversed (directed radially outwards) surface flow near the axis (Fig. 6(b)). The boundary layers caused by the accumulation of surfactant materials are shown in Figs. 6(c) and 6(d). When the surface viscosities are set to zero, the elastic production of surface azimuthal vorticity is localized (Fig. 6(c)). Comparing the elastic case with the clean surface case, we find that the presence of inviscid surfactants has virtually no effect on Γ; whereas, the viscous contributions are seen to cause substantial vortex line bending, particularly for $r < 0.65$ where the concentration of surfactant is largest in the viscoelastic case (Fig. 6(d)). Note that if the flow were planar two-dimensional, there would be no flow component corresponding to Γ, and hence the surface vorticity production associated with vortex line tilting, i.e., $\partial\Gamma/\partial z \neq 0$ at the interface, which is only active for viscous surfactants, would not exist. So, if the flow is planar two-dimensional, this mechanism of surface vorticity production, whose predominance depends on the viscous nature of the interface, is not present regardless of how viscous the interface may be. For planar two-dimensional flows, the vorticity has only one nonzero component and it corresponds essentially to η in the present axisymmetric flow, so surface viscosity effects will also be present in planar two-dimensional flows via the corresponding viscous terms in (2.5).

In comparing all four cases shown in Fig. 6, it is very striking that although the elastic production of surface vorticity is active with inviscid interfaces, it only produces a very localized effect and the resultant bulk flow is a small perturbation away from that when the surface is stress-free. However, inclusion of the surface viscosity terms causes a dramatic global change in the flow. The surface layer that results is as intense as the boundary layer due to the stationary no-slip top. The resultant bulk flow is very similar to that of the no-slip case, but the vortex breakdown recirculation cells on the axis are more intense for the viscoelastic case. In fact, although the same Re is used in both cases, the viscoelastic surfactant bulk flow has characteristics of a bulk flow with a no-slip top at a higher Re.

5 Conclusions

The viscoelastic effects due to the presence of insoluble surfactants on the surface of a swirling vortex flow have been investigated numerically. The hydrodynamic coupling between the bulk swirling flow and the surfactant-covered surface flow is provided via the tangential stress balance at the interface, and this balance is dependent upon the surface concentration of surfactant, which in turn is altered by the interaction of bulk and surface flows. The viscoelastic properties of surfactants are functions of the surfactant concentration, for which we are presently using ad hoc models until they are determined experimentally. We investigate not only the elastic influence caused solely by surface tension gradients of different surfactant groups and surfactant concentration, but also surface viscosity effects caused by both surface dilatational and shear viscosities. Comparisons among stress-free clean top surfaces, no-slip tops, and contaminated surface flows provide a first look at the dynamics of flows where the inner product of the surface velocity and surface vorticity is not identically zero and the surface viscosities are treated as functions dependent upon the surfactant concentration. It is clear from this preliminary investigation that the viscous properties of a surfactant influenced interface can have a dramatic quantitative and qualitative impact on both the interfacial and the bulk flows, not only local to the interface, but also globally. This is so even at relatively low concentration levels of surfactant. In a future study, we will include soluble surfactants, deforming free surfaces, as well as incorporating empirically determined viscoelastic properties of the surfactants into our numerical simulation.

Acknowledgments

We would like to thank Prof. Amir Hirsa for the many discussions and sharing his data. This work was partially funded by NSF grants DMS-9512483 and CTS-9896259 and some of the computations were performed at NCSA.

References

Adamson, A. W., 1982, *Physical Chemistry of Surfaces,* Wiley-Interscience Publication.

Ananthakrishnan, P., and Yeung, R. W., 1994, "Nonlinear Interaction of a Vortex Pair with Clean and Surfactant-Covered Free Surfaces," *Wave Motion,* Vol. 19, pp. 343–365.

Asher, W. E., and Pankow, J. F., 1991, "Prediction of Gas/Water Transport Coefficients by a Surface Renewal Model," *Environmental Science and Technology,* Vol. 25, pp. 1294–1300.

Boussinesq, J., 1913, "Sur l'existence d'une viscosité superficiecle, dans la mince couche de transition séparant un liquide d'un autre fluide contigu," *Comptes Rendus Hebdomadaires des Séances de l'Académie des Sciences,* Vol. 156, pp. 983–989.

Edwards, D. A., Brenner, H., and Wasan, D. T., 1991, *Interfacial Transport Processes and Rheology,* Butterworth-Heinemann, Washington DC.

Foda, M., and Cox, R. G., 1980, "The Spreading of Thin Liquid Films on a Water-Air Interface," *Journal of Fluid Mechanics,* Vol. 101, pp. 33–51.

Gains, G. L., 1966, *Insoluble Monolayers at Liquid-Gas Interfaces,* Interscience Publishers.

Grotberg, J. B., 1994, "Pulmonary Flow and Transport Phenomena," *Annual Reviews of Fluid Mechanics,* Vol. 26, pp. 529–571.

Hirsa, A., Harper, J. E., and Kim, S., 1995, "Columnar Vortex Generation and Interaction with a Clean or Contaminated Free Surface," *Physics of Fluids,* Vol. 7, pp. 2532–2534.

Hirsa, A., Korenowski, G. M., Logory, L. M., and Judd, C. D., 1997a, "Velocity Field and Surfactant Concentration Measurement Techniques for Free-Surface Flows," *Experiments in Fluids,* Vol. 22, pp. 239–248.

Hirsa, A., Korenowski, G. M., Logory, L. M., and Judd, C. J., 1997b, "Determination of Surface Viscosities by Surfactant Concentration and Velocity Field Measurements for an Insoluble Monolayer," *Langmuir,* Vol. 13, pp. 3813–3822.

Hirsa, A., Korenowski, G. M., Logory, L. M., Judd, C. J., and Kim, S., 1995, "Surfactant Effects on Vortex Flows at a Free Surface and the Relation to Interfacial Gas Transfer," *Air-Water Gas Transfer,* B. Jahne and E. C. Monahan, eds., AEON Verlag Publishing, Heidelberg, Germany, pp. 649–663.

Hunt, J. C. R., 1984, "Turbulent Structure and Turbulent Diffusion Near Gas-Liquid Interfaces," *Gas Transfer at Water Surfaces,* W. Brutsaert and G. H. Jurka, eds., D. Reidel, Boston pp. 67–82.

Kim, S., 1996, "An Experimental Investigation of a Columnar Vortex Terminating Normal to a Gas/Liquid or a Solid/Liquid Interface," Ph.D. thesis, Aeronautical Eng., Rensselaer Polytechnic Institute.

Lopez, J. M., 1990, "Axisymmetric Vortex Breakdown. Part 1. Confined Swirling Flow," *Journal of Fluid Mechanics,* Vol. 221, pp. 533–552.

Lopez, J. M., 1995, "Unsteady Swirling Flow in an Enclosed Cylinder with Reflectional Symmetry," *Physics of Fluids,* Vol. 7, pp. 2700–2714.

Lopez, J. M., and Shen, J., 1998, "An Efficient Spectral-Projection Method for the Navier-Stokes Equations in Cylindrical Geometries," *Journal of Computational Physics,* Vol. 139, pp. 308–326.

Lopez, J. M., and Weidman, P. D., 1996, "Stability of Stationary Endwall Boundary Layers During Spin-Down," *Journal of Fluid Mechanics,* Vol. 326, pp. 373–398.

Maru, H. C., and Wasan, D. T., 1979, "Dilational Viscoelastic Properties of Fluid Interfaces—II," *Chemical Engineering Science,* Vol. 34, pp. 1295–1307.

Poskanzer, A., and Goodrich, F. C., 1975, "A New Surface Viscometer of High Sensitivity: II. Experiments with Stearic Acid Monolayers," *Journal of Colloid and Interface Scienced,* Vol. 52, pp. 213–221.

Scriven, L. E., 1960, "Dynamics of a Fluid Interface," *Chemical Engineering Science,* Vol. 12, pp. 98–108.

Slattery, J. C., 1990, *Interfacial Transport Phenomena,* Springer-Verlag, NY.

Spohn, A., Mory, M., and Hopfinger, E. J., 1993, "Observations of Vortex Breakdown in an Open Cylindrical Container with a Rotating Bottom," *Experiments in Fluids,* Vol. 14, pp. 70–77.

Sternling, C. V., and Scriven, L. E., 1959, "Interfacial Turbulence: Hydrodynamic Instability and the Marangoni Effect," *American Institute of Chemical Engineers Journal,* Vol. 5, pp. 514–523.

Tryggvason, G., Abdollahi-Alibeik, J., Willmarth, W. W., and Hirsa, A., 1992, "Collision of a Vortex Pair with a Contaminated Free Surface," *Physics of Fluids A,* Vol. 4, pp. 1215–1229.

Tsai, W.-T., and Yue, K. P., 1995, "Effects of Soluble and Insoluble Surfactant on Laminar Interactions of Vortical Flows with a Free Surface," *Journal of Fluid Mechanics,* Vol. 289, pp. 315–349.

Wang, H. T., and Leighton, R. I., 1990, "Direct Calculation of the Interaction Between Subsurface Vortices and Surface Contaminants," *Proceedings of the 9th OMAE Conference,* Houston, TX, Feb., ASME, NY, Vol. I, Part A.

Richard E. Hewitt
Lecturer.

Peter W. Duck
Reader.

Department of Mathematics,
University of Manchester,
Oxford Road,
Manchester M13 9PL,
United Kingdom

Michael R. Foster
Professor.
Department of Aerospace Engineering,
Applied Mechanics and Aviation,
The Ohio State University,
Columbus, Ohio 43210

Peter A. Davies
Professor.
Department of Civil Engineering,
The University,
Dundee, DD1 4HN,
United Kingdom

Nonlinear Spin-Up of a Rotating Stratified Fluid: Theory

We consider the boundary layer that forms on the wall of a rotating container of stratified fluid when altered from an initial state of rigid body rotation. The container is taken to have a simple axisymmetric form with sloping walls. The introduction of a non-normal component of buoyancy into the velocity boundary-layer is shown to have a considerable effect for certain geometries. We introduce a similarity-type solution and solve the resulting unsteady boundary-layer equations numerically for three distinct classes of container geometry. Computational and asymptotic results are presented for a number of parameter values. By mapping the parameter space we show that the system may evolve to either a steady state, a double-structured growing boundary-layer, or a finite-time breakdown depending on the container type, rotation change and stratification. In addition to extending the results of Duck et al. (1997) to a more general container shape, we present evidence of a new finite-time breakdown associated with higher Schmidt numbers.

1 Introduction

The transient response of a contained fluid undergoing a spin-up from a state of rigid body rotation has been discussed for both homogeneous and stratified fluids; see for example, Greenspan and Howard (1963), Pedlosky (1967), Walin (1969), and Spence et al. (1992). However, conclusions drawn from investigations into the stratified spin-up problem have been based on containers with vertical walls.

Duck et al. (1997), subsequently referred to as DFH, considered the nonlinear boundary-layer problem for a conical container of viscous, stratified fluid, showing that the evolution for a fixed Schmidt number (the ratio of the two coefficients of momentum and density diffusion) could be entirely classified according to just two parameters. The parameters involved were shown to be the initial rotation rate (denoted by $\hat{W}_e$, which was taken to be positive, with a final rotation rate nondimensionalized to unity) and a "modified Burger number" that was defined in terms of the Burger number, the angle of the sidewalls to the horizontal, and the boundary-layer edge conditions. The parameter space was shown to have well-defined boundaries that separated three distinct regions in which the governing equations evolved to either a steady state, a growing boundary-layer or a finite-time singularity.

In this paper, we extend the analysis presented by DFH to more general forms of axisymmetric container. The analysis is presented for nonlinear changes in the rotation rate (of either sign) but we do restrict the final rotation to be in the same sense as the initial rotation; this is not a conceptual restriction however. Figures 1(*a*)–(*c*) show the three distinct cases that we consider; these are containers that have a cross-sectional shape defined by $z = R^\alpha$ in a cylindrical polar coordinate system (R, z, λ). The case considered by DFH corresponds to Fig. 1(*b*) (their analysis uses α to denote the quantity shown as $\hat{\alpha}$ in the figure). We distinguish the cases according to the sign of $(1 - \alpha)$ since it is this quantity that determines the appropriate solution expansion away from the "apex" of the container.

The governing boundary-layer equations are as given by DFH,

$$\frac{1}{r^2}\frac{\partial(r^2 v_r)}{\partial r} + \frac{1}{r}\frac{\partial v_\theta}{\partial \theta} = 0, \tag{1}$$

$$\frac{\partial v_r}{\partial t} + (q\cdot\nabla)v_r - \frac{v_\phi^2}{r} + \frac{dp}{dr} = \frac{1}{r^2}\frac{\partial^2 v_r}{\partial \theta^2} - B\sin\hat{\alpha}, \tag{2}$$

$$\frac{\partial v_\phi}{\partial t} + (q\cdot\nabla)v_\phi + \frac{v_\phi v_r}{r} = \frac{1}{r^2}\frac{\partial^2 v_\phi}{\partial \theta^2}, \tag{3}$$

$$\frac{\partial B}{\partial t} + (q\cdot\nabla)B - S v_r \sin\hat{\alpha} = \frac{1}{\sigma}\frac{1}{r^2}\frac{\partial^2 B}{\partial \theta^2}, \tag{4}$$

$$q\cdot\nabla \equiv v_r\frac{\partial}{\partial r} + \frac{v_\theta}{r}\frac{\partial}{\partial \theta}, \tag{5}$$

with boundary conditions $\partial B/\partial\theta = v_r = v_\theta = 0$, $v_\phi = r\omega(t)$ on $\theta = 0$, and with prescribed edge conditions as $\theta \to -\infty$. The reader is referred to DFH for details of the non-dimensionalisation. We have used a spherical polar coordinate system (r, θ^*, ϕ) centerd on the "apex," in which r is a radial coordinate relative to the axis of rotation, ϕ is an azimuthal coordinate and θ is a scaled boundary-layer coordinate (where $\theta(\nu/\Omega h^2)^{1/2} = \theta^* - (\pi/2 - \tan^{-1} R^{\alpha-1})$). Here h and Ω are a characteristic length scale and rotation rate, and ν is the kinematic viscosity of the fluid. In (2)–(5), $\hat{\alpha}$ denotes the local angle between the container and the horizontal, B is the buoyancy, S is a Burger number and $\omega(t)$ is the angular frequency of the container (which we take to be an impulsive change from $\hat{W}_e$ to unity at $t = 0$).

In the following sections we discuss the $\alpha > 1$ case (in Section 2) and the $\alpha < 1$ case (in Section 3), which contains

Contributed by the Fluids Engineering Division for publication in the JOURNAL OF FLUIDS ENGINEERING. Manuscript received by the Fluids Engineering Division November 5, 1997; revised manuscript received July 30, 1998. Guest Editor: D. T. Valentine.

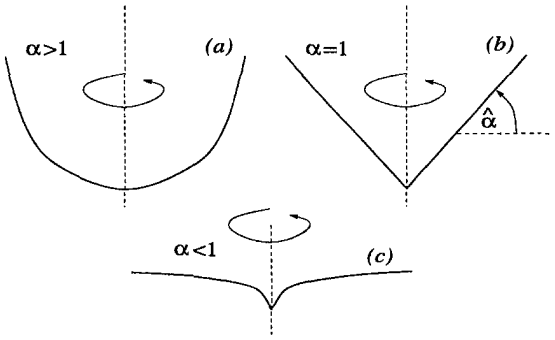

Fig. 1 The container geometries

two sub-cases that are discussed in Section 3.1 and Section 3.2. Finally, in Section 4, we compare the evolution type found in each case with that found for the conical container (corresponding to $\alpha = 1$) considered by DFH. The notation used in each section is defined independently.

2 The $\alpha > 1$ Container

A sensible balancing of terms in the boundary-layer equations, (2)–(5), for a container of the type shown in Fig. 1(*a*) leads to the following scalings as $r \to \infty$

$$v_r = r^{(2/\alpha)-1}\hat{U}(\Theta, t) + \ldots, \quad v_\phi = r^{1/\alpha}\hat{W}(\Theta, t) + \ldots, \quad (6)$$

$$v_\theta = r^{(2/\alpha)-2}(\hat{V}(\Theta, t) - \Theta\hat{U}(\Theta, t)) + \ldots, \quad (7)$$

$$B = r^{(2/\alpha)-1}\hat{B}(\Theta, t) + \ldots, \quad P = r^{2/\alpha}\hat{P} + \ldots, \quad (8)$$

where $\Theta = r\theta$. The above expansions follow directly from the scaling $R \sim r^{1/\alpha}$ with $\hat{\alpha} \to \pi/2$. Substitution of these expansions yields a set of governing equations within the boundary layer, which can be simplified by introducing

$$\hat{B}(\Theta) = B^*(\bar{\Theta}) - (\hat{W}_e^2 - \hat{B}_e), \quad \hat{U}(\Theta) = \alpha U^*(\bar{\Theta}), \quad (9)$$

$$\hat{V}(\Theta) = \sqrt{\alpha}V^*(\bar{\Theta}), \quad \hat{W}(\Theta) = W^*(\bar{\Theta}), \quad (10)$$

where $S = \alpha^2 S^*$, $\bar{\Theta} = \Theta/\sqrt{\alpha}$ and $\bar{t} = t/\alpha$. These substitutions effectively remove $\hat{P}$ and α from the boundary-layer equations. The boundary conditions for this system are $U^* = V^* = B^*_{\bar{\Theta}} = 0$, $W^* = 1$ on $\bar{\Theta} = 0$, and $U^* \to 0$, $W^* \to \hat{W}_e$, $B^* \to \hat{W}_e^2$, as $\bar{\Theta} \to -\infty$.

The azimuthal momentum equation is reduced to the heat equation, therefore there are no steady-state solutions to this problem for a general $\hat{W}_e$. Numerical investigations for $S^* > 0$, $\hat{W}_e > 0$ suggest that the system always evolves to a growing boundary layer. The evolution is characterized by an overall thickening of the boundary layer which is easily observed when the velocity or buoyancy profiles are examined. The analysis presented by DFH concerning the double structure of the growing boundary layer can also be applied here.

In an outer layer, $\eta = \bar{\Theta}/\sqrt{t} \sim O(1)$, we can introduce the following expansions (dropping the bar notation for t)

$$W^* = \bar{W}_0(\eta) + \ldots, \quad B^* = \bar{B}_0(\eta) + \ldots, \quad (11)$$

$$U^* = \frac{\bar{U}_0(\eta)}{t} + \ldots, \quad V^* = \frac{\bar{V}_0(\eta)}{\sqrt{t}} + \ldots. \quad (12)$$

The boundary conditions reduce to $\bar{W}_0 = \hat{W}_e$, $\bar{B}_0 = \hat{W}_e^2$, $\bar{U}_0 \to 0$ as $\eta \to -\infty$, and the solution must be matched with an inner layer. In the inner layer, which is $O(1)$ and immediately next to the container wall, the relevant expansions are

$$W^* = 1 + \frac{W_0(\bar{\Theta})}{\sqrt{t}} + \ldots,$$

$$B^* = 1 + \frac{B_0(\bar{\Theta})}{\sqrt{t}} + \ldots, \quad (13)$$

$$U^* = \frac{U_0(\bar{\Theta})}{\sqrt{t}} + \ldots, \quad V^* = \frac{V_0(\bar{\Theta})}{\sqrt{t}} + \ldots. \quad (14)$$

Matching conditions must be applied as $\bar{\Theta} \to -\infty$ together with no-slip, impermeability, and no net density flux at the wall. The solution in both regions can be obtained analytically and matched together to determine the complete leading-order form.

A comparison may be made with the numerical results using the asymptotic results

$$B^*(\bar{\Theta} = 0, t) = 1 + \frac{1}{\sqrt{t}}\left(\frac{2}{\sqrt{\pi}\left(\frac{\sigma S^*}{4}\right)^{1/4}}\right)(W_e^* - 1) + \ldots, \quad (15)$$

and

$$W^*_{\bar{\Theta}}(\bar{\Theta} = 0, t) = \frac{1}{\sqrt{t}}\left(-\frac{1}{\sqrt{\pi}}(W_e^* - 1)\right) + \ldots. \quad (16)$$

Figure 2 compares the value of B^* at the container wall with that predicted by the first two terms in the expansion (15) for $W_e^* = 0.5$, $S^* = 0.5$. The oscillatory behavior shown in the figure is not an artifact of the numerical method and can be related to the buoyancy frequency N.

3 The $\alpha < 1$ Container

The relevant expansions for a container of the type shown in Fig. 1(*c*) are

Nomenclature

Ω = a typical angular frequency
$\rho = \rho_o + \bar{\rho} + \rho'$ = the density field
$\bar{\rho}(z)$ = a stable linear stratification, $|\bar{\rho}| \ll \rho_o$
$\{r, \theta^*, \phi\}$ = a spherical polar coordinate system
θ = a scaled boundary layer coordinate
$\Theta = r\theta \in [0, -\infty)$ = a normal boundary layer coordinate
$\{z, R, \phi\}$ = a cylindrical coordinate system
α = the container is described by $z = R^\alpha$
t = a nondimensional timescale
ρ_o = a reference density
ρ' = a density perturbation, $|\rho'| \ll \rho_o$
$N^2 = -(g/\rho_0)\bar{\rho}_z$ = the Brunt-Väisälä frequency
$S = N^2/\Omega^2$ = the Burger number
σ = the Schmidt number
$\hat{W}_e = \Omega_i/\Omega_f$ = the relative rotation rate as $\Theta \to -\infty$
$\hat{\alpha}$ = a local wall-slope of the container

$$v_r = r\hat{U}(\Theta, t) + \ldots, \quad v_\phi = r\hat{W}(\Theta, t) + \ldots, \quad (17)$$

$$v_\theta = \hat{V}(\Theta, t) - \Theta\hat{U}(\Theta, t) + \ldots,$$

$$P = r^2\hat{P} + \ldots, \quad (18)$$

and $\Theta = r\theta$, which follow from the scaling $R \sim r$ with $\hat{\alpha} \to 0$. However, in this case there are two possible scalings for the buoyancy term B, namely

$$B = r^{2-\alpha}\hat{B}(\Theta, t) + \ldots, \quad \text{or} \quad B = r^{\alpha}\hat{B}(\Theta, t) + \ldots. \quad (19)$$

In the first of the above scalings, B is of sufficient magnitude for the density transport equation to remain coupled with the momentum equations. However, the Burger number, S, does not appear in the density transport equation in this case. The second scaling shown in (19) corresponds to balancing the $\hat{B}$ terms in the density transport equation with the inhomogeneous Burger-number term of $S\hat{U}$. In this case the buoyancy is not of sufficient magnitude for the coupling term to be present in the $\hat{U}$-momentum equation and the density transport equation remains decoupled. We examine both cases individually in the following sections.

3.1 The $B \sim r^{2-\alpha}$ Case. When this choice of scaling is made for B, a substitution of $B^* = \hat{B} + (\hat{W}_e^2 - \hat{B}_e)$ simplifies the radial momentum equation and the density transport equation and the term S^* plays the role of the Burger number. S^* is now defined solely in terms of the edge conditions as $S^* = (\hat{W}_e^2 - \hat{B}_e)(2 - \alpha)$. The boundary conditions for this system are as given previously.

We observe that the only difference between this case and that of the conical container (as discussed by DFH) are the definitions of B^* and S^*, together with a change of coefficient in the density transport equation.

3.1.1 The Parameter Space. Numerical investigation of this system reveals that the same three types of evolution that are found for the conical case of DFH are also obtained with this geometry of container. The asymptotic analyses of the growing boundary layer and the finite-time breakdown for this case are detailed below. We can categorize the behavior of the solution according to two parameters (as can be done for the $\alpha = 1$ case). For this particular geometry we observe that the relevant parameters are $\hat{W}_e$ and $\tilde{S}$ (defined below). A schematic of this parameter space is shown in Fig. 3, and displays three distinct regions corresponding to the three evolutionary types.

Region (i).

The region (i) shown in Fig. 3 represents those parameter values for which an evolution to a steady state is achieved. There is a critical value of S^*, denoted by S^*_{crit}, above which a steady solution cannot be located. We can consider the steady problem for a perturbation about this critical value by defining

$$S^* = S^*_{\text{crit}} + \delta, \quad (20)$$

which leads to a two-layer solution with regions in which $\Theta \sim O(1)$ and $\Theta \sim O(\delta^{-1})$. The sign of δ is determined as part of the expansion and therefore solutions can only be located on one "side" of the critical boundary S^*_{crit}.

There is a natural substitution that arises in this expansion, which is $\tilde{S} = S^* - (1 - \alpha)$. Steady-state solutions can only be located for $\tilde{S} < \tilde{S}_{\text{crit}}$ where $\tilde{S}_{\text{crit}} = S^*_{\text{crit}} - (1 - \alpha)$.

We note here that when $\hat{W}_e > 1$ unsteady calculations evolved to a finite-time breakdown even in the region for which a steady solution existed.

Region (ii).

The region (ii) in Fig. 3 consists of those values of $\tilde{S}$ and $\hat{W}_e$ for which the solution fails at a finite time. The scalings involved in the breakdown process are as given by DFH with only a minor difference in the coefficients involved in the governing equations. The character of the breakdown process is therefore the same in this region of the parameter space as that presented for the conical container.

A balancing of terms leads to an inner layer ($\eta = \Theta/(t_0 - t)^{1/2}$) with a lengthscale of $\Theta = O(\tau^{1/2})$ as $\tau \to 0$ (where $\tau = t_0 - t$, and t_0 is the time at breakdown). An analysis of this inner layer yields the following scalings

$$(\hat{U}, \hat{V}, \hat{W}, B^*)^T = (\tau^{-1}\hat{U}_1(\tilde{\eta}), \tau^{-(1/2)}\hat{V}_1(\tilde{\eta}), \tau^{-1}\hat{W}_1(\tilde{\eta}), \tau^{-2}\hat{B}_1(\tilde{\eta}))^T + \ldots, \quad (21)$$

where $\tilde{\eta} = \Theta/(t_0 - t)^{1/2}$. Substitution of these expansions into the governing equations yields a system of equations that form a nonlinear eigenvalue problem. These equations can be solved numerically by a finite-difference method with Newton iteration used to obtain the correct behaviour at $\tilde{\eta} = 0$. We found that the simplest way to iterate to a non-trivial solution was to use an appropriately scaled solution to the full unsteady numerical problem as a starting point in the iterative procedure. The scaled velocity components and buoyancy in the $\Theta = O((t_0 - t)^{1/2})$ region decay algebraically like

$$\hat{U}_1, \hat{W}_1 = O(\tilde{\eta}^{-2}), \quad \hat{V}_1 = O(1), \quad \hat{B}_1 = O(\tilde{\eta}^{-4}), \quad (22)$$

as $\tilde{\eta} \to -\infty$.

There are also two other layers, a passive inner-layer (where $\Theta \sim \tau^{-1}$) in which the no-slip conditions are satisfied, and an outer layer (where $\Theta = O(1)$).

A comparison of the numerical solution to the system of equations valid in the $\tilde{\eta} = O(1)$ region and scaled numerical solutions to the full problem, is not presented here. As noted above, there is very little difference between the inner-layer equations for this geometry of container and those for the conical container. Therefore, the reader is referred to the figures of DFH for examples of the agreement between the asymptotic solution and the unsteady solution as $t \to t_0$ for $\alpha = 1$; similar results are found in this $\alpha < 1$ case.

Numerical results indicate that the dividing boundary between the finite-time breakdown behavior and the growing boundary layer type of evolution is the curve $\tilde{S} = (2 - \alpha)[\hat{W}_e^2 - 1] + 1$. The appearance of this particular curve through parameter space as a boundary between evolution types is not arbitrary. We observe that for these parameter values there exist uniform B^* solutions to the problem, which have a velocity field that is equivalent to that found for the corresponding infinite rotating disk problem.

Region (iii).

An analysis of the growing boundary layer follows in the manner of section 2. In the outer, $\eta = \Theta/\sqrt{t} = O(1)$, region we have the same scalings (11)–(12).

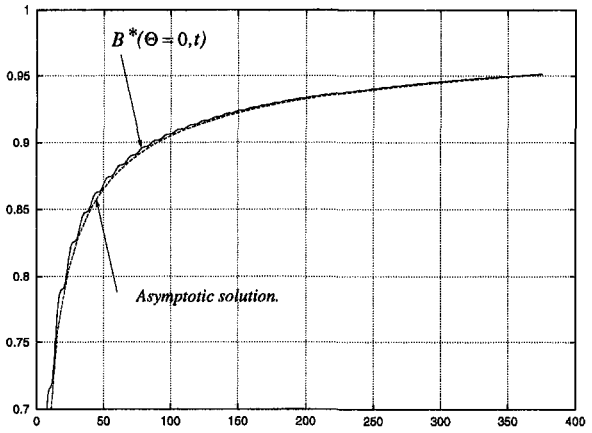

Fig. 2 Comparison of B^* ($\Theta = 0$, t) with the expansion (15); $\hat{W}_e = .5$, $S^* = .5$

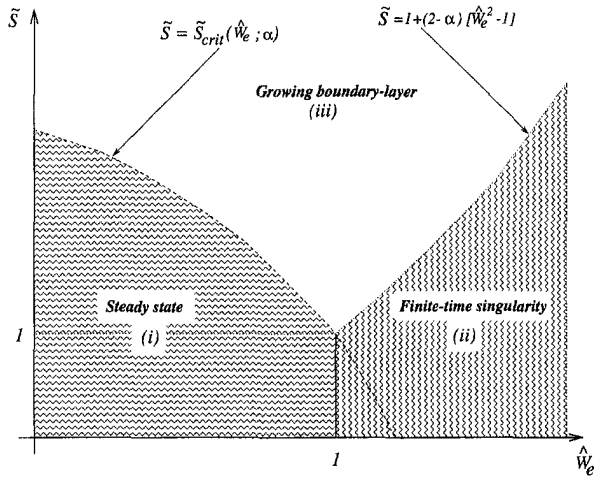

Fig. 3 Different flow regimes for $\sigma = 1$

The inner solution is equivalent to that presented by DFH when S^* is replaced by $\tilde{S}$ in their analysis. The same fourth-order shooting method that was applied by DFH can be applied here, showing excellent agreement with the numerics, although in the interests of brevity we do not present any figures of comparison here.

The growing boundary layer scenario is found for those parameter values in the region $\tilde{S} > \max\{\tilde{S}_{crit}(\hat{W}_e;\alpha), (2-\alpha)[\hat{W}_e^2 - 1] + 1\}$ when $\hat{W}_e > 0$. This region is denoted by (iii) in Fig. 3.

3.2 The $B \sim r^\alpha$ Case. When this choice of scaling is made for B we note that the momentum equations become decoupled from the density transport equation, which now includes a term that is dependent on the Burger number.

The boundary conditions on the velocity components are as given previously, but the buoyancy must now satisfy $\hat{B}_\Theta(\Theta = 0, t) = 0$ and $\hat{B}(\Theta, t) \to \hat{B}_e$ as $\Theta \to -\infty$. In this case the edge conditions for the azimuthal rotation and buoyancy can be prescribed independently since the large Θ form of the radial momentum equation determines the pressure constant to be $\hat{P} = \hat{W}_e^2/2$.

Obviously the initial value problem, from the point of view of the decoupled velocity components, is equivalent to that for the infinite rotating disk problem; see Von Kármán (1921), Bödewadt (1940). However, a numerical investigation of the whole system suggests that two types of behavior can be found for the decoupled buoyancy. Eventually, for the $\hat{B}$ term, we find that a steady-state solution is achieved, or an exponential growth is obtained depending on the the sign of $1 - \hat{W}_e$ (for $\hat{W}_e > 0$). When the system undergoes a spin up, a steady state is achieved, but in the spin-down case an exponential growth of the buoyancy is found and presumably, in this case, the density transport equation will eventually recouple with the momentum equations.

Since the numerical results suggest that $\hat{W}_e = 1$ is a dividing boundary between evolution types, we begin by investigating the steady solution to the density transport equation when $\hat{W}_e = 1 + \delta$. In this case the velocity components can be written as

$$\hat{U} = \delta u + \ldots, \quad \hat{V} = \delta v + \ldots, \quad \hat{W} = 1 + \delta w + \ldots, \quad (23)$$

and a simple linearized solution is available.

Now, considering the form of the density transport equation we see that it may be simplified (removing the Burger number dependence) by the substitutions $S^* = S + \alpha\hat{B}_e$, and $B^* = (\hat{B} - \hat{B}_e)/S^*$, to give

$$\frac{\partial B^*}{\partial t} + \alpha\hat{U}B^* + \hat{V}\frac{\partial B^*}{\partial\Theta} - \hat{U} = \frac{1}{\sigma}\frac{\partial^2 B^*}{\partial\Theta^2}. \quad (24)$$

The boundary conditions for this transformed buoyancy are $B^*_\Theta(\Theta = 0, t) = 0$ and $B^*(\Theta, t) \to 0$ as $\Theta \to -\infty$.

We can examine the steady states of (24) when $\hat{W}_e = 1 + \delta$ by using the solution (23). The solution in this linear limit has a double-layer structure consisting of a $\Theta = O(1)$ inner layer and a $\Theta = O(\delta^{-1})$ outer layer. In the inner layer the appropriate expansion for $\hat{B}$ is $\hat{B} = b_0 + O(\delta)$, where the leading order term b_0 is a constant. Similarly, in an outer layer defined by $\bar{\Theta} = \delta\Theta = O(1)$, we see that $\hat{B} = \bar{b}_0(\bar{\Theta}) + O(\delta)$, where $\bar{b}_0(\bar{\Theta}) = b_0\exp(-\sigma\bar{\Theta})$.

Thus the steady solution to the density transport equation involves a lengthening boundary-layer scale as $\hat{W}_e \to 1$, and cannot be continued to $\hat{W}_e > 1$ (i.e., $\delta > 0$) because we find that $\bar{\Theta} \in [0, -\infty)$, which leads to an exponentially growing solution. Thus a steady solution is eventually attained for $\hat{W}_e < 1$, however, for $\hat{W}_e \geq 1$ no such steady solution is possible. Numerical results for the spin-down case show that the solution to the density transport equation grows with time. When t is sufficiently large for $B^* \gg \hat{U}$, we can find a solution to (24) in the form $B^*(\Theta, t) = \tilde{B}(\Theta)\exp(\mu t)$, where μ and $\tilde{B}(\Theta)$ are determined by an eigenvalue problem.

Good comparisons between the large-time, exponential behaviour described above and unsteady computations with $\hat{W}_e > 1$ are readily obtained.

3.3 A New Finite-Time Breakdown. Recent results suggest that the parameter space diagram presented by DFH needs some modification for more general Schmidt numbers, σ. The numerical work of DFH was (mainly) presented for $\sigma = 1$, and it was noted that the parameter space remained largely unchanged at higher Schmidt numbers. The regime $\sigma \gg 1$ is of obvious practical importance since for a saline solution (as used in a typical laboratory experiment) the appropriate value is $\sigma \approx 700$.

A preliminary investigation of the $\sigma \gg 1$ limit suggested that the boundary layer separates into a thin buoyancy layer, in which the velocity components are Taylor series expansions from a thicker velocity boundary layer. The most significant effect from the point of view of the parameter space diagram was a shift of S^*_{crit}, the boundary that separates the steady state region from the growing boundary-layer region, to lower values of S^*. Recently, however, numerical computations of the governing boundary-layer equations (with $\alpha = 1$) for parameter values approaching $\hat{W}_e = 1$, and at more general (larger) values of σ, have revealed an interesting breakdown. A typical example of the breakdown is shown in Fig. 4, which shows profiles of $\hat{W}(\Theta, t)$ as $t \to t_0$, the time at breakdown. A comparison of this figure with similar results for the finite-time singularity obtained in the $\hat{W}_e > 1$, $S^* < \hat{W}_e^2$ region (as presented by DFH) reveals no similarities.

This new class of evolution is present in the case discussed in Section 3.1, although we have not shown the new region on Fig. 3 since no exact method of determining the boundary in parameter space has yet been discovered. It seems likely that the evolution is governed by a complex stability/existence problem involving the steady state solutions to the boundary-layer equations. No detailed analysis of the steady states and their stability has been performed, and this is an area that we hope to discuss in the near future. We should also note that even the stability problem for steady solutions to the swirling (homogeneous) flow above an infinite rotating disk has some unresolved complications (Bodonyi and Ng, 1984).

4 Discussion

We have extended the analysis of the boundary-layer problem discussed by DFH to include a more general class of axisymme-

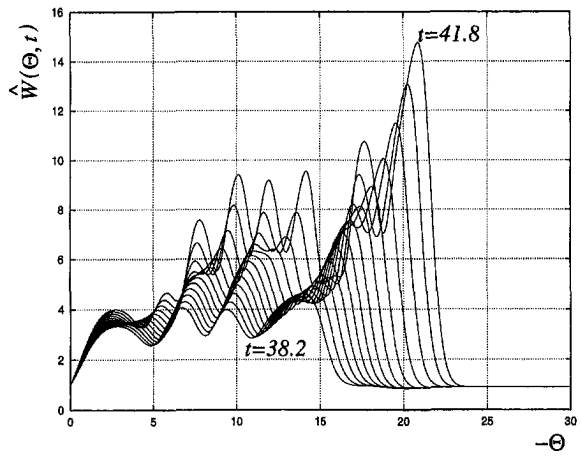

Fig. 4 An example of a new finite-time breakdown at $S^* = 0$, $\hat{W}_e = 0.9$, $\alpha = 1$ and $\sigma = 700$

tric container. The analysis is valid near the container walls and away from the axis of rotation. We place no bounds on the size of the change in rotation rate for the container, but do require that the final rotation is in the same sense as the initial rotation (i.e., $\hat{W}_e > 0$).

It was noted by DFH that the parabola $S^* = \hat{W}_e^2$ corresponds to considering the equations governing the homogeneous swirling flow above an infinite rotating disk. In fact, in a typical laboratory experiment with a linearly stratified fluid in a conical container, the $S^* < \hat{W}_e^2$ region of parameter space corresponds to a statically unstable interior stratification. Since we are only considering the boundary layer however, we do not restrict the parameter space, but do recognize that it must be interpreted correctly when applied to a specific experimental investigation. Nevertheless, it must be noted that the finite-time breakdowns discussed for nonlinear spin down ($\hat{W}_e > 1$) occur over relatively short timescales; typically within just a few background rotations even when the parameter values are only slightly within the breakdown region. It may therefore be possible for this mechanism to dominate in some local region of a typical laboratory experiment.

For the container type shown in Fig. 1(a) we have shown how the boundary-layer equations can be reduced to a form similar to those obtained in the $\alpha = 1$ case but without the advection terms. There are no nontrivial steady solutions and at all points in parameter space (S^*, $\hat{W}_e > 0$, for σ fixed) we find a growing boundary layer that can be described in terms of a double-layer structure for large times.

For the container type shown in Fig. 1(c) we have shown that there are two possible scalings that can be applied. If we scale the buoyancy in such a way that the density transport equation remains coupled to the momentum equations then we find an overall behaviour that can be described in the same manner as the conical container (after an appropriate redefinition of the parameters involved). In this case we find all three evolution types; a steady state, a growing boundary layer, and a finite-time singularity (of which there are two types). When scaling the buoyancy to balance the Burger number term in the density transport equation we find that an increase in the rotation rate of the container leads to both steady velocity profiles and a steady buoyancy profile across the boundary layer. When the rotation rate of the container is decreased however, we find that an exponential growth of the buoyancy term can occur and, presumably, after sufficient growth has occurred we cannot neglect the coupling effect between the momentum equations and the density transport equation.

Acknowledgment

The support of the EPSRC is gratefully acknowledged.

References

Bödewadt, U. T., 1940, "Die Drehströmung über festem Grund," *Zeitschrift fur Angewandte Mathematik und Mechaniker,* Vol. 20, pp. 241.

Bodonyi, R. J., and Ng, B. S., 1984, "On the Stability of the Similarity Solutions for the Swirling Flow Above an Infinite Rotating Disk," *Journal of Fluid Mechanics,* Vol. 144, p. 311.

Duck, P. W., Foster, M. R., and Hewitt, R. E., 1997, "On the Boundary Layer Arising in the Spin-Up of a Stratified Fluid in a Container with Sloping Walls," *Journal of Fluid Mechanics,* Vol. 335, p. 233.

Greenspan, H. P., and Howard, L. N., 1963, "On a Time-Dependent Motion of a Rotating Fluid," *Journal of Fluid Mechanics,* Vol. 17, p. 385.

Kármán, T. Von, 1921, "Über laminare und turbulente Reibung," *Zeitschrift fur Angewandte Mathematik and Physik,* Vol. 1, p. 244.

Pedlosky, J., 1967, "The Spin Up of a Stratified Fluid," *Journal of Fluid Mechanics,* Vol. 28, p. 463.

Spence, G. S. M., Foster, M. R., and Davies, P. A., 1990, "The Transient Response of a Contained Rotating Stratified Fluid to Impulsively Started Surface Forcing," *Journal of Fluid Mechanics,* Vol. 243, p. 33.

Walin, G., 1969, "Some Aspects of Time-Dependent Motion of a Stratified Fluid," *Journal of Fluid Mechanics,* Vol. 36, p. 289.

Richard E. Hewitt
Lecturer,
Department of Mathematics,
University of Manchester,
Oxford Road,
Manchester M13 9PL,
United Kingdom

Peter A. Davies
Professor,
Department of Civil Engineering,
The University,
Dundee, DD1 4HN,
United Kingdom

Peter W. Duck
Reader,
Department of Mathematics,
University of Manchester,
Oxford Road,
Manchester M13 9PL,
United Kingdom

Michael R. Foster
Professor,
Department of Aerospace Engineering,
Applied Mechanics and Aviation,
The Ohio State University,
Columbus, OH 43210

Fraser W. Smith
Lecturer,
Department of Civil Engineering,
The University,
Dundee, DD1 4HN,
United Kingdom

Nonlinear Spin-Up of a Rotating Stratified Fluid: Experimental Method and Preliminary Results

We consider the nonlinear spin-up of a rotating stratified fluid in a conical container. An analysis of similarity-type solutions to the relevant boundary-layer problem (Duck et al., 1997) has revealed three types of behavior for this geometry. In general, the boundary-layer evolves to either a steady state, a growing boundary-layer, or a finite-time singularity depending on the initial to final rotation rate ratio, and a "modified Burger number." We emphasize the experimental aspects of our continuing spin-up investigations and make some preliminary comparisons with the boundary-layer theory, showing good agreement. The experimental data presented is obtained through particle tracking velocimetry. We briefly discuss the qualitative features of the spin-down experiments which, in general, are dominated by nonaxisymmetric effects. The experiments are performed using a conical container filled with a linearly stratified fluid, the generation of which is nontrivial. We present a general method for creating a linear density profile in containers with sloping boundaries.

1 Introduction

The readjustment (spin-up) of a rotating fluid subsequent to an abrupt change in rotation rate of the bounding walls is a fundamental problem that has both geophysical and industrial relevance. The spin-up problem for homogeneous fluids has received a great deal of attention; see for example Greenspan and Howard (1963), Greenspan (1968), Wedemeyer (1964) and Greenspan and Weinbaum (1965). The level of interest can perhaps be attributed, apart from obvious practical applications, to an ability to pose the problem in terms of a very simple geometry. The linear analysis of Greenspan and Howard (1963) showed that the influence of the container geometry was minimal, and that the essential physical mechanisms are present in the unbounded flow between two infinite parallel planes.

The next obvious extension to the large body of work concerning spin-up mechanisms was to include the effect of density stratification. Attention has centred on the problem of spin-up within a circular cylinder (for both multi-layer and linear density gradients), with some debate over the results of the initial investigators. The correct description of the linear spin-up process was later presented by Walin (1969) and Sakurai (1969), who predicted that the effect of the stable stratification was to restrict the recirculation of fluid from the Ekman layers to a localised region near to the horizontal boundaries. The effect of this localised spin up is to create a quasi-steady state, which has a linear shear in the horizontal velocity component.

The recirculation process and penetration of the fluid ejected from the Ekman layers into the interior flow is governed by the ratio of buoyancy and Coriolis forces, as determined by the Burger number, $S = N^2/\Omega^2$, where $N^2 = -(g/\rho_o)d\bar{\rho}(z)/dz$ is the Brunt-Väisälä frequency (ρ_o and $\bar{\rho}(z)$ are a reference density and stable linear stratification respectively). This localized readjustment near to the horizontal boundaries eventually ceases as the difference in (local) angular frequency between the Ekman layer and adjacent fluid decreases. Therefore, a quasi-steady localised spin up is achieved on the fast $E^{-1/2}\Omega^{-1}$ timescale with a reduction to solid body rotation on a viscous timescale $E^{-1}\Omega^{-1}$; see for example Spence et al. (1992). When discussing stratified spin-up problems care must be taken concerning the definition of spin-up time. Since the readjustment is localised and thus position dependent, it is possible to achieve a flow that matches the new conditions very quickly in some regions of the container (notably adjacent to the horizontal boundaries). Nevertheless, on defining the (global) spin-up time to be that at which the bulk of the fluid has adjusted to the new conditions, we conclude that the time taken for a stratified fluid to spin up is $O(E^{-1/2})$ longer than for the equivalent homogeneous problem.

Contributed by the Fluids Engineering Division for publication in the JOURNAL OF FLUIDS ENGINEERING. Manuscript received by the Fluids Engineering Division November 5, 1997; revised manuscript received July 30, 1998. Guest Editor: D. T. Valentine.

The linear, stably stratified spin-up problem for a circular cylinder is obviously a rather specialised problem. In particular, it is unclear how the effects of density stratification, nonlinearity, background rotation and a more general container geometry will interact. One would intuitively expect that the introduction of boundaries that are neither perpendicular nor parallel to the vertical axis will establish a flow in which the effects of buoyancy are coupled into the usual Ekman boundary-layer. Until recently very little work has been presented concerning buoyancy effected Ekman layers, see for example MacCready and Rhines (1991) and Duck et al. (1997), subsequently referred to as DFH.

The analysis of Duck et al. considered (theoretically) the unsteady, nonlinear, boundary layer arising on the sloping wall of a conical container undergoing a spin-up to a final rotation that is in the same sense as the initial rotation. Their analysis showed that nonlinear changes in rotation rate can provide at least three qualitatively different evolutions. For the form of axisymmetric solutions considered, the eventual behaviour is either a steady state, growing boundary-layer or a finite-time singularity. Which of these three classes of evolution is obtained is determined by a two-dimensional parameter space (for fixed σ; the ratio of coefficients of momentum and density diffusion), involving the ratio of initial to final rotation rates ($\hat{W}_e$) and a modified Burger number (S^*); we reproduce the parameter space diagram of DFH in Fig. 1. This redefinition of the Burger number,

$$S^* = \hat{W}_e^2 + \sin\alpha(S\sin\alpha - \hat{B}_e), \qquad (1)$$

removes any dependence on the cone half-angle, and imposed pressure from the governing boundary-layer equations. Here, $\hat{B}_e$ denotes a buoyancy perturbation at the boundary-layer edge. We note that $\hat{B}_e < S\sin\alpha$ leads to $S^* > \hat{W}_e^2$ and thus an evolution to a finite time singularity, of the form discussed by DFH, can only be located for an "edge-buoyancy" above this critical value. The parameter space diagram presented in Fig. 1 is for Schmidt number of unity, for a saline solution the Schmidt number is much larger ($\sigma \approx 700$), which moves the boundary S^*_{crit} toward $S^* = 1$.

In Section 2 we briefly describe the experimental setup used to investigate the boundary-layer development, and also discuss (Section 2.1) the technique used to generate a linear density gradient within the cone. The global spin-up of a homogeneous fluid (with a free surface) in this geometry is a nontrivial problem that has not been fully addressed, however, we are mainly concerned here with only the boundary layer development and its comparison to the theoretical predictions made for an infinite container. In Section 3 we make some comparisons between the nonlinear boundary-layer theory of DFH and our experimental data. Finally, in Section 4 we discuss the qualitative features of spin-down cases and also the nature of the spin-up process (not only the boundary layer) in the bulk of the fluid.

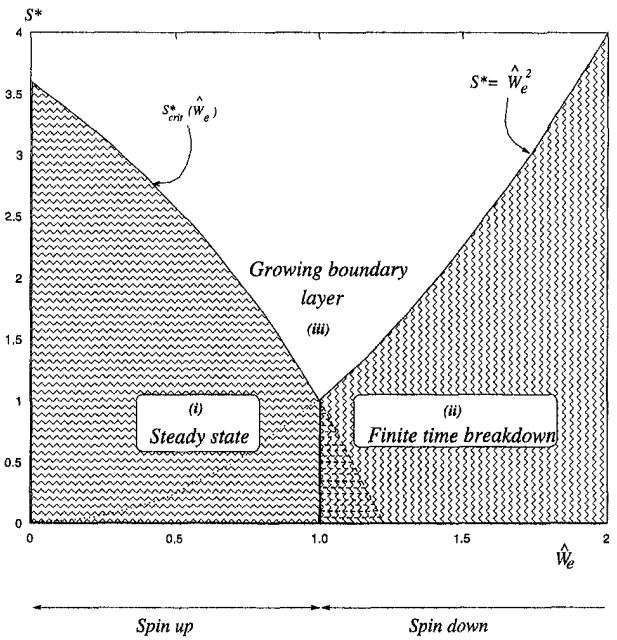

Fig. 1 Parameter space for $\sigma = 1.0$

2 Experimental Setup

A schematic of the experimental apparatus is shown in Fig. 2. The fluid within the cone is seeded with particles of a mean diameter less than 250 microns, then the unsteady evolution of the flow is visualized by illumination of these particles with a horizontal light sheet. The larger volume of unseeded fluid shown in Fig. 2 is used to reduce the optical difficulties associated with maintaining a horizontal light sheet through the container.

Density information is gathered with an aspirating conductivity probe that measures vertical density profiles near to the axis

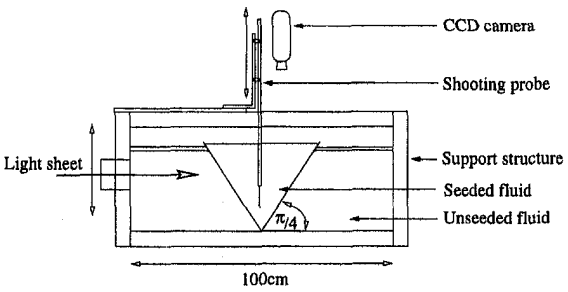

Fig. 2 Apparatus

Nomenclature

Ω = a typical angular frequency

$\rho = \rho_o + \overline{\rho} + \rho'$ = the density field

$\overline{\rho}(z)$ = a stable linear stratification, $|\overline{\rho}| \ll \rho_o$

α = the half-angle of the conical container

$S = N^2/\Omega^2$ = the Burger number

σ = the Schmidt number

$\hat{W}_e = \Omega_i/\Omega_f$ = the ratio of initial and final rotation rates

ω = a local angular frequency

h = a typical lengthscale

ρ_o = a reference density

ρ' = a density perturbation, $|\rho'| \ll \rho_o$

$N^2 = -(g/\rho_0)\partial\overline{\rho}/\partial z$ = the Brunt-Väisälä frequency

$B = g(\rho'/\rho_o)/(\Omega^2 h)$ = a nondimensionalized buoyancy

$E = (\nu/\Omega h^2)$ = the Ekman number

S^* = the modified Burger number

τ = a rotation number, $\tau = \Omega_f t/2\pi$

of rotation. In some experiments the profile was monitored at intervals throughout the readjustment phase and therefore measurements were restricted to the near-axis region; since this is the area of least fluid velocity this minimises any disturbance caused by the measurement action.

Typical laboratory parameter values used in this investigation are,

$$0.08 \leq h \leq 0.11 \text{ m}, \quad \nu \approx 10^{-6} \text{ m}^2 \text{ s}^{-1},$$
$$0 \leq N^2 \leq 5 \text{ s}^{-2}, \quad \sigma = 700,$$
$$\pi/10 \leq \Omega \leq \pi/4 \text{ rad s}^{-1}, \quad \alpha = \pi/4.$$

From the above data we see that a typical Ekman number is $E \sim 2 \times 10^{-4}$, for which we would expect stratified and homogeneous spin-up times of the order of 2 hours and 100 seconds respectively (for an angular frequency $\Omega = \pi/5$).

The height of the free surface above the apex of the container (measured while the container is at rest) was maintained at a constant 16.5 ± 0.2 cm throughout the experiments.

For moderate values of the buoyancy frequency, N, there was no evidence of any mixing or layering in the density profile during the experiments discussed below. In the homogeneous limit, $N \ll 1$, or equivalently when rotation effects dominate the dynamics, some small changes in the final measured profiles could be observed when compared to the data obtained prior to the rotation change; these effects are not thought to be significant in the cases we present here.

2.1 Generating Linear Density Profiles. To compare experimental results with the theoretical predictions on anything other than a local-analysis basis, care must be taken to generate linear density gradients that have a relatively constant buoyancy frequency. The traditional technique for creating a linearly stratified fluid is that suggested by Oster (1965), however this method relies on the container that is to be filled having a constant cross section. Using the double reservoir technique for a conical container (or any other more general axisymmetric container) yields profiles that, although repeatable, have a buoyancy frequency that varies with depth. Nevertheless, it is possible to construct a filling apparatus that is capable of generating linear density gradients in a conical container by modifying the approach of Oster.

We consider a conical container with a sidewall at an angle α to the horizontal, and a vertical coordinate system z, defined so that the apex is at $z = 0$ and the open top of the container is at $z = h > 0$. If the required density profile for our experiments is such that $\rho\,(z = h) = \rho_t$ and $\rho\,(z = 0) = \rho_b$, then

$$\rho(z) = \rho_t + \gamma(h - z), \tag{2}$$

where $\gamma = (\rho_b - \rho_t)/h$. The total volume of the container is

$$V_{\text{tot}} = \frac{\pi}{3} b^2 h, \tag{3}$$

where b is the radius of the container at height $z = h$, therefore $b = h \cot \alpha$.

Obviously, when filling the container, time is a passive parameter and any general technique will be best discussed in terms of fluid levels and volumes. In particular, for the cone defined above, we see that after a volume $\bar{V}$ has been transferred from a filling apparatus to the container, the fluid level in the cone is at $z = \bar{h}$, where

$$\bar{h} = \left\{ \frac{3\bar{V} \tan^2 \alpha}{\pi} \right\}^{1/3}. \tag{4}$$

The practicalities of filling from above via a float mechanism are rather involved in a conical geometry, therefore we use a displacement technique. A small diameter tube is placed along the axis of the container until within just a few millimeters of the base (if too close to the apex, a jet-like outflow from the filling tube can result in non-localised mixing). The density of fluid withdrawn from the filling tanks is then increased as the container fills, causing the initial fluid (of density ρ_t) to be displaced towards the upper levels. Because of this displacement of fluid caused by subsequent filling, the required density of a fluid element withdrawn from the filling apparatus when the fluid level in the cone is given by (4) is

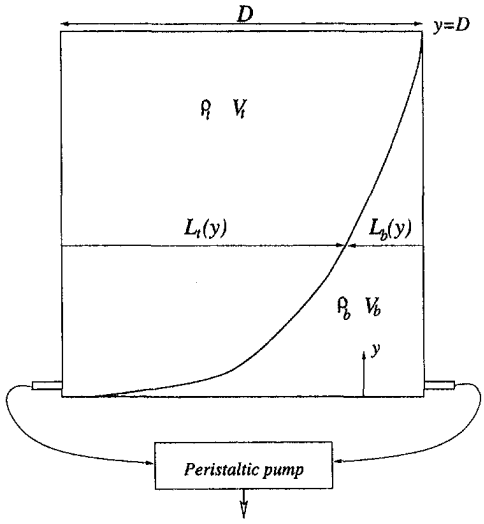

Fig. 3 Side view of the filling tank

$$\rho(\hat{h}) = \rho_t + \gamma(h - \hat{h}), \tag{5}$$

where

$$\hat{h} = (h^3 - \bar{h}^3)^{1/3}. \tag{6}$$

Thus, after removing a volume $\bar{V}$ from the filling apparatus, we require that the next element of fluid withdrawn has a density $\rho(\hat{h})$, where

$$\rho(\hat{h}) = \rho_b - \gamma\{h^3 - \bar{h}^3\}^{1/3}. \tag{7}$$

Now we can consider a filling tank as shown in Fig. 3, the dimensions of which are $(D \times D \times D)$, where D is chosen such that the total volume of the filling tank is equal to that of the conical container, thus $D = V_{\text{tot}}^{1/3} = h\beta^{-1/3}$ where $\beta = 3 \tan^2 \alpha/\pi$. The filling tank is divided into two separate regions by a partition defined by $L_b(y)$. Each sub-volume (V_t and V_b) is filled to the (open) top of the tank with a fluid of density ρ_t and ρ_b, respectively. Near the base of each sub-volume is an outlet, which are connected together and lead to a peristaltic pump. The pump is used to fill the conical container at a rate that is slow enough to maintain an equal depth of fluid in each sub-volume of the filling tank. The shape of the internal partition must be chosen so that the density of fluid withdrawn from the tank varies in the manner required to generate a linear profile in the cone.

Rewriting $\rho(\hat{h})$ as a function of the volume removed from the filling apparatus, $\bar{V}$, we see that

$$\rho(\hat{h}) = \hat{\rho}\,(\bar{V}) = \rho_b - \gamma\{h^3 - \beta\bar{V}\}^{1/3}. \tag{8}$$

To obtain this density we must have a partition, as shown in Fig. 3, that divides the container in the following manner,

$$\frac{\rho_b L_b + \rho_t L_t}{D} = \hat{\rho}\,(\bar{V}), \tag{9}$$

or equivalently, since $L_t = D - L_b$,

$$L_b = D\left\{1 - \left(\frac{h^3 - \beta\bar{V}}{h^3}\right)^{1/3}\right\}. \quad (10)$$

Therefore, in terms of the vertical coordinate y shown in Fig. 3, since $\bar{V} = D^2(D - y)$ and $D^3 = h^3/\beta$,

$$L_b(y) = D\left\{1 - \left(\frac{y}{D}\right)^{1/3}\right\}. \quad (11)$$

Although at first sight the wall angle α does not appear in the definition of the partition shape, the dependence is obviously included in the overall volume of the filling tank, as defined by D.

The required partition shape for the filling tank, as given by (11), is, in hindsight, an intuitively obvious result. Reconsidering the double reservoir technique, we can see that the two tanks are equivalent to a diagonal partition in our approach, that is $L_t(y) = y$. Therefore, for a container with a constant cross section, the fluid level will rise linearly with the volume removed from the filling tank, and since a diagonal partition causes the density of fluid withdrawn from the tank to increase proportionally with the volume removed, the final result is a linear gradient. For a conical container, the geometry is such that the fluid level in the cone rises like the cube root of the volume withdrawn from the filling tank. Therefore, to compensate for the conical geometry, we must alter the partition in order to provide a fluid density that also varies like the cube root of the volume withdrawn.

The above technique can be applied with few differences to any more general container; for axisymmetric containers the approach is essentially the same with just the volumes altered to the integral representation for a volume of revolution. In particular, it is hoped that the present experimental study will progress to more general axisymmetric containers, and cases for which there are discontinuities in the local angle of the container walls. This approach to generating linear gradients is particularly useful for some classes of container with discontinuous wall slope (for example, a cylindrical container with a conical base) since a filling tank can be constructed by a simple piecewise addition of the appropriate partition shapes. This technique may also be useful in applications where specific, nonuniform, profiles (even in containers with vertical sidewalls) are required to model particular industrial or geophysical problems.

3 Comparison With the Theory

It is possible to make a preliminary comparison between the particle tracking data obtained from spin-up experiments and the predictions of the DFH boundary-layer analysis. However, the coordinate system and nondimensionalization utilized in the theoretical approach needs some consideration before a direct comparison can be made. Care must be taken in making the appropriate conversion from the spherical polar coordinate system of DFH to the cylindrical polar coordinate system typical of a laboratory experiment.

To compare the results of the DFH boundary-layer analysis with those of the particle-tracking experiments we can examine a normalized, nondimensional angular frequency, ω (relative to a rotating frame of reference fixed with the container), against a nondimensional radial coordinate, $\bar{r}$, (relative to the axis of rotation) at nondimensional times $\bar{t}$, where we define

$$\omega(\bar{r}, \bar{t}) = \Omega_f(1 - \hat{W}(\Theta, \hat{t}))/|\Omega_i - \Omega_f|, \quad (12)$$

$$\bar{r} = 1 - \sqrt{2}\bar{E}^{1/2}\Theta, \quad (13)$$

$$\bar{E} = \sqrt{2}\nu/(\Omega_f h^2), \quad (14)$$

$$\bar{t} = \sqrt{2}\hat{t}. \quad (15)$$

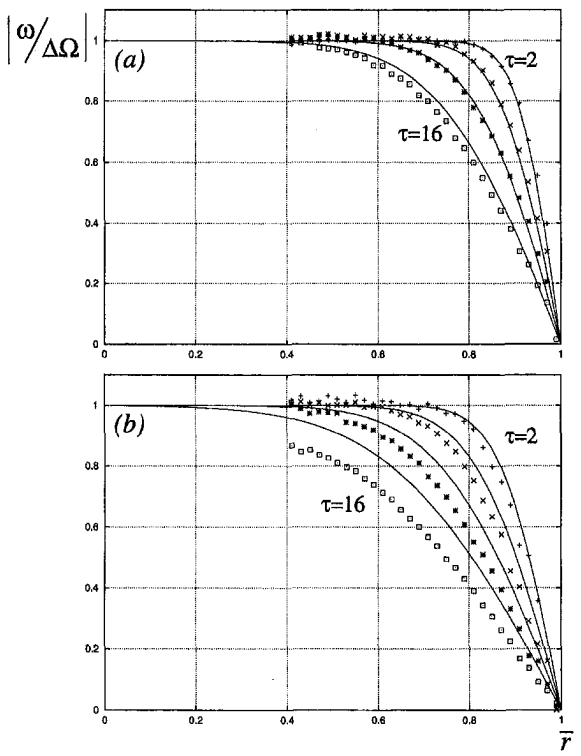

Fig. 4 A comparison between experiment and boundary-layer analysis predictions at τ = 2, 4, 8, 16. $\Delta\Omega = |\Omega_i - \Omega_f|$, Ω_i = 0 s^{-1}, $\Omega_f = \pi/5$ s^{-1} (spin-up from 0 → 6 rpm). (*a*) N^2 = 2.5 s^{-2} (S^* = 6.3), (*b*) N^2 = 4.4 s^{-2} (S^* = 11.2)

In Fig. 4 we present some comparisons of the normalized, local angular frequency obtained from particle tracking (the data points) with the corresponding prediction of the boundary-layer analysis at $\sigma = 700$ (the solid lines). The theoretical results are presented in the form (12)–(15) above. The data points shown in the figure are a segmented average of the particle tracking data obtained over the quarter of the cone viewed by the camera. The tracking interval over which the data is acquired is typically one or two seconds, depending on the particle density (in the sense of particles per unit area) within the light sheet. The camera used in the particle tracking process is mounted in the frame of the conical container, therefore the local angular frequency presented in the figure has $\omega = 0$ at the boundary $\bar{r} = 1$ and $\omega = 1$ in the interior $\bar{r} \ll 1$ (for sufficiently small times).

The two comparisons presented in Fig. 4 are for a spin up from rest to a final angular frequency of six revolutions per minute, corresponding to $\hat{W}_e = 0$ in the notation of DFH; obviously this flow is dominated by nonlinear effects. The buoyancy frequency is $N^2 = 2.5$ s^{-2} in Fig. 4(a) and $N^2 = 4.4$ s^{-2} in Fig. 4(b), corresponding to (on taking $B_e = 0$ for an initial comparison) $S^* = 6.3$ and $S^* = 11.2$, respectively. These two comparisons (5(a) and 5(b) represent a best and worst case, respectively, for the experiments performed.

The comparisons shown in Fig. 4 are over a timescale comparable to that required for homogeneous spin-up and there is clearly a remarkable level of quantitative agreement. The theoretical predictions of DFH are made with a boundary layer approximation, which, as can be seen from Fig. 4, is difficult to justify over any significantly larger timescale.

Although it is difficult to verify experimentally, the level of agreement between experiments (which cover a range of fluid depths) and theory suggests that the similarity solutions introduced by DFH were realised throughout the majority of the fluid depth.

3.1 Experimental Error. In the above comparisons we have taken $\hat{B}_e$ to be zero, effectively ignoring any density perturbation to the linear, interior stratification. Thus it is possible for S^* to deviate from the values at which the comparisons have been made if $\hat{B}_e$ is sufficiently large. Similarly, S^* depends on N, and the buoyancy frequency value that is used to define S^* is a local value at the light sheet level, measured while the container is at rest (the variation in N with z is negligible, away from the apex/free surface, for profiles generated by the method of Section 2.1). In none of the results have we allowed for the variation of the kinematic viscosity possible at high salinity levels, which, as noted by MacCready and Rhines (1991), can be as much as 10 percent for the range $\rho \in [1000, 1100]$ kg/m^3.

The length scale used in the non-dimensionalisation process is the radius of the light sheet (or equivalently the apex to light sheet distance since $\alpha = \pi/4$). This is determined by using the aspirating probe (whose position is known to ± 1 mm) to measure the z-position of the top and bottom of the light sheet and then averaging the two values. At the center of the conical container the light sheet is approximately 6 mm deep since some divergence is unavoidable.

We do not give any quantitative measure of the errors involved in the tracking process, or for deviations from a constant rotation rate of the table, and deformation of the free surface by centrifugal effects. There is little evidence that any of the above discrepancies in the experimental setup play a significant role in the dynamics of the boundary layer on the timescale we are considering.

4 Discussion

It has been shown that an analysis of the unsteady, nonlinear, boundary-layer equations, as presented by DFH, makes predictions for the spin-up of a linearly stratified fluid in a conical geometry that are in good quantitative agreement with experimental results. Agreement has been found over a wide range of parameter values, and (although not discussed above) when the modified Burger number is sufficiently small there is also some evidence of a sustained Ekman transport near the container wall, which is also in agreement with the parameter space diagram presented in the boundary layer analysis (region (i), Fig. 1).

The preliminary results presented above only show cases for which the rotation rate of the container has been increased and remains in the same sense as the initial rotation; corresponding to $0 < \hat{W}_e < 1$. We must note that the axisymmetric boundary layer analysis, although very successful in the spin up cases, does not provide even qualitative agreement with the experiments (in general) when $\hat{W}_e > 1$. These spin down cases are of particular interest since an analysis of the boundary-layer equations indicates that a finite-time singularity is possible, with an eruption of fluid from the boundary layer into the interior.

For values of $\hat{W}_e > 1$ with $\hat{W}_e - 1 \ll 1$ it is possible to obtain results that can be matched to the growing boundary layer scenario (especially for $N \gg 1$). Nevertheless, for a general (although still moderate) spin down experiment, the flow evolves through a transient stage dominated by what appears to be a centrifugal instability (i.e., a Taylor-Görtler instability).

There are a number of questions that remain unanswered in this work, in particular concerning the importance of the container geometry, a description of the physical mechanisms involved in the spin down process, and an analysis of the global spin up problem. The details of the global spin-up of fluid in such a conical container will be reported subsequently. Even for the case of a small-Ω change in a homogeneous fluid this geometry presents some new challenges owing to the absence of side-wall layers in the usual sense. Nonetheless, that analysis has been done, and spin-up occurs on an $E^{-1/2}\Omega^{-1}$ time scale as one would expect. The mechanism for stratified spin-up for small changes in Ω appears to be that discussed in Walin (1969) and in Spence et al. (1992). However, the nonlinear case is more problematic. Provided the spin-up occurs with the boundary-layer parameters in region (i) of Fig. 1, the mechanism appears to be essentially that of the linearised situation: Owing to a mismatch in flux of fluid in layer on the sloping wall and in the free-surface boundary layer, an eruption occurs in the upper corner of the container where those layers meet. That erupting fluid, with its larger angular momentum, enters the interior of the cone, but stratification effects distribute that momentum differentially in height. Only on a diffusive time scale, $\mathcal{O}(E^{-1/2}\Omega^{-1})$, is that angular momentum made uniform in height, completing the spin-up. However, for spin-up (or spin-down for that matter) in zones (ii) or (iii) of Fig. 1, the way in which the boundary layer imparts its new angular momentum to the fluid bulk, and the time scale over which that happens, is much less clear and is the subject of future work.

Acknowledgment

The support of the EPSRC is gratefully acknowledged. The authors would like to thank Dr. M. J. Coates and the late Dr. D. J. Tritton for helpful comments concerning this work.

References

Duck, P. W., Foster, M. R., and Hewitt, R. E., 1997, "On the Boundary Layer Arising in the Spin-Up of a Stratified Fluid in a Container with Sloping Walls," *Journal of Fluid Mechanics,* Vol. 335, pp. 233–259.

Greenspan, H. P., 1968, "The Theory of Rotating Fluids," Cambridge University Press.

Greenspan, H. P., and Howard, L. N., 1963, "On a Time-Dependent Motion of a Rotating Fluid," *Journal of Fluid Mechanics,* Vol. 17, pp. 385–404.

Greenspan, H. P., and Weinbaum, S., 1965, "On Nonlinear Spin-Up of a Rotating Fluid," *Journal of Mathematics and Physics,* Vol. 44, pp. 66–85.

MacCready, P., and Rhines, P. B., 1991, "Buoyant Inhibition of Ekman Transport on a Slope and Its Effect on Stratified Spin Up," *Journal of Fluid Mechanics,* Vol. 223, pp. 631–661.

Oster, G., 1965, "Density Gradients," *Scientific American,* Vol. 213, pp. 70–76.

Sakurai, T., 1969, "Spin Down Problem of a Rotating Stratified Fluid in Thermally Insulated Circular Cylinders," *Journal of Fluid Mechanics,* Vol. 37, pp. 689–699.

Spence, G. S. M., Foster, M. R., and Davies, P. A., 1992, "The Transient Response of a Contained Rotating Stratified Fluid to Impulsively Started Surface Forcing," *Journal of Fluid Mechanics,* Vol. 243, pp. 33–50.

Walin, G., 1969, "Some Aspects of Time-Dependent Motion of a Stratified Rotating Fluid," *Journal of Fluid Mechanics,* Vol. 36, pp. 289–307.

Wedemeyer, E. H., 1964, "The Unsteady Flow Within a Spinning Cylinder," *Journal of Fluid Mechanics,* Vol. 20, pp. 383–399.

Flow Structure in a Rayleigh-Bénard Cell Upon Impulsive Spin-Up

Peter Vorobieff
Research Associate.

Robert E. Ecke
Staff Member.

Center for Nonlinear Studies and Condensed Matter and Thermal Physics Group,
Los Alamos National Laboratory,
Los Alamos, NM 87545

We investigate convection in a cylindrical Rayleigh-Bénard cell with radius-to-height ratio $\Gamma = \frac{1}{2}$. The cell is subjected to impulsive spin-up about its vertical axis. We use TLC (thermochromic liquid crystal) imaging for temperature field measurements and PIV (particle image velocimetry) for velocity reconstruction of the transition in the range of Rayleigh numbers R from 5×10^7 to 5×10^8 and dimensionless rotation rates Ω from 0 up to 8×10^4. The initial (at rest) and the final (in steady rotation) states of the system are those of turbulent convection. The most persistent transient feature is a well-defined ring pattern characterized by a decrease in temperature, axial velocity directed downward and high azimuthal shear. The latter leads to formation of an azimuthally regular structure of Kelvin-Helmholz vortices. During the final stage of the transition, this vortical structure loses azimuthal regularity and an irregular pattern of vortices characteristic of turbulent rotating convection forms.

1 Introduction

Rayleigh-Bénard convection has received considerable scientific attention because of its importance for a very wide range of applications—from astrophysics to engineering, and because it provides a convenient model problem for investigations of phenomena from pattern formation (Cross and Hohenberg, 1993) to strong turbulence (Siggia, 1994). A fluid layer of height d heated from below and cooled from above remains stable and transmits heat by thermal diffusion only if the temperature difference across the layer ΔT does not exceed a critical value ΔT_c. For $\Delta T > \Delta T_c$, buoyancy-driven convection takes place in the layer, and heat is transported through it by a combination of diffusion and advection. The dimensionless parameters that govern the state of the flow in the simplest case of Rayleigh-Bénard convection are the Rayleigh number R, representing the amount of potential energy in the fluid, and the Prandtl number σ determined by the properties of the fluid:

$$R = \frac{\alpha g \Delta T d^3}{\nu \kappa}, \quad \sigma = \frac{\nu}{\kappa}, \tag{1}$$

where α is the coefficient of thermal expansion, g is the acceleration of gravity, ν is the kinematic viscosity of the fluid, and κ is the fluid coefficient of thermal diffusivity. Another dimensionless parameter of importance is the aspect ratio $\Gamma = r_0/d$ between the vertical and characteristic lateral dimensions (the latter being, for instance, the radius of a cylindrical convection cell r_0).

For Rayleigh numbers far above the onset of convection, $R \simeq 10^7$, convection is characterized by thermal plumes erupting from thin thermal boundary layers near the upper and lower boundaries. These thin layers control the convective heat transport (Siggia, 1994) because the interior flow is vigorously mixed by the turbulent flow which is only suppressed near the boundaries. High precision experiments on convection in helium gas demonstrated that scaling of heat transport with R was different from the classical scaling predictions. The two main alternatives to the classical picture are the mixing-zone theory of Castaing et al. (1989) and the large-scale circulation theory of Shraiman and Siggia (1990). The latter suggests that the interaction of the shear flow generated by large-scale circulation with the thermal boundary layers is responsible for the observed heat transport scaling. A tremendous amount of recent experimental work has failed to unequivocally support a single theoretical description of turbulent convection which remains a challenging problem in the physics of fluid turbulence.

The above is a very brief outline of the general problem of Rayleigh-Bénard convection. To this one can add a number of ingredients that extend the problem of convection in a variety of interesting directions. In particular, Rayleigh-Bénard convection in a rotating reference frame represents the characteristic features of many problems in diverse areas such as astrophysics, geophysics and engineering, and has been the subject of numerous studies. Rotation adds the influence of the Coriolis force whose strength is measured by the dimensionless rotation rate, $\Omega = \Omega_D d^2/\nu$ where Ω_D is the angular rotation rate about the vertical axis. The second force added by rotation is the centrifugal one that is either ignored completely as much smaller than the gravitational acceleration or conversely takes the place of gravity as the dominant source of buoyancy in the fluid. Here we consider the case of very weak centrifugal acceleration.

The linear stability analysis for rotating convection was carried out by Chandrasekhar (1953), and since the first experimental work of Nakagawa and Frenzen (1955), there have been many investigations of rotating convection, most of which are reviewed by Boubnov and Golitsyn (1995). In rotating turbulent convection, the main flow feature is the presence of vortices (plumes) with cyclonic or anticyclonic cores corresponding to converging or diverging flow, respectively, near the top and bottom boundaries. The number of vortices grows with the rotation rate (Boubnov and Golitsyn, 1986; Sakai, 1997). Several authors have reported the formation of regular structures in the flow if the rotating convection cell is subjected to rapid changes in either R (Dikarev, 1983; Zhong et al., 1993) or Ω (Boubnov and Golitsyn, 1986). Formation of axially regular features upon rapid spin-up from rest of the convection cell is the subject of the current study. We present time sequences of instantaneous temperature maps and velocity fields in the plane adjacent to the top of the cell that show the presence of rings of downwelling cold flow characterized by an abrupt change in azimuthal velocity. Our earlier investigation (1998) shows that the number of such rings grows with the final rotation rate and also depends on the Rayleigh number. As shear develops across

Contributed by the Fluids Engineering Division for publication in the JOURNAL OF FLUIDS ENGINEERING. Manuscript received by the Fluids Engineering Division November 5, 1997; revised manuscript received July 30, 1998. Guest Editor: D. T. Valentine.

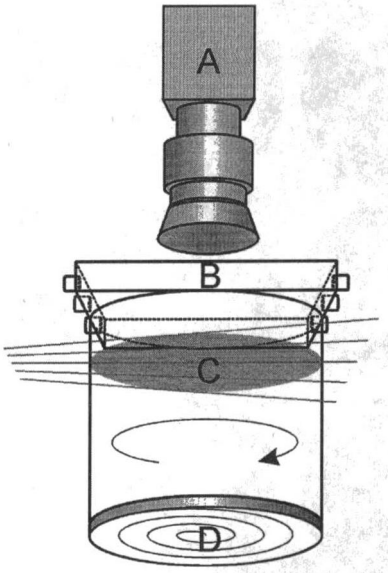

Fig. 1 Experimental setup. *A*—camera, *B*—cooling manifold, *C*—illuminated section of the cell, *D*—bottom plate with heater

the rings, Kelvin-Helmholz instability causes vortex roll-up, leading to destruction of the rings.

2 Experimental Details

A cylindrical Plexiglas cell of radius $r_0 = 6.35$ cm and height $d = 12.7$ cm is placed on a rotating table. The bottom boundary of the cell is an anodized aluminium plate attached to a disk-shaped heating element with the radius equal to that of the cell. The top boundary of the cell is a transparent sapphire window separating the cell from a cooling manifold through which temperature-controlled water is circulated. Thus, the top boundary of the cell is maintained at constant temperature T_t, while at the bottom boundary the heat current into the cell is constant, resulting in approximately constant bottom temperature T_b in steady rotating convection. A lighting system produces a thin (~3 mm) sheet of white light which illuminates horizontal sections of the cell, and a color digital video camera is positioned on the rotating table above the cell. Figure 1 presents a schematic view of the cell.

In the plane of the light sheet, instantaneous fields of temperature and horizontal velocity can be acquired. For temperature field acquisition, the flow is seeded with 5-μm microcapsules with thermochromic liquid crystals (TLC). TLCs selectively reflect incident white light and, within the range of their color play, the wavelength of the color they reflect varies monotonically with temperature, red corresponding to the lower end of the color play range, and blue to the upper. Thus, color digital images of the light sheet illuminating the flow in the cell seeded with TLC microcapsules can be converted to temperature maps by extracting their hue component and mapping the hue of each pixel to temperature. For velocity acquisition, we seed the flow with neutrally buoyant 250-μm polystyrene microspheres and apply the standard particle image velocimetry (PIV) technique to recover velocities from microsphere displacements between consecutive frames of digital video images of the flow. Details of TLC temperature mapping and PIV velocity acquisition in application to this problem, as well as the accuracy of both techniques, are discussed elsewhere (Vorobieff and Ecke, 1998). The error in temperature reconstruction does not exceed 0.1°C. We used a digital PIV system capable of acquiring thirty 640 × 480 frames per second. The spatial resolution of this system limited the size of the grid for the velocity data recovered to 27 by 27—sufficient to resolve the larger-scale features of the flow with 99 percent accuracy, but unable to recover information about features of sizes 0.5 cm and smaller.

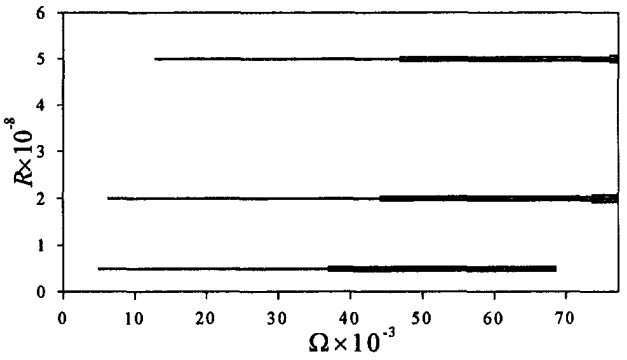

Fig. 2 Azimuthally regular spin-up patterns for $R = 5 \times 10^7$, 2×10^8 and 5×10^8. Single line—one ring, double line—two rings, triple line—three rings.

3 Observations

Upon spin-up, we observe a variety of transient flow patterns, often azimuthally regular. Figure 2 shows a summary of the latter in $R - \Omega$ parameter space.

Prior to discussing Fig. 2, let us consider a typical sequence of transient velocity/temperature maps for $R = 2 \times 10^8$ presented in Fig. 3. The cell undergoes impulsive spin-up from rest to a dimensionless $\Omega = 1.9 \times 10^4$. Velocity and temperature

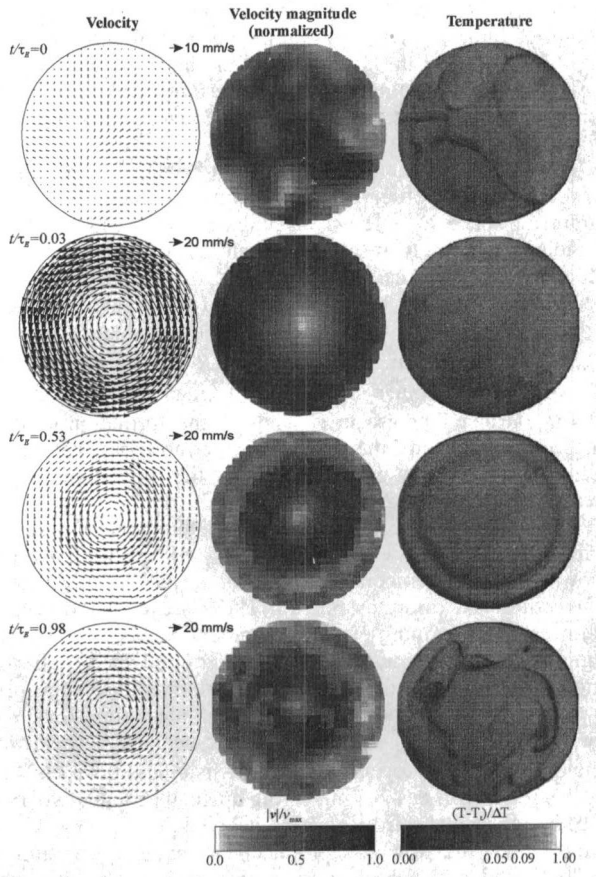

Fig. 3 Maps of instantaneous horizontal velocity (left column, velocity scale indicated for each map), velocity magnitude (center column, normalized by maximum velocity for each map) and temperature (right column) of spin-up to $\Omega = 1.9 \times 10^4$ at $R = 2 \times 10^8$. Dimensionless times are indicated in the figure.

were acquired in two separate runs of the experiment under identical conditions, but with different seeding particles. In both runs, the horizontal light sheet was positioned adjacent to the top boundary of the cell. The time in Fig. 3 has been nondimensionalized with the Ekman spin-up time $\tau_E = d/\sqrt{\nu\Omega_D}$, the characteristic time scale for the spin-up of a cylindrical container of isothermal fluid to a state of solid body rotation.

Immediately before spin-up (Fig. 3, $t/\tau_E = 0$), the flow is dominated by upwelling plumes of hot material separated by elongated zones of cool downwelling flow clearly visible in the temperature map. The characteristic velocity due to turbulent convection before spin-up is of the order of 2 mm/s. Upon spin-up ($t/\tau_E = 0.03$), the azimuthal velocity imparted to the water in the cell in the layer adjacent to the horizontal walls is of the order of $\Omega_D r_0 = 58$ mm/s. In the rotating reference frame, this corresponds to the core of the cell being in solid-body rotation with azimuthal velocity growing linearly with distance from the axis of the cell and then decreasing to zero in the area near the wall. The velocity distribution closely matches that predicted and measured by Weidman (1976a, b) for impulsive spin-up of a cylindrical cell without convection. It is also noteworthy that at the early stages of spin-up all the structures in the temperature field near the top of the cell are destroyed. As the flow evolves, colder fluid accumulates at the outer perimeter of the cell due to large-scale centrifugally-driven flow. At dimensionless time $t/\tau_E \sim 0.4$, a thin cold ring forms at a radius $r_r \simeq \frac{3}{4}r_0$. Formation of this ring is also associated with changes in the velocity field: the ring corresponds to a local minimum in the velocity profile (Fig. 3, $t/\tau_E = 0.53$). This feature of the velocity field is specific to spin-up with convection—neither Weidman's solution (1976a) nor the experiments produce velocity profiles with local minima for the non-convective spin-up problem. The next stage of the evolution is the roll-up of Kelvin-Helmholz vortices in the ring due to azimuthal shear ($t/\tau_E = 0.98$). After the formation of the cyclonic vortices, the flow loses its azimuthal regularity, resulting in the irregular vortex pattern characteristic of rotating convection at high Rayleigh numbers.

As reported in our previous work (1998), this pattern of flow evolution is observed over a considerable region of the parameter space $R - \Omega$ we investigated (Fig. 2). At a fixed Rayleigh number, there exists an interval of rotation rates at which one ring forms, with its radius showing a remarkably weak dependence on either R or Ω and remaining close to $r_r \simeq \frac{3}{4}r_0$. Spin-up to low Ω does not lead to ring formation, whereas when Ω exceeds a critical value for each R we observe formation of two rings, the inner still at $r_r \simeq \frac{3}{4}r_0$ and the outer at $r_r \simeq 0.94r_0$. Further increase in Ω leads to the formation of three rings during spin-up, the third and innermost ring having the radius $r_r \simeq 0.56r_0$. Again, the radii of the rings show only a weak dependence on R and Ω.

Figure 4 shows the time sequence of temperature maps for spin-up to $\Omega = 7.2 \times 10^4$ at $R = 2 \times 10^8$. The first image shows a typical temperature map for a state of nonrotating convection just prior to spin up. There are cooler downflow plumes/sheets forming elongated borders between the upwelling hotter flow. The next two images, acquired shortly after the impulsive spin-up of the cell, show the temperature maps prior to the formation of the ring. At dimensionless time $t/\tau_E \sim 1$, one observes an outer cold ring forming near the vertical wall. The ring at $r_r \simeq \frac{3}{4}r_0$ forms next, at dimensionless time 1.67, and at $t/\tau_E \sim 2$ vortices begin to roll up in the outer two rings and the innermost third ring becomes visible. At $t/\tau_E = 2.37$, evolution of the flow has produced a staggered structure of cyclonic and anticyclonic vortices in place of the two outer rings coexisting with the innermost ring. At later times, the inner ring is also destroyed by vortex roll-up, and the structure of the flow loses its regularity and eventually evolves to a steady rotating convection pattern. The rotation rates characterizing

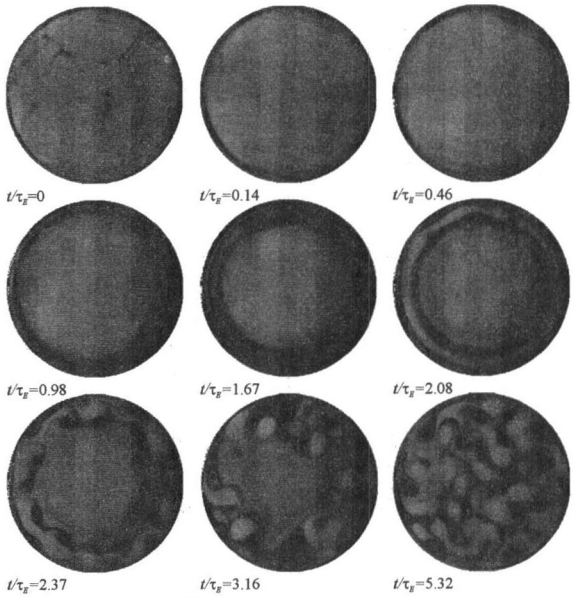

Fig. 4 Instantaneous TLC temperature maps of spin-up to $\Omega = 7.2 \times 10^4$ at $R = 2 \times 10^8$. Dimensionless times are indicated in the figure.

the transition from the flow pattern without rings to the one-ring pattern, from the one-ring pattern to the two-ring pattern, etc. increase with the Rayleigh number (Vorobieff and Ecke, 1998).

4 Conclusions

For the impulsive spin-up of a Rayleigh-Bénard cell, we produce time sequences of instantaneous horizontal velocity and temperature maps in the plane adjacent to the top cooled surface of the cell. The most prominent features of the flow morphology observed during the spin-up are axisymmetric ring-shaped zones of downwelling flow characterized by a local drop in temperature and azimuthal velocity. Whereas the number of the rings increases with the increase in the final rotation rate, the characteristic radii of the rings do not show a strong dependence on either R or Ω.

The flow evolution during spin-up can be divided into three stages. First, the flow structures typical of the non-rotating convection are destroyed by the acceleration of the cell, and a relatively uniform temperature field forms near the top boundary. At this stage, one can also observe accumulation of the cooler fluid near the vertical wall. During the first stage, the velocity distribution is consistent with that calculated and measured for the spin-up of a cylindrical cell without convection. In the second stage, cold downwelling ring(s) form. Azimuthal velocity undergoes sharp changes in the rings, and the velocity profiles no longer resemble ones typical for the no-convection spin-up. Finally, shear in the rings leads to roll-up of Kelvin-Helmholz vortices. The mechanism for the formation of the rings is related to the interaction of the boundary layer stability and the strong shear induced by impulsive spin up. The axisymmetric nature of the ring formation suggests that it is the radial component of the shear that is the important ingredient in the ring formation. As the fluid approaches solid body rotation, the magnitude of the shear at the boundaries decreases, reducing its stabilizing influence on the thermal boundary layer. In addition, during the spin up the boundary layer has been thickening because of the heat input from the boundaries. Eventually lateral instability of the boundary layer occurs. That this manifests itself in the formation of single or multiple rings is an interesting topic for future theoretical analysis and for other experiments.

Acknowledgment

This research is supported by the U.S. Department of Energy.

References

Boubnov, B. M., and Golitsyn, G. S., 1986, "Experimental Study of Convective Structures in Rotating Fluids," *Journal of Fluid Mechanics,* Vol. 167, pp. 503–531.

Boubnov, B. M., and Golitsyn, G. S., 1995, *Convection in Rotating Fluids,* Dordrecht; Boston, Kluwer Academic.

Castaing, B., Gunaratne, G., Heslot, F., Kadanoff, L., Libchaber, A., Thomae, S., Wu, X.-Z., Zaleski, S., and Zanetti, G., 1989, "Scaling of Hard Thermal Turbulence in Rayleigh-Bénard Convection," *Journal of Fluid Mechanics,* Vol. 204, pp. 1–39.

Chandrasekhar, S., 1953, "The Instability of a Layer of a Fluid Heated from Below and Subject to Coriolis Forces," *Proceedings of the Royal Society of London,* Series A, Vol. 217, pp. 306–327.

Cross, M. C., and Hohenberg, P., 1993, "Pattern-Formation Outside of Equilibrium," *Reviews of Modern Physics,* Vol. 65, pp. 851–1112.

Dikarev, S. N., 1983, "On the Influence of Rotation on the Convection Structure in a Deep Homogeneous Fluids," *Doklady Akademii Nauk SSSR,* Vol. 273, pp. 718–720.

Nakagawa, Y., and Frenzen, P., 1955, "A Theoretical and Experimental Study of Cellular Convection in Rotating Fluids," *Tellus A,* Vol. 7, pp. 1–21.

Sakai, S., 1997, "The Horizontal Scale of Rotating Convection in the Geostrophic Regime," *Journal of Fluid Mechanics,* Vol. 333, pp. 85–95.

Shraiman, B. I., and Siggia, E. D., 1990, "Heat-Transport in High-Rayleigh-Number Convection," *Physical Review A,* Vol. 42, pp. 3650–3653.

Siggia, E. D., 1994, "High Rayleigh Number Convection," *Annual Review of Fluid Mechanics,* Vol. 26, pp. 137–168.

Vorobieff, P., and Ecke, R. E., 1998, "Transient States During Spin-Up of a Rayleigh-Bénard Cell," *Physics of Fluids,* currently in press.

Weidman, P. D., 1976a, "On the Spin-Up and Spin-Down of a Rotating Fluid. Part 1. Extending the Wedemeyer Model," *Journal of Fluid Mechanics,* Vol. 77, pp. 685–708.

Weidman, P. D., 1976b, "On the Spin-up and Spin-Down of a Rotating Fluid. Part 2. Measurements and Stability," *Journal of Fluid Mechanics,* Vol. 77, pp. 709–735.

Zhong, F., Ecke, R. E., and Steinberg, V., 1993, "Rotating Rayleigh-Bénard Convection: Asymmetric Modes and Vortex States," *Journal of Fluid Mechanics,* Vol. 249, pp. 135–159.

J. Mang
PhD Student,
Institut für Strömungslehre
und Wärmeübertragung
Vienna University of Technology,
Vienna, Austria

E. Minkov
PhD Student,
Department of Computer Science,
Israel Institute of Technology, Haifa, Israel

U. Schaflinger
Professor,
Institut für Strömungslehre
und Wärmeübertragung,
Vienna University of Technology,
Vienna, Austria

M. Ungarish
Professor,
Department of Computer Science,
Israel Institute of Technology, Haifa, Israel

Particle Entrainment in a Bounded Rotating Flow With a Drain

A bathtub vortex is usually formed at the axis of a drain. In the presence of such a vortex, gravity separation of solid impurities lighter than the embedding fluid is modified by centrifugal separation and viscous resuspension. Both mechanisms are responsible for the agglomeration of impurities at the axis of the vortex. From there the impurities are easily sucked into the outlet. In the investigated case, a viscous fluid with a given initial rotation is spinning down in a container with endplates both at the bottom and the top. The amount of fluid withdrawn through a circular hole in the center of the vortex is constantly replaced by a radial influx. The resulting time-dependent flow was solved by means of a finite difference method taking into account the influence of Ekman layers at the bottom and the top. Subsequently, the process of centrifugal separation of particles lighter than the embedding fluid was studied in the aforementioned flow field. The results were compared with the particle motion in a classical Oseen vortex. For a simplified case an analytical solution was derived and compared with the corresponding numerical solution. Both results were found to be in good agreement.

Introduction

Gravity settling of solid impurities in a viscous laminar flow has many applications in industrial engineering. In the investigated case, a dilute suspension is flowing through a long non-rotating container with solid boundaries both at the bottom and the top. The suspended particles are approximately spherical and of uniform size and density. They are lighter than the embedding fluid. Gravity causes them to move up and form a layer of sediment on the top. At the bottom of the container, fluid is withdrawn through a circular outlet. Because of perturbations in the far field, the incoming fluid has a vorticity. As a consequence, gravity settling is modified by centrifugal separation and viscous resuspension, as will be described in the following.

The vorticity of the incoming fluid is transported to the drain where it is usually concentrated as a strong local vortex superimposing the sink flow, known as bathtub vortex (Fig. 1). An asymptotic solution of the Navier-Stokes equations for a similar steady vortex-flow was found by Lewellen (1962). In the unsteady flow under discussion, friction causes the vortex to spin down. At the top, viscous resuspension of the sediment is caused by the shear flow inside the Ekman layer. Centrifugal separation leads to the agglomeration of the suspended impurities at the axis of the vortex. From there the particles are easily sucked into the drain.

This work contains an analysis of the process of centrifugal separation in the flow field described above. The influence of the inner and outer Stewartson layers is neglected. To simplify the present calculations also the influence of gravity is neglected.

Particle Motion in a Classical Oseen Vortex

The time-decaying vortex is asymptotically approximated by a solid body rotation near the axis and by a potential vortex at large radii, Truckenbrodt (1991). To distinguish dimensional from dimensionless variables, the former will be marked by an upper asterisk. The velocity v^* with the components u^*, v^*, and w^* and pressure p^* of the Oseen vortex depend only on the radius r^* and the time t^*:

$$u^* = 0, \quad v^* = v^*(r^*, t^*), \quad w^* = 0, \tag{1}$$

$$p^* = p^*(r^*, t^*). \tag{2}$$

Integration of the azimuthal momentum equation leads to

$$v^*(r^*, t^*) = \frac{\Gamma_\infty^*}{2\pi r^*}\left[1 - \exp\left(\frac{-r^{*2}}{r_\delta^{*2}}\right)\right], \tag{3}$$

with

$$r_\delta^{*2} = 4\nu^*(t_0^* + t^*). \tag{4}$$

Γ_∞^* denotes the circulation at $r^* \to \infty$. The radius $r_0^*(t^*)$ is the radius of intersection between the two asymptotic cases of the free and the forced vortex. The constant t_0^* references the (viscous) initial state at $t^* = 0$.

Dimensionless variables are introduced by referring all lengths to $r_{\text{ref}}^* = r_0^*(0)$. The angular velocity will be referred to Ω_{ref}^* denoting the angular velocity of a potential vortex with Γ_∞^* at r_{ref}^*. Velocities will be referred to U_{ref}^* standing for the Stokesian centrifugal settling velocity of a single particle caused by Ω_{ref}^* at r_{ref}^*. The time t^* will be referred to $\tau^* = r_{\text{ref}}^*/U_{\text{ref}}^*$. Where necessary within the text, the properties of the continuous phase will be denoted by the subscript 1 and the properties of the dispersed phase by the subscript 2. For a dilute suspension the influence of the particle motion on the basic flow is negligible. Restricting the analysis to volume concentrations of the dispersed phase $\alpha \ll 1$ within the whole domain, ensures that the flow can be treated as a single phase flow. The influence of the Brownian diffusion can be neglected because the Peclet number,

$$\text{Pe} = \frac{U_{\text{ref}}^* r_{\text{ref}}^*}{\mathcal{D}^*} \ll 1, \tag{5}$$

Contributed by the Fluids Engineering Division for publication in the JOURNAL OF FLUIDS ENGINEERING. Manuscript received by the Fluids Engineering Division December 1, 1997; revised manuscript received July 30, 1998. Guest Editor: D. T. Valentine.

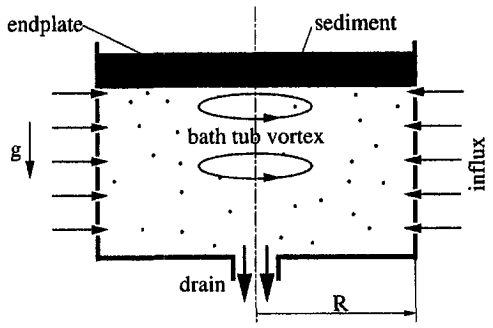

Fig. 1 Sketch of problem

with $\mathscr{D}^*$ being the Brownian diffusivity of the particles. We require that the Taylor number Ta meets the following condition:

$$\mathrm{Ta} = \frac{\Omega^*_{\mathrm{ref}} a^{*2}}{\nu^*} \ll 1, \tag{6}$$

where a^* denotes the radius of the solid impurities and ν^* is the kinematic viscosity of the liquid phase. Ta represents the ratio of Coriolis to viscous influences on a dispersed particle. From the condition for Ta the azimuthal velocity of the particle phase v_2^* is obtained as follows:

$$v_2^* \approx v_1^* = v^* = \omega^* r^*. \tag{7}$$

The particle Reynolds number

$$\mathrm{Re}_p = \frac{U^* a^*}{\nu^*} \ll 1. \tag{8}$$

Hence, the Stokesian velocity of a single spherical particle is given by

$$U^*_{st} = \frac{2a^{*2} v^{*2} \epsilon}{9\nu^* r^*}, \tag{9}$$

wherein ϵ denotes the relative density difference of the phases. Neglecting the inertial and viscous terms in the momentum balance of the mixture and taking into account the restrictions (6) and (8), the equation of the relative motion yields the drift flux of the dispersed phase in the radial direction $j^*_{12_r}$

$$j^*_{12_r} = U^*_{st}(r^*, t^*) f(\alpha). \tag{10}$$

For the hindrance function $f(\alpha)$, Richardson and Zaki (1954) postulated:

$$f(\alpha) = \alpha(1 - \alpha)^n, \tag{11}$$

with $n = 4.7$ following from experiments [Schaflinger (1985)]. The volume flux density of the dispersed phase in the radial direction is given by

$$j^*_{2_r} = \alpha j^*_r - j^*_{12_r}, \tag{12}$$

with $j^*_r = 0$ because the flow has no component in the radial direction. Insertion of Eq. (12) and the equation of global volume continuity into the continuity equation for the dispersed phase, given as

$$\frac{\partial \alpha}{\partial t^*} + \frac{1}{r^*} \frac{\partial (r^* j^*_{2_r})}{\partial r^*} = 0, \tag{13}$$

yields the (dimensionless) kinematic wave equation as described in Schaflinger (1990)

$$\frac{\partial \alpha}{\partial t} + U_{st}(r, t) f'(\alpha) \frac{\partial \alpha}{\partial r} = -\left(\frac{U_{st}(r, t)}{r} + \frac{\partial U_{st}(r, t)}{\partial r} \right) f(\alpha). \tag{14}$$

For $t = 0$, homogeneous concentration is assumed, i.e.,

$$\alpha = \alpha_0 \tag{15}$$

in the whole domain $0 < r < \infty$. Equation (14) was solved by the method of characteristics and, alternatively, by a finite difference scheme. Figure 2 shows the solutions for the particle concentration with the ratio $\tau^*_{\mathrm{ref}}/t^*_0 \approx 2 \cdot 10^{-2}$. It is seen that the impurities are concentrated at the axis as t is increasing. The results obtained by the two methods of integration show good agreement.

Solid Body Rotation in a Bounded Domain With an Influx

The time of formation of the Ekman layers is much shorter than the spin down-time τ^*_{sd}. For $t^* \ll \tau^*_{sd}$ the angular velocity ω^* is approximately constant.

In the following, we treat the bulk of the suspension apart from the boundary-layer flows near the horizontal and the vertical walls. We account for the effect of the Ekman layers near the bottom and the top plates by superimposing the secondary radial motion induced by the Ekman layers on the bulk flow. This is justified because the thickness of the Ekman layers $\delta^* = O[(\nu^*/\Omega^*)^{1/2}]$ is very small compared to the height of the container H^*. We assume that outside the Ekman layers $\partial/\partial z = 0$.

With the radial influx $q^* = Q^*/2\pi$ and the secondary flow according to Bödewadt (1940) the radial velocity is obtained as

$$u^* = \frac{1}{H^*} \left(-\frac{q^*}{r^*} + \kappa r^* \sqrt{\nu^* \omega^*} \right), \tag{16}$$

where $\kappa = 1.26$ is a dimensionless parameter and

$$\omega^* = \Omega^*_{\mathrm{ref}} = \text{const.} \tag{17}$$

for a solid body rotation. Inserting

$$j^*_r = u^* \tag{18}$$

and

$$j^*_{12_r} = U^*_{st}(r^*) f(\alpha) = -U^* r^* f(\alpha) \tag{19}$$

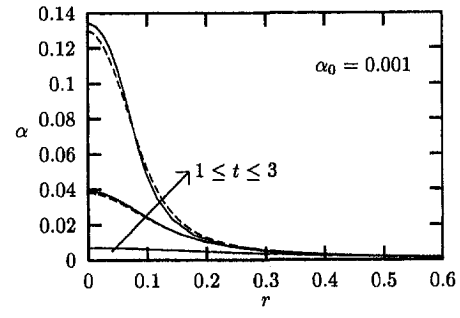

Fig. 2 Particle concentration $\alpha(r, t)$ in a classical Oseen vortex computed by a characteristic method (full curves) and a finite difference scheme (dashed curves); $\alpha_0 = 0.001$

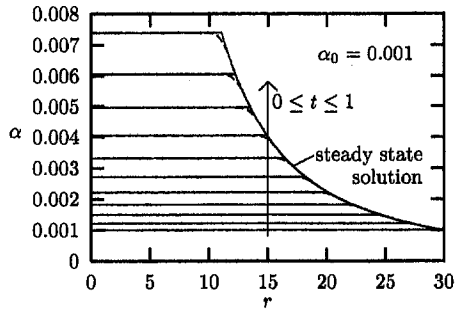

Fig. 3 Particle concentration $\alpha(r, t)$ for solid body rotation in a bounded domain with a drain computed by the method of characteristics (full curves) and a finite difference scheme (dashed curves); $\alpha_0 = 0.001$

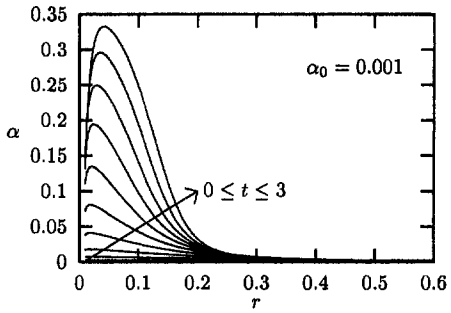

Fig. 5 Particle concentration $\alpha(r, t)$ in a time-dependent vortex flow with a drain, without consideration of Ekman layers; $\alpha_0 = 0.001$; configuration 1

into Eq. (13) and considering

$$\nabla \cdot j^* = 0, \tag{20}$$

we obtain

$$\frac{\partial \alpha}{\partial t} - \left[\frac{q}{r} + r(Uf'(\alpha) - d)\right]\frac{\partial \alpha}{\partial r} = 2Uf(\alpha). \tag{21}$$

In Eq. (21),

$$q = \frac{q^*}{r^*_{\text{ref}} H^* U^*_{\text{ref}}}, \tag{22}$$

$$U = 1, \tag{23}$$

$$d = \frac{\kappa\sqrt{\nu^* \Omega^*_{\text{ref}}}\, r^*_{\text{ref}}}{H^* U^*_{\text{ref}}}. \tag{24}$$

With R specifying the domain under consideration, the initial and the boundary conditions are given as

$$\alpha = \alpha_0 \; \forall 0 \le r \le R \quad \text{at} \quad t = 0 \tag{25}$$

and

$$\alpha = \alpha_0 \; \forall 0 < t < \infty \quad \text{at} \quad r = R, \tag{26}$$

respectively. For the case of a dilute suspension with $f(\alpha) \approx \alpha$, Eq. (21) can be solved analytically by the method of characteristics. For $t \to \infty$, α is only a function of r and $\alpha = \alpha_0$, given as (Ungarish, 1993),

$$\alpha = \alpha_0 \frac{1 + cR^2}{1 + cr^2}, \tag{27}$$

with

$$c = \frac{U - d}{q}. \tag{28}$$

This problem served as a test case for the code used for the analyses reported in the next section. Figure 3 shows both the analytical and a numerical solution.

Vortex With Influx and Ekman Layer Influence

Inserting Eq. (16) into the azimuthal momentum equation and dividing by r, we obtain an equation for ω which is now a function of r and t:

$$\frac{\partial \omega}{\partial t} + \left(-\frac{q}{r^2} + d\sqrt{\omega}\right)\left(2\omega + r\frac{\partial \omega}{\partial r}\right) = e\left(\frac{\partial^2 \omega}{\partial r^2} + \frac{3}{r}\frac{\partial \omega}{\partial r}\right), \tag{29}$$

with

$$e = \frac{\nu^* \tau^*_{\text{ref}}}{r^{*2}_{\text{ref}}}. \tag{30}$$

At $t = 0$, the angular velocity ω is equal to the angular velocity of an Oseen vortex given by Eq. (3). At the inner boundary, there is a no-shear condition for $t > 0$, i.e.,

$$\frac{\partial \omega}{\partial r} = 0 \quad \text{at} \quad r = 0. \tag{31}$$

At the outer boundary, we assume an influx with an angular velocity

$$\omega(R, t) = \omega(R, 0). \tag{32}$$

Substitution of Eqs. (12), (16), (18), (19), and (20) into Eq. (13) yields

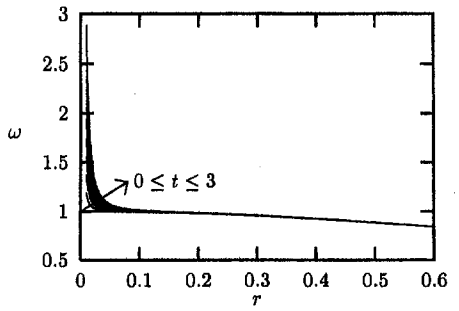

Fig. 4 Angular velocity $\omega(r, t)$ in a time-dependent vortex flow with a drain, without consideration of Ekman layers ($d = 0$); configuration 1: $e \approx 1 \cdot 10^{-8}$

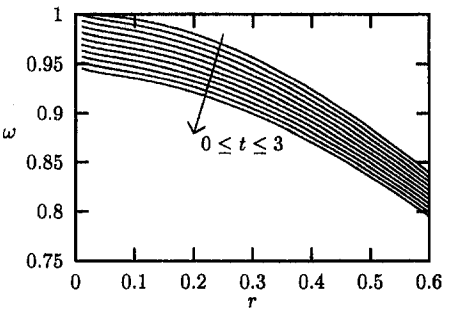

Fig. 6 Angular velocity $\omega(r, t)$ in a time-dependent vortex flow with a drain, without consideration of Ekman layers ($d = 0$); configuration 2: $e \approx 5 \cdot 10^{-3}$

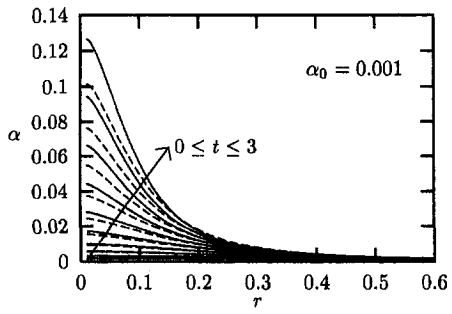

Fig. 7 Particle concentration $\alpha(r, t)$ in a time-dependent vortex flow, with (dashed curves) and without (full curves) consideration of Ekman layers ($d = 0$); configuration 2

$$\frac{\partial \alpha}{\partial t} - \left[\frac{q}{r} + r(Uf'(\alpha)\omega^2 - d\sqrt{\omega})\right]\frac{\partial \alpha}{\partial r} = U\left(\omega^2 + \frac{\partial(\omega^2 r)}{\partial r}\right) f(\alpha), \quad (33)$$

with the initial condition

$$\alpha = \alpha_0 \; \forall 0 < r \le R \quad \text{at} \quad t = 0 \quad (34)$$

and the boundary conditions

$$\frac{\partial \alpha}{\partial r} = 0 \; \forall 0 < t < \infty \quad \text{at} \quad r = 0, \quad (35)$$

$$\alpha = \alpha_0 \; \forall 0 < t < \infty \quad \text{at} \quad r = R. \quad (36)$$

Equations (29) and (33) can be integrated by means of a finite difference method.

We have found that the concentration profiles $\alpha(r, t)$ strongly depend on the properties of the particles and the suspending fluid. Figures 4, 5, 6, and 7 show $\alpha(r, t)$ and $\omega(r, t)$, respectively, for different dimensionless parameters e. The influence of the Ekman layers was neglected by setting $d = 0$. The radial influx convects the vorticity to the axis where it is concentrated as can be seen in Fig. 4. For the second configuration (Fig. 6), the viscosity ν^* is sufficiently large. Hence, internal friction counteracts the aforementioned effect.

The difference in the concentration profiles follows from the different behaviour of $\omega(r, t)$. In configuration 1, the particle concentration $\alpha(r, t)$ reaches higher values than in configuration 2 because the larger angular velocity $\omega(r, t)$ enhances the centrifugal separation. The high negative value of $\partial\omega/\partial r$ in configuration 1 near the axis of the vortex is responsible for the decline in α in this domain, where more impurities are withdrawn than are replaced.

For reasons of numerical stability we had to take a very small value for q^*. This is why there is almost no difference between the concentration profiles in configuration 2 (Fig. 7) and the Oseen vortex (Fig. 2). In Fig. 6, however, near the axis a small increase in $\omega(r, t)$ can be observed. It is caused by the influx.

Figure 7 shows the influence of the Ekman layer secondary flux ($d \neq 0$) for configuration 2. This motion in the outward direction hinders the concentration process. Its influence, however, is small compared to the influence of the viscosity.

Conclusions

We investigated the centrifugal separation of a monodispersed mixture in a nonrotating cylindrical domain with solid endplates both at the bottom and the top under the conditions

$$\mathrm{Ta} \ll 1 \quad \text{and} \quad \mathrm{Re}_p \ll 1.$$

Within the given range of parameters, a considerable increase in the particle concentration $\alpha(r, t)$ is achieved in very short dimensional times t^*. It was found that the concentration profiles as regards their shape and their absolute values, strongly depend on the kinematic viscosity ν^* of the suspending liquid. The secondary radial motion caused by the Ekman layers hinders the separation process.

As a further step it is intended to consider the influence of gravity and the mechanism of viscous resuspension of the sediment below the top plate inside the Ekman shear regions.

Acknowledgment

This work was supported by the Christian Doppler Laboratory for Continuous Solidification Processes and the Program of Scientific-Technological Cooperation Austria-Israel.

References

Bödewadt, U. T., 1940, "Die Drehströmung über festem Grunde," *Zeitschrift fur Angewandte Mathematik und Mechanik,* Vol. 20, p. 241.

Lewellen, W. S., 1962, "A Solution for Three-Dimensional Vortex Flows With Strong Circulation," *Journal of Fluid Mechanics,* Vol. 14, p. 420.

Richardson, J. F., and W. N. Zaki, 1954, "Sedimentation and Fluidization: Part I," *Transaction of the Institute of Chemical Engineers,* Vol. 32, p. 35.

Schaflinger, U., 1985, "Experiments on Sedimentation Beneath Downward-Facing Inclined Walls," *International Journal of Multiphase Flow,* Vol. 11, p. 189.

Schaflinger, U., 1990, "Centrifugal Separation of a Mixture," *Fluid Dynamics Research,* Vol. 6, p. 224.

Truckenbrodt, E., 1991, *Fluidmechanik,* Band 2, 3. Edition, Springer Berlin.

Ungarish, M., 1993, *Hydrodynamics of Suspensions,* Springer, Berlin.

Craig C. Jahnke
Visiting Assistant Professor,
Department of Mechanical, Aerospace,
Industrial and Manufacturing Engineering,
Polytechnic University, Brooklyn, NY 11201

Daniel T. Valentine
Associate Professor,
Department of Mechanical and
Aeronautical Engineering,
Clarkson University, Potsdam,
NY 13699-5725

Recirculation Zones in a Cylindrical Container

The flow field induced inside a cylindrical container by the rotation of the two end walls is described. It is shown that stagnation points leading to separation bubbles occur on the axis of rotation and/or the bottom end wall for certain ranges of the characteristic parameters; the Reynolds number, the aspect ratio of the container, and the ratio of the rotation rates of the end walls. Flow fields in a container of aspect ratio 2.0 are examined for Reynolds numbers from 100 to 3000 and ratios of the rotation rates of the top and bottom end walls from −0.10 to 1.0. For a range of ratios of the rotation rates of the top and bottom end walls and Reynolds numbers it is shown that ring vortices surrounding a columnar vortex core exist.

Introduction

Flows in closed cylindrical containers with one end wall rotating have been studied in great detail because under certain conditions stagnation points occur on the axis of rotation, leading to one or more separation bubbles. This phenomenon has been interpreted as a type of vortex breakdown. The structure of the single-bubble vortex breakdown phenomenon observed in the flow inside the cylinder is a type B breakdown as described by Leibovich (1984). Escudier (1984) showed experimentally that these separation bubbles tend to be axisymmetric in a large region of parameter space. Since flows in cylindrical containers with a rotating lid tend to be axisymmetric, computational investigations that solve the axisymmetric equations of motion can be used to study the details of these flows. This will further our understanding of vortex breakdown in general. These types of flows also have applications in chemical mixers and combustion chambers.

Vogel (1968, 1975) and Ronnenberg (1977) experimentally observed single bubble vortex breakdown in flows in a cylindrical container with one rotating end wall and mapped the region in Reynolds number-aspect ratio space where these breakdowns occurred. Escudier (1984) extended the previous work and mapped regions of one-, two- and three-bubble breakdowns as well as regions of oscillatory flows.

The computational study of Lugt and Haussling (1982) provides a preliminary glimpse into the onset of vortex breakdown in a cylinder caused by a rotating end wall. Lugt and Abboud (1987) extended this study and included the effects of thermal gradients to within the Boussinesq approximation. Lopez (1990), Brown and Lopez (1990), and Lopez and Perry (1992) describe the results of an extensive numerical investigation of the rotating end wall problem. They presented comparisons with the experimental observations reported by Escudier (1984), described the physical mechanism of the breakdown phenomenon in these flows, and described the details of two unsteady modes of motion (periodic internal separation and coalescence of bubbles).

Daube and Sorensen (1989) and Tsitverblit (1993) suggest that the unsteady flows occur as the result of a supercritical Hopf bifurcation as Reynolds number is increased beyond a critical value for an aspect ratio $\mathscr{AR} = H/R = 2.5$, where H is the height of the cylinder and R is its radius. This conjecture is plausible as Escudier (1984) did not find hysteresis at the location of the critical Reynolds number (he approached the critical value from above and below in his experimental investigation). Gelfgat et al. (1996a) determined the linear stability of the axisymmetric flows for aspect ratios between 1.0 and 3.5 and showed that oscillatory solutions indeed arise due to a supercritical Hopf bifurcation. Three modes of instability, depending on the aspect ratio of the container, were found to occur.

Spohn, Mory and Hopfinger (1993) and Spohn (1991) studied experimentally the flow with one rotating end wall, a fixed side wall and a free surface. This flow is analogous to the flow in the lower half-plane of a closed cylinder with both end walls rotating at the same rate if free surface effects are negligible. In that case the free surface acts as a pure-slip boundary. Spohn, Mory and Hopfinger found that recirculation bubbles occur for certain combinations of aspect ratio and Reynolds number and mapped regions of vortex breakdown and the boundary between steady and unsteady flow.

Valentine and Jahnke (1994) studied numerically the flow with both end walls rotating at the same rate and a fixed sidewall. Regions were mapped in Reynolds number-aspect ratio parameter space where different types of recirculation bubbles were found to occur. The evolution of the separation bubbles as the Reynolds number was varied for fixed aspect ratios was also discussed. The numerical results of Valentine and Jahnke compare favorably with the experimental results of Spohn, Mory and Hopfinger (1993) for aspect ratios larger than one, where free surface effects are negligible.

Roesner (1990) studied experimentally the flow in a cylinder with both end walls rotating and a fixed side wall. It was shown that a slight co-rotation of the second end wall tends to enhance the occurrence of recirculation bubbles while a slight counter-rotation of the second end wall tends to suppress formation of recirculation bubbles. Gelfgat et al. (1996b) determined steady and oscillatory solutions for this problem over a large region of parameter space. Linear stability analysis of the steady solutions showed that oscillatory solutions arise due to a supercritical Hopf bifurcation of the steady solution.

Watson and Neitzel (1996) studied the problem where the side wall and one end wall rotate at one angular velocity while the remaining end wall rotates at a different angular velocity. They determined regions in parameter space where recirculation regions occurred on the axis of the cylinder and analyzed whether the Brown and Lopez breakdown criteria could be used to predict incipient vortex breakdown. It was found that the criterion was not predictive, as it was only satisfied after a breakdown bubble had appeared.

In this paper we examine the recirculation bubbles (or 'vortex-breakdown' phenomena) that occur in flows in cylindrical containers when both end walls rotate at different rates with a fixed side wall. Significant changes are observed in the flow

Contributed by the Fluids Engineering Division for publication in the JOURNAL OF FLUIDS ENGINEERING. Manuscript received by the Fluids Engineering Division November 5, 1997; revised manuscript received July 7, 1998. Associate Technical Editor: D. P. Telionis.

field as the rotation rates of the bounding surfaces are varied. Several types of vortex breakdown occur including the well known internal-flow vortex breakdown that is predicted in the problem with only one end wall rotating as well as a breakdown in which a vortex ring surrounds a vortical core.

Computational Analysis

The geometry of the flow field analyzed in this study is a cylindrical container with rigid walls. The flow field driven by rotating the end walls is assumed to be axisymmetric. The equations describing the axisymmetric flow inside the cylindrical container are the equations for the azimuthal component of the vorticity, ω, the azimuthal component of the velocity (or swirl), v, and the meridional-plane stream function, ψ. The equations are:

$$\frac{\partial \omega}{\partial t} + \frac{1}{r}\frac{\partial ur\omega}{\partial r} + \frac{\partial w\omega}{\partial z} = 2\frac{v}{r}\frac{\partial v}{\partial z} + \frac{u\omega}{r} + \frac{1}{\mathrm{Re}}\left(\frac{\partial^2 \omega}{\partial r^2} + \frac{1}{r}\frac{\partial \omega}{\partial r} - \frac{\omega}{r^2} + \frac{\partial^2 \omega}{\partial z^2}\right), \quad (1)$$

$$\frac{\partial v}{\partial t} + \frac{1}{r}\frac{\partial urv}{\partial r} + \frac{\partial wv}{\partial z} + \frac{uv}{r} = \frac{1}{\mathrm{Re}}\left(\frac{\partial^2 v}{\partial r^2} + \frac{1}{r}\frac{\partial v}{\partial r} - \frac{v}{r^2} + \frac{\partial^2 v}{\partial z^2}\right), \quad (2)$$

$$\frac{\partial^2 \psi}{\partial r^2} - \frac{1}{r}\frac{\partial \psi}{\partial r} + \frac{\partial^2 \psi}{\partial z^2} = r\omega, \quad (3)$$

where

$$u = \frac{1}{r}\frac{\partial \psi}{\partial z}, \quad w = -\frac{1}{r}\frac{\partial \psi}{\partial r}, \quad (4)$$

and

$$\omega = \frac{\partial u}{\partial z} - \frac{\partial w}{\partial r}.$$

The u is the radial component of velocity and the w is the vertical component of velocity. The dimensionless parameter in Eqs. (1) and (2) is the Reynolds number, defined as $\mathrm{Re} = \Omega_t R^2/\nu$, where Ω_t is the rotation rate of the top end wall, R is the radius of the cylinder, and ν is the kinematic viscosity of the fluid inside the cylinder.

The no-slip boundary condition is imposed on all bounding surfaces of the cylindrical container while radial symmetry is imposed on the axis of the container. No-slip in the axial and radial velocities is imposed through the finite difference approximation to the definition of the vorticity in terms of the stream function, Eq. (3). Constant rotation rates are applied to the container side wall and the end walls, thus specifying constant azimuthal velocities on these surfaces. In addition, the condition of no mass flux through the container walls or the axis of symmetry is satisfied by imposing a zero value of the stream function on these surfaces. The boundary conditions are then:

$$a)\quad r = 0,\quad 0 \le z \le \mathscr{AR}:\quad \psi = 0,\quad \eta = 0,\quad v = 0$$

$$b)\quad 0 \le r \le 1,\quad z = \mathscr{AR}:\quad \psi = 0,\quad \frac{\partial \psi}{\partial z} = 0,\quad v = r$$

$$c)\quad r = 1,\quad 0 \le z \le \mathscr{AR}:\quad \psi = 0,\quad \frac{\partial \psi}{\partial r} = 0,\quad v = 0$$

$$d)\quad 0 \le r \le 1,\quad z = 0:\quad \psi = 0,\quad \frac{\partial \psi}{\partial z} = 0,\quad v = \beta r$$

where $\beta = \Omega_b/\Omega_t$, Ω_b is the rotation rate of the bottom end wall and Ω_t is the rotation rate of the top end wall. In the present work $\mathscr{AR} = 2$.

Steady solutions were calculated by: 1) using Eq. (4) to write Eqs. (1)–(3) in terms of ψ, v, and ω only, 2) setting all time derivatives equal to zero, 3) discretizing the resulting partial differential equations 4) applying a continuation method to the discretized equations. Second-order central differences are used to discretize the partial differential equations except at the boundaries where second-order one sided differences are used. The same pseudo arc-length continuation technique, based on the work of Doedel and Kernevez (1985), as used by Jahnke and Valentine (1996) is used here. A steady state was determined to have been reached when both (i) the residual of the discretized forms of Eqs. (1)–(3) and the boundary conditions was less than 10^{-6} at all grid points and (ii) the relative change of all variables in a Newton iterate was less than 10^{-6}. The Reynolds number and β are used as continuation parameters in the present study.

A nonuniform grid with 77 grid points in the radial direction and 137 grid points in the axial direction was used in the continuation computations. The nominal grid size in the radial and axial directions was 1/60, but extra grid points were packed near the bounding surfaces to resolve the boundary layers. Packing of grid points was obtained by progressively halving the grid size near the boundaries of the flow. This made it possible to use second ordered central differences throughout the flow field, even at grid points where the grid size changes by simply passing over a grid point when necessary. Additional details on the grid and numerical resolution can be found in Jahnke and Valentine (1996), including comparisons of results from three different grids.

Results and Discussion

The motivation for this study was to further our understanding of vortex breakdown in cylindrical containers. For the case of a single rotating lid, Brown and Lopez (1990) describe the physical mechanisms that lead to the occurrence of recirculation bubbles on the vortex core. The waviness of the streamlines near the vortex core is the result of a centrifugal wave and the resulting divergence of streamlines causes the production of negative azimuthal vorticity which induces the recirculation bubbles.

Brown and Lopez (1990) also point out that the core flow is nearly inviscid so angular momentum, $\Gamma = rv$, and head, $\mathscr{H} = P/\rho + (1/2)(u^2 + v^2 + w^2)$, are constant along streamlines. Since the centrifugal wave is primary to the vortex breakdown and the amplitude and wavelength of the wave depend on the initial values of Γ and $\mathscr{H}$, the history of the fluid particles entering the vortex core is important to the development of vortex breakdown. Indeed, Brown and Lopez (1990) point out that the influence of Reynolds number on vortex breakdown is mainly to change the distribution of Γ and $\mathscr{H}$ entering the vortex core.

Since the distribution of Γ and $\mathscr{H}$ entering the vortex core is affected by the boundary layers on the side wall and the stationary end wall, Valentine and Jahnke (1994) analyzed the flow in a cylindrical container with a pure slip boundary condition on the bottom end wall (equivalent to a midplane of symmetry for a container of twice the height). The distribution of Γ and $\mathscr{H}$ entering the vortex core is substantially different when a pure-slip boundary condition, as opposed to a no-slip boundary condition, is applied on the bottom end wall. As a result, the recirculation bubbles that occur when a pure slip condition is imposed on the bottom end wall are qualitatively different than the recirculation bubbles that occur when a no-slip condition is imposed on the bottom end wall. In particular recirculation bubbles occur at lower Reynolds numbers and evolve into toroidal vortices surrounding a vortical core when the pure slip boundary condition is used on the bottom end wall.

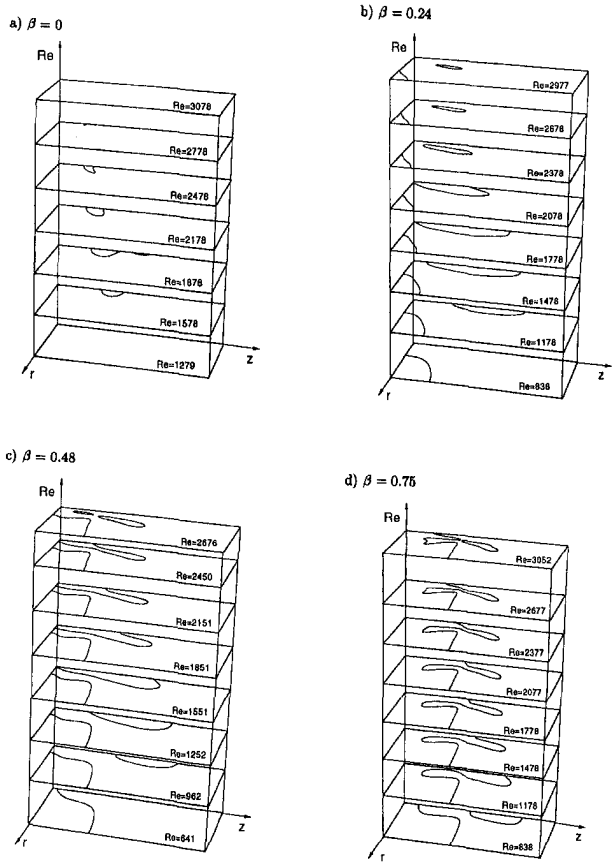

Fig. 1 Zero streamline contours

Based on this previous work we decided to examine the effect of rotating the bottom end wall along with the top end wall. Rotating the bottom end wall results in a centrifugal acceleration that causes a radial outflow along the bottom end wall and results in a recirculating region adjacent to the bottom end wall. Figure 1 shows, for $\mathcal{AR} = 2$, the zero streamlines as functions of Reynolds number for several values of β. For β equal to zero (fixed lower end wall) a single recirculation bubble occurs on the axis of rotation for Re = 1578 and a second bubble appears for Re = 1878. The second recirculation bubble disappears as the Reynolds number is increased while the first separation bubble moves toward the stationary end wall. Eventually the initial separation bubble also disappears. These results agree with Escudier (1984), Lopez (1990) and Gelfgat et al. (1996a, b). The movement of the separation points connected to the breakdown bubble is continuous. As a check for bifurcations of the flow field, the determinant of the Jacobian was evaluated in the continuation process. No sign changes were observed in any of the present calculations, so the bubbles occur as a result of the evolution of the flow field and are not a result of bifurcations. This agrees with the linear stability analysis of Gelfgat et al. (1996a, b).

A slight corotation of the bottom end wall changes the character of the breakdown bubble. Increasing β to 0.24 causes the recirculating region adjacent to the bottom end wall to grow larger as shown in Fig. 1(b). The bubble again appears initially as a slender vortex on the axis of rotation and resembles the slender body vortex discussed by Leibovich (1968). This bubble also migrates toward the bottom end wall as the Reynolds number is increased and the stagnation point closest to the bottom end wall moves onto the lower end wall and becomes a periodic point of the flow ($u = 0, w = 0, v \neq 0$). This point eventually moves back onto the axis of rotation as the Reynolds number is further increased. Eventually the two stagnation points come together and disappear resulting in a ring vortex that persists over a range of Reynolds numbers.

For $\beta = 0.48$ the topological features of the flow over most of the range of Reynolds numbers are qualitatively similar to the flow with $\beta = 0.24$. The recirculating region adjacent to the lower end wall is larger for larger values of β and a periodic point exists on the lower end wall for a much larger range of Reynolds numbers. One new feature is that the vortex ring that forms when the recirculating region detaches from the axis of rotation breaks into two rings for sufficiently large Reynold's numbers.

When $\beta = 0.75$, Fig. 1(d), the structure of the flow field is quite different than the structure of the flow field for smaller values of β. The recirculation bubble adjacent to the lower end wall is quite large and occupies most of the lower half of the meridional plane. At low Reynolds numbers a slender separation bubble occurs on the axis of rotation that is similar to the bubble that forms for lower values of β. As the Reynolds number is increased the separation points move towards the lower end wall. Near Re = 1100 the lower separation point of the recirculation bubble merges with the separation point of the lower recirculating region resulting in two recirculating regions separated by an undulating streamline. This flow field persists for Reynolds numbers up to 3000.

The above results concerning bubble onset and evolution are summarized in Fig. 2 which shows the critical values of Re and β at which separation bubbles first occur and at which transitions to different types of bubbles occur. It is seen that separation bubbles on the axis of rotation first occur at lower Reynolds numbers when the bottom end wall is rotated in the same direction as the rotation of the top end wall. The critical Reynolds number at which a separation bubble first appears on the axis of rotation increases very rapidly when the bottom lid is rotated in the direction opposite to that of the top lid (i.e., $\beta < 0$). For $\beta = -0.05$ no separation bubble was found to occur for Reynolds numbers up to 3000. This trend agrees with the experimental results of Roesner (1990). Gelfgat et al. (1996b) found recirculation bubbles for Re = 2000 and $\beta > -0.03$ and for larger negative values of β at Reynolds numbers above 3000.

To understand the effects of rotating the bottom lid, the case of $\beta = 0.48$ will be examined in detail. Figure 3 shows contour plots of the stream function, the swirl and the azimuthal vorticity for $\beta = 0.48$ and Re = 1000, 2000, 3100. Figure 3(a) shows that a separation bubble exists on the axis of rotation of the container and a recirculating region exists adjacent to the lower end wall for Re = 1000. It can be seen that one effect of the recirculating region in the lower corner is to decrease the effective height, and thus aspect ratio, of the container. Since vortex breakdown occurs at lower Reynolds numbers in lower aspect ratio containers (Escudier, 1984) the trend of earlier vortex breakdown with increasing rotation rate of the bottom end wall

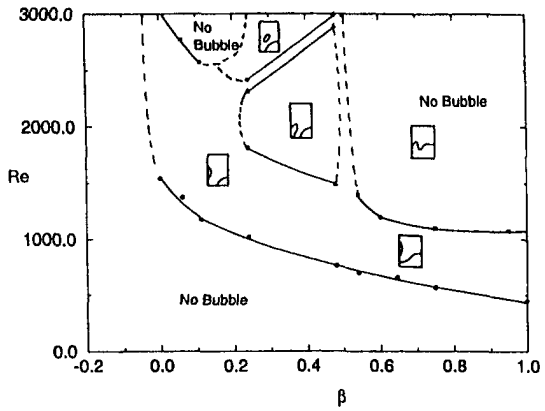

Fig. 2 Cartoons of recirculation regions

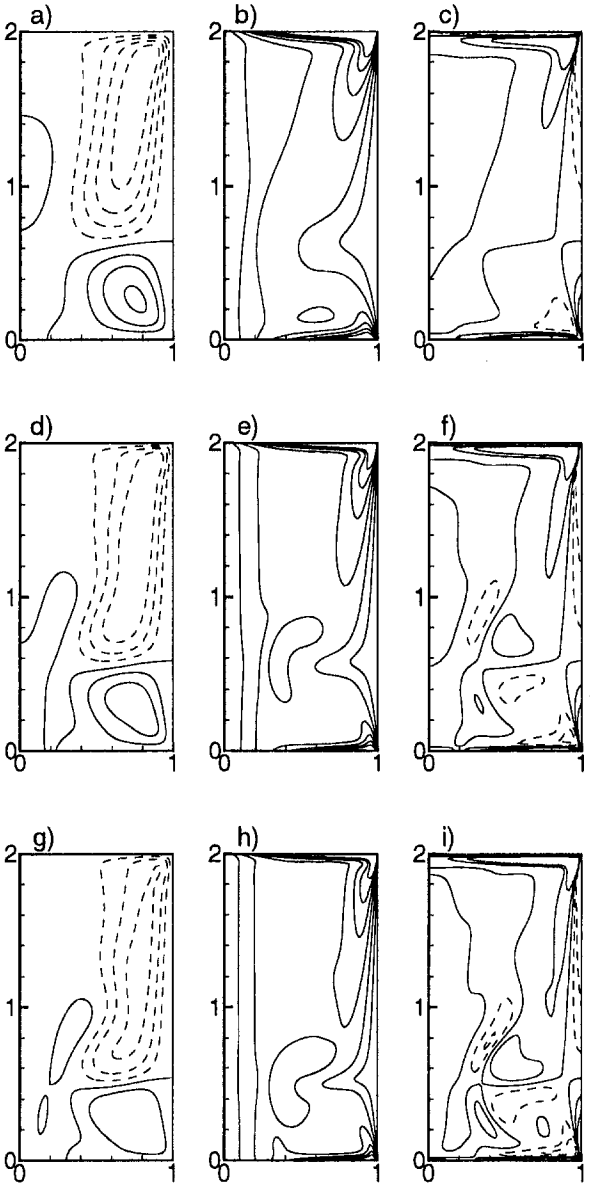

Fig. 3 Contour plots of the stream function (*a*, *d*, *g*), swirl (*b*, *e*, *h*) and azimuthal vorticity (*c*, *f*, *i*) for $\beta = 0.48$ and Re = 1000 (*a*, *b*, *c*), Re = 2000 (*d*, *e*, *f*), Re = 3100 (*g*, *h*, *i*)

may be partially explained by the decrease in the effective aspect ratio of the container as the rotation rate of the bottom lid is increased. For Re = 2000, Fig. 3(*d*), the breakdown bubble has moved toward the bottom end wall and the stagnation point closest to the bottom end wall has moved onto the end wall and become a periodic point of the flow ($u = 0$, $w = 0$, $v \neq 0$). The downward movement of the breakdown bubble with increasing Reynolds number is due to the increased negative azimuthal vorticity in the core region that results from vorticity tilting and stretching, $(v/r)(\partial v/\partial z)$. It is this increased negative azimuthal vorticity that causes the lower stagnation point to move onto the bottom end wall. It should be noted that the velocities in the r and z directions near the core are very small (as can be inferred from the streamlines).

Another effect of the recirculating region in the lower corner is to increase the swirl and thus the angular momentum turned toward the axis of rotation. The outer streamline of the recirculating region adjacent to the lower end wall acts similar to a pure-slip boundary to the meridional flow created by the top end wall. Very little dissipation of angular momentum occurs along this surface except in the boundary layers along the side wall and bottom end wall.

For the case of a fixed bottom end wall, the boundary layer present along the bottom end wall dissipates angular momentum as illustrated in Fig. 4, which shows contour plots of the stream function, the swirl, and the azimuthal vorticity for Re = 2000 and $\beta = 0$. Whereas Fig. 4(*b*) shows that the swirl does not increase as the fluid approaches the axis of rotation (because angular momentum is dissipated in the boundary layer along the fixed bottom end wall), Fig. 3(*e*) shows that the swirl increases as the fluid moves toward the axis of rotation (because angular momentum is conserved along the streamline separating the recirculating region adjacent to the lower end wall from the meridional flow produced by the top end wall).

As discussed by Brown and Lopez (1990) the distribution of Γ entering the vortex core along the axis of rotation is important to vortex breakdown. Since the core flow is essentially inviscid, the centrifugal wave that eventually leads to the breakdown is controlled by the upstream distribution of Γ and $\mathcal{H}$. Increased swirl entering the region of the vortex core results in a core region less receptive to radial disturbances causing the fluid to turn toward the top end wall at a greater distance from the core (cf. Figs. 3(*d*) and 4(*a*)). Note that the same contour levels are plotted in all figures so a direct comparison of the figures is possible.

The Brown and Lopez criterion that the helix angle of the velocity vector must be greater than the helix angle of the vorticity vector on a streamsurface near the core upstream of the breakdown bubble for breakdown to occur is satisfied for the flow with the rotating bottom end wall. It is found that the helix angle of the velocity is greater than the helix angle of the vorticity along the entire core except in the regions near and inside the breakdown bubble. The Brown and Lopez criterion is also satisfied before a breakdown bubble appears.

As the Reynolds number is further increased the periodic point on the lower end wall migrates back to the axis of rotation, becoming a stagnation point again, and the upper stagnation point on the axis of rotation moves downward. When the two stagnation points along the axis of rotation meet and annihilate each other the bubble does not collapse as is the case with the fixed bottom end wall, but a ring vortex is formed as shown in Fig. 3(*g*). The Brown and Lopez criterion for vortex breakdown was also applied to this flow and it was found to be satisfied in the entire core region except in the region of the ring vortex. Again it must be noted that the Brown and Lopez criterion for breakdown was developed for a flow situation quite different from the present case, but since the criterion concerns the necessary condition for the production of negative azimuthal vorticity on a diverging streamtube, a situation that occurs in the present flow, it is not surprising that it is satisfied for the flows under consideration here.

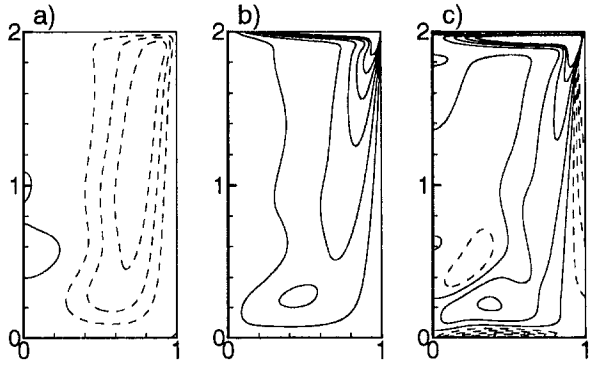

Fig. 4 Contour plots for $\beta = 0$, and Re = 2000; (*a*) stream function, (*b*) swirl. (*c*) Azimuthal vorticity

There is a notable decrease in the size and strength of the recirculating region adjacent to the lower end wall as the Reynolds number is increased. This occurs because there is an enhancement of the meridional flow induced by the upper end wall at the higher Reynolds number. Also, the effect of viscous diffusion along the stationary side wall is reduced as the Reynolds number in increased. Thus, the Ekman layer on the bottom end wall must counteract a stronger flow coming from the top end wall. Additionally, the Taylor-Proudman Theorem suggests that the meridional flow will become weaker as the axial rotation of the fluid is increased and the axial rotation of the fluid increases with Reynolds number as there is less dissipation.

Acknowledgment

Partial funding for this work was provided by the National Science Foundation under Grant Numbers INT-8819665 and CMS-9409025 and the National Aeronautics and Space Administration under Grant Number OSP-5039.

References

Brown, G. L., and Lopez, J. M., 1990, "Axisymmetric Vortex Breakdown. Part 2. Physical Mechanisms," *Journal of Fluid Mechanics,* Vol. 221, p. 553.

Daube, O., and Sorensen, J. N., 1989, "Simulation numérique de l'écoulement périodique axisymétrique dans une cavité cylindrique," *Comptes Rendus de l'Academie des Sciences des Paris,* Vol. 308, p. 463.

Doedel, E. J., and Kernevez, J. P., 1985, "Software for Continuation Problems in Ordinary Differential Equations with Applications," Preprint, California Inst. of Tech., Pasadena, CA.

Escudier, M. P., 1984, "Observations of the Flow Produced in a Cylindrical Container by a Rotating End Wall," *Experiments in Fluids,* Vol. 2, p. 189.

Gelfgat, A. Y., Bar-Yoseph, P. Z., and Solan, A., 1996a, "Stability of Confined Swirling Flow with and Without Vortex Breakdown," *Journal of Fluid Mechanics,* Vol. 311, p. 1.

Gelfgat, A. Y., Bar-Yoseph, P. Z., and Solan, A., 1996b, "Steady States and Oscillatory Instability of Swirling Flow in a Cylinder with Rotating Top and Bottom," *Physics of Fluids,* Vol. 8, p. 2614.

Jahnke, C. C., and Valentine, D. T., 1996, "Boundary Layer Separation in a Rotating Container," *Physics of Fluids,* Vol. 8, p. 1408.

Leibovich, S., 1968, "Axially-Symmetric Eddies Embedded in a Rotational Stream," *Journal of Fluid Mechanics,* Vol. 32, p. 529.

Leibovich, S., 1984, "Vortex Stability and Breakdown: Survey and Extension," *AIAA Journal,* Vol. 22, p. 1192.

Lopez, J. M., 1990, "Axisymmetric Vortex Breakdown. Part 1. Confined Swirling Flow," *Journal of Fluid Mechanics,* Vol. 221, p. 533.

Lopez, J. M., and Perry, A. D., 1992, "Axisymmetric Vortex Breakdown. Part 3. Onset of Periodic Flow and Chaotic Advection," *Journal of Fluid Mechanics,* Vol. 234, p. 449.

Lugt, H. J., and Abboud, M., 1987, "Axisymmetric Vortex Breakdown with and Without Temperature Effects in a Container with a Rotating Lid," *Journal of Fluid Mechanics,* Vol. 179, p. 179.

Lugt, H. J. and Haussling, H. J., 1982, "Axisymmetric Vortex Breakdown in Rotating Fluid within a Container," ASME *Journal of Applied Mechanics,* Vol. 49, p. 921.

Roesner, K. G., 1990, "Recirculating Zones in a Cylinder with Rotating Lid," *Topological Fluid Mechanics, Proc. IUTAM Symp. Cambridge,* 1989 (Moffat, K.; Tsinober, A.), London, Cambridge University Press.

Ronnenberg, B., 1977, "Ein selbstjustierendes 3-Komponenten-Laserdoppler-anemometer nach dem Vergleichsstrahlverfahren, angewandt für Untersuchungen in einer stationären zylinder-symmetrischen Drehströmung mit einem Rückstromgebiet," Max-Planck-Institut für Strömungsforschung, Göttingen, Bericht, 20.

Spohn, A., 1991, "Ecoulement et éclatement tourbillonaires engendré par une disque tournant dans une enceinte cylindrique," Thèse de Doctorat d'Université, Université Joseph Fourier Grenoble I.

Spohn, A., Mory, M., and Hopfinger, E. J., 1993, "Observations of Vortex Breakdown in an Open Cylindrical Container with a Rotating Bottom," *Experiments in Fluids,* Vol. 14, pp. 70–77.

Tsitverblit, N., 1993, "Vortex Breakdown in a Cylindrical Container in the Light of Continuation of a Steady Solution," *Fluid Dynamics Research,* Vol. 11, p. 19.

Valentine, D. T., and Jahnke, C. C., 1994, "Flows Induced in a Cylinder with Both End Walls Rotating," *Physics of Fluids,* Vol. 6 (8), pp. 2702–10.

Vogel, H. U., 1968, "Experimentelle Ergebnisse über die laminare Strömung in einem zylindrischen Gehäuse mit darin rotierender Scheibe," Max-Planck-Institut für Strömungsforschung, Göttingen, Bericht 6.

Vogel, H. U., 1975, "Rückströmungsblasen in Drallströmungen. Festschrift 50 Jahre," Max-Planck-Institut für Strömungsforschung, Göttingen, Bericht, 1925.

Watson, J. P., and Neitzel, G. P., 1996, "Numerical Evaluation of a Vortex-Breakdown Criterion," *Physics of Fluids,* Vol. 8, p. 3063.

T. Mullin
Professor,
Department of Physics and Astronomy,
The University of Manchester,
Manchester M13 9PL, United Kingdom

S. J. Tavener
Associate Professor,
Department of Mathematics,
Pennsylvania State University,
State College, PA

K. A. Cliffe
Chief Mathematical Modeller,
AEA Technology, Harwell, United Kingdom

On the Creation of Stagnation Points in a Rotating Flow

We report the results of a numerical study of the creation of stagnation points in a rotating cylinder of fluid where both endwalls are rotated. Good agreement is found with previous results where the stagnation points are formed on the core of the primary columnar vortex. Novel phenomena have been uncovered at small aspect ratios where stagnation occurs off-axis directly and the secondary vortex which is created forms a toroid. The case is then considered of a small cylinder placed along the center of the flow and despite the qualitatively different boundary condition, the phenomena are found to be robust.

1 Introduction

The steady flow in a cylinder where one or both endwalls rotate has been the subject of a great deal of numerical and experimental research. The case where one endwall rotates was first studied by Vogel (1968) in a combined numerical and experimental investigation. He showed that the primary flow was a columnar vortex which developed a pair of stagnation points midway along its central core above a certain Reynolds number, Re. An axisymmetric secondary recirculation was thus created and Vogel suggested that this situation could be considered as a weak steady form of the important and yet ill-understood problem of vortex breakdown (see e.g., Hall, 1972). This interpretation of events is still not widely accepted (see e.g., Keller, 1995) and perhaps this focus of the debate detracts from what is an interesting internal vortex flow. It is appealing in that it is one of the few fluid mechanical situations where close quantitative comparison can be made between numerical calculation and experimental observation. It also has technological implications for a diverse range of flow situations such as swirl combustion chambers, flow between shrouded computer disks and in satellite fuel containers. In all of these situations, a deeper understanding of the origin and location of stagnation points could prove vital in gaining insight into the origins of time dependence and hence more complicated motions.

Vogel's original work was extended by Escudier (1984) who carried out a systematic experimental study. He established the range of existence of the secondary vortices in terms of the two control parameters Re and the aspect ratio Γ. In particular, he showed that the secondary vortices exist over a finite range of Re, i.e., they appear above a certain value of Re and disappear above a greater one. He also showed that they do not form for $\Gamma \leq 1.0$ and that multiple steady vortices and time-dependence exists at sufficiently large Γ and Re.

Escudier's results have stimulated several numerical and experimental investigations. Perhaps the most extensive discussion of the phenomena are given in a series of papers by Lopez and his collaborators (1990a, 1990b, 1992). These results are broadly in agreement with Escudier's observations and the insight gained from the numerical investigation has been used to establish a criterion for the onset of the secondary recirculation. Further numerical investigations were performed by Tsitverblit (1993) who used continuation methods with the steady Navier Stokes equations to show that the secondary vortices do not appear critically at a bifurcation point but rather evolve smoothly with increase of Re.

In more recent investigations the focus of attention has moved towards variants of the original problem. These include counter and co-rotation of both ends of the cylinder by Jahnke and Valentine (1996) and Gelfgat, Bar-Yoseph and Solan (1996), flow with a free surface by Hyun (1985) and Spohn, Mary and Hopfinger (1993) and symmetric rotation of both ends by Valentine and Jahnke (1994). The counter and corotation of ends has been found to either suppress or enhance the secondary vortex, respectively. It is the configuration where both ends co-rotate at the same speed which is the subject of our investigation, since it provides new and interesting features which are not present in the original problem of a singly rotated end.

Valentine and Jahnke's work was inspired by Spohn et al.'s experiments with a free surface. They show that by changing the end boundary from a stationary wall as in the original problem, to a free surface, so the upper limiting Re for the recirculation is removed. Their calculations are for the case where the aspect ratio is greater than one. Instead of disappearing as Re is increased, the recirculation intensifies and migrates from the central core to a point off-axis. Hence, the stagnation point becomes a circular stagnation line or periodic point of the flow and the recirculation bubble forms a torus. In Valentine and Jahnke's numerical model both ends rotate at the same speed so that the central plane is equivalent to the free surface of the experiment. Now, two pairs of stagnation points are formed at sufficiently large Re so that a pair of recirculation bubbles are equally disposed about the mid-plane. It is established that there is no upper limit to the existence of the secondary recirculation bubbles and broad agreement between theory and experiment is obtained. In addition, the bubbles are also found to migrate from the core to off-axis locations as Re is increased, so that a toroidal bubble is formed and the stagnation points become periodic points of the flow as in the free surface experiments. These results were confirmed and extended to include the onset of time-dependence by Lopez (1995) for the symmetric driven ends case with aspect ratio 1.5.

The aim of the present study is to extend the parameter range studied by Valentine and Jahnke to include aspect ratios smaller than one where novel phenomena are uncovered. We study the steady, axisymmetric Navier Stokes equations using the numerical continuation program called ENTWIFE (Cliffe, 1996) which we have used extensively to obtain good quantitative agreement between calculation and experiment for Taylor-Couette flows (see e.g., Cliffe, Kobine and Mullin, 1992). The weight of numerical and experimental evidence suggests that the creation of the secondary recirculation is a steady axisymmetric

Contributed by the Fluids Engineering Division for publication in the JOURNAL OF FLUIDS ENGINEERING. Manuscript received by the Fluids Engineering Division November 5, 1997; revised manuscript received July 9, 1998. Guest Editor: D. T. Valentine.

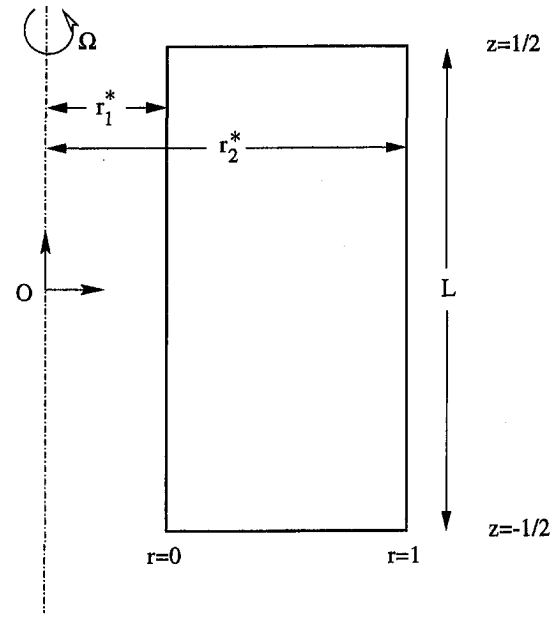

Fig. 1 Schematic of the computational domain

phenomenon and hence this approach seems justified. We then consider the situation where a thin solid cylinder is placed along the central core. This qualitative change in the inner boundary condition is, perhaps surprisingly, shown to have little effect on the results. We consider the cases where the inner cylinder rotates with the endwalls and where it is stationary and compare and contrast the results. Finally, we investigate the effects of increasing the diameter of the inner cylinder to see if the phenomena persist into parameter regimes normally associated with Taylor-Couette flows.

2 Formulation of the Problem and Numerical Technique

We computed steady, axisymmetric flows of an incompressible Newtonian fluid in bounded cylindrical or annular domains. The restriction to axisymmetric flows enabled the computations to be performed in two-dimensional (radial) domains, as shown in Fig. 1. Superscripts (*) denote dimensional quantities. Three different flow configurations were investigated. In each case the top and bottom surfaces rotated with the same angular velocity Ω. We considered; (i) no inner cylinder (for which $r_1^* = 0$), (ii) a stationary inner cylinder, and, (iii) an inner cylinder rotating with angular velocity Ω.

The primative variable formulation of the incompressible steady, axisymmetric Navier-Stokes equations was solved via the finite-element method, using quadrilateral elements with biquadratic interpolation of the velocity field and discontinuous piecewise linear interpolation of the pressure field. The length and velocity scales, and therefore the Reynolds number and aspect ratio, depended upon the problem at hand.

(i): No Inner Cylinder. The natural length and velocity scales were the radius of the container r_2^* and Ωr_2^* respectively. The Reynolds number, $R = \Omega(r_2^*)^2/\nu$ and the aspect ratio, $\Gamma = L^*/r_2^*$. We defined $r = r^*/r_2^*$, $z = z^*/\Gamma r_2^*$, $u_r = \Gamma u_r^*/\Omega r_2^*$, $u_\theta = u_\theta^*/\Omega r_2^*$ and $u_z = u_z^*/\Omega r_2^*$. The computational domain was therefore

$$\{(r, z) \in [0, 1] \times [-0.5, 0.5]\}$$

and the boundary conditions were

$$\begin{cases} u_r = 0 \\ u_\theta = r, \quad \text{on} \quad z = \pm 0.5 \\ u_z = 0 \end{cases}$$

$$\begin{cases} u_r = 0 \\ \dfrac{\partial u_\theta}{\partial r} = 0, \quad \text{on} \quad r = 0 \\ \dfrac{\partial u_z}{\partial r} = 0 \end{cases}$$

$$\begin{cases} u_r = 0 \\ u_\theta = 0, \quad \text{on} \quad r = 1 \\ u_z = 0 \end{cases}$$

(ii): Stationary Inner Cylinder. The natural length and velocity scales were the gap width $d^* = r_2^* - r_1^*$ and Ωr_1^* respectively. The Reynolds number, $R = \Omega r_1^* d^*/\nu$, the aspect ratio, $\Gamma = L^*/d^*$, and the radius ratio $\eta = r_1^*/r_2^*$. We defined $r = (r^* - r_1^*)/d^*$, $z = z^*/\Gamma d^*$, $u_r = \Gamma u_r^*/\Omega r_1^*$, $u_\theta = u_\theta^*/\Omega r_1^*$ and $u_z = u_z^*/\Omega r_1^*$. The computational domain was again

$$\{(r, z) \in [0, 1] \times [-0.5, 0.5]\}$$

and the boundary conditions were

$$\begin{cases} u_r = 0 \\ u_\theta = 1 + \left(\dfrac{1-\eta}{\eta}\right) r, \quad \text{on} \quad z = \pm 0.5, \\ u_z = 0 \end{cases}$$

$$\begin{cases} u_r = 0 \\ u_\theta = 0, \quad \text{on} \quad r = 0, 1. \\ u_z = 0 \end{cases}$$

(iii): Rotating Inner Cylinder. The length and velocity scales were the same as for (ii) and the same nondimensionalization was applied. The boundary conditions were

$$\begin{cases} u_r = 0 \\ u_\theta = 1 + \left(\dfrac{1-\eta}{\eta}\right) r, \quad \text{on} \quad z = \pm 0.5, \\ u_z = 0 \end{cases}$$

$$\begin{cases} u_r = 0 \\ u_\theta = 1, \quad \text{on} \quad r = 0 \\ u_z = 0 \end{cases}$$

$$\begin{cases} u_r = 0 \\ u_\theta = 0, \quad \text{on} \quad r = 1. \\ u_z = 0 \end{cases}$$

Most of the calculations were carried out using 24 × 28 elements but some were also performed using 48 × 56 elements to check details. No appreciable difference was found between the results. Appropriate corner refinement of the finite-element mesh and smoothing of the velocity discontinuities was employed. Details of both may be found in Tavener, Mullin and Cliffe (1990). Arclength continuation methods were used to follow solution branches in (R, Γ, η) parameter space. The

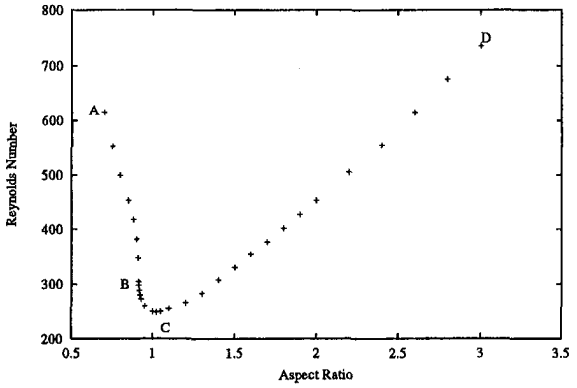

Fig. 2 Plot of domain of existence of recirculation bubble on the (Re, Γ) plane. The bubble exists above the curve ABCD.

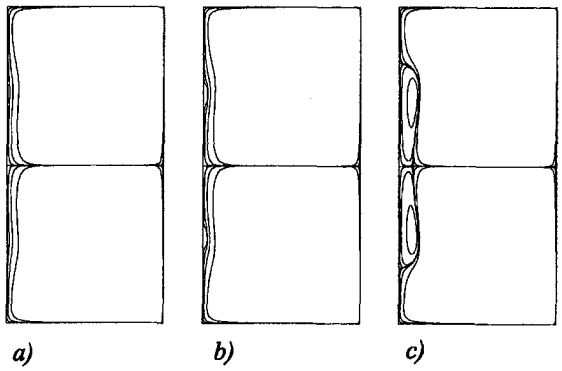

Fig. 3 Half-plane streamline plots for $\Gamma = 2$ and (*a*) Re = 450 (*b*) Re = 455 and (*c*) Re = 500. In each case there is no inner cylinder present. In each figure $\psi = \pm 1 \times E^{-7}$ to $\pm 1 \times E^{-4}$ in steps of $1 \times E^{-1}$ and 0.

streamfunction was computed from the primative variable solution.

As pointed out by Tsitverblit (1993), the onset of the recirculation bubble is a continuous process and so an estimate of its appearance requires an extra criterion. This is not a straightforward procedure since the bubble is typically very weak compared with the primary vortex and the spatial location depends on Γ. The first point is often not commented on in the literature where streamlines for the primary and secondary vortices are most often plotted using non-uniform scaling to emphasise the bubble. This has the obvious advantage of enhancing the structure of the bubble but it may give a misleading impression of its strength. The effect of the weakness of the bubble is compounded by the varying spatial location of its onset and this rendered all attempts to automatically detect its appearance ineffective.

The method we used to detect the first onset of the bubble was to simply visually inspect the streamline plots calculated for fixed Γ when Re was increased in ~1 percent steps. A bubble was deemed to be present when a visable area was first enclosed by the zero streamline. In practice, the bubble grows rapidly with Re and so we are confident that this is a reliable criterion which is robust. Moreover, our results are in good quantitative agreement with the limited data set available from Valentine and Jahnke (1994) who used alternative methods.

3 Results

The results for the boundary of the range of existence of the secondary recirculations on the (Re, Γ) plane for the case of no inner cylinder are shown in Fig. 2. We have decided to show the results as a series of points rather than a fitted curve to emphasise that these are estimates of the bubble onset obtained using the methods described above. For parameter values below the line of points labeled ABCD, only the primary vortex exists and the secondary recirculation bubbles form when this curve is crossed by varying either Re or Γ.

In the aspect ratio range *C* to *D* two pairs of stagnation points are formed on the core of the primary vortex. We show a typical sequence of streamline plots for this range of Γ in Fig. 3. All the streamline plots are shown in the computational domain

$$\{(r, z) \in [0, 1] \times [-0.5, 0.5]\}$$

shown schematically in Fig. 1. This corresponds to one half of a cross-sectional slice through the axisymmetric domain. We have chosen small streamline values to emphasise the bubble and hence omitted those for the primary vortex which are typically two to three orders of magnitude greater. They were calculated for $\Gamma = 2.0$ and (*a*) Re = 450, (*b*) Re = 455, and (*c*) Re = 500. It can be seen that the recirculations appear on axis between Re = 450 and 455 and subsequently increase in size and strength as Re is increased.

The next sequence of streamline plots shown in Fig. 4 were calculated at $\Gamma = 0.8$ and (*a*) Re = 500, (*b*) Re = 505, and (*c*) Re = 520 and are typical of events at onset in the aspect ratio range *A* to *B* in Fig. 2. Distortion of the streamline patterns such as in Fig. 4(*a*), is first seen at Re ~ 450. However, flow reversal and the enclosure of a detectable area by the zero streamline is first evident at Re = 505 as in Fig. 4(*b*). The recirculations now form a toroidal vortex whose inner and outer limits are set by circles of stagnation lines around the generator of the cylinder. Hence the stagnation points are now periodic points of the flow. These toroidal vortices have been reported previously by Valentine and Jahnke (1994) and Spohn et al. (1993), but in those cases the bubbles were initially formed on the core and they subsequently migrated to an off-axis position as Re was increased. We believe that the present results are the first calculations of the direct onset of these toroidal vortices.

In the aspect ratio range B to C in Fig. 2, a mixed stage is observed where there is a pair of stagnation points on the axis and a single circular stagnation line off-axis. Thus there is a smooth change in the type of recirculation bubble formed at onset involving the coalescence of pairs of stagnation points. For large Γ a pair of on-axis bubbles is formed at onset while for small Γ a toroidal vortex develops. It is clear that there is no lower limit to the aspect ratio range for the existence of these secondary vortices. These results are in agreement with the speculation of Spohn et al. who suggested that this should be the case but were unable to pursue this point in their experimental investigation due to technical difficulties.

The above results show that stagnation points need not necessarily form initially on the central core of the flow. Indeed, Jahnke and Valentine (1996) have shown that separation may also occur on the outer boundary of the cylinder when it is made to rotate. All of this evidence suggests that if a small cylinder is placed along the central core of the flow then one might expect toroidal vortices to appear above a certain range

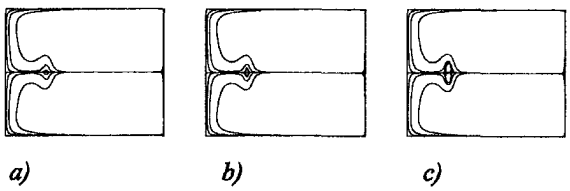

Fig. 4 Half-plane streamline plots for $\Gamma = 0.8$ and (*a*) Re = 500 (*b*) Re = 505 and (*c*) Re = 520. In each case there is no inner cylinder present. In each figure $\psi = \pm 1 \times E^{-7}$ to $\pm 1 \times E^{-4}$ in steps of $1 \times E^{-1}$ and 0.

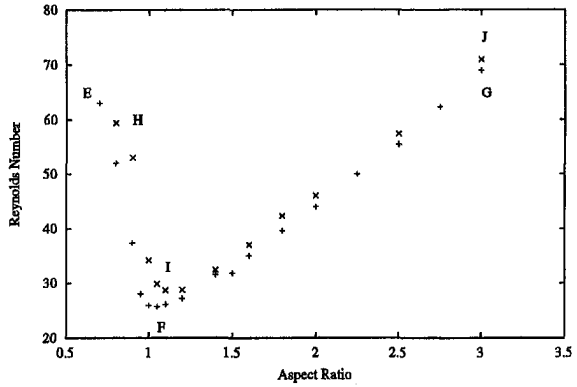

Fig. 5 The range of existence of the recirculating bubbles with inner cylinders present plotted as a function of Re and Γ. The locus labeled EFG is for a rotating inner cylinder and HIJ for a stationary one. In both cases the radius ratio is set to 0.1.

of Re. We therefore decided to investigate this possibility and the results for the range of existence of these secondary vortices are shown in Fig. 5.

We studied two different versions of the problem. In one, the inner cylinder rotated with the ends while in the other it remained stationary. The set of points for the case where the inner cylinder rotates with the ends is labeled EFG while that for a stationary cylinder is labeled HIJ in Fig. 5. The radius ratio of the two cylinders was set to 0.1 for all of these calculations. It is immediately clear that they have the same qualitative form as each other and are also the same as the set shown in Fig. 2 where there is no inner cylinder present. The locus of points for the stationary cylinder case is above that for the rotating one indicating that rotation assists the onset of the recirculation bubble.

It may also be seen in Fig. 5 that the minima of the curves are all at approximately the same aspect ratio in all three cases. The scaling for Re now involves the radius of the inner cylinder and the gap width which is the convention for Taylor-Couette flows. Hence the ratio of this Reynolds number and that defined for the case when no inner cylinder is present involves

$$\eta(1 - \eta).$$

Thus the minimum for the case of a rotating cylinder would be ≈28.0 and that for a stationary one is ≈32.0. Hence in the cases where an inner cylinder is present the minimum is ~10 percent of the corresponding value for no cylinder.

We show in Figs. 6 and 7 the streamline sequences for the onset of the bubbles for aspect ratios 2 and 0.8 where a rotating inner cylinder is present. The sequences for a stationary inner

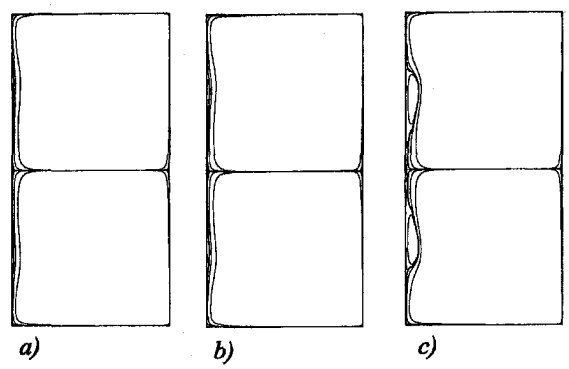

Fig. 6 Half-plane streamline plots for Γ = 2.0 and (*a*) Re = 43 (*b*) Re = 44 and (c) Re = 50. In each case a rotating cylinder is present at the left-hand edge of the figure. In each figure $\psi = \pm 1 \times E^{-7}$ to $\pm 1 \times E^{-4}$ in steps of $1 \times E^{-1}$ and 0.

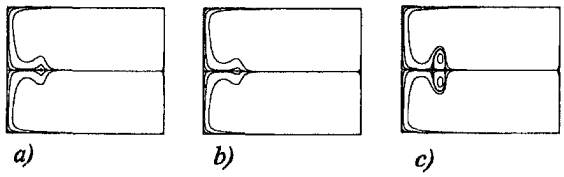

Fig. 7 Re = 52 and (*c*) Re = 60. In each case a rotating cylinder is present at the left-hand edge of the figure. In each figure $\psi = \pm 1 \times E^{-7}$ to $\pm 1 \times E^{-4}$ in steps of $1 \times E^{-1}$ and 0.

cylinder exhibit the same features except that they are displaced to slightly higher Reynolds numbers. It can be seen that the streamline patterns are qualitatively similar to those shown in Figs. 3 and 4 when there was no inner cylinder present. A pair of toroidal recirculation bubbles are formed near the inner cylinder at the larger value of Γ and as an off-axis toroidal vortex for Γ = 0.8. The formation sequence shown in Fig. 6 is perhaps less distinct than in the case when there is no cylinder present but when viewed in detail it can still be distinguished. Hence, the addition of a small cylinder has not produced any qualitatively different features. There are some weak effects but they are subtle and will require more research before any definite statements can be made.

We now turn our attention to the effect of the radius ratio of the two cylinders on the onset of the stagnation points in these rotating flows. This investigation was carried out using the case where the inner cylinder rotates with the ends. We show in Fig. 8 the Reynolds number for the onset of the bubble at Γ = 1 plotted as a function of the radius ratio η. A curve has been fitted through the calculated data points using least squares. It can be seen that the Reynolds number for onset is greatly affected by η and rises steeply as $\eta \to 0.5$. At these Reynolds numbers in Taylor-Couette type flows a strong time dependence would occur and so it is unlikely that they will be observable in an experiment. However, flows with similar vortex structure have been found in Taylor-Couette and related flows by Lensch (1988) and Kobine and Mullin (1994). Both cases involved experiments with a single primary vortex which developed a small secondary vortex above a certain range of Reynolds numbers. Hence the situation is analogous to the present one but the relationship plotted in Fig. 8 suggests that any link may be coincidental.

The lower curve shown in Fig. 8 was obtained using the relationship $250\eta(1 - \eta)$ which should hold if there is a simple scaling between the case with no cylinder and the present one. If the onset of the bubble is unaffected by the presence of the cylinder the Reynolds numbers with and without the inner boundary should have a simple geometrical relationship. It can be seen that this is a reasonable approximation for values of η

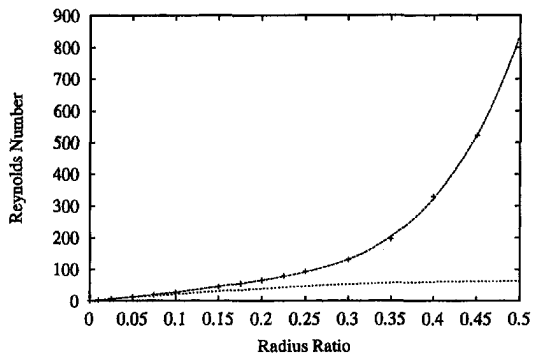

Fig. 8 Graph of the onset Reynolds number for a recirculation bubble for aspect ratio 1.0 plotted as a function of radius ratio. A curve has been fitted to the calculated points. The lower curve shows the relationship $250\eta(1 - \eta)$.

≤ 0.1 and thereafter the inner cylinder has a strong effect on the flow field.

4 Conclusions

The numerical results reported here agree with previous calculations and observations for the onset of recirculation bubbles within internal rotating flows. We have extended the investigation to small aspect ratios and found the first evidence for the direct onset of off-axis toroidal bubbles which ought to be observable in an experiment. We have also shown that the flow is relatively insensitive to qualitative changes in the inner boundary condition which were achieved by introducing solid cylinders along the central axis. This is true as long as the radius ratio of the two cylinders is less than 0.1.

Acknowledgments

We are grateful to Pedro Reis for help with preparing the manuscript.

References

Brown, G. L., and Lopez, J. M., 1990, "Axisymmetric Vortex Breakdown. Part 2. Physical Mechanisms," *Journal of Fluid Mechanics,* Vol. 221, pp. 553–576.

Cliffe, K. A., 1996, "ENTWIFE (Release 6.3) Reference Manual: ENTWIFE, INITIAL DATA and SOLVER DATA Commands," AEAT-0823.

Cliffe, K. A., Kobine, J. J., and Mullin, T., 1992, "The Role of Anomalous Modes in Taylor-Couette Flow," *Proceedings of the Royal Society of London,* Series A, Vol. 439, pp. 341–357.

Escudier, M. P., 1984, "Observations of the Flow Produced by a Rotating End Wall," *Experiments in Fluids,* Vol. 2, pp. 189–196.

Gelfgat, A. Y., Bar-Joseph, P. Z., and Solan, A., 1996, "Steady States and Oscillatory Instability of Swirling Flow in a Cylinder with Rotating Top and Bottom," *Physics of Fluids,* Vol. 8, pp. 2614–2625.

Hall, M. G., 1972, "Vortex Breakdown," ASME *Annual Reviews of Fluid Mechanics,* Vol. 4, pp. 195–218.

Hyun, J. M., 1985, "Flow in an Open Tank with a Free Surface Driven by the Spinning Bottom," ASME JOURNAL OF FLUIDS ENGINEERING, Vol. 107, pp. 495–499.

Jahnke, C. C., and Valentine, D. T., 1996, "Boundary Layer Separation in a Rotating Container," *Physics of Fluids,* Vol. 8, pp. 1408–1414.

Keller, J. J., 1995, "On the Interpretation of Vortex Breakdown," *Physics of Fluids,* Vol. 7, pp. 1695–1702.

Kobine, J. J., and Mullin, T., 1994, "Low-Dimensional Bifurcation Phenomena in Taylor-Couette Flow with Discrete Azimuthal Symmetry," *Journal of Fluid Mechanics,* Vol. 275, pp. 379–405.

Lensch, B., 1988, "Uber die Dynamik der Einwirbelstromung im Taylor-Zylinder," Diplomarbeit, University of Kiel, Germany.

Lopez, J. M., 1990, "Axisymmetric Vortex Breakdown. Part 1. Confined Swirling Flow," *Journal of Fluid Mechanics,* Vol. 221, pp. 533–552.

Lopez, J. M., 1995, "Unsteady Swirling Flow in an Enclosed Cylinder with Reflectional Symmetry," *Physics of Fluids,* Vol. 7, pp. 2700–2714.

Lopez, J. M., and Perry, A. D., 1992, "Axisymmetric Vortex Breakdown. Part 3. Onset of Periodic Flow and Chaotic Advection," *Journal of Fluid Mechanics,* Vol. 234, pp. 449–472.

Spohn, A., Mory, M., and Hopfinger, E. J., 1993, "Observations of Vortex Breakdown in an Open Cylindrical Container with a Rotating Bottom," *Experiments in Fluids,* Vol. 14, pp. 70–77.

Tavener, S. J., Mullin, T., and Cliffe, K. A., 1991, "Novel Bifurcation Phenomena in a Rotating Annulus," *Journal of Fluid Mechanics,* Vol. 229, pp. 483–497.

Tsitverblit, N., 1993, "Vortex Breakdown in a Cylindrical Container in the Light of Continuation of a Steady Solution," *Fluid Dynamics Research,* Vol. 11, pp. 19–35.

Valentine, D. T., and Jahnke, C. C., 1994, "Flows Induced in a Cylinder with Both End Walls Rotating," *Physics of Fluids,* Vol. 6, pp. 2702–2710.

Vogel, H. U., 1968, "Experimentelle Ergebnisse über die laminare Strömung in einem zylindrischen Gehäuse mit darin rotierender Scheibe," Max-Planck-Institut für Strömungsforschung, Göttingen, Bericht, Vol. 6.

The Interaction of Spinning Liquid Film With Swirling Gas in Cylindrical Vessel—Experiments and Numerical Simulations

Avi Birk
Senior Scientist/Engineer.

James DeSpirito
Senior Engineer.

U.S. Army Research Laboratory,
Weapons and Materials
Research Directorate,
Aberdeen Proving Ground, MD 21005-5066

Experimental flow visualizations and numerical simulations of the interaction of a spinning liquid film with a swirling gas in a cylindrical vessel are reported. A gas/liquid flow that simulates the high-pressure conditions of combustion was successfully visualized in a transparent test chamber. The test chamber was a mockup of a liquid propellant gun ignition system component called the hydrodynamically-stabilized combustor. Water-glycerol mixtures were used for the liquid, and ballistically compressed helium-nitrogen was used for the gas. The liquid is injected tangentially along the cylindrical test chamber wall where it spreads as a spinning film. The gas is then injected tangentially and interacts with the liquid. The flows were insensitive to the tilt angle of the test chamber and only mildly sensitive to the liquid viscosity. Liquid entrainment by the gas and subsequent atomization occurs promptly (within 2 ms) after the onset of gas injection, and the flow in the test chamber vent passage is a swirling, transonic, two-phase flow. Two types of three-dimensional simulations of the liquid and gas injection into the test chamber were performed using the CRAFT Navier-Stokes code. The first type was of the initial liquid flow only. The second type was of the high-pressure gas injection into the chamber, with the liquid initialized in an annulus around the chamber surface with a swirl velocity. The numerical simulations were successful in capturing the primary characteristics of the flow phenomena observed in the experimental flow visualizations. This included yielding the observed liquid flow patterns before gas injection and capturing the cellular structure observed after gas injection.

Introduction

The fluid dynamic/combustion system concept described in this paper was investigated during the development of the ignition system for a large-caliber, regenerative liquid propellant gun under the U.S. Army's Liquid Propellant Gun program. The regenerative liquid propellant gun, which is described in more detail by Klingenberg et al. (1997a), uses two moving pistons to inject the liquid propellant (LP) during the combustion process. The two pistons are designed such that an annular injector is formed when there is an axial separation between them. Before ignition, the liquid propellant is located in a separate reservoir. An external ignition system is required to raise the pressure and temperature in the combustion chamber to start the injection process and ignite the LP.

A program requirement was that the ignition system for the large-caliber, regenerative liquid propellant gun also used the same LP as the gun system, rather than a solid propellant charge. This was a development issue because of the large amount of LP charge (100 to 200 cm^3) that was required in the igniter main-stage combustor. To date, the only reliable, stable way to combust these large liquid propellant charges was using the regenerative injection method, with the LP injection rate controlled by the piston motion. The use of the regenerative injection concept for the ignition system was deemed too complex. Instead, a staged combustor concept was explored that used increasing size chambers in which the initial LP loading density (ratio of LP mass to total chamber volume) was about 0.2 to 0.35 g/cm^3. A problem that was encountered when using these simple medium-loading density combustors was the occurrence of high-amplitude pressure waves that caused damage to the chamber or internal components of the ignition system. A new igniter main-stage concept was developed in an attempt to use the fluid dynamics of the liquid and gas injection to stabilize the combustion of the LP igniter charge. This concept was called the hydrodynamically stabilized combustor (also called the HDSC). Experimental testing of the HDSC concept showed that it was still subject to combustion anomalies (Hanson, 1995). Since the HDSC concept offered other important advantages, such as an ignition system that could potentially be independent of gun elevation, further investigation into the fluid dynamic aspects of the HDSC concept was desired. The experimental and computational results described in this paper are two results of this investigation.

The HDSC, whose sketch is shown in Fig. 1, uses tangential injection to centrifugally spin a LP film on cylindrical walls, thus preventing unreacted liquid from draining into the gun combustion chamber, downward through the HDSC centerline vent. After termination of the LP injection, a separate (smaller) charge of LP is ignited in a prestage initiator (not shown) and the resulting high-pressure, hot gas enters tangentially into the HDSC in the same direction as the spinning liquid. The hot gas and the LP are injected tangentially through single ports that are at the same azimuthal location on the chamber wall. The gas inlet port diameter is 9.53 mm and is located the farthest from the exit port (102 mm), while the LP inlet port diameter is 3.18 mm and is located 69 mm from the exit port. The hot gas interacts with the spinning LP, ignites it, and converts it to high-pressure (ca. 100 MPa), hot fluid that flows into the gun combustion chamber through the 20.62-mm vent. It was hoped

Contributed by the Fluids Engineering Division for publication in the JOURNAL OF FLUIDS ENGINEERING. Manuscript received by the Fluids Engineering Division July 17, 1997; revised manuscript received July 6, 1998. Associate Technical Editor: C. L. Merkle.

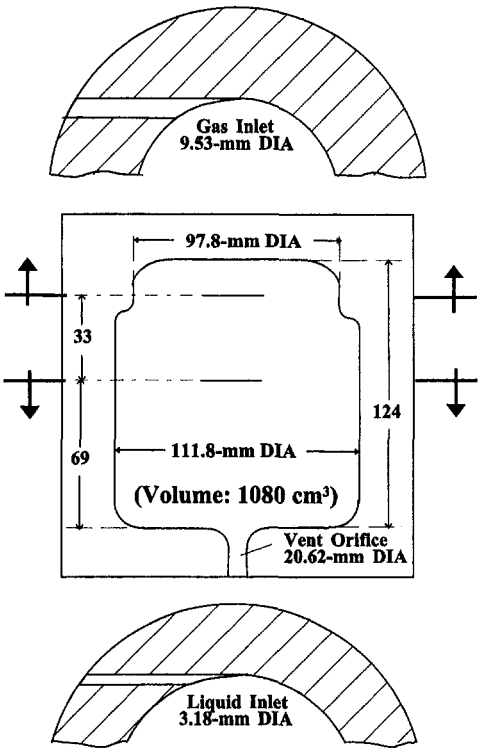

Fig. 1 Geometry of the HDSC

that the swirling motion of the liquid/gas would (*a*) provide for a gun-elevation independent ignition system and (*b*) stabilize the combusting surface of the LP and prevent combustion instabilities. However, combustion instabilities still occurred. Because uneven distribution of liquid on the walls of the HDSC just prior to ignition can cause the instabilities, we decided to conduct a flow visualization study of the liquid/gas distribution using a transparent replica of the HDSC and insert fluids. In addition to aiding the gun developers in redesigning the HDSC, the flow visualizations would be useful in validating, at least qualitatively, a numerical simulation of the liquid/gas interaction. The replica tested in this study will hereon be called the "test chamber," while the actual component of the gun ignition system will continue to be referred to as the HDSC.

The flows in this study are unique, and the authors are not aware of previous studies of such flows. Although the first phase of the injection process involves only the liquid, the three-dimensional geometry and the free surface boundary conditions defy analytic solution of the flow. The second phase of the injection process is vastly more complex, and it involves the gas injection and the gas/liquid interaction prior to ignition. The gas enters the chamber through a complex-shaped inlet as an underexpanded jet and expands in a spinning configuration axially toward the choked vent orifice of the test chamber. Because of its high shear velocity (almost sonic once expanded beyond the inlet), the gas entrains the spinning liquid film violently. As summarized by Kuo and Cheung (1995), many studies of liquid entrainment by shear flow have been conducted. However, they cannot be applied directly to the case at hand, because, although the liquid entrainment mechanisms of shear flow are universal, their correlations are highly empirical and process dependent. Therefore, we based our choice of the simulant fluids on universal flow mechanisms and practicality of use. This paper describes the results of flow visualizations and numerical simulations of the two phases of the liquid/gas flow in the test chamber.

Approach

Flow Visualization Tests. The developer of the ignition system hardware drove the objectives of the flow visualization. The HDSC was already in the testing phase of its development, and design modifications to improve its performance were required rather quickly. We were asked to visualize the fluid flow in the first two phases of the HDSC process at three tilts (elevations), 0, 40, and 75 deg; and with three liquid charges of 100, 140, and 180 cm^3 (corresponding to loading densities of 0.132, 0.185, and 0.238 g/cm^3). Desired data are liquid velocities and retention time in the spinning configuration, pressurization rate, gas velocities, void fractions, and liquid particle sizes. During the test program, only average liquid velocity, liquid retention time in spinning configuration, and pressurization rates could be practically obtained. Notwithstanding, good quality photographic data that elucidated the HDSC flow processes and verified the adequacy of the numerical simulations were obtained.

We selected water-glycerol mixtures for the test liquids because they do not precipitate (like salts or sugars) and because they have advantageous properties—their surface tensions are within 10% of the surface tension of the actual LP (67 dyne/cm), their densities (1—1.2 g/cm^3) approach the LP density (1.43 g/cm^3), and their viscosity range (1—36 cp) overlaps the LP viscosity (7.1 cp). A mixture of 50/50 nitrogen-helium was selected for test gas because of its low molecular weight (thus simulating the actual combustion gas), and efficient ballistic compression to high pressure and temperature.

The experimental system is designed for good photographic access and ease of cleaning and setup; its schematic is shown in Fig. 2. The system consists of four major components: the transparent test chamber, the gas vessel, the igniter, and the liquid vessel. The entire assembly can be tilted to test the effects of gravity. The test chamber is comprised of three (203-mm OD) highly polished clear acrylic slabs bolted together with three bolts. The gas vessel is a modified Autoclave o-ring closure reactor-vessel, model OR0050SL30. Its smooth bore contains a piston for ballistic compression of the vessel gas. The vessel is equipped with a 607L Kistler pressure transducer. The igniter is mounted onto the rear of the gas vessel. It is equipped with a 607C Kistler pressure transducer. The liquid vessel is an Allenair (gas/hydraulic) cylinder, model SSED-2-1/2*5 SR-R-HTP.

The gas and liquid vessels are connected to the test chamber via injection tubes made from Autoclave 9/16-in tubes (14.2-mm OD, 7.9-mm ID). The injection tubes slide fit into the test chamber wall web and are sealed peripherally with o-rings. The tubes' bores intersect tangentially with the inner surface of the test chamber and form the injection ports. The injection axes are on the same plane. (See also Fig. 1.) The liquid injection tube assembly contains a check valve with a 172-kPa (25-psi) cracking pressure. The gas injection tube assembly is fitted to the gas vessel via a modified Autoclave filter. A brass seal disc (9.5-mm OD), pressure-fit into a disc retainer unit at the filter's

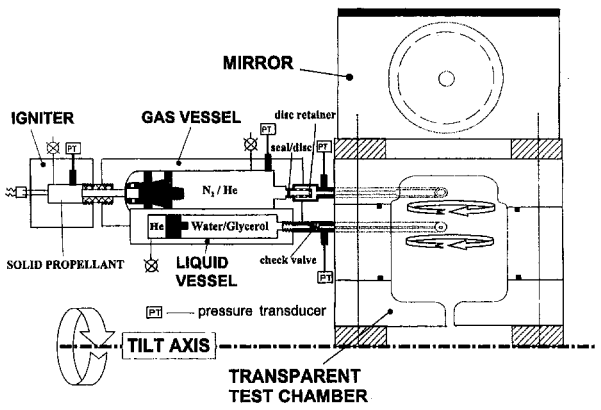

Fig. 2 Schematic of the experimental setup

inlet, seals the gas vessel from the test chamber. The disc unseats during ballistic compression in the gas vessel, when the pressure exceeds 25 MPa. Unlike a rupture disc, it does not introduce debris into the chamber. The liquid and gas injection tubes are each equipped with a Kistler 601B1 pressure transducer close to their injection ports. The pressure transducer in the liquid tube effectively measures the liquid injection pressure and, once the gas injection starts, the wall pressure in the test chamber at the liquid port location.

A motion-picture camera initiates the test via a timer-sequencer. First, the liquid is injected into the test chamber by applying 6-MPa helium on the rear of the liquid-vessel piston. After a preset time (0.25–0.32 s), the igniter is fired, and the ballistically compressed gas is injected into the chamber. The vented liquid is continuously collected, and its final volume is measured. Data are recorded on a Nicolet 420 Wave Recorder.

A Photec IV 16-mm motion picture camera equipped with a 45-mm f/2.8 Mamiya-Sekor Model M645 lens and a wide-angle attachment was used for high-speed (5000 frames/s) cinematography. Rolls of 16-mm Kodak 2253 Ektachrome film were used. Video was taken (60-fields/s, 1-ms/frame exposure time) with a JVC Professional CCD Color Video Camera Model BY-10U, equipped with a zoom lens. Four 640-W tungsten halogen lamps were used for illumination. A mirror mounted at 45 deg on the top of the test chamber facilitated composite photography of the side and top views. To enhance photographic details, the liquid was colored deep blue using a minute amount of methylene blue.

Numerical Simulations. The objective of the numerical study was to determine the feasibility of modeling the liquid and gas injection processes in the HDSC ignition system. The numerical study was undertaken after the flow visualization study was nearly complete. Therefore, the numerical study used the test conditions of the flow visualization study as inputs. Specifically, one flow visualization test was chosen as the baseline for the numerical simulation. If the results of the numerical study compared well with flow visualization results, then it was hoped that the model could be used to further study some of the physics of the concept or, if run times were reasonable, be used as an engineering design tool.

The CRAFT Navier-Stokes code (Sinha et al., 1992) was used to perform transient, three-dimensional simulations of inert liquid and gas injection and mixing in the test chamber. The CRAFT code is based on the TUFF aerodynamic code developed by Molvik and Merkle (1989). It is a three-dimensional, finite-volume code that uses an implicit, upwind scheme based on that of Roe (1981). A Total-Variation-Diminishing (TVD) technique of Chakravarthy and Osher (1983) is used to obtain higher order accuracy without spurious oscillation behavior. A large-eddy simulation (LES) approach is used for turbulence modeling, i.e., the large-scale turbulent structure is directly simulated by the flow solver while the small-scale (on the order of the grid cell size) dissipative structures are modeled. In the code version used in the present study, a third-order accurate TVD scheme, second-order time integration, and a simple small-scale (sub-grid) turbulence model were used. A summary of the CRAFT code numerics and modifications for short-duration transient, chemically reacting, multiphase flows is provided by Hosangadi et al. (1995). Hosangadi et al. (1995) also present several fundamental numerical validation studies that demonstrate the capability of the CRAFT code to analyze problems involving finite-rate combustion, turbulence with large-scale vortical structures and transient wave processes particular to gun propulsion systems. The CRAFT code was successfully used to simulate flows in the electrothermal-chemical gun and the regenerative liquid propellant gun (Hosangadi et al., 1995; Hosangadi et al., 1996; Madabhushi et al., 1995). All calculations were performed in serial mode on the Silicon Graphics Inc. Power Challenge Array (SGI-PCA) system located at the DOD High Performance Computing Center at Aberdeen Proving Ground, Maryland.

The test chamber geometry required that a three-dimensional calculation be performed. A grid of 51 × 51 × 61 (150,000 computational cells) was developed using the GRIDGEN grid generation program (Steinbrenner and Chawner, 1994) and was used for all simulations. Figure 3(*a*) shows a view of the outside surface of the computational grid, indicating the location of the liquid and gas inlets and the exit vent of the test chamber. Figure 3(*b*) shows a close-up of the inlet regions. The liquid inlet area consisted of 48 cells and the gas inlet area consisted of 52 cells. The liquid and gas inlets were projections of circles, of the respective diameter, onto the inside surface of the test chamber, representing the interface of the tangential inlet and the inside surface of the test chamber. As shown in Fig. 3(*b*), the gas inlet intersected the chamber wall in the reduced diameter region (Fig. 1). The liquid inlet was specified as a fixed inflow velocity boundary condition. The gas inlet was specified as an inflow boundary condition where the static pressure and temperature and velocity vector direction cosines were specified. The exit vent was specified as a non-reflecting boundary that properly handles the choke flow exit condition. The grid was nearly uniform in the interior region of the computational domain and no attempt was made to resolve the boundary layer along the test chamber wall so that the computational cost would be reduced. An inviscid, "slip," boundary condition was used at the chamber walls. The grid was generated such that the circular boundary of the chamber wall made up the four "sides" of the computational domain so that there was no "centerline" boundary in the computational domain.

Results

Flow Visualization Tests. The sequence of tests is given in Table 1. Three tilt angles were tested—0, 40, and 75 degrees. The liquid was injected at a rate of 460 ± 10 cm^3/s—close to the rate in the HDSC. The gas was injected within 0.25—0.32 s after the end of the liquid injection, just as in the HDSC. The gas injection parameters were picked to minimize the mainte-

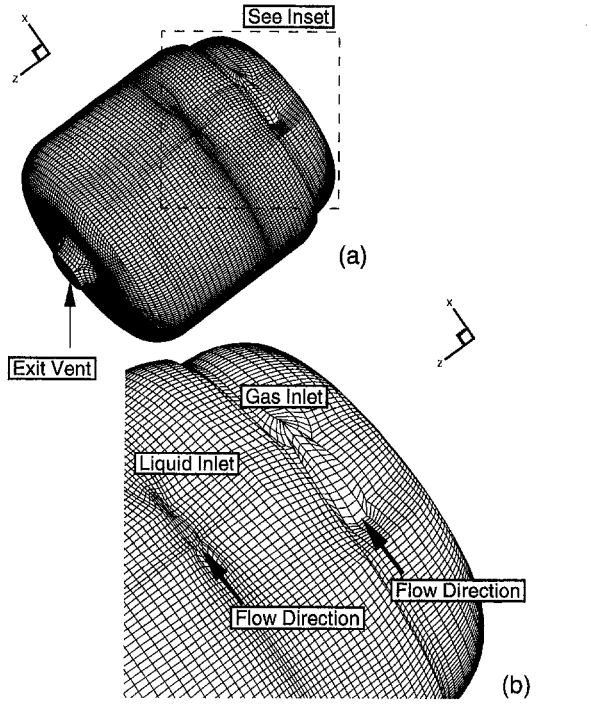

Fig. 3 Computational grid used in simulations: (*a*) three-dimensional view of HDSC chamber and (*b*) close-up of gas and liquid inlets

Table 1 Test matrix

Test no.	Liquid volume (cm^3) (amount injected of W-water, G-glycerol)	Gas injection initial pressure in gas vessel (MPa)/amount of IMR in igniter (g)
1–3	140W	None
4–6	140 .5W/.5G	|
7, 8	140 .25W/.75G	|
9–11	100 .5W/.5G	|
12–14	180 .5W/.5G	|
15	100W	5.2/6
16, 17	140W	5.2/6
18–20	140 .5W/.5G, 100W, 140W	5.2/6, 5.2/10, 8/7
21–25	140W	8/7.5

nance expenditures (such as repolishing the wall adjacent to gas inlet) but still yield realistic data.

Pressure Data. Typical pressure data of a nominal test (No. 24) are shown in Fig. 4. For simulation of the HDSC flow, the period of interest is the liquid injection, the intermission between liquid injection and gas injection, and the first 3 ms of the gas injection. Figure 4(*a*) shows the liquid injection pressure and, once the gas is injected, the gas pressure in the test chamber. Figure 4(*b*) shows the first 3 ms of the static gas pressure in the gas jet slightly upstream the gas inlet, and the pressure on the test chamber wall at the liquid inlet location. (The latter pressure, shown multiplied by a factor of 10, is much lower than the former indicating that the underexpanded gas jet has greatly expanded when it reaches the location of the liquid injection port.) Experimentally, the gas inlet pressure pulsated because the piston in the gas vessel rebounded back and forth in a damped spring-mass fashion. The 3-ms duration corresponds to about half of the period between the first (and highest) and second pressure peak. The nominal peak pressure of the igniter was 170 MPa and this resulted in a (stagnation) peak pressure of about 50 MPa in the gas vessel.

Because of excessive erosion of the inner surface of the test chamber, only one maximum-pressure test (No. 19) was conducted (reaching peak pressures of 165, 33, and 2.9 MPa in the gas vessel, gas inlet, and liquid inlet respectively). Yet, the visual records from that test feature flow phenomena that are similar to those recorded in the nominal pressure tests. Therefore, the data can be extended to the HDSC.

Visualization Data. Selected video and cinematic records were rendered digital and stored as image files on a personal computer. The video frames were frame-grabbed from the VCR (480*640 pixels). The cinematic films were scanned using a KODAK film scanner (1024*1546 pixels) and stored as sequences of 5 frames/image pictures on KODAK Photo-CDs. The image files were color-processed for detail enhancement and for printing using Adobe Photoshop software.

The visual records are most meaningful when observed as movies or video in full color. Representative video pictures are shown in Fig. 5(*a*). The pictures show the clear test chamber from the side, with the top view observed through a mirror (and therefore reversed). The pictures show the spreading angle of the liquid and its containment in a film on the curved wall, including the stepped diameter curved wall. Representative cinematic pictures are shown in Fig. 5(*b*). The pictures show cellular structures of the liquid film on the walls after gas injection. The milky appearance of the inner chamber reflection and the vent indicate liquid spray in the bulk of the chamber and liquid discharge through the vent.

The visual records portrayed interesting aspects of the flow that were found in all the tests. They are as follows:

1. The liquid is expected to spread on the wall because a pressure gradient exists between the centrifugal pressure in the center of the flow and the atmospheric pressure on its edges. Indeed, the liquid spreads on the curved walls but not with even thickness. An even-thickness liquid film would have contained the largest amount of liquid injected, 180 cm^3, in an annular volume below the 97.8-mm stepped diameter (Fig. 1). Experimentally, the liquid film covered the gas injection port and spreads upward on the stepped diameter curved wall, even in the case of the 100-cm^3 injection.

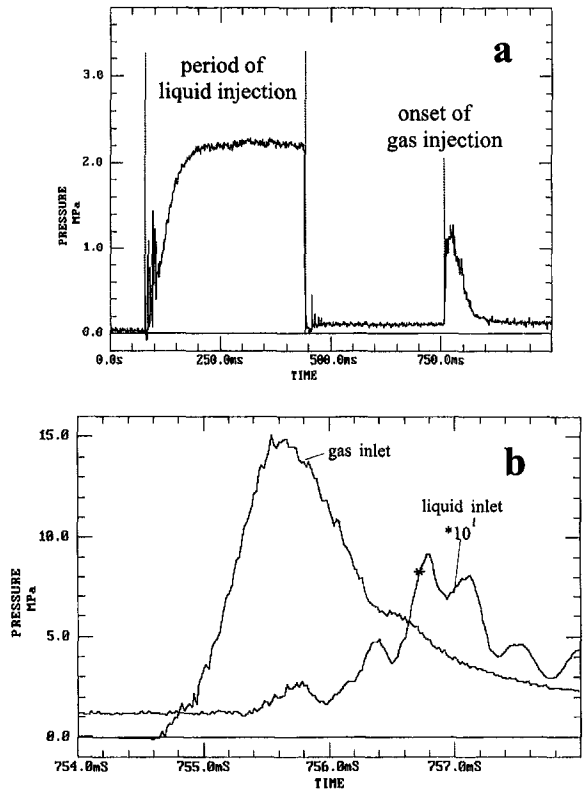

Fig. 4 Pressure traces of test 24: (*a*) at liquid inlet, (*b*) at gas and liquid inlet after the onset of gas injection

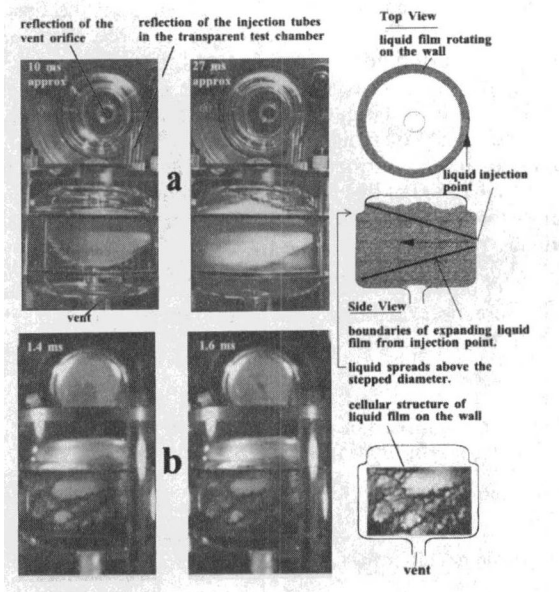

Fig. 5 Visual records of test 24: (*a*) video pictures of onset of liquid injection, (*b*) cinematic pictures of gas injection

2. During the liquid injection, the liquid spreads on the curved wall within an angle of 55 ± 5 deg from the injection port, independent of the liquid tested.
3. The spinning liquid pulsated axially with a sub-10-Hz frequency.
4. No liquid vents from the test chamber before gas injection. In tests Nos. 1–14, where only liquid was injected, the liquid continued to spin on the wall after the termination of its injection for a certain "retention" period. We define this period as the time interval from the termination of the liquid injection until gravity caused the liquid film to sag 5 cm down the walls in zero tilt configuration or to drip from the walls in tilted configurations. (The retention periods are given in Table 2 and are accurate to within ±0.017 s (as 0.017 s is the duration of a video frame).)
5. After the termination of the gas injection, the liquid spread back over the curved wall and resumed its spinning motion.

The retention times are very important with respect to the timing of prestage ignition in the HDSC. It is desired to inject the combustion gas in the HDSC when the LP spins on the wall and does not block the gas inlet and the HDSC vent. As Table 2 indicates, even for the lowest liquid charge (100 cm^3) and the highest viscosity (36 cp) there is a long (in gun firing time scale) window of opportunity (0.3 s) for gas injection. Therefore, variations in liquid viscosity are not problematic with respect to the HDSC ignition concept. The liquid resumes its spinning motion once the gas injection pressure drops, a fact that is of no consequence for the HDSC—in the HDSC the LP is ignited by the injected gas and burns rapidly at high pressure.

It was very difficult to determine the liquid velocities on the test chamber walls. Turbulence features in the liquid effectively serve as flow markers, but they can be followed only for a maximum of three frames when photographed at 5000 frames/s. The liquid port injection velocity at full injection pressure is calculated to be about 43 m/s. From the photography, it is estimated that upon termination of the liquid injection, the mid-wall circumferential velocity of the liquid film velocity is 25 ± 5 m/s, and it relaxes to 9 ± 5 m/s before the gas injection. The liquid collapses downward along the walls (in 0 deg tilt) or drops onto the bottom (in 75 deg tilt) once its velocity drops below 1 m/s and the gravitational acceleration overcomes the centrifugal acceleration.

In general, the visualization data reveal that the tilt angle and choice of liquid had no discernible influence on the observed gas/liquid interaction phenomena. We suppose that for the tested conditions, fluid momentum transfer effects overshadow any viscosity and surface tension effects. Therefore, for ease of operation, most of the gas injection tests were conducted with water and at a 0 deg tilt angle. The gas action on the liquid asymmetrically redistributes the liquid on the wall. The complete visualization of this phenomenon required cinematography from different camera angles. Analysis of the complete set of cinematic pictures indicate the following:

1. The liquid film on the wall shears away unevenly under the action of the gas and forms twisting cellular structures.
2. A portion of the sheared liquid is deposited on the liquid film on the opposite side from the gas injection port.
3. Liquid starts to vent from the test chamber after 0.6 ms from the onset of gas injection.

The unevenness of the liquid distribution is an important observation. It is suspected that such distribution is the cause for measured pressure spikes during the HDSC combustion process. This is addressed further in the Discussion section.

Table 2 Post-injection retention period (a) of the liquid (b) in spinning configuration

Liquid volume (cm^3)	100	140	180
Time (s)	0.38	0.48	0.60

(a) Times do not differ for more than 0.034 s for injections at different tilt angles.
(b) For a .5W/.5G liquid mixture (viscosity = 6 cp). Add 0.05 s for W (1 cp) and subtract 0.08 s for .25W/.75G (36 cp).

Numerical Simulations. Two cases were computed. The first case included only liquid injection. The second case included gas injection into the chamber that had an annular ring of liquid initialized along the test chamber wall with a swirl component of velocity. The flow visualization test 24 was used as the baseline for these two numerical simulations. This test was performed with 140 g water (see Table 1) and those were the properties given to the liquid in the simulation. The helium-nitrogen gas mixture (50/50 by mole) properties were: molecular weight, 16 kg/kg-mol; specific heat ratio, 1.498; and a specific heat (constant pressure) of 1562 J/kg-K.

Liquid Injection Simulation. In the liquid injection simulation case, only the first 27 ms of the injection was simulated. This was necessary because of the impracticality of simulating the full injection period (400 ms) with the relatively long computational times required for the simulation (2.7 minutes per iteration with a maximum time step of 1.0×10^{-5} s). Simulating only the early part of the liquid injection was a reasonable simplification based on the flow visualization observation that the liquid was in a stable, swirling motion with a slowly decaying velocity for most of the injection period. Although the characteristics of this early portion of the liquid injection are not critical to the operation of the HDSC, it is a good reference point for determining how well the numerical calculation does in simulating the liquid injection characteristics.

The initial chamber conditions in the simulation were set as gas at a uniform pressure and temperature, 1 MPa and 300 K, respectively. Specifying a constant velocity at the liquid inlet cells controlled the injection of liquid. The velocity unit vectors were oriented tangential to the chamber wall, with no initial axial component. The specification of inlet liquid and gas was controlled by specifying the cell gas volume fraction, ϕ_g. The inflow of liquid was specified by setting ϕ_g equal to 1.0×10^{-5}. The inflow liquid velocity was specified at 31.6 m/s, which was calculated from the experimental pressure data as the average injection velocity during the first 20 ms of injection (the very early region of the "liquid injection" pressure profile in Fig. 4(*a*)].

Figures 6(*a*) and 6(*b*) show the evolution of the liquid injection into the test chamber at two times. In the top portion of Fig. 6, a liquid mass fraction isosurface of 0.7, representing a dense spray, is shown. The bottom portion of Fig. 6 shows shaded contours of liquid mass fraction in a plane that cuts through the liquid inlet and is perpendicular to the chamber axis. The liquid jet, injected tangentially at 31.6 m/s, is seen to spread axially, covering the cylindrical part of the test chamber wall (Fig. 6(*a*)). The liquid is observed to remain along the wall with the dense spray just inside the liquid region (Fig. 6 (*b*)). The axial component of the liquid velocity is due to the pressure gradient that is generated between the center of the flow and the edges by the centrifugal forces.

The simulation at 8.0 ms (Fig. 6(*a*)) compares with the left image of Fig. 5(*a*), which shows the liquid injection at about 10 ms. The liquid jet has traversed about half-way around the test chamber wall at this time in both the simulation and the flow visualization test. The liquid jet is moving faster in the computation than in the experimental flow visualization. This is likely due to the fixed inlet specification, which does not take into account the experimental startup transient that is noticeable in Fig. 4(*a*), and the slip-wall boundary condition. The simula-

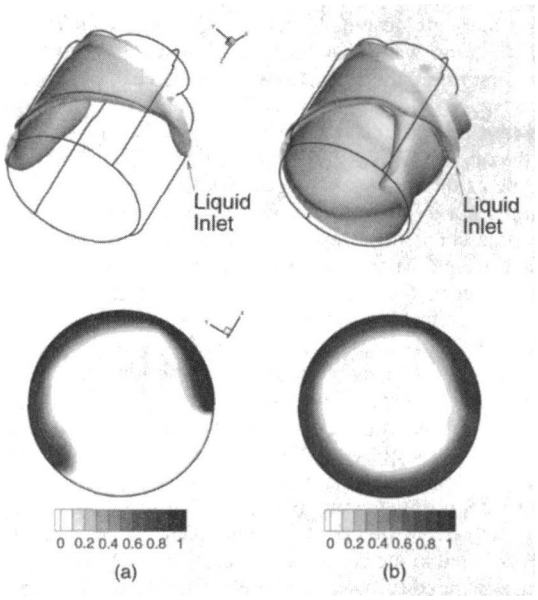

Fig. 6 Time evolution of liquid injection into test chamber at (*a*) 8 ms, and (*b*) 16 ms. Upper figure: Liquid mass fraction isosurface level 0.7. Lower figure: Liquid mass fraction shaded contours.

tion at 16.0 ms (Fig. 6(*b*)) compares with the right image of Fig. 5(*a*), which shows the liquid injection at about 27 ms. At this time both the simulation and the test show that the liquid jet has traversed around the chamber wall a little more than one complete revolution. This can be seen in the simulation by observing that the 0.7 level isosurface has moved past the injection orifice while the liquid jet is still spreading from the inlet. Although difficult to make out clearly due to still-picture limitations, this can also be observed in the test result (right image of Fig. 5(*a*)), where the dense spray is observed to have flowed past the jet inlet. The spreading angle of the jet in the simulation was measured to be about 45 deg, which is reasonably close to the 55 ± 5 deg measured in the experiment. Although the comparisons with the test results are mostly qualitative, they show that the numerical simulation successfully captures the physical characteristics of the early liquid injection into the test chamber.

Gas Injection Simulation. The gas injection simulation was not a continuation of the liquid injection simulation. Instead, the chamber was initialized with liquid in an annulus around the inside surface of the test chamber. Figure 7 shows a cross section of the chamber with liquid mass fraction contours showing the initialization of the liquid in the chamber. The chamber was initialized by setting the ϕ_g value in the first two cells next to the chamber wall to give 140 cm^3 of liquid (water) in the chamber. Only one cell was initialized as liquid in the stepped-diameter (smaller diameter) region. Using two cells made the annulus of liquid approximately 5 mm thick. If the cells were initialized as all liquid ($\phi_g \cong 0$) the amount of liquid would be well over 140 cm^3. The value of ϕ_g to give 140 cm^3 of liquid in a gas/liquid mixture was calculated to be 0.36833. An estimate of the actual annular film thickness was too difficult to discern from the flow visualization experiments. However, the liquid was observed to spread over the smaller diameter region of the chamber so it was initialized in this way. The remainder of the cells in the chamber represented the nitrogen-helium mixture ($\phi_g \cong 1.0$). Both the liquid and the gas were set to 1 MPa and 300 K. An initial uniform swirl velocity of 10 m/s was set for all cells in the chamber. This velocity was estimated from the flow visualization tests as the velocity directly prior to gas injection.

The injection of the gas into the test chamber was simulated by using the experimental pressure-time data (Fig. 4(*b*)). This pressure, which was measured in the gas inlet, was used as the static pressure in a row of ghost cells outside the gas inlet cells. The inflow velocity was then calculated as part of the solution. The velocity was specified to be tangential to the chamber wall, with no axial component. The temperature of the incoming gas was set to 300 K.

The simulation was run until 3.1 ms with a maximum time step of 5.0×10^{-7} and took about 380 hours of CPU time on a single processor of the SGI-PCA. Although the flow visualization was recorded for more than 50 ms, the combustion in the HDSC takes place in the first 2–4 ms. Therefore, this is a reasonable time period since only the early part of the gas injection is relevant for determining the state of the liquid when combustion takes place in the HDSC.

The cellular structure observed in the experiments (Fig. 5(*b*)) was also evident in the simulation. Liquid mass fraction isosurfaces (0.7 and 0.85) are shown in the top portion of Fig. 8. Note that in Fig. 8, for clarity, only the front half of the computational volume (closest to the observer) was made visible. The lower portion in Fig. 8 shows filled contours of liquid mass fraction in a cross-section that cuts through the gas inlet (the dashed line in the upper portion of the figure). The view

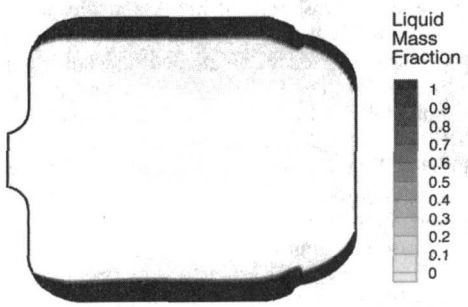

Fig. 7 Shaded contours of liquid mass fraction showing initial location of liquid in gas injection simulation

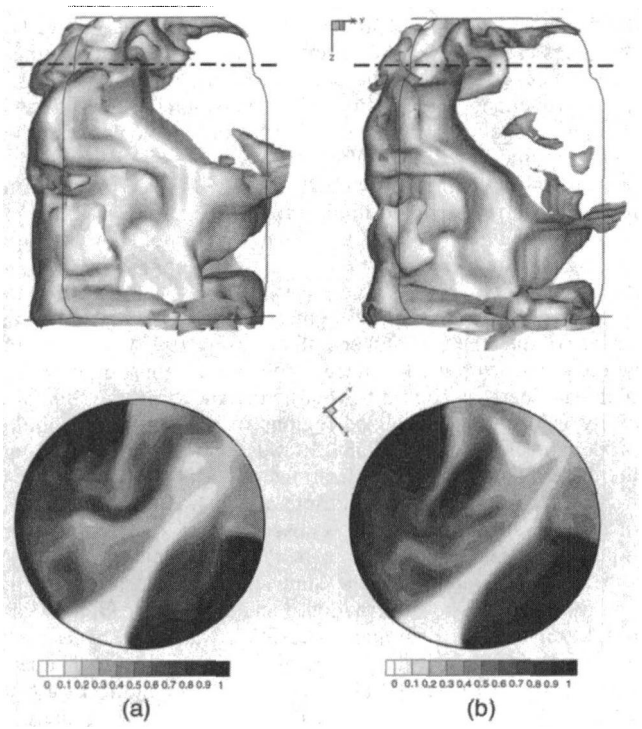

Fig. 8 Side view of liquid mass fraction isosurfaces (0.7 and 0.85) (upper figure) and shaded contours of liquid mass fraction in gas inlet plane at (*a*) 1.4 ms and (*b*) 1.6 ms after gas injection

is from below the chamber. The gas jet (lightest region in lower figure) is observed to move across the chamber at an angle of about 75 deg, rather than tangentially along the chamber wall. Although the gas jet is expected to expand and have a component in the radial direction, this large radial component is likely due to error induced by the inflow boundary condition, i.e., setting the flow direction nearly parallel to the boundary. Since the goal of the simulation was not to obtain quantitative measurements, we believe qualitative comparisons of the gross characteristics of the liquid/gas interaction can still be made with the flow visualizations. Although the still-picture illustrations may be limiting, but we believe that both the flow visualizations and the simulation show similar gross characteristics of the flow—liquid entrained in eddies that are produced by the dynamics of the gas jet. A liquid spray is observed in the test chamber vent in the experiment at both times shown in Fig. 5(*b*). Liquid was also observed in the chamber vent in the simulation, although it was at a mass fraction lower than 0.7 at the first time shown in Fig. 8.

The total amount of mass lost from the test chamber by the end of the computation (3.1 ms) was a little less than 0.3 g. The rate of the mass leaving the chamber was very low during the computation but increased at about 1.0 ms, indicating the point at which liquid likely began leaving the chamber in addition to gas. Experimentally, it was not practical to measure the flow rate of the test chamber effluent. Of course, it is this type of information, not possible to measure in the experiment, that drives the desire to perform the numerical simulations.

Discussion

The most important observation from both the experimental flow visualizations and the flow simulations was the "cellular" structure of the gas/liquid interaction. The term cellular, perhaps not the best description, was used after viewing the experimental flow visualizations, which only allowed viewing the contact of the flow with the clear test chamber wall (Fig. 5). From the flow simulation results it was observed that some of the liquid was engulfed in three-dimensional vortical structures (Fig. 8) that give a similar cellular appearance if viewed by their contact with the chamber wall. These vortical, or eddy, structures are important because they can lead to high-loading-density pockets of thermally and chemically "preconditioned" liquid propellant. The "explosive" combustion of these pockets of liquid propellant were believed to be a probable cause of the high-amplitude pressure spiking that was observed in a high-pressure jet research facility (Birk et al., 1995) and the ignition phase of the regenerative liquid propellant gun (Hosangadi et al., 1996; Klingenberg et al., 1997b). High-amplitude pressure spiking was the nature of the combustion anomalies present in the actual HDSC igniter. The pressure spikes were believed to be the cause of localized pitting that was observed on the inside surface of the HDSC chamber wall (Hanson, 1995). This would be consistent with the localized, explosive combustion postulation. The inert gas/liquid flow structure shown in Fig. 8 could easily lead to such localized regions of preconditioned liquid propellant in the actual HDSC. It was evident after observing the experimental flow visualizations that a design change was necessary since the gas/liquid interaction was not in the form of a stable shear layer but was susceptible to these pockets of liquid propellant.

The fluid dynamics of the supersonic gas jet appeared to control the gas/liquid interaction, including the location of liquid accumulation. A similar observation was made by Hosangadi et al. (1996) in simulations of the interaction of a supersonic gas jet with an initially static puddle of liquid in a test chamber. The domination of the flow characteristics by the gas jet is a likely reason for the insensitivity to chamber tilt angle and mild sensitivity to liquid viscosity that was observed in the experimental flow visualizations.

To numerically test the effect of viscosity, a second gas injection simulation was run with a liquid viscosity 100 times that in the first simulation. All other parameter settings were the same as in the original gas simulation. The effect of the substantial increase in viscosity appeared to be a small change in the time-history of the flow with the primary flow characteristics the same as those in the first gas injection simulation. Comparing liquid mass fraction isosurfaces from each simulation at the same time showed large eddy structures of almost equivalent size and shape. There was only a small difference in the size and location of the smaller eddies. The effect of viscosity on the flow structure is believed to be too small to affect the combustion anomalies observed in the HDSC. The effect of viscosity on the liquid injection simulation was not investigated because the experimental flow visualizations showed that the liquid viscosity had little effect on the state of the liquid at the beginning of gas injection. The hydrodynamics of the gas injection phase dominated the flow process.

The LES turbulence approach used in the CRAFT code allowed the direct numerical simulation of the large eddies that were observed in the gas injection simulation. This is in contrast to time-averaged turbulence modeling methods, which may not have been able to resolve the highly transient nature of the process. Although the true numerical accuracy of these simulations cannot be estimated, Hosangadi et al. (1995) previously validated the CRAFT code with other cases involving two-phase, liquid/gas flows with large-scale vortical structures. The complexity of the system and the pressure regime involved limited the validation of these simulations to qualitative comparisons with the experimental flow visualizations.

Summary and Conclusions

Experimental flow visualizations and numerical simulations of the interaction of a spinning liquid film with a swirling gas in a cylindrical vessel were reported. The experimental flow visualizations showed that the flows were insensitive to the tilt angle of the test chamber, and only mildly sensitive to the liquid viscosity. The liquid jet spreading angle was measured to be 55 ± 5 deg. No liquid was observed to vent from the test chamber before the onset of gas injection. Liquid entrainment by the gas and atomization occurred promptly, within 2 ms after the onset gas injection. The liquid film was redistributed by the gas unevenly on the walls, and it featured twisting cellular structures.

The liquid injection simulation showed a very similar liquid flow pattern, with a jet spreading angle of 45 deg. The gas injection simulations captured the cellular structure observed in the experiments and was shown to be the effect of large eddy structures interacting with the test chamber wall. The calculation showed that a negligible amount of liquid (about 0.3 g) vented from the test chamber during the first 3.1 ms of gas injection. A second gas injection simulation with 100 times the liquid viscosity of the first gas simulation resulted in minor changes to the primary flow characteristics.

The complexity of the system and the pressure regime limited both the amount of quantitative diagnostics that was obtainable in the experimental flow visualizations and the data available for numerical validation. The numerical simulations were successful in capturing the primary characteristics of the flow phenomena observed in the test chamber flow visualizations. This included showing that the combustion anomalies observed in actual HDSC firings may be due to the localized combustion of accumulated liquid propellant. Although limited to mostly qualitative information, we believe that the numerical simulations have the potential to determine the effect of geometry and other configuration changes.

Acknowledgments

This work was sponsored by the Program Manager, Crusader, Picatinny Arsenal, NJ. This work was also supported in part by

a grant of high-performance computing time from the DOD Aberdeen High Performance Computing Center, Power Challenge Array System.

References

Birk, A., McQuaid, M., and Gross, M., 1995, "The Influence of Flow Dispersers on 30-mm Gun-Type Annular Jets—XM46 Combustion and Flash X-ray Photography of Aqueous NaI Solutions," U.S. Army Research Laboratory, ARL-TR-720, Aberdeen Proving Ground, MD, Apr.

Chakravarthy, S. R., and Osher, S., 1983, "Numerical Experiments with the Osher Upwind Scheme for the Euler Equations," *AIAA Journal,* Vol. 21, No. 9, pp. 1241–1248, Sept.

Hanson, J., 1995, Private Communication, Lockheed Martin Defense Systems, Pittsfield, MA.

Hosangadi, A., Sinha, N., and Dash, S. M., 1995, "Multi-Dimensional Simulation of ETC Gun Flowfields," U.S. Army Research Laboratory, ARL-CR-240, Aberdeen Proving Ground, MD, Aug.

Hosangadi, A., Kenzakowski, D. C., Sinha, N., and Dash, S. M., 1996, "Combustion Instabilities in Interior Ballistic Flowfields," AIAA-96-3078, Lake Buena Vista, FL, July.

Klingenberg, G., Knapton, J. D., Morrison, W. F., and Wren, G. P., 1997a, "Liquid Propellant Gun Technology," *Progress in Astronautics and Aeronautics,* Vol. 175, AIAA, Wash. DC, pp. 329–378.

Klingenberg, G., Knapton, J. D., Morrison, W. F., and Wren, G. P., 1997b, "Liquid Propellant Gun Technology," *Progress in Astronautics and Aeronautics,* Vol. 175, AIAA, Wash. DC, p. 370.

Kuo, K. K., and Cheung, F. B., 1995, "Droplet Entrainment of Breakup by Shear Flow," U.S. Army Research Laboratory, ARL-CR-276, Aberdeen Proving Ground, MD, Oct.

Madabhushi, R. K., Hosangadi, A., Sinha, N., and Dash, S. M., 1995, "Large Eddy Simulation Studies of Vortex Shedding with Application of LPG Instabilities Using the CRAFT Navier-Stokes Code," U.S. Army Research Laboratory, ARL-CR-241, Aberdeen Proving Ground, MD, Aug.

Molvik, G. A., and Merkle, C. L., 1989, "A Set of Strongly Coupled, Upwind Algorithms for Computing Flows in Chemical Nonequilibrium," AIAA-89-0199, Reno, NV, Jan.

Roe, P. L., 1981, "Approximate Reimann Solvers, Parameter Vectors, and Difference Schemes," *J. Comp. Phy.,* Vol. 43, pp. 357–372.

Sinha, N., Dash, S. M., and Hosangadi, A., 1992, "Applications of an Implicit, Upwind Navier-Stokes Code, CRAFT, to Steady/Unsteady Reacting, Multi-phase Flowfields," AIAA-92-0837, Reno, NV, Jan.

Steinbrenner, J. P., and Chawner, J. R., 1994, "The GRIDGEN Version 9 Multiple Block Grid Generation Software," MDA Engineering, Inc., Report 94-01, June.

A Three-Dimensional Analysis of Rotordynamic Forces on Whirling and Cavitating Helical Inducers

Luca d'Agostino
Associate Professor,
Università degli Studi di Pisa, Pisa, Italy

Fabrizio d'Auria
ESA Post-Doctoral Scholar,
California Institute of Technology,
Pasadena, CA 91125

Christopher E. Brennen
Professor,
Division of Engineering and
Applied Science,
California Institute of Technology,
Pasadena, CA 91125

This paper investigates the linearized dynamics of three-dimensional bubbly cavitating flows in helical inducers. The purpose is to understand the impact of the bubble response on the radial and tangential rotordynamic forces exerted by the fluid on the rotor and stator stages of whirling turbomachines under cavitating conditions. The flow in the inducer annulus is modeled as a homogeneous inviscid mixture, containing vapor bubbles with a small amount of noncondensable gas. The effects of several contributions to the damping of the bubble dynamics are included in the model. The governing equations of the inducer flow are written in "body-fitted" orthonormal helical Lagrangian coordinates, linearized for small-amplitude perturbations about the mean flow, and solved by modal decomposition. The whirl excitation generates finite-speed propagation and resonance phenomena in the two-phase flow within the inducer. These, in turn, lead to a complex dependence of the lateral rotordynamic fluid forces on the excitation frequency, the void fraction, the average size of the cavitation bubbles, and the turbopump operating conditions (including, rotational speed, geometry, flow coefficient and cavitation number). Under cavitating conditions the dynamic response of the bubbles induces major deviations from the noncavitating flow solutions, especially when the noncondensable gas content of the bubbles is small and thermal effects on the bubble dynamics are negligible. Then, the quadratic dependence of rotordynamic fluid forces on the whirl speed, typical of cavitation-free operation, is replaced by a more complex behavior characterized by the presence of different regimes where, depending on the whirl frequency, the fluid forces have either a stabilizing or a destabilizing effect on the inducer motion. Results are presented to illustrate the influence of the relevant flow parameters.

1 Introduction

The combined effects of destabilizing rotordynamic fluid forces and cavitation represent the main fluid dynamic phenomena that adversely affect the dynamic stability and performance of high power density turbopumps (Brennen, 1994). This can lead to very serious problems ranging from fatigue failure to sudden destructive damage of the machine (Jery et al., 1985; Franz et al., 1990). Rotordynamic fluid forces under cavitating conditions have long been known to play an important role in promoting the development of self-sustaining lateral motions (whirl) of the impeller (Rosenmann, 1965). Recent experiments carried out in the Rotor Force Test Facility at the California Institute of Technology by Franz et al. (1990) and Bhattacharyya (1994) showed that cavitation significantly affects the rotordynamic fluid forces on axial flow inducers. In general, cavitation has been found to have a destabilizing effect on the whirl motion. In the present context, it is important to note that cavitation replaces the characteristic quadratic behavior of the noncavitating rotordynamic fluid forces with a more complex dependence on the whirl speed, thereby undermining the traditional expansion of the rotordynamic fluid forces in terms of stiffness, damping and inertia matrices. Bhattarcharyya (1994) tentatively correlated these changes to the development of reverse (possibly oscillatory) flow at lower flow coefficients, implicitly postulating some form of interaction between cavitation, backflow and whirl motion.

The present research aims at obtaining some fundamental understanding of the basic fluid dynamic phenomena responsible for the observed behavior of the rotordynamic fluid forces in whirling and cavitating inducers. In particular, the main purpose of this study consists of investigating to what extent this behavior results from the dynamic response of the bubbles in the cavitating flow through the inducer under the excitation provided by the whirl motion. The flow is studied using the linear perturbation approach used by the authors in their previous dynamic analyses of bubbly liquids (d'Agostino and Brennen, 1983, 1988, 1989; d'Agostino, Brennen and Acosta, 1988; Kumar and Brennen, 1993; d'Auria, d'Agostino and Brennen, 1994, 1996), extending earlier two-dimensional results (d'Auria, d'Agostino and Brennen, 1995) to account for the presence of the inducer blades and the occurrence of significant tangential components of the rotordynamic fluid forces. By introducing suitable simplifications, this approach leads to a fully three-dimensional boundary value problem for a linear Helmholtz equation in the complex amplitude of the pressure perturbation. Solution to this equation can be efficiently obtained by separation of variables. Despite its intrinsic limitations, the results of the theory are consistent with the general features of the available experimental data. Hence, it appears that the present analysis correctly captures some of the fundamental fluid dynamic phenomena in whirling inducers under cavitating conditions and can usefully contribute to the understanding of the rotordynamic fluid forces and instabilities in a number of important turbomachinery applications.

Contributed by the Fluids Engineering Division for publication in the JOURNAL OF FLUIDS ENGINEERING. Manuscript received by the Fluids Engineering Division January 21, 1998; revised manuscript received May 5, 1998. Associate Technical Editor: J. Katz.

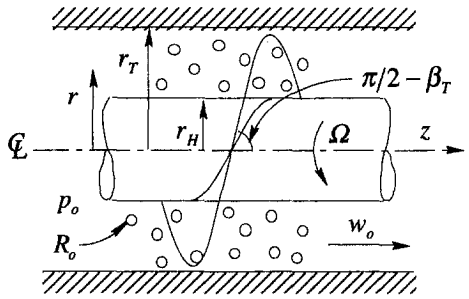

Fig. 1 Schematic of the flow configuration and inducer geometry

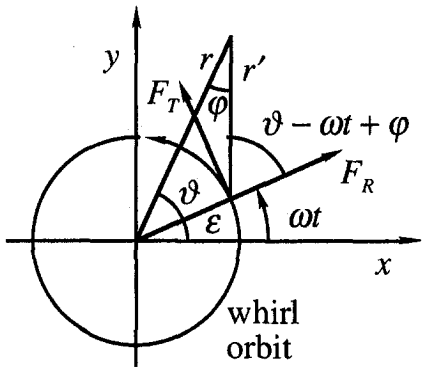

Fig. 2 Schematic of whirl motion, coordinates and rotordynamic forces

2 Linearized Dynamics of a Bubbly Flow in a Whirling Impeller

We address the problem of the flow of an incompressible liquid of velocity $\mathbf{u}$, pressure p, and density, ρ_L, in a helical inducer rotating with velocity, Ω, and whirling on a circular orbit of small eccentricity, ϵ, at angular speed, ω. We define an absolute (inertial) system of cylindrical coordinates (r, ϑ, z), fixed on the axis of the duct surrounding the inducer, and relative cylindrical coordinates, (r', ϑ', z'), fixed in the impeller, as illustrated in Figs. 1 and 2. Hence, to the first order in the eccentricity, the coordinate transformation is:

$$r = r' - \epsilon \cos(\vartheta - \omega t),$$

$$\vartheta' = \vartheta - \Omega t + \frac{\epsilon}{r} \sin(\vartheta - \omega t) \quad \text{and} \quad z' = z$$

A number of simplifying assumptions are introduced in order to obtain a soluble set of equations that still reflects the dynamics of a whirling inducer in a bubbly mixture. The relative motion of the two phases, whose dynamic role is insignificant in the present linearized approximation (d'Agostino and Brennen, 1989), is neglected. Viscous effects are also neglected, except in the bubble dynamics where they contribute to the damping. As shown in Fig. 1, an infinite helical inducer is considered, with N radial blades, zero blade thickness, hub radius r_H, tip radius r_T, tip blade angle β_T, and constant pitch:

$$P = 2\pi r_T \tan \beta_T = 2\pi r' \tan \beta$$

The mean flow conditions are specified by the flow coefficient, ϕ, and the cavitation number, σ, assuming fully-guided forced-vortex flow with axial velocity $w_o = \phi\Omega r_T$, angular velocity $\Omega_o = \Omega(1 - \phi \cot \beta_{oT})$, zero radial velocity u_o, and uniform mean pressure $p_o = p_{Vo} + \sigma\rho_L\Omega^2 r_T^2/2$ (neglecting centrifugal effects), where p_{Vo} is the vapor pressure of the liquid.

Cavitation is modeled by a uniform distribution of small spherical bubbles of unperturbed radius, R_o, and void fraction, $\alpha \ll 1$. The dynamics of vapor-gas bubbles is modeled as proposed by Nigmatulin et al. (1981), assuming uniform internal pressure, equal gas and vapor temperatures, and linear subsonic bubble oscillations. For assigned values of the pressure, temperature, and surface tension of the surrounding liquid it is possible to determine the amount of non-condensable gas stabilizing a bubble of given radius (d'Auria et al., 1997). The effects of compressibility, inertia, and energy dissipation due to the viscosity of the liquid and the transfer of heat and mass between the two phases are included in the model. In this model, the vapor-gas bubbles, when excited at frequency ω_L, behave as second-order harmonic oscillators:

$$(-\omega_L^2 - i\omega_L 2\lambda + \omega_B^2)\hat{R} = -\frac{\hat{p}}{\rho_L R_o} \tag{1}$$

where $\hat{R}$ and $\hat{p}$ are the complex amplitudes of the bubble radius and liquid pressure perturbations:

$$\tilde{R} = R - R_o = \mathrm{Re}\{\hat{R} \exp(-i\omega_L t)\} \quad \text{and}$$

$$\tilde{p} = p - p_o = \mathrm{Re}\{\hat{p} \exp(-i\omega_L t)\}.$$

Assuming that the gas and vapor densities are negligible when compared to the liquid density and solving the energy equation at $R = R_o$, the damping coefficient $\lambda = \lambda(\omega_L)$ and the bubble natural frequency $\omega_B = \omega_B(\omega_L)$ are obtained as:

Nomenclature

a = sound speed
b = boundary equation
$\mathbf{e}$ = unit vector
E = bubble thermodynamic function
F = force
i = imaginary unit
j = blade index
J = Bessel function of the first kind
k = wave number, thermal conductivity
l = hub excitation mode index
m = blade excitation mode index
n = cross-flow helical coordinate
N = number of blades
p = pressure
P = blade axial pitch
r = radial coordinate
R = bubble radius
s = streamwise helical coordinate
t = time
$\mathbf{u}$ = velocity vector
u, v, w = velocity components
x, y, z = Cartesian coordinates
Y = mass fraction, Bessel function of the second kind
α = void fraction
β = blade angle
γ = specific heat ratio
ϵ = whirl eccentricity
ϑ = azimuthal coordinate
λ = bubble damping coefficient
μ = eigenvalue
ν = kinematic viscosity
ρ = density
σ = cavitation number
τ = bubble volume
φ = angle
ϕ = flow coefficient
ω = frequency, whirl angular speed
Ω = rotational speed

Subscripts and Superscripts

B = bubble, blade
G = gas
H = hub
I = inducer
L = liquid, Lagrangian
M = bubbly mixture
p = pressure
R = radial
T = tangential, blade tip
v = volume
V = vapor
VG = vapor-gas mixture
o = unperturbed or reference value

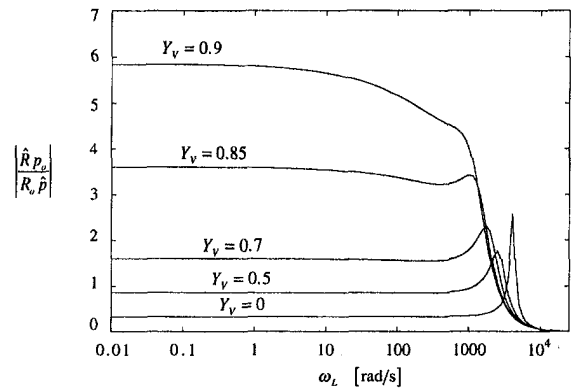

Fig. 3 "Cold bubble." Radius response, $|\hat{R}p_o/R_o\hat{p}|$, of a 1 mm radius gas-vapor bubble in water at $p_o = 5 \cdot 10^3$ Pa, $T_o = 293$ K, as a function of the excitation frequency, ω_L, for different values of the bubble vapor content: $Y_V = 0$ (noncondensable gas bubble), $Y_V = 0.5$, $Y_V = 0.7$, $Y_V = 0.85$, and $Y_V = 0.9$ (from d'Auria et al., 1997).

$$2\lambda = \frac{3p_{Bo}}{\rho_L R_o^2 \omega_L} \operatorname{Im}\left\{\frac{\gamma_{VG}}{E(\omega_L)}\right\} + \frac{4\nu_L}{R_o^2} \tag{2}$$

$$\omega_B^2 = \frac{3p_{Bo}}{\rho_L R_o^2} \operatorname{Re}\left\{\frac{\gamma_{VG}}{E(\omega_L)}\right\} - \frac{2S}{\rho_L R_o^3} \tag{3}$$

which are similar to the expressions of Chapman and Plesset (1972) and Prosperetti (1984, 1991). Here γ_{VG} is the specific heat ratio of the vapor-gas mixture inside the bubble, ν_L and S are the kinematic viscosity and the surface tension of the liquid, and $p_{Bo} = p_o + 2S/R_o$ is the bubble internal pressure, which is the sum of the partial pressure of the vapor, p_{Vo}, and of the non-condensable gas, p_{Go}. The quantity $E = E(\omega_L)$ accounts for the bubble compressibility, interfacial phase changes, heat transfer, mass diffusion, and inertial effects (Nigmatulin et al., 1981).

It is important to note that the dynamic behavior of vapor-gas bubbles changes dramatically when the temperature is such that interfacial heat transfer limits the bubble dynamics (Brennen, 1995). This is illustrated in Figs. 3 and 4, where the response of bubbles with different vapor content is plotted as a function of the excitation frequency for $p_o = 5000$ and 40,000 Pa, respectively corresponding to temperatures of 20° and 70° Celsius. In both cases the normalized amplitude of the bubble response increases rapidly with the vapor content. However, vapor-gas bubbles at 20°C are much more compliant than those

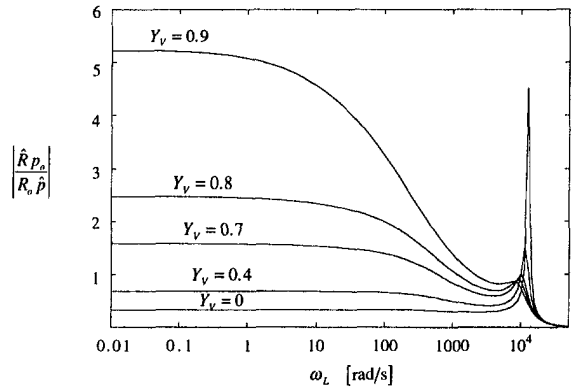

Fig. 4 "Warm bubble." Radius response, $|\hat{R}p_o/R_o\hat{p}|$, of a 1 mm radius gas-vapor bubble in water at $p_o = 4 \cdot 10^4$ Pa, $T_o = 343$ K, as a function of the excitation frequency, ω_L, for different values of the bubble vapor content: $Y_V = 0$ (noncondensable gas bubble), $Y_V = 0.4$, $Y_V = 0.7$, $Y_V = 0.8$, and $Y_V = 0.9$ (from d'Auria et al., 1997).

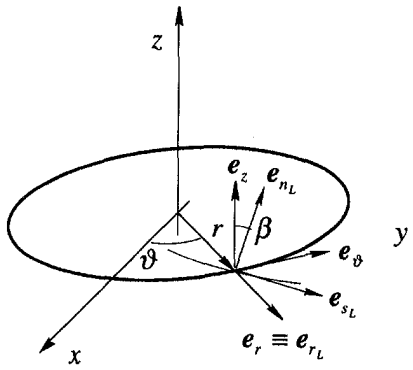

Fig. 5 Schematic of the transformation from the cylindrical coordinates r, ϑ, z to the orthogonal helical coordinates r_L, s_L, n_L

at 70°C. This has important consequences for the forces acting on the inducer.

The perturbation velocities must satisfy the kinematic conditions on the hub, $D(r' - r_H)/Dt = 0$, on the outer casing, $D(r - r_T)/Dt = 0$, and on the blade:

$$\frac{D}{Dt}\left\{\vartheta' + \frac{z'}{r_T}\cot\beta_T - \vartheta_j'\right\} = 0$$

where $\vartheta_j' = 2\pi(j-1)/N$ identifies the angular position of the jth blade ($j = 1, 2, \ldots N$). It is convenient to analyze the flow in body-fitted Lagrangian helical coordinates:

$$r_L = r, \quad s_L = \frac{\vartheta - \Omega_o t}{2\pi}\cos^2\beta - \frac{z - w_o t}{P}\sin^2\beta,$$

$$n_L = \frac{N}{2\pi}(\vartheta - \Omega_o t) + \frac{N}{P}(z - w_o t)$$

moving with the mean flow at axial velocity, w_o, and angular speed, Ω_o, and normalized so that s_L and n_L are incremented by 1 for one rotation about the axis (see Fig. 5). Then, the linearized kinematic conditions for the Lagrangian velocity perturbations ($\tilde{u}$, $\tilde{v}$, $\tilde{w}$) on the solid surfaces are found to be:

$$\tilde{u} = \epsilon\omega_L \sin\left(2\pi s_L + \frac{2\pi}{N} n_L \sin^2\beta - \omega_L t\right)$$

on the hub $\quad r_L = r_H$

$$\tilde{u} = 0 \quad \text{on the casing} \quad r_L = r_T$$

and:

$$\tilde{w} = \epsilon\frac{P\omega_L\cos\beta}{2\pi r_L}\cos\left(2\pi s_L + \frac{2\pi}{N} n_L \sin^2\beta - \omega_L t\right)$$

on the blades $\quad n_L = 1, 2, \ldots N$

where $\omega_L = \omega - \Omega_o$ is the frequency of the bubble excitation in the Lagrangian frame. Finally, appropriate boundary conditions at the inlet and exit of the inducer are needed. Here, for simplicity, we impose periodic conditions $\hat{p}(s_L) = \hat{p}(s_L + 1)$, consistent with the original assumption that the inducer is long in the axial direction.

Generalizing the derivation of d'Agostino and Brennen (1988), linearization of the fluid dynamic equations of the bubbly mixture in rotating coordinates for time-harmonic fluctuations with frequency ω_L and irrotational absolute velocity perturbations yields the following Helmholtz equation for the pressure field:

$$\nabla^2\hat{p} + k^2(\omega_L)\hat{p} = 0 \tag{4}$$

where the free-space wave number, k, is determined using the principal branch of the complex square root from the dispersion relation:

$$\frac{1}{a_M^2(\omega_L)} = \frac{k^2(\omega_L)}{\omega_L^2} = \frac{1}{a_{Mo}^2}\left(\frac{\omega_{Bo}^2}{\omega_B^2 - \omega_L^2 - i\omega_L 2\lambda}\right)$$

Here $a_M(\omega_L)$ is the complex (dissipative) and dispersive (frequency dependent) speed of propagation of harmonic disturbances of angular frequency, ω_L, in the free bubbly mixture, and a_{Mo} is the low-frequency sound speed, given by:

$$a_{Mo}^2 = \frac{\omega_{Bo}^2 R_o^2}{3\alpha(1-\alpha)}$$

where $\omega_{Bo}^2 = \omega_B^2(0)$ is the natural frequency of oscillation of a single bubble at isothermal conditions ($\omega_L \to 0$) in an unbounded liquid. Assuming uniform mean pressure in the inducer, k is constant and, neglecting Coriolis forces ($\Omega_o \approx 0$), to this order of approximation, the complex velocity and pressure perturbations are related, as usual, by $i\omega_L\rho_L(1-\alpha)\hat{\mathbf{u}} = \nabla\hat{p}$.

With the above boundary conditions, the homogeneous Helmholtz equation for the pressure represents a well-posed complex boundary value problem for $\hat{p}$. If the blade angle $\beta = \beta(r)$ is approximated by a constant value β_o at some suitable mean radius r_o, the separable solution (Lebedev, 1965) in the blade channel $j-1 \le n_L \le j$ is:

$$\hat{p} = \sum_{l=0}^{+\infty} a_l R_{Hl}(r_L)\cos\left[2\pi(n_L - j + 1)\right]e^{i(2\pi s_L - \omega_L t)} + \sum_{m=0}^{+\infty} R_{Bm}(r_L)\{c_{m,j}\cos\left[\mu_m(n_L - j + 1)\right] - c_{m,j-1}\cos\left[\mu_m(n_L - j)\right]\}e^{i(2\pi s_L - \omega_L t)} \tag{5}$$

where:

$$a_0 = \epsilon\rho_L(1-\alpha)\omega_L^2 r_H \int_{j-1}^{j} \exp\left(i\frac{2\pi}{N}n_L \sin^2\beta_o\right)dn_L$$

$$a_l = 2\pi l\epsilon\rho_L(1-\alpha)\omega_L^2 r_H \times \int_{j-1}^{j} \exp\left(i\frac{2\pi}{N}n_L \sin^2\beta_o\right)\cos\left[l\pi(n_L - j + 1)\right]dn_L \quad \text{for} \quad l \neq 0$$

$$c_{m,j} = \frac{\epsilon N\rho_L(1-\alpha)\omega_L^2}{i2\pi\mu_m \sin\mu_m} \frac{\displaystyle\int_{r_H}^{r_T} \exp\left(i\frac{2\pi}{N}j\sin^2\beta_o\right)R_{Bm}(r_L)dr_L}{\displaystyle\int_{r_H}^{r_T}\frac{N^2 r_L}{P^2\cos^2\beta_o}R_{Bm}^2(r_L)dr_L}.$$

In these equations $R_{Hl}(r_L)$ and $R_{Bm}(r_L)$ are the modal solutions corresponding to the hub and blade excitation, given in terms of the Bessel functions of the first and second kind and order $\nu = \cos\beta_o$ by:

$$R_{Hl}(r_L) = \frac{1}{B_l r_H}\frac{J_\nu(B_l r_L)Y'_\nu(B_l r_T) - Y_\nu(B_l r_L)J'_\nu(B_l r_T)}{J'_\nu(B_l r_H)Y'_\nu(B_l r_T) - Y'_\nu(B_l r_H)J'_\nu(B_l r_T)}$$

$$R_{Bm}(r_L) = J_\nu(B_m r_L)Y'_\nu(B_m r_T) - Y_\nu(B_m r_L)J'_\nu(B_m r_T)$$

where B_m are the (infinite and positive) zeros of the equation:

$$J'_\nu(Br_H)Y'_\nu(Br_T) - Y'_\nu(Br_H)J'_\nu(Br_T) = 0$$

and B_l and μ_m are the principal square roots of:

$$B_l^2 = k^2(\omega_L) - \frac{l^2\pi^2 N^2}{P^2\cos^2\beta_o} \quad \text{and}$$

$$\mu_m^2 = \frac{P^2\cos^2\beta_o}{N^2}\left[k^2(\omega_L) - B_m^2\right]$$

In the presence of bubble dynamic damping, the series for $\hat{p}$ in Eq. (5) converges rapidly and only the first few terms are needed in the computations.

In the special case of no bubble dynamic damping, k^2 is real and the boundary value problem for $\hat{p}$ is self-adjoint with real eigenvalues, μ_m^2. If, in particular, $k^2 r_T^2 < \cos^2\beta_o$, then all eigenvalues μ_m^2 are negative. Given the functional dependence of the solution, this condition and the dispersion relation identify the cut-off frequency:

$$\omega_L^* = \omega^* - \Omega_o \approx \omega_{Bo}\Big/\left(1 + \frac{3\alpha(1-\alpha)r_T^2}{R_o^2\cos^2\beta_o}\right)^{1/2} \tag{6}$$

beyond which no wave-like propagation of the blade excitation takes place in the n_L-direction. From the above equations it also appears that resonance occurs in response to the hub and blade excitation when $B_l = B_m$ and $\mu_m = l\pi$, respectively. This leads to an infinite set of natural frequencies:

$$\omega_{Llm} = \omega_{lm} - \Omega_o = \omega_{Bo}\Big/\left(1 + \frac{3\alpha(1-\alpha)/R_o^2}{B_m^2 + l^2\pi^2N^2/P^2\cos^2\beta_o}\right)^{1/2} \tag{7}$$

for $l > 0$, $m > 0$. Notice that, consistent with the results of previous dynamic analyses of bubbly flows (d'Agostino and Brennen, 1983, 1988, 1989; d'Agostino et al., 1988; d'Auria, d'Agostino and Brennen, 1994, 1995, 1996), ω_L^* and ω_{Llm} never exceed the resonance frequency ω_{Bo} of an individual bubble, and become much lower when a "cloud interaction" parameter, β, becomes significantly greater than unity. In the present case, $\beta = \alpha L^2/R^2$ where $L = r_T$.

The rotordynamic fluid force per unit length on the inducer is:

$$\mathbf{F} = -\frac{1}{\pi\epsilon P\rho_L\Omega^2 r_T^2}\int_{S_I}(p - p_o)d\mathbf{S} \tag{8}$$

where S_I is the surface of the inducer (hub and blade surfaces) for one interval $0 \le \vartheta \le 2\pi$.

Upon integration, the radial and tangential components, F_R and F_T, of the rotordynamic force on the inducer are more compactly represented in complex form by:

$$F = F_R - iF_T \tag{9}$$

Due to the linear nature of the solution, it is possible to synthesize the rotordynamic forces by examining the separate contributions from the hub and blade motion. With the notation of Eq. (9), the rotordynamic force on the hub generated by the hub motion is:

$$F^{(HH)} = F_R^{(HH)} - iF_T^{(HH)} = -\frac{1}{\pi\epsilon P\rho_L\Omega^2 r_T^2}\sum_{j=1}^{N}\sum_{l=0}^{+\infty}\frac{\pi P r_H}{N}a_l R_{Hl}(r_H)I_{l,j} \tag{10}$$

where:

$$I_{l,j} = \int_{j-1}^{j}\exp\left(-i\frac{2\pi}{N}n_L\sin^2\beta_o\right)\cos\left[l\pi(n_L - j + 1)\right]dn_L$$

Similarly, the rotordynamic force on the hub generated by the blade motion is:

$$F^{(HB)} = F_R^{(HB)} - iF_R^{(HB)} = -\frac{1}{\pi\epsilon P\rho_L\Omega^2 r_T^2} \times \sum_{j=1}^{N}\sum_{m=0}^{+\infty}\frac{\pi P r_H}{N} R_{Bm}(r_H)(c_{mj}A_{mj} - c_{mj-1}B_{mj}) \quad (11)$$

where:

$$A_{mj} = \int_{j-1}^{j} \exp\left(-i\frac{2\pi}{N} n_L \sin^2\beta_o\right)\cos\left[\mu_m(n_L - j + 1)\right]dn_L$$

$$B_{mj} = \int_{j-1}^{j} \exp\left(-i\frac{2\pi}{N} n_L \sin^2\beta_o\right)\cos\left[\mu_m(n_L - j)\right]dn_L$$

The complex representation of the rotordynamic force on the blades generated by the hub motion is:

$$F^{(BH)} = F_R^{(BH)} - iF_T^{(BH)} = \frac{1}{\pi\epsilon P\rho_L\Omega^2 r_T^2} \times \left\{\sum_{j=1}^{N}\sum_{l=0}^{+\infty} i\frac{Pa_l}{2}\int_{r_H}^{r_T} R_{Hl}(r_L)e^{-i(2\pi/N)(j-1)\sin^2\beta_o}dr_L - (-1)^l\sum_{j=1}^{N}\sum_{l=0}^{+\infty} i\frac{Pa_l}{2}\int_{r_H}^{r_T} R_{Hl}(r_L)e^{-i(2\pi/N)j\sin^2\beta_o}dr_L\right\} \quad (12)$$

and, finally, the rotordynamic force on the blades generated by the blade motion is:

$$F^{(BB)} = F_R^{(BB)} - iF_T^{(BB)} = \frac{1}{\pi\epsilon P\rho_L\Omega^2 r_T^2} \times \left\{\sum_{j=1}^{N}\sum_{m=0}^{+\infty} i\frac{P}{2}(c_{mj} - c_{mj-1}\cos\mu_m) \times \int_{r_H}^{r_T} R_{Bm}e^{-i(2\pi/N)(j-1)\sin^2\beta_o}dr_L - \sum_{j=1}^{N}\sum_{m=0}^{+\infty} i\frac{P}{2}(c_{mj}\cos\mu_m - c_{mj-1}) \times \int_{r_H}^{r_T} R_{Bm}e^{-i(2\pi/N)j\sin^2\beta_o}dr_L\right\} \quad (13)$$

Then, the rotordynamic forces on the inducer are simply synthesized as:

$$F = F_R - iF_T = F^{(HH)} + F^{(HB)} + F^{(BH)} + F^{(BB)} \quad (14)$$

The modes R_{Hl}, due to the hub motion, are analogous to the earlier two-dimensional flow solution (d'Auria et al. 1995), except for relatively minor modifications introduced by the helical nature of the flow. These mostly contribute to the radial component of the rotordynamic force. On the other hand, the modes R_{Bm}, due to the blade motion are essentially three-dimensional and generate significant contributions to the tangential forces.

The entire flow has therefore been determined in terms of the material properties of the two phases, the geometry of the impeller, the nature of the excitation, and the assigned quantities ϕ, σ, α, and R_o.

3 Results and Discussion

The calculated rotordynamic forces acting on the inducer as a consequence of the whirl motion are strongly dependent on the propagation of pressure disturbances through the blade channels. The general features of this propagation (behavior in space and time, dependence on the flow parameters, resonances and cut-off frequencies, etc.) have already been examined (d'Auria et al., 1995) and will not be reviewed here in detail.

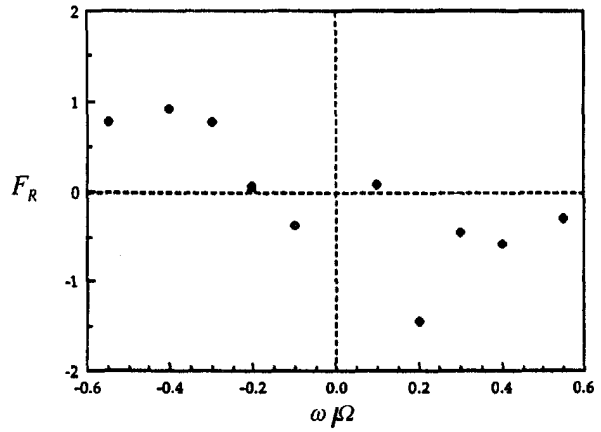

Fig. 6 Experimentally measured radial rotordynamic force on the test inducer as a function of the whirl speed ratio ω/Ω under cavitating conditions at ϕ = 0.049 and σ = 0.106 (adapted from Bhattacharyya, 1994)

The rotordynamic fluid forces predicted by the present model will be compared with the experimental results obtained by Bhattacharyya (1994) for a helical inducer (r_T = 5.06 cm, r_H/r_T = 0.4, β_T = 9°, ϵ = 0.254 mm) operating in water at Ω = 3000 rpm with flow coefficients of ϕ = 0.049 and ϕ = 0.074 (not corrected for hub blockage) and different values of the cavitation number, σ.

Figures 6 and 7 show some typical experimental data at a flow coefficient, ϕ = 0.049, and a cavitation number σ = 0.106. Notice that the forces do not vary quadratically with the whirl frequency, ω, and that their behavior is characterized by multiple zero crossings. The radial force (Fig. 6) is essentially negative for $\omega/\Omega > -0.2$, and has a minimum at $\omega/\Omega \cong 0.2$. Similar behavior was observed for other cavitation numbers (Bhattacharya, 1994). In the tangential forces (Fig. 7), the most interesting feature is the strong positive (destabilizing) peak at $\omega/\Omega \cong 0.2$. This peak was present in all of the experiments of Bhattacharyya (1994); it increased in magnitude as the cavitation number, σ, increased and the flow coefficient, ϕ, decreased.

Typical results for the radial and tangential rotordynamic forces predicted by the present theory for the same inducer at ϕ = 0.049, and σ = 0.106 are displayed in Fig. 8 as a function of the whirl speed ratio ω/Ω. Despite the differences between

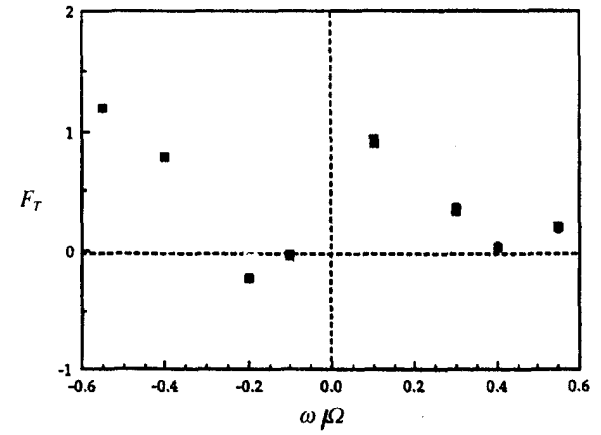

Fig. 7 Experimentally measured tangential rotordynamic force on the test inducer as a function of the whirl speed ratio ω/Ω under cavitating conditions at ϕ = 0.049 and σ = 0.106 (adapted from Bhattacharyya, 1994)

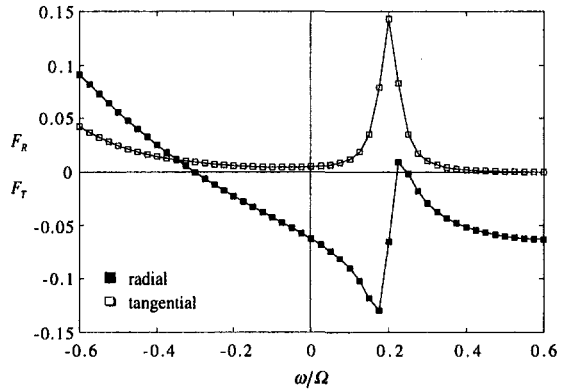

Fig. 8 Radial and tangential rotordynamic forces on the test inducer as a function of the whirl speed ratio ω/Ω under cavitating conditions at ϕ = 0.049, T_o = 293 K, α = 0.005, R/r_T = 0.01, p_o = 2255 Pa, and Y_V = 0.875

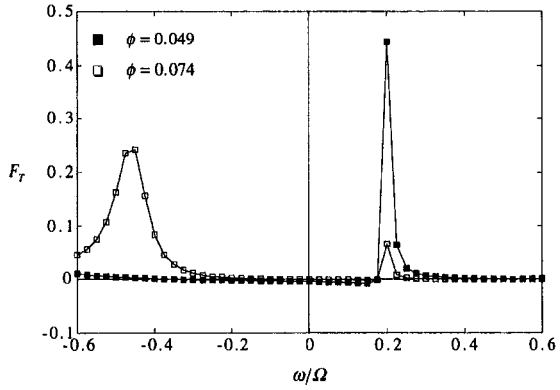

Fig. 10 Tangential rotordynamic force on the test inducer as a function of the whirl speed ratio ω/Ω under cavitating conditions at α = 0.03, T_o = 293 K, R/r_T = 0.01, p_o = 2255 Pa, for two different values of the flow coefficient, ϕ

theory and experiment (notice, for example, that the magnitude of the forces is off by one order of magnitude), the main qualitative features of the forces are correctly reproduced. Note that, consistent with experimental results, the radial force, F_R, is essentially negative for $\omega/\Omega > -0.3$. In addition, the zero crossing for positive whirl ratios and the minimum at $\omega/\Omega \cong 0.2$ have been reproduced by the computations. More important, in view of its implications for rotordynamic stability, Fig. 8 shows that the strong positive peak in the tangential force and its location ($\omega/\Omega \cong 0.2$) are also reproduced by the theory. Figure 9 presents results for various void fractions. As the void fraction increases, the magnitude of the peak in the tangential force increases. This is physically consistent with the experimental observations of Bhattacharyya (1994), who observed the same increase as the cavitation number, σ, decreased. Figure 10 presents results for various flow coefficients and demonstrates that a similar effect occurs as ϕ decreases.

These results are strongly influenced by bubble dynamics effects. The corresponding value of the cloud interaction parameter $3\alpha(1 - \alpha)r_T^2/R_o^2$ (as defined by d'Agostino and Brennen, 1989) is much larger than unity, thus indicating that extensive bubble dynamic and resonant phenomena are likely to occur in the inducer flow.

Finally, we turn our attention to the influence of thermal effects on the rotordynamic forces. Figure 11 shows the behavior of the tangential force for different values of the temperature in the liquid. It may be observed that, as the temperature in the flow increases, the peak decreases in magnitude and eventually disappears. This behavior results from the different bubble response at different temperatures, as exemplified by Figs. 3 and 4.

A few brief remarks on the discrepancies between the present theory and experimental results are appropriate. First, the magnitude of the rotordynamic forces is systematically underestimated. A plausible cause for this discrepancy is the variation of cavitation in the radial direction in the blade channels. Also the (rather unrealistic) assumptions that all bubbles have the same radius and therefore the same resonant dynamic behavior results in more localized peaks than those observed. Finally, the present theory necessarily neglects the secondary flows that are inevitably present in cavitating inducers (Brennen, 1994).

4 Conclusions

The results of this study show that bubble dynamics cause major modifications of the rotordynamic forces on cavitating inducers.

The propagation of the whirl-induced disturbances within the inducer is significantly modified by the large reduction of the sonic speed in the bubbly cavitating flow. The spectral response of the rotordynamic fluid forces is strongly correlated to the cloud interaction parameter, $3\alpha(1 - \alpha)r_T^2/R_o^2$, and the relative magnitude of the excitation and bubble resonance frequencies. Most of the paper focuses on cavitation that is uninhibited by thermal effects though we also demonstrate the damping effects introduced when thermal effects become important.

The computations show that the rotordynamic fluid forces on the inducer in bubbly cavitating flows no longer vary quadratically with the whirl frequency, as in noncavitating conditions.

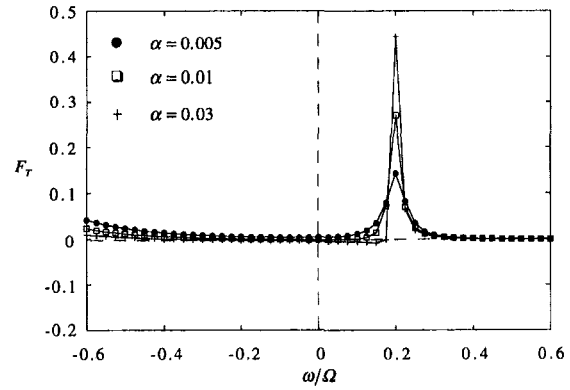

Fig. 9 Tangential rotordynamic force on the test inducer as a function of the whirl speed ratio ω/Ω under cavitating conditions at ϕ = 0.049, T_o = 293 K, R/r_T = 0.01, p_o = 2255 Pa, for three different values of the void fraction, α

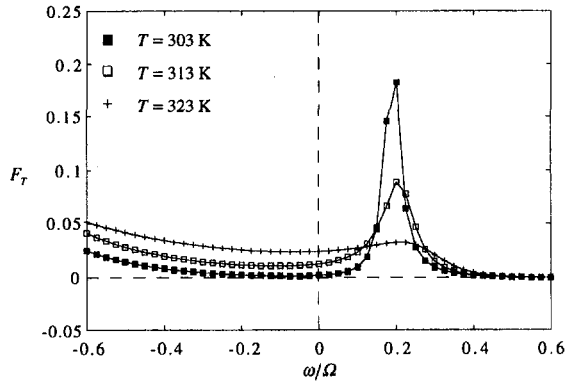

Fig. 11 Tangential rotordynamic force on the test inducer as a function of the whirl speed ratio, ω/Ω, under cavitating conditions at ϕ = 0.049, R_o/r_T = 0.007, p_L = 35000 Pa, and three different temperature levels

The theory qualitatively reproduces the main characteristics of the rotordynamic forces (though there are significant quantitative discrepancies). In particular, the occurrence of a strong destabilizing peak in the tangential force is correctly predicted, including the frequency at which it occurs and the evolution of the magnitude with cavitation number and flow coefficient. These results provide the first real insight into the complex physical phenomena observed experimentally.

Acknowledgments

This research project was carried out on internal funds by CentroSpazio, Ospedaletto (Pisa) Italy, as well as under a European Space Agency External Post-Doctoral Fellowship. Financial support was also provided by a grant from the Foundation Blanceflor Boncompagni-Ludovisi, född Bildt. The authors would like to express their gratitude to Mr. Riccardo Marsili, undergraduate student at Pisa university, for carrying out most of the computations, to Prof. Mariano Andrenucci, Director of Centrospazio, and Prof. Renzo Lazzeretti of the Aerospace Engineering Department, University of Pisa, Pisa, Italy, for their friendly encouragement in the completion of the present work.

References

Bhattacharyya, A., 1994, "Internal Flows and Force Matrices in Axial Flow Inducers," Ph.D. thesis, Division of Engineering and Applied Science, California Institute of Technology, Pasadena, CA.

Brennen, C. E., 1994, *Hydrodynamics of Pumps,* Concepts ETI, Inc. and Oxford University Press.

Brennen, C. E., 1995, *Cavitation and Bubble Dynamics,* Oxford University Press.

Chapman, R. B., and Plesset, M. S., 1972, "Nonlinear Effects in the Collapse of a Nearly Spherical Cavity in a Liquid," ASME *Journal of Basic Engineering,* Vol. 94, pp. 172–183.

d'Agostino, L., and Brennen, C. E., 1988, "Acoustical Absorption and Scattering Cross-Sections of Spherical Bubble Clouds," *Journal of the Acoustical Society of America,* Vol. 84 (6), pp. 2126–2134.

d'Agostino, L., and Brennen, C. E., 1989, "Linearized Dynamics of Spherical Bubble Clouds," *Journal of Fluid Mechanics,* Vol. 199, pp. 155–176.

d'Agostino, L., Brennen, C. E., and Acosta, A. J., 1988, "Linearized Dynamics of Two-Dimensional Bubbly and Cavitating Flows over Slender Surfaces," *Journal of Fluid Mechanics,* Vol. 192, pp. 485–509.

d'Auria, F., d'Agostino L. and Brennen C. E., 1994, "Linearized Dynamics of Bubbly and Cavitating Flows in Cylindrical Ducts," ASME FED Vol. 194, pp. 59–66.

d'Auria F., d'Agostino L. and Brennen C. E., 1995, "Bubble Dynamic Effects on the Rotordynamic Forces in Cavitating Inducers," ASME FED Vol. 201, pp. 47–54.

d'Auria F., d'Agostino L., and Brennen C. E., 1996, "Dynamic Response of Ducted Bubbly Flows to Turbomachinery-Induced Perturbations," ASME JOURNAL OF FLUIDS ENGINEERING, Vol. 118, pp. 595–601.

d'Auria, F., d'Agostino, L., and Burzagli, F., 1997, "Linear Stability of Parallel Two-Dimensional Shear Layers Containing Vapor-gas Bubbles," ASME FEDSM, Vancouver, BC, June 22–26.

Franz, R., Acosta, A. J., Brennen, C. E., and Caughey, T. K., 1990, "The Rotordynamic Forces on a Centrifugal Pump Impeller in the Presence of Cavitation," ASME JOURNAL OF FLUIDS ENGINEERING, Vol. 112, pp. 264–271.

Jery, B., Brennen, C. E., Caughey, T. K., and Acosta, A. J., 1985, "Forces on Centrifugal Pump Impellers," *Second International Pump Symposium,* Houston, Texas, April 29–May 2.

Lebedev, N. N., 1965, *Special Functions and Their Applications,* Prentice Hall.

Nigmatulin, R. I., Khabeev, N. S., and Nagiev, F. B., 1981, "Dynamics, Heat and Mass Transfer of Vapor-Gas Bubbles in a Liquid," *International Journal of Mass Transfer,* Vol. 24(6), pp. 1033–1044.

Prosperetti, A., 1984, "Bubble Phenomena in Sound Fields: Part One," *Ultrasonics,* Mar., pp. 69–78.

Prosperetti, A., 1991, "The Thermal Behavior of Oscillating Gas Bubbles," *Journal of Fluid Mechanics,* Vol. 222, pp. 587–616.

Rosenmann, W., 1965, "Experimental Investigations of Hydrodynamically Induced Shaft Forces with a Three Bladed Inducer," *Proceedings of the ASME Symposium on Cavitation in Fluid Machinery,* pp. 172–195.

R. Hirschi
Research Associate.

Ph. Dupont
Research Associate.

F. Avellan
Professor.

Laboratory of Hydraulic Machines,
Swiss Federal Institute of Technology,
1007 Lausanne, Switzerland

J.-N. Favre

J.-F. Guelich

Sulzer Pumps Ltd.,
8401 Winterthur, Switzerland

E. Parkinson
Hydro-Vevey Ltd.,
1800 Vevey, Switzerland

Centrifugal Pump Performance Drop Due to Leading Edge Cavitation: Numerical Predictions Compared With Model Tests

The aim of this paper is to present the results obtained with a 3-D numerical method allowing the prediction of the cavitation behavior of a centrifugal pump and to compare this prediction to model tests. The influence of the diffuser on the pump performances, for a cavitating flow, is taken into account by performing coupled computations. The proposed method, which allows the performance drop prediction, consists of assuming the cavity interface as a free surface boundary of the computation domain and in computing the single phase flow. The unknown shape of the interface is determined using an iterative procedure matching the cavity surface to a constant pressure boundary (p_v). The originality of the method is that the adaptation process is done apart from the flow calculation, allowing to use any available code.

Introduction

Cavitation behavior prediction of hydraulic machines, such as inception σ_{ui} and standard σ_{us} cavitation coefficients, partial cavity length and its associated performance drop is of high interest for the manufacturers.

When upgrading existing hydraulic installations or designing new geometries, the cavitation guarantees are often the main limiting features. A precise prediction of this phenomenon by numerical simulation is then essential. In recent years, models to predict cavitation development have been refined and applied with success on isolated profiles, for steady (Lemonnier and Rowe, 1988; Dupont and Avellan, 1991) and unsteady flows (Delannoy and Kueny, 1990; Kubota et al., 1992). Some 3-D models, based on potential, S1/S2 and Euler flow computation were also developed, but without taking into account the 3-D turbulent and viscous effects of the cavity on the flow (Kinnas and Fine, 1993; Maitre et al., 1993).

The aim of this paper is to present results obtained with a new 3D numerical method allowing the cavitation behaviour prediction of pumps. This method considers the cavity interface as a free surface boundary of the computation domain. As it has been done on a 2D profile by Yamaguchi and Kato (1983), the cavity shape is iteratively modified until the pressure at its interface is constant and equal to the vapor pressure (p_v). This method has the advantage of being independent of the flow computation code. However, the iterative process could be quite time consuming if starting from the solid surface of the blade. So, an original procedure is used to estimate an initial cavity shape. This approach has been successfully validate on a twisted elliptical hydrofoil, for nonconfined flows showing important 3D effects (Hirschi and Dupont, 1998). To present the accuracy of the proposed method on hydraulic machines, numerical calculations performed on a centrifugal pump (n_q = 15) and a pump-turbine (n_q = 66) with a commercial Navier-Stokes code (TASCflow®) are compared with measurements. Particular operating points are chosen to predict the impeller cavitation behaviour.

These calculations are done in 3 steps: First, a cavitation free flow computation is performed, in order to define the hydraulic performances and the cavitation inception coefficient σ_{ui}, which is predicted using the minimum pressure coefficient calculated over the blade. Then, the initial cavity shape is established as a function of the cavitation coefficient. Finally, the cavitation coefficient σ_{us}, corresponding to the beginning of the performance drop, is determined by a direct computation of the pump flow, taking into account the flow modification due to the cavitation sheet. The comparison with the measurements is done defining a local cavitation coefficient, based on the σ_u cavitation coefficient measured during the model tests (Avellan, 1993; Dupont et al., 1993).

The cavitation behavior prediction of the impeller is only possible if the velocity field at its inlet is well known. As no experimental surveys of the impeller inlet flow were done for the pump n_q = 15, a flow computation of the inlet pipe is performed in order to define the velocity field and the evolution of the absolute flow angle at its outlet.

On Fig. 1 is represented the flow characteristics at this location. Figure 1 brings to the fore the quality of the resulting flow distribution. The angular variations in comparison with the ideal angle of 90 degrees are lower than 0.1 degree and the meridional velocity is quite constant across the radial direction. For the pump-turbine, experimental surveys have been performed and are represented on Fig. 2. We can observe also a very good quality of the flow field. Considering these results, one can assume the velocity field to be axial and constant at the outlet of the inlet pipe. This condition will be used as an inlet condition for all impeller flow computations.

Contributed by the Fluids Engineering Division for publication in the JOURNAL OF FLUIDS ENGINEERING. Manuscript received by the Fluids Engineering Division September 24, 1997; revised manuscript received September 24, 1998. Associate Technical Editor: B. Schiarvello.

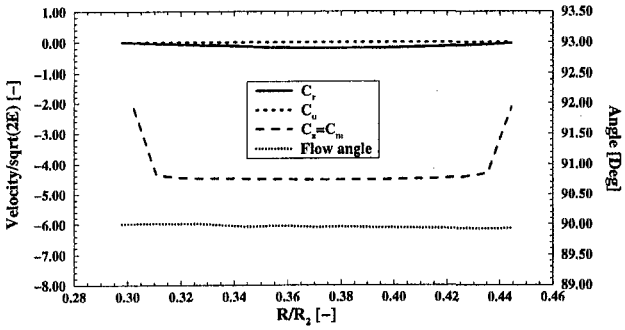

Fig. 1 "Numerical" survey of the velocity components at the outlet of the inlet pipe

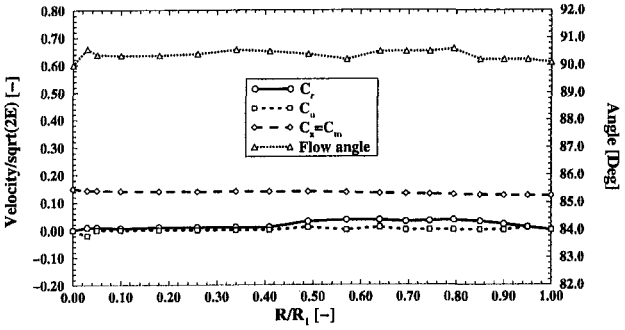

Fig. 2 Experimental survey of the velocity field at the pump-turbine inlet (RMS error = 2.3 percent)

Cavity Modeling

In the proposed method, the cavity prediction is done independent from the flow computation code. As the cavity shape has an influence on the mean flow, an iterative process needs to be applied between the CFD code and the cavitation prediction one. Based on the pressure distribution along the cavity given by the CFD computation, a deformation algorithm is used to modify the interface shape in order to reach a constant pressure equal to the vapor pressure along it. In the equilibrium calculation at the interface, only the pressure term is taken into account, neglecting the shear rate tensor term as well as the surface tension at the interface (Hirschi, 1998). After each cavity adaptation, the mesh of the flow domain needs to be adapted to the new cavity interface and a flow computation is performed using the previous solution extrapolated on the new mesh as an initial solution. As this iterative process could be quite time consuming if beginning with a zero cavity thickness, an initial cavity shape is used.

Cavity Surface Tracking Method. The cavity shape is adapted step by step according to the pressure distribution obtained with the flow computation at the previous iteration. If one considers t the subscript corresponding to the calculated values at the previous iteration, the expression of the modified cavity thickness $\vec{e}$ at the abscissa ξ along the streamline η is given by:

$$\vec{e}(\xi, \eta, t+1) = \vec{e}(\xi, \eta, t) + \lambda C_2[c_p(\xi, \eta, t) + \chi_c] \cdot \vec{n}(\xi, \eta, t) \quad (1)$$

where $\vec{n}$ represents the normal direction to the cavity interface at the point (ξ, η, t) and λ is function of the flow confining, which depends mainly on the blade to blade distance for hydraulic machines. C_2 is a factor depending on a relaxation coefficient C_1.

$$C_2 = \frac{[2 - 2^{(1-C_1)}]}{1 + \mathcal{R}(\xi, \eta, t)} \quad [0 \le C_2 \le 1] \quad (2)$$

$$C_1 = \begin{cases} 1 & \text{if } |c_p(\xi, \eta, t) + \chi_c| > S_{cp} \\ \dfrac{|c_p(\xi, \eta, t) + \chi_c|}{S_{cp}} & \text{otherwise} \end{cases} \quad (3)$$

The coefficient $\mathcal{R}$, which corresponds to the local curvature of the cavity is given by $|(\partial^2 \vec{e}/\partial s^2)(\xi, \eta, t)|$. This coefficient allows to avoid oscillations in regions where high thickness gradients occur, such as the beginning or the closure of the cavity. S_{cp} corresponds to the root mean square of the difference $\delta(\xi, \eta, t)$ between the pressure coefficient at the abscissa ξ and the local cavitation coefficient value χ_c, according to the cavity length ($L_c = f(\eta, t)$).

Nomenclature

Cp = pressure coefficient $Cp = (p - p_1)/(\frac{1}{2}\rho U_1^2)$
E = massic energy J/kg
Fr = Froude number Fr = $C/\sqrt{2gR_2}$
H = head m
L_c = cavity length m
NPSE = net positive suction energy J
P = power W
Q = flow rate m^3/s
R = impeller radius (generic) m
R = bubble radius m
S, A = area m^2
S_{cp} = standard deviation of Cp
T = torque Nm
Z = altitude m
e = cavity thickness m
k = turbulent kinetic energy $k = \frac{1}{2}\overline{c_i'^2}$ J/kg
k_{rd} = coefficient of viscous losses
l_r = length of the cavity closure region m
n = rotation speed rpm
p = static pressure N/m^2
p_v = vapor pressure N/m^2
s = curvilinear abscissa m
$\vec{c}, C$ = absolute velocity m/s
$\vec{r}$ = position vector m
$\vec{u}, U$ = circumferential velocity m/s
$\vec{n}$ = normalized vector m/s
α = absolute flow angle °
ϵ = precision criterion
$\vec{\Omega}, \omega$ = angular rotation speed s^{-1}
ρ = density kg/m^3
ξ, η = local curvilinear coordinates m
n_q = specific speed $n_q = n(gQ^{1/2})/(E^{3/4})$
χ_c = local cavitation coefficient
$\chi_c = (p_1 - p_v)/(\frac{1}{2}\rho U_1^2)$
φ = flow rate coefficient
$\varphi = Q/(\pi\omega R^3)$
ψ = energy coefficient
$\psi = (2E)/\omega^2 R^2)$
σ_u = net positive suction energy coefficient
$\sigma_u = (2\text{NPSE})/(\omega^2 R_1^2)$
ψ_r = loss energy coefficient
$\psi_r = k_{rd}(R_2^2 A_2^2)/(R_1^2 A_1^2)\varphi_2^2$
RMS = Root mean square value

Subscripts

3 = pump outlet
2 = impeller outlet
1 = impeller inlet
0 = pump inlet
x = reference to a particular streamline
t = reference to the previous time step
o = section of reference
bep = reference to the best efficiency point
* = referred to the cavitation free value
m, r, u = reference to velocity component (m: meridional, r: radial, u: circumferential)

$$S_{cp} = \sqrt{\frac{1}{L_c}\int_{\xi=0}^{\xi=L_c} [\delta(\xi, \eta, t) - \overline{\delta}(\eta, t)]^2 d\xi} \quad (4)$$

$$\delta(\xi, \eta, t) = c_p(\xi, \eta, t) + \chi_c \quad (5)$$

with $\overline{\delta}(\eta, t)$ the average value of $\delta(\xi, \eta, t)$ defined as:

$$\overline{\delta}(\eta, t) = \frac{1}{L_c}\int_{\xi=0}^{\xi=L_c} \delta(\xi, \eta, t) d\xi \quad (6)$$

In most of cases, the cavity beginning does not correspond to the blade leading edge, so the deformation starts at the abscissa ξ where the following condition is respected:

$$\left|\frac{\partial^2 \vec{e}}{\partial s^2}(\xi, \eta, t)\right| > 0 \quad (7)$$

The convergence of the iterative deformation process is obtained when the standard deviation S_{cp} is less than a given precision ϵ.

Initial Cavity Shape. If one assumed that an attached cavity corresponds to the transition of a high number of bubbles, known as the saturation phenomenon (Arn et al., 1996), then the use of the Rayleigh-Plesset equation could be justified to estimate an initial cavity shape. The envelope of bubbles in evolution over the blade is used to define the initial cavity shape as shown on Figure 3. The radius instead of the diameter of the bubble is chosen to define this envelope. This is based on the experimental observation of a hemispherical shape of the bubbles in evolution along a solid wall and on a measured height of these bubbles corresponding roughly to their planform radius (see Arn et al., 1998). This bubble radius evolution is calculated along mesh lines in the main flow direction using the pressure distribution obtained for the non-cavitating condition. The bubble growth is ensured using the critical bubble radius as initial radius according to the minimum pressure along the considered mesh line.

Cavity Closure Condition. The free surface tracking method is applicable as long as the constant pressure condition along the interface is valid. As one can expect, this is no more the case in the cavity closure region. In this special region, one can observe a non stationary two-phase flow, which can not be treated by the proposed approach. In order to avoid this problem, a specific model for the cavity closure needs to be used, which gives an averaged value of the pressure distribution.

The cavity closure model developed in this study is very similar to the one used by Yamaguchi and Kato (1983). It is based on the fact that the physics at the cavity closure is similar to a collapsing bubble cloud which size could be roughly evaluated using a Rayleigh model. In our case the cavity closure is defined using the maximum cavity thickness as the initial radius and calculating the bubble radius evolution, neglecting the viscous effects, the surface tension and the inner state of the bubble. The resulting bubble envelope is used as the cavity closure

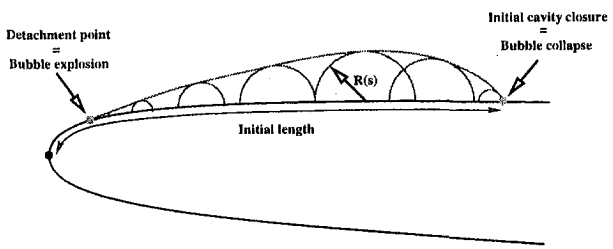

Fig. 3 Initial cavity shape = bubble radius evolution envelope

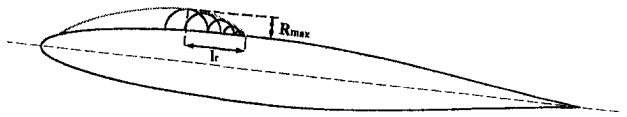

Fig. 4 Cavity closure model based on the Rayleigh time

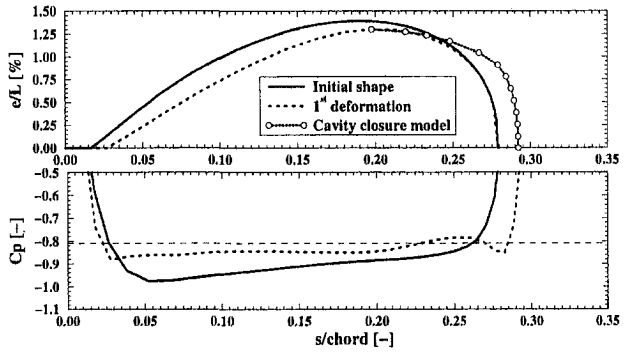

Fig. 5 Cavity shape and corresponding pressure distribution before and after the first deformation

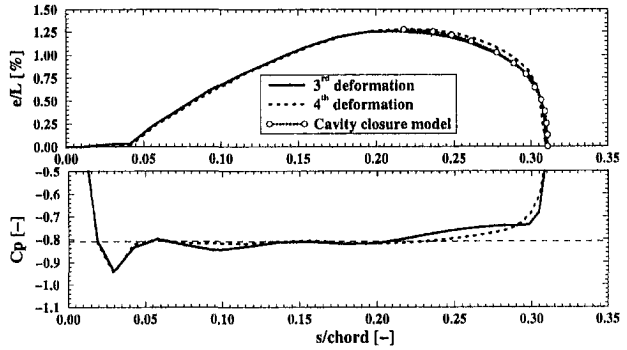

Fig. 6 Cavity shape and corresponding pressure distribution before and after the fourth deformation

shape, applied from the maximum thickness of the modified cavity up to its closure, as shown on Fig. 4.

An application example of this modeling on a 2D profile (NACA009 section) is shown on Figs. 5 and 6, from the first iteration to the last one. Only the cavity interface is represented.

Flow Computation. Eight operating points of the $n_q = 15$ pump are calculated using a Reynolds averaged Navier-Stokes finite volume code (ASC, 1995). The turbulence is taken into account using the well known $k - \epsilon$ model. A "wall-function" is used to model the flow in the low Reynolds number region near solid walls. This way allows to relate the near wall tangential velocity to the wall shear stress by means of a logarithmic relation. An uniform axial velocity field is imposed at the impeller inlet. As an outlet condition, the pressure is set to zero on one node of the domain outlet. An upstream turbulence level of 5 percent and a turbulence mixing length of 10 percent of R_2 is imposed. For cavitating computations, two different boundary conditions have been applied along the cavity interface. The first one corresponds to a slip condition and the second one considers the interface as a solid wall. As described in the work of Hirschi (1998), no major difference has been observed between the two solutions.

The mesh of the blade to blade channel, shown on Fig. 7, is a single structured block with 95 nodes in the flow direction, 41 from suction to pressure side and 17 from hub to shroud.

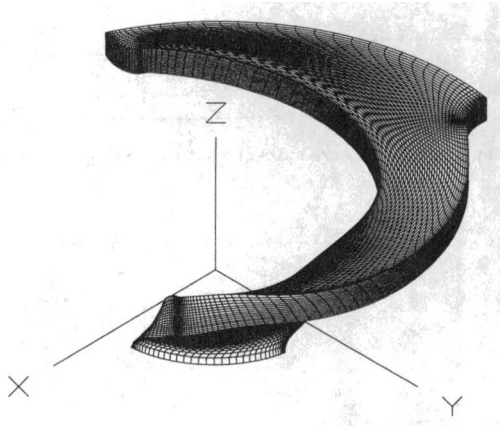

Fig. 7 3D view of a blade to blade channel mesh of the impeller

Results

Cavitation Inception. A cavitation coefficient is defined as a function of the local pressure value p_{1x} at a point of the impeller low pressure section. Generally, the pressure in this section is not uniform and at each considered mean streamline corresponds a different pressure value p_{1x}. Thus, it is unrealistic to use this coefficient to evaluate the cavitation risk of a machine. However, it is possible to establish a relation between this coefficient and the reference conditions at the low pressure section of the machine (Franc et al., 1995).

$$\chi_c = \sigma_u + \frac{R_2^2}{R_1^2}\left\{\frac{\psi_2}{\mathrm{Fr}^2}\frac{Z_o - Z_{1x}}{2R_1} - \left[1 + \frac{1}{tg^2\alpha_{1x}}\right]\frac{R_2^2A_2^2}{R_1^2A_1^2}\varphi_2^2 - \psi_{r0\div 1x}\right\} \quad (8)$$

In spite of its relative complexity, the previous relation shows clearly that the local cavitation coefficient value, which controls the cavitation development in the impeller, is strongly influenced by the operating point $\varphi - \psi$ of the machine, and this, even if the net positive suction energy coefficient is constant. The cavitation inception condition, in terms of local cavitation coefficient and static pressure, is given by the condition $\chi_c \leq -Cp_{\min}$ where $Cp_{\min}$ represents the minimum value of the calculated static pressure coefficient in the impeller. In the case of a pump with an axial shaft ($Z_o = Z_{1x}$) and an axial inlet velocity field ($\alpha_{1x} = \pi/2$), this condition is given by:

$$\sigma_u \leq -Cp_{\min} + [1 + k_{rd}]\frac{R_2^4A_2^2}{R_1^4A_1^2}\varphi_2^2 \quad (9)$$

On Fig. 8 are compared the cavitation inception curves obtained with different criteria. The first one was determined with the minimum pressure coefficient calculated, the second one with the cavitation inception criterion defined as a cavity length equal to 2% of the outlet radius of the impeller. The last one corresponds to the measurement obtained with this same criterion of 2 percent. These results show that the measurements are very well predicted if one used the same criterion. In this particular case: relative high NPSE of the installation, the economic interest was to use a normal impeller as suction impeller in order to save the additional cost of an optimized suction impeller. Even if the σ_u/ψ_{bep} value is maximum in the range of the best efficiency point ($\varphi_2 = 0.8-1.$), which corresponds to a bad cavitation behaviour, the results is sufficient and acceptable for this case. For such a pump of a small specific speed, an estimation of the leakage flow between the impeller and the casing on shroud side, in order to calibrate the real flow inside the impeller, is also essential for an useful comparison.

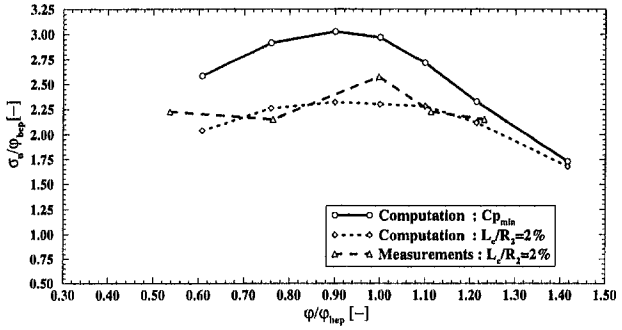

Fig. 8 Pump n_q = 15: cavitation inception prediction compared with measurements (RMS error = 4.5 percent)

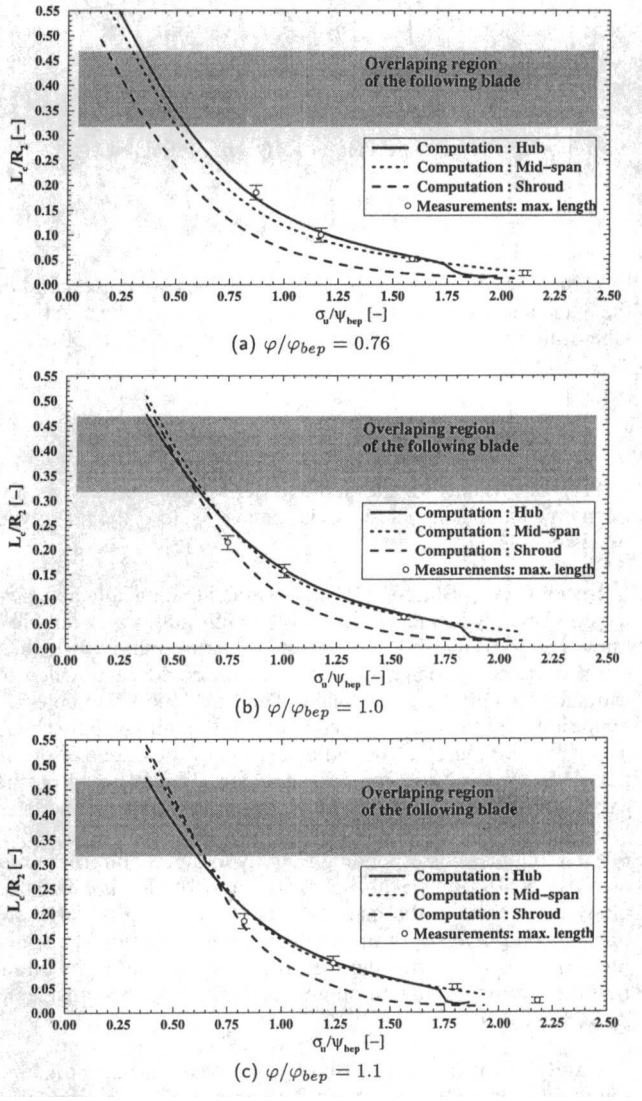

Fig. 9 Predicted cavity lengths compared with measurements on a n_q = 15 pump: φ_2/φ_{bep} = 0.76, 1.0, and 1.1

Cavity Length. On Fig. 9 are reported the estimated cavity lengths, for the n_q = 15 pump, on three streamlines, from hub to shroud, for three operating points. The cavity lengths represented on these graphics correspond to the bubble collapse location calculated by the Rayleigh-Plesset equation.

The comparison with the measurements shows that in the case of this low specific speed pump, this initial length is sufficiently

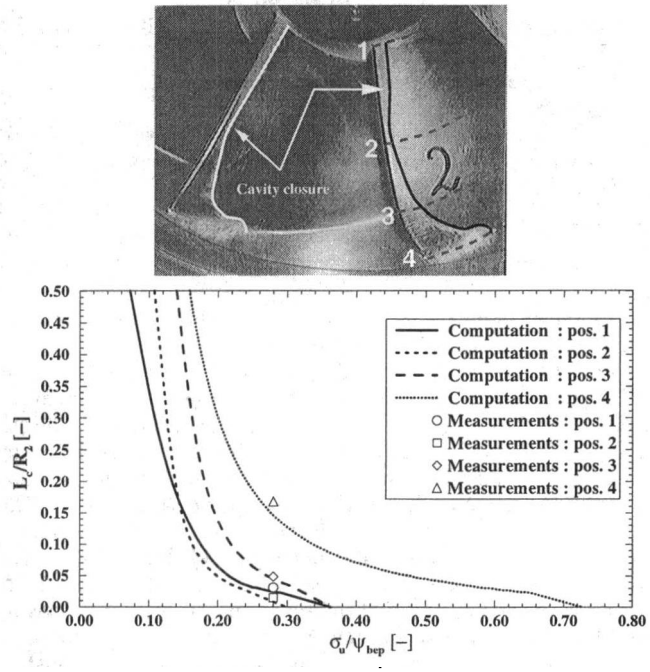

Fig. 10 Predicted cavity lengths compared with measurements on a n_q = 66 pump-turbine at part load: σ_u/ψ_{bep} = 0.43, φ_2/φ_{bep} = 0.9 (RMS error = 4.2 percent)

predictive for a wide range of σ_u. However, this approach is accurate as far as the cavity length is smaller than a characteristic length for which the flow modifications induced by the cavity are no more neglectable. For higher cavitation development, it is then necessary to applied the deformation method in order to take into account these flow modifications.

To demonstrate the accuracy of this method for higher specific speed values, we have represented on Fig. 10 the cavity lengths prediction obtained on a n_q = 66 pump-turbine for a low cavitation development. We can see that this method predicts also very well the cavitation development across the impeller span.

Cavity Deformation. Once the initial cavity is determined, its shape is iteratively modified until the calculated pressure at its interface is constant and equal to the vapor pressure. The pressure coefficient distributions obtained along different grid lines after a cavitation free flow computation and for a σ_u/ψ_{bep} value of 0.265 are compared on Fig. 11, for the pump n_q = 15. The cavity effect on the pressure distribution corresponds to the constant pressure region on the suction side. A three-dimensional representation of the cavitation sheet is shown on Fig. 12.

Head Drop Computation. The energy loss due to the cavitation development is determined by comparing the transferred energy E_t given by the impeller with the energy provided to the flow E for different cavitation coefficient values. This is expressed by:

$$E = E_t - E_r \tag{10}$$

where E_t represents the transferred energy, E the provided energy and E_r the lost energy.

Transferred Energy. The energy transferred through the impeller, and the corresponding energy coefficient, are given by:

$$E_t = \frac{P_t}{\rho Q} = \frac{\vec{T}_t \cdot \vec{\Omega}}{\rho Q} \rightarrow \psi_t = \frac{2E_t}{\omega^2 R_2^2} \tag{11}$$

The transferred torque $\vec{T}_t$ is determined by the pressure and the viscous forces integration on the blades and impeller side walls:

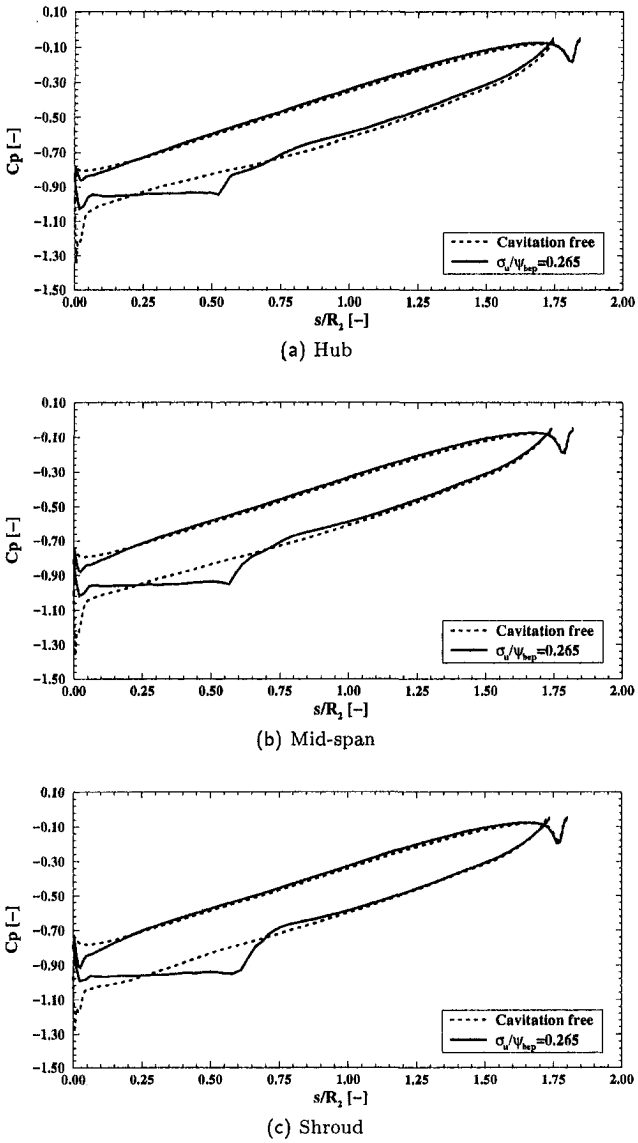

Fig. 11 Pressure coefficient distribution without and with cavitation for σ_u/ψ_{bep} = 0.265: φ_2/φ_{bep} = 1.21

$$\vec{T}_t = \int_{S_{\text{imp}}} \vec{r} \wedge (p\vec{n})ds + \int_{S_{\text{imp}}} \vec{r} \wedge (\bar{\bar{\tau}}\vec{n})ds \tag{12}$$

where S_{imp} represents the blades and impeller side walls, p the calculated static pressure, $\vec{r}$ the position vector and $\bar{\bar{\tau}}$ the constraints tensor, which corresponds to the molecular and turbulent viscosity.

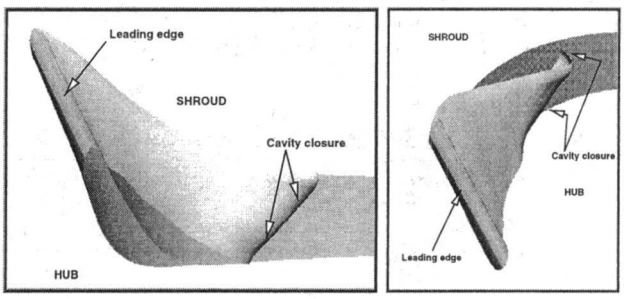

Fig. 12 Pump n_q = 15: 3D view of the cavitation sheet

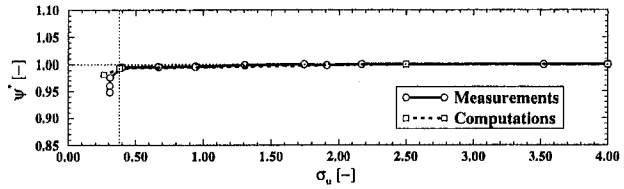

(a) Diffuser A ($RMS\ error = 0.6\%$)

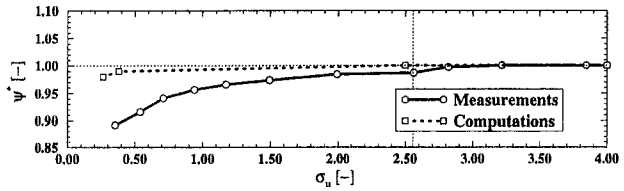

(b) Diffuser B ($RMS\ error = 0.9\%$)

Fig. 13 Predicted and measured head drop for two different diffuser geometries. The impeller geometry and the flow rate are identical for both cases.

Provided Energy. The energy provided to the flow, and the corresponding energy coefficient, are calculated using the hydraulic energy difference between the low pressure and the high pressure section of the machine, and expressed by:

$$E = gH_3 - gH_0 \rightarrow \psi = \frac{2E}{\omega^2 R_2^2} \tag{13}$$

with

$$gH = \frac{\int_A \left(\frac{p}{\rho} + gz + \frac{c^2}{2}\right)\vec{c}\,\vec{n}dA}{\int_A \vec{c}\,\vec{n}dA} \tag{14}$$

Comparison Computations—Measurements. In a previous study (Hirschi et al., 1996), we observed that the performance drop due to cavitation could change with the diffuser geometry. Indeed, measurements done at same flow rate ($\varphi_2/\varphi_{bep} = 1.21$), for a same impeller ($n_q = 15$) and two different diffuser geometries show a different cavitation behaviour, as shown on Fig. 13. The main difference between the two diffusers (A and B) is the throat ratio at inlet and outlet, been respectively 1.25 and 1.16. To analyse the diffuser influence on the performance drop, we have done cavitation development predictions using coupled impeller-diffuser flow calculations. On Fig. 15 is represented the calculated geometry including the impeller blades with the attached cavity and the diffuser blades. We have reported for both diffusers, on Tables 1 and 2, the evolution of the calculated provided energy ψ, relatively to the noncavitating condition, for three relative σ_u values. This evolution is calculated for each component (impeller and diffuser) of the pump. We have also compared on the same tables the transferred energy to the provided one for the entire pump. One can first observe that the transferred energy ψ_t remains constant with cavitation coefficient for both diffusers. This means that, even if the pressure distribution on the blades is

Table 1 Provided and transferred energy with diffuser A

	diffuser A			
ψ_c/ψ_{bep}	ψ^*_{imp} [−]	ψ^*_{dif} [−]	ψ^*[−]	ψ_t^* [−]
cav. free.	1.0825	−0.0825	1.	1.109
0.383	1.078	−0.084	0.994	1.108
0.265	1.069	−0.087	0.982	1.103

Table 2 Provided and transferred energy with diffuser B

	diffuser B			
ψ_c/ψ_{bep}	ψ^*_{imp} [−]	ψ^*_{dif} [−]	ψ^*[−]	ψ_t^* [−]
cav. free.	1.148	−0.148	1.	1.175
0.383	1.143	−0.153	0.99	1.176
0.265	1.13732	−0.157	0.98	1.175

modified by cavitation, the total torque is not changed by the cavity development. This demonstrates that, for such cavity extensions, the performance drop is not due to a modification of the transferred energy ψ_t but to an increase of the turbulence losses, as shown by the turbulence kinetic energy evolution given on Fig. 14. This increase of the turbulence losses is shown to be mainly located into the impeller for both diffusers, and particularly in the cavity closure region for $\sigma_u/\psi_{bep} = 0.265$. It is also very interesting to notice that the cavity corresponding to $\sigma_u/\psi_{bep} = 0.383$ does not generate any identifiable increase of turbulence in the closure region. We can then deduced that a cavity development could improve the blade behaviour as a results of a zero pressure gradient on the cavity is more favourable than a positive gradient concerning the energy transfer between the mean flow and the turbulent structures.

The comparison of the provided energy between calculations and measurements for the three cavitation conditions and the two diffusers, given on Fig. 13, leads to the following observations. For the diffuser A, the beginning of the performance drop σ_{us} is very well predicted by the calculation. For the diffuser B, even if there is a small difference in the turbulence kinetic energy at the impeller outlet, the comparison is much less convincing. One can imagine that these differences are due to phenomenon which are not taking into account by the computation, such as unsteady behaviour or cavitation development on the diffuser blades (Hirschi, 1998).

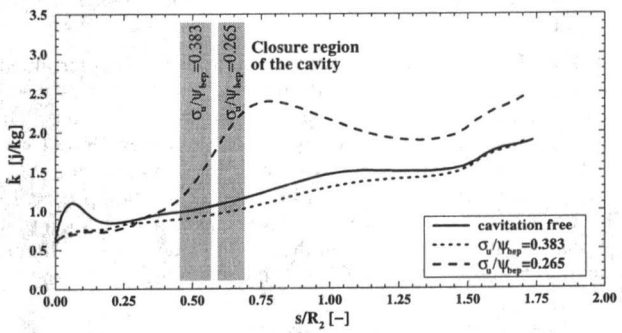

(a) Diffuser A

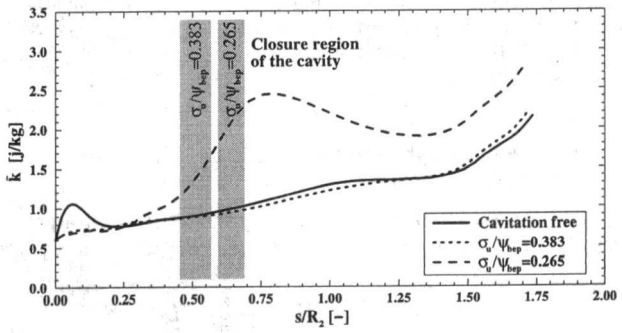

(b) Diffuser B

Fig. 14 Turbulence kinetic energy evolution along the impeller blade in function of the cavitation development

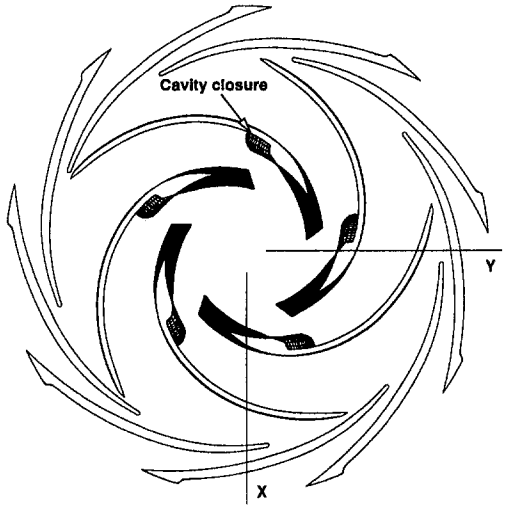

Fig. 15 Impeller and diffuser blades. The impeller mesh takes into account the cavity surface.

Conclusion

Considering an impeller geometry, its behavior and its main cavitation characteristics can be described with the results of a 3-D Navier-Stokes computation, using models of cavitation developments. The predicted behaviour of the cavitating flow in a centrifugal pump, using the proposed method, compares very well with the measurements.

The pressure level corresponding to cavitation inception is determined for all calculated operating points and compared with measurements. The mean standard deviation between the measured and calculated points is less than 4 percent. This point only depends on the flow computation codes accuracy to predict the minimum pressure coefficient along the blade.

The cavity lengths computation using the Rayleigh-Plesset equation provides very good results. Indeed, the measured cavity lengths behaviour is faithfully reproduced by the calculation, and this for all measured operating points.

The prediction of the performance drop beginning is done by a direct flow computation taking into account the cavitation sheet. Coupled computations were performed in order to take into account the influence of the diffuser geometry observed on measurements. Unfortunately, these behavior differences were not point out with the numerical simulations. This leads us to think that these differences are mainly due to unsteady phenomenon and/or cavitation development in the diffuser. However, the very good results obtained with this method shows that, with our present modelling, the performance drop prediction is possible as far as the performance drop is only due to the cavitation development on the impeller blades in the operating range characterized by sheet cavitation regime. To conclude, the results analysis of this study demonstrates that the presented method provides an interesting tool for the 3-D cavitation development prediction in hydraulic machines.

Acknowledgments

The authors are particularly grateful to all the members of the IMHEF Cavitation research group. We wish to thank SULZER Pumps and Hydro-Vevey S.A. which made possible the publication of this paper and the staff of the test-rigs who performed the measurements. This work is financially supported by the Swiss Federal "Commission pour la Technologie et l'Innovation," SULZER Pumps, Hydro-Vevey S. A. and Rolla S. P. Propeller.

References

Arn, C., Dupont, P., and Avellan, F., 1996, "Efficiency Alteration of FRANCIS Turbines by Travelling Bubble Cavitation," *Hydraulic Machinery and Cavitation,* Valencia, Spain, Proceedings of the XVIII IAHR Symposium.

Arn, C., Dupont, P., and Avellan, F., 1998, "Prediction of Francis Turbines Efficiency Alteration due to Travelling Bubble Cavitation," *Third International Symposium on Cavitation,* Vol. 1, pp. 81–85, Grenoble, France, Cavitation 98.

ASC, 1995, *Theory Documentation,* Advanced Scientific Computing.

Avellan, F., 1993, "Cavitation Tests of Hydraulic Machines: Procedures and Instrumentation," Washington, ASME Winter Annual Meeting.

Delannoy, Y., and Kueny, J., 1990, "Two Phase Flow Approach in Unsteady Cavitation Modeling," *Cavitation and Multiphase Flow Forum,* Vol. 98, Toronto, ASME.

Dupont, P., and Avellan, F., 1991, "Numerical Computation of Leading Edge Cavity," *CAVITATION '91,* Vol. 116, pp. 47–54, Portland, Oregon, ASME Summer Annual meeting.

Dupont, P., Parkinson, E., and Walther, W., 1993, "Cavitation Development in a Centrifugal Pump: Numerical and Model Tests Predictions," Washington, ASME Winter Annual Meeting.

Franc, J., Avellan, F., Belahadji, B., Billard, J., Briançon-Marjollet, L., Frechou, D., Fruman, D., Karimi, A., Kueny, J., and Michel, J., 1995, *La Cavitation,* Presses universitaires de Grenoble.

Hirschi, R., 1998, Prédiction par Modélisation Numérique Tridimensionnelle des Effets de la Cavitation à Poche dans les Turbomachines Hydrauliques, Ph.D. thesis, Ecole Polytechnique Fédérale de Lausanne.

Hirschi, R., and Dupont, P., 1998, "Partial Sheet Cavities Prediction on a Twisted Elliptical Planform Hydrofoil Using a Fully 3-D Approach," *Third International Symposium on Cavitation,* Vol. 1, pp. 245–249, Grenoble, France, Cavitation 98.

Hirschi, R., Dupont, P., Avellan, F., Favre, J.-N., Guelich, J.-F., and Handloser, W., 1996, "Leading Edge Cavitation in a Centrifugal Pump: Numerical Predictions Compared with Model Tests," *Hydraulic Machinery and Cavitation,* Vol. 1, pp. 604–613, Valencia, Spain, *Proceedings of the XVIII IAHR Symposium.*

Kinnas, S. A., and Fine, N. E., 1993, "A Numerical Nonlinear Analysis of the Flow Around Two- and Three-Dimensional Partially Cavitating Hydrofoils," *J. Fluid Mech.,* Vol. 254, pp. 151–181.

Kubota, A., Kato, H., and Yamaguchi, H., 1992, "A New Modelling of Cavitating Flows: A Numerical Study of Unsteady Cavitation on a Hydrofoil Section," *J. Fluids Mech.,* Vol. 240, pp. 56–96.

Lemonnier, H., and Rowe, A., 1988, "Another Approach in Modelling Cavitating Flows," *J. Fluid Mech.,* Vol. 195, pp. 557–580.

Maitre, T., Kueny, J., Geai, P., and Kaenel, A. V., 1993, "Numerical Prediction of Three-Dimensional Partial Cavitation in a Rocket Turbopump Inducer," ASME Summer Annual meeting, Washington.

Yamaguchi, H., and Kato, H., 1983, "On Application of Nonlinear Cavity Flow Theory to Thick Foil Sections," *Proc. of Second Int. Conf. on Cavitation,* pp. 167–174, Edinburgh, England, Institution of Mechanical Engineers.

Hitoshi Soyama
Associate Professor,
Department of Machine Intelligence and Systems, Tohoku University, Sendai, Japan

Andrzej Lichtarowicz
Reader (Retired),
Department of Mechanical Engineering, University of Nottingham, Nottingham, NG7 2RD, United Kingdom

Takahiro Momma
Deputy Chief,
Nuclear Power Department, Construction Group, Kajima Corporation, Tokyo, Japan

Edward J. Williams
Senior Lecturer,
Department of Mechanical Engineering, University of Nottingham, Nottingham, NG7 2RD, United Kingdom

A New Calibration Method for Dynamically Loaded Transducers and Its Application to Cavitation Impact Measurement

The erosion produced by cavitation is a serious problem in hydraulic machinery. During investigations of the dynamic loading generated by collapsing cavitation on a surface, a dynamic pressure transducer was developed. The piezoelectric polymer PVDF (Polyvinylidene fluoride) was used as the pressure sensitive material. A novel method of dynamic calibration has also been developed. The transducer is loaded through pencil lead by a beam supported at its other end on a knife edge and loaded at the center by weights. As the static load is increased, the pencil lead breaks and the load is released suddenly. The unloading time is faster than for any other conventional calibration method and is of the same order as cavitation loading. Descriptions of the developments of both the calibration method and the transducer are given. The principal advantages of the new method are the short pulse duration and the simplicity of the test procedure.

The paper is an extension of the previously reported work by Momma and Lichtarowicz (1994), giving further information on the operating characteristics of the transducer in comparison with the traditional ball-dropping method.

1 Introduction

During investigation of the relationship between the loading produced by cavitation and the resulting erosion, a transducer has been developed for measuring the dynamic loads involved. Cavitation loading consists of repeated high intensity impacts caused by collapsing cavitation bubbles. The rise time of the signal can be the order of a few microseconds and its magnitude can reach 10 GPa according to some authors (Jones and Edwards, 1960). Piezoelectric transducers are suitable for such operating conditions. Okada et al. (1989 and 1994) used piezoelectric crystals and Momma (1991), Momma and Lichtarowicz (1994), Hoam (1994), and Arndt et al. (1995) used the piezoelectric polymer, PVDF (Polyvinylidene Fluoride). PVDF transducers were also used for shock wave work by Henckels and Takayama (1986) and by Bauer and Moulard (1987). For cavitation work, piezo-films require electrical insulation from the water and protection from damage caused by the high cavitation loads, which are concentrated on very small impact areas.

The transducer measures the total force generated on its surface and, only in the case when the pressure is uniform over the transducer area, can it be calculated from equation;

$$\text{Pressure} = \text{Force/Transducer area} \qquad (1)$$

In the case of cavitation, the impact area can be obtained from the size of the "pits" produced by plastic deformation in the early stages of the exposure to cavitation. The number of pits in each size group can be counted using a microscope or, more conveniently, using image analysis techniques. The number of pits of a specific size had to be correlated with the same number of force impacts counted from the transducer signal. If the number of pits of chosen size and the number of pulses of some magnitude corresponded, it was assumed that that magnitude pulse had made the pit size. Hence, the pressure produced by cavitation could be obtained.

The experimental work was carried out using an apparatus where a cavitating jet impinged on a soft aluminium target placed normal to the flow. Damage was in the form of pitted or eroded rings (Momma, 1991; Momma and Lichtarowicz, 1993 and 1995).

2 Experimental Apparatus and Procedures

2.1 Transducer. PVDF film has two important properties that make it particularly suitable for dynamic force measurement. The first is the high velocity of sound in the material (c = 2200 m/s), which for 110 μm thick film, gives the high natural frequency of

$$f_N = \frac{c}{2t} = 10 \text{ MHz} \qquad (2)$$

The second is the high piezoelectric stress constant (-3.39×10^{-5} (V/m)/Pa). This gives excellent response and a signal with low noise without the need for amplification.

The film is pliable and can easily be cut to any desired shape using a knife or scissors. It can be obtained in sheet form, either uncoated or coated on both sides with metallic paint or vapour deposited metal film. The metallic paint can be scratched out to leave the desired shape for the transducer and terminals.

Figure 1 shows the transducer mounted on a stainless-steel target. The transducer consists of a 110 μm thick PVDF film, coated on both sides with metallic paint, two electrical terminals attached on either side to the electrodes, two or three layers of Kapton (polyamide) tape with adhesive on one side and a bottom layer of Kapton tape stuck with its adhesive to the PVDF tape. The top tapes provide outer protection and the bottom tape provides electrical insulation. The bottom Kapton tape is bonded to the stainless steel base by the "rim cement" used to bond tubular bicycle tyres to the wheel rim. Both epoxy and cyanoacrylic adhesives dissolve the silver paint on PVDF film. This

Contributed by the Fluids Engineering Division for publication in the JOURNAL OF FLUIDS ENGINEERING. Manuscript received by the Fluids Engineering Division October 20, 1996; revised manuscript received May 15, 1998. Associate Technical Editor: J. Katz.

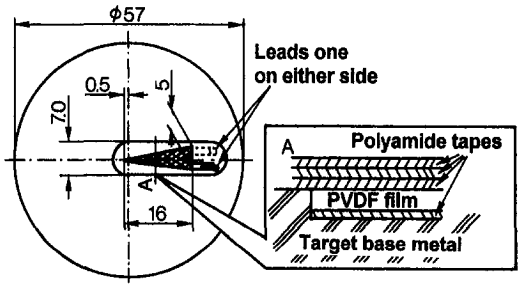

Fig. 1 PVDF piezo-film assembly for a transducer

affects the capacitance so the calibration constant is not uniform over the sensitive area and may also change with time.

The most fragile parts of the transducer are the connection points between the metallic-paint terminals and the wires leading outside. The wires are mechanically connected to the terminals and the joints are painted over with conducting paint. The connections are therefore located outside the maximum erosion zone. The size range of the rectangular transducers was 0.14 ~ 27 mm^2 and that of the triangular transducers was 41 ~ 45.38 mm^2. Large triangular transducers were used to "catch" all zones of cavitation erosion along the radius of the specimen.

2.2 Pulse Height Measuring System. In order to carry out the pulse height analysis, an analogue measurement system with an input pulse height gate circuit was designed, as shown in Fig. 2. The system consists of the piezo-film transducer, the input pulse gate circuit, a digital voltmeter, a digital oscilloscope and a counter. The input signal detected by the transducer is transmitted to the gate circuit (comparator) and any pulse whose peak exceeds the pre-set threshold level generates a trigger signal to activate the counter. By changing the preset level from low to high, an accumulated pulse height distribution can easily be obtained. The circuit consists of two parts, an operational amplifier (magnification ×1 and ×5.83) and a comparator. Since the output voltage from the PVDF transducer was sufficiently high (approximately 10 V), higher amplification was not needed. Furthermore, since the signal from the transducer was very clean, noise filters and pulse holding circuits were not required.

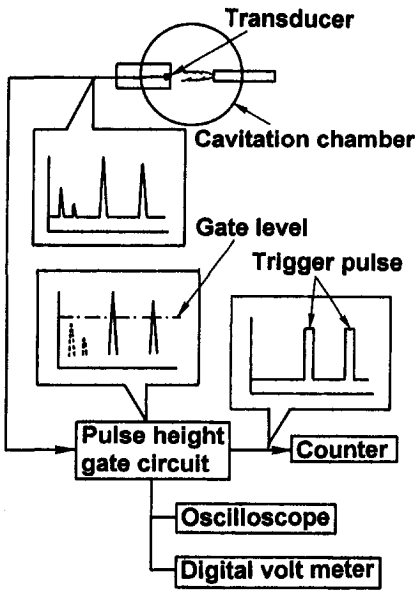

Fig. 2 Diagram of the pulse height counting system

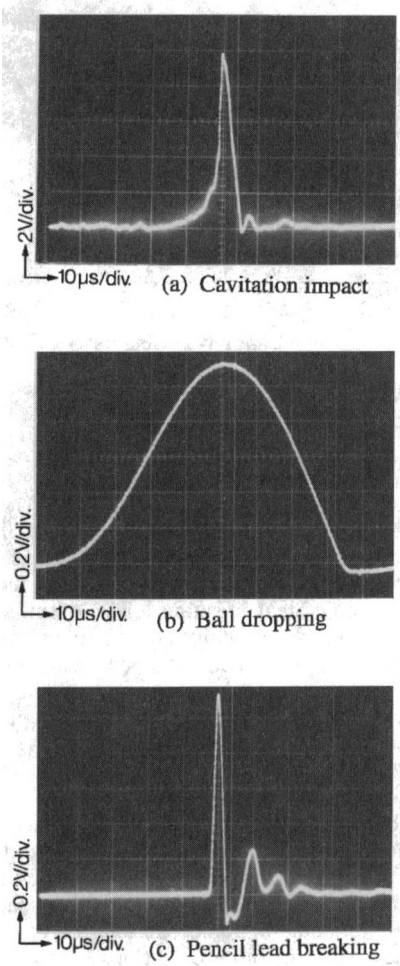

Fig. 3 Output signal from the PVDF transducer

2.3 Calibration Methods. The most common method of dynamic calibration is a dropping-ball technique. For this, small steel balls are dropped from different heights, h_1, onto the transducer and the rebound heights, h_2, are measured. The impact and rebound velocities can then be calculated from conservation of energy.

$$v_n = \sqrt{2gh_n} \quad (n = 1, 2) \tag{3}$$

The average force F_{av} is obtained from momentum conservation considerations.

$$F_{av} = \frac{m(v_1 + v_2)}{\tau} \tag{4}$$

In our tests, the impact duration time τ was determined experimentally using a digital storage oscilloscope with a sampling rate of 100 MHz. The average force is calculated from;

$$F_{av} = \frac{m(1 + \sqrt{e})\sqrt{2gh_1}}{\tau} \tag{5}$$

where $e = h_1/h_2$ is the average coefficient of restitution.

Figure 3(*a*) and (*b*) show a typical cavitation pulse and a calibration pulse produced by a steel ball. The ball-dropping method produces a pulse whose duration is at least four times the cavitation pulse duration and its rise rate is very much slower. Because of these shortcomings, coupled with rather cumbersome photographic measurement of the rebound height, this calibration method is unattractive.

A reliable dynamic calibration method was required, which produced a more realistic pulse shape and was simpler to use.

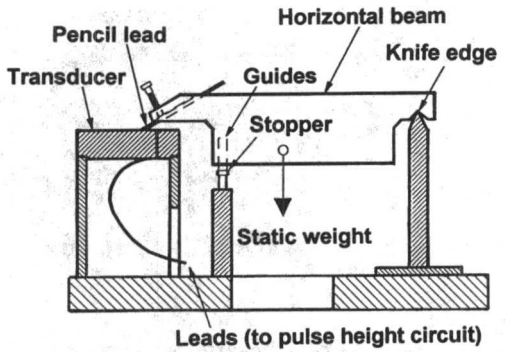

Fig. 4 Calibration apparatus using the pencil lead breaking tool

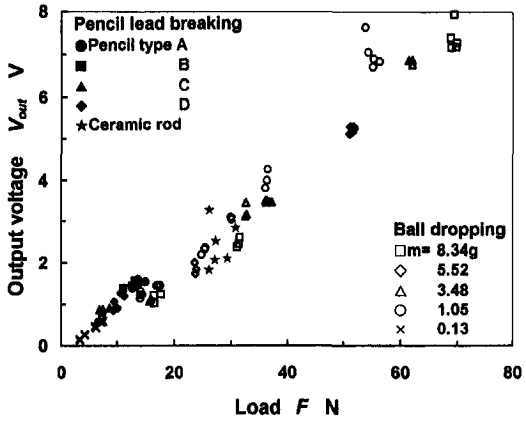

Fig. 5 Effect of load on output voltage

It is generally easier to release a load quickly (e.g., by breaking a weak link holding the load) than to apply it. The calibration method developed uses a pencil lead as the weak link. When a bending load is applied to an extended pencil lead, it will snap and release the load. The good quality control of modern pencil leads results in consistent breaking loads. A similar technique is commonly used for calibrating acoustic emission transducers. Figure 4 shows diagrammatically the main parts of the calibration apparatus. A horizontal beam is supported at one end on a knife edge and on the other by an inclined pencil lead resting on the transducer. The center of the beam is loaded by a pan holding a plastic water bottle and metal weights. The weight of the pan can be slowly increased by pouring in water until the pencil lead breaks. From the weight of the device, the amount of water poured into the bottle and the geometry of the loading points, it is possible to calculate the load applied to the transducer. A 2 mm diameter pencil lead normally used for drawing was used here, although a number of alternatives are available on the market. The suitability of various types is discussed in Appendix 1. The load at which the pencil lead breaks can be changed by altering the protruding length of the lead. Other brittle materials like glass or ceramic rod can be used instead of the pencil lead to obtain higher breaking loads.

A typical calibration pulse produced by the breaking pencil lead method is shown in Fig. 3(*c*). The rise time compares favourably with that of the cavitation pulse.

Cavitation impacts can be produced by micro-jets or shock waves. In case of micro-jets, it is clear that calibration using the pencil lead breaking method is valuable. In the case of shock waves, Sanada et al. (1986) have calibrated a similar PVDF transducer using a shock wave caused by an explosion in the water. They reported that the resulting output voltage from the PVDF sensor was proportional to the output voltage from a crystal type transducer (Kistler 601H), thus providing a cross-calibration. In comparison, the pencil lead breaking method has the advantage of its simplicity.

2.4 Cavitating Jet Apparatus. The apparatus described by Momma and Lichtarowicz (1995) was used to measure cavitation loading in this study. A cylindrical nozzle with a diameter of 2 mm and length of 5 mm was fitted. The stand-off distance s is measured from the upstream edge of the nozzle throat since the flow separation begins at this point and the flow does not reattach itself to the nozzle throat.

The cavitation number σ of such a jet is defined in terms of the upstream pressure, p_1, and downstream pressure, p_2, and is

$$\sigma = \frac{p_2 - p_v}{p_1 - p_2} \tag{6}$$

where p_v is the vapor pressure of the test water. In the case of a cavitating jet, because $p_v \ll p_2 \ll p_1$, the cavitation number can be simplified to

$$\sigma = \frac{p_2}{p_1} \tag{7}$$

In our apparatus, the cavitation number could be set by changing either the upstream pressure or the downstream pressure.

The range of test conditions were as follows: upstream pressure p_1 = 8–12 MPa, downstream pressure p_2 = 0.24–0.36 MPa, cavitation number σ = 0.02–0.0375. The range of Reynolds number R_e at the nozzle outlet is about $2.5 \times 10^5 - 3.1 \times 10^5$ and the range of the velocity at the nozzle outlet, given by Bernoulli equation, is about 126–155 m/s.

3 Results

3.1 Effect of Pulse Duration at Calibration. Figure 5 compares the output voltages from the PVDF transducer produced by the pencil lead breaking and ball-dropping methods. For the ball-dropping method, five different balls (mass = 0.13–8.34 g) were dropped from heights ranging from 3 to 266 mm onto the transducer. The rebound height was recorded using a camera, whose shutter was opened. The load range for the pencil lead breaking method was extended by using 2 mm diameter ceramic rods. It is important to select a ceramic that will break cleanly. The authors feel that pencil leads are best since the results are very repeatable (see Appendix 1). It can be seen in Fig. 5 that the points are approximately on a line that passes through the origin and that the scatter of the data for the ball-dropping method increases as the load rises.

In order to investigate the reason for the scatter of the calibration constants, Fig. 6 illustrates the relation between the pulse duration and the calibration constant. The same data as in Fig. 5

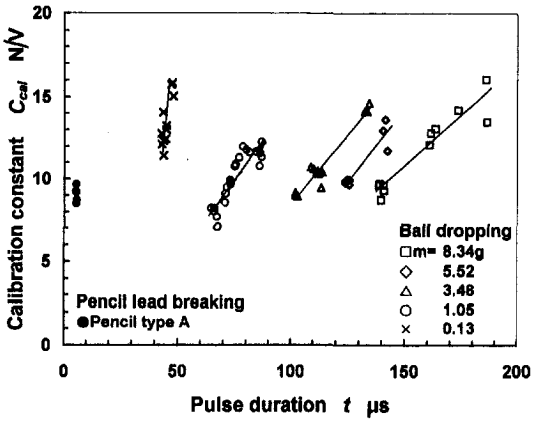

Fig. 6 Effect of pulse duration on calibration constant

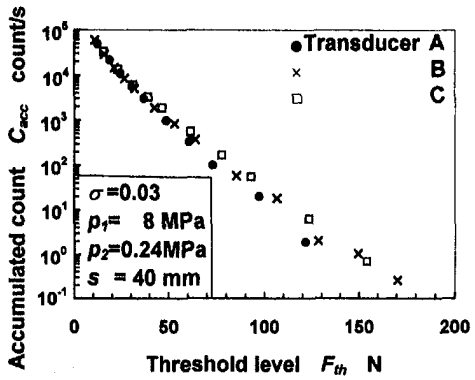

Fig. 7 Repeatability of pulse height distribution for different transducers

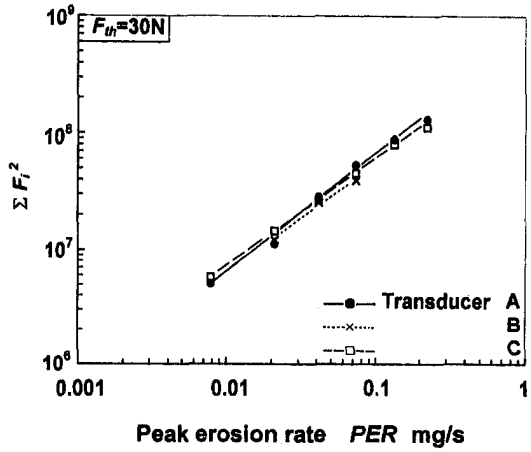

Fig. 8 Repeatability of pulse height analysis

is used. The calibration constant from the ball-dropping method increases with pulse duration for each mass, and is close to that of the pencil lead breaking method only for the shortest duration for each ball. This indicates that the calibration constant of the ball-dropping method is affected by the pulse duration, which in turn depends on the mass of the ball and the drop-height, h_1. As the pulse duration produced by the pencil lead breaking method is of the same order as that of cavitation loading, it can be said that it is better than the ball-dropping method for measuring dynamic loading such as cavitation.

3.2 Repeatability of the Transducer. In any measurement system, the transducers used should be of such quality that, when one is replaced, the new results must be repeatable. Figure 7 shows the pulse height distribution obtained in the same apparatus under the same flow condition, but taken on separate occasions by three different PVDF transducers using the same counting and measuring system. Each transducer was triangular in shape (see Fig. 1) but had a different included angle. Details of the transducers and their calibration constants are shown in Table 1. Considering the differences in their size and their calibration constants, the accumulated count results show good repeatability.

When pulse height analysis has been used for the measurement of cavitation loads on a surface, it has been shown (Stinebring et al., 1980; Momma and Lichtarowicz, 1995) that

$$\sum F_i^2 \propto (\mathrm{PER})^n \qquad (8)$$

where F_i is the pulse height and PER is the peak erosion rate. The pulse height is measured above a threshold value that depends on the material and represents the level at which plastic deformation appears.

Figure 8 illustrates the excellent correlation between the pulse height data and the peak erosion rate. The same three transducers were used and the erosion specimens were made from the same piece of aluminium. The same threshold value of 30 N was chosen.

The standard deviation of each ΣF_i^2 value is 5–15 percent, even though the greatest difference between the calibration constants is about 50 percent. For a given transducer, repeated tests on similar specimens resulted in a standard deviation of 15 percent. From these results it can be concluded that transducers calibrated using the pencil lead breaking method produced very repeatable results.

Table 1 Calibration constant and geometry of transducers

Transducer	Calibration constant (*N/V*)	Area (mm^2)	Angle (degrees)
A	12.15	45.38	18.9
B	10.67	44.10	23.1
C	15.46	41.25	17.2

Table 2 Effect of Kapton tape on calibration constant and pulse duration for the pencil-lead-breaking method

Number of protection layers	Calibration constant (*N/V*)	Pulse duration (μs)
2	10.44 (0.74)	5.90 (0.36)
3	11.49 (0.84)	5.64 (0.32)
4	11.51 (0.73)	5.66 (0.26)
6	11.59 (1.54)	5.97 (0.30)

(The values in brackets show standard deviations for each case.)

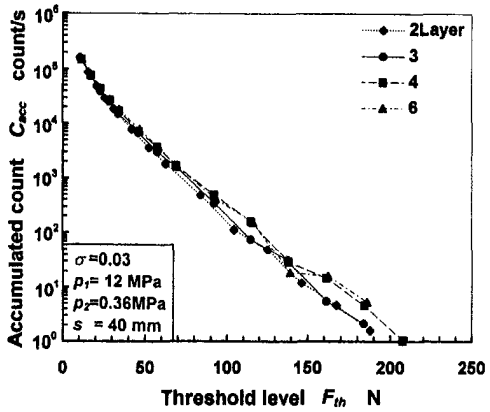

Fig. 9 Effect of protection tapes on the pulse height distribution

3.3 Effect of Protection Tapes. The presence of two or three tapes on top of the sensor area of the transducer raised the question of whether they caused attenuation or distortion of the signal from the piezo-film. In order to check this, test runs in the cavitating jet erosion apparatus were made with two, three, four and six layers of protective tape on top of the transducer. The transducer used had a triangular area of 44.1 mm^2 (approximately 6.0 mm wide and 15 mm high). The calibration constant and pulse duration from the pencil lead breaking method are shown in Table 2. The calibration constant increases by only 11 percent when the number of protective layers is increased from two to six and the pulse durations all lie within one standard deviation of each other. The pulse height distribution given in Fig. 9, which includes the calibration constant, shows that any attenuation effect due to the protection tapes is negligibly small for the range of the number of layers tested.

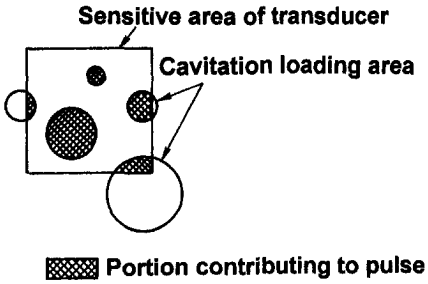

Fig. 10 Relation between a small transducer and large size cavitation loading schematic diagram

Similar results were obtained from the ball-dropping method, except that the pulse durations were ten times longer (see Appendix 4).

Momma and Lichtarowicz (1994) reported similar results using transducers calibrated with two protective layers and further illustrate the negligible effect of increasing the number of protective tapes.

3.4 Effect of Transducer Size. The effect of the size of the transducer was also investigated. While a small transducer has attractions, if its size is not sufficiently large when compared with the size of the cavitation pits, the readings may be misleading.

Figure 10 shows a possible cavitation loading pattern on a small transducer. "Over the edge" loading will give a reduction in the magnitude of the pulse height signal. This is well illustrated in Fig. 11, which shows the variation of the pulse height with the sensitive area of the transducer. The apparent reduction in pulse height for transducer with areas below 25 mm^2 shows the over the edge effect well. With a 2 mm diameter pencil lead cut at the contact end at 30°, the footprint of the loading area is elliptical with a major axis of 4 mm and an area of 6.3 mm^2. Any transducer that cannot accommodate this area fully will show this over the edge effect when it is being calibrated. In Figs. 11 and 12, the dashed lines indicate regions where this occurs. Figure A2 in Appendix 2 shows the same effects when the pencil lead is moved into the narrower parts of the transducer. Smaller sizes of transducer can still be calibrated using 2 mm diameter leads, provided that an extension piece with a suitable contact point is fitted at its end.

Figure 12 shows two sets of points obtained from different batches of PVDF film. Both show the same trends.

3.5 Calibration of Transducers Under Water. All of the above calibrations were carried out in air; a practice followed by all researchers who use the ball-dropping method. As the transducers were intended for use under water, pencil lead breaking calibrations were repeated under this condition. A calibration of 8.4 ± 0.5 N/V in air was found to be 8.0 ± 0.5 N/V under water, showing that there was no significant difference between the two test conditions.

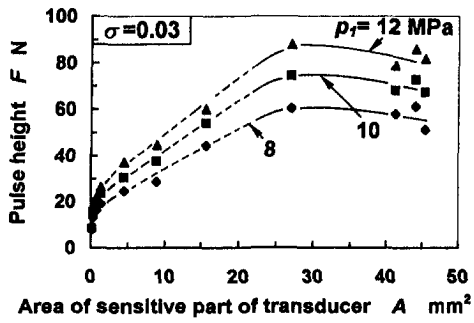

Fig. 11 Variation of pulse height at an accumulated count of 1.0 count/(mm^2s) with the area of sensitive part of the transducer

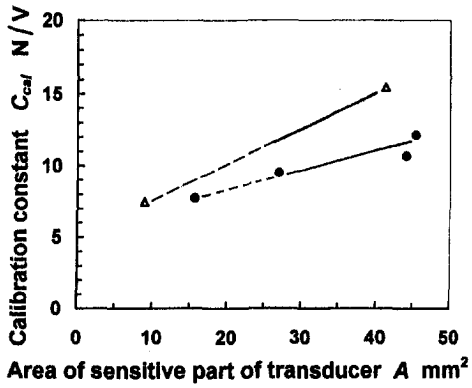

Fig. 12 Effect of the sensitive area on the calibration constant

4 Conclusions

1. A new calibration method for dynamically loaded transducers has been developed to replace the currently used ball-dropping method.
2. The method is simple and convenient to use as the results can be read directly from the oscilloscope without using photographs.
3. The pulse duration of this method is almost the same as the duration of the cavitation pulse. In contrast, the pulse duration for the ball-dropping method is about 8–10 times longer.
4. The calibration load can be altered by changing the grade, diameter and/or length of the lead. Other materials like glass or ceramic rods can also be used.
5. The transducer is capable of surviving severe cavitation loading. Its protection system is made from Polyamide (Kapton) tapes that can be placed in layers to increase protection. The top protection layer can be changed without affecting calibration.
6. The transducer is thin and flexible so it can be mounted on curved surfaces.
7. The pulse height data obtained from the PVDF transducer has an excellent correlation with the peak erosion rate.

Acknowledgements

The first author wishes to thank the Japan Society for the Promotion of Science for the Postdoctoral Fellowship for Research Abroad. The third author wishes to thank the Kajima Corporation for providing funds for his support during his doctoral studies. All the authors thank the University of Nottingham for providing the facilities.

References

Arndt, R. E. A., Ellis, C. R., and Paul, S., 1995, "Preliminary Investigation of the Use of Air Injection to Mitigate Cavitation Erosion," ASME JOURNAL OF FLUIDS ENGINEERING, Vol. 117, pp. 498–504.

Bauer, F., and Moulard, H., 1988, "State-of-the-Art in the Research Work of Piezoelectric PVF_2 Polymer Shock Gauges," *Shock Waves in Condensed Matter*, pp. 627–630.

Dutta, P. K., and Kalafut, J., 1990, "Evaluation of PVDF Piezopolymer for Use as Stock Gauge," Special Report, 90-223, US Army Corps of Engineers.

Henckels, A., and Takayama, K., 1986, "A Study of Shock Wave Propagation Phenomena in PMMA and Glass," Report of Institute of High Speed Mechanics, Tohoku University, Vol. 52, pp. 28–43.

Hoam, N. T., 1994, "Development et validation d'une methode analytique de prevision de l'erosion de cavitation," PhD thesis, L'Institut National Polytechnique de Grenoble.

Jones, I. R., and Edwards, D. N., 1960, "An Experimental Study of the Forces Generated by the Collapse of Transient Cavities in Water," *Journal of Fluid Mechanics*, Vol. 7, pp. 596–609.

Momma, T., 1991, "Cavitation Loading and Erosion Produced by Cavitating Jet," PhD thesis, University of Nottingham.

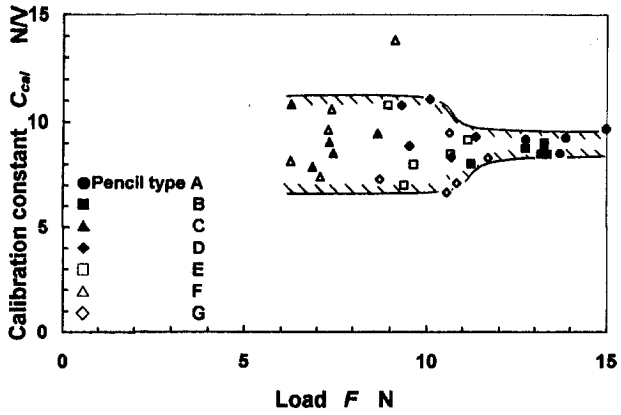

Fig. A1 Calibration constant for various pencil types

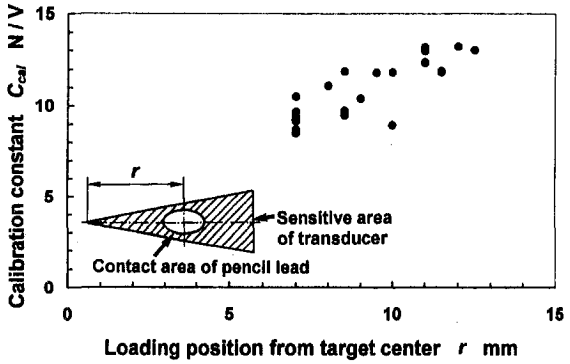

Fig. A2 Calibration constant as a function of the distance between target center and loading point

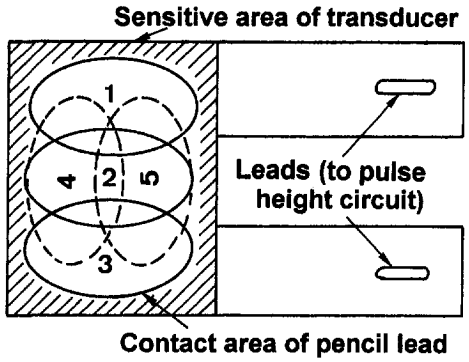

Fig. A3 Calibration constant of a rectangular shape transducer for various loading position

Momma, T., and Lichtarowicz, A., 1993, "Some Experiments on Cavitation Damage Produced by a Submerged Jet," *Proceedings of the 2nd ASME/JSME Nuclear Engineering Conference,* San Francisco, Vol. 2, pp. 877–884.

Momma, T., and Lichtarowicz, A., 1994, "A New Calibration Method for Dynamically Loaded Transducers," *Proceedings of Fluid Measurement and Instrumentation,* Lake Tahoe, FED-Vol. 183, pp. 103–107.

Momma, T., and Lichtarowicz, A., 1995, "A Study of Pressure and Erosion Produced by Collapsing Cavitation," *Wear,* Vol. 186–187, pp. 425–436.

Okada, T., Iwai, Y., and Awazu, K., 1989, "A Study of Cavitation Bubble Collapse pressure and Erosion Part 1: A Method for Measurement of Collapse Pressure," *Wear,* Vol. 133, pp. 219–232.

Okada, T., Iwai, Y., Ishimaru, H., and Maekawa, N., 1994, "Measurement and Evaluation of Cavitation Bubble Collapse Pressures," *JSME International Journal* Series A, Vol. 37, pp. 37–42.

Sanada, N., Takayama, K., Onodera, O., and Ikekuchi, J., "Interaction of an Air bubble with a Shock Wave Generated by a Micro-Explosion in Water," *Trans. Japan Society of Mechanical Engineers,* Vol. 52, pp. 2779–2786 (in Japanese).

Stinebring, D. R., Holl, J. W., and Arndt, R. E. A., 1980, "Two Aspects of Cavitation Damage in the Incubation Zone: Scaling by Energy Considerations and Leading Edge Damage," ASME JOURNAL OF FLUIDS ENGINEERING, Vol. 102, pp. 481–4

APPENDIX 1

Comparison of Pencil Leads

A number of different pencil leads are available on the market and their breaking strength and its repeatability varies considerably. Figure A1 illustrates the calibration constant for various types of pencil lead as a function of the breaking load. All have the same diameter of 2 mm. The average value and the standard deviation of the calibration constant for each type are shown in Table A1. Each pencil lead was tested five times and in all cases the protruding length was 14.6 ± 1.0 mm.

The average calibration constant remained almost constant for all leads (Table A1). However, the repeatability for "weak leads" (C to G) was much worse than for "strong leads" (A and B), as shown by the standard deviations. Thus, "strong leads" produce better repeatability. If the protruding length is changed considerably, the optimum pencil lead might be different. The conditions will change also if the material or diameter of the brittle element is changed.

Table A1 Calibration constants for various pencil leads

	Calibration constant (*N/V*)	
Types of pencil	Average	Standard deviation
A	9.07	0.45
B	8.55	0.37
C	9.15	1.11
D	9.68	1.20
E	8.68	1.42
F	9.92	2.51
G	7.77	1.14

Table A2 Effect of the position of the pencil lead on the calibration constant

Position of pencil lead	Calibration constant (*N/V*)
1	9.39
2	9.15
3	9.74
4	9.28
5	9.85

APPENDIX 2

Location of Calibration Load

The effects on the calibration constant of moving the location of the pencil lead are shown in Fig. A2. The calibration constant increases by about 30 percent as the distance from the target center and the width of the triangular transducer increase. For a rectangular transducer (see Fig. A3 and Table A2), it remains nearly constant (±4 percent), irrespective of its position.

APPENDIX 3

The Accuracy of the Calibration Method

The applied load consisted of a standard weight and a flask into which water was poured until the pencil lead was heard to break. For a pouring rate of 50 ml/s and the human reaction time to the sound of the beam hitting the stop is about 0.2 s, the consequent error for a total load of 2 kg is less than 10 g (0.5 percent). The accuracy of positioning the pencil load is ±2 mm/80 mm, or ±2.5 percent. The output pulse varied between 1.0–1.6 V and was measured by the digital oscilloscope to an accuracy of 0.2 percent. The sampling rate was 100 MHz.

The largest variation was the breaking load of the pencil lead and this was less than 5 percent of the average value of the calibration constant.

APPENDIX 4

Effect of Protection Tapes on the Ball-Dropping Method

In order to investigate the effect of the protection tapes on the ball-dropping method, the calibration constant was measured with different numbers of layers. From Eq. (5), the calibration constant C_{cal} is given by;

$$C_{cal} = \frac{F_{av}}{V_{out}} = \frac{m(1 + \sqrt{e})\sqrt{2gh_1}}{\tau V_{out}} \quad \text{(A1)}$$

A 0.70005 g steel ball was dropped from 99 mm onto a PVDF transducer covered with different numbers of protection tapes. The calibration constant was affected by the coefficient of restitution, the pulse duration and the output voltage caused by the ball impact. Table A3 shows the calibration constant with these parameters, normalized with respect to the value for two layers. The average pulse duration, the average output voltage and average coefficient of restitution for two layers were 48.7 μs, 2.728 V and 0.235, respectively, and the averaged calibration constant was then 10.39 N/V. In equation (A1), the coefficient of restitution appears in the term $(1 + \sqrt{e})$, so that the normalized coefficient of restitution in Table A3 is represented by $(1 + \sqrt{e})/(1 + \sqrt{0.235})$. As expected, the pulse duration increased slightly with the increase in the number of protection tapes, due to the increase in thickness of the elastic layer. However, the increase of the pulse duration was only 28 percent, despite a three-fold increase in the thickness. The normalized coefficient of restitution and the pulse duration also increased, but the output voltage decreased. The calibration constant increased slightly. Overall, this means that the output decreased by about 9 percent (six layers) due to the attenuation of the tapes and it can be concluded that the effect of the protection tapes was negligibly small.

Table A3 Nondimensional parameters for the ball-dropping method

Number of protection layers	Calibration constant	Pulse duration	Output voltage	Coefficient of restitution
2	1.0	1.0	1.0	1.0
3	1.06	1.06	0.90	1.08
4	1.07	1.07	0.86	1.10
6	1.09	1.09	0.78	1.15

Prediction of Cavitation Erosion: An Energy Approach

F. Pereira
Research Associate.

F. Avellan
Professor.

Ph. Dupont
Research Associate.

IMHEF-EPFL,
Institut de Machines Hydrauliques
et de Mécanique des Fluides,
Swiss Federal Institute of Technology,
Av. de Cour 33, 1007 Lausanne,
Switzerland

The objective is to define a prediction and transposition model for cavitation erosion. Experiments were conducted to determine the energy spectrum associated with a leading edge cavitation. Two fundamental parameters have been measured on a symmetrical hydrofoil for a wide range of flow conditions: the volume of every transient vapor cavity and its respective rate of production. The generation process of transient vapor cavities is ruled by a Strouhal-like law related to the cavity size. The analysis of the vapor volume data demonstrated that vapor vortices can be assimilated to spherical cavities. Results are valid for both the steady and unsteady cavitation behaviors, this latter being peculiar besides due to the existence of distinct volumes produced at specific shedding rates. The fluid energy spectrum is formulated and related to the flow parameters. Comparison with the material deformation energy spectrum shows a remarkable proportionality relationship defined upon the collapse efficiency coefficient. The erosive power term, formerly suggested as the ground component of the prediction model, is derived taking into account the damaging threshold energy of the material. An erosive efficiency coefficient is introduced on this basis that allows to quantify the erosive potential of a cavitation situation for a given material. A formula for localization of erosion is proposed that completes the prediction model. Finally, a procedure is described for geometrical scale and flow velocity transpositions.

Introduction

The present work has been initiated in the frame of the multidisciplinary and long-standing problem of the prediction of cavitation erosion in hydraulic machines.

The energy approach is based on the determination of the energy spectrum associated with a leading edge cavitation. The collapse of vapor cavities at the rear part of an attached cavity is known to be capable of damage on most types of materials. However, the experimental determination of this spectrum has not been attainable up to now and, as a consequence, no prediction model has received enough consensus to be widely applied.

Prior investigators have put forth great effort in (*i*) understanding the fluid mechanisms originating such extremely high stresses, and (*ii*) improving the performance of materials.

There is a global agreement about the fact that cavitation erosion results from the repeated collapse of vapor structures in the neighborhood of rigid boundaries. However, the basic mechanism has been much debated. The focus of prior work may be categorized as described below.

The first explanation, even though theoretical, has been proposed by Rayleigh (1917) whose model describes the time evolution of the radius of a vapor bubble in an infinite fluid medium at constant pressure. A local and very high pressure peak appears in the final collapse stage. Fujikawa and Akamatsu (1980) showed that this pressure peak was associated with a shock wave that they pointed out as the main damaging factor.

Kornfeld and Suvorov (1944), Vogel et al. (1989) demonstrated that vapor bubbles do not collapse spherically in the neighborhood of solid boundaries or when subjected to pressure gradients. They observed a liquid microjet threading the bubble and finally striking and damaging the boundary.

Although the damaging process is certainly a combination of these two mechanisms, recent works indicate that the shock wave is probably the predominant one: Avellan and Farhat (1989), Fortes-Patella and Reboud (1993).

The generation process of vapor cavities by a leading edge cavity has been often described (Knapp et al., 1970; Kubota et al., 1987; Farhat et al., 1993). In particular, steady and unsteady behaviors have been reported. The former situation is characterized by small scale vapor cavities shed with no obvious periodicity. Instead, the unsteady cavitation is recognizable by the periodic shedding of large scale vapor structures, ruled by a Strouhal law. Often called cloud cavitation, this behavior is generally considered as the most erosive situation.

Therefore, cloud cavitation has motivated and yet motivates a great amount of experimental and numerical research work: noise generation (Bark and Berlekom, 1978), erosion (Franc and Michel, 1988; Kato et al., 1996), cloud collapse (Soyama et al., 1992), bubble interaction and shock wave propagation (Mørch, 1981; Chahine and Duraiswami, 1992).

Along with the prediction problem, transposition laws are needed in what concerns testing of hydraulic machines, to transpose prediction outputs from laboratory tests on small scale model to full scale machine. Attempts have been made in the past in that direction: Thiruvengadam (1971), Kato (1975).

Notably, Bourdon et al. (1990) and Farhat et al. (1993) developed the notion of erosive power through the P_{er} term, introduced as a scaling factor for cavitation erosion in hydraulic machines. Promising results were obtained (Farhat, 1994), and stimulated and oriented the present study.

The only reasonable approach to the problem of predicting cavitation erosion consists in the conciliation of the two aspects of the phenomenon: fluid and material. Specifically, this should be done through the determination of the erosive potential of the cavitation situation under consideration. Unfortunately, it appears from our literature review that very few studies are related to the understanding of the energy transfer between the main flow and the material. Hammitt (1963) is a pioneer in this aspect as he hypothesized a model for cavitation erosion based on the knowledge of the energy spectrum $\mathbf{n}(E_c)$, where E_c is the potential energy of a vapor cavity.

In our study, we consider the problem of cavitation erosion following the so-called energy approach inspired by this investigator. This approach appears to be particularly suitable for the definition of an erosion prediction tool. Moreover, the erosive

Contributed by the Fluids Engineering Division for publication in the JOURNAL OF FLUIDS ENGINEERING. Manuscript received by the Fluids Engineering Division July 11, 1997; revised manuscript received April 30, 1998. Associate Technical Editor: J. Katz.

power term P_{er} is a privileged basis towards this definition. We intend to validate the energy approach by the measurement and analysis of two ground components of P_{er}: V_c and f_c. The third term, Δp, is accessible either from direct pressure measurements (see Farhat, 1994; Pereira, 1997), or from flow computation, and therefore is not considered in the frame of the current work.

Cavitation tests are performed in the IMHEF's high speed cavitation tunnel, on a symmetrical hydrofoil NACA 65012 (chord length is 100 mm). Steady and unsteady cavitation behaviors are studied.

In a first part, a new event counting technique combined with a wavelet analysis is presented as to determine the rate of production of transient vapor vortices by the leading edge cavity. Afterwards, a visualization technique, combining principles of stereometry and tomography, is introduced to determine the volume of vapor cavities through their tridimensional reconstruction.

Results are discussed in the second part. On the one hand, the generation process of transient vapor cavities is analyzed on a statistical basis from which an analytical formulation of the production rate is carried out. On the other hand, data from the volume reconstruction are analyzed with a view to the modeling of volumes while ensuring the cohesion with the production laws.

In a third and concluding part, we perform a global synthesis where we develop the formalism of the energy approach. The energy spectrum is analytically expressed as a function of the main flow parameters. The erosive power term P_{er} is derived while integrating the concept of damaging threshold energy introduced by Hammitt (1963). Then, prediction and transposition aspects are considered and formulated according to these fundamental definitions. Finally, elements for an experimental validation of the energy approach are presented, comparing the spectrum of the fluid energy and that of the material deformation energy.

Production Rate of Vapor Cavities

Principle and Instrumentation. A technique is brought into operation to carry out the production rate of transient vapor cavities (also referred to as vortices) in relation with their characteristic size λ. The setup is depicted in Fig. 1. A coherent light beam provided by a 5 W laser source is focused on a reflecting area of the hydrofoil. The beam is pointed onto the closure region of the main cavity and is oriented perpendicularly

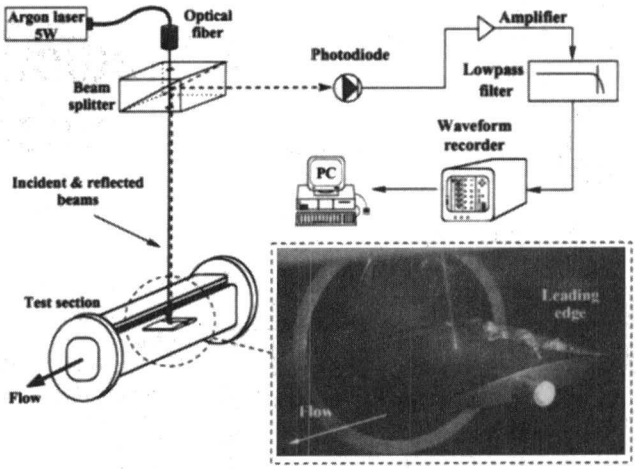

Fig. 1 Production rate of vapor vortices: experimental setup

to the profile surface so that the incident and the reflected beams have the same path.

By means of a splitter cube, the reflected beam is deflected 90° towards an ultrafast photodiode (rise time: 1 ns). The voltage signal output of this sensor is filtered and amplified to compensate losses due to the successive passages through the splitter cube. Therefore, the voltage signal is ideally maximum when total reflection is observed and attenuated when a vapor cavity passes through the beam.

Three hypotheses are considered: (*i*) Vapor cavities are opaque and diffusive objects; (*ii*) The characteristic size λ of a cavity corresponds to its longitudinal maximum extent; (*iii*) Vapor cavities are produced spanwise according to the same process (though with a phase shifting that currently is not measured).

Provided an adequate signal processing, the cavity characteristic size λ may be determined from the knowledge of the light extinction time and of the convection velocity C_c. The production rate of cavities in a given size range comes out from their counting over the measurement period.

The photodiode signal is filtered at 100 kHz and sampled at 200 kHz over multiple time periods of 2.6 s each.

Data Processing and Analysis. The wavelet analysis, and namely the continuous wavelet transform (CWT, see Farge, 1992), was found to be the most appropriate technique to deter-

Nomenclature

C_c = convection velocity, $m \cdot s^{-1}$
C_{ref} = upstream flow velocity, $m \cdot s^{-1}$
d_{eq} = equivalent diameter of vapor cavity, m
E_a = acoustical energy of vapor cavity, J
E_c = potential energy of vapor cavity, J
E_d = damaging energy of material, J
E_m = maximum potential energy of vapor cavity, J
E_s = minimal damaging energy of material, J
f_c^{λ} = shedding frequency of cavities with size λ, Hz
f_c = main shedding frequency, Hz
i = flow angle of incidence, °
l = length of main cavity, m
L = chord of hydrofoil, m
$\mathbf{n}$ = frequency histogram, s^{-1}
$\hat{\mathbf{n}}$ = statistical density, $\hat{\mathbf{n}}(\lambda)$ $m^{-1} \cdot s^{-1}$, $\hat{\mathbf{n}}(E_c)$, $J^{-1} \cdot s^{-1}$
$\hat{\mathbf{N}}$ = statistical distribution, s^{-1}
$\tilde{\mathbf{N}}$ = normalized distribution, $\tilde{\mathbf{N}} = \hat{\mathbf{N}}/C_{ref}$, m^{-1}
p_{ref} = upstream pressure, Pa
p_v = vapor pressure, Pa
P_{er} = erosive power, W
R_m = bubble initial radius, m
t_r = Rayleigh time, s
V_c = volume of transient vapor cavity, m^3
x_c = abscissa of collapse location, m
δ_c = displacement of convected vapor cavity, m
Δp = pressure difference in the main cavity closure region, Pa
$\lambda_{x,y,z}$ = main dimensions of a vapor cavity, m
α, β = statistical class parameters
C_p = pressure coefficient, $C_p = (p - p_{ref})/(\frac{1}{2}\rho C_{ref}^2)$
$C_{p_{max}}$ = C_p in the main cavity closure region
η_{co} = collapse efficiency, $\eta_{co} = \hat{\mathbf{n}}(E_d)/\hat{\mathbf{n}}(E_c)$
η_{er} = erosive efficiency, $\eta_{er} = 1 - (E_s/E_m)^{2/3}$
λ_{er} = erosive power coefficient
σ = cavitation coefficient, $\sigma = (p_{ref} - p_v)/(\frac{1}{2}\rho C_{ref}^2)$
S_c = production rate constant, $S_c \simeq 86.87\ 10^{-3}$
S, S_c^{α} = Strouhal numbers, $S = (f_c l)/C_{ref}$ $S_c^{\alpha} = S_c \alpha/(1 + \alpha)$
RMS = root mean square error on least squares fitted data

mine the production rate of vapor cavities accordingly to their individual characteristic length. In contrast with the Fourier transform, this analysis is particularly suitable for random and transient signals, being yet applicable to the detection of periodicities (as expected in the case of cavitation unsteadiness).

The original wavelet analysis is a convolution of the original signal $f(t)$ with a wavelet function $\psi(t)$, the so-called mother wavelet. The CWT is a generalization procedure of this convolution operation that uses a family of wavelet functions $\psi_{\kappa,\tau}(t)$ continuously translated (parameter τ) and dilated (parameter κ). Thus, it performs a transformation between the physical time space t and a time-scale space (t, ϕ). The complex-valued Morlet wavelet is currently used. The following analysis is obtained:

$$\tilde{f}(\kappa, \tau) = \langle \psi_{\kappa,\tau} | f \rangle = \kappa^{-1/2} \int_{\mathbf{R}} \psi^* \left(\frac{t - \tau}{\kappa} \right) f(t) dt \quad (1)$$

ψ^* is the complex conjugate of ψ and $\tilde{f}$ is the CWT of $f(t)$.

Another important aspect of this transform is the conservation of energy locally (and therefore globally), see Lewalle (1994). The CWT is usually represented by the energy density map: local energy spectral density plotted versus time t and scale ϕ.

Because the water fluid contains microbubbles of undissolved air, the light signal may get noisy. Therefore, the voltage signal from the photodiode is processed in a two steps procedure before the wavelet analysis: (*i*) Subtraction of the off-cavitation voltage; (*ii*) Envelope in a frequency range of 0–100 kHz (using the Hilbert transform).

Finally, the cavity characteristic size λ is related to the ϕ scale through the following relation: $\lambda = K(C_c/\phi)$, where K is a normalization coefficient and C_c is the convection velocity of the vapor structure in the closure region of the main cavity. Considering the experimental results carried out by Kiya and Sasaki (1983) (0.5 C_{ref}) and Farhat (1994) (0.65 C_{ref}), we take $C_c = 0.6\ C_{\text{ref}}$. We emphasize the fact that this convection velocity is only valid at the measurement location.

It is noteworthy that the primary concepts in the wavelet analysis are those of time and scale, whereas frequency is clearly a secondary quantity obtained from the repetition of individual events. Let an event be the occurrence of a cavity of size λ at an instant t. An algorithm (see Pereira, 1997) is developed that locates every maximum appearing in the energy map, thus giving an equal importance to low and high energy events. The resulting image is called the structure map from which the event histogram $\mathbf{n}$ is carried out. Dividing this quantity by the measurement period gives the frequency f_c^{λ} associated to the size class λ. We refer $\hat{\mathbf{n}}$ as the statistical density and $\hat{\mathbf{N}}$ as the statistical distribution associated to class λ.

Eight data segments of 32 k-samples each ($\approx$164 ms) are processed. The ϕ scale is divided into 9 octaves with 16 voices each (therefore, we have 144 λ classes). Lengths λ in the range 0.5 to 100 mm are considered.

Volume of Vapor Cavities

Principle and Instrumentation. The quantification of two phase phenomena in terms of volume or shape data is technically complex. Most current visualization techniques are only applicable when geometrical characteristics are considered steady in time, such as in the case of the leading edge cavity: laser sheet (Farhat et al., 1993), high speed photography (Lehman, 1966), holography (Maeda et al., 1991), tomography (Levinthal and Ware, 1972), etc. However, the vapor structures produced by a leading edge cavity are characterized by a very short lifetime, an extremely changing shape and are conveyed by the flow at high speeds (up to 50 $\text{m} \cdot \text{s}^{-1}$ in the test section of the IMHEF-LMH's cavitation tunnel).

To quantify the geometrical characteristics of these transient vapor vortices, we developed a technique combining principles of tomography and stereometry, see Pereira (1997). The basic and intuitive principle is that the volume of an object in space (moving or not) can be estimated out from simultaneous contours taken from a minimum of two noncollinear lines of sight. Contours define, in the 3-D space, cylinders (or cones) that encompass the object being observed. They intersect each other and form a common volume that overestimates the real volume. Accuracy can be increased with a higher number of contours.

Four black and white frame transfer CCD cameras are arranged around the test section according to Fig. 2.

In monoshot mode, the CCD integration period (20 ms) starts on a TTL signal input. Afterwards, the image information is transferred onto a storage section where it remains until a TTL readout signal is received. Information is finally converted to standard video signal and output to a 8-bits frame grabber. Archiving is done on S-VHS video tape. Special electronic hardware was developed for the conditioning of the video signal as well as for the camera control from a remote computer (addressing, multiplexing, triggering, gain control and synchronization between video devices). A compact mechanical mounting has been designed for each camera, allowing precise positioning (1 rotation and translation on 3 axes). Lighting is undertaken by two flash point sources placed around the test section. Flashes are triggered randomly during camera integration period to avoid any coupling with the phenomenon being observed. The trigger pulse is transmitted through an optical fiber in order to protect electronics hardware from electromagnetic disturbances.

Images are acquired simultaneously on all four cameras and readout sequentially according to the above sequence. The cycle takes 140 ms from acquisition to storage and is repeated 512 times at the corresponding frequency ($\approx$7 Hz).

Data Processing and Analysis. Volume extraction goes through 4 steps: (*i*) image enhancement: normalization to full pixel range (256 grey levels) and thresholding; (*ii*) contour extraction by gradient operator; (*iii*) contour closing; (*iv*) volume intersection. The intersection operation is the core of the volume reconstruction (see Pereira, 1997). This procedure is applied to all possible pairs of object contours. An orthogonal parallelepiped is drawn out that encompasses the intersection points and is divided into voxels (discrete volume elements). Each voxel is defined by a center, an elementary volume and a norm. This norm is equal to unity if the projection of the associated center on at least one image plane is inside the corresponding contour, 0 if on the contour and -1 on the outside.

Total volume of object under consideration is the summation of all elementary volumes from voxels whose norm is zero or unity. Figure 3 shows the graphical display of the final reconstructed volume of an upside down U-shaped vapor vortex. Upper four photographs are the simultaneous images from the CCD cameras and bottom figures show the reconstructed cavity. It clearly demonstrates the ability of the technique to closely catch complex 3-D structures.

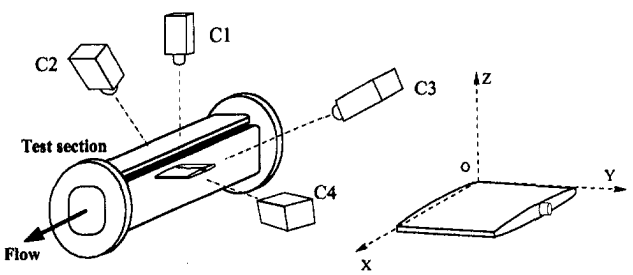

Fig. 2 Cameras arrangement around test section and world coordinates system

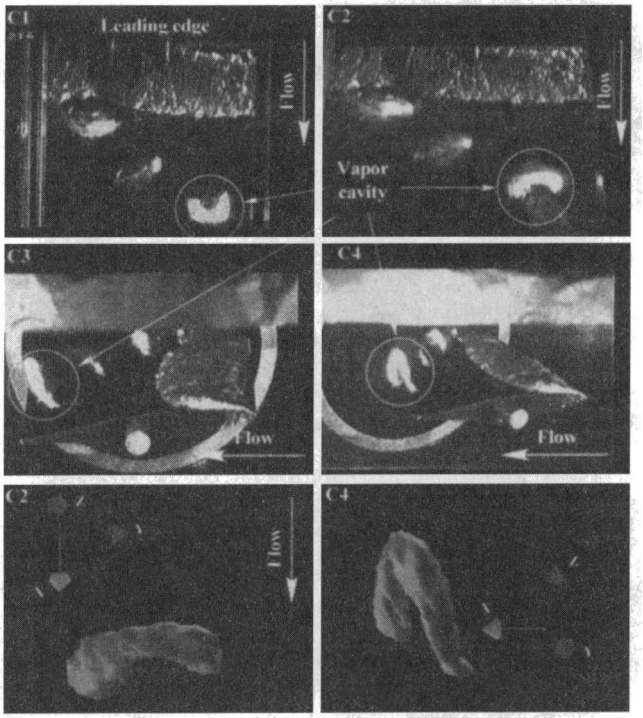

Fig. 3 Reconstruction of a vapor volume

Calibration. Calibration of a stereoscopic system is the process by which we determine the geometrical and optical characteristics of a camera (intrinsic parameters) and/or the 3-D position and orientation in the world space of the image sensor (extrinsic parameters). Eleven parameters (6 extrinsic and 5 intrinsic) are determined by our algorithm (see Pereira, 1997). World space coordinates may be derived from multiple image data and vice versa. Minimum measurable volume is 0.44 mm^3.

Flow Conditions

We explored 2 flow angles of incidence (4 and 6 deg), 3 main cavity lengths (l/L = 20, 30, 40 percent) and 5 upstream flow velocities (C_{ref} = 15, 20, 25, 30, 32 $m \cdot s^{-1}$). The cavitation coefficient σ is adjusted to obtain the correct main cavity length, which is checked under continuous lighting by means of a graduated video monitor. As soon as flow parameters are considered steady in time, 128 measurements are performed and averaged over a period of 30 s before the image acquisition loop.

Results and Discussion

Production Rate of Vapor Cavities. Figure 4 represents $\tilde{\mathbf{N}}$, which is the event statistical distribution $\hat{\mathbf{N}}$ (number of events $\geq\lambda$ per unit of time) divided by the respective mean flow velocity C_{ref}. $\tilde{\mathbf{N}}$ is plotted versus structure size λ. Only sizes below 50 mm are reported since structures with characteristic size greater than the main cavity mean length can reasonably be put aside.

It follows from these graphs (see Pereira, 1997) that the distributions $\hat{\mathbf{N}}$ are ruled by the relation $\hat{\mathbf{N}}(\lambda) = kC_{ref}/\lambda$, where k is a constant. The analytical formulation of the event density $\hat{\mathbf{n}}(\lambda)$ can be derived from this analysis:

$$\hat{\mathbf{n}}(\lambda) = k\frac{C_{ref}}{\lambda^2}, \quad k \simeq 86.87\ 10^{-3} \pm 12\ 10^{-5} \qquad (2)$$

The number of events per unit of time $\mathbf{n}(\lambda)$ is given by the following relation:

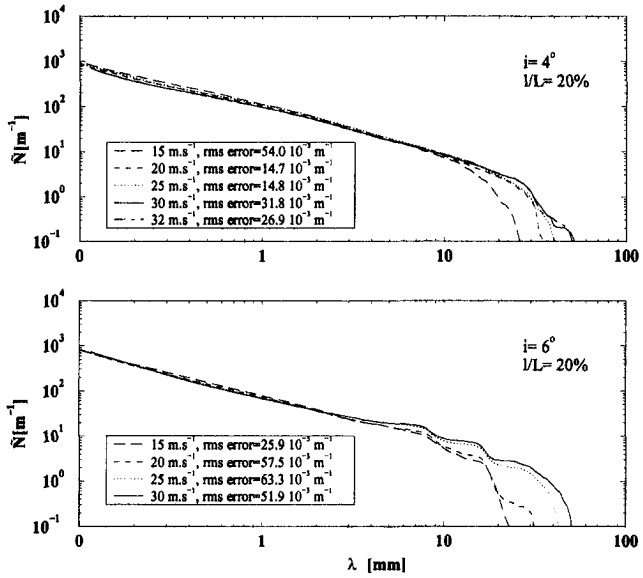

Fig. 4 Normalized distributions $\tilde{N} = \hat{N}/C_{ref}$ versus λ. i = 4°, 6°, l/L = 20%

$$\mathbf{n}(\lambda) = \int_{\lambda}^{\lambda+\Delta\lambda} \hat{\mathbf{n}}(\zeta)d\zeta \qquad (3)$$

$\mathbf{n}(\lambda)$ is the so-called production rate (or shedding frequency) of vapor cavities in the interval $[\lambda, \lambda + \Delta\lambda]$, and will be now referred to as f_c^{λ}. We show that f_c^{λ}, C_{ref} and λ are linked by the relation

$$\frac{\lambda f_c^{\lambda}}{C_{ref}} = S_c\frac{\alpha}{1+\alpha} = S_c^{\alpha}, \quad S_c \simeq 86.87\ 10^{-3} \pm 12\ 10^{-5} \qquad (4)$$

where α is a parameter defining the density class width: $\alpha \in \mathbf{R}^+ | \Delta\lambda = \alpha\lambda$. S_c is the production rate constant and is equal to k of relation (2). S_c^{α} tends to S_c as α grows to infinity.

Figure 5 represents the values of S_c^{α} when formula (4) is applied to the experimental histograms $\mathbf{n}$. In the case of our analysis, we have $\alpha \simeq 43.3\ 10^{-3}$. S_c^{α} is found constant and close to $3.8\ 10^{-3}$ over the whole λ scale. This result fully validates the above reasoning and shows that the generation

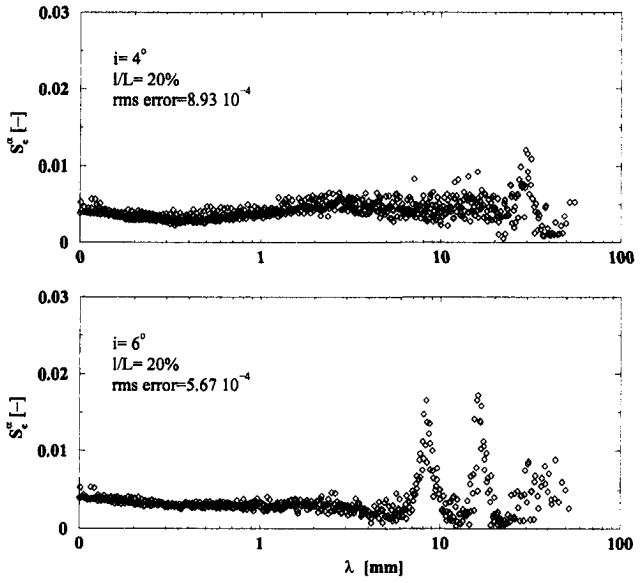

Fig. 5 Strouhal number S_c^{α} versus λ. i = 4°, 6°, l/L = 20%

process of the transient vapor cavities is truly ruled by the Strouhal-like law of Eq. (4), provided α is chosen (even arbitrarily).

The unsteady case ($i = 6$ deg) is characterized by two particular λ values that we call λ_1 and λ_2. We show that these singular lengths are essentially defined by the main cavity mean length according to the following relations: $\lambda_1 \simeq 0.44l$ and $\lambda_2 \simeq 0.85l$. Considering the uncertainties related to the convection velocity determination, we point out that these values are comparable with the $\frac{1}{3}$ and $\frac{2}{3}$ values that are commonly found in the literature as far as the generation process of vapor cavities in the unsteady situation is discussed. As a matter of fact, these results are coherent with the 3-parts cyclic generation sketches proposed by Le et al. (1993) and Kubota et al. (1987).

Finally, let f_c be the sum of frequencies f_c^{λ} of events whose dimension λ is in the close vicinity of λ_1 and λ_2. f_c is called the macroscopic or main shedding frequency. Figure 6 represents this frequency versus the reduced frequency C_{ref}/l.

This graph clearly shows that the production rate of vapor cavities inside these two λ classes is controlled by the well-known Strouhal law based on the main cavity length and on the upstream flow velocity:

$$S = \frac{f_c l}{C_{\text{ref}}} \quad \text{with} \quad S \approx 0.3 \tag{5}$$

This result is perfectly coherent with those found in literature related to unsteady cavitation behavior: Simoneau et al. (1989), Farhat et al. (1993), Farhat (1994), Kubota et al. (1987), Le et al. (1993).

Volume of Vapor Cavities. We showed (Pereira, 1997) that the most relevant information, with respect to the volume of vapor cavities, were the dimensions λ_x, λ_y, and λ_z, respectively the chordwise, the spanwise, and the vertical extents.

Figure 7 shows that there exist linear relationships between λ_x, λ_y, and λ_z. We have reported couples (λ_x, λ_y) and (λ_y, λ_z) (values are divided by l), accompanied by the corresponding linear regression. λ_x and λ_y are identical with a slope coefficient close to unity, for both the steady and unsteady cases ($\lambda_y \approx 0.851\lambda_x$ and $\lambda_y \approx 1.035\ \lambda_x$, respectively). Graphs related to (λ_y, λ_z) show that the cavity height is about 60% higher than λ_y (slopes are 1.629 and 1.582, respectively for $i = 4$ deg and $i = 6$ deg). Besides, the unsteady case ($i = 6$ deg) is characterized by two secondary trends indicating that there exist two

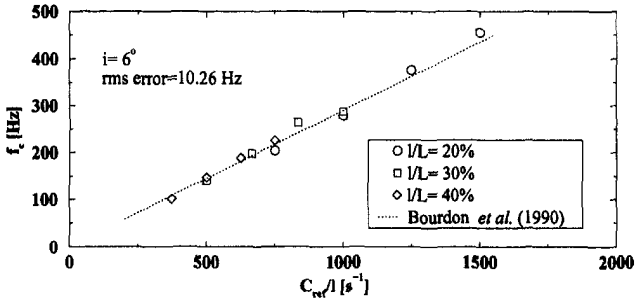

Fig. 6 Shedding frequency f_c versus reduced frequency C_{ref}/l. $i = 6°$, $l/L = 20, 30, 40\%$

additional volume families that confirm the following relations: $\lambda_z \approx 0.197\lambda_y$ and $\lambda_z \approx 0.562\lambda_y$. As established by Pereira (1997), we also have $\lambda_y \approx 1.61\lambda_x$ and $\lambda_y \approx 2.17\lambda_x$. It is also noticeable that the longitudinal and transversal dimensions (λ_x and λ_y) rarely exceed half of the main cavity length l in the steady situation. Instead, for $i = 6$ deg, λ_x and λ_y may equal it, while appearing the aforementioned two specific types of volumes. These remarks are in full agreement with the visual observations.

Because experimental volume data were not available up to now, vapor structures produced by the leading edge cavity were usually considered to be spherical volumes (Kato, 1975; Selim, 1985; Baiter, 1982). Our immediate purpose is to check the validity of this hypothesis. Let $d_{eq} = \sqrt[3]{(6/\pi)V_c}$ be the equivalent diameter. Figure 8 represents dimensions $\lambda_{x,y,z}$ versus d_{eq}. In the steady case (4 deg), these dimensions vary linearly with the equivalent diameter and slopes are similar to that found above between λ_x, λ_y and λ_z. For $i = 6$ deg (unsteady behavior), multiple trends appear on graph (d_{eq}, λ_z). The main trend indicates that λ_z is about 60 percent greater than d_{eq}. Secondary trends are related to the specific volumes that characterize the unsteady case. Slopes are close to that found between λ_z and λ_y (Fig. 7).

As a consequence, d_{eq} is representative of dimensions $\lambda_{x,y,z}$ of vapor volumes. Table 1 reports the relationships between $\lambda_{x,y,z}$ and d_{eq} as well as the constants that provide, from the single knowledge of the main cavity mean length, the $\lambda_{x,y,z}$ dimensions of the macroscopic structures produced in the un-

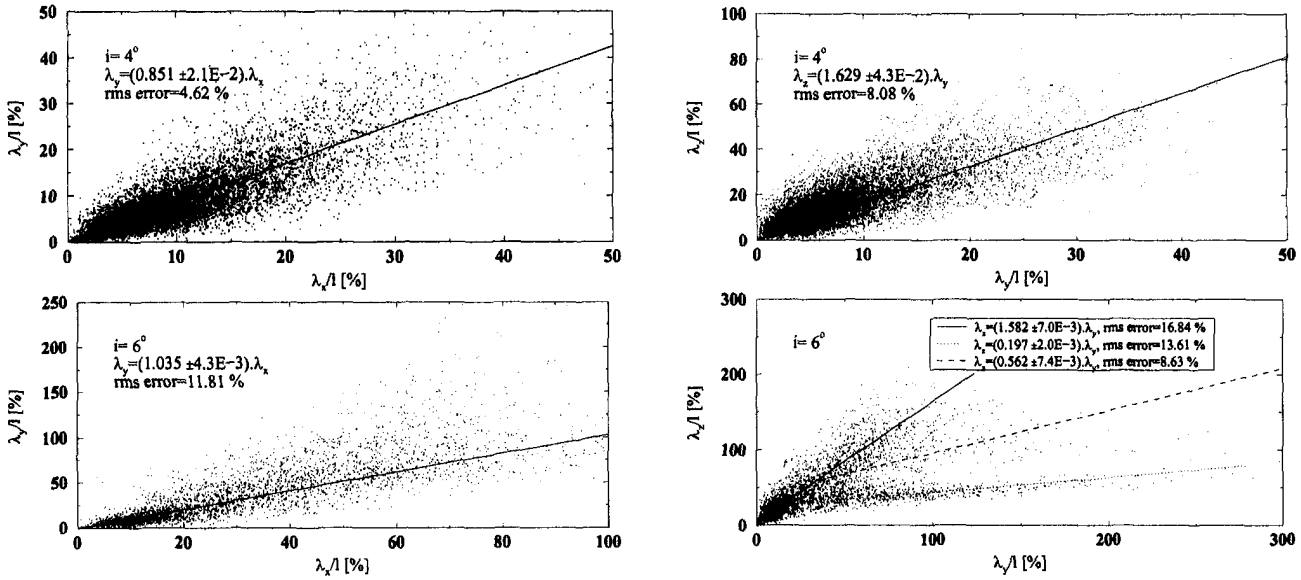

Fig. 7 Relationships between dimensions $\lambda_{x,y,z}$. $i = 4°, 6°$, $C_{ref} = 15, 20, 25, 30, 32\ m \cdot s^{-1}$, $l/L = 20, 30, 40\%$

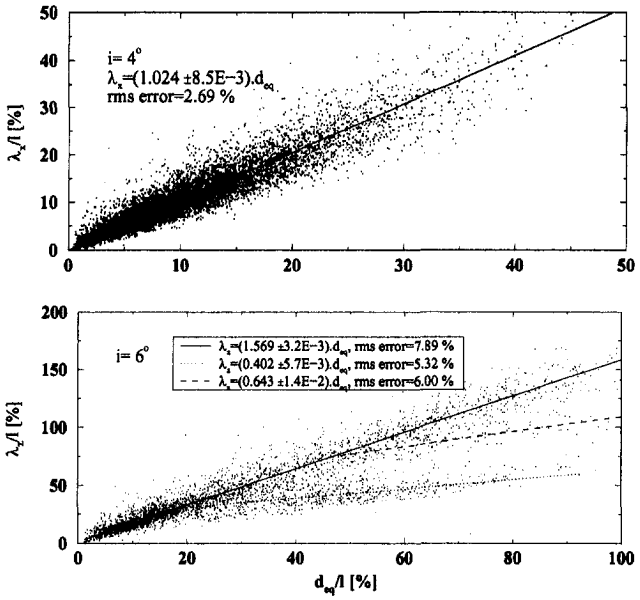

Fig. 8 $\lambda_{x,y,z}$ **versus the equivalent diameter** d_{eq}. i = 4°, 6°, C_{ref} = 15, 20, 25, 30, 32 m · s^{-1}, l/L = 20, 30, 40%

steady cavitation behavior. These characteristic dimensions are coherent with visual observations and high speed visualizations: Farhat (1994), Brennen (1994), Kubota et al. (1987).

Energy Approach: Formalism and Validation

The energy spectrum suggested by Hammitt (1963) describes the energy transfer between the fluid and the material. This concept is illustrated on Fig. 9, for different cavitation extents: the coordinate axis represents the frequency histogram $\mathbf{n}(E_c)$ of cavities with potential energy inside the interval $[E_c, E_c + \Delta E_c]$.

Hammitt emphasizes the fact that he takes into account only the cavities that effectively produce damage, suggesting that an energy E_s exists beyond which damage takes place. This threshold, reported on Fig. 9, depends on the mechanical properties of the material under consideration. Thus, the damaging energy is proportional to the surface under the curve corresponding to the cavitation extent, with $E_c \geq E_s$.

Energy Density. The energy density $\hat{\mathbf{n}}(E_c)$ is related to the event density $\hat{\mathbf{n}}(\lambda)$ by

$$\hat{\mathbf{n}}(E_c)dE_c = \hat{\mathbf{n}}(\lambda)d\lambda \tag{6}$$

where λ is the longitudinal maximum extent of cavities, as hypothesized formerly. Furthermore, Table 1 shows that the dimensions $\lambda_{x,y,z}$, and specifically the longitudinal one, are proportional to d_{eq}, with $d_{eq} \propto \sqrt[3]{V_c}$. Thus, the potential energy E_c of a cavity may be expressed by

Table 1 Dimensional characteristics of vapor volumes

Steady		Unsteady		
Eq. (4)	Eq. (5)	Eq. (4)		Eq. (5)
$\lambda_x \approx d_{eq}$	—	$\lambda_x \approx d_{eq}$		$\lambda_x = 0.44\ l$
$\lambda_y \approx d_{eq}$	—	$\lambda_y \approx d_{eq}$	1	$\lambda_y = 0.71\ l$
$\lambda_z \approx 1.6\ d_{eq}$	—	$\lambda_z \approx 1.6\ d_{eq}$		$\lambda_z = 0.14\ l$
				$\lambda_x = 0.85\ l$
			2	$\lambda_y = 1.84\ l$
				$\lambda_z = 1.04\ l$

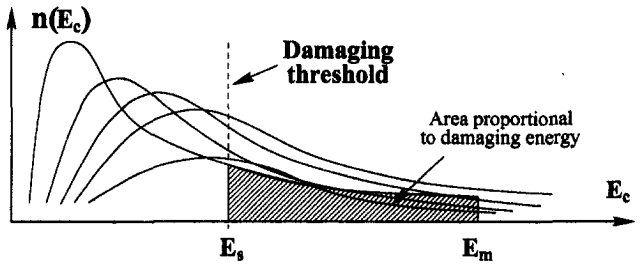

Fig. 9 Energy spectra according to Hammitt (1963)

$$E_c = \Delta p V_c \propto \Delta p \lambda^3, \quad \Delta p = \tfrac{1}{2}\rho(\sigma + C_{p_{\max}})C_{\text{ref}}^2 \tag{7}$$

According to (7), we have $\lambda \propto E_c^{1/3}\Delta p^{-1/3}$. Thus, Eq. (6) becomes, using (2):

$$\hat{\mathbf{n}}(E_c) \propto C_{\text{ref}}\Delta p^{1/3}E_c^{-4/3} \tag{8}$$

Let $E_m = \Delta p \cdot l^3$ be the reference energy. E_m is normally associated with the maximum volume generated by the main cavity. However, we do not know the relationship between this volume and the current flow conditions, so we assume that this volume is proportional to l^3. This hypothesis is true in the unsteady situation, as suggested by Table 1.

The energy density $\hat{\mathbf{n}}(E_c)$ is finally given by

$$\hat{\mathbf{n}}(E_c) = K_0 S_c \frac{C_{\text{ref}}}{l} E_m^{1/3}E_c^{-4/3}, \quad K_0 = \sqrt[3]{\frac{\pi}{162}} \tag{9}$$

Energy Spectrum. The number per time unit of vapor cavities whose energy E_c is inside the interval $[E_c, E_c + \Delta E_c]$ is given by the relation:

$$\mathbf{n}(E_c) = \int_{E_c}^{E_c+\Delta E_c} \hat{\mathbf{n}}(\epsilon)d\epsilon \tag{10}$$

We introduce the parameter β that acts on E_c as α does on λ: $\beta \in \mathbf{R}^+ | \Delta E_c = \beta E_c$. Moreover, according to (6), we have the following relation:

$$\mathbf{n}(E_c) = \mathbf{n}(\lambda) = \int_{\lambda}^{\lambda+\Delta\lambda} \hat{\mathbf{n}}(\zeta)d\zeta = S_c \frac{C_{\text{ref}}}{\lambda} \frac{\alpha}{\alpha + 1} \tag{11}$$

Comparing coefficients from relations (10) and (11), we obtain the formulation of $\mathbf{n}(E_c)$:

$$\mathbf{n}(E_c) = K_1 S_c \frac{C_{\text{ref}}}{l} \left(\frac{E_m}{E_c}\right)^{1/3} [1 - (1 + \beta)^{-1/3}] \tag{12}$$

with

$$\beta = (1 + \alpha)^3 - 1 \quad \text{and} \quad K_1 = \sqrt[3]{\frac{\pi}{6}} \tag{13}$$

Spectrum $\mathbf{n}(E_c)$ is fully determined by the flow parameters. It differs from existing models based on theoretical probability laws selected to fit the closest possible the spectrum suggested by Hammitt (1963): Kato (1975), Selim (1985).

Collapse Efficiency. We assume that a vapor cavity induces damage if the energy resulting from the collapse is greater than the material threshold E_s. The damaging energy E_d issued from the cascade from flow to material is only a part of the initial fluid energy E_c. Knapp et al. (1970) estimated experimentally, being to our knowledge the only literature reference with regard to this aspect, that only 1 cavity in 30000 produces damage. Inspired on previous works (Ross, 1977; Baiter, 1982), we reintroduce the notion of collapse efficiency through the term η_{co}, which is a function of numerous parameters (energy

dissipation during collapse, distance of collapse to the wall, physical properties of fluid and material, roughness, pressure fluctuations, . . .). η_{co} is defined by the ratio between the spectrum of energy E_d absorbed by the material and that of energy E_c provided by the vapor cavities (with $E_c \geq E_s$):

$$\eta_{co} = \frac{\hat{\mathbf{n}}(E_d)}{\hat{\mathbf{n}}(E_c)} = \frac{\mathbf{n}(E_d)}{\mathbf{n}(E_c)} \tag{14}$$

Thus, η_{co} is only related to that part of collapses having energy larger than the threshold energy. It differs in that from the "energy efficiency" introduced by Reboud and Fortes-Patella (1996) as the ratio E_d/E_c, this being a measure of the effective energy transfer from flow to material. η_{co} is rather a macroscopic efficiency that integrates both the generation process and this energy cascade. We hypothesize that the collapse efficiency η_{co} is constant over the complete energy scale above E_s.

Erosive Power. The erosive power P_{er} (using the same terminology as Farhat et al., 1993) is the integral per time unit of energies contributing to the damage process (i.e., $E_c \geq E_s$):

$$P_{er} = \int_{E_s}^{E_m} \hat{\mathbf{n}}(\epsilon)\epsilon d\epsilon = K_2 S_c \frac{C_{\text{ref}}}{l} E_m \Phi_{\text{er}}, \quad K_2 = \sqrt[3]{\frac{\pi}{48}} \tag{15}$$

where E_m is the upper bound of energies. Term Φ_{er} is given by the relations:

$$\Phi_{er} = 1 - F^{2/3}, \quad F = \frac{E_s}{E_m} \tag{16}$$

Erosive Efficiency. We introduce the erosive efficiency η_{er} as the ratio between the erosive power and the total power of vapor cavities. η_{er} is a continuously decreasing function of the energy threshold E_s:

$$\eta_{er} = \frac{P_{er}}{\int_0^{E_m} \hat{\mathbf{n}}(\epsilon)\epsilon d\epsilon} = \Phi_{er} \tag{17}$$

The denominator represents the total energy per time unit and is proportional to the energy flux $(C_{\text{ref}}E_m)/l$.

Transposition. We consider two flows geometrically similar and with the same cavitation development (thus similar with regard to the cavitation coefficient σ). Fluid is unchanged.

The problem of transposition consists in studying the influence of a change of the flow velocity and/or of the geometrical scale. Let π_1 and π_2 be the transposition parameters: $\pi_1 = C'_{\text{ref}}/C_{\text{ref}}$ and $\pi_2 = l'/l$. C'_{ref} and l' are, respectively, the mean velocity and the main cavity length of the new flow. The cavity length is taken as the reference geometrical length due to the σ similarity.

Using Eqs. (15) and (16), the transposed erosive power P'_{er} is given by:

$$P'_{er} = \lambda_{er} P_{er}, \quad \lambda_{er} = \pi_1^3 \pi_2^2 \frac{1 - \Gamma F^{2/3}}{\eta_{er}}, \quad \Gamma = \pi_1^{-4/3} \pi_2^{-2} \tag{18}$$

λ_{er} is the erosive power coefficient: it allows the transposition of the erosive power P_{er}, both in velocity and in geometrical scale. It also includes the damaging energy threshold E_s as well as the macroscopic flow parameters of the original flow (through the erosive efficiency η_{er}).

Location of Collapse. According to the theoretical model developed by Rayleigh (1917), the time between the instant of application of pressure and the instant of zero radius is given by the Rayleigh time $t_r \cong 0.915\ R_m\sqrt{\rho/\Delta p}$, where R_m is the initial and maximum radius of the bubble. Four hypotheses are given: (*i*) According to Table 1, $\lambda = \lambda_x \simeq d_{\text{eq}}$; consequently, we can state that $R_m \approx \lambda/2$; (*ii*) Cavity is convected with the flow velocity $C_c = kC_{\text{ref}}$, $k \approx 0.6$; (*iii*) Δp is constant during t_r; (*iv*) Volume of cavity is maximum at abscissa l.

The displacement of a cavity is $\delta_c = t_r C_c$. Thus, using Eq. (7), the chordwise location of the collapse is given by

$$x_c = l\left[1 + K_3\left(\frac{E_c}{E_m}\right)^{1/3}(\sigma + C_{p_{\max}})^{-1/2}\right]$$

$$K_3 = \frac{0.915k}{\sqrt{2}}\sqrt[3]{\frac{6}{\pi}} \tag{19}$$

The collapse location is independent of the mean flow velocity, for a given flow incidence i and a given cavitation coefficient σ. This result is coherent with the works performed by Simoneau et al. (1989) and N'Guyen et al. (1987). For a given set of flow conditions, δ_c is proportional to λ. As a consequence, the collapse or pit density (number of collapses/pits per time unit and per length unit) may be expressed by: $\hat{\mathbf{n}}(\delta_c)d\delta_c = \hat{\mathbf{n}}(E_c)dE_c$. Equation (19) also points out that the beginning of the damaged area is fully determined when E_c equals E_s.

Experimental Validation: Elements. Pitting data is available from former erosion tests done independently of the present work, although on the same hydrofoil and for a subset of the flow conditions considered here. Cavitation tests were performed on Copper samples. Surface measurement was done using a laser profilometer and processed by a software developed by Fortes-Patella (1994) and co-workers. In addition to the geometrical characteristics of pits, the software provides the acoustical energy E_a associated to each pit and calculated according to the numerical simulation developed by this author.

Recent works (see Reboud and Fortes-Patella, 1996) indicate that the material deformation energy E_d is proportional to E_a, yet for a given material as long as this is strongly dependent upon the elastic properties of the material. As a consequence, we will use the terminology E_d instead of E_a to make clear distinction between flow and material. This is consistent since E_a is derived from material deformation data by the numerical simulation.

Figure 10 represents the energy spectra $\mathbf{n}(E_c)$ (fluid), calculated according to relation (12), and $\mathbf{n}(E_d)$ (material). Both are expressed per unit of surface. A remarkable proportionality relationship is noticed. The experimental spectra are fitted by power laws using a least squares method and are found to have exponents that closely match the theoretical exponent $-\frac{1}{3}$ of Eq. (12): -0.341 for $l/L = 20$ percent and -0.364 for $l/L = 40$ percent. One can estimate the collapse efficiency using Eq. (14). Figure 11 represents the value of η_{co} and shows that it remains fairly constant over the whole range of energies, thus confirming the hypothesis we made above.

Mean ratios between number of pits and number of cavities are found to be very low, ranging from 10^{-5} to 10^{-4}, as reported in Table 2. As a matter of fact, E_d can be much smaller than E_c or E_a, as reported by Reboud and Fortes-Patella (1996).

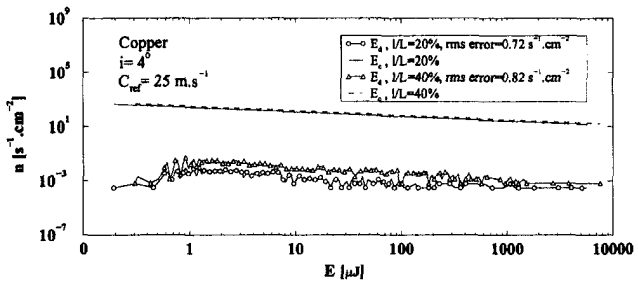

Fig. 10 Comparison of energy spectra between flow and material

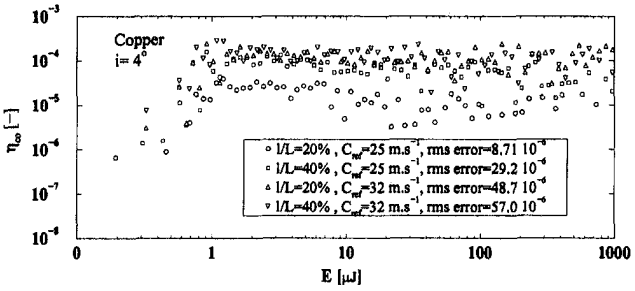

Fig. 11 Collapse efficiency $\eta_{co} = \hat{n}(E_d)/\hat{n}(E_c)$

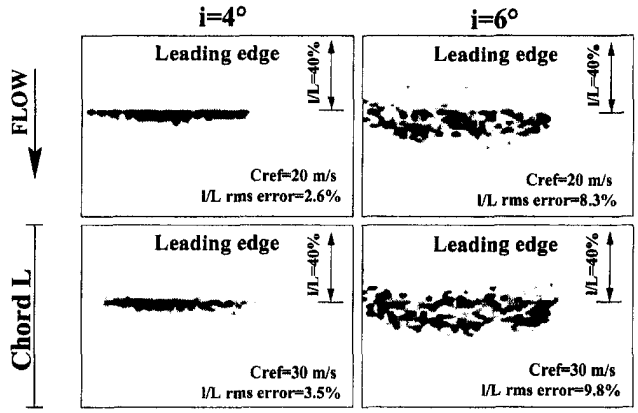

Fig. 12 Collapse locations of vapor cavities, top view: i = 4 deg, 6 deg, C_{ref} = 20, 30 m·s^{-1}, l/L = 40 percent

Moreover, the statistical density of vapor cavities decreases rapidly with their energy (see Eq. (9)). Yet, factors not fully understood, such as the distance of collapse to the wall, may be the main cause of such low values. Though, these values are quite coherent with those estimated experimentally by Knapp et al. (1970).

η_{co} is highly dependent upon the flow conditions. Curves relative to 25 m·s^{-1} and 32 m·s^{-1} point out that mean η_{co} increases with C_{ref}. These results are consistent with increased erosion observed by Simoneau et al. (1989). Influence of cavity length at constant velocity is not clearly established. Although flow parameters may act directly on η_{co}, they certainly have an indirect influence through complex phenomena: cloud structure, shock wave propagation, ... These influences are beyond the objectives of the current study.

Relation (19) is used to determine the collapse area. Two main comments are suggested by the resulting collapse images of Fig. 12, confirmed by direct observation of eroded areas: (*i*) As stated earlier, the location of collapse is independent of C_{ref}; however, the distribution of collapses around the mean position changes: collapses move downstream when C_{ref} increases; this effect is mainly attributed to inertial forces and agrees with observed elongation of the main cavity with increasing C_{ref} (Dupont, 1991); (*ii*) For the unsteady case (6 deg), the collapse area enlarges around the mean position of the closure region; indeed, the energy spectrum widens and moves to higher energies, in particular because of the appearance of the characteristic volumes (see Table 1).

Conclusion

The production rate f_c^{λ} of transient vapor cavities generated by a leading edge cavity is ruled by a Strouhal law S_c^{α} depending on the characteristic cavity size λ, the mean flow velocity C_{ref}, the class width parameter α, and the constant $S_c \approx 86.87\ 10^{-3}$. This law applies to both the steady and the unsteady cavitation behaviors. This latter situation is, besides, characterized by the production of vapor volumes arranged into two distinct λ classes. The ratios between the mean λ values of those classes and the main cavity mean length l give values very close to $\frac{1}{3}$ and $\frac{2}{3}$, whatever the flow conditions are. The corresponding production rate is controlled by the well-known Strouhal law based on C_{ref} and l, with $S \approx 0.3$.

Combining stereometry and tomography principles, volume of transient vapor vortices is reconstructed. Despite the complexity and variety of volumes, remarkable linear relationships are found between main dimensions (chordwise, spanwise and vertical extents) and the diameter d_{eq} of a corresponding equivalent spherical volume. This applies equally to both behaviors, with specific relationships for the unsteady case.

The fluid energy spectrum $\mathbf{n}(E_c)$, E_c being the potential energy of a vapor cavity, is expressed exclusively as a function of flow global parameters, production rate constant S_c, maximum potential energy E_m (defined by main cavity length l) and E_c.

The comparison between the fluid energy spectrum $\mathbf{n}(E_c)$ and the material deformation energy spectrum $\mathbf{n}(E_d)$ carried out from former pitting experiments shows a remarkable proportionality relationship defined by the collapse efficiency η_{co}. Values of η_{co} in the range 10^{-5} to 10^{-4} are found, depending on flow conditions. This relationship between the fluid and the material sides of the cavitation erosion problem confirms the well-founded nature of the energy approach and validates it.

The erosive power term P_{er} is defined as a function of flow parameters, constant S_c and of the erosive efficiency η_{er}. This efficiency is dependent upon the damaging energy threshold E_s defined by the mechanical properties of the material. A simple model based on the Rayleigh's theory is introduced that locates the erosion area according to E_s. The eroded area does not depend on the flow velocity, but essentially on the pressure gradient in the closure region of the main cavity. Quite good correlation is found with experiment.

Provided flow geometries are homologous, fluids are unchanged and cavitation coefficient is identical, the ratio between E_c spectra is equal to the ratio between velocities if velocity transposition is considered. If geometrical scale changes, the ratio between spectra per surface unit is inversely equal to the square of the geometrical ratio. Finally, the erosive power coefficient λ_{er} is introduced as to transpose P_{er}.

A study over a number of materials of engineering interest covering a wide range of mechanical properties should be engaged in order to establish correlations between these properties and E_s. Furthermore, the influence of flow parameters on the material deformation energy spectrum could be clarified in order to better understand their role on the collapse efficiency η_{co}. Finally, the determination of the maximal fluid energy E_m in relation with flow parameters is of relevance to define the upper limit of the fluid energy spectrum and thus to improve the accuracy of the erosive power term.

Table 2 Mean collapse efficiency $\overline{\eta_{co}} = \overline{\hat{n}(E_d)/\hat{n}(E_c)}$

i [°]	C_{ref} [m·s^{-1}]	σ [-]	l/L [%]	$\overline{\eta_{co}}$ [-]
4°	25	1.25	20	16.5 10^{-6}
		1.12	40	69.1 10^{-6}
	32	1.26	20	122.8 10^{-6}
		1.13	40	128.6 10^{-6}

Acknowledgments

The authors wish to thank the members of the IMHEF cavitation research group. This work was financially supported by Électricité de France and the Swiss Federal Commission d'Encouragement à la Recherche Scientifique.

References

Avellan, F., and Farhat, M., 1989, "Shock Pressure Generated by Cavitation Vortex Collapse," *International Symposium on Cavitation Noise and Erosion in Fluid Systems,* Vol. FED 88, pp. 119–125, San Francisco, ASME Winter Annual Meeting.

Baiter, H.-J., 1982, "Estimates of the Acoustic Efficiency of Collapsing Bubbles," *International Symposium on Cavitation Noise,* Phoenix, AZ, ASME.

Bark, G., and Berlekom, W. B., 1978, "Experimental Investigations of Cavitation Dynamics and Cavitation Noise," *12th Symposium on Naval Hydrodynamics,* pp. 470–493, Washington, D.C., ONR.

Bourdon, P., Simoneau, R., Avellan, F., and Farhat, M., 1990, "Vibratory Characteristics of Erosive Cavitation Vortices Downstream of a Fixed Leading Edge Cavity," *15th Symposium on Modern Technology in Hydraulic Energy Production,* Vol. I, Belgrade (Yugoslavia), IAHR, Paper H3, 12 pp.

Brennen, C. E., 1994, "Observations of Cavitating Flows," *20th Symposium on Naval Hydrodynamics,* ONR, Invited Lecture.

Ceccio, S. L., and Brennen, C. E., 1991, "Observations of the Dynamics and Acoustics of Travelling Bubble Cavitation," *Journal of Fluid Mechanics,* Vol. 233, pp. 633–660.

Chahine, G. L., and Duraiswami, R., 1992, "Dynamical Interactions in a Multi-Bubble Cloud," ASME JOURNAL OF FLUIDS ENGINEERING, Vol. 114, pp. 680–686.

Chien, C. H., and Aggarwal, J. K., 1985, "Reconstruction and Matching of 3-D Objects Using Quadtrees/Octrees," *Third Workshop on Computer Vision,* pp. 49–54, Bellaire, MI.

Dupont, Ph., 1991, "Étude de la Dynamique d'une Poche de Cavitation Partielle en Vue de la Prédiction de l'Érosion dans les Turbomachines Hydrauliques," Ph.D. thesis, École Polytechnique Fédérale de Lausanne, Institut de Machines Hydrauliques et de Mécanique des Fluides (IMHEF-LMH), No. 931.

Farge, M., 1992, "Wavelet Transforms and their Applications to Turbulence," *Annual Review of Fluid Mechanics,* Vol. 24, pp. 395–457.

Farhat, M., 1994, "Contribution à l'Étude de l'Érosion de Cavitation: Mécanismes Hydrodynamiques et Prédiction," Ph.D. thesis, École Polytechnique Fédérale de Lausanne, Institut de Machines Hydrauliques et de Mécanique des Fluides (IMHEF-LMH), No. 1273.

Farhat, M., Pereira, F., and Avellan, F., 1993, "Cavitation Erosion Power as a Scaling Factor for Cavitation Erosion in Hydraulic Machines," *4th International Symposium on Bubble Noise and Cavitation Erosion in Fluid Systems,* Vol. FED 176, pp. 95–104, New Orleans, LA, ASME Winter Annual Meeting.

Fortes-Patella, R., 1994, "Analyse de l'Érosion de Cavitation par Simulations Numériques d'Impacts," Ph.D. thesis, Institut National Polytechnique de Grenoble, CREMHyG, Grenoble, France.

Fortes-Patella, R., and Reboud, J. L., *1993,* "Numerical Analysis for Evaluating Cavitation Erosion Phenomenon," *Cavitation and Multiphase Flow Forum,* Washington D.C., ASME.

Franc, J. P., and Michel, J. M., 1988, "Unsteady Attached Cavitation on an Oscillating Hydrofoil," *Journal of Fluid Mechanics,* Vol. 193, pp. 171–189.

Fujikawa, S., and Akamatsu, T., 1980, "Effects of the Non-equilibrium Condensation of Vapour on the Pressure Wave Produced by the Collapse of a Bubble in a Liquid," *Journal of Fluid Mechanics,* Vol. 97, pp. 481–512.

Hammitt, F. G., 1963, "Observations on Cavitation Damage in a Flowing System," ASME *Journal of Basic Engineering,* pp. 347–367.

Kato, H., 1975, "A Consideration on Scaling Laws of Cavitation Erosion," *International Shipbuilding Progress,* Vol. 22, pp. 305–327.

Kato, H., Konno, A., Maeda, M., and Yamaguchi, H., 1996, "Possibility of Quantitative Prediction of Cavitation Erosion Without Model Test," ASME JOURNAL OF FLUIDS ENGINEERING, Vol. 118, pp. 582–588.

Kiya, M., and Sasaki, K., 1983, "Structure of a Turbulent Separation Bubble," *Journal of Fluid Mechanics,* Vol. 137, pp. 83–113.

Knapp, R. T., Daily, J. W., and Hammitt, F. G., 1970, "Cavitation," *Engineering Societies Monographs,* McGraw-Hill, NY, 578 pp.

Kornfeld, M., and Suvorov, L., 1944, "On the Destructive Action of Cavitation," *Journal of Applied Physics,* Vol. 15, pp. 495–506.

Kubota, S., Kato, H., Yamaguchi, H., and Maeda, M., 1987, "Unsteady Structure Measurement of Cloud Cavitation on a Foil Section Using Conditional Sampling Technique," *International Symposium on Cavitation Research Facilities and Techniques,* Vol. FED 111, pp. 204–210, Boston, ASME.

Le, Q., Franc, J. P., and Michel, J. M., 1993, "Partial Cavities: Global Behavior and Mean Pressure Distribution," ASME JOURNAL OF FLUIDS ENGINEERING, Vol. 115.

Lehman, A. F., 1966, "Determination of Cavity Volumes Forming on a Rotating Blade," 11th International Towing Tank Conference, Tokyo, Japan.

Levinthal, C., and Ware, R., 1972, "Three-dimensional Reconstruction from Serial Sections," *Nature,* Vol. 236, pp. 207–210.

Lewalle, J., 1994, "Wavelet Analysis of Experimental Data: Some Methods and the Underlying Physics," 25th Fluid Dynamics Conference, Colorado Springs, CO, AIAA, p. 2281.

Maeda, M., Yamaguchi, H., and Kato, H., 1991, "Laser Holography Measurement of Bubble Population in Cavitation Cloud on a Foil Section," *International Symposium on Cavitation,* Vol. FED 116, pp. 67–75, ASME.

Mørch, K. A., 1981, "Cavity Cluster Dynamics and Cavitation Erosion," *International Cavitation and Polyphase Flow Forum,* pp. 1–10, Boulder, CO, ASME-ASCE.

N'Guyen, T. M., Franc, J.-P., and Michel, J.-M., 1987, "On Correlating Pitting Rate and Pressure Peak Measurements in Cavitating Flows," *International Symposium on Cavitation Research Facilities and Techniques,* Vol. FED 57, pp. 207–216, ASME.

Pereira, F., 1997, "Prédiction de l'Érosion de Cavitation: Approche Énergétique," Ph.D. thesis, École Polytechnique Fédérale de Lausanne, Institut de Machines Hydrauliques et de Mécanique des Fluides (IMHEF-LMH), No. 1592.

Rayleigh, Lord, 1917, "On the Pressure Developed in a Liquid During the Collapse of a Spherical Void," *Philosophical Magazine and Journal of Science,* 34, No. 6, pp. 94–98.

Reboud, J. L., and Fortes-Patella, R., 1996, "Étude de l'Interaction Fluide-Structure en Érosion de Cavitation," *Proceedings des Troisièmes Journées Cavitation,* pp. 183–192, Grenoble, SHF (Société Hydrotechnique de France).

Ross, D., 1977, "Sound Radiation from Collapsing Cavitation Bubbles," 9th International Congress on Acoustics (ICA), Madrid (Spain), Paper L35, 6 pp.

Selim, S. M. A., 1985, "A Theoretical Study on Cavitation Erosion Rate," Cavitation in Hydraulic Structures and Turbomachinery, Albuquerque, NM, ASCE/ASME Mechanics Conference.

Simoneau, R., Avellan, F., and Kuhn de Chizelle, Y., 1989, "On Line Measurement of Cavitation Erosion Rate on a 2D NACA Profile," *International Symposium on Cavitation Noise and Erosion in Fluid Systems,* Vol. FED 88, pp. 95–102, San Francisco, ASME Winter Annual Meeting.

Soyama, H., Kato, H., and Oba, R., 1992, "Cavitation Observations of Severely Erosive Vortex Cavitation Arising in a Centrifugal Pump," *3rd International Conference on Cavitation,* pp. 103–110, I.Mech.E.

Thiruvengadam, A., 1971, "Scaling Laws for Cavitation Erosion," *Symposium on Flow of Water at High Speeds,* pp. 405–425, Leningrad, USSR, IUTAM.

Vogel, A., Lauterborn, W., and Timm, R., 1989, "Optical and Acoustic Investigations of the Dynamics of Laser-Produced Cavitation Bubbles near a Solid Boundary," *Journal of Fluid Mechanics,* Vol. 206, pp. 299–338.

Cavitation Nuclei Population and Event Rates

Zhenhuan Liu
Graduate Student.

Christopher E. Brennen
Professor.

Division of Engineering
and Applied Science,
California Institute of Technology,
Pasadena, CA 91125

To model the processes of cavitation inception, noise and damage, it is necessary to generate a model of the cavitation event rate which can then be coupled with the consequences of the individual events to produce a complete synthesis of the phenomenon. In this paper we describe recent efforts to connect the observed event rates to the measured distributions of cavitation nuclei in the oncoming stream. Comparisons are made between the observed event rates and event rates calculated from measured nuclei distributions using an algorithm which includes the dynamics of the nuclei motion and growth. Various complications are explored including the effect of the boundary layer, the relative motion between the nucleus and the liquid, the observable bubble size effect, and the effect of bubble growth on neighboring nuclei. All of these are seen to have important influences on the event rate, and therefore, on cavitation inception and other macroscopic consequences. We demonstrate that it is possible to predict the correct order of magnitude of the event rate when an attempt is made to model the important flow complications.

1 Introduction

In order to synthesize the cumulative effects of a stream of traveling cavitation bubbles, it is necessary to supplement the details of individual events with the rates at which these events occur. Many investigators have anticipated a relationship between the cavitation event rate and the concentration of cavitation nuclei in the oncoming stream (see, for example, Schiebe, 1972; Keller, 1972, 1974; Keller and Weitendorf, 1976; Kuiper, 1978; Gates and Acosta, 1978; Meyer et al., 1992). At first sight this seems like a straightforward problem of computing the flux of nuclei into the region for which $C_p < -\sigma$. However, many complications arise which make this analysis more difficult than might otherwise appear and we shall discuss some of the specific issues below. But these difficulties do not account for the lack of experimental research into the relationship. Rather, the difficulties involved in the accurate measurement of the incoming nuclei number distribution function, $N(R)$, have been responsible for the delay in any detailed, quantitative investigation of this component of the problem. (Note that $N(R)dR$ is the number of nuclei with size between R and $R + dR$ per unit volume.) As Billet (1985) remarked in his review of nuclei measurement techniques, the only reliable method of obtaining $N(R)$ has been the extremely time-consuming procedure of surveying a reconstruction of an in situ hologram of a small volume of tunnel water (Gates and Bacon, 1978). However, the time and effort required to construct one $N(R)$ distribution by this method has seriously limited the scope of these investigations.

The recent development of light scattering instruments employing phase Doppler techniques (Saffman et al., 1984; Tanger et al., 1992) has improved the situation. In our laboratory, we have succeeded in validating and calibrating a Phase Doppler Anemometer (PDA) made by Dantec by taking simultaneous measurements with the PDA and a holographic system (Liu et al., 1993). The great advantage of the PDA system is the speed with which $N(R)$ can be measured. After validation, the PDA system could then be used with confidence for investigations of the nuclei population dynamics in a water tunnel (Liu et al., 1993 and 1994) and of the aforementioned relation between $N(R)$ and the cavitation event rate (Liu et al., 1993, Liu and Brennen, 1994).

In this paper, we first present the experimental observations of cavitation event rates on a Schiebe headform with simultaneous measurement of the nuclei distribution in the upcoming stream. We then present an analytical model to synthesize the event rates from the measured nuclei distributions. Then we compare the predicted event rates with cavitation observations in two water tunnels with quite different nuclei population dynamics.

2 Observations of Nuclei Population and Event Rates

The experiments were performed in the Low Turbulence Water Tunnel (LTWT) and the High Speed Water Tunnel (HSWT) at Caltech. Detailed descriptions of these two water tunnels can be found in other literature (see Gates, 1978 and Liu and Brennen, 1995), and will not be repeated here. Figure 1 shows a sketch of the experimental setup. A Schiebe headform with 5.08 cm diameter was installed at the center of the water tunnel. The free-stream nuclei number distribution was measured by a Phase Doppler Anemometer (PDA), which was calibrated by comparing the results with those obtained by a holographic method (Liu et al., 1993). On the other hand, the cavitation event rate on the Schiebe headform was measured by three flush-mounted electrodes on the headform surface (Ceccio and Brennen, 1992 and Kuhn de Chizelle et al., 1992).

In Fig. 2, we present a typical comparison of the nuclei number density distributions in the LTWT and in the HSWT. Also plotted in the figure are measurements in other facilities (Arndt and Keller, 1976; Peterson et al., 1972, 1975; Feldberg and Shlemenson, 1971; Keller and Weitendorf, 1976; and Gates and Bacon, 1978) and in the ocean (Cartmill and Su, 1993). As expected, substantial differences in the nuclei number density distributions in the two water tunnels were found. Although the shapes of the distributions are similar, the differences in the magnitudes were as much as two orders of magnitude. The typical nuclei concentration in the LTWT is quite large, about 100 cm^{-3}; while the nuclei concentration in the HSWT is low at about 1 cm^{-3}. Billet (1985) and Gindroz and Billet (1994) presented useful reviews of the subject of nuclei concentrations and distributions. They found that for deaerated water, typical concentrations are of the order of 20 cm^{-3} with sizes ranging from about 5 μm to about 20 μm. We conclude that the LTWT is nuclei rich and the HSWT is nuclei poor. This was expected

Contributed by the Fluids Engineering Division for publication in the JOURNAL OF FLUIDS ENGINEERING. Manuscript received by the Fluids Engineering Division August 8, 1995; revised manuscript received October 2, 1997. Associate Technical Editor: J. Katz.

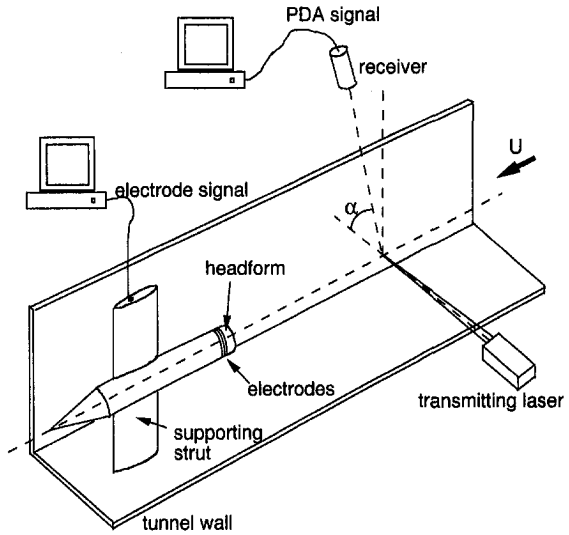

Fig. 1 Experimental setup for the simultaneous measurement of the cavitation nuclei distribution in the water tunnel and the cavitation event rate on a Schiebe headform

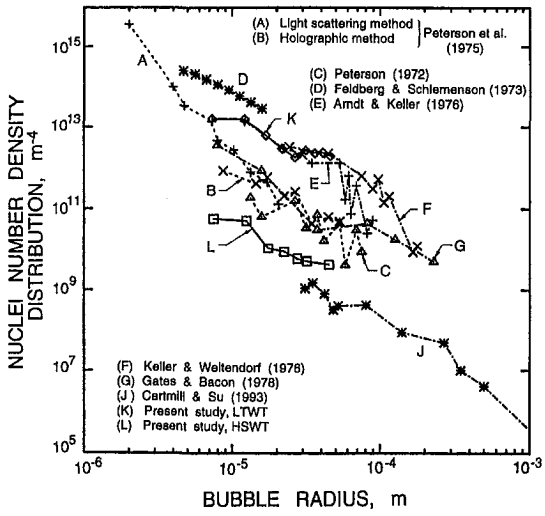

Fig. 2 A comparison of the nuclei number density distributions in the Low Turbulence Water Tunnel and the High Speed Water Tunnel with measurements in other facilities and in the ocean. The uncertainty in the ordinate is ±5 percent.

since the HSWT has an effective resorber while the LTWT does not; related studies (Liu, 1995, Liu et al., 1993) demonstrated that, as a result, the two facilities have quite different nuclei population dynamics. Consequently, comparative experiments in the two tunnels were expected to provide a valuable range of nuclei populations.

Figure 3 presents the measurements of the event rates on a Schiebe headform in the LTWT and HSWT tunnels. Note that the cavitation event rates increase dramatically as the cavitation number is decreased. However, the event rates can vary by as much as a decade at the same cavitation number. At the same cavitation number, the larger free stream nuclei concentrations correspond to the larger cavitation event rates. As one would expect, the event rates observed at the same cavitation number in the LTWT are much higher than in the HSWT, because of the much higher nuclei population in the LTWT.

During the tests in the HSWT, cavitation experiments were performed at various speeds and air contents. Again, it was clear that the nuclei population had a strong effect on the cavitation event rate as illustrated on the right in Fig. 3. This resulted in a significant effect on the cavitation inception number. For example, at a velocity of 9.4 m/s and a nuclei concentration of 0.8 cm^{-3}, the cavitation inception number was 0.47. After air injection, the nuclei concentration rose to 12 cm^{-3}, and cavitation inception occurred at $\sigma_i = 0.52$. In contrast, in the LTWT, the cavitation inception number in the LTWT was about 0.57, and the nuclei concentration was about 100 cm^{-3}. In the HSWT, attached cavitation occurred soon after traveling bubble cavitation. This implies that attached cavitation occurs more readily when the nuclei population is low. Similar phenomenon was also observed by Li and Ceccio (1994) on a cavitating hydrofoil. In their observations, when the nuclei concentration in the

Nomenclature

C = nuclei concentration
C_P = coefficient of pressure, $(p - p_\infty)/\frac{1}{2}\rho U^2$
C_{PM} = minimum C_P on a given streamline
C_{PMS} = minimum value of C_P on the headform surface
$C^*_{\beta 1}$ = constant
D = headform diameter
E = cavitation event rate
$N(R)$ = nuclei density distribution function
R = radius of a cavitation nucleus
$\dot{R}$, $\ddot{R}$ = dR/dt, d^2R/dt^2
R_C = critical cavitation nucleus radius
R_M = minimum observable bubble radius
$R_{\max}$ = maximum cavitation bubble radius
R_0 = initial nucleus radius
S = surface tension
U = upstream tunnel velocity
U_M = maximum velocity corresponding to C_{PMS}
f_1, f_2, f_3 = numerical factors effecting the cavitation event rate
n_i = bubble/bubble interaction effect
p = fluid pressure
p_∞ = free stream pressure
p_{G0} = initial gas pressure in a bubble
p_c = blake critical pressure
$p_{\min}$ = undisturbed liquid pressure
p_v = vapor pressure
q = flow velocity
r = distance from the center of a bubble
r_H = headform radius
r_K = radius of curvature of streamlines near minimum pressure point
r_S = radius of minimum pressure point
r_e = critical radius
y = distance normal to body surface
y_M = maximum y value of the $C_P = -\sigma$ isobar
s, s_0 = coordinate along a streamline and the location of minimum pressure point
t_G = time available for bubble growth
u, u_M = fluid velocity, fluid velocity just outside boundary layer
v = velocity of a bubble normal to streamline
ρ = fluid density
σ = cavitation number, $(p_v - p_\infty)/\frac{1}{2}\rho U^2$
σ_{cri} = threshold cavitation number
σ_i = inception cavitation number
σ_i' = cavitation number variation
ξ, λ = factors in the chosen analytical expression for $N(R)$
ν = kinematic viscosity of fluid
μ = fluid viscosity
δ, δ_2 = thickness and momentum thickness of the boundary layer
ϵ = displacement of a bubble normal to a streamline
Σ = function defined by Eq. (15)
Σ' = $d\Sigma/d(r/r_H)$

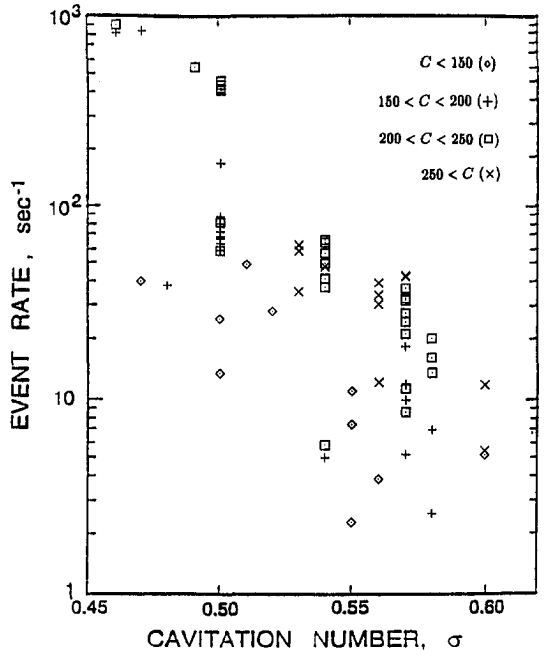

Fig. 3 Left: Variations in the cavitation event rates with cavitation number on a 5.08 cm Schiebe body in the LTWT at a speed of 9 m/s. Data are plotted for various ranges of free stream nuclei concentration, C (cm^{-3}): $C < 150$ (◇); $150 < C < 200$ (+); $200 < C < 250$ (□) and $250 < C$ (×).

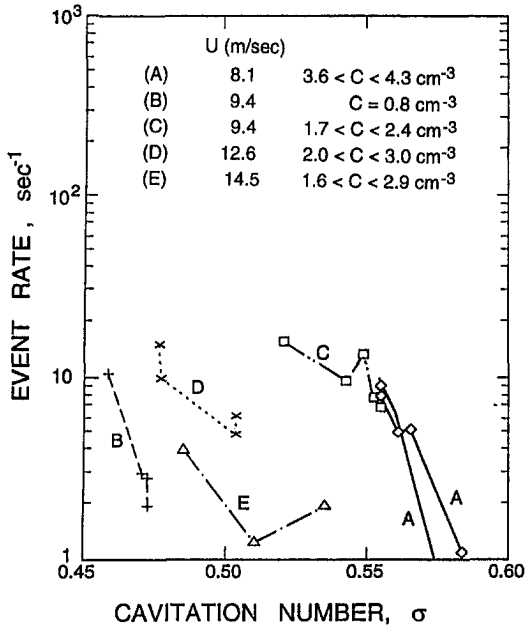

Fig. 3 Right: Observed cavitation event rates on a 5.08 cm Schiebe body in the HSWT at various tunnel speeds and nuclei concentrations. The data are plotted for various tunnel speeds and nuclei concentrations. The uncertainty in the ordinate is ±5 percent.

water was high, traveling bubble cavitation occurred before attached cavitation was observed. But when the nuclei concentration was low, no traveling bubble cavitation was observed before attached cavitation occurred. They ascribe the cause of this phenomenon to laminar boundary separation on the hydrofoil. However, we are not sure about the cause on the Schiebe headform since it does not exhibit laminar boundary layer separation in the region of low pressure where these events were observed.

By comparing the event rates for conditions C and E in Fig. 3 (right), it can be seen that, at the constant nuclei concentration level, the cavitation event rate decreased with increasing tunnel velocity, which is the inverse of what would be expected. All the numerical and analytical simulations (Ceccio and Brennen, 1992; Meyer et al., 1992; Liu et al., 1993) predict that the event rate increases with oncoming velocity, provided that the nuclei population remains the same. This velocity effect on the cavitation event rate was also observed by Kuhn de Chizelle et al. (1992, 1995). Since they were unable to measure the nuclei population in the oncoming flow, Kuhn de Chizelle et al. speculated that the free nuclei population was decreased by the increase in tunnel pressure necessary to achieve the same cavitation number at a higher speed. The investigations of nuclei population dynamics in a water tunnel by Liu et al. (1993) support that explanation. However, the current data shows that the event rates decrease with an increasing tunnel speed even when the nuclei concentrations are at the same level. This phenomenon is not understood. A possible explanation is that the PDA mistakenly counted more solid particles as microbubbles at the higher tunnel velocities. Since the population of solid particles increased with speed, perhaps the number of microbubbles decreased even though the total nuclei concentration remained the same. It may also be the case that there exists some, as yet unrecognized, mechanism in the relation between the nuclei population and the cavitation event rate.

3 An Analytical Model for Cavitation Event Rate

A simple synthesis of the cavitation event rate from the nuclei distribution in the on-coming stream was presented by Ceccio and Brennen (1992). Here we explore this relationship further and comment on other factors which could significantly effect the event rate. We will use a nuclei number distribution function, $N(R)$, defined such that, per unit volume, the number of nuclei with radii between R and $R + dR$ is given by $N(R)dR$. From the measurement of free stream nuclei distribution in our laboratory (see Liu et al., 1993), a characteristic form for $N(R)$ is

$$N(R) = C\frac{\log e}{(2\pi)^{1/2}\lambda R}\exp\left(-\frac{(\log R - \log \xi)^2}{2\lambda^2}\right) \quad (1)$$

where C is the nuclei concentration. By adjusting the values of ξ and λ, the distribution function (1) can be made to fit most observed nuclei distribution functions. It is preferable to the more frequently used power law because it allows simulation of the peak in the population which is often observed (at $R = \xi$) and of the fact that the population of large bubbles is very small.

The principal problem in synthesizing the event rate is to evaluate how many of these nuclei are convected into the region of low pressure near the minimum pressure point on the surface of the body and how many therefore grow to observable macroscopic vapor bubbles. Some simplifying observations allow us to avoid lengthy numerical computations of the bubble dynamics (using the Rayleigh-Plesset equation) for every nucleus size, every streamline, every cavitation number, etc. Meyer et al. (1989, 1992) conducted a detailed numerical study of this kind which included most of the effects studied here. In this paper we present a much simpler analytical approach which, though more approximate, is probably as accurate as the current experimental data would merit. First, we shall employ various relations pertaining to spherical bubble dynamics despite the tact that, as shown by Ceccio and Brennen (1992), the actual cavitation bubbles are far from spherical. However, Kuhn de Chizelle et al. (1995) also showed that the Rayleigh-Plesset equation gives a reasonable though crude estimate of the bubble dimensions and we therefore adopt this approximation here. However, in doing so we note that Kuhn de Chizelle et al. (1995) also demonstrated increasing departure from sphericity and from the

Rayleigh-Plesset equation for the larger bubbles at low cavitation numbers and we make reference to this in discussing the results.

Ceccio and Brennen (1992) observed while carrying out numerical integration of the Rayleigh-Plesset equation that, for a given cavitation number, σ, and minimum pressure coefficient, C_{PM}, all nuclei above a certain critical size, $R = R_C$, would grow to roughly the same observable bubble size and therefore would be registered as "cavitation events." Furthermore, the critical size, R_C, appeared to be almost independent of the details of the pressure/time history and a function only of the difference between the minimum pressure and the vapor pressure (represented non-dimensionally by $(-C_{PM} - \sigma)$), the upstream velocity, U, the fluid density, ρ, and surface tension, S. Specifically,

$$R_C = \frac{8\beta S}{3\rho U^2(-C_{PM} - \sigma)} \tag{2}$$

fitted the bubble dynamic calculations very well when the empirical parameter $\beta \approx 1$. This expression is, of course, consistent with the stability analyses put forward first by Flynn (1964) and Johnson and Hsieh (1966). Its use does save a great deal of computational effort. Furthermore, it means that we need not concern ourselves with the detailed pressure/time history along the entire length of each streamline but can simply focus on the region around the minimum pressure point.

However, it is necessary to determine how the minimum pressure coefficient, C_{PM}, varies from streamline to streamline. Here again we will use a simple analytic expression derived from much more complex computations. A panel method was developed to solve the potential flow around any axisymmetric headform. This was used to calculate the potential flow around the Schiebe headform. Such calculations suggested that the pressure gradient, dp/dy, normal to the surface in the vicinity of the minimum pressure point could be approximated by $\rho U_M^2/r_K$ where $U_M = U(1 - C_{PMS})^{1/2}$ and C_{PMS} are, respectively, the velocity and pressure coefficient at the minimum pressure point on the surface of the body (exterior to the boundary layer) and r_K is a measure of the radius of curvature of the streamlines in this region. For the Schiebe body ($C_{PMS} = -0.78$) it is found that $r_H/r_K = 2.5$ provides an approximate representation of the variation in the minimum pressure coefficient, C_{PM}, on a streamline with the distance y of that streamline from the surface. The actual variation of C_{PM} with y from the potential flow calculation is shown in Fig. 4 along with several approximations. With $dp/dy = \rho U_M^2/r_K$ it follows that

$$C_{PM} = C_{PMS} + 2y(1 - C_{PMS})/r_K \tag{3}$$

This expression allows us to evaluate from Eq. (2) the critical nuclei size, $R_C(y)$, for each streamline. Clearly, R_C increases with the distance, y, of the streamline from the surface. A larger critical size means that fewer of the available nuclei will generate cavitation events. The process is terminated on that streamline which just touches the isobar $C_{PM} = -\sigma$ for then the minimum pressure is equal to the vapor pressure and no cavitation events will occur on this streamline or any outside it. Consequently, we need only be concerned with a region near the surface given by

$$0 < y \leq y_M f_3 \tag{4}$$

where

$$y_M = \frac{(-C_{PMS} - \sigma)}{2(1 - C_{PMS})} r_K \tag{5}$$

and $f_3 = 1$. Different values of f_3 which is a function of R_M/r_H will be used later to examine the influence of a minimum observable bubble size, R_M. Using the relations (2) and (3) and disregarding any possible effects of the boundary layer or of relative motion between the nucleus and the flow one can then construct an event rate from the nuclei number distribution as follows. The volume flow rate passing through two stream surfaces a distance, dy, apart at the minimum pressure point (see Fig. 5) is given by

$$2\pi r_S U(1 - C_{PMS})^{1/2} f_1(y) dy \tag{6}$$

where $f_1(y) = 1$, but different values will be used later to account for the same boundary layer effects. The variable r_S is the radial distance from the axis of symmetry to the minimum pressure point (on the Schiebe body $r_S/r_H \approx 0.75$). It follows from Eq. (6) that the cavitation event rate in the stream tube, dE, is given by

$$dE = 2\pi r_S U(1 - C_{PMS})^{1/2} f_1(y) dy \times \int_{R_C(y)}^{\infty} \frac{N(R)dR}{f_2(R, y)(1 + n_i)} \tag{7}$$

where $f_2(R, y) = 1$, but different values will be used later to account for screening effects due to relative motion between the nuclei and the liquid. Also $n_i = 0$, but different values will be used later to account for the bubble/bubble interactions. In the above equation it follows from Eqs. (2) and (3) that

$$R_C(y) = \frac{8\beta S}{3\rho U^2}\left[-\sigma - C_{PMS} - \frac{2y(1 - C_{PMS})}{r_K}\right]^{-1} \tag{8}$$

Note that $R_C(y \to y_M) \to \infty$. It follows that the total cavitation event rate, E, will be

$$E = \int_0^{y_M f_3} 2\pi r_S U(1 - C_{PMS})^{1/2} f_1(y) \times \int_{R_C(y)}^{\infty} \frac{N(R)dR}{f_2(R, y)(1 + n_i)} dy \tag{9}$$

where $f_3 = 1$, but different values will be used to account for the observable bubble size effect.

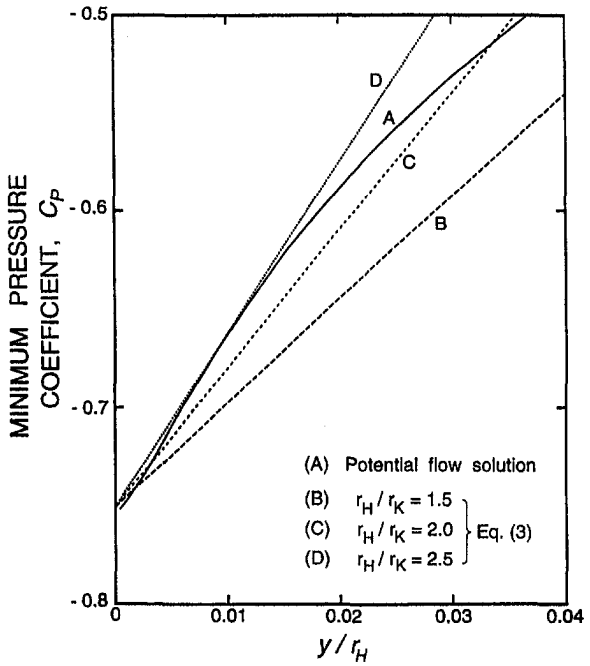

Fig. 4 Variation in the minimum pressure coefficient, C_{PM}, on a streamline for a Schiebe headform with the distance y of that streamline from the surface of the body near the minimum pressure point

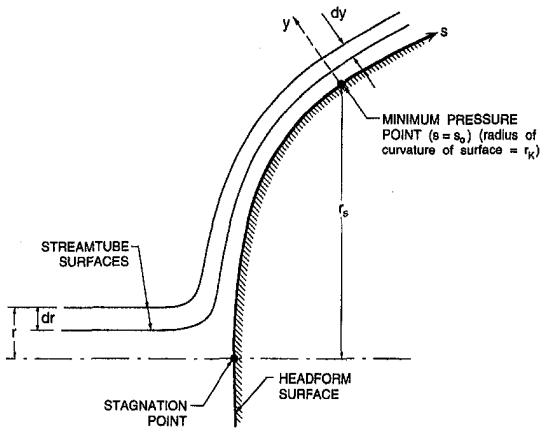

Fig. 5 Schematic showing a typical annular stream tube upstream of the headform and in the neighborhood of the minimum pressure point

3.1 Boundary Layer Effect. The above analysis neglected the effects which the presence of a boundary layer might have on the pressure/time history experienced by a potential cavitation nucleus. Several such effects can be envisaged. These include the fact that the boundary layer will reduce the volume flow rate of fluid traveling close to the headform and thus reduce the supply of nuclei. It will also increase the residence time of the bubbles in a thin layer very close to the surface, though estimates of this effect indicate that it is not a major factor. It may also alter the shape of the isobars near the surface. Here we will explore only the first of these effects. To do so we assume a simple form for the boundary layer profile near the minimum pressure point, namely,

$$\frac{u}{U_M} = \begin{cases} 2\left(\frac{y}{\delta}\right) - 2\left(\frac{y}{\delta}\right)^3 + \left(\frac{y}{\delta}\right)^4 & \text{for} \quad y < \delta \\ 1 & \text{for} \quad y \geq \delta \end{cases} \tag{10}$$

where δ is the boundary layer thickness. If δ_2 is the momentum thickness, it follows that $\delta_2 = 0.133\delta$ and using the modified Thwaites method to solve for the laminar boundary layer thickness (Thwaites, 1949, Rott and Crabtree, 1952), we find that

$$\frac{\delta_2}{r_H} \approx 0.68\left(\frac{\nu}{r_H U}\right)^{1/2} \tag{11}$$

Then, to account for the decrease in volume flow rate due to the boundary layer, the expressions (6), (7), and (9) should include values for $f_1(y)$ different from unity, namely

$$f_1(y) = \begin{cases} 2\left(\frac{y}{\delta}\right) - 2\left(\frac{y}{\delta}\right)^3 + \left(\frac{y}{\delta}\right)^4 & \text{for} \quad y < \delta \\ 1 & \text{for} \quad y > \delta \end{cases} \tag{12}$$

with $\delta = 5.10(\nu r_H/U)^{1/2}$.

It is also true that the boundary layer will affect the shape of the isobars and therefore cause some alteration of the expressions (3), (5), and (8); we have not included this effect in the present analysis.

3.2 Bubble Screening Effects. In their study of the potential cavitation of nuclei, Johnson and Hsieh (1966) recognized that the relative motion between a nucleus and the liquid might play an important role in determining the number of nuclei which enter the region in which the pressure is below the vapor pressure. Specifically they recognized that a bubble "screening" effect would occur in which the nuclei are forced away from the body due to the large pressure gradients normal to the streamlines in the vicinity of the stagnation point. This outward displacement would be larger for the larger bubbles. Because one is concerned only with streamlines very close to the stagnation streamline and the body surface and because the streamline curvature and therefore the pressure gradient normal to the streamline is much larger in the vicinity of the stagnation point than anywhere else, we may evaluate this screening effect by focusing attention on the stagnation point flow alone. In order to obtain an estimate of this effect we shall assume that the nuclei under consideration (of radius R) are all sufficiently small that the Reynolds number of the relative motion is much smaller than unity. Then the velocity, v, of the nucleus in a direction normal to the streamline is given by

$$v = \frac{2}{9}\frac{R^2}{\mu}\left(\frac{\partial p}{\partial n}\right) \tag{13}$$

where $\partial p/\partial n$ is the local pressure gradient normal to the streamline. Then the total displacement, ϵ, across the streamlines is given by

$$\epsilon = \int_A^B v dt = \int_A^B \frac{v}{|q|}\, ds \tag{14}$$

where $|q|$ is the magnitude of the fluid velocity, the coordinate s is measured along a streamline, A is a point far upstream and B is a location after the large pressure gradients in the vicinity of the stagnation point have been experienced. Note that ϵ will, of course, differ from streamline to streamline and will therefore be a function of r defined as the radial position of the streamline far upstream of the body (see Fig. 5). Thus

$$\frac{\epsilon(r/r_H)}{r_H} = \frac{2R^2U}{9\nu r_H}\int_A^B \frac{1}{\rho U^2}\frac{\partial p}{\partial(n/r_H)}\frac{U}{|q|}\, d\left(\frac{s}{r_H}\right)$$

$$= \frac{2R^2U}{9\nu r_H}\Sigma(r/r_H) \tag{15}$$

where $\Sigma(r/r_H)$ is used to denote the dimensionless integral on the previous line.

Since the stagnation point flow is the same on any blunt axisymmetric body it is appropriate to choose to examine the stagnation region in the potential flow around a sphere in order to evaluate $\Sigma(r/r_H)$. This is a non-trivial calculation, and the details will be omitted here for the sake of brevity. The result is the function $\Sigma(r/r_H)$ presented in Fig. 6; for convenience this can be approximated by the empirical relation

$$\Sigma(r/r_H) = \Gamma(r/r_H)^\gamma \tag{16}$$

where $\Gamma \approx 1.69$, $\gamma \approx 0.5$.

Having evaluated the screening displacement it can be applied to the evaluation of the event rate in the following way. A nucleus of radius R which is on the streamline at radius r far upstream will, when it reaches the low pressure region, be on the streamline which is the following distance, y, from the body surface:

$$\frac{y}{r_H} = \frac{1}{2(1 - C_{PMS})^{1/2}}\frac{r^2}{r_S r_H} + \frac{2}{9}\left(\frac{R}{r_H}\right)^2\frac{r_H U}{\nu}\Sigma(r/r_H) \tag{17}$$

Thus the stream tube between y and $y + dy$ will contain all the nuclei of radius R which were present in the upstream flow between radii r and $r + dr$ (Fig. 5) where

$$\frac{dy}{r_H} = \frac{rdr}{(1 - C_{PMS})^{1/2} r_S r_H} f_2(R, y) \tag{18}$$

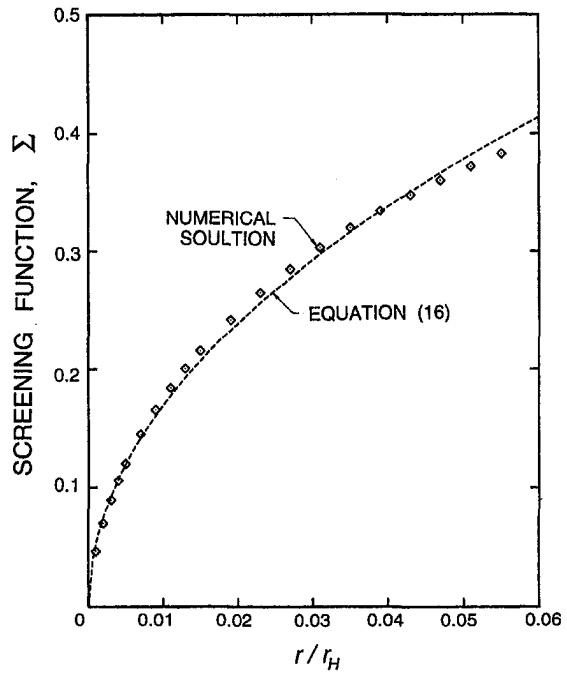

Fig. 6 The function $\Sigma(r/r_H)$ for the stagnation point flow in the potential flow around a sphere

and

$$f_2(R,y) = 1 + \frac{2}{9}\left(\frac{R}{r_H}\right)^2\left(\frac{r_H U}{\nu}\right)(1 - C_{PMS})^{1/2}\left(\frac{r_S}{r_H}\right)\frac{r_H}{r}\Sigma' \quad (19)$$

where Σ' denotes $d\Sigma/d(r/r_H)$ and r and y are related by Eq. (17). Since the liquid flow between y and $y + dy$ is still given by the expression (6), it follows that the actual nuclei number distribution function for the stream tube between y and $y + dy$ is $N_E(R, y)$ where

$$N_E(R, y) = N(R)/f_2(R, y) \quad (20)$$

Consequently, the screening effect alters the event rate by introducing a value for $f_2(R, y)$ different from unity in the expression (9), namely that given by Eq. (19).

3.3 Observable Cavitation Bubble Size Effect. Normally, experimental observation can only detect cavitating bubbles when they achieve a certain observable size, say R_M, and in this section we shall incorporate this "observable cavitation bubble size effect" in our analysis. This requires an analysis of the maximum size, $R_{\max}$, achieved by the cavitation bubble. To do so we approximate the pressure coefficient near the minimum pressure point by

$$C_P = C_{PMS} + \frac{2y(1 - C_{PMS})}{r_K} + \frac{C_{P1}^*|s - s_0|}{r_H}$$

$$= C_{PM} + \frac{C_{P1}^*|s - s_0|}{r_H} \quad (21)$$

where s is a coordinate measured along a streamline and $s = s_0$ is the minimum pressure location and C_{PM} is given by Eq. (3). The value of the constant C_{P1}^* is about 1.39. It follows that the time of residence of the bubble in the region $-C_P \le \sigma$ on a given streamline distance y from the surface is given by

$$t_G = \frac{2(-\sigma - C_{PM})}{UC_{P1}^*(1 - C_{PMS})^{1/2}} r_H \quad (22)$$

The bubble growth rate is given approximately by

$$\frac{dR}{dt} = U(-\sigma - C_{PM})^{1/2} \quad (23)$$

where C_{PM} is given by Eq. (3). It follows that the maximum size reach by a cavitating bubble, $R_{\max}$, will be given roughly by

$$\frac{R_{\max}}{r_H} = \frac{2(-\sigma - C_{PM})^{3/2}}{C_{P1}^*(1 - C_{PMS})^{1/2}} \quad (24)$$

Only those bubbles whose maximum size, $R_{\max}$, is greater than a certain radius, R_M, are regarded as observable cavitation events. By solving $R_{\max} \ge R_M$ for y, we have

$$y \le y_M f_3(R_M/r_H) \quad (25)$$

where

$$f_3\left(\frac{R_M}{r_H}\right) = 1 - \frac{\left[\frac{1}{2}\left(\frac{R_M}{r_H}\right)C_{P1}^*(1 - C_{PMS})^{1/2}\right]^{2/3}}{(-\sigma - C_{PMS})} \quad (26)$$

and y_M is given by (5). Notice that as $R_M \to 0$, $f_3(R_M/r_H) \to 1$. And when

$$\sigma_{crt} = -C_{PMS} - \left[\frac{1}{2}\left(\frac{R_M}{r_H}\right)C_{P1}^*(1 - C_{PMS})^{1/2}\right]^{2/3} \quad (27)$$

$f_3(R_M/r_H) = 0$, which means that if $\sigma \ge \sigma_{crt}$, no bubble with a size greater than R_M will occur. Hence σ_{crt} is the threshold cavitation number. For example, for $C_{PMS} = -0.78$ and $R_M/r_H = 0.04$, σ_{crt} is 0.67, which is significantly less than $-C_{PMS} = 0.78$.

3.4 The Effect of Bubble/Bubble Interactions. As a bubble grows in the low pressure region, the pressure field close to the bubble is altered. Within a certain distance close to the growing bubble the pressure perturbation due to bubble growth increases the local pressure above the critical pressure at which a nuclei will cavitate. Thus, any other nuclei in this volume will not cavitate. In this section we explore this bubble/bubble interaction effect in more detail.

To quantify the effect, we need to calculate the liquid volume in which the local pressure is larger than the Blake (Blake, 1949) critical pressure, p_c,

$$p_c = p_v - \frac{4S}{3}\left[\frac{2S}{3p_{G0}R_0^3}\right]^{1/2} \quad (28)$$

When a bubble is growing, the pressure perturbation in the surrounding liquid is given by

$$\frac{p(r) - p_{\min}}{\rho} \approx \frac{R}{r}(R\ddot{R} + 2(\dot{R})^2) \quad (29)$$

where $p_{\min}$ is the undisturbed liquid pressure. When $R \gg R_0$, the pressure perturbation can be simplified using the Rayleigh-Plesset equation and written as

$$p(r) - p_{\min} = \frac{4}{3}\frac{R}{r}(p_v - p_{\min}) \quad (30)$$

For another nucleus to cavitate, the local pressure must be smaller than the Blake critical pressure. Solving for $p(r) < p_c$, we find the radius of the volume within which another nucleus will not cavitate is:

$$r < \frac{4}{3}\frac{(-C_P - \sigma)}{(-C_P - \sigma - \sigma')}R \tag{31}$$

where σ' is given by

$$\sigma' = \frac{1}{3}\left(\frac{8S}{\rho U^2 R_0}\right)\left[\frac{1}{6}\left(\frac{8S}{\rho U^2 R_0}\right)\frac{1}{\sigma + \left(\frac{8S}{\rho U^2 R_0}\right)}\right]^{1/2} \tag{32}$$

Now, the minimum pressure which a nucleus experiences in flow of the type considered here is a function of the streamline offset, y, normal to the headform surface. And the bubble size at the point where the pressure reaches the minimum pressure is approximately half of the maximum bubble size, $R_{\max}/2$. Thus the critical radius is given by

$$r_e = \frac{4}{3}\frac{(-C_{PM}(y) - \sigma)}{(-C_{PM}(y) - \sigma - \sigma')}\left(\frac{R_{\max}}{2}\right) \tag{33}$$

and, only those nuclei outside $r = r_e$ can cavitate.

It follows that the number of nuclei which will not cavitate due to the pressure perturbation surrounding a growing bubble is

$$n_i = \int_0^\infty \frac{4}{3}\pi\left[r_e^3 - \left(\frac{R_{\max}}{2}\right)^3\right]N(R_0)dR_0 \tag{34}$$

In other words, only one nucleus out of $1 + n_i$ nuclei will actually cavitate. Thus, the effective nuclei number density distribution is given by

$$\frac{N(R)}{1 + n_i} \tag{35}$$

where

$$n_i = \frac{1}{6}\pi R_{\max}^3 \int_0^\infty N(R_0) \times \left[\frac{64}{27}\left(\frac{-C_{PM}(y) - \sigma}{-C_{PM}(y) - \sigma - \sigma'}\right)^3 - 1\right]dR_0 \tag{36}$$

Note that the effect of bubble interactions, n_i, is proportional to the cube of the maximum bubble size, $R_{\max}$, which, in turn, is proportional the headform size. This means that, for a small model, bubble interactions may not be very important for the cavitation event rate. But for a large model, interactions may be very important. We do not know that this scaling effect has been recognized before. We also note that when $n_i \gg 1$, it follows that $1 + n_i \approx n_i$, and this implies that, when the bubble interactions become large ($n_i \gg 1$), the event rate becomes independent of the nuclei concentration. This may help to explain the fact that, when the nuclei population is sufficiently large, quantities like the inception number tend to become independent of the nuclei concentration.

4 Results of the Analytical Model

In this section we shall evaluate the various effects on the cavitation event rate and compare the results of the analytical model with the measured cavitation event rates. For this purpose we select a particular nuclei number distribution of the form given by Eq. (1), namely,

$$C = 100\ \text{cm}^{-3}$$
$$\xi = 9.8\ \mu\text{m}$$
$$\lambda = 0.49 \tag{37}$$

These values produce a nuclei distribution which is similar in shape to that of many of the nuclei number distributions which have been measured in the Low Turbulence Water Tunnel and the High Speed Water Tunnel. We note that the concentration, C, of 100 cm^{-3} is also consistent with values obtained by other researchers (see, for example, Billet, 1985). When viewing the analytical results in Fig. 7, one should remember that the cavitation event rates scale almost linearly with concentration C and therefore the results for other values of concentration C are easily obtained. Furthermore, we shall use a minimum observable radius, R_M, of 1 mm since this is the limit of the electrode instrumentation used to detect the cavitation events (see also Ceccio and Brennen, 1992).

First, we present in Fig. 7 typical results calculated for a 5.08 cm Schiebe body at a tunnel speed of 9 m/s. The event rates are calculated from Eq. (9) using the assumed nuclei concentration and distribution (Eqs. (1) and (37)). The individual changes in the event rate due to four separate effects described in Sections 3.1 to 3.4 are shown in the figure, namely the boundary layer flux effect (f_1), the bubble screening effect (f_2), the observable bubble size effect (f_3) and the bubble/bubble interaction effect (n_i). Note that all these effects can produce significant alterations in the event rate, and, together, can account for more than an order of magnitude reduction in the event rate in the present calculation. Among all the effects, the bubble screening effect causes the largest reduction in the event rate. At large cavitation numbers, the effect of bubble/bubble interactions causes little or no reduction in the cavitation event rate. However, at low cavitation numbers, it causes significant reduction because the interactions between bubbles are more intensive at low cavitation numbers due to the larger and more numerous bubbles. The boundary layer flow rate effect is more pronounced at large cavitation numbers since the boundary layer thickness approaches the thickness of the low pressure region in which nuclei cavitate. Also note that the observable cavitation bubble size effect generates a sharp threshold at a cavitation number of about 0.6.

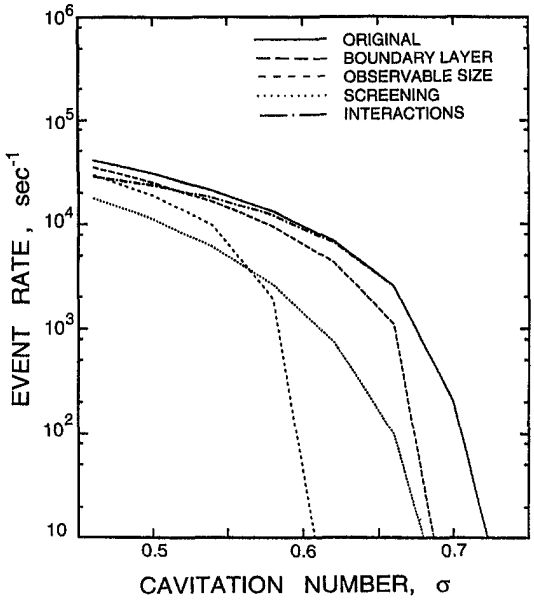

Fig. 7 Typical event rates calculated using an assumed but typical nuclei distribution for flow around a 5.08 cm Schiebe body at a velocity of 9 m/s. Original: Basic method not including the additional effects included in other lines. Boundary layer: As original but including the boundary layer flux effect. Observable size: As original but including only "observable" bubbles larger than 1 mm in radius. Screening: As original but including the bubble screening effect. Interactions: As original but including the bubble/bubble interaction effect.

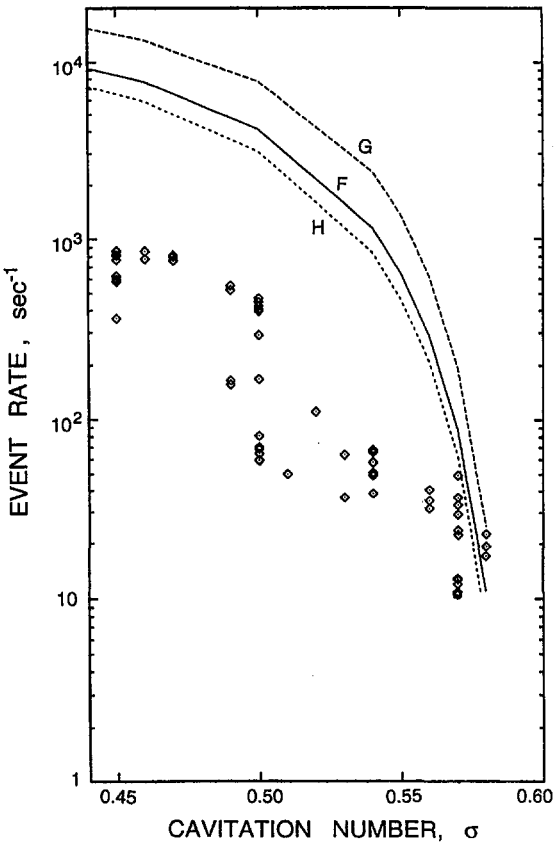

Fig. 8 Left: A comparison of observed cavitation event rates (◇) on a 5.08 cm Schiebe body in the LTWT at a speed of 9 m/sec with anticipated event rates based on simultaneously measured nuclei distributions. The numerical results are plotted as (F): event rates calculated using intermediate nuclei concentrations, (G): event rates calculated using the largest nuclei concentrations, (H): event rates calculated using the smallest nuclei concentrations.

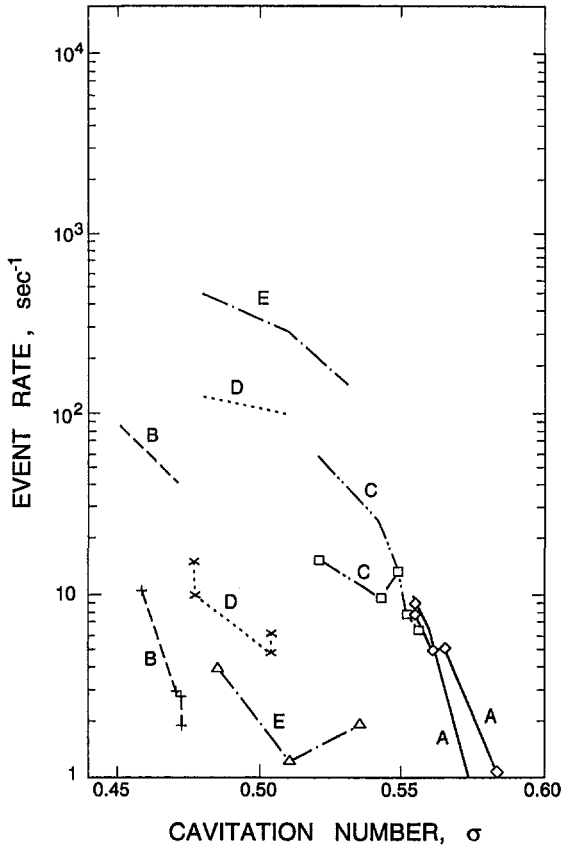

Fig. 8 Right: A comparison of observed cavitation event rates (lines with symbols) on a 5.08 cm Schiebe body in the HSWT reproduced from Fig. 3 with the anticipated event rates (corresponding lines without symbol) based on simultaneously measured nuclei distributions. The uncertainty in the ordinate is ±5 percent.

The effects of the boundary layer flow rate and of bubble screening varied slightly with flow velocity and headform scale. The effects of bubble/bubble interactions, however, varied significantly with headform size since the bubble size increases as the headform size increases. As the headform size increases, the reduction of the cavitation event rate at low cavitation numbers due to bubble/bubble interactions increases with the cube of the headform radius. For the values chosen and at a cavitation number of $\sigma = 0.46$ the bubble interaction factor, n_i, is 0.9 for a headform radius of 2.5 cm. At the same cavitation number, but with a headform radius of 25 cm, the bubble/bubble interaction factor, n_i, is 900, which implies significant reduction in the cavitation event rate. Note, however, in practice that the cavitation on the headform transitioned to fully-attached cavitation long before bubble/bubble interactions reach that level.

Figure 8 presents a comparison between the experimentally measured event rates and the event rates calculated from the analytical model by using the simultaneously measured nuclei distributions. Note that the event rates are in rough agreement at the larger cavitation numbers but that a progressively increasing discrepancy develops as the cavitation number decreases and the event rate increases. At the present time the reason for this discrepancy is not known Though we make several suggestions in the next section.

The information on event rates can be used to produce cavitation inception numbers simply by selecting a certain event rate criterion for inception. In figure 9 we make a qualitative comparison between the inception numbers observed in the LCC experiments of Kuhn de Chizelle et al. (1992) and those calculated from the model using an assumed but typical nuclei distribution function. Both the observed and calculated σ_i are based on an arbitrarily chosen critical event rate of 50 events per second. Comparing the predicted and measured cavitation inception numbers, we note that the trends with changing headform size are consistent. Moreover, the predicted values are also close to those observed experimentally. But the change of the predicted inception numbers with velocity are the reverse of the experiment observations. This is a reflection of the same unresolved velocity scaling issue discussed at the end of Section 2.

We must conclude that two outstanding issues still remain. First the observed event rates at low cavitation numbers are at least one order of magnitude smaller than one would predict based on the anticipated nuclei distributions. Perhaps only a small fraction of the "potential" nuclei actually do cavitate but more detailed study is needed to confirm this. Secondly the changes with tunnel velocity cannot be explained at present. One suspects that the observed effects may be the result of changes in the nuclei population with changes in the tunnel operating condition (pressure and velocity). On-line monitoring of nuclei content and explorations of how the nuclei content changes with operating condition seem essential prerequisites for answering the questions posed by this study. Moreover, it seems clear that cavitation inception criteria are a natural consequence of the event rate variations and that the above recommendations are also an essential prerequisite to an understanding of inception and the scaling effects of cavitation.

5 Conclusions

The present paper describes investigations of the relationship between the cavitation nuclei distributions in the incident free

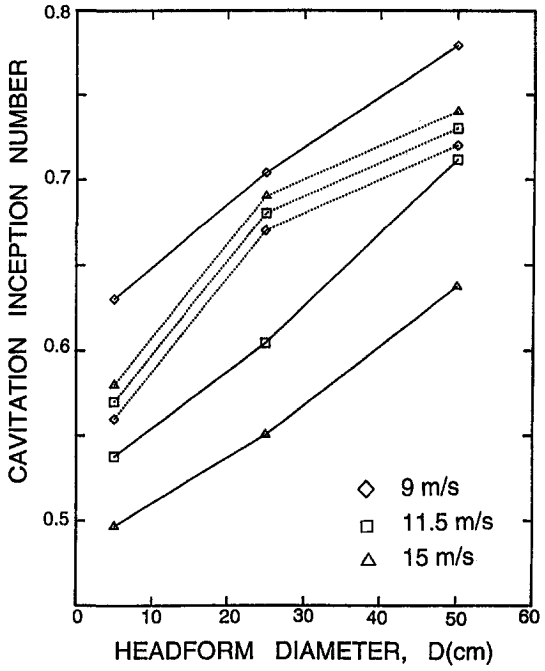

Fig. 9 A comparison of cavitation inception numbers observed in the scaling experiments of Kuhn de Chizelle et al. (1992) (dotted lines) and those predicted by the analytical model based on a critical event rate of 50 s^{-1}, an assumed but typical nuclei distribution and a minimum observable bubble radius of 1 mm (solid lines). Data are shown for three different speeds.

stream and the cavitation event rates on an axisymmetric headform. The cavitation event rates and the nuclei populations in two water tunnels were simultaneously measured. The event rates increase with increasing nuclei population and decreasing cavitation number as expected. However they decrease with increasing tunnel speed even when the nuclei concentrations are similar. This is the inverse of what would be expected.

A simple analytical model is presented for the connection between the nuclei distribution and the event rate. The changes in the cavitation event rate due to several complicating factors are explored; these factors are the reduction of volume flow rate by the boundary layer, the bubble screening effect near the stagnation point, the interactions between bubbles and the effect of a minimum observable cavitation bubble size. Among all these effects, bubble screening results in the largest reduction in the cavitation event rate. However, the effect of bubble/bubble interactions becomes increasingly important with increasing body size and decreasing cavitation number. Combined, all these effects give rise to a reduction in the event rate of an order of magnitude.

The scaling of the predicted cavitation event rate with body size, cavitation number and nuclei population agrees with the experimental observations. At larger cavitation numbers, the predicted cavitation event rates agree quantitatively with the experimental observations in the Low Turbulence Water Tunnel and in the High Speed Water Tunnel. However, two outstanding issues still remain. First the observed event rates at lower cavitation numbers are about an order of magnitude smaller than one would predict based on the actual nuclei distributions. This may be due to the fact that only a fraction of the observed nuclei actually cavitate or it may be due to some other effect not included in the model. One possible effect could be due to the large departure from bubble sphericity; since Kuhn de Chizelle et al. (1995) showed increasing departure from sphericity at low cavitation numbers, this might contribute to the larger discrepancies under those conditions. Other factors might be the increased importance of bubble/bubble interactions at lower cavitation numbers. The other issue which remains is that the changes with tunnel velocity cannot be fully explained at present.

With regard to the possibility that only a fraction of the counted nuclei actually cavitate, we should note that there is some uncertainty regarding the role played by solid particles in the present experiments. Though, in theory, the PDA system should measure only spherical bubbles, in fact, due to the validation level settings some solid particles may also be counted. These may or may not act as nuclei. On the other hand, the validation process may eliminate some bubbles. These uncertainties are, to some extent, resolved by the calibration using the holographic measurements, though that calibration was only possible for nuclei larger than 18 μm. Therefore some of the discrepancies could be caused by the uncertainties associated with solid particles.

When the model for the event rates is used along with some chosen criterion in order to predict the cavitation inception number, the results are consistent with those observed experimentally in so far as the trend with headform size is concerned. The trend with velocity is, of course, at odds with the experiments because of the discrepancy in the event rate discussed above.

Acknowledgments

The authors would like to thank Dr. Yan Kuhn de Chizelle, Dr. Kotaro Sato, Pavel Svitek, Fabrizio D'Auria, Garrett Reisman, Yi-chun Wang, and Elizabeth McKenney for help with the experiments, and Professor Allan Acosta for his advice. This work was supported by the Office of Naval Research under contract number N-00014-91-K-1295.

References

Arndt, R. E. A., and Keller, A. P., 1976, "Free Gas Content Effects on Cavitation Inception and Noise in a Free Shear Flow," *Proceedings, IAHR Conference on Two Phase Flow and Cavitation in Power Generation Systems,* Grenoble, France, pp. 3–16.

Billet, M. L., 1985, "Cavitation Nuclei Measurement—A Review," *Proceedings, ASME Cavitation and Multiphase Flow Forum,* pp. 31–38.

Blake, W. K., 1949, "The Onset of Cavitation in Liquids: I," Technical Report, Acoustics Research Laboratory, Harvard University, Tech. Memo. No. 12.

Cartmill, J. W., and Su, M. Y., 1993, "Bubble Size Distribution Under Saltwater and Freshwater Breaking Waves," *Journal of Dynamics of Atmospheres and Oceans,* Vol. 20, pp. 25–31.

Ceccio, S. L., and Brennen, C. E., 1992, "Observations of the Dynamics and Acoustics of Traveling Bubble Cavitation," *Journal of Fluid Mechanics,* Vol. 233, pp. 633–660.

Feldberg, L. A., and Shlemenson, K. T., 1971, "The Holographic Study of Cavitation Nuclei," *Proceedings, IUTAM Symposium on Non-Steady Flow of Water at High Speed,* Leningrad, USSR, pp. 239–42.

Flynn, H. G., 1964, *Physics of Acoustic Cavitation in Liquids,* Academic Press.

Gates, E. M., and Acosta, A. J., 1978, "Some Effects of Several Free-Stream Factors on Cavitation Inception on Axisymmetric Bodies," *Proceedings, 12th Symposium on Naval Hydrodynamics,* pp. 86–108.

Gates, E. M., and Bacon, J., 1978, "A Note on the Determination of Cavitation Nuclei Distributions by Holography," *Journal of Ship Research,* Vol. 22(1), pp. 29–31.

Gindroz, B., and Billet, M. L., 1994, "Nuclei and Propeller Cavitation Inception," *Proceedings, Cavitation and Gas-Liquid Flow in Fluid Machinery and Devices,* ASME, FED, Vol. 190, pp. 251–260.

Johnson, V. E. and Hsieh, T., 1966, "The Influence of the Trajectories of Gas Nuclei on Cavitation Inception," *Proceedings, 6th Symposium on Naval Hydrodynamics,* Washington D.C., pp. 163–182.

Keller, A. P., 1972, "The Influence of the Cavitation Nucleus Spectrum on Cavitation Inception, Investigated With a Scattered Light Counting Method," ASME *Journal of Basic Engineering,* pp. 917–925.

Keller, A. P., 1974, "Investigations Concerning Scale Effects of the Inception of Cavitation," *Proceedings, Conference on Cavitation,* IMechE, pp. 917–925.

Keller, A. P. and Weitendorf, E. A., 1976, "Influence of Undissolved Air Content on Cavitation Phenomena at the Propeller Blades and on Induced Hull Pressure Amplitudes," *Proceedings, IAHR Symposium on Two Phase Flow and Cavitation in Power Generation System,* Grenoble, France, pp. 65–76.

Kuhn de Chizelle, Y., Ceccio, S. L., and Brennen, C. E., 1995, "Observations, Scaling and Modeling of Traveling Bubble Cavitation," *Journal of Fluid Mechanics,* Vol. 293, pp. 99–126.

Kuhn de Chizelle, Y., Ceccio, S. L., Brennen, C. E., and Shen, Y., 1992, "Cavitation Scaling Experiments with Headforms: Bubble Dynamics," *Proceedings, 19th Symposium on Naval Hydrodynamics,* Seoul, Korea.

Kuiper, G., 1978, "Scale Effects on Propeller Cavitation Inception," *Proceedings, 12th Symposium on Naval Hydrodynamics,* Washington DC, pp. 400–429.

Li, C. Y., and Ceccio, S. L., 1994, "Observations of the Interactions of Cavitation Bubbles with Attached Cavities," *Proceedings, Cavitation and Gas-Liquid Flow in Fluid Machinery and Devices,* ASME. FED, Vol. 190, pp. 283–290.

Liu, Z., 1995, "Nuclei Population Dynamics and Cavitation," Ph.D. thesis, California Inst. of Technology, Pasadena.

Liu, Z., and Brennen, C. E., 1995, "Models of Cavitation Event Rates," *Proceedings, CAV95 International Symposium on Cavitation,* Deauville, France, pp. 321–328.

Liu, Z., and Brennen, C. E., 1994, "The Relation Between the Nuclei Population and the Cavitation Event Rate for Cavitation on a Schiebe Body," *Proceedings, ASME Symposium on Cavitation and Gas Liquid Flows in Fluid Machinery,* pp. 261–266.

Liu, Z., Kuhn de Chizelle, Y., and Brennen, C. E., 1993, "Cavitation Event Rate and Nuclei Distributions," *Proceedings, ASME 4th International Symposium on Cavitation Inception,* New Orleans.

Liu, Z., Sato, K., and Brennen, C. E., 1994, "Cavitation Nuclei Population Dynamics in a Water Tunnel," *Proceedings, ASME Cavitation and Multiphase Flow Forum,* Washington D.C..

Meyer, R. S., Billet, M. L., and Holl, J. W., 1989, "Free Stream Nuclei and Cavitation," *Proceedings, International ASME Symposium on Cavitation Inception,* pp. 55–62.

Meyer, R. S., Billet, M. L., and Holl, J. W., 1992, "Free Stream Nuclei and Traveling Bubble Cavitation," ASME JOURNAL OF FLUIDS ENGINEERING, Vol. 114, pp. 672–679.

Peterson, F. B., 1972, "Hydrodynamic Cavitation and Some Considerations of the Influence of Free Gas Content," *Proceedings, 9th Symposium on Naval Hydrodynamics,* Vol. 2, Paris, France, pp. 1131–1186.

Peterson, F. B., Danel, F., Keller, A., and Lecoffe, Y., 1975, "Determination of Bubble and Particulate Spectra and Number Density in a Water Tunnel with Three Optical Techniques," *Proceedings, 14th International Towing Tank Conference,* Ottawa, Canada, Vol. 2, pp. 27–52.

Rott, N., and Crabtree, L. F., 1952, "Simplified Laminar Boundary Layer Calculations for Bodies of Revolution and for Yawed Wings," *Journal of Aeronautical Sciences,* Vol. 19, pp. 553–565.

Saffman, M., and Buchhave, P., 1984, "Simultaneously Measurement of Size, Concentration and Velocity of Spherical Particles by a laser Doppler Method," *Proceedings, 2nd International Symposium on Applications of Laser Anemometry to Fluid Mechanics,* Lisbon.

Schiebe, F. R., 1972, "Measurement of the Cavitation Susceptibility of Water Using Standard Bodies," Technical report, St. Anthony Falls Hydraulic Laboratory, University of Minnesota, Report No. 118.

Tanger, H., and Weitendorf, E. A., 1992, "Applicability Tests for the Phase Doppler Anemometer for Cavitation Nuclei Measurements," ASME JOURNAL OF FLUIDS ENGINEERING, Vol. 114(3), pp. 443–449.

Thwaites, B., 1949, "Approximate Calculations of the Laminar Boundary Layer," *Aeronautics Quarterly,* Vol. 1, pp. 245–280.

T. Brattberg
Ph.D. Student.

H. Chanson
Senior Lecturer,
Fluid Mechanics, Hydraulics and
Environmental Engineering.

L. Toombes
Ph.D. Student.

Department of Civil Engineering,
The University of Queensland,
Brisbane QLD 4072,
Australia

Experimental Investigations of Free-Surface Aeration in the Developing Flow of Two-Dimensional Water Jets

Turbulent water jets discharging into the atmosphere are often characterized by a substantial amount of free-surface aeration. The effects can be detrimental or beneficial. In any case, the knowledge of the air entrainment mechanisms is essential for an optimum design. New experimental data are presented in the developing flow region of two-dimensional water jets discharging into air. The results indicate that the air diffusion takes place rapidly downstream of the nozzle and it is nearly independent of the momentum transfer process. Further, the distribution of air bubble frequency may be related to the air content distribution by a parabolic relationship.

Accuracy

The error on the positions $\{x, y, z\}$ of the probes was less than:

	Δx	Δy	Δz
Experiment No. 1:	<1 cm	<0.025 mm	<1 mm
Experiment No. 2:	<1 cm	<0.025 mm	<1 mm
Experiment No. 3:	<0.1 mm	<0.1 mm	<1 mm

The error on the discharge measurement was less than 2%.

The error on the air concentration (void fraction) measurements was estimated as: $\Delta C/C = 2\%$ for $5 < C < 95\%$, $\Delta C/C = 0.001/(1 - C)$ for $C > 95\%$, and $\Delta C/C = 0.001/C$ for $C < 5\%$.

The accuracy of the clear-water velocity data was normally estimated as: $\Delta V/V = 1\%$.

The error on the mean air-water velocity measurements was estimated as: $\Delta V/V = 5\%$ for $5 < C < 95\%$.

The minimum detectable bubble chord length was about 200 μm in a 2 m/s flow and 80 μm in a 8 m/s jet based upon a data acquisition frequency of 10 kHz per channel.

Introduction

Turbulent water jets discharging into the atmosphere are often characterized by a substantial amount of free-surface aeration. Applications include water jets at bottom outlets to dissipate energy, jet flows downstream of a spillway ski jump, mixing devices in chemical plants and spray devices, water jets for fire-fighting, jet cutting (e.g., coal mining) and with Pelton turbines. A related case is the ventilated cavity flow, observed downstream of blunt bodies, on the extrados of foils and turbine blades and on spillways (i.e., aeration devices).

The effects of air entrainment can be detrimental (e.g., loss of jet momentum) or beneficial (e.g., mixing enhancement). In any case, knowledge of the air entrainment mechanisms is essential for an optimum design. Some experimental results are available on the free-surface aeration of circular water jets (e.g., Heraud, 1966; Ervine and Falvey, 1987; Ruff et al., 1989; Tseng et al., 1992) but there is little information on the free-surface aeration of two-dimensional water jets (see review in Chanson, 1997a).

The present paper describes new experiments performed with two-dimensional water jets discharging into air. Three experimental configurations were used (Fig. 1). It is the purpose of the study to present new experimental evidence of the air-water flow properties in the developing shear layer immediately downstream of the nozzle (i.e., $x/d_o < 20$, where d_o is the nozzle thickness). Altogether the results provide new information on the air entrainment mechanisms, the advective diffusion of air bubbles, the momentum exchange process and the distributions of entrained bubble sizes. Full details of the experimental data were reported in Chanson (1995a), Chanson and Toombes (1997), and Chanson and Brattberg (1997).

Experimental Apparatus

Experimental Channels. Three experimental configurations of two-dimensional water jets were used at the University of Queensland (Fig. 1, Table 1). Experiment No. 1 is basically a water wall jet (0.03 m thick, 0.5 m wide). Experiment No. 2 is an air-water free-shear layer at an abrupt drop ($\Delta z = 0.13$ m, $W = 0.5$ m). The third experiment is a vertical free-falling jet: it consists of a two-dimensional jet issuing from a 0.012 m slot nozzle and discharging downwards. The PVC jet support is 0.35 m long.

The discharge was measured with a Venturi-type device (i.e., Dall™ tube) in experiments No. 1 and No. 2, and with orifice meters in experiment No. 3. The error on the discharge measurement was less than 2 percent.

For experiments Nos. 1 and 2, the vertical probe translation was controlled by a fine adjustment travelling mechanism connected to a Mitutoyo™ digimatic scale unit (Ref. No. 572-503). The error on the vertical position of the probe was less than 0.025 mm and the accuracy on the longitudinal position of the probe was estimated as $\Delta x < 1$ cm. In experiment No. 3, the displacement of the probes in the direction normal to the jet support and along the jet direction were controlled by two fine adjustment travelling mechanisms (made in-house) and the positions were measured with two Lucas Schaevitz Magnarules Plus™ (MRU-012 and MRU-036 in the normal and longitudinal directions, respectively). The error in the longitudinal and normal positions of the probes was less than 0.1 mm in each direction.

Contributed by the Fluids Engineering Division for publication in the JOURNAL OF FLUIDS ENGINEERING. Manuscript received by the Fluids Engineering Division August 29, 1997; revised manuscript received July 6, 1998. Associate Technical Editor: M. Sommerfeld.

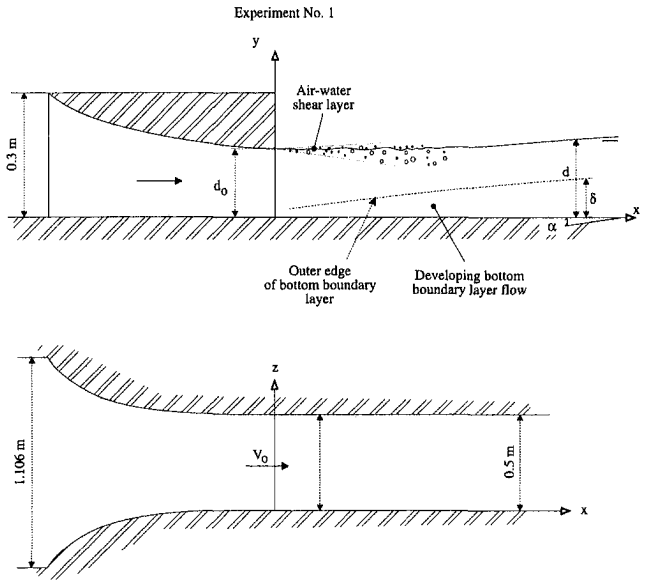

Experiment No. 1

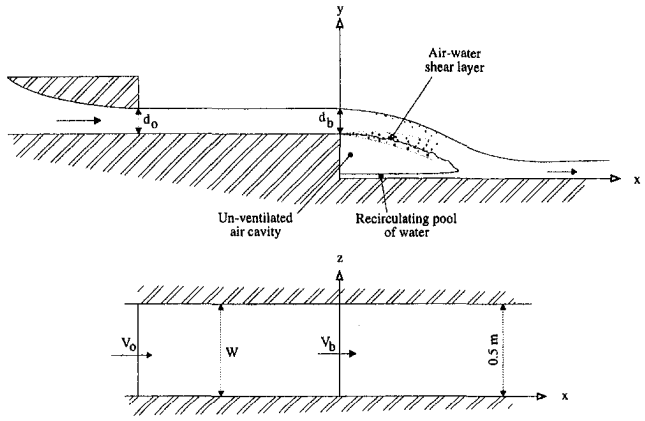

Experiment No. 2

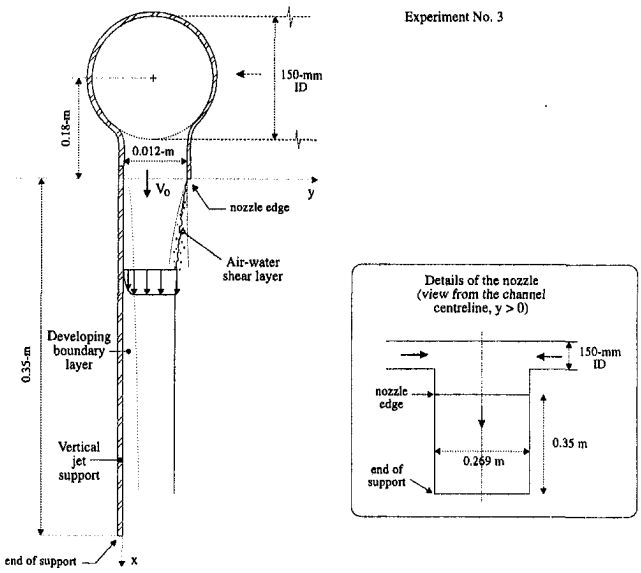

Experiment No. 3

Fig. 1 Sketch of the experiments

Instrumentation. The air-water flow properties were recorded using two types of conductivity probes made at the University of Queensland, based on an earlier design (Chanson, 1995a, Cummings and Chanson, 1997). A single-tip conductivity probe (inner electrode ∅ = 0.35 mm, outer electrode ∅ = 1.42 mm) was used to perform air concentration measurements only in experiments Nos. 1 and 2.

A two-tip conductivity probe was used to record simultaneously the air concentration, air-water velocity and bubble frequency in experiment No. 3. Each tip is identical with an internal concentric electrode (∅ = 25 μm, platinum electrode). The tip spacing is 8 mm.

Both conductivity probes were excited by an electronic system (air bubble detector Ref. AS25240) designed with a response time less than 10 μs. The measurements were recorded with a scan rate ranging from 10 to 20 kHz per channel.

In addition, clear water jet velocities were measured with a Pitot tube (external diameter ∅ = 3.3 mm).

Discussion. At low void fractions, the air-water mixture consists of air bubbles surrounded continuously by water. At large void fractions, the mixture is predominantly water droplets surrounded by air. For void fractions between 0.3 and 0.7, the flow is a homogeneous mixture but the air-water flow structures are not well understood. In the present study, the writers define an air bubble as a volume of air surrounded continuously or

Nomenclature

C = air concentration defined as the volume of air per unit volume of air and water; it is also called void fraction
ch_{ab} = bubble chord length (m)
$(ch_{ab})_{mean}$ = mean bubble chord length (m)
D_t = turbulent diffusivity (m^2/s)
d = jet thickness (m) measured perpendicular to the flow direction
d_o = jet thickness (m) at the nozzle
F_{ab} = air bubble frequency (Hz)
$(F_{ab})_{max}$ = maximum air bubble frequency (Hz) recorded in a cross-section
f_{ab} = dimensionless bubble frequency: $f_{ab} = F^*_{ab}\sqrt{x^* d_o}/V_o$
g = gravity constant: $g = 9.80$ m/s^2
q = volume discharge per unit width (m^2/s)
t = dimensionless variable
u = dimensionless variable
V = velocity (m/s)
V_o = mean flow velocity (m/s) at nozzle
W = channel width (m)
X = longitudinal coordinate (m)
x = distance along the flow direction (m)
y = distance (m) measured normal to the flow direction
α = angle between the flow direction and the horizontal
Δ = error
Δz = drop height (m)
ρ = density (kg/m3)
μ = dynamic viscosity
∅ = diameter (m)

Subscripts

w = water flow
o = nozzle flow conditions

Table 1 Experimental flow conditions

Ref. (1)	Slope α (deg.) (2)	Deflector and nozzle geometry (3)	Nb of Exp. (4)	V_o (m/s) (5)	d_o (m) (6)	Comments (7)
Experiment No. 1[a]	4.0	Elliptical convergent (10:1 contraction in flow thickness and 2.2:1 in jet width).	1	5.0	0.03	Wall jet issued from a smooth convergent nozzle. W = 0.5 m. Single-tip conductivity probe.
Experiment No. 2[b]	0	Elliptical convergent (10:1 contraction in flow thickness and 2.2:1 in jet width).	1	5	0.03	Nappe flow at an abrupt drop (Δz = 0.131 m). W = 0.5 m. Single-tip conductivity probe scanned at 8 kHz (for 150 s).
Experiment No. 3[c]	89	S-shaped convergent (12.5:1 jet thickness contraction followed by a 50 mm straight section).	7	1.4 to 7.9	0.012	Vertical free-falling jet. W = 0.269 m. Double-tip conductivity probe scanned at 10 kHz (per channel).

Notes: d_o, V_o: initial nozzle thickness and flow velocity; slope: streamline angle with horizontal at nozzle.
[a]: data reported in Chanson (1995); [b]: data reported in Chanson and Toombes (1997); [c] data reported in Chanson and Brattberg (1997).

not by water interfaces. Practically it is an air entity detected by the leading tip of the probe between two consecutive air-water interface events.

Further, the bubble frequency, at a given position $\{x, y\}$ is defined as the number of air bubbles detected by the leading tip of the conductivity probe per unit time.

Experimental Results

Free-Surface Aeration. For all investigated flow conditions (Table 1), substantial free-surface aeration was always observed immediately downstream of the nozzle (Figs. 2 to 4). Figures 2 to 4 present typical distributions of air concentration C, dimensionless velocity V/V_o and dimensionless bubble frequency $f_{ab} = F_{ab}*\sqrt{x*d_o/V_o}$, where x is the distance from the nozzle in the flow direction, y is the distance normal to the jet support, V is the mean air-water velocity, V_o is the nozzle velocity, d_o is the jet thickness at the nozzle and F_{ab} is the air bubble frequency.[1] Note on Fig. 3 that the upper free-surface of the nappe is not a free-shear layer. The upper nappe entrainment process was analyzed and discussed elsewhere (Chanson, 1989).

[1] The air bubble frequency is defined as the number of air bubbles detected by the probe leading tip per second.

In all the experiments, the air concentration distributions follow closely a solution of the diffusion equation:

$$C = \frac{1}{2}*\left(1 - \text{erf}\left(\frac{1}{2}*\sqrt{\frac{V_o}{D_t}}*\frac{y}{x}\right)\right) \quad (1)$$

where D_t is the turbulent diffusivity, assumed independent of the transverse direction y and the function erf is defined as:

$$\text{erf}(u) = \frac{2}{\sqrt{\pi}}*\int_0^u \exp(-t^2)*dt \quad (2)$$

Equation (1) was developed and validated for two-dimensional free-shear layers by Chanson (1989, 1995). The above result (Eq. (1)) may be extended to the developing flow region of a two-dimensional water jet discharging into the atmosphere. Note that Eq. (1) is not valid when the jet core becomes aerated.

Velocity Distribution. Distributions of mean air-water velocity and bubble frequency for experiment No. 3 are presented in Fig. 4. In the near-flow field (i.e., $x/d_o < 17$), the transfer of momentum from the water jet to the air is negligible and the air-water velocity is not affected by the advective diffusion of air bubbles (Fig. 4). For the free-falling jet experiments, the free-stream velocity satisfied the Bernoulli equation:

$$V = V_o*\sqrt{1 + \frac{2*g*x}{V_o^2}} \quad \text{for} \quad C < 0.99 \quad \text{and} \quad x/d_o < 17 \quad (3)$$

Note that the developing boundary layer along the jet support was small and could not be detected with the instrumentation.

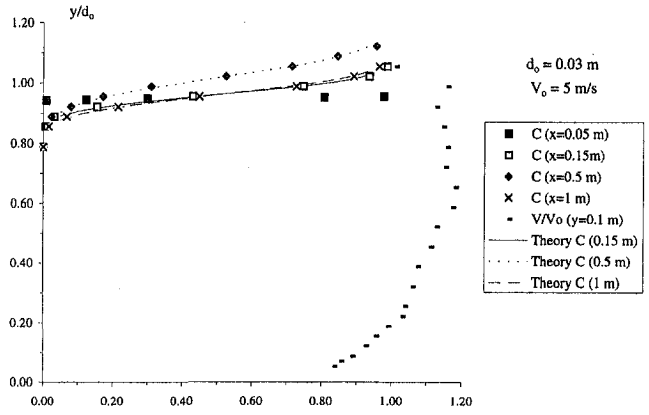

Fig. 2 Air concentration distributions (Experiment No. 1, V_o = 5 m/s, d_o = 0.03 m), comparison with Eq. (1). Uncertainty estimates vert. axis *y/do*: error = 0.003 (or 0.3%); horiz. axis *C*: error = 2%; *V/Vo* error = 5%.

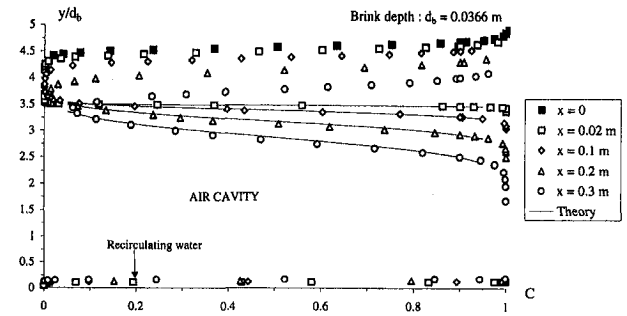

Fig. 3 Air concentration distributions (Experiment No. 2, V_o = 5 m/s), comparison with Eq. (1). Uncertainty estimates vert. axis *y/db*: error = 0.0017 (or 0.17%); horz. axis *C*: error = 2%.

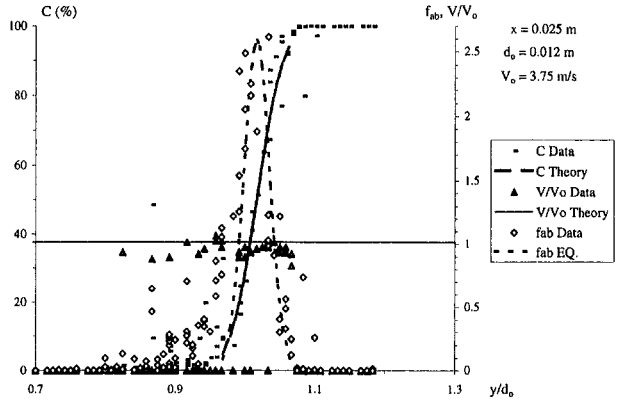

Fig. 4(*a*) $x/d_o = 2.1$

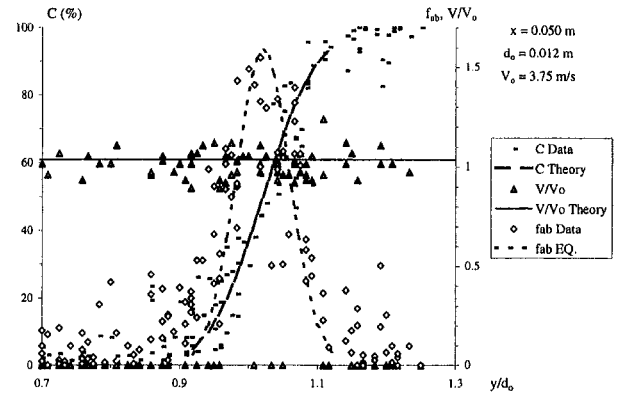

Fig. 4(*b*) $x/d_o = 4.2$

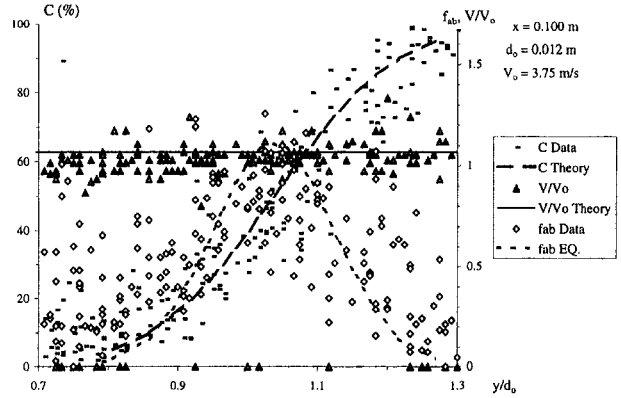

Fig. 4(*c*) $x/d_o = 8.3$

Fig. 4 Air-water flow characteristics in the free-falling jet (Experiment No. 3, V_o = 3.75 m/s, d_o = 0.012 m): distributions of air concentration *C*, dimensionless mean air-water velocity V/V_o and dimensionless bubble frequency $f_{ab} = F^*_{ab}\sqrt{x^*d_o/V_o}$. Uncertainty estimates horz. axis y/d_o: error = 0.00033 (or 0.033%) vert. axis *C*: error = 2%; *V/vo* error = 5%; fab error = 0 (no error on bubble count)

That is, the boundary layer thickness was less than 3.5 mm at $x = 0.2$ m for V_o ranging from 1.4 to 7.9 m/s.

Bubble Frequency. The air bubble frequency distributions exhibit a characteristic shape at each cross-section (Fig. 5). A maximum $(F_{ab})_{max}$ is observed at about 50 percent air content

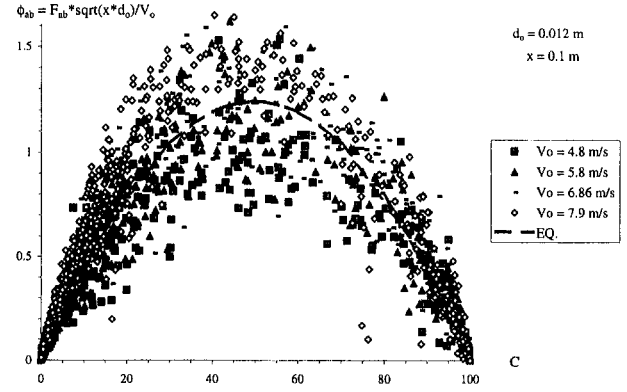

Fig. 5 Dimensionless bubble frequency $f_{ab} = F^*_{ab}\sqrt{x^*d_o/V_o}$ as a function of the air content (Experiment No. 3) comparison with Eq. (4). Uncertainty estimates vert. axis fab: error = 0 (no error on bubble count); horz. axis *C*: error = 2%.

and the bubble frequency tends to zero at very-low and very-large air contents. Overall the dimensionless air bubble frequency distributions are best correlated by a parabolic function:

$$\frac{F_{ab}}{(F_{ab})_{max}} = 1 - 4*(C - 0.5)^2 \qquad (4)$$

For the experiments, the dimensionless maximum bubble frequency $((F_{ab})_{max}*\sqrt{x*d_o/V_o})$ was observed to be independent of the jet velocity and distance from the nozzle. Hence Eq. (4) may be rewritten as:

$$f_{ab} = 1.242*(1 - 4*(C - 0.5)^2)$$

$$\text{for} \quad \rho_w * \frac{V_o * x}{\mu_w} > 1.5E + 5 \qquad (5)$$

where f_{ab} is the dimensionless bubble frequency: $f_{ab} = F_{ab}*\sqrt{x*d_o/V_o}$. For $\rho_w*V_o*x/\mu_w < 1.5E + 5$, the coefficient of proportionality differs from 1.242 but the bubble frequency distributions follow closely the parabolic shape (i.e., Eq. (4)).

It is worth noting that the same observation (i.e., Eq. (4)) was obtained in fully-developed supercritical flows (Chanson, 1997b), suggesting that the air-water flow structure might be similar.

Chord Length Distributions. Bubble chord length distributions were recorded using the double-tip conductivity probe in experiment No. 3. The data give some information on the characteristic sizes of air bubbles, air pockets, foam bubbles, bubbles in water projections, and air volumes between water projections. The results (Fig. 6) are presented in the form of cumulative bubble chord length distributions, at various positions from the nozzle and for various nozzle velocities V_o. Note that each figure presents the cumulative probability of all the points for $0 < C < 0.90$ at a fixed distance x and, in each figure, the histogram columns represent the probability of a bubble chord length in 0.5 mm intervals: e.g., the probability of a chord length from 2.0 to 2.5 mm is represented by the column labelled 2.5. The last column (i.e., 100 mm) indicates the probability of bubble chord lengths larger than 100 mm. The results (Fig. 6) show the broad spectrum of bubble chord lengths observed at each cross-section: i.e., from less than 0.5 mm to larger than 100 mm. This is observed both in the low air-content region ($C < 0.5$) and in the high air-content region ($0.5 < C < 0.9$). In both regions, the distributions are skewed with a preponderance of small bubble sizes relative to the mean. The probability of bubble chord lengths is the largest for bubble sizes between 0 and 1.5 mm for $C < 50$ percent and between

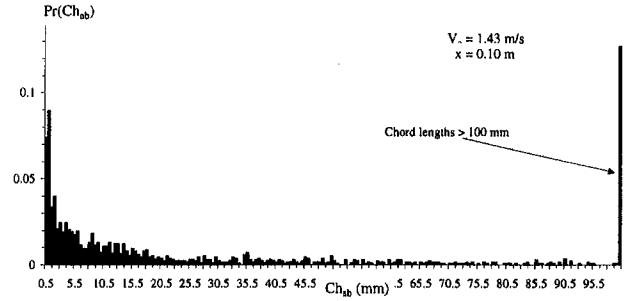

Fig. 6(*a*) V_o = 1.43 m/s, d_o = 0.012 m, x = 0.10 m – chord length interval: 0.5 mm

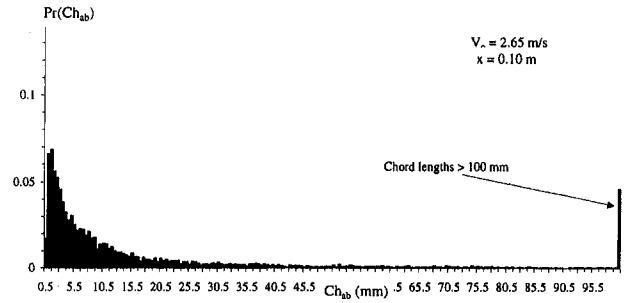

Fig. 6(*b*) V_o = 2.65 m/s, d_o = 0.012 m, x = 0.10 m – chord length interval: 0.5 mm

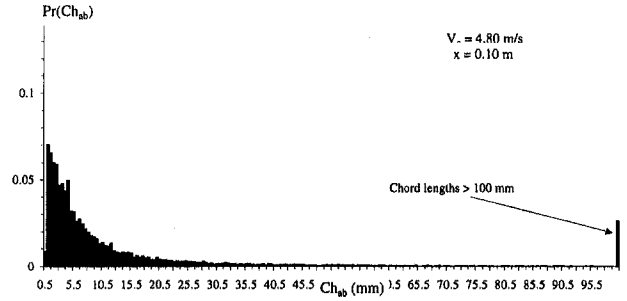

Fig. 6(*c*) V_o = 4.80 m/s, d_o = 0.012 m, x = 0.10 m – chord length interval: 0.5 mm

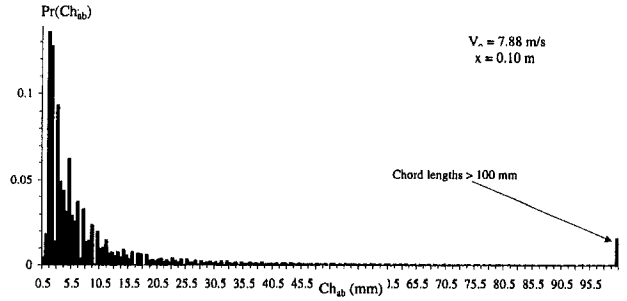

Fig. 6(*d*) V_o = 7.88 m/s, d_o = 0.012 m, x = 0.10 m – chord length interval: 0.5 mm

Fig. 6 Cumulative bubble chord length distributions

0 and 2.0 mm for $0.5 < C < 0.9$. It is worth noting the large amount of bubbles larger than 100 mm. These may be large air packets and air volumes surrounding water structures (e.g. droplets).

For V_o = 3.75 m/s, measurements performed at various distances from the nozzle suggest that most entrained air bubbles have small sizes close to the nozzle ($x < 0.1$ m), and that the distributions of chord length are redistributed toward larger sizes further downstream. Note, in any case, the significant amount of large chord length bubbles ($ch_{ab} > 100$ mm).

Discussion

Air Bubble Diffusion. With two-dimensional water jets, the advective diffusion of entrained air bubbles (i.e., Eq. (1)) has been observed with several configurations (see review in Chanson, 1997a, Figs. 2 to 4 in this paper). For all the new experiments, the authors estimated the turbulent diffusivity D_t, satisfying Eq. (1), from the best fit of the data (Table 2). It must be emphasized that the reported values are based on the crude assumption of D_t being independent of the transverse direction y.

Figure 7 presents the dimensionless diffusivity $D_t/(V_o * d_o)$ as a function of the Reynolds number $\rho_w * V_o * d_o/\mu_w$, where V_o and d_o are the characteristics jet velocity and thickness, respectively. The results, presented with logarithmic scales, indicate some scatter suggesting that the Reynolds number might not be the only relevant parameter. Nevertheless, the order of magnitude of the results is consistent with other types of air-water shear flows (see Chanson, 1997a, pp. 216–223). Although the three different experimental geometries (wall jet, free shear layer, free-falling jet) are expected to have different momentum transfer characteristics, the close results of diffusivity coefficients suggest that the air diffusion process is little affected by the geometry and the momentum transfer process.

Note that the data of experiment No. 3 might suggest an increase in dimensionless diffusivity with increasing Reynolds numbers. It is believed that the trend is related to the modification of inflow turbulence with increasing discharge and it is atypical. Experiments Nos. 1 and 2 had both a long smooth-convergent section while the convergent section was very short (i.e., less than 0.2 m) in experiment 3.

Characteristic Bubble Sizes. For any bubble size shape, bubble size distribution and chord length distribution, the mean chord length size (i.e., number mean size) is related to the air content, velocity and bubble frequency by:

$$(ch_{ab})_{\text{mean}} = \frac{CV}{F_{ab}} \tag{6}$$

Equation (6) is mathematically true in bubbly flows (i.e., air bubbles surrounded continuously by water). At the air-water interfaces of high-velocity water jets, Equation (6) is not exactly correct but it still gives an order of magnitude of a characteristic mean bubble size.

Equations (1), (3), (4), and (6) may be combined to deduce the distributions of mean bubble size in the air-water shear flow. For $C < 50$ percent, the mean bubble size (Eq. (6)) is a constant and the order of magnitude is about: $(ch_{ab})_{\text{mean}} \sim 1$ cm. For $C > 0.5$, Eq. (6) predicts a drastic increase of mean chord length with distance from the jet support (or jet centreline) which is consistent with the chord length distribution data.

Conclusion

New experiments have been performed with three types of two-dimensional water jets discharging into air: a wall jet flow, a free shear layer, and a free-falling jet. In each experiment, the distributions of air concentrations follow closely a solution of the diffusion equation (Eq. (1)) and the estimated

Table 2 Air bubble diffusion properties in two-dimensional water jets discharging into air

Ref. (1)	Run (2)	V_o m/s (3)	d_o m (4)	D_t m²/s (5)	$\frac{D_t}{V_o * d_o}$ (6)	X m (7)
Chanson (1988)[a]	860-1	10.71	0.020	1.41E-3	6.58E-3	0.093
	860-2	10.71	0.020	1.55E-3	7.24E-3	0.093
	870-1	10.65	0.032	2.17E-3	6.37E-3	0.199
	870-2	10.65	0.032	1.42E-3	4.17E-3	0.199
	871-1	9.54	0.032	1.50E-3	4.91E-3	0.173
	871-2	9.54	0.032	1.04E-3	3.41E-3	0.173
	872-1	12.01	0.033	2.81E-3	7.09E-3	0.199
	872-2	12.01	0.033	1.71E-3	4.31E-3	0.199
	873-1	8.72	0.031	7.29E-4	2.70E-3	0.146
	873-2	8.72	0.031	8.04E-4	2.97E-3	0.146
	874-1	7.00	0.030	4.52E-4	2.15E-3	0.15
	874-2	7.00	0.030	4.21E-4	2.00E-3	0.15
	1050	7.56	0.035	7.56E-4	2.86E-3	0.153
	1051	10.56	0.035	1.70E-3	4.60E-3	0.391
	880-1	6.21	0.069	3.58E-4	8.35E-4	0.156
	880-2	6.21	0.069	3.36E-4	7.84E-4	0.156
Low (1986)[a]	A7	4.61	0.046	5.58E-4	2.63E-3	0.288
	A8	5.19	0.047	4.86E-4	1.99E-3	0.327
	A9	5.71	0.053	9.99E-4	3.30E-3	0.342
	A10	6.64	0.057	2.93E-3	7.74E-3	0.44
	A11	8.36	0.056	1.63E-3	3.48E-3	0.349
Present study Experiment No. 1	Run P5	5.00	0.030	9.17E-4	6.11E-3	0.15
Experiment No. 2	Q75_St2CL	4.10	0.037	2.56E-3	1.69E-2	0.2
Experiment No. 3	FJ-2-100	1.43	0.012	2.65E-5	1.54E-3	0.1
	FJ-3-100	2.65	0.012	1.06E-4	3.33E-3	0.1
	FJ-4-100	3.75	0.012	2.70E-4	6.00E-3	0.1
	FJ-5-100	4.80	0.012	4.49E-4	7.80E-3	0.1
	FJ-6-100	5.83	0.012	5.03E-4	7.19E-3	0.1
	FJ-7-100	6.86	0.012	8.09E-4	9.83E-3	0.1
	FJ-8-100	7.88	0.012	8.96E-4	9.48E-3	0.1

Notes: X: considered interval (i.e., $0 < x < X$); [a] data reanalyzed by Chanson (1997a).

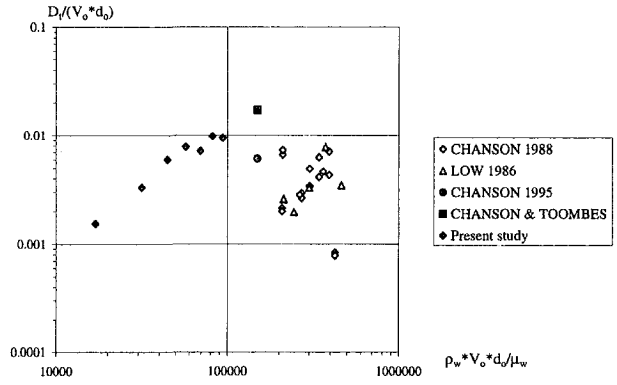

Fig. 7 Dimensionless diffusivity $D_t/(V_o^* d_o)$ as a function of the Reynolds number $\rho_w * V_o * d_o / \mu_w$ (Table 2)

turbulent diffusivity coefficients are of a similar order of magnitude. In experiment No. 3, the velocity and bubble frequency distributions were recorded also. Bubble chord length data show a wide range of entrained bubble sizes (from 0 to over 100 mm chord length). The relationship between the void fraction and the bubble frequency is a parabolic law (Eq. (4)), identical to that observed in self-aerated open channel flows.

Further experiments are necessary to extend the range of flow conditions as well as to investigate the interaction between the momentum shear flow and the air diffusion process.

Acknowledgments

The authors want to thank particularly Professor C. J. APELT, University of Queensland who supported this project since its beginning. They acknowledge the support of the Department of Civil Engineering at the University of Queensland which provided the experimental facility and the financial support of Australian Research Council (Ref. No. A89331591). The first and third authors were supported by Postgraduate scholarships sponsored by the Australian Research Council and the University of Queensland, respectively.

References

Chanson, H., 1988, "A Study of Air Entrainment and Aeration Devices on a Spillway Model." Ph.D. thesis, Ref. 88-8, Dept. of Civil Engrg., University of Canterbury, New Zealand.

Chanson, H., 1989, "Study of Air Entrainment and Aeration Devices." *Journal of Hydraulic Research,* IAHR, Vol. 27, No. 3, pp. 301–319.

Chanson, H., 1995, "Air Bubble Entrainment in Free-surface Turbulent Flows. Experimental Investigations." Report CH46/95, Dept. of Civil Engineering, University of Queensland, Australia, June, 368 pages (ISBN 0 86776 611 5).

Chanson, H., 1997a, *Air Bubble Entrainment in Free-surface Turbulent Shear Flows,* Academic Press, London, UK, 401 pp.

Chanson, H., 1997b, "Air Bubble Entrainment in Open Channels. Flow Structure and Bubble Size Distributions." *International Journal of Multiphase Flow,* Vol. 23, No. 1, pp. 193–203.

Chanson, H., and Brattberg, T., 1997, "Experimental Investigations of Air Bubble Entrainment in Developing Shear Layers," Report CH48/97,

Dept. of Civil Engineering, University of Queensland, Australia, Oct., 309 pp.

Chanson, H., and Toombes, L., 1997, "Flow Aeration at Stepped cascades," Research Report No. CE155, Dept. of Civil Engineering, University of Queensland, Australia, June, 110 pp.

Cummings, P. D., and Chanson, H., 1997, "Air Entrainment in the Developing Flow Region of Plunging Jets. Part 2 Experimental." ASME JOURNAL OF FLUIDS ENGINEERING, Vol. 119, Sept.

Ervine, D. A., and Falvey, H. T., 1987, "Behaviour of Turbulent Water Jets in the Atmosphere and in Plunge Pools," *Proc. Instn Civ. Engrs., London,* Part 2, Mar. Vol. 83, pp. 295–314. Discussion: Part 2, Mar.–June 1988, Vol. 85, pp. 359–363.

Heraud, D., 1966, "Dispersion des Jets Liquides; Influence des Rugosités de Paroi," ('Dispersion of Liquid Jets: Influence of the Wall Roughness.') Ph.D. thesis, University Grenoble 1, France (in French).

Low, H. S., 1986, "Model Studies of Clyde Dam Spillway aerators." Research Report No. 86-6, Dept. of Civil Eng., Univ. of Canterbury, Christchurch, New Zealand.

Tseng, L. K., Ruff, G. A., and Faeth, G. M., 1992, "Effects of Gas Density on the Structure of Liquid Jets in Still Gases." *AIAA Journal,* Vol. 30, No. 6, pp. 1537–1544.

Instability of Taylor Vortex and Nonaxisymmetric Modes in Flow Between Rotating Porous Cylinders

Chin-Hwa Kong
Professor.

Chi-Kuo Lee
Graduate Student.

Department of Naval Architecture
& Ocean Engineering,
National Taiwan University,
73 Chow-Shan Rd., Taipei, Taiwan, R.O.C.

A numerical solution of linear differential equations governing the instability of Taylor vortex and nonaxisymmetric modes in flow between rotating porous cylinders is present. Solutions take into account the presence of a radial flow between the two rotating cylinders. The critical Reynolds number and corresponding critical axial and azimuthal wavenumber are shown for different values of radius ratio, ratio of angular velocities of the inner and outer cylinders. The results show that not only the critical Reynolds number but the oscillatory onset mode of nonaxisymmetric disturbances can be altered when a radial flow is superimposed on the circular Couette flow. The weak inward flow has a destablizing effect for wide-gap, corotating system of positive and large μ (ratio of angular velocities Ω_1 and Ω_2), and the weak outward flow has a destablizing effect for small gap, co-rotating system and all counter-rotating system. The most unstable mode of instability depends not only on the angular speed ratio of both cylinders but also the strength of radial flow.

Introduction

The stability of a viscous flow between two concentric rotating cylinders is of both academic and engineering application interest. Taylor (1923) considered the stability problem both theoretically and experimentally and obtained a perfectly good agreement. He got a criterion for the onset of a secondary motion in the form of cellular toroidal vortices spaced more or less regularly along the axis of the cylinder. Later workers (DiPrima, 1955; Chandrasekhar, 1961; Meksyn, 1961; Duty and Reid, 1964; DiPrima and Swinney, 1985) used different approaches to solve this problem for μ (ratio of the angular velocities of the two cylinders) very negative and large. They all solved this problem for axisymmetric disturbances with small-gap assumption, where the mean flow can be replaced by its average value. Krueger et al. (1966) considered the fully linear Taylor problem for negative μ, and found that in narrow-gap approximation, when μ is less than -0.78, the most unstable disturbance is no longer axisymmetric but nonaxisymmetric. As μ decreases below this value the most unstable mode changes from m (azimuthal wavenumber) $= 0$ to $m = 1$, but then takes a higher values in rapid succession. This phenomenon has already been found experimentally by Coles (1965) and Snyder (1968). Nonaxisymmetric disturbances usually corresponding to unsteady onset shows a very different feature from steady onset, which is well assumed in instability problems of the closed type, i.e., Taylor problem and Bénard problem. Perturbation growth rates (σ) are usually assumed to be zero in the formulation of the two problems, but σ is actually not zero for unsteady onset. This makes the problem more complicated and difficult to solve.

Another interesting problem in this case is the effects of an additional flow on the stability of a viscous flow between two rotating cylinders. For example, Chandrasekhar (1960), DiPrima (1960), Chung and Astill (1977), and Babcock et al. (1991) showed that an axial flow in the annulus stabilizes the circular Couette flow. At the same time, the stability problem for viscous flow between porous cylinders with a radial flow also has been widely investigated. Chang and Sartory (1967, 1969), Min and Lueptow (1994), Kolyshkin and Vaillancourt (1997) predicted that inward radial velocity and strong outward velocity stabilize the flow, while weak outward velocity destabilizes the flow. Bahl (1970) made the narrow-gap approximation and concluded that an radially inward velocity stabilizes the flow, while an radially outward velocity destabilizes the flow. Similar type of flow occurs during the dynamic filtration process in biotechnology. By using a rotating inner porous cylinder and stationary nonporous outer cylinder, as a suspension of fluid and particles moves axially between the cylinders, the filtrate passes radially through the wall of the inner cylinder and the concentrate is collected at the exit end of the annulus, opposite to the entrance end (Kroner et al., 1987; Wronski et al., 1989). The porous cylinders in this paper can be treated as a rotating shear filter in which the suspension is filled from outer porous wall and filtrate is collected inside the inner porous wall.

So far the combination of Taylor problem and radial flow has not yet been solved theoretically for nonaxisymmetric disturbance. This may be important in biotechnology. Nonaxisymmetric onset may cause the different washing effect, and quite different effect in preventing plugging. The authors tried to understand the change of instability mode due to radial velocity variation by using a completely linear stability analysis with arbitrary gap width, in which three-dimensional disturbances of both stationary and oscillatory modes are considered. First, we compare the calculated results with those of previous studies for axisymmetric modes, with radial velocity control to confirm the computer code. Then the nonaxisymmetric mode shifts occurring in Taylor vortex flow are examined for different values of radial velocity. The results show general stability characteristics and the nature of nonaxisymmetric modes, as well as the corresponding travelling waves in the azimuthal direction.

Problem Formulation and Method of Solution

Let r, θ, z denote the usual cylindrical coordinates, and let u_r, u_θ, u_z be the components of velocity in the positive r-, θ-, z-directions, respectively. We consider an incompressible viscous

Contributed by the Fluids Engineering Division for publication in the JOURNAL OF FLUIDS ENGINEERING. Manuscript received by the Fluids Engineering Division September 22, 1997; revised manuscript received July 6, 1998. Associate Technical Editor: J. A. C. Humphrey.

Table 1 Comparison the results of present study (A) and those of Krueger et al. (1966, B) for Taylor problem $\alpha = 0$

			a_c		Ta_c^*		$-\sigma_r$	
η	μ	m	A	B	A	B	A	B
0.95	0	0	3.127	3.128	3509.71	3509.9	0.000	0.000
	−1.0	4	3.680	3.680	20067.9	20072	23.358	23.358
	−1.5	6	4.003	4.002	45289.8	45307	43.622	43.616
	−2.0	7	4.484	4.483	91234.8	91298	64.163	64.147
0.90	−1.0	3	3.722	3.721	23855.6	23861	26.897	26.896
0.80	−1.0	2	3.835	3.835	36750.8	36767	33.008	33.009
0.70	−1.0	2	3.985	3.984	60085.0	60099	48.474	48.472
0.60	−1.0	2	4.458	4.456	113959	114043	72.649	72.626
0.50	−.75	1	5.868		131587		51.945	
0.20	−.10	0	4.250		82090.3		0.000	

Table 2 Comparison of the results of the present study (A) and those of Donnelly et al. (1965, C), Chung et al. (1977, D), Min et al. (1994, E), for Taylor problem $m = 0$, $\alpha = 0$, $\mu = 0$

	Ta_c				a_c			
η	A	C	D	E	A	C	D	E
0.95	184.99	184.98	184.99	184.99	3.128	3.128	3.128	3.128
0.90	131.61	131.61	—	131.62	3.129	3.129	—	3.129
0.85	108.31	108.31	—	108.32	3.130	3.130	—	3.131
0.75	85.78	85.78	85.78	85.78	3.135	3.136	3.135	3.135
0.50	68.186	68.186	68.189	68.188	3.163	3.163	3.151	3.162

fluid in the absence of a body force which contained within two infinite long cylinders, both cylinders are made of porous material, with the z-axis as their common axis. If we let r_1, r_2 and Ω_1, Ω_2 denote the radii and angular velocities of the inner and outer cylinders, respectively, the flow is driven not only by the rotation but also the radial velocity between the two cylinders. The Navier-Stokes equations and continuity equation admit a steady solution in terms of the velocities:

$$u_r = \alpha\nu/r, \quad u_\theta = Ar^{\alpha+1} + B/r, \quad u_z = 0 \tag{1}$$

here $\alpha = u_1 r_1/\nu$ is the radial Reynolds number, where u_1 denotes the radial velocity through the inner porous cylinder, with a positive value stands for a outward velocity from the center of cylinder. And since $(\partial p/\partial r = -\rho(u_r(\partial u_r/\partial r) - (u_\theta^2/r))$, we can substitute $(\partial p/\partial r)$ into perturbed momentum equation in r-direction and need not calculate $p(r)$ directly. The constants are

$$A = \frac{-\Omega_1\eta^2(1-\mu/\eta^2)}{r_2^\alpha(1-\eta^{\alpha+2})}, \quad B = \frac{\Omega_1 r_1^2(1-\mu\eta^\alpha)}{1-\eta^{\alpha+2}} \tag{2}$$

where μ is the ratio of the angular velocities and η is the ratio of the radii, and $\alpha = -2$ is a avoiding point.

To study the stability, following the deviation of Krueger et al. (1966), of this flow we superpose a general disturbance on the basic solution, substitute in the equations of motion, continuity equation and neglect the high order terms. Since the coefficients in the resultant disturbance equations depend only on r, it is possible to seek solutions for velocities, pressure perturbations u_r', u_θ', u_z', p' of the form below to obtain the ordinary differential equations

$$\{u_r', u_\theta', u_z'\} = d_1\Omega_1\{u(x), v(x), w(x)\}\exp[i(\omega t + m\theta + \lambda z)]$$
$$p' = \rho\nu\Omega_1 p(x)\exp[i(\omega t + m\theta + \lambda z)] \tag{3}$$

where $x = (r - r_1)/(r_2 - r_1)$.

It is noted that m must be an integer for the reason the azimuthal wave must be countable and the λ must be real for the solution must be bounded at $z \to \pm\infty$, while the parameter ω is in general complex.

If we replace the pressure term $\pi(x)$ by introducing a new variable $X(x)$ defined by

$$\pi(x) = D^*u(x) - X(x) \tag{4}$$

where

Nomenclature

a = nondimensional axial wavenumber
A, A^* = basic velocity parameter
B, B^* = basic velocity parameter
d_1 = gap between the two cylinders
D, D^* = differential symbols
F, G, H = some functional forms
m = azimuthal wavenumber
M = parameter for calculation
N = temperature parameter
p = pressure perturbation
r, θ, z = cylindrical coordinates
r_1, r_2 = radii of the inner and outer cylinders, respectively
ω = perturbation growth rate
t = time
Ta = Reynolds number
u_1 = radial velocity through the wall of inner porous cylinder
u_r, u_θ, u_z = velocity perturbations
α = radial Reynolds number
δ = ratio of gap to inner radius
$\eta = r_1/r_2$
λ = axial wavenumber
$\mu = \Omega_2/\Omega_1$
ν = kinematic viscosity
π = pressure parameter
ξ = nondimensional radial distance
ρ = density of the fluid
σ = nondimensional growth rate
σ_r, σ_i = real and imaginary parts of σ
Ω_1, Ω_2 = angular velocities of the inner and outer cylinders, respectively
Ω^* = nondimensional angular velocity

Table 3 The critical value Ta_c and corresponding values of m, a_c, and $-\sigma_r$ for assigned values of η, μ, and α

η	μ	α	m	a_c	Ta_c	$-\sigma_r$
0.95	−1.00	−10	5	3.90	378.40	34.372
		−8	5	3.86	361.59	32.757
		−6	5	3.82	346.00	31.290
		−1	4	3.70	311.20	23.910
		1	4	3.66	298.39	22.832
		4	4	3.62	281.05	21.426
		8	3	3.55	260.61	15.485
		10	3	3.52	250.90	14.817
0.85	−1.00	−8	4	5.20	368.03	80.826
		−6	3	4.34	309.33	57.758
		−3	3	4.04	241.25	43.326
		1	3	3.80	182.00	32.227
		3	2	3.62	159.53	20.803
		5	2	3.53	142.33	18.305
		7	1	3.42	127.91	8.525
		10	0	3.26	111.40	0.000
0.75	−1.00	−1	2	4.02	198.88	48.099
		4	1	3.59	109.97	13.963
		8	0	3.28	83.29	0.000

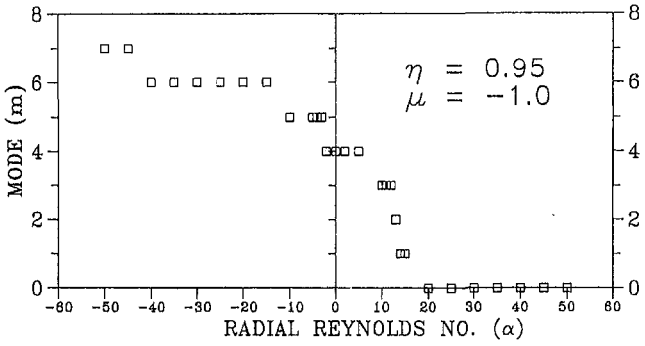

Fig. 1 The most unstable modes (m) for variation of radial Reynolds number (α) for $\eta = 0.95$, $\mu = -1.0$

$$\pi(x) = \frac{d_1}{\nu} p(x)$$

$$r = r_1 + xd_1, \quad D = d/dx, \quad D^* = d/dx + \xi(x),$$

$$\xi(x) = \delta/(1 + \delta x), \quad \delta = d_1/r_1, \quad d_1 = r_2 - r_1 \qquad (5)$$

In order to get the sets of ODE's, it is convenient to let $Y = D^*v(x)$, $Z = Dw(x)$, and make use of continuity equation to replace D^*u, we obtain the following system of six first-order equations

$$Du = -im\xi(x)v - iaw - \xi(x)u \qquad (6)$$

$$Dv = Y - \xi(x)v \qquad (7)$$

$$Dw = Z \qquad (8)$$

$$DX = M(x)u + 2[im\xi^2(x) - \mathrm{Ta}\,\Omega^*]v - 2\alpha\xi^2(x)u - im\alpha\xi^2(x)v - ia\alpha\xi(x)w \qquad (9)$$

$$DY = [M(x) + m^2\xi^2(x)]v - im\xi(x)X + ma\xi(x)w + \alpha\xi(x)Y - [2im\xi^2(x) - (\alpha + 2)\,\mathrm{Ta}\,A^*/\xi^\alpha]u \qquad (10)$$

$$DZ = [M(x) + a^2]w - iaX + am\xi(x)v + \alpha\xi(x)Z - \xi(x)Z \qquad (11)$$

where

$$M(x) = a^2 + m^2\xi^2(x) + i[\sigma + m\,\mathrm{Ta}\,\Omega^*]$$

$$\Omega^* = A^*/\xi^\alpha(x) + B^*\xi^2(x),$$

$$A^* = \frac{d_1^{1+\alpha}}{\Omega_1 r_1} A, \quad B^* = \frac{B}{\Omega_1 r_1 d_1},$$

$$a = \lambda d_1, \quad \sigma = \omega d_1^2/\nu, \quad \mathrm{Ta} = \frac{\Omega_1 r_1 d_1}{\nu}, \qquad (12)$$

The parameters presented above Ta, a, α and σ are rotational Reynolds number, axial wavenumber, radial Reynolds number, and perturbation growth rate, respectively.

The boundary conditions are

$$u = v = w = 0 \quad \text{at} \quad x = 0 \quad \text{and} \quad x = 1 \qquad (13)$$

The eigenvalue problem formed by (6)–(11) together with boundary condition (13) can be of the form

$$F(\mu, \eta, m, a, \sigma, \alpha, \mathrm{Ta}) = 0 \qquad (14)$$

The marginal state is characterized by σ_i, the imaginary part of σ, equal to zero. In this nonaxisymmetric case, the exchange of stability, i.e., σ is assumed to be identically zero, cannot be assured to be a priori, since the oscillatory mode is its nature for nonzero azimuthal waves. Hence not only σ is complex, but all the variables u, v, w . . . are also complex. This makes the problem (6)–(11) change to a set of 12 first-order ODE's with the same boundary condition (13) to another form

$$G(\mu, \eta, m, a, \sigma_r, \alpha, \mathrm{Ta}) = 0,$$

$$H(\mu, \eta, m, a, \sigma_r, \alpha, \mathrm{Ta}) = 0, \qquad (15)$$

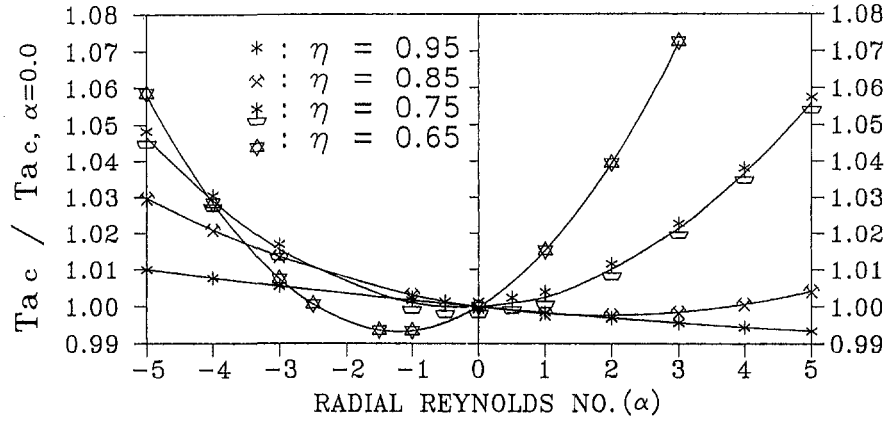

Fig. 2 The variation of critical Reynolds number (Ta_c) for various η with $\mu = 0.4$

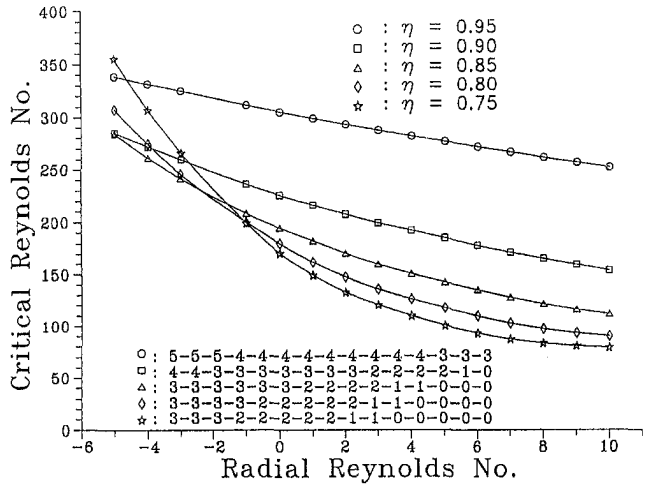

Fig. 3 Relationship associated with critical Reynolds number (Ta_c) and radial Reynolds number (α) for $\mu = -1.0$

where G and H are real-valued functionals with σ_r (real part of σ) to be determined. For given value of μ, and α, we seek for the minimum real positive Ta over real a and integer $m \geq 0$, for which there exists a solution for (15) with σ_r not equal to zero. The value of Ta to be solved is the critical Reynolds number Ta_c for assigned parameters stated above, the disturbances then are determined by the corresponding values a_c and m, which are called critical axial and azimuthal wave numbers, respectively.

The eigenvalue problem (15) can be solved as Walowit et al. (1964) via a Galerkin method. Here we solve the two-point eigenvalue problem by a shooting technique, which makes the problem an initial-value problem, together with a unit-disturbance method. This method has been widely used by, for example, DiPrima (1960), Harris and Reid (1964), Krueger et al. (1966), Soundalgekar et al. (1990), Min and Lueptow (1994), and Kong and Liu (1994) for similar hydrodynamic stability problems. Procedures of Krueger et al. and Min et al. are preferred here so as to see the details. A faster convergence of the iteration, which determines the critical Reynolds number, σ_r and corresponding axial wave number a_c, is obtained by utilizing a hybrid algorithm developed by Powell (1970) on the basis of a modified Newton-Raphson scheme, as well as the steepest-descent iteration instead of bivariate used by Krueger et al.

Results and Discussions

Verifying our computer code so as to ensure the correctness of (6)–(11) and boundary condition (13). Since our program is to investigate the nonaxisymmetric mode in circular viscous flow under the effects of a radial velocity, we first check our results (A) with those by Krueger et al. (1966) (B) in Table 1. We should note that the Taylor number $Ta^* = -4((1-\eta)/\eta)^2(\mu - \eta^2)/(1-\eta^2)\ Ta^2$ here. Second, our axisymmetric results (A) are compared with those by Donnelly et al. (1965) (C), Chung et al. (1977) (D) and Min et al. (1994) (E) in terms of a_c, Ta_c for the case $\alpha = 0$. It is shown in Table 2. The comparisons in both tables are in good agreement; errors in most cases are no more than 1.0 percent, and we estimate that the errors mainly result from the different numerical approach we chose. In Table 3, there is the summary of our present research.

In Fig. 1, which confirms the result of Krueger et al. (1966): ". . . for $R_1/R_2 = 0.95$, $\Omega_1/\Omega_2 = -1$, the wave-number in the azimuthal direction of the critical disturbance is $m = 4 \ldots$," at the same time, it is clear that strong outward velocity is a benefit to axisymmetric disturbances, and the nonaxisymmetric disturbances of higher modes prefer strong inward velocity. In fact, our results show that at $\eta = 0.95$, if $\mu \leq -0.80$, the most unstable disturbances are indeed nonaxisymmetric ones, and the modes depend upon the μ, η, and α. Similar phenomenon can be found in the research for radial temperature gradient acts on the region between two coaxial cylinders by Kong and Liu (1994).

Since the research by Min and Lueptow (1994), Kolyshkin and Vaillancourt (1997) are all focused on the instability arising from counter-rotating mechanism, we will extend their results by adding the corotating effects here. In Fig. 2, we can find for small gap cases (e.g., $\eta = 0.95, 0.85$) with positive and large μ (we take $\mu = 0.4$ here), the first instabilities still appear in $\alpha > 0$, but for wide gap ones, the lowest Taylor numbers appear in $\alpha < 0$, and we have verified that all modes appear in this range are all axisymmetric. In Fig. 3, for $\mu = -1$, we change the gap sizes from $\eta = 0.75 \sim 0.95$, the radial inward flows cannot destabilize the flow field any more, then we can conclude that the weak inward flow has a destabilizing effect for wide-gap, corotating system of positive and large μ, and the weak outward flow has a destabilizing effect for small gap, corotating system and all counter-rotating system.

As our earlier concept: in the absence of radial velocity, the critical Reynolds number of the flow field is inversely proportional to the gap width. But since the radial velocity is present, the smallest Reynolds numbers may not be wide gap ones. In Fig. 3, we can find that the inward velocity enhances the critical Reynolds numbers for all gap sizes, but as the η decreases, the effect increases rapidly. Therefore, on the influence of inward flow, the wide gap cases may show higher critical Reynolds numbers than small gap ones. From the results obtained by Min and Lueptow, Kolyshkin and Vaillancourt, the strong outward flow has the stabilized effect, too. And the same phenomenon may occur in large, positive α. If we check Fig. 3 for $\alpha = 0$, the onset modes for $\eta = 0.95, 0.90, 0.85, 0.80, 0.75$, are 4, 3, 3, 2, 2, respectively. This also coincides with the result obtained by Krueger et al. in their Table 2. For most cases, at the same radial flow strength, the unstable modes for larger ηs are always larger or equal to smaller ηs, and when the inward flow becomes stronger, the unstable modes become higher and higher; but the unstable modes will decrease when outward flow becomes stronger. Unlike critical Reynolds numbers, the critical axial wave numbers show less regularity in the absence of radial flow, but since the effect of radial inward flow becomes stronger, the critical axial wave number increases as its gap size increases, and the axial wave number decreases as the α increases, but

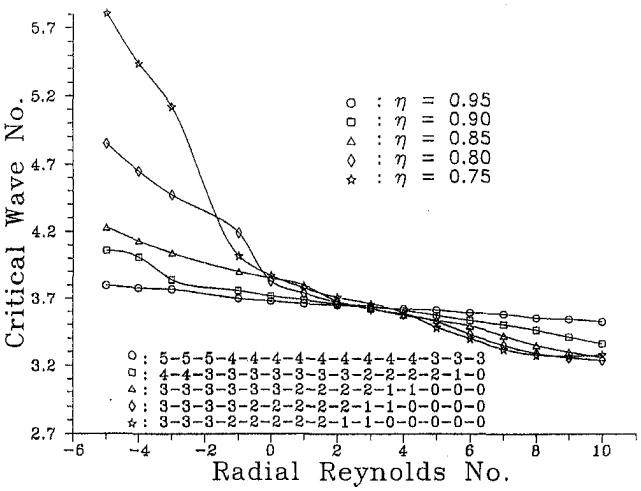

Fig. 4 Relationship associated with critical wave number (α_c) and radial Reynolds number (α) for $\mu = -1.0$

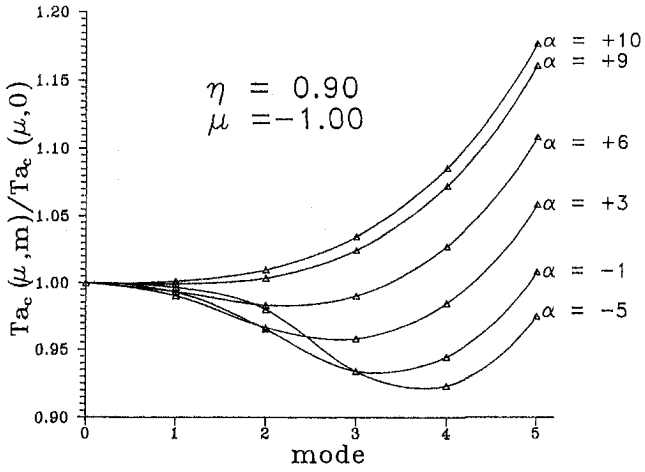

Fig. 5(*a*) The variation of $Ta_c(\mu, m)/Ta_c(\mu, 0)$ with $\eta = 0.90$, $\mu = -1.0$ for assigned values of α

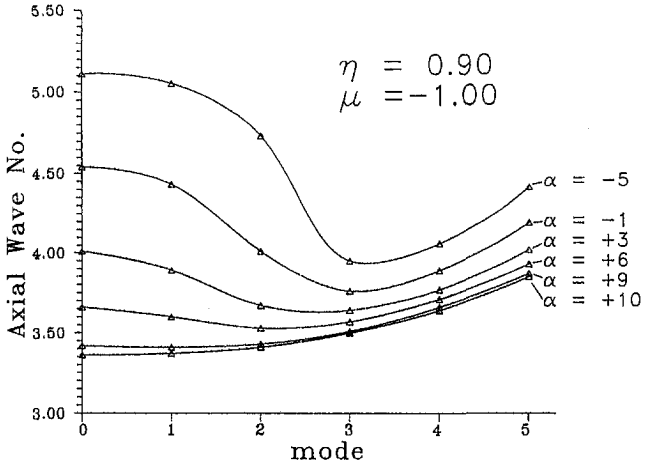

Fig. 5(*b*) The variation of $a_c(\mu, m)$ with $\eta = 0.90$, $\mu = -1.0$ for assigned values of α

instead of decreasing, the axial wave number will increase while the radial outward flow becoming more stronger (see Fig. 4).

Although the smallest axial wave numbers are not wholly corresponding to the smallest Taylor numbers (i.e., critical Reynolds numbers) in the mode evolution, but the smallest axial wave numbers always appear near the most unstable modes. For $\alpha = -5$ in Fig. 5(a), the most unstable mode is 4, and we can check Fig. 5(b) and find the smallest value of axial wave numbers for $\alpha = -5$ is at $m = 3$, and for the case of $\alpha = -1$, both the smallest axial wave number and Reynolds number appear at $m = 3$.

Conclusions

The instability of Taylor vortex flow between rotating porous cylinders is indeed affected by a radial velocity. The nonaxisymmetric mode can be altered by the strength of the radial velocity and the angular speed ratio of both cylinders. For strong inward flow, nonaxisymmetric modes prevail, but for strong outward flow, axisymmetric modes prevail.

The weak inward flow has a destabilizing effect for wide gap, corotating system of large μ, and the weak outward flow has a destabilizing effect for corotating system of small μ and all counter-rotating system. Both strong inward flow and strong outward flow have a stabilizing effect. Whether the gap is wide or not, for large $-\mu$, the nonaxisymmetric modes predominate. And in the presence of inward flow, wide gap systems may show stronger stability than small gap ones. We wish that the results obtained from the present study could be a benefit to the research of dynamic filtration process in biotechnology.

References

Bobcock, K. L., Ahlers, G., and Cannell, D. S., 1991, "Noise-Sustained Structure in Taylor-Couette Flow with Through Flow," *Physics Review Letters,* Vol. 67, p. 3392.

Chandrasekhar, S., 1960, "The Hydrodynamic Stability of Viscid Flow Between Coaxial Cylinders," *Proceedings of the National Academy of Sciences of the United States of America,* Vol. 46, p. 141.

Chandrasekhar, S., 1961, *Hydrodynamic and Hydromagnetic Stability,* Clarendon, Oxford.

Chang, T. S., and Sartory, W. K., 1967, "Hydromagnetic Stability of Dissipative Flow Between Rotating Permeable Cylinders: Part 1. Stationary Critical Modes," *Journal of Fluid Mechanics,* Vol. 27, p. 65 with corrections noted in *Journal of Fluid Mechanics,* Vol. 36, p. 193.

Chung, K. C., and Astill, K. N., 1977, "Hydrodynamic Instability of Viscous Flow Between Rotating Coaxial Cylinders With Fully Developed Axial Flow," *Journal of Fluid Mechanics,* Vol. 81, p. 641.

Coles, D., 1965, "Transitions in Circular Couette Flow," *Journal of Fluid Mechanics,* Vol. 21, p. 385.

DiPrima, R. C., 1955, "Application of Galerkin Method to Problem in Hydrodynamic Stability," *Quarterly of Applied Mathematics,* Vol. 13, p. 55.

DiPrima, R. C., 1960, "The Stability of a Viscous Fluid Between Rotating Cylinders With an Axial Flow," *Journal of Fluid Mechanics,* Vol. 9, p. 621.

DiPrima, R. C., and Swinney, H. L., 1985, "Instabilities and Transition in Flow Between Concentric Rotating Cylinders," in *Topics in Applied Physics, Hydrodynamic Instabilities and the Transition to Turbulence,* Swinney, H. L., and Gollub, J. P., eds., Springer-Verlag, Berlin, pp. 139–180.

Donnelly, R. J., Schwarz, K. W., and Roberts, P. H., 1965, "Experiments on the Stability of Viscous Flow Between Rotating Cylinders: VI. Finite-Amplitude Experiments," *Proceedings of the Royal Society of London,* Series A 283, p. 531.

Duty, R. L., and Reid, W. H., 1964, "On the Stability of Viscous Flow Between Rotating Cylinders," *Journal of Fluid Mechanics,* Vol. 20, p. 81.

Harris, D. L., and Reid, W. H., 1964, "On the Stability of Viscous Flow Between Rotating Cylinders. Part 2. Numerical Analysis," *Journal of Fluid Mechanics,* Vol. 20, p. 95.

Kolyshkin, A. A., and Vaillancourt, R., 1997, "Convective instability boundary of Couette flow between rotating porous cylinders with axial and radial flows," *Physics Fluids,* Vol. 9, p. 910.

Kong, C.-H., and Liu, I-C., 1994, "The Stability of Nonaxisymmetric Circular Couette Flow With a Radial Temperature Gradient," *Physics Fluids,* Vol. 6, p. 2617.

Kroner, K. H., Nissinen, V., and Ziegler, H., 1987, "Improving Dynamic Filtration of Microbial Suspensions," *Biotechnology,* Vol. 5, p. 921.

Krueger, E. R., Gross, A., and DiPrima, R. C., 1966, "On the Relative Importance of Taylor-vortex and Nonaxisymmetric Mode in Flow Between Rotating Cylinders," *Journal of Fluid Mechanics,* Vol. 24, p. 521.

Meksyn, D., 1961, *New Method in Boundary-layer Theory,* Pergamon, Oxford.

Min, K., and Lueptow, R. M., 1994, "Hydrodynamic Stability of Viscous Flow Between Rotating Porous Cylinders With Radial Flow," *Physics Fluids,* Vol. 6, p. 144.

Powell, M. J. D., 1970, *Numerical Method for Nonlinear Algebraic Equations,* Gordon and Breach, New York.

Snyder, H. A., 1968, "Experiments on Rotating Flows Between Noncircular Cylinders," Physics Fluids, Vol. 11, p. 1599.

Soundalgekar, V. M., Takhar, H. S., and Ali, M. A., 1990, "Effects of a Radial Temperature Gradient on the Stability of a Wide-Gap Annulus," *International Journal of Energy Research,* Vol. 14, p. 597.

Taylor, G. I., 1923, "Stability of a Liquid Contained Between Two Rotating Cylinders," *Philosophical Transactions of the Royal Society of London,* Series A 20, p. 289.

Walowit, J., Tsao, S., and DiPrima, R. C., 1964, "Stability of Flow Between Arbitrarily Spaced Concentric Cylindrical Surfaces Including the Effect of a Radial Temperature Gradient," ASME *Journal of Applied Mechanics,* Vol. 86, p. 585.

Wronski, S., Molga, E., and Rudniak, L., 1989, "Dynamic Filtration in Biotechnology," *Bioprocess Engineering,* Vol. 4, p. 99.

M. T. Lund[1]
Graduate Research Assistant.

C. Q. Jian[2]
Graduate Research Assistant.

P. E. Sojka
Associate Professor.

J. P. Gore
Professor.

M. V. Panchagnula[3]
Graduate Research Assistant.

Thermal Sciences and Propulsion Center,
School of Mechanical Engineering,
Purdue University,
West Lafayette, IN 47907-1003

The Influence of Atomizing Gas Molecular Weight on Low Mass Flowrate Effervescent Atomizer Performance

The relationship between atomizing gas molecular weight and spray mean drop size, Rosin-Rammler distribution parameter, and number averaged drop velocity is reported for a low mass flowrate effervescent atomizer-produced spray. Experimental data at lower gas-liquid ratios (GLR's) demonstrate that an increase in the molecular weight of the atomizing gas increases mean drop size and decreases number averaged drop velocity. The increase in mean drop size is attributed to an increase in the thickness of the liquid annulus at the nozzle exit and a subsequent increase in the diameter of ligaments formed there. The decrease in number averaged velocity results from a decrease in jet momentum rate. A model developed to explain the atomization process indicates that the gas flow is choked at higher GLR's.

Introduction

Effervescent atomization studies have been reported by a number of researchers, with topics considered ranging from the influence of nozzle geometry and liquid physical properties on mean drop size to the structure of the spray. For instance, Wang et al. (1987) and Lefebvre et al. (1988) demonstrated that atomizer performance is independent of injector geometry and final orifice diameter while Roesler and Lefebvre (1989) reported that nozzle performance is nearly independent of mixing tube porosity. Buckner and Sojka (1991) showed that mean drop size is independent of viscosity for Newtonian liquids while Buckner and Sojka (1993) report no consistent variation in mean drop size with consistency index or flow behavior index for power law non-Newtonian liquids.

More recently, in a study closely related to this one, Lund et al. (1993) showed that an increase in surface tension reduces mean drop size, while an increase in viscosity leads to a slight increase in SMD. Lund et al. then developed a simple analytical model based on liquid and gas continuity, liquid and gas momentum conservation, annular flow at the nozzle exit (supported by their high speed photographs), and Weber's (1931) model for ligament breakup in order to explain the observed mean drop size versus surface tension and viscosity behavior.

A companion paper by Lund and Sojka (1994) discusses the spatial structure of low mass flowrate effervescent atomizer produced sprays. These authors indicate that the increase in mean drop size with an increase in distance from the spray centerline results from a droplet size dependent competition between inertia and drag, which allows the larger drops to penetrate farther in the radial direction. They also show that the increase in mean drop size with axial distance from the nozzle is due to turbulent mixing within the spray cone.

Finally, Lee and Sojka (1993) report a marked decrease in nozzle performance for viscoelastic liquids. They concluded that fluid relaxation time is the rheological parameter that controls mean drop size.

Each of the previous studies was concerned with nozzle performance when using air as the atomizing gas. While air would be the most common choice, there are applications where an atomizing gas other than air is desirable. An obvious example is a combustor where dual fuel operation is required; a relatively heavy oil would be the primary fuel and methane the atomizing gas and pilot fuel. A less obvious example is the two-phase jet that exits a ruptured oil well, with the Kuwait fires being a case in point. Here, crude oil and gases (usually some mixture of methane, ethane and propane) exit the well head in a two-phase stream and burn when ignited. Because of the size of an operating well head, such fires are impossible to reproduce in the laboratory and difficult to investigate in the field. Fortunately, a sub-scale model of an oil well fire can be constructed using a low mass flowrate effervescent atomizer with a crude oil feed rate of 0.5 g/s providing a manageable firing rate of about 30 kW (Dutta et al., 1994).

Shifting from air to methane as the atomizing gas may influence mean drop size in the dual fuel combustor case and therefore impact combustion efficiency, pollutant formation, radiation heat transfer to the walls, and soot formation through variations in evaporation rate. In addition, when natural gas is used to atomize the oil, there will be variations in chemical composition that may lead to unacceptable swings in combustor performance if the molecular weight of the atomizing gas has a strong effect on nozzle performance. The composition of gas exiting an uncapped crude oil well head will vary from well to well so the influence of atomizing gas molecular weight on mean drop size is of interest to those simulating oil well fires.

These two applications motivated the present study into the influence of atomizing gas molecular weight on effervescent atomizer performance. These applications also motivated the choice of crude oil as the liquid to be sprayed and the low mass flowrates (0.5 g/s and below).

The following sections present the results of this study in terms of (i) Sauter mean diameter (SMD) and Rosin-Rammler distribution parameter (q) versus atomizing gas molecular weight (MW) at varying levels of gas-to-liquid ratio by mass (GLR) all for a single crude oil mass flowrate, and (ii) number averaged drop velocity versus atomizing gas molecular weight,

[1] Currently with Procter & Gamble, Cincinnati, OH.
[2] Currently with Vortec Corp., Philadelphia, PA.
[3] Currently with Delavan, Bamberg, SC.

Contributed by the Fluids Engineering Division for publication in the JOURNAL OF FLUIDS ENGINEERING. Manuscript received by the Fluids Engineering Division November 29, 1994; revised manuscript received August 6, 1998. Associate Technical Editor: D. E. Stock.

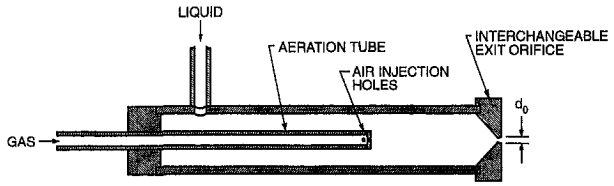

Fig. 1 Effervescent atomizer

again for a single crude oil mass flowrate. The experimental data are then compared to predictions provided by a model based on the one developed by Lund et al. (1993) in order to explain why a change in gas molecular weight influences effervescent atomizer performance at low GLR's.

Experimental Apparatus

The effervescent atomizer and liquid supply system of Lund et al. (1993) were used throughout this study. A schematic of the nozzle is provided in Fig. 1.

Alberta Sweet crude oil was chosen as the liquid to be sprayed because of its obvious application to oil well fires and because it is representative of residual fuel oils that might be burned in a dual fuel application. Alberta Sweet crude oil has a viscosity of 0.005 kg/m-s (5 cP), a surface tension of approximately 0.03 N/m (30 dynes/cm), and a density of 816 kg/m^3.

Atomizing gas was supplied using the system shown in Fig. 2. It consists of a pair of high pressure gas cylinders that supply helium and carbon-dioxide to a cylindrical stainless steel mixing chamber, with rotameters and metering valves included in each gas line to independently control the mass flowrates. The gas mixture was then routed to the injector's atomizing gas port.

Gas mixture molecular weights were varied between 8, half that of methane, and 44, that of propane, to span the range of possible (i) well head fire gas components and (ii) gas-phase fuels typical of combustion systems. Real gas effects were determined to be negligible by showing that the He and CO_2 compressibility factors were within 3% of unity for all conditions considered here.

A Malvern 2600 particle size analyzer was used to obtain line-of-sight number density based drop size data while an Aerometrics Phase/Doppler Particle Analyzer (P/DPA) was used to collect complementary flux based drop size data and velocity distributions. The Malvern was employed because it facilitates rapid collection of nozzle performance data. Malvern results can, however, suffer from inaccuracies due to droplet size-velocity correlations. For that reason P/DPA data were also collected since results obtained using this instrument are not subject to drop size-velocity correlation related limitations.

All Malvern data were obtained using a 300 mm focal length lens and reduced by fitting the scattered light profile to a Rosin-Rammler drop size distribution. Results are reported as Sauter mean diameter and the Rosin-Rammler distribution parameter.

The P/DPA was fitted with a 495 mm transmitting lens and a 300 mm collimating lens and operated in the 30 degree forward

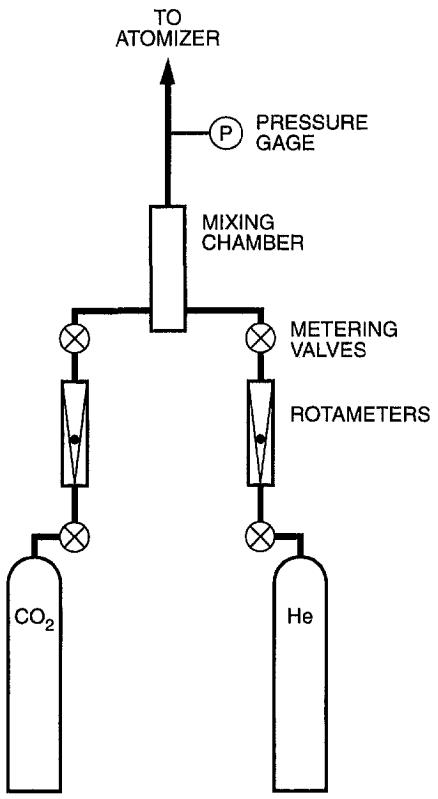

Fig. 2 Gas supply system

scattering mode. This permitted measurement of drop diameters between 3.34 and 117 microns and axial velocities between 0 and 25 m/s. Validation rates were consistently above 90 percent. All P/DPA data are reported as either SMD or number averaged drop velocity.

Both P/DPA and Malvern data were collected on the spray axis at a point 150 mm downstream of the nozzle exit orifice. All data were acquired at room temperature, which was nearly constant at 293 K (68 F).

Results

Representative results are shown in Figs. 3 through 6. Figures 3 and 4 present Malvern measured SMD and q versus molecular weight for GLR's ranging from 0.05 to 0.50. The crude oil mass flowrate is 0.5 g/s in all cases; GLR was therefore varied by adjusting the atomizing gas mass flowrate. Error bars are not included on these figures because they would be smaller than the symbols: the standard deviation relative to the mean is less than 4.0 percent for all the SMD data and less than 4.5 percent for all the q data.

The data demonstrate that mean drop size increases slightly with atomizing gas molecular weight for GLR's of 0.15 and

Nomenclature

C = a constant in the gas-phase momentum equation
C_{fi} = interfacial friction coefficient, dimensionless
d = diameter, m
GLR = gas-to-liquid ratio by mass, dimensionless
$\dot{m}$ = mass flowrate, kg/s
MW = atomizing gas molecular weight, kg/kg-mole
p = pressure, Pa
R_u = universal gas constant, J/kgmole-K
sr = gas-liquid velocity slip ratio, dimensionless
T = temperature, K
α = void fraction, dimensionless
μ = viscosity, kg/m-s
ρ = density, kg/m^3
σ = surface tension, kg/s^2

Subscripts

g = gas
l = liquid
L = ligament
o = nozzle exit orifice

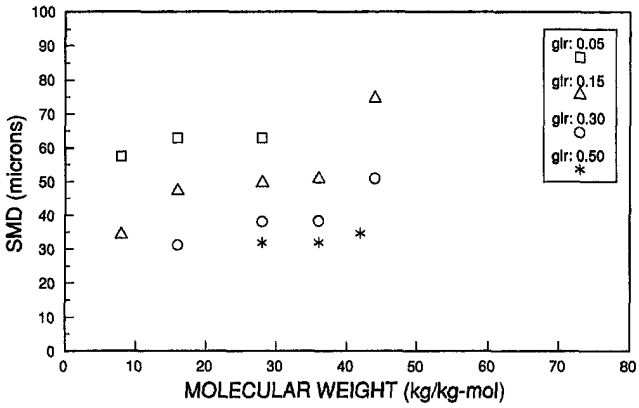

Fig. 3 Malvern measured Sauter mean diameter (SMD) versus atomizing gas molecular weight for four gas-liquid ratios (GLR's). The uncertainty in SMD measurements is estimated to be 6 percent (95 percent confidence interval), while the uncertainty in GLR measurements is estimated to be 5 percent (95 percent confidence interval).

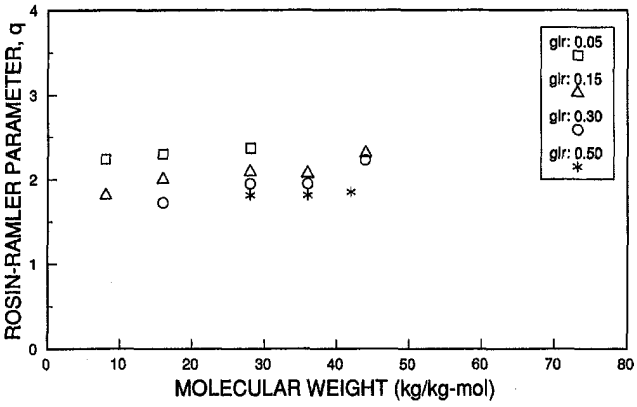

Fig. 4 Malvern measured Rosin-Rammler size distribution parameter (q) versus atomizing gas molecular weight for four gas-liquid ratios (GLR's). The uncertainty in q is estimated to be 6 percent (95 percent confidence interval), while the uncertainty in GLR measurements is estimated to be 5 percent (95 percent confidence interval).

below. However, the influence of atomizing gas molecular weight in insignificant for GLR's above 0.15. In addition, the width of the drop size distribution decreases slightly as molecular weight goes up. Finally, there is no systematic influence of GLR on the relationship between q and molecular weight.

The observation that mean drop size increases slightly with atomizing gas molecular weight at low GLR's is supported by the GLR = 0.05 and 0.15 P/DPA measured mean drop size data presented in Fig. 5. This figure also indicates that the influence of molecular weight on SMD is insignificant for GLR's above 0.15. Error bars are not included in Fig. 5 since the standard deviation relative to the mean for this data is always less than 4.0 percent and the error bars are therefore smaller than the symbols.

The disparity between Malvern and P/DPA measured SMD's is due to the two different methods used to sample the drops: the Malvern provides a number density based measurement and does not account for drop size-velocity correlations, whereas the P/DPA provides a flux based measurement and returns data that are therefore insensitive to drop size-velocity correlations.

Figure 6 shows that number averaged drop velocity decreases slightly with an increase in atomizing gas molecular weight and increases substantially with an increase in GLR. The latter behavior was also observed by Lund and Sojka (1994) when using air as the atomizing gas. Error bars are not included in Fig. 6 since the standard deviation relative to the mean is less

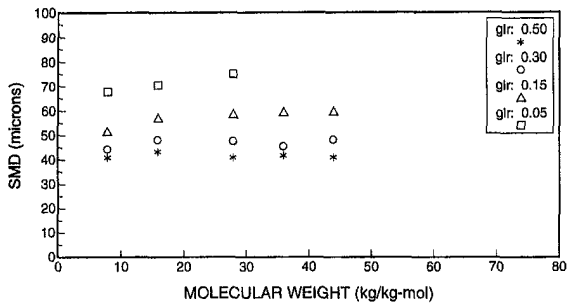

Fig. 5 P/DPA measured Sauter mean diameter versus atomizing gas molecular weight for four gas-liquid ratios (GLR's). The uncertainty in SMD measurements is estimated to be 6 percent (95 percent confidence interval), while the uncertainty in GLR measurements is estimated to be 5 percent (95 percent confidence interval).

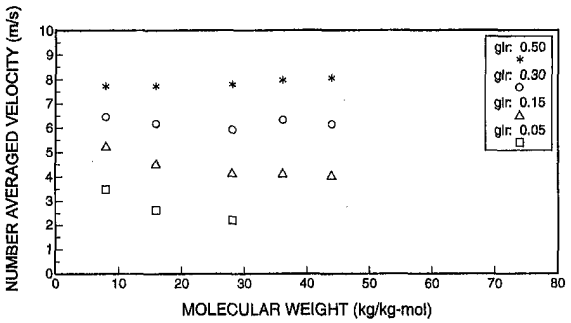

Fig. 6 Number averaged velocity versus atomizing gas molecular weight for four gas-liquid ratios (GLR's). The uncertainty in velocity measurements is estimated to be 4 percent (95 percent confidence interval), while the uncertainty in GLR measurements is estimated to be 5 percent (95 percent confidence interval).

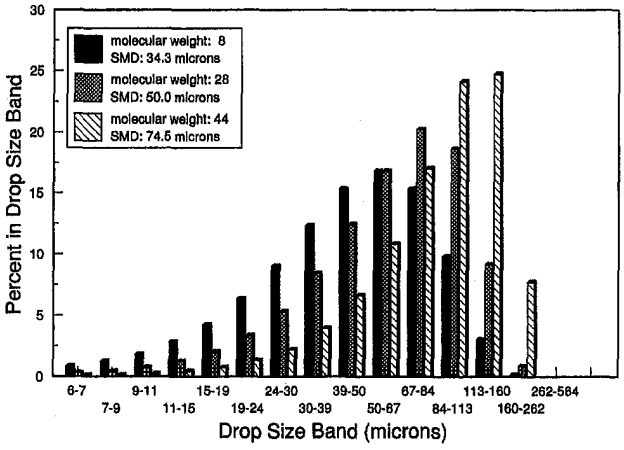

Fig. 7 Weight percent in each size band for three different atomizing gas molecular weights. The uncertainty in weight percentages is estimated to be 10 percent.

than 1.6 percent in all cases and the error bars are therefore smaller than the symbols.

Figure 7 provides a qualitative illustration of how changes in atomizing gas molecular weight shift spray mass between various size classes. The data are for a GLR of 0.15, however the behavior is indicative of all GLR's investigated. As can be seen, the width of the drop size distribution remains nearly unchanged, but mass is continually shifted from the larger drop categories to the smaller ones as atomizing gas molecular weight is reduced.

Analysis

The mean drop size and velocity behavior illustrated in Figs. 3, 5, and 6 is analyzed using a modified version of the model developed by Lund et al. (1993). The Lund et al. model assumes that each ligament formed at the nozzle exit orifice behaves as a liquid jet with its fluid mechanic instabilities described by Weber's (1931) analysis. As such, the length of a ligament is assumed to correspond to the wavelength of the fastest growing disturbance

$$\lambda_{\text{opt}} = \sqrt{2}\pi d_L\left(1 + \frac{3\mu_l}{\sqrt{\rho_l \sigma d_l}}\right)^{1/2} \tag{1}$$

with each cylindrical ligament eventually forming a single spherical drop. Conservation of mass yields the following expression for the drop Sauter mean diameter

$$\text{SMD} = \left[\frac{3}{2}\sqrt{2}\pi d_L^3\left(1 + \frac{3\mu_l}{\sqrt{\rho_l \sigma d_l}}\right)^{1/2}\right]^{1/3} \tag{2}$$

The ligament diameter, d_L, is found by first applying gas and liquid continuity to the annular flow at the nozzle exit orifice to determine the thickness of the liquid film there, then assuming that an integer number of ligaments exist in that film, and finally applying liquid continuity again to determine the ligament diameter.

Two key changes were made to Lund et al.'s original analysis. The first change was to include the effect of compressibility in the atomizing gas governing equations and was motivated by the fact that the gas phase Mach numbers exceeded 0.38 for all GLR's considered in this study. Lund et al. treated their gas phase as incompressible since their lower GLR's resulted in Mach numbers that were much lower than the ones considered here.

Gas phase compressibility was incorporated through a one-dimensional momentum equation

$$\frac{dp}{\rho_g} + V_g dV_g = 0 \tag{3}$$

which was coupled with the ideal gas equation of state

$$p = \frac{\rho_g R_u T}{MW} \tag{4}$$

While it is true that the gas flow at the nozzle exit is not inviscid, inviscid flow was assumed as a first approximation when applying the gas phase momentum equation with the interaction between the two phases at the interface included through the slip ratio expression. Viscous calculations including turbulence are much more complicated and may require constants for which values are not available. Hence, the model has been kept simple to suit the availability of input information.

The limiting thermodynamic paths, viz. adiabatic and isothermal expansion through the nozzle, were both considered. A comparison of predicted and measured drop sizes showed that the gas phase followed a thermodynamic path much closer to isothermal expansion than adiabatic. This is attributed to the intimate contact between the gas and liquid phases, which results in the liquid phase acting as a thermal reservoir for the gas. Substituting Eq. (4) into Eq. (3), making use of the isothermal assumption, and integrating yields Eq. (5)

$$\frac{R_u T}{MW}\ln\left(\frac{\rho_g R_u T}{MW}\right) + \frac{V_g^2}{2} = C \tag{5}$$

where C is a constant.

The second change to Lund et al.'s model was to modify the slip ratio correlation originally proposed by Ishii (1977)

$$sr = \sqrt{\frac{\rho_l}{\rho_g}}\sqrt{\frac{\sqrt{\alpha}}{1 + 75(1 - \alpha)}} \tag{6}$$

to account for the influence of mass flow rate on velocity slip. This traditional formula has been derived based on a one-dimensional drift flux model of two-phase fully developed annular flow in pipes. Ishii's correlation was chosen by Lund et al. after their photographs of the region immediately upstream of the nozzle exit showed the presence of annular two-phase flow. The following paragraph provides justification for this change.

The parameter 75 in Eq. (6) was originally introduced in a correlation developed by Wallis (1969) for the interfacial friction factor

$$C_{fi} = 0.005[1 + 75(1 - \alpha)] \tag{7}$$

Equation (7) was then used by Ishii when deriving his slip ratio expression for fully developed annular flow in pipes. In arriving at the value of 75, Wallis noted that the friction factor is a function of mass flow rate and that the slope of the C_{fi} versus $(1 - \alpha)$ curve increases as the liquid mass flow rate increases. However, no quantitative information was provided relating that slope to the liquid mass flowrate. Consequently, the value of 75 was scaled for the mass flowrates considered in this study.

The mass flow rate scaling was accomplished by matching predictions of mean drop size based on the model described here to the experimental SMD data of Lund et al. while varying the parameter 75. Mean drop size was calculated using Eqn. (2), which requires the measured liquid density, surface tension and viscosity, and the ligament diameter. The ligament diameter was determined via the approach discussed after Eq. (2); this calculation requires the gas core diameter. The gas core diameter was determined from

$$\frac{\pi}{4} d_g^2 = \alpha \frac{\pi}{4} d_o^2 \tag{8}$$

The void fraction is in turn related to the slip ratio, the (known) gas-to-liquid ratio, and the gas and liquid densities (Todreas and Kazimi, 1989)

$$\alpha = \frac{1}{1 + \dfrac{sr\rho_g}{GLR\rho_l}} \tag{9}$$

If Eq. (5) is rewritten in terms of the known gas mass flow rate, the void fraction, and the gas density

$$\frac{R_u T}{MW}\ln\left(\frac{\rho_g R_u T}{MW}\right) + \frac{\dot{m}_g^2}{2\left(\rho_g \dfrac{\pi}{4} d_o^2\right)^2} = C \tag{10}$$

Equations (6), (9), and (10) contain only three unknowns: α, ρ_g, and sr. They were solved iteratively using Newton's method.

Solution of Eqs. (6), (9), and (10) using the parameter value of 75 exhibited best agreement when compared to Lund et al.'s 0.8 g/s SMD data. Comparison of model predictions to data taken at 1.0 and 1.2 g/s indicated that the parameter value should be increased to 340 and 640, respectively. Note that an increase in the parameter value q with mass flow rate is consistent with Wallis' suggestion that the slope of the C_{fi} versus $(1 - \alpha)$ curve should increase with $\dot{m}$.

The approach for determining sr employed in this study yields acceptable agreement between experimental results and model predictions. However, a superior approach would be to independently determine the parameter q. This may be the subject of a future study.

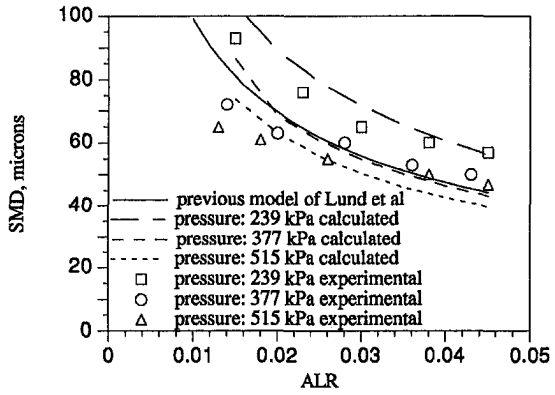

Fig. 8 Comparison of Lund et al. data with predictions using our model. The uncertainty in SMD measurements is estimated to be 6 percent (95 percent confidence interval), while the uncertainty in GLR measurements is estimated to be 5 percent (95 percent confidence interval).

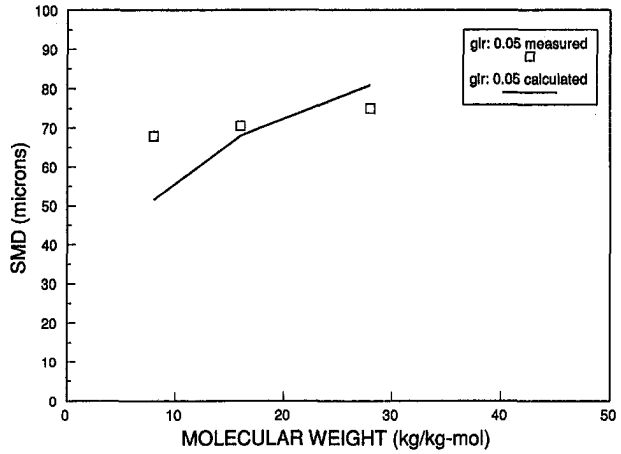

Fig. 9 Comparison of low GLR data from this study with predictions using our model. The uncertainty in SMD measurements is estimated to be 6 percent (95 percent confidence interval).

Figure 8 illustrates the level of agreement between the experimentally obtained data of Lund et al. and model predictions that result from adjusting the Ishii parameter for the various mass flow rates. Error bars have not been included since the standard deviation relative to the mean is less than 5.6 percent with the result that the symbols are larger than the error bars in all cases.

The parameter values used to obtain the predictions presented in Fig. 8 were then extrapolated to the 0.5 g/s crude oil data collected during this study using a power law approach. A value of 10 was obtained. A comparison of model predictions (using the value of 10) to the P/DPA data of Fig. 5 is presented in Fig. 9. It is limited to a GLR of 0.05 since the model indicates the gas flow chokes at higher values and sonic or supersonic flow cannot be treated by the current analysis. As Fig. 9 shows, qualitative agreement is achieved, with an increase in atomizing gas molecular weight leading to a small increase in mean drop size at this low GLR. The model indicates that this behavior results from a five step process: (i) an increase in atomizing gas molecular weight increases the gas density; (ii) the increase in gas density in turn decreases the diameter of the gas core at the nozzle exit; (iii) the decrease in the diameter of the gas core increases the thickness of the liquid annulus; (iv) the increase in the thickness of the liquid annulus produces larger diameter ligaments at the nozzle exit; and (v) these larger diameter ligaments lead directly to larger drops (as shown in Figs. 3 and 5).

The model also indicates why Fig. 6 shows a decrease in number averaged drop velocity upon an increase in atomizing gas molecular weight: raising the atomizing gas molecular weight reduces the velocity slip ratio. The decrease in velocity slip ratio leads to lower momentum rates at the nozzle exit, and therefore lower droplet velocities.

Summary

An increase in atomizing gas molecular weight is shown to have a slightly adverse effect on the performance of a low mass flowrate effervescent atomizer at low gas-to-liquid ratios (GLR ≤ 0.15) by raising the mean drop size, but to have an insignificant effect at higher GLR's. A comparison of experimental data with predictions based on a modified version of the model of Lund et al. (1993) indicates that the increase in mean drop size results from a thickening of the liquid annulus as atomizing gas molecular weight is increased. Increasing the thickness of the liquid annulus leads directly to larger diameter ligaments at the nozzle exit and, hence, larger drops. An increase in atomizing gas molecular weight also decreases drop velocity. The model indicates that the observed decrease in drop velocity is due to a reduction in jet momentum rate at the nozzle exit. Finally, the model indicates the gas flow chokes for gas-liquid ratios much over 0.08.

Acknowledgments

The authors acknowledge the National Science Foundation's equipment grant for providing the Phase/Doppler Particle Analyzer used during this study, and the National Institute for Standards and Technology for financial support (CQJ and JPG). Dr. David D. Evans is the NIST grant monitor.

References

Buckner, H. N., and Sojka, P. E., 1991, "Effervescent Atomization of High-Viscosity Fluids. Part I: Newtonian Liquids," *Atomization and Sprays,* Vol. 1, pp. 239–252.

Buckner, H. N., and Sojka, P. E., 1993, "Effervescent Atomization of High-Viscosity Fluids. Part II: Non-Newtonian Liquids," *Atomization and Sprays,* Vol. 3, pp. 157–170.

Dutta, P., Gore, J. P., Sivathanu, Y. R., and Sojka, P. E., 1994, "Global Properties of High Liquid Loading Turbulent Crude Oil + Methane/Air Spray Flames," *Combustion and Flame,* Vol. 97, pp. 251–260.

Ishii, M., 1977, "One-Dimensional Drift-Flux Model and Constitutive Equations for Relative Motion Between Phases in Various Two-Phase Flow Regimes," Argonne National Laboratory Rept. ANL 77-47.

Lee, W. Y., and Sojka, P. E., 1993, "The Influence of Fluid Viscoelasticity on Low Mass Flow Rate Effervescent Atomization," pp. 129–135 in *Fluid Mechanics and Heat Transfer in Sprays,* ASME FED-Vol. 178/HTD-Vol. 270, J. W. Hoyt, T. J. O'Hern, C. Presser, A. K. Gupta, and R. L. Alpert, eds.

Lefebvre, A. H., Wang, X. F., and Martin, C. A., 1988, "Spray Characteristics of Aerated-Liquid Pressure Atomizers," *AIAA Journal Prop. & Power,* Vol. 4, pp. 293–298.

Lund, M. T., Sojka, P. E., Lefebvre, A. H., and Gosselin, P. G., 1993, "Effervescent Atomization at Low Mass Flowrates. Part I: The Influence of Surface Tension," *Atomization and Sprays,* Vol. 3, pp. 77–89.

Lund, M. T., and Sojka, P. E., 1994, "Effervescent Atomization at Low Mass Flowrates. Part II: The Structure of the Spray," *Atomization and Sprays,* submitted.

Roesler, T. C., and Lefebvre, A. H., 1989, "Studies on Aerated-Liquid Atomization," *International Journal Turbo and Jet Engines,* Vol. 6, pp. 2221–230.

Todreas, N. E., and Kazimi, M. S., *Nuclear Systems I: Thermal Hydraulic Fundamentals,* Hemisphere, New York.

Wallis, G. B., *One Dimensional Two Phase Flow,* McGraw-Hill, New York.

Wang, X. F., Chin, J. S., and Lefebvre, A. H., 1987, "Influence of Gas Injector Geometry on Atomization Performance of Aerated-Liquid Nozzles," *Heat Transfer in Furnaces,* ASME HTD, Vol. 74, pp. 11–18.

Weber, C., 1931, "Disintegration of Liquid Jets," *Z. Agnew. Math. Mech.,* Vol. 11, pp. 136–159.

Elements of an Approach to the Assessment of Systematic Uncertainty in Transient Measurements

Paul K. Maciejewski
Visiting Assistant Professor,
Department of Mechanical Engineering,
University of Connecticut,
191 Auditorium Road, U-139,
Storrs, CT 06269-3139

Although there has been an increasing interest in experimental research investigating time-dependent fluid phenomena, accepted methods for assessing and reporting measurement uncertainty, i.e., those contained in ANSI/ASME PTC 19.1-1998, do not consider issues pertaining specifically to the assessment of uncertainty in transient measurements. Complementing the author's previous work which presented a method for assessing the random component of uncertainty in transient measurements, this paper presents a method for assessing the systematic component of uncertainty in transient measurements.

Introduction

Recently, Maciejewski (1996) proposed a method for assessing the random component of uncertainty in transient measurements. However, application of this method presupposes that one has direct access to a time series of data which represents the desired measured variable. In practice, however, the desired measured variable, i.e., the unobserved input to one's measurement system, is not directly observed: It must be constructed from the observed output from one's measurement system in a manner that accounts for the dynamics of the system. The aims of the present study are to provide a method for estimating a time series for the unobserved input to a measurement system and to provide a method for assigning a value for the systematic component of uncertainty to each member of this time series.

If the time response of the measurement system is sufficiently small compared to the time variation of the measured variable, then the measured variable and the output from the measurement system will be directly related through the static calibration of the measurement system. In this case, one can construct an observed time series for the measured variable corresponding to the measured time series for the output of the measurement system without regard to the dynamic characteristics of the measurement system, i.e., the systematic component of uncertainty in the observed time series can be assessed directly by the methods given in ANSI/ASME PTC 19.1-1998 (in press). However, if the time response of the measurement system is not sufficiently small compared to the time variation of the measured variable, then the output from the measurement system will be related to the measured variable via the dynamic characteristics of the measurement system. In this case, one must construct an observed time series for the measured variable corresponding to the measured time series for the output of the measurement system while accounting for the dynamic characteristics of the measurement system.

Although the investigation of time-dependent phenomena is not new, apparently the treatment of measurement uncertainty in these phenomena is relatively new. Neither the current American National Standard for Measurement Uncertainty, ANSI/ASME PTC 19.1-1998 (in press), nor the International Organization for Standardization's *Guide to the Expression of Uncertainty in Measurement* (1993), nor the National Institute of Standards and Technology's *Guidelines for Evaluating and Expressing the Uncertainty of NIST Measurement Results* (Taylor and Kuyatt, 1994) give any mention to issues pertaining specifically to the assessment of uncertainty in transient measurements. The studies on measurement uncertainty presented by Kline and McClintock (1953), Moffat (1982, 1988) and many others also do not address issues pertaining specifically to the assessment of uncertainty in transient measurements. Alwang (1991) describes many of the issues pertaining specifically to the assessment of uncertainty in transient measurements, but he does not advance any comprehensive method for assessing uncertainty in transient measurements. The study of Maciejewski (1996), which provides a method for assessing the random component of uncertainty in transient measurements, complements the present study which provides a method for assessing the systematic component of uncertainty in transient measurements. The development of methods for assessing uncertainty in transient measurements should be of particular interest to researchers in fluids engineering, since the *Journal of Fluids Engineering's* "Policy on Reporting Uncertainties in Experimental Measurements and Results" (1991) requires that papers published in the *Journal of Fluids Engineering* present assessments of uncertainty in experimental results.

The treatment of systematic uncertainty in transient measurements presented in this paper will be restricted to measurement systems that can be adequately modeled as time-invariant, i.e., to measurement systems with no drift in calibration. The analysis will also be restricted to measurement systems whose output is digitally sampled, e.g., by means of an A/D converter, at discrete times. Figure 1 presents a schematic of a typical measurement system. Figure 2 presents an example of the continuous output, $R(t)$, from a first-order, linear, time-invariant measurement system with static gain $\kappa = 2$ and time constant $\tau = 0.25$ when the continuous input is given by $Q(t)$.

Systematic Uncertainty in Transient Measurements.

A differential equation which models the behavior of a measurement system establishes a relation between the observed output from that measurement system, $R(t)$, and the unobserved input, $Q(t)$. For example, suppose a measurement system is linear and time-invariant such that its dynamic response can be modeled as a linear, second-order, ordinary differential equation with constant coefficients as follows:

Contributed by the Fluids Engineering Division for publication in the JOURNAL OF FLUIDS ENGINEERING. Manuscript received by the Fluids Engineering Division February 5, 1998; revised manuscript received August 25, 1998. Guest Editor: H. W. Coleman.

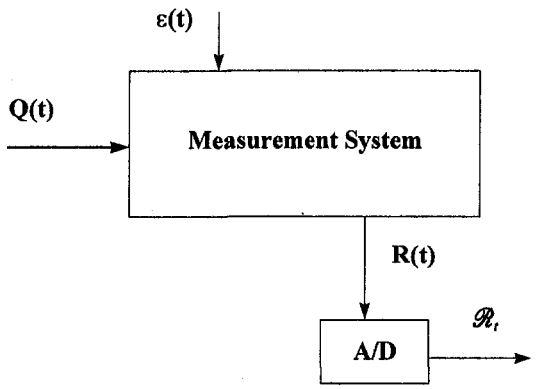

Fig. 1 Schematic of a typical measurement system

$$Q(t) = a_0R(t) + a_1dR(t)/dt + a_2d^2R(t)/dt^2 \quad (1)$$

where $Q(t)$ is the continuous input to the measurement system and $R(t)$ is the continuous output from the measurement system. In principle, if the model coefficients, a_0, a_1, and a_2, have been determined by means of some appropriate calibration procedure, and if the output from the measurement system, $R(t)$, is observed, then the unknown input to the measurement system, $Q(t)$, could be constructed from Eq. (1). Presumably, Eq. (1) could also be used as a basis for constructing an estimate of the systematic uncertainty in $Q(t)$.

In practice, one often observes a discretely sampled record of the output from a measurement system, $\mathscr{R}_t$, a record which includes the influence of systematic error sources. In this case, one can infer a time series for the input to the measurement system, Q_t, from a time series constructed to represent the output from the measurement system, R_t, and the parameters which characterize the dynamic response of the measurement system, a_i. For example, a discrete time approximation to Eq. (1) might be written as follows:

$$Q_t = a_0R_t + a_1\Delta R_t/\Delta t + a_2\Delta^2R_t/\Delta t^2 \quad (2)$$

where

$$\Delta R_t = (R_{t+1} - R_{t-1})/2$$

$$\Delta^2R_t = R_{t+1} - 2R_t + R_{t-1}$$

and Δt is the difference in time between consecutive members in one's representation of the output time series, R_t. [The form of the discrete approximation to the continuous model for the dynamics of the measurement system is selected at the discretion of the analyst. The particular central difference scheme presented in Eq. (2) is merely an example.] Given suitable estimates for the coefficients that appear in Eq. (2), and given that the sampling rate for the output time series is adequate to represent $R(t)$, the unobserved input to the measurement system, Q_t, can be constructed directly from Eq. (2). Furthermore, by means of Eq. (2), one can treat Q_t, which is not directly measured, as if it were simply a result that is calculated from a set of variables for which estimates have been made and for which uncertainties have been evaluated. From this perspective, Q_t can be estimated from the Eq. (2), and the uncertainty in Q_t can be estimated by the conventional methods given in ANSI/ASME PTC 19.1-1998 (in press) for determining the uncertainty in an experimental result. Accordingly, the systematic uncertainty in the unobserved input to the measurement system, U_{Qt}, can be estimated as follows:

$$U_{Qt} = [\sum_{i=0}^{2}(\theta_{ai}U_{ai})^2 + \sum_{j=-1}^{1}\{(\theta_{Rt+j}U_{Rt+j})^2 + \sum_{k=-1}^{1}\theta_{Rt+j}\theta_{Rt+k}\rho_{jk}U_{Rt+j}U_{Rt+k}(1-\delta_{jk})\} + (\theta_{\Delta t}U_{\Delta t})^2]^{1/2} \quad (3)$$

where

$$\theta_{a0} \equiv \partial Q_t/\partial a_0 = R_t$$

$$\theta_{a1} \equiv \partial Q_t/\partial a_1 = \Delta R_t/\Delta t$$

$$\theta_{a2} \equiv \partial Q_t/\partial a_2 = \Delta^2R_t/\Delta t^2$$

$$\theta_{Rt-1} \equiv \partial Q_t/\partial R_{t-1} = -a_1/2\Delta t + a_2/\Delta t^2$$

$$\theta_{Rt} \equiv \partial Q_t/\partial R_t = a_0 - 2a_2/\Delta t^2$$

$$\theta_{Rt+1} \equiv \partial Q_t/\partial R_{t+1} = a_1/2\Delta t + a_2/\Delta t^2$$

$$\theta_{\Delta t} \equiv \partial Q_t/\partial \Delta t = -a_1\Delta R_t/\Delta t^2 - 2a_2\Delta^2R_t/\Delta t^3$$

and U_{ai}, U_{Rt+j}, U_{Rt+k}, and $U_{\Delta t}$ are estimates of the systematic component of uncertainty in the i^{th} coefficient, a_i, the systematic components of uncertainty in the $(t+j)^{th}$ and $(t+k)^{th}$ members of the output time series, R_{t+j} and R_{t+k}, and the systematic component of uncertainty in the time step, Δt, respectively. Adapting the work of Brown et al. (1996) to the present context, the terms involving the correlation coefficients between U_{Rt+j} and U_{Rt+k} (i.e., the ρ_{jk}) account for correlations among the systematic uncertainties in successive members of R_t. In the expression for U_{Qt} given in Eq. (3), the uncertainty in Q_t is a function of time, since the values of R_{t+j} and R_{t+k} vary with time.

More generally, if the discrete time input to a measurement system is related to the discrete time output from the measurement system by a relation of the following form:

$$Q_t = f(R_{t-J}, \ldots, R_t, \ldots, R_{t+JJ}; a_0, a_1, \ldots, a_I) \quad (4)$$

then the uncertainty in Q_t, U_{Qt}, can be estimated as follows:

$$U_{Qt} = [\sum_{i=0}^{I}(\theta_{ai}U_{ai})^2 + \sum_{j=-J}^{JJ}\{(\theta_{Rt+j}U_{Rt+j})^2 + \sum_{k=-J}^{JJ}\theta_{Rt+j}\theta_{Rt+k}\rho_{jk}U_{Rt+j}U_{Rt+k}(1-\delta_{jk})\} + (\theta_{\Delta t}U_{\Delta t})^2]^{1/2} \quad (5)$$

Nomenclature

a_i = coefficient in dynamic equation for measurement system
f_c = cutoff frequency associated with $R(t)$
$Q(t)$ = continuous input to measurement system
Q_t = discrete representation of $Q(t)$
$R(t)$ = continuous output from measurement system
$\mathscr{R}_t$ = discrete time series sampled from $R(t)$
R_t = discrete representation of $R(t)$ constructed from $\mathscr{R}_t$
t = time
U = systematic uncertainty
X_t = time series introduced to construct R_t from $\mathscr{R}_t$
Y_t = time series introduced to construct R_t from $\mathscr{R}_t$
Z_t = time series introduced to construct R_t from $\mathscr{R}_t$
δ_{jk} = Kronecker delta: $\delta_{jk} = 1$ if $j = k$; $\delta_{jk} = 0$ otherwise
$\epsilon(t)$ = random error input to measurement system
κ = static gain
ϕ = time between successive observations in a sample
Φ = time period for entire sample
θ = sensitivity
ρ = correlation coefficient
τ = time constant

where

$$\theta_{ai} \equiv \partial f/\partial a_i$$

$$\theta_{Rt+j} \equiv \partial f/\partial R_{t+j}$$

$$\theta_{\Delta t} \equiv \partial f/\partial \Delta t$$

and ρ_{jk} is the correlation coefficient between U_{Rt+j} and U_{Rt+k}. Both Q_t and U_{Qt} are functions of time, since R_t is a function of time. Unlike the treatment of systematic uncertainty in steady-state measurements, the systematic component of uncertainty in transient measurements can only be assessed after one acquires his/her data. The functional relation, f, need not be linear in R_t.

Specification of Sampling Rate and Reconstruction of Measurement System Output

The construction of an estimate of the unobserved input to a measurement system from the observed output of that measurement system can be conceived as a two step process. In the first step, one must sample the output from the measurement system at a rate that is adequate for representing $R(t)$. For band-limited functions or truncated segments of band-limited functions, the maximum time interval between samples that produces data that is adequate for representing $R(t)$ is determined by the Nyquist frequency, i.e., $\phi_{\max} = 1/2f_c$. The time series sampled from the output of the measurement system will be designated $\mathcal{R}_t$. In the second step, one must evaluate $R(t)$ at points in time suitable for the purposes of estimating Q_t and U_{Qt}. The points in time at which one evaluates $R(t)$ for the purposes of estimating Q_t and U_{Qt} are not constrained by the rate at which one samples $R(t)$. The time series consisting of the points at which one evaluates $R(t)$ for the purpose of estimating Q_t and U_{Qt} will be designated R_t.

In practical terms, one can treat the output from a measurement system as a truncated segment of a band-limited function. From this perspective, however, the output from that measurement system is conceived as being discontinuous at the beginning and at the end of the data record. These discontinuities create difficulties in reconstructing $R(t)$ from the sampled data by means of convolution with a conventional interpolating function, i.e., $2f_c$ SINC $(2f_ct)$. These difficulties can be avoided by processing the sampled data as follows:

(1) If $\mathcal{R}_0$ is the value of the first observation in the data record corresponding to time $t = 0$ and $\mathcal{R}_N$ is the value of the last observation in the data record corresponding to time $t = \Phi$, then construct a new time series, X_t, whose members are given as follows:

$$X_j = \mathcal{R}_j - \{(\mathcal{R}_N - \mathcal{R}_0) \times \sin[(\pi/2)(t/\Phi)] + \mathcal{R}_0\} \quad (6)$$

where $\mathcal{R}_j$ and X_j are the j^{th} observations in $\mathcal{R}_t$ and X_t, respectively. These observations correspond to time $t = j\phi$, where ϕ is the time interval between successive observations in the sample.

(2) Attach the negative reflection of X_t to the beginning of X_t to construct a new time series Y_t.

(3) Concatenate a series of replications of Y_t to the beginning and to the end of Y_t to create a strictly periodic time series Z_t.

(4) One can now evaluate a convolution integral of Z_t with a conventional interpolating function to evaluate $Z(t)$. This convolution integral can be expressed as the following serial product:

$$Z(t) = \sum_{j=-\infty}^{\infty} 2f_c \text{ SINC } [2f_c(t - j\phi)]Z_j\phi \quad (7)$$

(5) On the interval of time between $t = 0$ and $t = \Phi$, $R(t)$ can now be evaluated as follows:

$$R(t) = Z(t) + \{(\mathcal{R}_N - \mathcal{R}_0) \times \sin[(\pi/2)(t/\Phi)] + \mathcal{R}_0\} \quad (8)$$

One can use Eq. (8) to construct the time series R_t, which can then be used for the purpose of estimating Q_t using a model of the form given in Eq. (4). The systematic uncertainty in the values of the constructed time series R_t, U_{Rt}, required for the purpose of estimating U_{Qt} using Eq. (5), may be taken to be equivalent to the systematic uncertainty in the observations of the sampled time series $\mathcal{R}_t$, $U_{\mathcal{R}t}$. For further elaboration on this point, see Bracewell (1986).

An Example

Suppose one plans to use a measurement system which can be modeled as a first-order, linear, time-invariant measurement system characterized as follows:

$$\tau dR(t)/dt + R(t) = \kappa Q(t) \quad (9)$$

where κ is its static gain and τ is its time constant. (A model of this form might be appropriate for a thermocouple probe that one plans to use to measure transient temperature variations in a convective environment in which the heat transfer coefficient between the thermocouple probe and the surrounding fluid is constant.) This model governing the behavior of the measurement system can be approximated in discrete time as follows:

$$\tau(R_t - R_{t-1})/\Delta t + R_t = \kappa Q_t \quad (10)$$

Since the primary aim of the analysis is to use a representation of the measurement output from the measurement system, R_t, in order to construct an estimate of the unobserved input to the measurement system, Q_t, one can use Eq. (10) to express Q_t in terms of κ, τ, Δt, R_t and R_{t-1} as follows:

$$Q_t = 1/\kappa[\tau(R_t - R_{t-1})/\Delta t + R_t] \quad (11)$$

The uncertainty in Q_t can be estimated as follows:

$$U_{Qt} = [(\theta_\kappa U_\kappa)^2 + (\theta_\tau U_\tau)^2 + (\theta_{\Delta t} U_{\Delta t})^2 + (\theta_{Rt} U_{Rt})^2 + (\theta_{Rt-1} U_{Rt-1})^2 + 2\theta_{Rt}\theta_{Rt-1}\rho_{RtRt-1}U_{Rt}U_{Rt-1}]^{1/2} \quad (12)$$

where

$$\theta_\kappa \equiv \partial Q_t/\partial \kappa = -1/K^2[\tau(R_t - R_{t-1})/\Delta t + R_t]$$

$$\theta_\tau \equiv \partial Q_t/\partial \tau = 1/\kappa[(R_t - R_{t-1})/\Delta t]$$

$$\theta_{\Delta t} \equiv \partial Q_t/\partial \Delta t = -1/\Delta t^2[\tau(R_t - R_{t-1})/\kappa]$$

$$\theta_{Rt} \equiv \partial Q_t/\partial R_t = 1/\kappa[\tau/\Delta t + 1]$$

$$\theta_{Rt-1} \equiv \partial Q_t/\partial R_{t-1} = 1/\kappa[-\tau/\Delta t]$$

and ρ_{RtRt-1} is the correlation between U_{Rt} and U_{Rt-1}. In this expression, it is clear that the uncertainty in Q_t is a function of time, since the values of R_t and R_{t-1} vary with time.

For example, suppose the true input to the measurement system in question is given by the function $Q(t)$ represented in Fig. 2, and the true output from the measurement system is given by the function $R(t)$ also represented in Fig. 2. Furthermore, suppose $R(t)$ is sampled over the time interval between $t = 0$ and $t = \frac{1}{3}$ at a rate at or above that determined by its Nyquist frequency, and the time series R_t is constructed from the sampled time series $\mathcal{R}_t$ using Eqs. (6) – (8). Assume calibration results for the measurement system in question establish $\kappa = 2 \pm 0.2$ at 95% confidence and $\tau = 0.25 \pm 0.025$ at 95% confidence. Finally, suppose the systematic uncertainty in Δt is 0.001, the systematic uncertainty in R_t (and R_{t-1}) is 0.001, and the correlation between the systematic uncertainties in R_t and

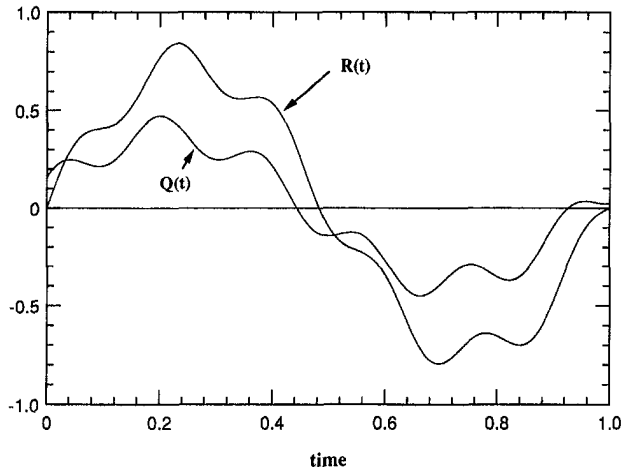

Fig. 2 Measurement system response, $R(t)$, to a time-dependent variable, $Q(t)$

R_{t-1} is 1. Employing this information in combination with the proposed methods for assessing the input time series [Eq. (11)] and its systematic uncertainty [Eq. (12)], Fig. 3 represents the construction of an estimate for an unobserved input discrete time series, Q_t (indicated by the plotted symbols), as well as the construction of an estimate for its systematic uncertainty, U_{Q_t} (indicated by the corresponding error bounds).

Criteria for Neglecting to Compensate for Measurement System Dynamics

As indicated earlier, there may be circumstances in which it may not be necessary to account for the dynamics of the measurement system when estimating the measured variable and the systematic uncertainty in the measured variable, provided that the time response of the measurement system is sufficiently small compared to the time variation of the measured variable. If, with respect to the time variation of the measured variable, the model for the dynamic response of the measurement system, f, is adequately approximated by a static calibration, g, i.e.:

$$Q_t = f(R_{t-J}, \ldots, R_t, \ldots, R_{t+JJ}; a_0, a_1, \ldots, a_I) \quad (13)$$
$$\approx g(R_t; b_0, b_1, \ldots, b_K)$$

then one can justify using the simpler relation, g, in place of the more involved relation, f, provided that the differences in estimates of Q_t employing f and g are a small fraction of the overall uncertainty in Q_t. As an illustration, if $\tau = 0.00025$ for the measurement system described in the example given in the preceding section, then the model $Q_t = R_t/\kappa$ is within ± 0.00016 of the dynamic model for Q_t given in Eq. (11). Since the systematic uncertainty in Q_t is greater than ± 0.00114 in this case, one can justify the use of the simpler model.

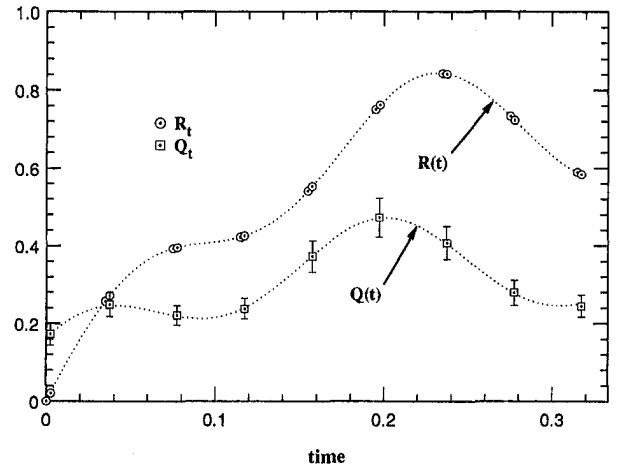

Fig. 3 Estimates of the desired measured variable, Q_t, and its uncertainty, U_{Q_t}

Discussion

The assessment of systematic uncertainty in transient measurements is equivalent to the assessment of the accuracy with which one is able to construct an estimate of the unobserved input to a measurement system, in the absence of sources of random uncertainty in the measurement process, from the observed output from that measurement system while accounting for the dynamics of the measurement system. The proposed method for estimating the values of the unobserved measured variable and for assessing the systematic uncertainty in these values can be summarized in the following series of steps. First, one should construct a difference equation for the output from the measurement system which will adequately approximate the dynamic behavior of the measurement system. Parameters which appear in the difference equation for the output from the measurement system ought to be estimated by means of a suitable set of calibration experiments. Second, one should sample the output from the measurement system at a rate which permits an adequate representation of $R(t)$. For a truncated segment of a band-limited function sampled at a rate at or above the Nyquist frequency, $R(t)$ can be reconstructed by means of Eqs. (6)–(8). Third, in order to interpret the output from the measurement system, one should construct a time series for the desired measured variable, Q_t, employing a discrete time series representing the output from the measurement system, R_t, in combination with the difference equation for the measurement system [see Eq. (4)]. Finally, one should estimate the systematic uncertainty in the desired measured variable by conventional methods for assessing uncertainty in an experimental result. To this end, one should employ the difference equation for the measurement system used to estimate the time series for the desired measured variable in order to determine the sensitivity of the desired measured variable to (i) the uncertainty in each of the parameters used to characterize the measurement system, (ii) the uncertainty in the output from the measurement system, and (iii) the uncertainty in the difference in time between members of the output time series [see Eq. (5)].

Detailed issues pertaining to the calibration of instruments for the purpose of measuring time-dependent variables are beyond the scope of the present paper. However, in order to assess the systematic uncertainty in transient measurement by the methods proposed above, one must have an adequate model for the dynamic behavior of the measurement system and a means to evaluate both the parameters and the uncertainty in the parameters associated with the model. For example, the specification of a first-order, linear, time-invariant measurement system would require an estimate of its static gain, its time constant, and the uncertainty in these parameters. Furthermore, in this case, one should also present some evidence confirming that a first-order, linear, time-invariant model is appropriate for the measurement system. Issues of calibration are closely related to the issues of system identification of dynamic systems as treated in the literature of control theory. An introduction to system identification of dynamic systems from the perspective of digital control theory is presented by Franklin and Powell (1980).

It must be emphasized that the proposed method will provide adequate estimates of a time series for the desired measured variable and its systematic uncertainty only if the output from the measurement system is sampled at a rate which permits an

adequate representation of the measurement system's response to the anticipated time characteristics of the desired measured variable. One should always perform a pretest analysis in which one attempts to reconstruct a known function for the input to the measurement system, whose time characteristics are representative of the input signal that may be encountered during the actual measurement process, via the difference equation for the measurement system used to estimate the time series for the desired measured variable.

Once one has constructed a time series for the desired measured variable, Q_t, then one is in a position to assess the random component of uncertainty in Q_t employing the methods presented in Maciejewski (1996). The total uncertainty in Q_t is then the root-sum-square combination of the systematic component of uncertainty, assessed by the methods presented in this paper, and the random component of uncertainty, assessed by the methods presented in Maciejewski (1996).

The proposed method for assessing systematic uncertainty in transient measurements represents a synthesis of ideas either adopted or adapted from the following areas of inquiry: (*i*) the identification and modeling of the behavior of dynamic systems, (*ii*) the propagation of uncertainty to an experimental result, (*iii*) the specification of sampling rate and the processing of sampled data, and (*iv*) the calibration of measurement systems. Undoubtedly, future developments in each of these areas of inquiry will contribute to an evolution of methods for assessing systematic uncertainty in transient measurements. Indeed, the need to advance a method for the assessment of systematic uncertainty in transient measurements might well serve to motivate new developments in each of these areas of inquiry.

Conclusion

Given an adequate, discrete-time model for the dynamic characteristics of a measurement system, and given that the output from that measurement system is sampled at a rate that is adequate for representing the time characteristics of the measurement system's response to the unobserved input to the measurement system via this model, one can construct a time series for the desired measured variable using a model of the form given in Eq. (4) and an estimate of the systematic uncertainty for each member of the time series for the desired measured variable using Eq. (5).

References

Alwang, W. G., 1991, "The Analysis of Uncertainty in Transient Measurements," ISA Paper No. 91-060.

Anon., in press, "Measurement Uncertainty," ANSI/ASME PTC 19.1-1998, American Society of Mechanical Engineers, New York.

Anon., 1991, "Journal of Fluids Engineering Policy on Reporting Uncertainties in Experimental Measurements and Results," ASME JOURNAL OF FLUIDS ENGINEERING, Vol. 113, pp. 313–314.

Anon., 1993, "Guide to the Expression of Uncertainty in Measurement," International Organization for Standardization, Geneva, Switzerland.

Bracewell, R. N., 1986, *The Fourier Transform and Its Applications,* 2nd Edition, Revised, McGraw-Hill, New York, pp. 189–215.

Brown, K. K., Coleman, H. W., Steele, W. G., and Taylor, R. P., 1996, "Evaluation of Correlated Bias Approximations in Experimental Uncertainty Analysis," *AIAA Journal,* Vol. 34, pp. 1013–1018.

Franklin, G. F., and Powell, J. D., 1980, *Digital Control of Dynamic Systems,* Addison-Wesley, Reading, MA, pp. 207–246.

Kline, S. J., and McClintock, F. A., 1953, "Describing Uncertainties in Single-Sample Experiments," *Mechanical Engineering,* Vol. 75, pp. 3–8.

Maciejewski, P. K., 1996, "Elements of an Approach to the Assessment of Random Uncertainty in Transient Measurements," ASME JOURNAL OF FLUIDS ENGINEERING, Vol. 118, pp. 90–95.

Moffat, R. J., 1982, "Contributions to the Theory of Single-Sample Uncertainty Analysis," ASME JOURNAL OF FLUIDS ENGINEERING, Vol. 104, pp. 250–260.

Moffat, R. J., 1988, "Describing the Uncertainties in Experimental Results," *Experimental Thermal and Fluid Science,* Vol. 1, pp. 3–17.

Taylor, B. N., and Kuyatt, C. E., 1994, "Guidelines for Evaluating and Expressing the Uncertainty of NIST Measurement Results," NIST Technical Note 1297, National Institute of Standards and Technology, Washington, DC.

Some Explicit Analytical Solutions of Unsteady Compressible Flow

Ruixian Cai
Academician,
Institute of Engineering Thermophysics,
Academia Sinica,
P.O. Box 2706, Beijing 100080 China

The analytical solutions of different flows are meaningful in theory. In addition, they are very useful to CFD also as the standard solutions to check the numerical solutions and to develop numerical differencing schemes, grid generation methods and so forth. However, very few analytical solutions have been known for the compressible flow, especially the unsteady flow. Some explicit analytical solutions of unsteady compressible flow have been derived since the early nineties and are given in this paper, which include the 1-D isentropic unsteady flow, 1-D unsteady flow with friction, heat transfer as well as with shock, and 2-D isentropic unsteady flow.

Introduction

The analytical solutions in fluid mechanics have had very important meaning. Many analytical solutions of steady incompressible potential flow played a key role in the early development of fluid mechanics. However, the governing equations of unsteady compressible flow are highly nonlinear, hence, it is very difficult to find out the analytical solution of such flow. According to the knowledge of the author, no explicit analytical solution of unsteady compressible flow has been found in the open literature so far. In order to fill in the gaps in the field of unsteady compressible fluid mechanics, it is meaningful in theory to find out some analytical solutions.

Moreover, besides theoretical meaning, analytical solutions can also be applied to check the accuracy, convergence and effectiveness of various numerical computation methods and their differencing schemes, grid generation ways and so on. The analytical solutions are therefore very useful even for the newly rapidly developing computational fluid dynamics. For example, several analytical solutions which can simulate the 3-D potential flow in turbomachine cascades were given by the author (Cai et al., 1984). These solutions have been used successfully by some numerical calculation scientists to check their computational methods and computer codes (Cai et al., 1984; Zhu and Liu, 1988; Xu et al., 1989; Gong and Cai, 1990; Shen et al., 1996). Therefore, several analytical solutions of unsteady compressible flow are given in this paper to develop the theory of unsteady fluid flow and to serve as the standard solutions for numerical calculations. The derivation procedure in this paper is not a general or classical mathematical one. Basically it is a trial and error method with the help of inspiration, experience, and fortune. A common means to simplify the derivation is to assume some parameters to be constant before deducing, sometimes even assuming that the physical dependent variables are given or constant and then to conversely derive the independent variables. In addition, since the main aim is to obtain explicit solutions of governing equations, the initial and boundary conditions are indeterminate before derivation and deduced from the solutions afterward. It makes the derivation procedure easier also. However, for a given analytical solution, its correctness can be proven easily by substituting it into the governing equations.

Contributed by the Fluids Engineering Division for publication in the JOURNAL OF FLUIDS ENGINEERING. Manuscript received by the Fluids Engineering Division June 25, 1997; revised manuscript received December 4, 1997. Associate Technical Editor: M. S. Cramer.

Analytical Solutions of 1-D Unsteady Flow Without Shock

Governing Equations. The governing equations for unidirectional 1-D unsteady flow of prefect gas can be derived as follows (Shapiro, 1954)

$$\frac{\partial \rho}{\partial t} + \rho \frac{\partial u}{\partial x} + u \frac{\partial \rho}{\partial x} + \rho u \frac{1}{A} \frac{dA}{dx} = 0$$

$$\frac{\partial u}{\partial t} + u \frac{\partial u}{\partial x} + \frac{1}{\rho} \frac{\partial p}{\partial x} + \sqrt{\frac{\pi}{A}} f u^2 = 0$$

$$(k-1)\rho\left(q + \sqrt{\frac{\pi}{A}} f u^3\right) = \frac{\partial p}{\partial t} + u \frac{\partial p}{\partial x} - k \frac{p}{\rho}\left(\frac{\partial \rho}{\partial t} + u \frac{\partial \rho}{\partial x}\right) \quad (1)$$

Generally, the functions of friction, heat transfer and area change $f(x, t)$, $q(x, t)$, and $A(x)$ are given, then the unknown analytical functions in Eq. (1) are $p(x, t)$, $\rho(x, t)$ and $u(x, t)$ which have to satisfy Eq. (1) as well as the following conditions: $p > 0$, $\rho > 0$, $A > 0$, $u \geq 0$ and $f \geq 0$. In addition, the sonic speed and Mach number can be expressed as:

$$a = \sqrt{kp/\rho} \quad (2)$$

$$M = u/a \quad (3)$$

Isentropic Flow Solutions. In this case, $f = 0$ and $q = 0$. three families of isentropic unsteady flow solutions can be derived with different area changes:

(1) A = const. A solution can be found as follows:

$$p = \text{const} = p_o$$

$$\rho = \text{arbitrary } \rho(x - u_o t)$$

$$u = \text{const} = u_o \quad (4)$$

The boundary and initial condition can be obtained by substituting given values of x and t into Eq. (4). It is the same for following solutions and will not superfluously dwell again. It is the simplest solution which represents the constant area, no friction, no heat transfer, constant velocity and pressure unsteady flow. The unsteadiness is owing to the fact that the density of inlet and outlet flow is variable. It can be obtained from Eq. (4) that $d\rho/dt = 0$ and $\rho = \rho(-u_o t)$ at $x = 0$. It

means that each gas particle travels in the path with constant density, only the density of gas particles at inlet changes with time, and all particles go ahead in sequence with their own density as moving solid particles.

(2) $A = C_3/(C_o x + C_2)$. A solution can be found as follows:

$$p = \text{const}$$

$$\rho = \text{const}$$

$$u = 2C_o(C_o x + C_2)/(2C_o^2 t + C_1) \tag{5}$$

It is a simple solution also, only area and velocity are variable and they offset each other to keep the density and then all thermodynamic parameters constant. So, it seems to be an incompressible solution as the density is constant. However, it can be treated as a special case of compressible solution with a finite sonic speed $a = \sqrt{kp/\rho} = \text{const}$.

When all constants C_i are positive, velocity and area are positive also, and velocity is a monotonically decreasing positive function of the time independent variable, $u \to 0$ when $t \to \infty$. The flow of this solution can be a subsonic, supersonic, or transonic flow depending on the interested time and geometric region as well as the values of various constants.

(3) $A = C_3(C_o x + C_2)^{[2/(k-1)C_6]^2-1}$. A solution can be found as follows:

$$p = C_4 R \left\{ \frac{2C_o(C_o x + C_2)}{\left[\frac{4}{(k-1)C_6^2} + 2\right] C_o^2 t + C_1} \right\}^{2k/(k-1)} \left(\frac{1}{C_6^2 kR}\right)^{k/(k-1)}$$

$$\rho = C_4 \left\{ \frac{2C_o(C_o x + C_2)}{\left[\frac{4}{(k-1)C_6^2} + 2\right] C_o^2 t + C_1} \right\}^{2/(k-1)} \left(\frac{1}{C_6^2 kR}\right)^{1/(k-1)}$$

$$u = 2C_o(C_o x + C_2) \Big/ \left\{ \left[\frac{4}{(k-1)C_6^2} + 2\right] C_o^2 t + C_1 \right\} \tag{6}$$

It can be deduced from Eqs. (2), (3), and (6) that the constant C_6 is actually the Mach number. Therefore, this solution is a constant Mach number flow. When all constants C_i are positive, the velocity and thermodynamic parameters—pressure, density and sonic speed for $x \geq 0$ are monotonically decreasing positive functions of the time independent variable, approaching to zero with $t \to \infty$. However, the total offset effect keeps the Mach number constant.

It can be seen from the flow area expression that $A = \text{const}$ when Mach number $M = 2/(k-1)$, and the flow path will be divergent or convergent when M is less or larger than $2/(k-1)$. The flow path will be a linear plane or linear conical divergent tube when $M = \sqrt{2}/(k-1)$ or $M = 2/[\sqrt{3}(k-1)]$.

It seems that for subsonic region the exponent in area expression would be too high and unrealistic. Actually, the gradient of area change can be small enough by selecting appropriate values of arbitrary constants C_o and C_2. For example, if $C_o \approx 10^{-3}C_2$, both total flow area change and its local gradient are small for $M > 0.5$ in the region $0 \leq x \leq 1$.

Constant Friction Coefficient and Constant Flow Area Solutions. In this case, $A = \text{const}$ and $f = \text{const}$. Let $\phi = f\sqrt{\pi/A} = \text{const}$ to simplify the expressions, some analytical solutions can be derived for different heat transfer functions as follows:

(4) $q = -1/(\phi^2 t^3)$, the solution can be found as follows:

$$p = \text{const}$$

$$\rho = \text{const}$$

$$u = 1/(\phi t) \tag{7}$$

It is a very simple solution also. The pressure and density keep constant and the velocity is a function of time only. The physical field at a certain time is a homogeneous field, but the velocity and cooling amount decrease with time. Because of the cooling effect and unsteady effect, the velocity along the flow path with friction and constant pressure can be constant at a certain time. The Mach number can be supersonic or subsonic depending on the values of various constants and the interested time region.

(5) $f = 0$ and $q = [k/(k-1)]p_o(C_1/C_5)[(C_1 x + C_3)/(C_1 t + C_2)]^{1+(C_4/C_1)}$. A solution can be found as follows:

$$p = \text{const} = p_o$$

$$\rho = C_5(C_1 t + C_2)^{C_4/C_1}/(C_1 x + C_3)^{1+(C_4/C_1)}$$

$$u = (C_1 x + C_3)/(C_1 t + C_2) \tag{8}$$

The heat transfer of this solution is unsteady also. When all constants are positive (C_4 can be excepted), the density and velocity are larger than zero and the heat transfer is heating, the Mach number can be subsonic, supersonic or transonic depending on the values of constants and the time and geometric region interested.

(6) $q = -[k/(k-1)]p_o[C_3\phi e^{-\phi x}(C_3\phi e^{-\phi x} + C_1)^{(C_4/C_1)+1}]/[C_5(C_1 t + C_2)^{(C_4/C_1)+1} e^{-\phi(C_4/C_1)x}] - \phi[(C_3 e^{-\phi x} + C_1/\phi)/(C_1 t + C_2)]^3$. A solution can be found as follows:

$$p = \text{const} = p_o$$

$$\rho = C_5[(C_1 t + C_2)e^{-\phi x}]^{C_4/C_1}/[C_3\phi e^{-\phi x} + C_1]^{(C_4/C_1)+1}$$

$$u = (C_3 e^{-\phi x} + C_1/\phi)/(C_1 t + C_2) \tag{9}$$

Similar to the former solution: the pressure is constant, the density and velocity are positive in the region $t > 0$ and $x > 0$ when all constants are positive (C_4 can be excepted). The flow can be subsonic, supersonic, or transonic but the heat transfer is cooling.

(7) $q = -[k/(k-1)]p_o\{C_1\phi \cdot \exp(-\phi x)/C_3 \cdot \exp[C_2 t + \phi x - C_2 \cdot \exp(\phi x)/(C_1\phi)]\} - \phi C_1^3 \cdot \exp(-3\phi x)$. A solution can be found as follows:

Nomenclature

A = flow area
a = sonic speed
C = constant
f = friction coefficient
k = specific heat ratio
M = Mach number
p = pressure
q = heat transfer per unit flow rate
R = gas constant
T = absolute temperature
t = time
u = velocity component in x direction
v = velocity component in y direction
x = abscissa
y = coordinate
ρ = density
$\phi = f\sqrt{\pi/A}$

Superscript

* = after shock

Subscripts

0, 1, 2, 3 . . . = different constant
f = shock front surface
r = shock rear surface

$$p = \text{const} = p_o$$

$$\rho = C_3 \cdot \exp[C_2 t + \phi x - C_2 \cdot \exp(\phi x)/(C_1 \phi)]$$

$$u = C_1 \cdot \exp(-\phi x) \tag{10}$$

In this case, pressure is constant and velocity is steady, only the heat transfer and density are unsteady. Actually, $q = -\phi u[(k/(k-1))(p_o/\rho) + u^2]$ and the heat transfer is cooling; in addition, $d\rho/dt = \phi u \rho$. In order to provide a positive velocity and density, C_1 and C_3 have to be larger than zero. If $C_2 = 0$, this solution degenerates into a steady one.

(8) $q = -C_1\sqrt{C_1/\phi} \cdot \{\exp[2\sqrt{C_1\phi}(t + C_2)] - 1\}/\{\exp[2\sqrt{C_1\phi}(t + C_2)] + 1\}\{[1/(k-1)] + \{\exp[2\sqrt{C_1\phi}(t + C_2)] - 1\}/\{\exp[2\sqrt{C_1\phi}(t + C_2)] + 1\}^2\}$. A solution can be found as follows:

$$p = -C_1\rho_o x + C_3$$

$$\rho = \text{const} = \rho_o$$

$$u = \sqrt{\frac{C_1}{\phi}} \cdot \frac{\exp[2\sqrt{C_1\phi}(t + C_2)] - 1}{\exp[2\sqrt{C_1\phi}(t + C_2)] + 1} \tag{11}$$

In this case, density is constant, pressure is steady and linear with geometric coordinate, velocity and heat transfer are unsteady but independent of geometric coordinate and actually $q = -u[(C_1/(k-1)) + \phi u^2]$. When $C_1 > 0$ and $C_2 > -t$, u is larger than zero; when $C_3 > C_1\rho_o x$, p is larger than zero. In addition, the heat transfer in this solution is cooling.

When friction disappears, the solution degenerates into $q = -C_1 u/(k-1)$ and $u = C_1(t + C_2)$, the expressions of p and ρ do not change.

Constant Flow Area and Variable Friction Coefficient Solutions. (9) If $f = f(t)$ and $q = -Af(t)/\{\pi[\int f(t)dt]^3\}$, a set of solutions can be found as:

$$p = \text{const}$$

$$\rho = \text{const}$$

$$u = \sqrt{A} \Big/ \left[\sqrt{\pi} \int f(t)dt\right] \tag{12}$$

Actually, the solution (4) is a special case of this solution with $f(t) = \text{const}$. If $\int f(t)dt$ can be integrated to obtain an explicit expression, then the analytical solution is easy to be derived.

Therefore, there are infinite solutions in this case.

(10) Let $f = -\sqrt{A/\pi}(\partial p/\partial x)/\rho_o u_o^2$, $q = [(\partial p/\partial t) + u_o(\partial p/\partial x)]/[(k-1)\rho_o] - \sqrt{\pi} f u_o^3/\sqrt{A}$, then the solution will be:

$$p = \text{arbitrary } p(x, t)$$

$$\rho = \text{const} = \rho_o$$

$$u = \text{const} = u_o \tag{13}$$

It is a simple solution also, the density and velocity are constant, only the pressure (as well as the friction coefficient and heat transfer) is the function of time and location. It can be deduced from the expression of f that $\partial p/\partial x$ has to be not larger than zero to ensure $f \geq 0$. In addition, there are infinite solutions also in this case and it is easier to obtain analytical solutions comparing with the former case since only differentiation exists in the expressions, and arbitrary analytical functions are differentiable in principle.

For example, if $p = -\rho_o u_o^2\{C_1 \exp(-C_2 t) + C_3\}x + C_4\}\sqrt{\pi/A}$, then $f = C_1 \exp(-C_2 t) + C_3$ and $q = \sqrt{\pi} u_o^2\{C_1 C_2 \exp(-C_2 t)x - k u_o[C_1 \exp(-C_2 t) + C_3]\}/[(k-1)\sqrt{A}]$.

Solutions With Area Change (11) If $A = A(x)$, $f = 0$ and $q = [k/(k-1)] \cdot (p_o u_o/A) \cdot (dA/dx)/\{C_2 \cdot \exp[C_1 x/u_o - \ln A(x) - C_1 t]\}$, a set of solutions will be found as follows:

$$p = \text{const} = p_o$$

$$\rho = C_2 \cdot \exp[C_1 x/u_o - \ln A(x) - C_1 t]$$

$$u = \text{const} = u_o \tag{14}$$

The constant C_2 in this solution has to be larger than zero to ensure $\rho > 0$. The heat transfer is cooling or heating when the area change is convergent or divergent. The expression of heat transfer can be simplified as $q = [k/(k-1)] \cdot (p_o u_o/\rho A) \cdot (dA/dx)$.

(12) If $A = [C_4 \cdot \exp(-\sqrt{\pi/C_1} \cdot x) + \sqrt{C_1/\pi}]^{-1}$, $f = \{C_1[C_4 \cdot \exp(-\sqrt{\pi/C_1} \cdot x) + \sqrt{C_1/\pi}]\}^{-1/2}$ and $q = -\sqrt{\pi/C_1}\{C_2[C_4 \cdot \exp(-\sqrt{\pi/C_1} \cdot x) + \sqrt{C_1/\pi}]/(C_2 t + C_3)\}^3$, a solution can be found as follows:

$$p = \text{const} = p_o$$

$$\rho = \text{const} = \rho_o$$

$$u = C_2[C_4 \exp(-\sqrt{\pi/C_1} \cdot x) + \sqrt{C_1/\pi}]/(C_2 t + C_3) \tag{15}$$

The expression of q in this case can be simplified as $q = -\sqrt{\pi/C_1} \cdot u^3$.

(13) if $A = C_4/(C_1 x + C_3)$, $f = C_5[C_4/(C_1 x + C_3)]^{n/2}$ and $q = -\sqrt{\pi} C_5 C_4^{(n-1)/2} \cdot (C_1 x + C_3)^{(7-n)/2} \cdot [(7-n)k - 4]/[(7-n)(k-1)(C_1 t + C_2)^3]$, a solution can be found as follows (n is a constant):

$$p = -2\rho_o C_5\sqrt{\pi} C_4^{(n-1)/2}(C_1 x + C_3)^{(7-n)/2}/[C_1(7-n)(C_1 t + C_2)^2] + C_6$$

$$\rho = \text{const} = \rho_o$$

$$u = (C_1 x + C_3)/(C_1 t + C_2) \tag{16}$$

All parameters (except q) can be positive in a semi-infinite region of (x, t) provided that each constant C_i is positive. In addition, it is necessary that $n \neq 7$ to ensure p is not infinite.

Analytical Solutions of 1 D Unsteady Flow With Shock

Governing Equations. The governing relations for the parameters just in front of and behind the normal shock in 1-D flow are shown as follows (Shapiro, 1954):

$$M_r^2 = [M_f^2 + 2/(k-1)]/[2kM_f^2/(k-1) - 1]$$

$$T_r/T_f = 2(k-1)[1 + (k-1)M_f^2/2][2kM_f^2/(k-1) - 1]/[(k+1)M_f]^2$$

$$p_r/p_f = [2kM_f^2 - (k-1)]/(k+1)$$

$$\rho_r/\rho_f = (p_r/p_f)/(T_r/T_f)$$

$$u_r/u_f = \rho_f/\rho_r$$

$$A_r = A_f \tag{17}$$

Similar to common practice it is assumed that the thickness of the shock is infinite thin. In addition, the geometric position of the shock is considered steady, only the absolute strength of shock and the parameters in the upstream and downstream fields of the shock are unsteady. Therefore, there are no unsteady terms in Eq. (17). Furthermore, it is assumed that there is only one shock in the flow field which position is at $x = 0$; the flow is isentropic outside the shock. Then, the duty to establish an analytical solution of an unsteady 1-D flow with shock is equivalent to finding out unsteady analytical solutions of isentropic flow in the region $x \leq 0$ and $x \geq 0$ respectively, and their parameters at $x = 0$ have to satisfy Eq. (17).

Unsteady Analytical Solution. (14) It is found out that the abovementioned isentropic constant Mach number solution (3) can be modified to satisfy Eq. (17), which expressions are as follows:
In the region $x < 0$:

$$u = 2C_o(C_o x + C_2) \Big/ \left\{ C_o^2 \left[\frac{4}{(k-1)M_f^2} + 2 \right] t + C_1 \right\}$$

$$T = u^2/(kRM_f^2)$$

$$p = C_4 R T^{k/(k-1)}$$

$$\rho = C_4 T^{1/(k-1)}$$

$$A = C_3(C_o x + C_2)^{[2/(k-1)M_f]^2-1} \tag{18}$$

and in the region $x > 0$:

$$u^* = 2C_o^*(C_o^* x + C_2^*) \Big/ \left\{ C_o^{*2} \left[\frac{4}{(k-1)M_r^2} + 2 \right] t + C_1^* \right\}$$

$$T^* = u^{*2}/(kRM_r^2)$$

$$p^* = C_4^* R T^{*k/(k-1)}$$

$$\rho^* = C_4^* T^{*1/(k-1)}$$

$$A^* = C_3^*(C_o^* x + C_2^*)^{[2/(k-1)M_r]^2-1} \tag{19}$$

The constants C_i and C_i^* are not independent, the relations between them are as follows:

$$C_o^* = C_o \sqrt{\{4/[(k-1)M_f^2] + 2\}/\{4/[(k-1)M_r^2] + 2\}}$$

$$C_1^* = C_1$$

$$C_2^* = C_2$$

$$C_3^* = C_3 \cdot C_2^{[2/(k-1)]^2(1/M_f^2 - 1/M_r^2)}$$

$$C_4^* = C_4 \frac{2kM_f^2 - k + 1}{k+1} \times \left\{ \frac{(k+1)^2 M_f^2}{2(k-1)[1 + (k-1)M_f^2/2][2kM_f^2/(k-1) - 1]} \right\} \tag{20}$$

M_f and M_r in abovementioned relations are the constant Mach number in front of and in rear of the shock, they are not independent and have to satisfy the first equation of relations (17) and M_f has to be larger than unity.

If each C_i is positive and $C_2 > -C_o x_{\min}$ ($x_{\min} < 0$ which is the minimum value of x in the region of interest), then all thermodynamic parameters, velocity and flow area will be positive.

The one-dimensional flow area of this solution is continuous along the flow path. However, the flow area gradient is not continuous at the shock position, it means the flow channel has a corner at $x = 0$. If $M_f > 2/(k-1)$, the flow channel is convergent in front of the shock and divergent after the shock, if $M_f < 2/(k-1)$, whole channel is divergent but the divergence angle is larger in rear of the shock, if $M_f = 2/(k-1)$ the channel area is constant in front of the shock but still divergent after the shock.

The initial and boundary conditions can be derived from Eqs. (18) and (19) with given initial time value and geometric boundary values. The variations of Mach number, flow area and velocity of this solution are presented in Figs. 1, 2, and 3 with $k = 1.4$, $M_f = \sqrt{2}$, $C_o = C_1 = C_3 = C_4 = 1$ and $C_2 = 100$. The variations of temperature, pressure, and density are qualitatively similar to the variation of velocity.

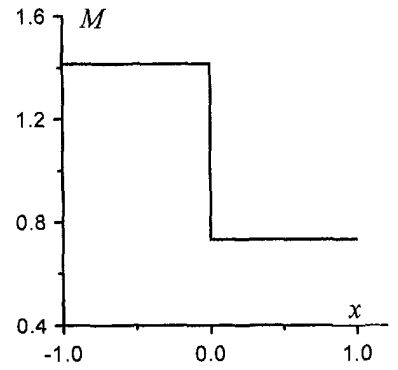

Fig. 1 The variation of Mach number

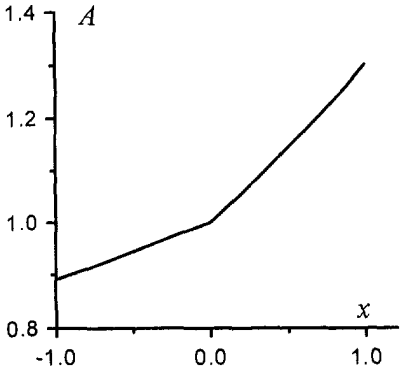

Fig. 2 The variation of flow area

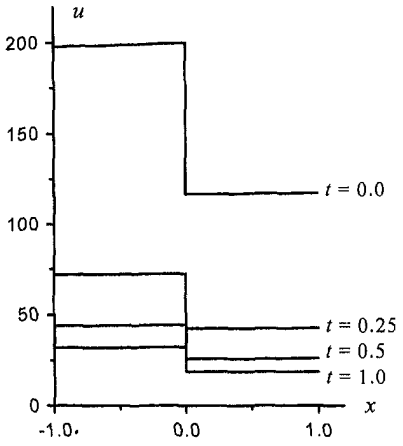

Fig. 3 The variation of velocity

Analytical Solution of 2-D Unsteady Isentropic Flow

Governing Equations. The governing equations for 2-D unsteady isentropic flow of perfect gas are as follows:

$$\frac{\partial \rho}{\partial t} + \frac{\partial(\rho u)}{\partial x} + \frac{\partial(\rho v)}{\partial y} = 0$$

$$\left(\frac{\partial}{\partial t} + u\frac{\partial}{\partial x} + v\frac{\partial}{\partial y} \right) u + \frac{1}{\rho}\frac{\partial p}{\partial x} = 0$$

$$\left(\frac{\partial}{\partial t} + u\frac{\partial}{\partial x} + v\frac{\partial}{\partial y}\right)v + \frac{1}{\rho}\frac{\partial p}{\partial y} = 0$$

$$p/\rho^k = \text{Const.}$$

$$p = \rho RT \tag{21}$$

Analytical Special Solution. (15) It is found out that an explicit analytical special solution of governing equations (21) can be expressed as follows:

$$u = 2C_oC_5[C_o(C_5x - \sqrt{1 - C_5^2}y) + C_2][(k+1)C_o^2t + C_1]^{-1} + C_3\sqrt{1 - C_5^2}$$

$$v = -2C_o\sqrt{1 - C_5^2}[C_o(C_5x - \sqrt{1 - C_5^2}y) + C_2][(k+1)C_o^2t + C_1]^{-1} + C_3C_5$$

$$p = C_4R(k-1)^{2k/(k-1)}(kR)^{-k/(k-1)}C_o^{2k/(k-1)}[C_o(C_5x - \sqrt{1 - C_5^2}y) + C_2]^{2k/(k-1)}[(k+1)C_o^2t + C_1]^{-2k/(k-1)}$$

$$\rho = C_4(k-1)^{2/(k-1)}(kR)^{-1/(k-1)}C_o^{2/(k-1)}[C_o(C_5x - \sqrt{1 - C_5^2}y) + C_2]^{2/(k-1)}[(k+1)C_o^2t + C_1]^{-2/(k-1)}$$

$$T = (k-1)^2(kR)^{-1}C_o^2[C_o(C_5x - \sqrt{1 - C_5^2}y) + C_2]^2[(k+1)C_o^2t + C_1]^{-2} \tag{22}$$

The reasonable range of constant C_5 is $|C_5| \leq 1$. When $C_5 = 1$, the solution (22) degenerates into an analytical solution with constant velocity component v; when $C_5 = 1$ and $C_3 = 0$, it degenerates further into a one-dimensional unsteady solution with constant Mach number $M = 2/(k-1)$.

The initial and boundary conditions of solution (22) can be derived by setting up the boundaries of time and space regions of interest. It represents an unsteady supersonic flow with unsteady boundary. The general shape of the unsteady flow line is an inclined logarithmic curve. For example, when $C_5 = 0$ the expression of the unsteady flow lines can be integrated as:

$$y = C_3[(k+1)C_o^2t + C_1]\ln(C_ox + C_2)/C_o^2 + C_6 \tag{23}$$

Figure 4 represents the variation of streamlines with time when $C_o = 1$, $C_1 = 1$, $C_2 = 1$, $C_3 = 0.5$, $C_5 = 0$, $C_6 = 0$ and 0.6 as well as $k = 1.4$.

Summary

Some explicit analytical solutions of unsteady compressible flow have been derived and given, which include 1-D isentropic unsteady flow, 1-D constant friction coefficient and constant channel area unsteady flow with heat transfer, 1-D constant channel area unsteady flow with variable friction coefficient and heat transfer, 1-D unsteady flow with variable channel area, friction coefficient and heat transfer, 1-D isentropic unsteady flow in front of and in rear of an unsteady absolute strength shock and 2-D isentropic unsteady flow.

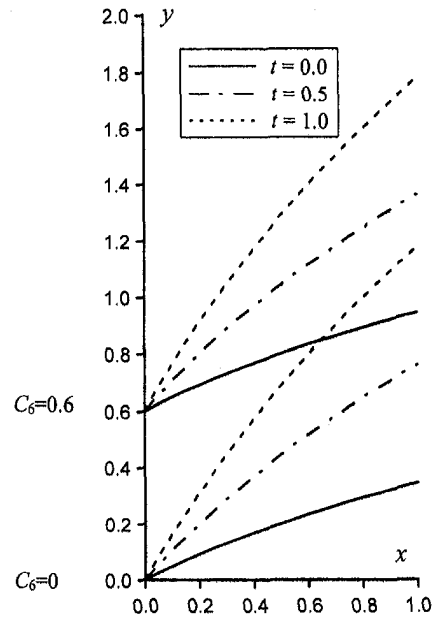

Fig. 4 The variation of streamline

According to the knowledge of the author, no analytical unsteady compressible solutions have been published in the open literature. The abovementioned solutions will be valuable to the theory of unsteady aerodynamics, especially to the CFD as the standard solutions to check the numerical solutions and to develop the numerical computation approaches such as the differencing schemes, grid generation methods and so forth.

Acknowledgment

The study is supported by the Chinese National Key Fundamental Research Project No. 85-39 and Project 59546007 of National Science Foundation of China.

The solution (1) is proposed by a referee to generalize the original solution $\rho = C_2\exp[C_1(x - u_ot)/u_o]$ given by the author as a special case of solution (11).

References

Cai, R., Jiang, H., and Sun, C., 1984, "Some Analytical Solutions Applicable to Verify 3-D Numerical Methods in Turbomachines," IMechE Conf. Publications C80/84, pp. 255–263.

Gong, Y., and Cai, R., 1989, "3D MSLM—A new Engineering Approach to the Inverse Problem of 3D Cascade," ASME paper 89-GT-48.

Shapiro, A. H., 1954, *The Dynamics and Thermodynamics of Compressible Fluid Flow*, The Ronald Press, New York.

Shen, M., Liu, Q., and Zhang, Z., 1996, "Calculating 3-D Transonic Flow of Turbomachine in the Generalized von Mises Coordinates," *Scientia in China* (Series E), Vol. 29, No. 4, pp. 325–332 (in Chinese).

Xu, J., et al., 1989, "Three Dimensional Imcompressible Flow Solution of an Axial Compressor Using Pseudostream-Functions Formulation," ASME paper 89-GT-319.

Zhu, S., and Liu, Z., 1988, "An Investigation of Numerical Method of 3-D Flow Field in the Blade Passage of Centrifugal Pump (Compared with Analytical Solution)," *Journal of Engineering Thermophysics*, Vol. 9, No. 3, 242–244. (in Chinese).

Turbulence Measurements of a Longitudinal Vortex Generated by an Inclined Jet in a Turbulent Boundary Layer

X. Zhang
Senior Lecturer,
Department of Aeronautics
and Astronautics,
University of Southampton,
Southampton SO17 1BJ, United Kingdom

A longitudinal vortex in a flat-plate turbulent boundary layer was examined in a wind tunnel experiment using Laser Doppler Anemometry. The vortex was produced by an inclined round jet ($D = 14$ mm) in the turbulent boundary layer ($\delta_{0.99} \approx 25$ mm). The jet nozzle was positioned at pitch and skew angles of 45 deg to the oncoming stream, and the jet speed ratios (jet speed/freestream flow speed) were 0.5, 1.0, and 1.5. The flow was characterized by embedded vortices, induced high turbulent kinetic energy peak, local areas of high primary shear stress, and negative shear stress. Two types of normal stress evolution were observed: (a) low normal stress beneath the vortex on the upwash side and high normal stress above the center of the vortex, caused by spanwise momentum transfer and local turbulent production; (b) high normal stress beneath the vortex on the upwash side and high normal stress coinciding with the center of the vortex, produced by spanwise and transverse momentum transfer of a vortex away from the wall with turbulent convection playing an important role. The study provided a database for numerical modeling effort.

1 Introduction

It has been known that a longitudinal vortex, once created, is able to maintain its strength in a boundary layer (Shabaka et al., 1985). Thus it is possible to utilize the vortex and/or a spanwise distribution of vortices to create (*i*) spanwise momentum transfer, and (*ii*) transverse convection. Possibilities then exist for turbulent flow control, including heat transfer enhancement and separation/stall prevention, etc. The arrangement of the vortex or vortices in terms of the size and position within the boundary layer is itself a complex issue, which is further complicated when the vortices are produced by various means, e.g., vanes, winglets and jets (Wallis, 1956). Studies based on one device will not necessarily be applicable to another. In the past, longitudinal vortices generated by vanes and winglets have been studied extensively (Bushnell, 1993). The purpose of this study is to examine the turbulent stress in a flat-plate turbulent boundary layer with an embedded longitudinal vortex generated by an inclined jet. It follows an earlier experimental examination of the mean properties of the flow (Zhang and Collins, 1997).

Past studies with direct relevance to the present study were performed by Wallis (1956), Johnston and his co-workers (Johnston and Nishi, 1990 and Compton and Johnston, 1991), Zhang and Collins (1993), Zhang (1995), and Selby et al. (1992) where either an inclined jet or an array of jets were used. Past measurements have concentrated on the mean flow features. Among these studies Johnston and Nishi (1990) and Compton and Johnston (1991) performed well-executed measurements. A survey of the past studies suggests that there is a lack of information on the turbulent stress field, which is important in validating numerical models. A closely related area is the research on solid vortex generators, which has produced databases of turbulent stress field. Shabaka et al. (1985) showed that the circulation around the vortex embedded in the boundary layer was almost conserved, being reduced only by the spanwise-component of the surface shear stress. The behavior of the various components of eddy viscosity suggested that simple empirical correlations for these quantities used in a number of turbulence models are not likely to yield accurate flow predictions. Cutler and Bradshaw (1993) measured a similar flow field but with a different arrangement of vortex generator. They also showed the complexity of the flow near the separation line and in the vortices and the interaction was expected to be difficult to model. Shizawa and Eaton (1992) measured longitudinal vortex development in a three-dimensional turbulent layer. They pointed out the existence of a negative primary stress area in the boundary layer. These studies are experimental in nature and were performed with either hot-wire anemometry or pressure probes. In the current study, we examine the inclined jet induced vortex flow and cover an area spanning the near-field where the primary vortex is formed and far-field where the dominant physics are turbulent production and dissipation. It is reasonable to believe the flow field would be at least equally complicated.

2 Description of Experiment

The experimental study formed part of an overall investigation of streamwise vortices generated by air jets, including numerical simulation (Zhang and Collins, 1993). The model tests were conducted in the R. J. Mitchell wind tunnel, which has a low speed closed circuit with a 3.5 m × 2.6 m test section. The tests were run at a freestream speed (U_∞) of 20 m/s. The freestream turbulence level was 0.3 percent. In the tests, a round jet nozzle was attached to a flat-plate with its exit flush with the plate surface (Fig. 1). The jet interacts with the oncoming boundary layer. A sketch of the test arrangement is given in Fig. 1, where the local Laser Doppler Anemometry (LDA) measurement coordinates are employed. The plate was 2.43 m in length and 10 mm in thickness with an elliptic leading edge (Fig. 1(*b*)). It was installed across the span of the test section at a height of 0.9 m above the tunnel floor. The boundary-layer transition was fixed by a 10 mm wide sand band located 100 mm downstream of the leading edge. A flat-plate boundary layer was produced by this arrangement (see Fig. 2). Spanwise measurements confirmed the boundary layer was two-dimen-

Contributed by the Fluids Engineering Division for publication in the JOURNAL OF FLUIDS ENGINEERING. Manuscript received by the Fluids Engineering Division May 12, 1997; revised manuscript received July 6, 1998. Associate Technical Editor: J. K. Eaton.

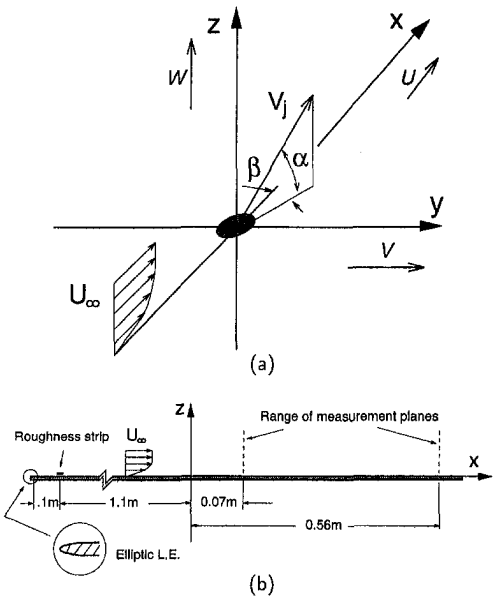

Fig. 1 Schematics of (*a*) coordinates system based on LDA measurement coordinates and (*b*) model dimensions

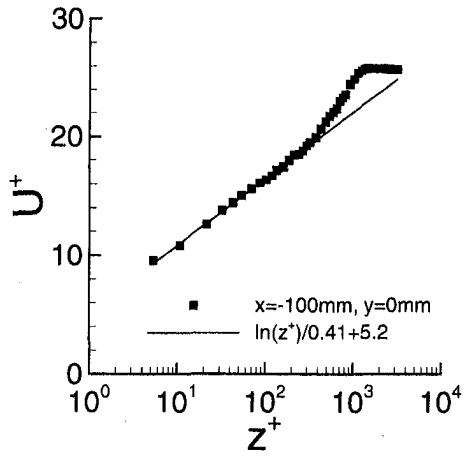

Fig. 2 Mean oncoming flow profile and the logarithmic law-of-the-wall

sional with a skin friction coefficient of 0.0033 at $x = -100$ mm (Zhang and Collins, 1997). The jet nozzle was formed by a straight, round tube of 14 mm diameter. The length of tube was 100 mm. The tube was connected to a compressed air supply and pressure controlled by a Fisher valve. The pitch angle of the jet, α, and the skew angle, β, were 45 deg. The velocity ratios (ratio of jet speed/freestream speed), λ, were 0.5, 1.0, and 1.5.

For each flow setting, Laser Doppler Anemometry (LDA) measurements were conducted on cross-planes (normal to the wall) at $x = 5$, 10, 20, 30, and $40D$. The LDA system is a three-component DANTEC system. It consists of a 5 W Ar-ion laser generator, a 60 × 33 safety cover, a 60 × 40 transmitter, six 60 × 24 Fibre manipulators, two 60 × 10/60 × 11 transducers, two 55 × 12 expanders, and two 55 × 59 lenses. Seeding was provided by two DANTEC 55L18 seeding generators. The seedings were released into the nozzle flow after the Fisher valve; we found this practice created very small disturbances to the flow. The number of measurement points in a plane ranged from 720 to 790. The nearest sampling point was 0.95 mm from the wall. The LDA signals were analyzed using three DANTEC Burst Spectrum Analyzers. On average, a total of 5000 bursts (instantaneous samples) were collected for each point. The typical coincidence rate was above 30 percent, which gave at least 1500 samples per point for the stress analysis. The measured data are presented in terms of velocity vectors, streamwise vorticity, normal stresses ($\overline{uu}$, $\overline{vv}$, $\overline{ww}$), shear stresses ($\overline{uv}$, $\overline{vw}$, $\overline{uw}$), and stress production and convection. Natural cubic splines were used to obtain the derivatives of U, W, V with respect to the measurement coordinates x, y, z.

In presenting the data, unless otherwise stated the velocity is normalised by U_∞ and length scales by D.

The likely uncertainties in the mean flow and positional measurements were given by Zhang and Collins (1997). Uncertainty in the pitch and skew angles of the jet is ±0.25 deg. Uncertainty in the measurement position is approximately ±0.16 mm. For the turbulent stress measurements, an estimation of the 95 percent uncertainties was obtained following the procedures given by Benedict and Gould (1996). In Fig. 3, examples are given of uncertainties of normal stress, $\overline{uu}$, and primary shear stress, $-\overline{uw}$, measurements. Typical values are: $\overline{uu}$, $\overline{ww} < \pm 13$ percent; $\overline{vv}$, $\overline{uv}$, $\overline{vw} < \pm 16$ percent; and $\overline{uw} < \pm 13$ percent. As the number of samples varied in the measurement, the estimation of the final uncertainties was difficult. The above numbers represented the worst cases. In general, it was found that around the center of the vortex and near the wall the uncertainties were higher. The smoothness of the results suggested that the actual uncertainties were better than the numbers quoted above.

3 Results and Discussion

Major features of the mean flow field were discussed by Zhang and Collins (1997). Here, only a summary of the measured vortex parameters are listed in Table 1. We note in Table 1 the circulation level, Γ, is listed. In calculating Γ, we have neglected the contribution from data with $\Omega \geq -0.02$ to avoid misleading results due to noise. The data are provided in aid of later discussions of turbulent stress evolution. In presenting the results, we often use the term "near-field." In fact, for the current vortex flow, it is rather difficult to define a near-field. If we were to use the formation of a single, dominant vortex as a guide, then the near-field would end between $x = 5D$ and $10D$ for the present flow. It is worth noting from the mean flow study that the secondary flow at the three jet speeds is characterized by a longitudinal vortex, which in appearance is similar to that generated by a winglet/vane (Shizawa and Eaton,

Nomenclature

D = jet hydraulic diameter
U, V, W = mean velocity components in x, y, z directions
U^+ = dimensionless, sublayer-scaled, velocity, U/u_τ
u, v, w = fluctuating velocity components in x, y, z directions
u_τ = friction velocity
x, y, z = cartesian coordinates
z^+ = dimensionless, sublayer-scaled, distance, $u_\tau z/\mu$
α = jet pitch angle
β = jet skew angle
λ = jet velocity ratio, V_j/U_∞
Ω = longitudinal vorticity, $(\partial W/\partial y - \partial V/\partial z)D/U_\infty$
Γ = circulation level normalized by U_∞/D^3

Subscripts

( )$_\infty$ = free-stream condition
( )$_j$ = jet flow condition

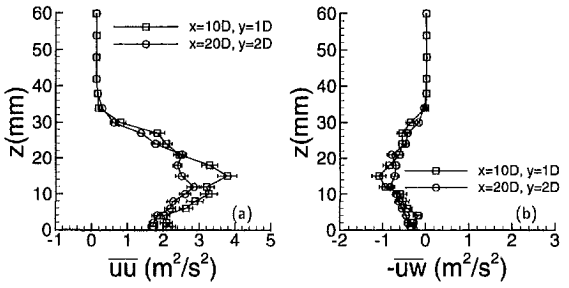

Fig. 3 Examples of 95 percent uncertainty in normal and shear stress measurements across the boundary layer: (*a*) $\overline{uu}$ and (*b*) $-\overline{uw}$

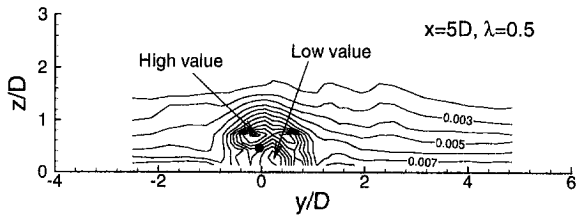

Fig. 4 $\overline{uu}/U_\infty^2$ contours at λ = 0.5. ●—center of the vortex

1992). However, it does have its own special characters. An area of counter-rotating vorticity exists to the right of the main vortex. This is more apparent at $x = 5D$ for the λ = 1.5 jet, where a counter-rotating vortex exists in the secondary vectors (see Zhang and Collins, 1997). This particular feature will introduce a convective mechanism into the secondary flow. Between $x = 5D$ and $10D$, this counter-rotating vortex disappears and the main vortex dominates. The strength of the vortex quantified by the magnitude of Ω drops sharply after the first measurement station at $x = 5D$ (see Table 1). We have noticed that after $x \approx 30D$, the reduction in circulation level, Γ, and Ω is small but the size of the vortex is increased. At λ = 1.0, the measured Γ drops from −0.612 at $x = 5D$ to −0.464 at $x = 10D$, −0.342 at $x = 20D$ and −0.263 at $x = 30D$. This suggests that the turbulence dissipation begins to play a bigger role. One interesting feature of the mean flow is the relative position of the local maximum vorticity (Ω_m) to the center of vortex. At λ = 0.5 and 1.0, and λ = 1.5 at $x = 5D$, the position of the maximum local vorticity lies to the right and beneath the center of vortex on the upwash side (Compton and Johnston, 1991). A similar feature was also discussed by Westphal (1987). In the case of λ = 1.0, Ω_m always lies about $0.3D$ beneath the center. However, at λ = 1.5 the location of the maximum local vorticity and the center of vortex coincide, suggesting a different type of vortex development.

The normal stress distributions are found to be rather similar. As such we only present examples of normal stress in the longitudinal direction ($\overline{uu}$ in Figs. 4–6) at selected locations. For all the normal stresses, the affected area inside the boundary layer is obviously increased as the vortex size enlarges downstream, and their maximum values are reduced. As to the magnitude, all normal stresses seem to be comparable with each other. At $x = 5D$, the measured normal stress values are high. This is caused by the wake after the jet and the value quickly decreases downstream at the three jet speed ratios. The characteristics of the $\overline{uu}$ distribution are different for the three jets. At λ = 0.5 the main vortex cannot be observed at $x = 40D$. As the result of the break-up of the vortex, the $\overline{uu}$ distribution is similar to that of a typical two-dimensional turbulent boundary layer. At $x = 5D$, local areas of high $\overline{uu}$ distribution are located above the center of the vortex and a local area of low $\overline{uu}$ distribution beneath it. At $x = 20D$, a local peak value can still be observed but this feature quickly disappears and at $x = 40D$ is no longer present. An interesting feature is that the local high $\overline{uu}$ is located above the center of the vortex and the local low $\overline{uu}$ beneath it and to the right side (on the upwash side). This feature is also present for the λ = 1.0 flow but not for the λ = 1.5 flow (see the following discussion). At λ = 1.0 (Fig. 5), the characteristics of the $\overline{uu}$ distribution are broadly similar to those at λ = 0.5, though the λ = 1.0 jet is seen to produce larger modification to the flat plate boundary layer. At $x = 5D$, the cross-plane distribution of $\overline{uu}$ shows two local areas of high $\overline{uu}$ distribution, on both sides of the center of vortex. The one to the left is located slightly below of the center of the vortex and the one to the right is located slightly above. This feature is similar to that of a normal jet in cross-flow where two contra-rotating vortices roll up inside the jet. In the present flow, the high $\overline{uu}$ distribution is closely associated with the forming of the main vortex and will eventually dominate the flow. One can surmise that for the λ = 0.5 jet this feature could still exist at an upstream cross-plane but disappears following the formation of the main vortex. At λ = 1.5 (Fig. 6), the characteristics of the $\overline{uu}$ distribution differs from those at λ = 1.0. It is clear that the boundary layer is modified significantly by the embedded vortex. Initially though at $x = 5D$ the cross-plane distribution of $\overline{uu}$ is similar to the λ = 1.0 flow in that there are again two local areas of high $\overline{uu}$ distribution, on both sides of the center of the vortex. Farther downstream of $x = 5D$, the normal stress distribution shows different characteristics. We have seen that at λ = 1.0 the local area of high $\overline{uu}$ is located above the center of the vortex to the right. The local area of low $\overline{uu}$ is located beneath the center and to the right on the upwash side. However, at λ = 1.5, this feature is not present. Instead, the local area of high $\overline{uu}$ coincides with the center of the vortex. The local area of low $\overline{uu}$ beneath the center of the vortex is rather small and is located slightly to the left on the downwash side. On the upwash side there is an area of high normal stress on the downwash side.

In analyzing the evolution of the normal stress, we examined the turbulence production and convection of the stresses (Shizawa and Eaton, 1992) and concentrated on $\overline{uu}$. We employed the cartesian tensor notation. The turbulence production of stress τ_{ij} is given as $-\tau_{ik}\partial\bar{v}_j/\partial x_k - \tau_{jk}\partial\bar{v}_i/\partial x_k$ and the convection term is given as $\bar{v}_k\partial\tau_{ij}/\partial x_k$. In calculating these terms we assumed a "slender flow" and omitted the contribution due to

Table 1 Vortex development

	λ = 0.5			λ = 1.0			λ = 1.5		
	$x = 5D$	$20D$	$40D$	$x = 5D$	$20D$	$40D$	$x = 5D$	$20D$	$40D$
Ω_c	−0.387	−0.072	n/a	−0.769	−0.156	−0.105	−1.389	−0.612	−0.339
y_c/D	−0.039	0.621	n/a	0.244	0.653	0.969	0.252	0.553	0.991
z_c/D	0.462	0.718	n/a	0.732	0.863	1.079	1.154	1.519	1.679
Ω_m	−0.435	−0.087	n/a	−1.025	−0.206	−0.198	−1.725	−0.632	−0.341
y_m/D	0.056	0.614	n/a	0.353	0.915	1.210	0.409	0.555	1.028
z_m/D	0.395	0.439	n/a	0.434	0.569	0.794	1.067	1.458	1.672
Γ	−0.350	−0.331	−0.031	−0.612	−0.342	n/a	−1.284	−0.991	−0.749

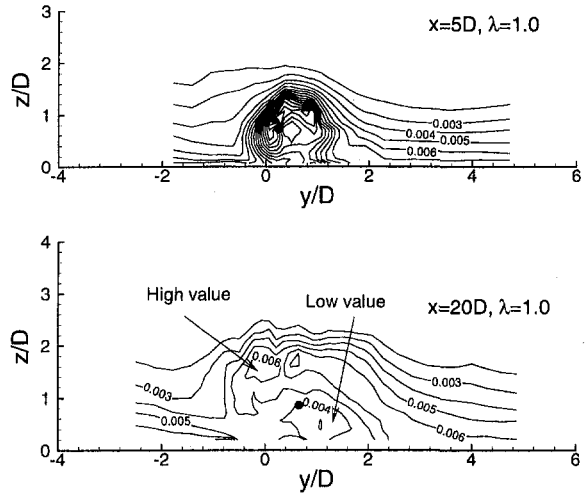

Fig. 5 $\overline{uu}/U_\infty^2$ contours at $\lambda = 1.0$

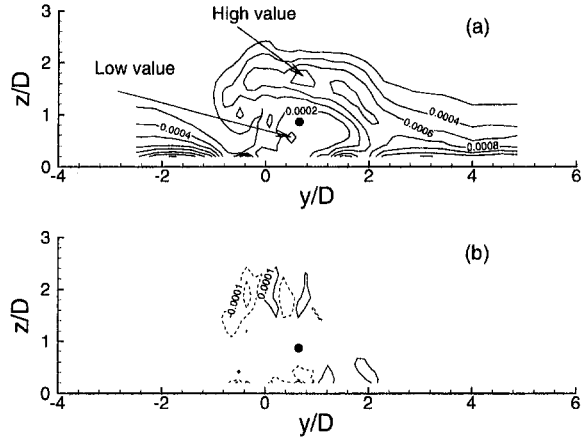

Fig. 7 (*a*) Turbulence production of $\overline{uu}$ at $\lambda = 1.0$ and $x = 20D$; (*b*) turbulence convection of $\overline{uu}$. Contour variables normalized by U_∞^3/D.

the longitudinal flow variation. In Fig. 7 the dominant physics in the stress production is the turbulence production term. The local low value area in the turbulence production is located beneath the center of the vortex and coincides with the local area of low normal stress on the upwash side of the vortex. This feature also exists at $\lambda = 0.5$, indicating the same physics. The convection term, in contrast, is rather weak. It is also important to note that there are no negative areas in the normal stress turbulence production at this location. An examination of the turbulence production and convection of the normal stress at $\lambda = 1.5$ reveals different characteristics, pointing to different physics (Fig. 8). First, in the turbulence production distribution, a local high value area is located beneath the center of the vortex and on the upwash side. This contributes to the observed high normal stress in that area. Equally important is the contribution from the convective mechanism (Fig. 8(*b*)), which differs from that at $\lambda = 1.0$. Also at $\lambda = 1.5$, an area of low turbulence production occupies an area surrounding the center of the vortex, leading to rapid reduction in the normal stress in that area. It seems that the $\lambda = 0.5$ and 1.0 jets possess a different physical mechanism in modifying the near-wall flow than the $\lambda = 1.5$ jet. The vortex flows generated by the $\lambda = 0.5$ and 1.0 jets create vortices embedded inside the boundary layer. The vortices generate areas of local velocity variation, leading to production (or reduction) of the normal stress in the near-wall region. At $\lambda = 1.5$, a vortex of much larger strength is produced and located farther away from the wall. This vortex creates spanwise and transverse momentum transfer, much in the traditional winglet/vane vortex generator fashion. Partly as a result of the convective mechanism, a local area of high normal stress is produced beneath the center of the vortex and on the upwash side. It seems that although the modifications to the normal stress field in the boundary layer are significant, the effect on the near-wall region is perhaps not as effective as the $\lambda = 0.5$ and 1.0 jets. This observation has implications in turbulent flow control applications. The stress distributions possess features similar to those in a solid vortex generator flow. There are other different features. For example, the local area of high normal stress near the core of the vortex, though significant, does not have the large, almost singular feature as that reported by Cutler and Bradshaw (1993). There may be several reasons for this: the vortex is embedded in the boundary layer and thus the turbulence diffusion plays an important role; and the jet flow allows for less longitudinal velocity drop than that in a winglet/vane flow.

The measured shear stresses also point to a bigger distortion in the boundary layer at $\lambda = 1.5$. The measured primary shear

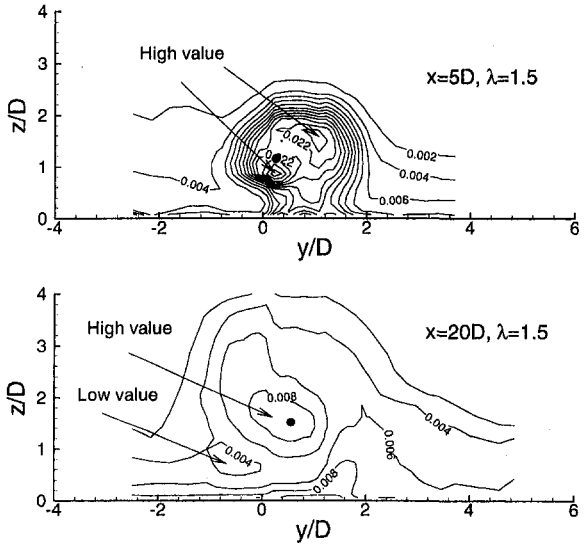

Fig. 6 $\overline{uu}/U_\infty^2$ contours at $\lambda = 1.5$

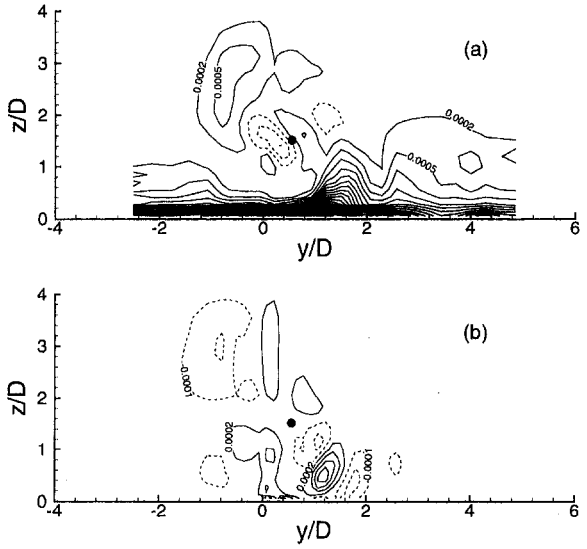

Fig. 8 (*a*) Turbulence production of $\overline{uu}$ at $\lambda = 1.5$ and $x = 20D$; (*b*) turbulence convection of $\overline{uu}$. Contour variables normalised by U_∞^3/D.

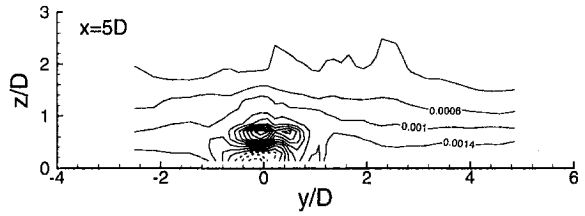

Fig. 9 $-\overline{uw}/U_\infty^2$ contours at $\lambda = 0.5$

stress $-\overline{uw}$ does reveal an important feature of the flow, namely the existence of an area of negative $-\overline{uw}$ between the center of the vortex and the wall (see Figs. 9–11). This area of negative $-\overline{uw}$ is located directly beneath a local area of high $-\overline{uw}$. The areas of low primary shear stress and high primary shear stress are separated in the transverse direction by the center of the vortex. This characterizes the flow at all the jet speed ratios tested. At $\lambda = 0.5$, the negative value exists at $x = 5D$ and the minimum negative $-\overline{uw}/U_\infty^2$ is -5.06×10^{-4}. This negative area of $-\overline{uw}$ was not observed at $x = 20D$ and $40D$. At $\lambda = 1.0$, the minimum negative value of $-\overline{uw}/U_\infty^2$ drops sharply from -2.30×10^{-3} at $x = 5D$ to -1.75×10^{-3} at $x = 10D$, -3.86×10^{-4} at $x = 20D$, and -4.58×10^{-5} at $x = 30D$. Similar development is also noticed at $\lambda = 1.5$. However, at $\lambda = 1.5$, the stress distribution differs from that at $\lambda = 1.0$ in that the local area of high $-\overline{uw}$ spreads out to an area outside the otherwise 2-D boundary layer. Shizawa and Eaton (1992) have pointed out that for a three-dimensional vane produced longitudinal vortex flow the negative area of $-\overline{uw}$ is caused by the mean flow velocity distribution which introduces sign change in the velocity gradient. The present observation supports their view. It is clear that the vortex introduces a wake flow leading to the negative $-\overline{uw}$ area.

Analysis of $\overline{uv}$ and $\overline{vw}$ also reveals complex patterns (Figs. 12–13). At $\lambda = 0.5$ the main vortex is broken-up downstream, leading to a slightly different shear stress pattern from those at $\lambda = 1.0$ and 1.5 (Fig. 12). Figure 12 also shows local near-wall $\overline{uv}$ distribution due to the strong convective effect of the vortex at $\lambda = 1.5$. We will now concentrate on the secondary

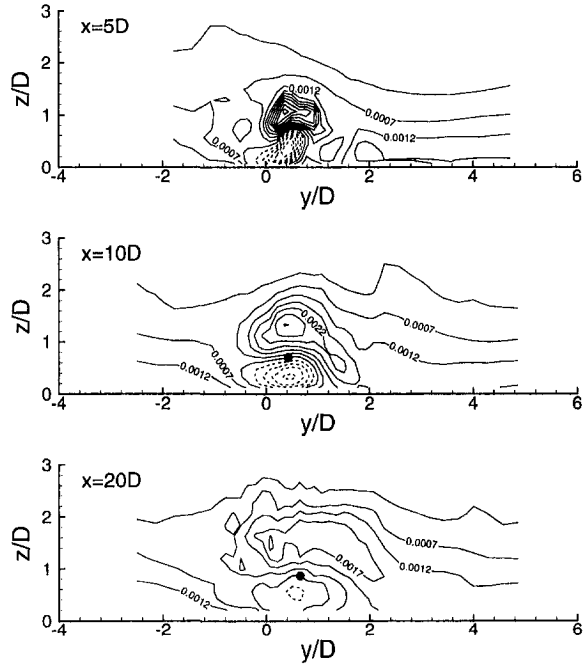

Fig. 10 $-\overline{uw}/U_\infty^2$ contours at $\lambda = 1.0$

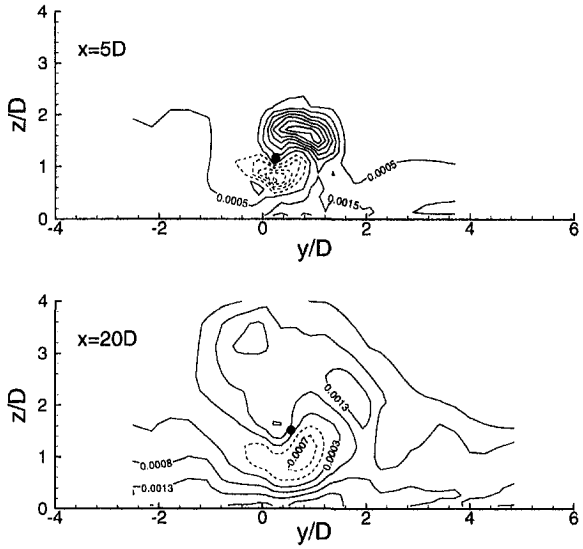

Fig. 11 $-\overline{uw}/U_\infty^2$ contours at $\lambda = 1.5$

shear stress $\overline{vw}$. At $\lambda = 1.0$ and 1.5, there are two local areas of positive $\overline{vw}$ on both sides of the center of the vortex ("butterfly" shaped distribution), and a local area of negative $\overline{vw}$ on top of these positive shear stress areas. The center of the vortex is located amongst the three particular distributions of the shear stress. The butterfly distribution is associated with the counter-rotating vortices generated by the initial jet and boundary layer interaction. However, the spanwise moment in the positive y-direction due to the inclined jet tends to modify the shape of the butterfly distribution, leading to a single area of positive $\overline{vw}$ much like the shape at $\lambda = 0.5$ and $x = 20D$. The local

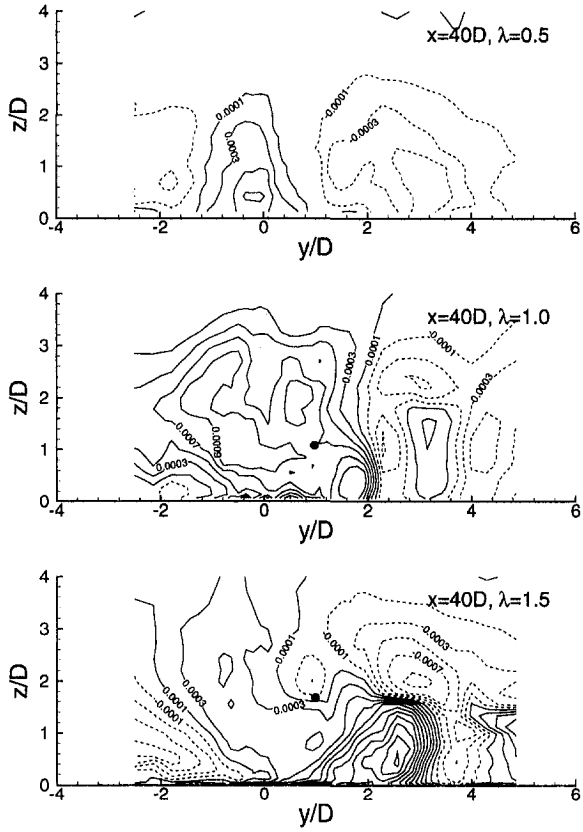

Fig. 12 $\overline{uv}/U_\infty^2$ contours

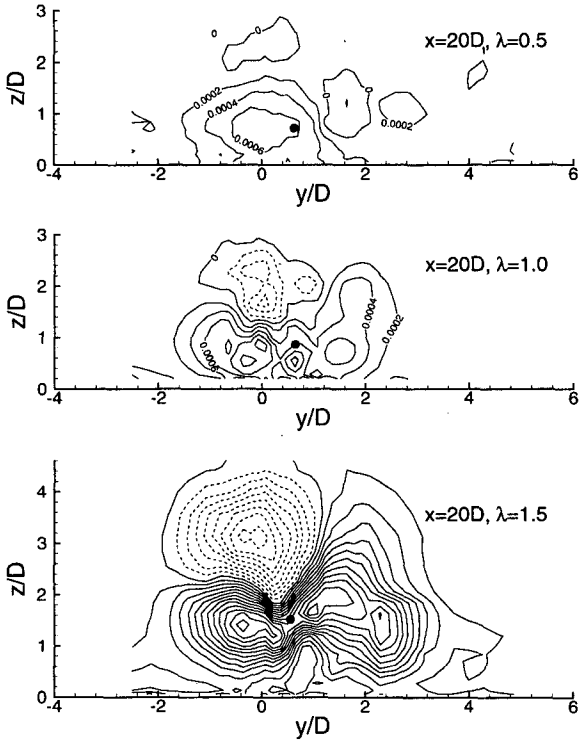

Fig. 13 $\overline{vw}/U_\infty^2$ contours

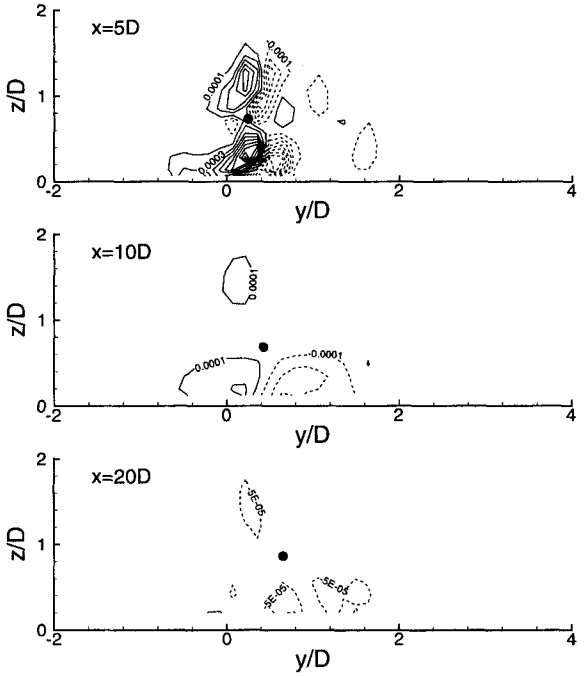

Fig. 15 Turbulence convection of $\overline{uw}$ at $\lambda = 1.0$. Contour variables normalized by U_∞^3/D.

area of high $\overline{vw}$ to the right of the center of the vortex tends to spread out to a larger cross-plane area as it evolves downstream. In fact, measurements suggest the shear stress in this area is always larger initially but will drop relatively quickly downstream. This phenomenon will be explained later when the stress production and convection are discussed. The particular shear stress distribution exists for all the measured cross-planes at $\lambda = 1.0$ and 1.5. Again, the size of the vortex increases and the peak value of $\overline{vw}$ drops downstream. For example, at $\lambda = 1.0$, the peak positive $\overline{vw}/U_\infty^2$ value drops from 4.81×10^{-3} at $x = 5D$ to 1.95×10^{-3} at $x = 10D$, 1.07×10^{-3} at $x = 20D$, and 7.24×10^{-4} at $x = 30D$. Our measurement suggests that the level of shear stresses varies significantly across the cross-plane. For solid vortex generators, past measurements have suggested a smaller $\overline{vw}$ typically at least four times smaller than $\overline{uw}$ (Shizawa and Eaton, 1992). This is not observed for the inclined jet produced vortex flow.

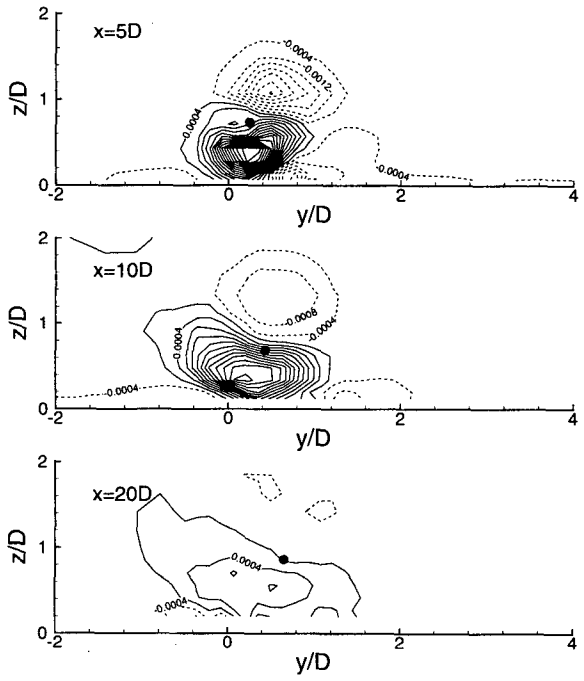

Fig. 14 Turbulence production of $\overline{uw}$ at $\lambda = 1.0$. Contour variables normalized by U_∞^2/D.

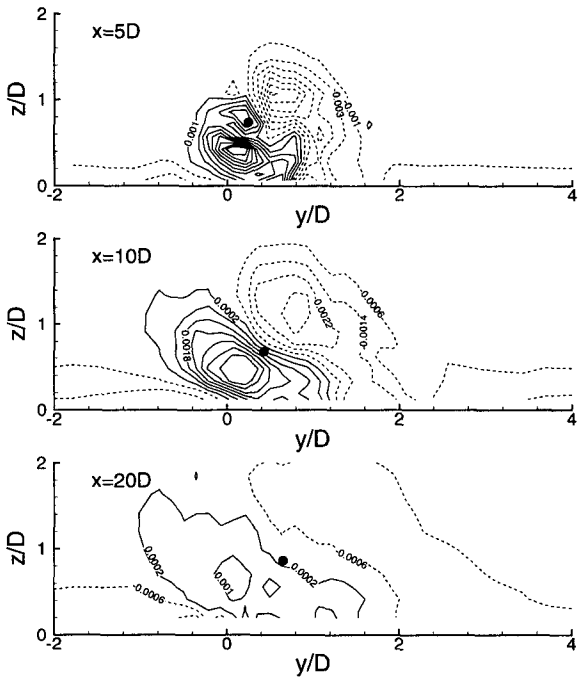

Fig. 16 Turbulence production of $\overline{vw}$ at $\lambda = 1.0$. Contour variables normalized by U_∞^3/D.

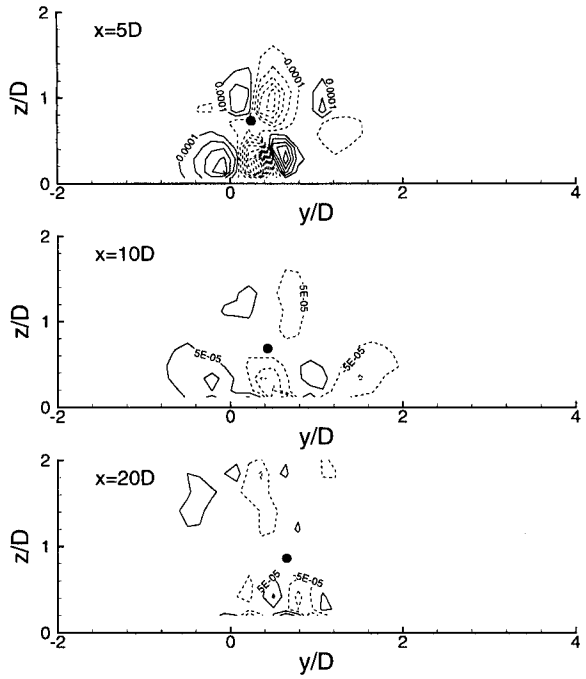

Fig. 17 Turbulence convection of $\overline{vw}$ at $\lambda = 1.0$. Contour variables normalized by U_∞^3/D.

Contributions to the primary stress $\overline{uw}$ and secondary shear stress $\overline{vw}$ in terms of turbulence production and convection are calculated. Here only selected $\lambda = 1.0$ results are presented as others are similar (Figs. 14–17). We note that at $x = 5D$ the turbulent convection plays a relatively important role in defining the shear stress production in the near-wall region and around the center of the vortex. However, farther downstream, the contribution from the convection is at least an order of magnitude smaller than the production. This is expected as the vortex is rather weak. The major physics in defining the stress production and distribution is thus the turbulence production and dissipation (not measured). This agrees with the observation by Shizawa and Eaton (1992). However, the distribution of the turbulence production (Figs. 14 and 16) are different from the results obtained for a 3-D flow and a solid vortex generator. A local high $\overline{uw}$ production corresponds to the negative $-\overline{uw}$ in Fig. 10. This area of high $\overline{uw}$ production is larger than the area occupied by negative $\overline{uw}$ production above it. In Fig. 16, areas of positive $\overline{vw}$ production co-exist. The negative $\overline{vw}$ production to the right of the center of the vortex acts to reduce the value of the high $\overline{vw}$ on the right of the vortex (see Fig. 13). As a result of this, farther downstream of the jet exit, the area of positive $\overline{vw}$ to the right of the vortex would eventually disappear.

4 Summary

This study examines the turbulent flow field produced by an inclined jet in a flat-plate turbulent boundary layer. The measurements suggest that complex flow physics exist around the center of the vortex and in the near-wall region. Therefore two-equation turbulence models will not be able to reproduce all the major physics, particularly between the vortex and the wall where areas of negative primary shear stress, and local low normal stress exist. The study is therefore justified in that it provides a database for numerical predictions employing stress models.

The initial secondary flow field is influenced by the turbulent wake behind the jet. While a main vortex is produced, an induced counter-rotating vortex (or vorticity) is also generated which characterizes the flow. The main vortex eventually dominates. The normal stresses exhibit different characteristics at the three jet speed ratios. At $\lambda = 0.5$ the main vortex breaks up relative quickly and the turbulent flow field thus has different features from those at $\lambda = 1.0$ and 1.5. A very significant difference though exists between the $\lambda = 0.5$ and 1.0 jets and the $\lambda = 1.5$ jet. At $\lambda = 0.5$ and 1.0, a local area of high normal stress is located above the center of the vortex and an area of local low normal stress below it on the upwash side. Local turbulence production dominates the normal stress generation process. A major contributing factor in the process is the spanwise momentum transfer and resulting velocity variation caused by the embedded vortex. At $\lambda = 1.5$, there is a local area of high normal stress coinciding with the center of the vortex and an area of low normal stress located beneath the center on the upwash side. A smaller area of low normal stress also exists beneath the vortex but to the downwash side. While the local turbulence production is still the dominant factor, the convective mechanism also plays an important role. The primary shear stress $-\overline{uw}$ has a local negative area just below the center of the vortex and an area of high $-\overline{uw}$ above it. The negative $-\overline{uw}$ area is caused by the wake region created by the main vortex. This feature persists downstream. While initially the convection mechanism contributes to the shear stress generation process, farther downstream as the single longitudinal vortex is formed, the turbulence production makes the largest contribution to the shear stress production in the flow, being an order of magnitude higher than the convection mechanism.

Acknowledgment

The study is supported under EPSRC grant GR/J17722. The author wishes to thank M. W. Collins for many helpful discussions during the course of the study.

References

Benedict, L. H., and Gould, R. D., 1996, "Towards Better Uncertainty Estimates for Turbulence Statistics," *Experiments in Fluids,* Vol. 22, No. 2, pp. 129–136.

Bushnell, D. M., 1993, "Longitudinal Vortex Control-Techniques and Applications," *Aeronautical Journal,* Oct., pp. 293–303.

Compton, D. A., and Johnston, J. P., 1991, "Streamwise Vortex Production by Pitched and Skewed Jets in a Turbulent Boundary Layer," AIAA Paper 91-0038.

Cutler, A. D., and Bradshaw, P., 1993, "Strong Vortex/Boundary Layer Interaction. Part II. Vortex Flow," *Experiments in Fluid,* Vol. 14, pp. 393–401.

Johnston, J. P., and Nishi, M., 1990, "Vortex Generator Jets—A Means for Flow Separation Control," *AIAA Journal,* Vol. 28, No. 6, pp. 989–994.

Selby, G. V., Lin, J. C. and Howard, F. G., 1992, "Control of Low-Speed Turbulent Separated Flow Using Jet Vortex Generators," *Experiments in Fluids,* Vol. 12, No. 6, pp. 394–400.

Shabaka, I. M. M. A., Mehta, R. D., and Bradshaw, P., 1985, "Longitudinal Vortices Imbedded in Turbulent Boundary Layer. Part 1. Single Vortex," *Journal of Fluid Mechanics,* Vol. 155, pp. 37–57.

Shizawa, T., and Eaton, J. K., 1992, "Turbulent Measurements for a Longitudinal Vortex Interacting with a Three-Dimensional Turbulent Boundary Layer," *AIAA Journal,* Vol. 30, No. 1, pp. 49–55.

Wallis, R. A., 1956, "A Preliminary Note on a Modified Type of Air-Jet for Boundary-Layer Control," ARC, CP-513, London, U.K.

Westphal, R. V., Eaton, J. K., and Pauly, W. R., 1987, "Interaction Between a Vortex and a Turbulent Boundary Layer in a Streamwise Pressure Gradient," *Turbulent Shear Flow 5,* Springer-Verlag, pp. 267–277.

Zhang, X., and Collins, M. W., 1993, "Flow and Heat Transfer in a Turbulent Boundary Layer Through Skewed and Pitched Jets," *AIAA Journal,* Vol. 31, No. 9, pp. 1590–1599.

Zhang, X., 1995, "Co- and Contra-Rotating Streamwise Vortices in a Turbulent Boundary Layer," *Journal of Aircraft,* Vol. 32, No. 6, pp. 1095–1101.

Zhang, X., and Collins, M. W., 1997, "Nearfield Evolution of a Longitudinal Vortex Generated by an Inclined Jet in a Turbulent Boundary Layer," ASME JOURNAL OF FLUIDS ENGINEERING, Vol. 119, pp. 934–939.

Spatial Structure of Negative $\partial\tilde{u}/\partial y$ in a Low R_θ Turbulent Boundary Layer

Joseph C. Klewicki
Associate Professor.

Rodney B. Hill
Mechanical Engineer.

Physical Fluid Dynamics Laboratory,
Department of Mechanical Engineering,
University of Utah,
Salt Lake City, UT 84112

Multiple line Molecular Tagging Velocimetry (MTV) measurements are used to explore the flow fields associated with wall region negative $\partial\tilde{u}/\partial y$ in a low R_θ turbulent boundary layer. Velocity and velocity gradient statistical profiles establish the present flow as a canonical flat plate boundary layer. Spatial correlations of $\partial u/\partial y$ in the (x, y) plane, and the probability of observing negative $\partial\tilde{u}^+/\partial y^+$ exceeding a negative threshold of -0.25 reveal the highly significant presence of negative $\partial\tilde{u}/\partial y$ in the region $25 \leq y^+ \leq 35$. Examination of the instantaneous flow fields underlying the conditional pdf indicates that there are two primary contributing motions: (i) streamwise shear layers and (ii) compact regions containing $\pm\partial\tilde{u}/\partial y$. The importance of these motions to wall region turbulence production is discussed.

Introduction

Research over the past thirty years has revealed the existence and importance of coherent vortical motions in wall bounded turbulence (e.g., Willmarth, 1975, Robinson, 1991). Accompanying and fostering these findings have been significant advances regarding the capability to obtain spatially resolved measurements of the vorticity and velocity gradient fields (e.g., Wallace and Foss, 1995). This emphasis, in large part, stems from the notion that velocity gradients and vorticity are optimal relative to revealing the evolution and dynamical significance of wall region coherent motions. In connection with this general view, a growing number of studies (e.g., Jimenez et al., 1988; Falco et al., 1990; Rajagopalan and Antonia, 1993) have identified the statistically significant existence of instantaneous near-wall spanwise vorticity, $\tilde{\omega}_z = (\partial\tilde{v}/\partial x - \partial\tilde{u}/\partial y)$, having sign opposite that of the mean vorticity, Ω_z (i.e., positive in a coordinate system in which the flow is in the positive x direction and y increases in the direction normal to the wall). Owing to the dominance of the $\partial\tilde{u}/\partial y$ contribution to $\tilde{\omega}_z$ near the wall (e.g., Klewicki and Falco, 1996), these positive $\tilde{\omega}_z$ motions are predominantly characterized by negative $\partial\tilde{u}/\partial y$. A primary motivation of the present work is based upon previous results by Klewicki et al. (1994) indicating strong associations between motions bearing negative $\partial\tilde{u}/\partial y$ and the $\partial\overline{uv}/\partial y$ Reynolds stress gradient, as well as the transport of u^2. The goal of the present work is to characterize the spatial structure of these motions through the study of highly resolved measurements and analysis of instantaneous $\tilde{u}(y)$ and $\partial\tilde{u}/\partial y(y)$ profiles.

Experimental Conditions and Techniques

The present study explores a two dimensional (in the mean) zero pressure gradient turbulent boundary layer over a smooth surface. As is typical, x increases in the flow direction, and y increases in the direction normal to the wall. Fluctuating velocity components are denoted u, v and w in the x, y and z directions respectively. Vorticity component fluctuations are denoted by ω_x, ω_y and ω_z. Mean quantities are denoted by upper case symbols, and instantaneous quantities are identified with a tilde (e.g., $\tilde{\omega}_z = \Omega_z + \omega_z$). Inner normalizations (i.e., using ν and $u_\tau = \sqrt{\tau_w/\rho}$, where τ_w is the mean wall shear stress, $\mu\partial U/\partial y|_{y=0}$) are denoted by a superscript "+."

Flow Facility and Conditions. The experiments were conducted in a recirculating water channel having test section dimensions 15 cm × 15 cm × 105 cm. The zero pressure gradient boundary layer studied developed along the lower wall of the test section. The measurements were acquired at downstream locations between 69 cm and 73 cm from the test section inlet. In order to fix the location of transition, the flow was tripped at the test section inlet using a 1.6 mm diameter threaded rod. The free stream velocity was 0.242 m/s, and the axial free-stream turbulence intensity was less than 0.5 percent. The momentum deficit thickness Reynolds number R_θ ($=U_\infty\theta/\nu$) at the measurement station was 500. Owing to the large number of measurements near the wall, determination of the mean shear utilized the slope of the mean velocity profile in the viscous sublayer ($y^+ \leq 3$). This method, when possible to implement, is believed superior to the Clauser plot technique, since it is more direct.

Molecular Tagging Velocimetry. Multiple line Molecular Tagging Velocimetry (MTV) was used to measure instantaneous $\tilde{u}(y)$ velocity profiles at a number of streamwise locations simultaneously. Note that this technique was previously called Laser Induced Photochemical Anemometry (LIPA). Owing, however, to the fact that the technique can be used in both liquids and gases the more generic acronym MTV is now used (see, Gendrich and Koochesfahani 1996). The version of the technique employed herein is described in detail in Hill and Klewicki (1996), and thus only a brief recap is now provided.

MTV relies on the relatively long emission lifetime of certain ultra-violet light activated phosphors. The present experiments used the photoluminescent chemical $1 - BrNp \cdot G\beta - CD \cdot ROH$ Ternary Complex (hereafter $G\beta - CD$) developed by Ponce et al. (1993). Excitation by a 308 nm light pulse (produced by a Lumonics EX-700 excimer laser) yields visible spectrum emission (green) that can be imaged by our gated intensified CCD camera (ITT model 4577) up to about 10 ms after the laser pulse. The time delay between when the laser fires and when the camera shutters is controlled by a pulse/delay generator. During this time delay, the line of excited $G\beta - CD$ displaces as a result of the fluid motion. Duration of the camera exposure is set at less than 20 percent of the delay. Generation of multiple lines was accomplished by a series of pinholes in an aluminum plate. With this method it is inherently easier to produce a set of co-planar parallel lines than with a

Contributed by the Fluids Engineering Division for publication in the JOURNAL OF FLUIDS ENGINEERING. Manuscript received by the Fluids Engineering Division September 24, 1997; revised manuscript received August 26, 1998. Associate Technical Editor: S. Banerjee.

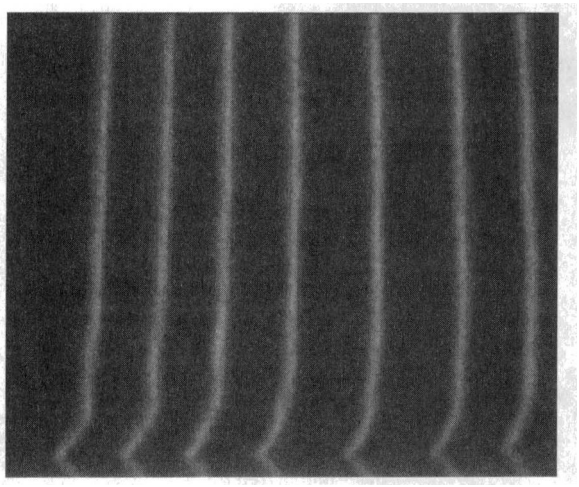

Fig. 1 Video image of displaced MTV lines

stepped mirror device. For the multiple line method, determination of velocity relies on the pointwise subtraction of undisplaced (non-time delayed) line positions from the displaced (time delayed) line positions. (By curve fitting the region of maximum intensity transverse to the line at each pixel location along the line, these positions were determined to a resolution of less than 0.3 pixel.) For short time delays, Δt, the instantaneous velocity nominally perpendicular to the line may then be determined by the Lagrangian formula, $u = \Delta x/\Delta t$. An image of a displaced set of lines is shown in Fig. 1.

Apart from errors associated with the uncertainties in the measurement of Δx and Δt, when using the multiple line method there is an additional error associated with the inability to track unique material elements. For a line arrangement measuring $\tilde{u}$ and $\partial\tilde{u}/\partial y$, Hill and Klewicki (1996) show that this relative error is described by the relation,

$$\frac{\delta\tilde{u}}{\tilde{u}} = \Delta t \frac{\tilde{v}}{\tilde{u}} \frac{\partial\tilde{u}}{\partial y}, \tag{1}$$

where, $\delta\tilde{u}$ is the error, and $\tilde{v}$ is the component of velocity tangential to the MTV line. This relation indicates that for fixed time delay, significant relative errors can result under the condition of simultaneously large $\partial\tilde{u}/\partial y$ and $\tilde{v}/\tilde{u}$. Using wall region boundary layer data, where both $\partial\tilde{u}/\partial y$ and $\tilde{v}/\tilde{u}$ become relatively large, Hill and Klewicki (1996) show that to within a 95 percent confidence interval (20:1 odds) use of typical time delays and camera magnifications yield maximum errors resulting from this effect of about 1.3 percent. Overall the maximum error in the instantaneous velocity along the line is estimated to be less than 4 percent for the present experiments.

Velocity and Velocity Gradient Profiles. The statistical analyses herein utilized 3000 independent (nonsequential) video frames containing 7 instantaneous profiles each, as indicated in Fig. 1. According to the analysis of Klewicki and Falco (1990) this number of independent trials results in uncertainties (resulting from the lack of statistical convergence) in the rms of the velocity gradient of less than 1 percent, and even smaller for velocity statistics. Based upon this and the errors inherent to the MTV technique discussed above, the maximum uncertainty in any of the statistical profiles presented herein are conservatively estimated to be less than 5 percent. The streamwise spacing between each profile is between $27 < \Delta x^+ < 38$. Each $\tilde{u}(y)$ profile extends from the wall out to $y^+ \cong 170$. The Δy^+ spacing between the individual measurements within each profile is 0.92 viscous units (186 individual $\tilde{u}(y)$ measurements per profile).

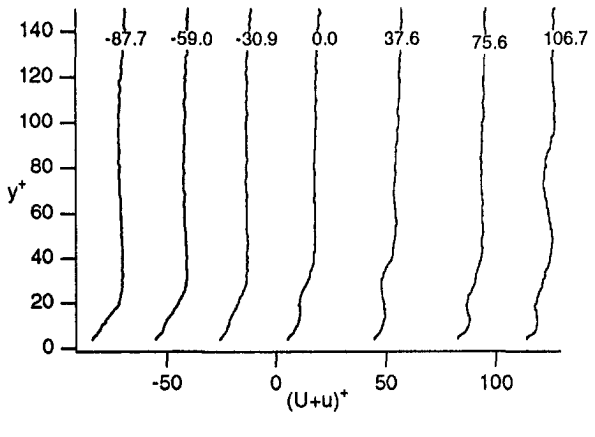

Fig. 2(a)

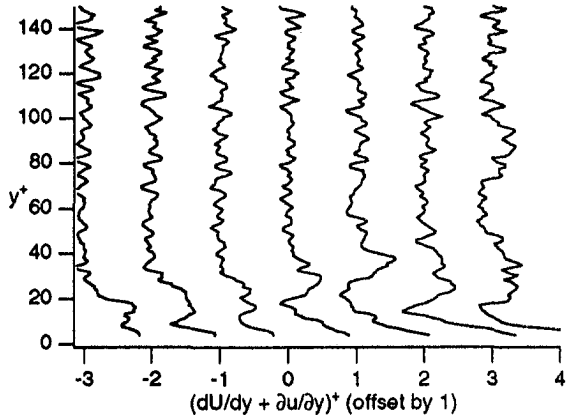

Fig. 2(b)

Fig. 2 (a) $\tilde{u}^+(y^+)$, and (b) $\partial\tilde{u}^+(y^+)$. Numbers at the top of the velocity profiles indicate relative x^+ positions.

Example sets of inner normalized $\tilde{u}(y)$ and $\partial\tilde{u}/\partial y(y)$ profiles are shown in Fig. 2. In this figure, the $\tilde{u}(y)$ profiles are offset along the abscissa according to their Δx^+ separation, while the

Nomenclature

pdf = probability density function
R_θ = momentum deficit thickness Reynolds number, $U_\infty\theta/\nu$
$R(\Delta y^+)$ = spatial correlation for probe separation in wall normal direction
u, v, w = streamwise, wall normal and spanwise velocity components
U_∞ = free-stream velocity
u_τ = friction velocity, $\sqrt{\tau_w/\rho}$
x, y, z = streamwise, wall normal and spanwise Cartesian coordinates
δ = boundary layer thickness
ν = kinematic viscosity
ρ = mass density
τ_w = mean wall shear stress, $\mu\partial U/\partial y|_{y=0}$
θ = momentum deficit thickness
$\omega_x, \omega_y, \omega_z$ = streamwise, wall normal and spanwise vorticity components

Subscripts/Superscripts

$(\ )'$ = denotes r.m.s. value of a fluctuating quantity
$\overline{(\ )}$ = denotes time averaged quantity
$(\tilde{\ })$ = denotes total (i.e., mean plus fluctuating) quantity
$(\ )^+$ = denotes normalization by ν and u_τ

Table 1 Boundary layer integral parameters

R_θ	U_∞ [m/s]	u_τ [m/s]	δ [mm]	θ [mm]	δ^* [mm]
500	0.242	0.0121	16.5	1.9	3.0

$\partial\tilde{u}/\partial y(y)$ profiles are offset by 1.0. The gradient profiles were obtained by differentiating the velocity profiles. This was done by taking the derivative of a sliding second order curve-fit of the $\tilde{u}(y)$ data. For the case of time derivatives, this technique has been shown to be more robust in the presence of noise relative to multiple point finite difference techniques (Klewicki 1989). The effects of spatial resolution were explored by varying the number of points in the curve-fit between 5 and 11. Based upon these results, the conditional and instantaneous analyses of the velocity derivative profiles utilized a 5 point fit having a net spatial extent of 4.6 viscous units. The effects of spatial resolution on the inner normalized rms gradient, $(\partial u/\partial y)'^+$, profile are explored further below.

Results

Results are first presented that establish the present flow as a canonical zero pressure gradient boundary layer. Time averaged spatial structure is revealed through spatial correlations. Conditional information is then used to relate to the presence of negative $\partial\tilde{u}/\partial y$ to long time structure. Lastly, the instantaneous spatial distributions of $\partial\tilde{u}/\partial y$ underlying the observed conditional structure are examined.

Statistics and Correlations. Table 1 presents the integral parameters describing the boundary layer studied. These parameters exhibit good consistency with a typical flat plate turbulent boundary layer-albeit at very low R_θ. Figure 3 shows inner normalized mean velocity data for the seven profiles measured. For convenience, u_τ was determined from the middle profile and subsequently used to normalized all of the profiles. A comparison between the present results and the logarithmic mean profile according to Coles (1968) parameters is also given in Fig. 3. The present profiles show good agreement in the slope but rise above the level of the Coles line. Similar observations have been made at higher R_θ (e.g., Blackwelder and Haritonidis 1983) when u_τ is derived from sublayer velocity gradient data rather than a Clauser plot. As prescribed by the current method of determining u_τ, the sublayer velocity profile follows closely to the $u^+ = y^+$ curve.

The scatter in the u'^+ versus y^+ curves of Fig. 4 is slightly greater than in the mean profiles, although the curves exhibit good agreement with established boundary layer data (e.g., Gad-el-Hak and Bandyopadhyay, 1994). In particular, the peak

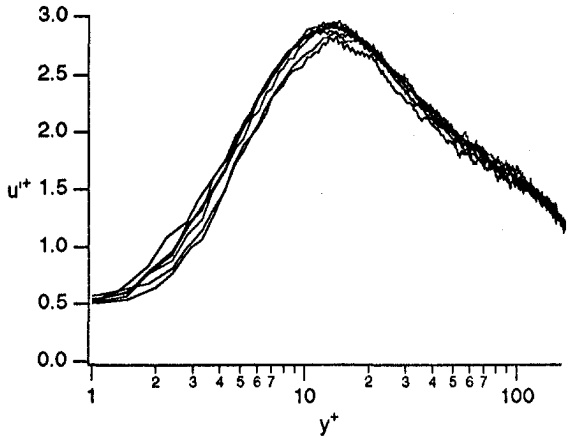

Fig. 4 Inner normalized rms u profiles

in the profile occurs at $y^+ \cong 12$. On the other hand, the magnitude of the peak value (near 2.9) is about 10 percent larger than what other studies at similar Reynolds number report (e.g., Wei and Willmarth 1989, Klewicki 1989). Profiles of the skewness and kurtosis of the axial fluctuations (not shown) also agree well with previous high resolution studies.

Figure 5 shows the present inner normalized $\partial u/\partial y$ rms profiles as derived using a 5 point and 11 point sliding curve fit of the instantaneous velocity profile data. The wall-normal extent of these curve-fits correspond to 10.1 and 4.6 viscous units, respectively. As expected, the 11 point curve-fit has a greater smoothing effect on the gradient data, resulting in a noticeable attenuation of the rms. The present results are also compared with the hot-wire probe based ω_z' results of Balint et al. (1990) and Klewicki and Falco (1990), and the numerically derived profile of Spalart (1988). Previous measurements (e.g., Klewicki and Falco 1996) have established that the near-wall rms profiles of $\partial u/\partial y$ and ω_z are very similar. Figure 5 indicates very good agreement between the 11 point curve-fit data and the data of Balint et al., and the the 5 point curve-fit data and the data of Klewicki and Falco. These results suggest that, given low signal noise, two point finite difference based gradient measurements result in very similar attenuation as the present curve-fits covering the same Δy^+. These results also reinforce the previous assertion by Klewicki and Falco (1990) that spatial resolution is the main reason underlying the difference between the two hot-wire based profiles. As expected, the mean gradient profile (not shown), as derived from time averaging the instantaneous gradient profiles, is not noticably affected by the num-

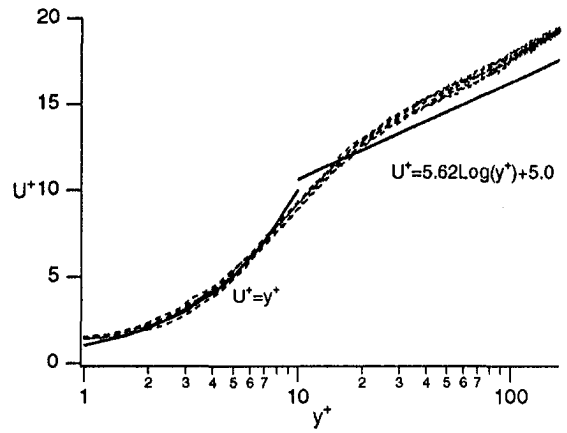

Fig. 3 Logarithmic mean velocity profiles

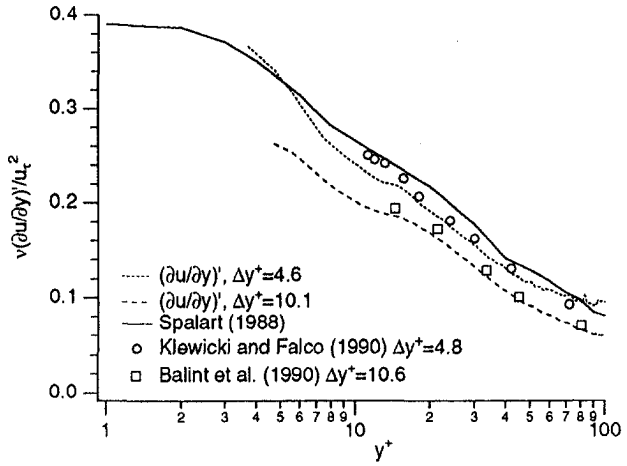

Fig. 5 Inner normalized rms $\partial u/\partial y$ profiles

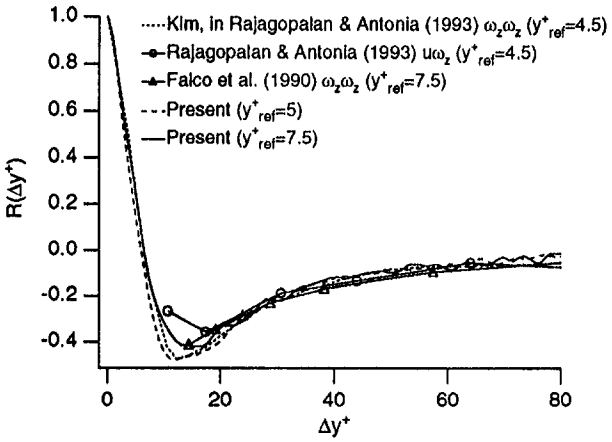

Fig. 6 Two point $\partial u/\partial y$ correlations as a function of wall normal probe separation

ber points in the curve-fit (for the range of points studied). The present higher resolution rms profile generally agrees well with the profile of Spalart (R_θ = 660), although the slope of the curves differ noticably near the wall. Similar observations have previously been made between hot-wire based measurements and these simulation results (Klewicki and Falco, 1996).

Previous correlations derived from a reference probe in or near the sublayer and a second probe positioned at the same x and z coordinates but greater y locations provide strong evidence for the existence of negative $\partial\tilde{u}/\partial y$ in the buffer layer (Falco et al., 1990, Rajagopalan and Antonia, 1993, Klewicki and Metzger, 1996). In particular, these studies show that the joint probability density function associated with the negative peak in the correlations of Fig. 6 largely arise from negative buffer layer $\partial u/\partial y$ (and often $\partial\tilde{u}/\partial y$) occurring in conjunction with highly positive $\partial\tilde{u}/\partial y$ in the sublayer. Of course, the other contributions to the negative correlation (which are also significant) must arise from positive buffer layer $\partial\tilde{u}/\partial y$ occurring in conjunction with negative $\partial u/\partial y$ in the sublayer. Rajagopalan and Antonia (1993) and Klewicki et al. (1994) generically associate the presence of negative and positive buffer layer $\partial\tilde{u}/\partial y$ with sublayer sweeps and ejections respectively. The present two point $\partial u/\partial y$ correlations also exhibit the strong negative peak, and show excellent agreement with the other data of Fig. 6.

Overall spatial structure of the $\partial u/\partial y$ fluctuations in the (x, y) plane is revealed in Figs. 7(a–d). These figures present the spatial distribution of correlation coefficient iso-contours for different reference points (y^+ = 5, 15, 30, 50) along the middle profile of the set of seven. The results of Fig. 7(a) for reference position at y^+ = 5 reveal that the axial extent of the negative correlation indicated in Fig. 6 is substantial. Specifically, the −0.4 correlation contour extends more than $100x^+$. Perhaps even more significantly, the 0.4 contour extends greater than $200x^+$. In general, the correlation contours for reference positions at y^+ = 5, 15, 30 indicate a shallow angle with the wall. Based upon numerous previous results (e.g., Jimenez et al., 1988, Johansson et al., 1991) this feature probably results largely from the presence of near-wall shear layers.

On the other hand, the wall-normal extent of the correlations is much smaller. In contrast to reference positions farther from the wall, the positive and negative peaks in Fig. 7(a) occur at essentially zero x^+ offset. As the reference point moves outward from the wall (Figs. 7(b, c), significant regions of negative correlation develop both above and below the dominant positive peak. In addition, the relative positions of the lower two peaks develop an x^+ offset ($\cong 30x^+$ in Fig. 7(c)), and the streamwise extent of the correlation contours decreases significantly. For reference position at y^+ = 50 (Fig. 7(d)), the magnitude and extent of the strong negative sublayer correlation observed for reference points closer to the wall attenuates significantly. The upper positive/negative correlation peak pair shown in Fig. 7(c) is also consistently revealed in Fig. 7(d). As must be the case, however, the position of the dominant positive peak shifts to the reference point.

Conditional Structure. The adjacent positive and negative correlation peaks in Figs. 7(a–d) strongly reinforce the importance of negative $\partial u/\partial y$ (and possibly $\partial\tilde{u}/\partial y$) in the near-wall region. This is particularly true for increasing y^+, since the value of the mean gradient decreases rapidly across the buffer region. The presence of the correlation peak near y^+ = 30, for reference positions both above and below y^+ = 30, further suggests that negative $\partial\tilde{u}/\partial y$ may be particularly prevalent in the upper buffer region. To explore this further, a negative threshold based analysis of the instantaneous $\partial\tilde{u}/\partial y$ profiles was performed.

Figure 8 shows probability density functions (pdfs) associated with the observation of negative $\partial\tilde{u}^+/\partial y^+$ conditioned on increasingly negative thresholds. Interestingly, this figure shows that at low threshold magnitudes (−0.05, −0.1), there is essentially uniform probability of observing negative $\partial\tilde{u}/\partial y$ in the range $30 < y^+ < 170$. With increasing threshold, however, the pdfs develop increasingly sharp peaks near y^+ = 30. Note that the magnitude of $(\partial u/\partial y)'$ exceeds that of dU/dy near y^+ = 20. Nearer the wall the mean greatly exceeds the rms. Farther from the wall, the rms decreases more slowly than the mean. Thus, with regard to the probability of observing large negative $\partial\tilde{u}/\partial y$, Fig. 8 indicates that the decrease in the frequency of negative $\partial u/\partial y$ fluctuations having large amplitude relative to the mean with increasing y^+ has a greater diminishing effect than does the positive mean gradient near the wall (that must be exceeded by high amplitude negative $\partial u/\partial y$ fluctuations to generate negative $\partial\tilde{u}/\partial y$).

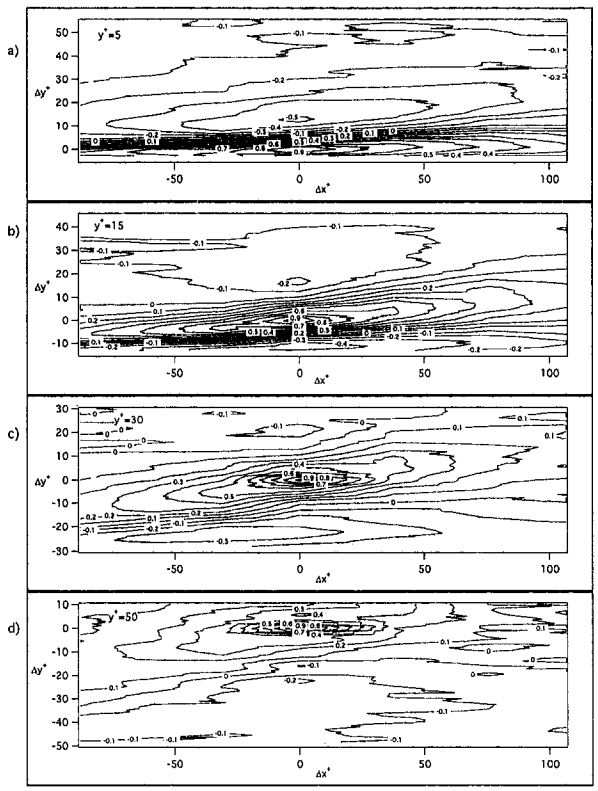

Fig. 7 Spatial correlations of $\partial u/\partial y$ in the (x, y) plane. Wall-normal location of the reference position indicated in the upper left of each frame.

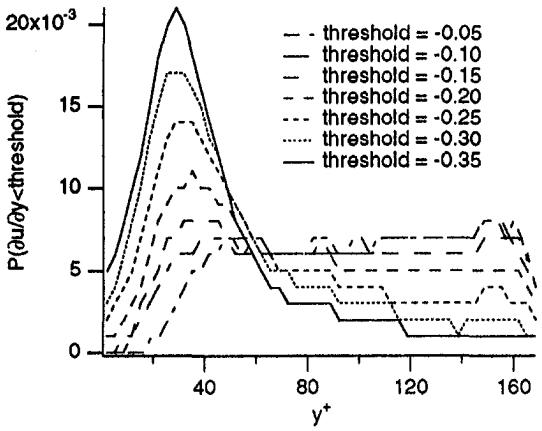

Fig. 8 Probability of observing $\partial\tilde{u}/\partial y$ exceeding a given negative threshold

Conditional averaging was conducted in order to better understand the flow fields associated with the presence of negative buffer layer $\partial\tilde{u}^+/\partial y^+$. Based on the results of Fig. 8, negative $\partial\tilde{u}^+/\partial y^+$ is most likely to occur in the region $25 \leq y^+ \leq 35$ for negative thresholds exceeding magnitudes of 0.2. Given this, the presence of $\partial\tilde{u}^+/\partial y^+ \leq -0.25$ in the region $25 \leq y^+ \leq 35$ was used to conditionally select instantaneous flow fields. Figures 9(a, b) show the average $\tilde{u}^+(y^+)$ and $\partial\tilde{u}^+/\partial y^+(y^+)$ profiles that result from application of this conditioning on the center profile of the set of 7. The number of instantaneous realizations in the ensemble underlying the profiles of Fig. 9 is 63. Thus, identifying this condition relative to all seven of the profiles would yield an ensemble of about 440, or about 15 percent of the total ensemble of 3000. Recognizing, however, that not all of these events are independent, it is likely that an event of this type occurs somewhere in the field of view of the measurements about 10 percent of the time.

Somewhat surprisingly, the profiles adjacent to the conditioned (center) profile do not reveal highly distinctive structure. In particular, the presence of negative $\partial\tilde{u}^+/\partial y^+$ is barely noticable in the third and fifth profiles of Fig. 9(b) and in the sublayer all of the gradient profiles approach something near the mean value of 1.0. On the other hand, the upstream $\partial\tilde{u}^+/\partial y^+$ profiles have noticably steeper slope for $y^+ < 20$ than those downstream. At the wall, a negative second derivative of $\tilde{u}(y)$ indicates a favorable pressure gradient. Although subtle, the two velocity profiles of either side of the center profile (Fig. 9(a)) indicate inflectional behavior. Starting with the third profile, the point of inflection moves outward with increasing downstream location.

Instantaneous Physics. The presence of negative buffer layer $\partial\tilde{u}/\partial y$ is likely to have association with more than one characteristic flow configuration. In fact, the lack of definitive structure in Fig. 9 suggests that the underlying instantaneous flows may have features that cancel under the process of ensemble averaging. To explore this further, the instantaneous realizations underlying the conditional averages of Figs. 9 were examined. The results from this analysis indicate that the instantaneous flow configurations may be classified into 3 main categories.

1. Near-wall shear layers of extended streamwise dimension.
2. Spatially compact motions often containing adjacent regions of positive and negative $\partial\tilde{u}/\partial y$.
3. Other motions, which do not fit into the first two categories.

Example instantaneous flow fields falling under categories 1 and 2 are given in Figs. 10(a, b), respectively. Of the total of 63 events examined, 28 (44 percent) were of the shear layer type exemplified in Fig. 10(a), 21 (33 percent) were of the spatially compact type shown in Fig. 10(b) and 14 (22 percent) were other types of motions.

In the case of the shear layers (Fig. 10(a)), negative $\partial\tilde{u}/\partial y$ develops under the strong positive $\partial\tilde{u}/\partial y$ tip of the shear layer. Jimenez et al. (1988) identify this phenomenon as an important mechanism for the regeneration of sublayer ejections. Of the 28 shear layer events identified, 5 had association with a strong sweep-like motion occurring upstream of the detection point, and 6 were associated with negative $\partial\tilde{u}/\partial y$ occurring above the shear layer, rather than below it. The more compact motion depicted in Fig. 10(b) is consistent with the considerable body of evidence by Falco (see, Falco, 1991) describing the advection of intermediate scale eddies toward the surface, resulting in significant redistribution of sublayer vorticity. Of the 21 compact motions identified, 14 indicated a strong association with the generation of a localized sweep that subsequently forms a shear layer at a location underneath and downstream. Similar kinematics have been previously described by Falco (1983, 1991) to result in sublayer pocket generation. These results are also in good agreement with the ω_z measurements of Rajagopalan and Antonia (1993) and Klewicki et al. (1994) indicating that positive buffer layer $\tilde{\omega}_z$ imposes a localized sweep on the sublayer.

Summary

The spatial structure of the flow fields associated with wall layer negative $\partial\tilde{u}/\partial y$ was explored through the use of multiple line MTV measurements. Statistical profiles and two-point wall-

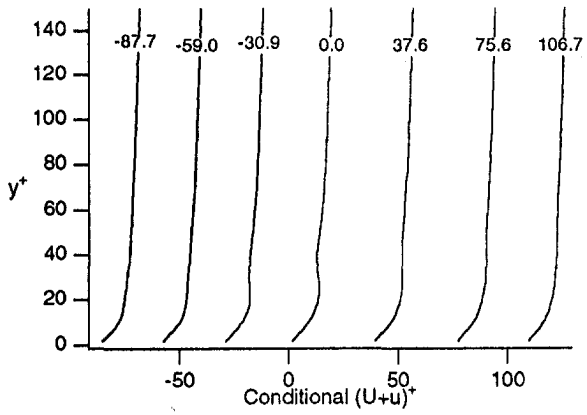

Fig. 9(a)

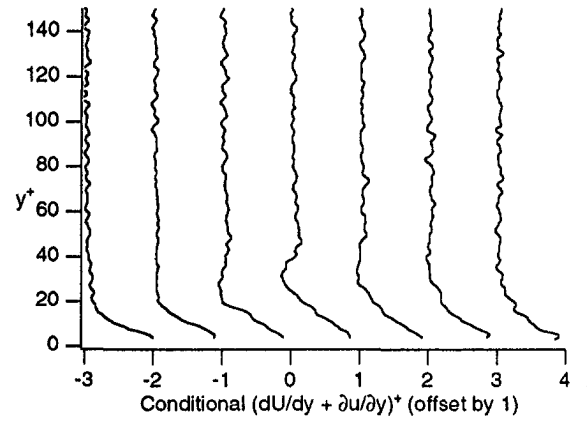

Fig. 9(b)

Fig. 9 Conditional profiles of (a) $\tilde{u}^+(y^+)$, and (b) $\partial\tilde{u}^+(y^+)$. Numbers at the top of the velocity profiles indicate relative x^+ positions.

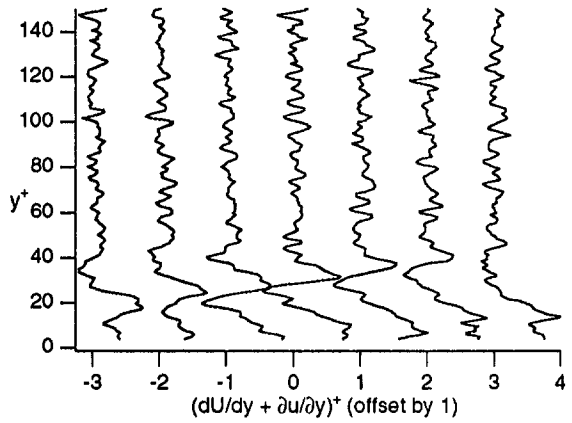

Fig. 10(*a*)

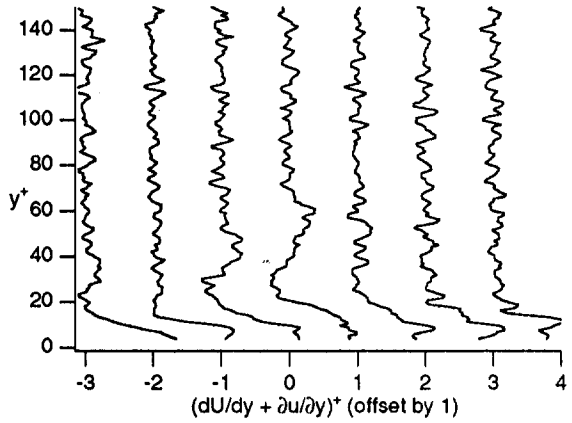

Fig. 10(*b*)

Fig. 10 Instantaneous $\partial\tilde{u}/\partial y < 0$ profiles associated with (*a*) shear layers and (*b*) spatially compact motions

normal correlations of $\partial u/\partial y$ indicate very good agreement with previous hot-wire based and numerical experiments. Correlations of $\partial u/\partial y$ in the (x, y) plane indicate that for reference positions $y^+ < 30$ the non-zero contours are highly distributed in the streamwise direction. For reference positions farther from the wall the correlation contours become significantly more localized in space. Overall, the spatial correlations reveal the existence of positive and negative contour peaks (up to 3) with wall-normal spacings between 15 and 25 viscous units. Conditional results indicate that for low magnitude negative thresholds the probability of observing negative $\partial\tilde{u}/\partial y$ is nearly uniform across most of the wall layer. For larger magnitude thresholds, however, the region $25 \leq y^+ \leq 35$ becomes the predominant location for observing negative $\partial\tilde{u}/\partial y$. Conditional $\tilde{u}(y)^+$ and $\partial\tilde{u}^+/\partial y^+$ profiles (based on a threshold of -0.25) indicate surprisingly subtle structure. Examination of the instantaneous profiles underlying these conditional results indicates that the majority of the contributing flow fields fall in two categories that have partially opposing features. These categories are identified as streamwise shear layers and spatially compact motions comprised of $\pm\partial\tilde{u}/\partial y$.

Overall, the present results are felt to further clarify the nature of those motions associated with negative $\partial\tilde{u}/\partial y$ in the wall region. The importance of these motions to engineering applications relates to their documented significance regarding the turbulence production process and its correlation with, for example, skin friction. Regarding control applications, the present results indicate that strategies designed to influence the generation of negative $\partial\tilde{u}/\partial y$ must contend with at least two apparently distinct types of motions.

Acknowledgment

This work was partially supported by the National Science Foundation under grant number CTS-9120076.

References

Balint, J.-L., Vukoslavcevic, P., and Wallace, J. M., "The Transport of Enstrophy in a Turbulent Boundary Layer," *Near-Wall Turbulence: 1988 Zoran P. Zaric Memorial Conference,* S. J. Kline and N. H. Afgan, eds., Hemisphere Publishing Corp., New York, pp. 932–950.

Blackwelder, R. F., and Haritonidis, J. H., 1983, "Scaling of the Bursting Frequency in Turbulent Boundary Layers," *Journal of Fluid Mechanics,* Vol. 132 pp. 87–103.

Coles, D. E., 1968, "A Young Persons Guide to the Data," *Proceedings, AFOSR-IFP-Stanford Conference on Computation of Turbulent Boundary Layers,* D. E. Coles and E. A. Hirst, eds., Stanford University, Stanford, CA.

Falco, R. E., 1983, "New Results, A Review and Synthesis of the Mechanism of Turbulence Production in Boundary Layers and its Modification," AIAA paper no. 83-0377.

Falco, R. E., 1991, "A Coherent Structure Model of the Turbulent Boundary Layer and its Ability to Predict Reynolds Number Dependence," *Philosophical Transactions of the Royal Society of London,* Series A, Vol. 336, pp. 103–129.

Falco, R. E., Klewicki, J. C., and Pan, K., 1990, "Production of Turbulence in Boundary Layers and Potential for Modification of the Near-Wall Region," *Structure of Turbulence and Drag Reduction,* A. Gyr, ed., Springer-Verlag, Berlin, pp. 59–68.

Gad el Hak, M., and Bandyopadhyay, P., 1994, "Reynolds Number Effects in Wall-Bounded Turbulent Flows," *Applied Mechanics Reviews,* Vol. 147, pp. 307–364.

Gendrich, C. P., and Koochesfahani, M. M., 1996, "A Spatial Correlation Technique for Estimating Velocity Fields Using Molecular Tagging Velocimetry (MTV)," *Experiments in Fluids,* Vol. 22, pp. 67–77.

Hill, R. B., and Klewicki, J. C., 1996, "Data Reduction Methods for Flow Tagging Velocity Measurements," *Experiments in Fluids,* Vol. 20, pp. 142–152.

Jimenez, J., and Moin, P., Moser, R., and Keefe, L., 1988, "Ejection Mechanisms in the Sublayer of a Turbulent Channel Flow," *Physics of Fluids,* Vol. 31, pp. 1311–1313.

Johansson, P. H., Alfredsson, J., and Kim, J., 1991, "Evolution and Dynamics of Shear Layer Structures in Near-Wall Turbulence," *Journal of Fluid Mechanics,* Vol. 224, pp. 579–599.

Klewicki, J. C., 1989, "Velocity-Vorticity Correlations Related to the Gradients of the Reynolds Stress in Parallel Turbulent Wall Flows," *Physics of Fluids A,* Vol. 1, pp. 1285–1288.

Klewicki, J. C., and Falco, R. E., 1990, "On Accurately Measuring Statistics Associated with Small Scale Structure in Turbulent Boundary Layers Using Hot-Wire Probes," *Journal of Fluid Mechanics,* Vol. 219, pp. 119–142.

Klewicki, J. C., Murray, J. A., and Falco, R. E., 1994, "Vortical Motion Contributions to Stress Transport in Turbulent Boundary Layers," *Physics of Fluids,* Vol. 6, pp. 277–286.

Klewicki, J. C., and Falco, R. E., 1996, "Spanwise Vorticity Structure in Turbulent Boundary Layers," *International Journal of Heat and Fluid Flow,* Vol. 17, pp. 363–376.

Klewicki, J. C., and Metzger, M. M., 1996, "Viscous Wall Region Structure in High and Low Reynolds Number Turbulent Boundary Layers," AIAA paper no. 96-2009.

Ponce, A., Wong, P. A., Way, J. J., and Nocera, D. G., 1993 "Intense Phosphorescence Triggered by Alcohols upon Formation of a Cyclodextrin Ternary Complex," *Journal of Physical Chemistry,* Vol. 97, pp. 1137–1143.

Rajagopalan, S., and Antonia, R. A., 1993, "Structure of the Velocity Field Associated with Spanwise Vorticity in the Wall Region of a Turbulent Boundary Layer," *Physics of Fluids A,* Vol. 5, pp. 2502–2510.

Robinson, S. K., 1991, "Coherent Motions in the Turbulent Boundary Layer," *Annual Review of Fluid Mechanics,* Vol. 23, pp. 601–639.

Spalart, P., 1988, "Direct Simulation of a Turbulent Boundary Layer up to R_θ = 1410," *Journal of Fluid Mechanics,* Vol. 187, pp. 61–98.

Wallace, J. M., and Foss, J. F., 1995, "The Measurement of Vorticity in Turbulent Flows," *Annual Review of Fluid Mechanics,* Vol. 27, pp. 469–514.

Wei, T., and Willmarth, W. W., 1989, "Reynolds Number Effects on the Structure of Turbulent Channel Flow," *Journal of Fluid Mechanics,* Vol. 204, pp. 57–95.

Willmarth, W. W., 1975, "Structure of Turbulence in Boundary Layers," *Advances in Applied Mechanics,* Vol. 15, pp. 159–254.

Identification of Coherent Structure in Turbulent Shear Flow With Wavelet Correlation Analysis

Hui Li
Department of Mechanical Engineering,
Faculty of Engineering,
Kagoshima University,
1-21-40, Korimoto,
Kagoshima City, Japan
Mem. ASME

In order to identify coherent structure of turbulent shear flow, a new combination of familiar techniques of signal processing, called wavelet correlation analysis, is developed based on the wavelet transform. The wavelet correlation analysis provides the unique capability for decomposing the correlation of arbitrary signals over a two-dimensional time delay-period plane. By analyzing two superposition functions implicating several pure frequencies, the correlation of periodic oscillations at several frequencies can well be separated and observed clearly. Coherent structures in the intermediate region of a plane turbulent jet are investigated using the wavelet correlation method. It is shown that the wavelet correlation analysis can extract the most essential scales governing features of eddy motions. The coherent structure information and apparent flapping behaviors are clearly revealed over a two-dimensional time-period plane.

Introduction

The topic of wavelet analysis is both very old and very new, because its roots can be traced back at least a century to the work of Weierstrass (1895), who described a family of functions that are constructed by superimposing scaled copies of a given base function. Another important early milestone was Haar's (1910) construction of the first orthonormal system of compactly supported functions, now called the Haar basis. As a tool for analysis of multiscale signals, the concept of wavelet transforms was first formalized in early 1980s by Morlet and Grossmann for the analysis of seismic data (Morlet et al., 1982; Goupillaud et al., 1984). They also outlined the mathematical foundations of the wavelets in 1984 (Grossmann and Morlet, 1984). Since then wavelets have been developed extensively by mathematicians and others. Over the last 15 years, exciting new developments in wavelet theory have attracted much attention and sparked new research in many fields, including pure and applied mathematics, physics, computer science, medicine, biology, and engineering. Few subjects have attracted scientists and engineers in other discipline as much attention as wavelets. New tools are available for efficient data compression, image analysis, and signal processing, and there is a great deal of activity in developing wavelet methods for use in these fields. The same features that make wavelets useful in these (and other) fields also make wavelets a natural and attractive choice to use in many areas of statistical data analysis.

The application of the wavelet analysis in the field of fluid mechanics started in 1988. Farge (1992, 1996) has given recent summaries of applications of wavelet analysis in the area of fluid mechanics. Numerous papers on this topic have been published rapidly, but from the view of fluids engineering these researchers can be broadly split into two categories. (1) Extracting the characters of turbulent or eddy structure from the wavelet analysis of experimental data and simulation data, and (2) developing turbulence modeling and numerical methods based on wavelet bases. In this study, we focus on the wavelet analysis of experimental data. In 1989 Argoul et al. used the wavelet transform to analyze the wind-tunnel turbulence data and provided the visual evidence of the celebrated Richardson cascade. From then the wavelet transform was widely used to reveal various turbulent or eddy structure, such as in fully developed turbulence (Yamada and Ohkitani, 1990; Bacry et al., 1991; Benzi and Vergassola, 1991), jets (Everson et al., 1990; Lewalle et al., 1994; Gordeyev et al., 1995; Gordeyev and Thomas, 1995; Li and Nozaki, 1995; Walker et al., 1995; Li, 1997a–d; Li et al., 1998a–c), boundary layers (Liandrat and Moret-Bailly, 1990; Benaissa et al., 1993; Kaspersen, 1996), bounded jets (Li et al., 1997), wall jets (Sullivan and Pollard, 1996), mixing layers (Dallard and Browand, 1993; Dallard and Spedding 1993), wake flows (Higuchi et al., 1994), surface wave fields (Spedding et al., 1993), multiphase flows (Li and Tomita, 1997, 1998), and others. Now, the wavelet transform has become a standard tool or software kit in identification of flow structure. Several new diagnostics (Farge, 1992; Li, 1997c) developed from the wavelet transform were employed to analyze structure of turbulence and eddy analysis. They offer the potential of extracting the essence of structure feature from flow fields, which are lost if using traditional statistics methods.

The aim of this paper is to apply the wavelets to analyzing the coherent structures in the near field of a turbulent plane jet. Since the coherent structure of a turbulent jet was first studied by Crow and Champagne (1971), the physics of a plane turbulent jet has been widely investigated for several decades (Gutmark, 1976; Moum et al., 1979; Goldschmidt et al., 1981; Gervantes and Goldschmidt, 1981; Krothapalli et al., 1981; Weir et al., 1981; Mumford, 1982; Antonia et al., 1983; Oler et al., 1984; Yoda et al., 1992; Tomas and Chu, 1993; Quinn, 1994; Hsiao and Huang, 1994). It has become a well-known fact that the large-scale eddy motion of the plane turbulent jet exhibits a symmetric, periodic and apparent flapping motion in similarity region. Coherent structures are known to exist and be responsible for most of the momentum transfer in plane turbulent jets. Furthermore, many identification techniques, such as visualization, spectra analysis, spatial correlation functions, education schemes, proper orthogonal decomposition, stochastic estimation, pattern recognition, and wavelet transform, are well established to determine coherent structures. However, the local pe-

Contributed by the Fluids Engineering Division for publication in the JOURNAL OF FLUIDS ENGINEERING. Manuscript received by the Fluids Engineering Division November 22, 1996; revised manuscript received June 9, 1998. Associate Technical Editor: F. Giralt.

riod with respect to space-time changes continuously for the turbulence and large-scale eddy motion, and the coherent structure in both time and period spaces has not yet been clarified. Identification of coherent structure requires the acquisition of detailed quantitative data on such structure characteristics as size, strength, convection velocity, etc. Neither the Fourier analysis nor the traditional correlation method gives us sufficient information. To solve these problems two methods, (1) more powerful identification techniques and (2) simultaneous multipoints or full field measurements, must be considered. In present study we focus on the development of the new identification technique.

The major motivation of this paper is to develop a new correlation method based on the wavelet transform, referred to as the wavelet correlation analysis. This approach can overcome limitations of the traditional correlation method which only describes the correlation of signals in terms of time delay, and assist analysis of the similarity structure of signals in terms of scale and time delay. The traditional correlation method still plays an important role, but it had been hiding the essence of the similarity feature since it lacks frequency resolution. Then the experimental fluctuating velocities at various spatial locations in the near field of a plane turbulent jet are analyzed by the wavelet correlation analysis to reveal coherent structures over a two-dimensional time-period plane, and to extract the most essential scales governing the features of eddy motions.

Definition of Continuous Wavelet Transform

The continuous wavelet transform of a real square integrable function $f(t) \in L^2(\Re)$ (where $L^2(\Re)$ denotes the Hilbert space of measure) at a location b, relative to a real integrable analyzing wavelet $\psi(t)$ at scale a, can be defined as

$$Wf(b, a) = \frac{1}{a}\int_{-\infty}^{\infty} f(t)\,\overline{\psi\left(\frac{t-b}{a}\right)}\,dt. \tag{1a}$$

Equivalently,

$$Wf(b, a) = \langle f, \psi_{b,a}\rangle, \tag{1b}$$

where $Wf(b, a)$ is called the wavelet coefficient, $^-$ stands for complex conjugate and

$$\psi_{b,a} = \frac{1}{a}\overline{\psi\left(\frac{t-b}{a}\right)}.$$

It can be seen that $\psi_{b,a}$ plays the same role as $e^{i\omega t}$ in the definition of the Fourier transform. The continuous wavelet transform is commonly viewed as a numerical microscope whose optics, magnification, and position are given by $\psi(t)$, a, and b, respectively.

In Fourier space the wavelet transform can be expressed as

$$Wf(b, a) = \frac{1}{2\pi}\int_{-\infty}^{\infty} \hat{f}(\omega)\overline{\hat{\psi}_{b,a}(\omega)}\,e^{ib\omega}d\omega, \tag{2}$$

where $\hat{f}$ and $\hat{\psi}$ are the Fourier transforms of f and ψ, respectively.

In order to understand the time-frequency localization properties of wavelet transforms, we need to study the behaviors of the standard deviation of $|\psi_{b,a}(t)|^2$ and $|\hat{\psi}_{b,a}(\omega)|^2$, i.e., $\sigma_{\psi_{b,a}}$ and $\sigma_{\hat{\psi}_{b,a}}$. It is easy to verify the following relationships:

$$\sigma_{\psi_{b,a}} = \sqrt{a}\,\sigma_{\psi_{0,1}} \quad \text{and} \quad \sigma_{\hat{\psi}_{b,a}} = \frac{\sigma_{\hat{\psi}_{0,1}}}{a^{2/3}}. \tag{3}$$

From the above relationships it can be easily seen that $\sigma_{\psi_{b,a}}$ increases and $\sigma_{\hat{\psi}_{b,a}}$ decreases with increasing the scale a, and vice-versa. This indicates that wavelet transform can detect high frequency components of signals with sharper time resolution and low frequency components of signals with sharper frequency resolution. This advantage overcomes the limitations of using a fixing scale of window in the short-time Fourier transform.

An arbitrary function satisfying the admissibility condition of wavelet may be used as an analyzing wavelet. Several well-defined wavelet functions, such as Haar, Paul, French hat, m-th derivatives of the Gaussian, Mexican hat, Morlet and Gabor wavelet, are commonly used as the analyzing wavelet. The choice of the appropriate wavelet function is at the user's disposal and depends on the kind of information that we want to extract from the signal. In this paper we adopt the continuous wavelet transform and the Morlet wavelet function (a complex-valued function), which often appeared in fluid mechanics. The Morlet wavelet function is given by

$$\psi(t) = \pi^{-1/4}e^{-i\omega_0 t}\,e^{-t^2/2}. \tag{4a}$$

which satisfies $\|\psi\|^2 = 1$, and its Fourier transform is written as

$$\hat{\psi}(\omega) = \sqrt{2}\pi^{1/4}e^{-(\omega-\omega_0)^2/2}. \tag{4b}$$

It is obvious that the Morlet wavelet function $\psi(t)$ is localized around $t = 0$, and $\hat{\psi}(\omega)$ is localized around the central of passing band $\omega_c = \omega_0$. In practical applications of signal processing it has been found that a particularly useful value for ω_c is the one for which the wavelet scale a represents the period. Therefore, the central of passing band is defined as $\omega_c = \omega_0 = 2\pi$ in this paper. Then $\psi_{b,a}(t)$ is centered at the position b with the standard deviation $\sqrt{a}/2$, and $\hat{\psi}_{b,a}(\omega)$ is centered at the central of passing band $2\pi/a$ with the standard deviation $\sqrt{\pi/2a^3}$. This wavelet function is complex, enabling one to extract information about amplitude and phase of the process being analyzed. Using the Morlet wavelet function, wavelet coefficients of Eq. (1) can describe a signal as localized strength of a signal over a two-dimensional time-period plane.

Wavelet Auto-Correlation Function

In any nonstationary situation, such as in human speech, music, velocity signals of turbulence and others, signals contain various frequency components that rapidly change with time in complex ways. The traditional auto-correlation method is quite capable in identifying the self-similarity structure. However, it cannot extract the information of the self-similarity structure in frequency space and had been hiding the essence of the self-similarity feature since it lacks frequency resolution. The traditional auto-correlation method is well suited to analyze the periodic signals and is not suited for complex signal analysis. Although the wavelet transform can describe *when* those frequency components occurred, more powerful techniques must be developed to gain deeper insight into the complex self-similarity behavior of signals.

As described in the previous section, wavelet coefficients can describe a signal as localized strength of the signal in both time and period or frequency spaces. The modulus, real part, and phase of wavelet coefficients have been employing to describe the characteristics of a signal. Therefore the all traditional statistics method may be applied. In order to obtain the self-similarity structure of a signal for various scales at any given time delay, at first, we unfold the signal into a two-dimensional time-period plane by the wavelet transform. Then we use its wavelet coefficients to define an auto-correlation function, called the *wavelet auto-correlation function* $WC(a, \tau)$, by the following formula.

$$WC(a, \tau) = \lim_{T\to\infty}\frac{1}{T}\int_{-2/T}^{2/T}\overline{Wf(b, a)}Wf(b+\tau, a)db, \tag{5}$$

where τ is time delay of wavelet coefficients in the wavelet space, or the time delay of the signal $f(t)$. It is evident that the wavelet auto-correlation function can provide important self-

similarity features on a two-dimensional period-time delay plane, and then extracts the most essential frequencies governing the self-similarity features of signals.

The wavelet auto-correlation function $WC(a, \tau)$ can also be written in Fourier space

$$WC(a, \tau) = \frac{1}{2\pi}\int_{-\infty}^{\infty} S(\omega)|\hat{\psi}(a\omega)|^2 e^{i\tau\omega}d\omega. \quad (6)$$

Equation (6) is very similar to the wavelet transform of Eq. (2) in either form or the physical sense. Equation (6) represents the relationship between wavelet space and Fourier space, and demonstrates the characteristic of $WC(a, \tau)$ as a local filter, in which the Fourier power spectrum $S(\omega)$ is filtered by $|\hat{\psi}(a\omega)|^2$ in Fourier space.

We define a local wavelet power spectrum density function $WP(a, \omega)$ as follows

$$WP(a, \omega) = S(\omega)|\hat{\psi}(a\omega)|^2. \quad (7)$$

Substituting Eq. (7) into Eq. (6), we obtain

$$WC(a, \tau) = \frac{1}{2\pi}\int_{-\infty}^{\infty} WP(a, \omega)e^{i\tau\omega}d\omega. \quad (8)$$

With the inverse Fourier transform the above equation becomes

$$WP(a, \omega) = \int_{-\infty}^{\infty} WC(a, \tau)e^{-i\tau\omega}d\tau. \quad (9)$$

From Eq. (8) and (9) it is obvious that $WP(a, \omega)$ may be defined as the Fourier transform of $WC(a, \tau)$, and $WC(a, \tau)$ may be obtained from the inverse Fourier transform of $WP(a, \omega)$. This relationship is same as the Wiener-Khintchine theorem of the traditional auto-correlation.

If a complex-valued function is used as the analyzing wavelet, the wavelet coefficient becomes a complex-valued function. Hence $WC(a, \tau)$ is also a complex-valued function from the definition of the wavelet auto-correlation function in Eq. (5) or (6). In order to extract information of the self-similarity structure of signals, the modulus $MWC(a, \tau)$ and the phase $\theta WC(a, \tau)$ of wavelet auto-correlation function are employed to express the strength of auto-correlation and the average phase difference for different time delay of signals at a given period, respectively. The real part of wavelet auto-correlation function $RWC(a, \tau)$ is used to reveal the information of positive and negative correlation.

In this paper, we define a wavelet auto-correlation coefficient $RWR(a, \tau)$, which is normalized with respect to the wavelet auto-correlation function at $\tau = 0$ or the wavelet power spectrum density function $RWC(a, 0)$, as follows:

$$RWR(a, \tau) = \frac{RWC(a, \tau)}{RWC(a, 0)}, \quad (10)$$

where $RWR(a, 0) = 1$ and $|RWR(a, \tau)| \leq 1$.

Wavelet Cross-Correlation Function

In identifying the spatial turbulent structure or coherent structures and its evolution in time, the cross-correlation analysis between velocity components measured at two separated points in flow filed is most used. A difficulty with the traditional cross-correlation method, however, is that the cross-correlation function only provides information about the cross-correlation behavior in terms of time delay but no information about correlation behaviors in scale space at each scale due to lack of scale resolution.

In analogy with the wavelet auto-correlation, we first unfold, respectively, two different signals $f_x(t)$ and $f_y(t)$ into their two-dimensional time-period planes using the wavelet transform, in order to yield the period resolution. Then their wavelet coefficients, $Wf_x(b, a)$ and $Wf_y(b, a)$, are used to define a cross-correlation function, called the *wavelet cross-correlation function* $WC_{xy}(a, \tau)$, by the following formula.

$$WC_{xy}(a, \tau) = \lim_{T\to\infty}\frac{1}{T}\int_{-2/T}^{2/T} \overline{Wf_x(b, a)}\, Wf_y(b + \tau, a)db, \quad (11)$$

where τ is a time delay between two signals. The wavelet cross-correlation function has the following two characteristics. (1) Since the wavelet cross-correlation function is obtained by integration of wavelet coefficients over time plane, contributions of different period to the correlation are kept reasonably separated. (2) This separation is achieved without excessive loss of resolution in time variable due to use of the wavelet transform (of course, subject to the limitation of the uncertainty principle). The two characteristics exhibit the property known as time-period localization. Therefore, the wavelet cross-correlation function can describe important statistical correlation features between two different signals on a two-dimensional scale-time delay plane, and extract the most essential scales governing the correlation features, which is lost if using traditional method.

In Fourier space, the wavelet cross-correlation function $WC_{xy}(a, \tau)$ can also be written as

$$WC_{xy}(a, \tau) = \frac{1}{2\pi}\int_{-\infty}^{\infty} S_{xy}(\omega)|\hat{\psi}(a\omega)|^2 e^{i\tau\omega}d\omega, \quad (12)$$

where $S_{xy}(\omega)$ is the traditional cross-spectrum. Expression (12) represents the relationship between the wavelet and Fourier spaces, and describes the characteristic of $WC_{xy}(a, \tau)$ as a local filter, in which the Fourier power spectrum $S_{xy}(\omega)$ is filtered by $|\hat{\psi}(a\omega)|^2$ in Fourier space. Here we define a local wavelet cross-spectrum function $WP_{xy}(a, \omega)$ as

$$WP_{xy}(a, \omega) = S_{xy}(\omega)|\hat{\psi}(a\omega)|^2. \quad (13)$$

Substituting Eq. (13) into Eq. (12), we obtain

$$WC_{xy}(a, \tau) = \frac{1}{2\pi}\int_{-\infty}^{\infty} WP_{xy}(a, \omega)e^{i\tau\omega}d\omega. \quad (14)$$

Carrying out an inverse Fourier transform the above equation becomes

$$WP_{xy}(a, \omega) = \int_{-\infty}^{\infty} WC_{xy}(a, \tau)e^{-i\tau\omega}d\tau. \quad (15)$$

From Eqs. (14) and (15), $WP_{xy}(a, \omega)$ can be defined as the Fourier transform of $WC_{xy}(a, \tau)$, and $WC_{xy}(a, \tau)$ can be obtained from the inverse Fourier transform of $WP_{xy}(a, \omega)$. This relationship is very similar to the Wiener-Khintchine theorem of the traditional cross-correlation.

In order to characterize the cross-correlation, we may use a modulus of wavelet cross-correlation coefficients $MWR_{xy}(a, \tau)$ and a phase of wavelet cross-correlation function $\theta WC_{xy}(a, \tau)$ to describe the strength of cross-correlation and the average phase difference between two signals in terms of time delay and period. However, $MWR_{xy}(a, \tau)$ can not provide an information of negative cross-correlation. Therefore, it is convenient to introduce a real part of wavelet cross-correlation coefficients $RWR_{xy}(a, \tau)$ by

$$RWR_{xy}(a, \tau) = \frac{RWC_{xy}(a, \tau)}{\sqrt{RWC_x(a, 0)RWC_y(a, 0)}}, \quad (16)$$

where $RWC_x(a, 0)$ and $RWC_y(a, 0)$ are the real parts of wavelet auto-correlation functions at $\tau = 0$.

Wavelet Correlation Analysis of Superposition Functions

First, the following function, which is a superposition of n pure frequencies at frequencies $\omega_1, \omega_2 \ldots \omega_n$,

$$f(t) = \sum_{k=1}^{n} \mathrm{Exp}(i\omega_k t). \quad (17)$$

is analyzed by the wavelet transform.

Clearly, the superposition principle tells us the wavelet transform of a superposition function is the superposition of the respective transforms. Using Eq. (1) the wavelet transform of function (17) can be written as

$$Wf(b, a) = \sum_{k=1}^{n} \exp(i\omega_k b)\overline{\hat{\psi}(a\omega_k)}. \quad (18)$$

If $\hat{\psi}(\omega)$ has zero imaginary part, the real part and imaginary part of wavelet coefficient correspond to the wavelet transform of the real part and imaginary part of the superposition function, respectively.

Consider the following two superposition functions,

$$f_x(t) = \sum_{j=1}^{n} \mathrm{Exp}(i\omega_j t) \quad \text{and} \quad f_y(t) = \sum_{k=1}^{n} \mathrm{Exp}(i\omega_k t). \quad (19)$$

Using Eq. (12) the wavelet cross-correlation solution of the above two functions (Eq. (19)) can be obtained as

$$WC_{xy}(a, \tau) = \sum_{j=1}^{n}\sum_{k=1}^{n} \hat{\psi}(a\omega_j)\overline{\hat{\psi}(a\omega_k)}\,\mathrm{Exp}(i\omega_j\tau) \lim_{T\to\infty}\frac{1}{T}\int_{-T/2}^{T/2} \times \mathrm{Exp}(i(\omega_j - \omega_k)b)db. \quad (20a)$$

From the above equation, the analyzing solution of the wavelet cross-correlation function can be written as the following formula.

(1) If $\omega_j \neq \omega_k$, then $\lim_{T\to\infty}\frac{1}{T}\int_{-T/2}^{T/2} \mathrm{Exp}(i(\omega_j - \omega_k)b)db = 0$,

Thus $WC_{xy}(a, \tau) = 0$.

(2) If $\omega_j = \omega_k$, then $\lim_{T\to\infty}\frac{1}{T}\int_{-T/2}^{T/2} \mathrm{Exp}(i(\omega_j - \omega_k)b)db = 1$,

Thus $WC_{xy}(a, \tau)$

$$= \sum_{j=1}^{n}\sum_{k=1}^{n} \hat{\psi}(a\omega_j)\overline{\hat{\psi}(a\omega_k)}\,\mathrm{Exp}(i\omega_j\tau). \quad (20b)$$

From the above relationships, it is obvious that the real part of wavelet cross-correlation function (Eq. (20*b*)) gives the cross-correlation between the real parts of two superposition functions.

Consider, for example, two different functions contain the superposition of three pure frequencies ($n = 3$) at frequencies $\omega_1 = \pi/4$, $\omega_2 = \pi/2$, $\omega_3 = \pi$ and $\omega_1 = \pi/4$, $\omega_2 = \pi/2$, $\omega_3 = 2\pi$, respectively. It is evident that two functions have common frequencies at $\pi/4$ and $\pi/2$. Using Eq. (21), the real part of the wavelet cross-correlation function $RWC_{xy}(a, \tau)$ is calculated with the help of the Morlet wavelet function, and is shown on the (a, τ) plane representation in Fig. 1. From the distributions of $RWC_{xy}(a, \tau)$, we can obtain the cross-correlation at various periods and time delay.

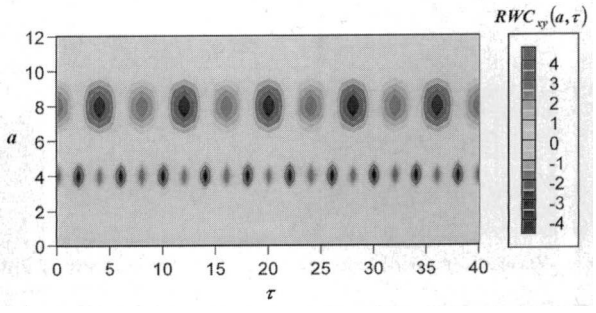

Fig. 1 Wavelet cross-correlation analysis of two superposition functions

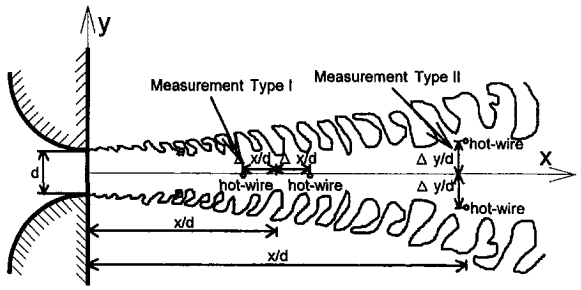

Fig. 2 Sketch of the experimental configuration

Two groups of periodic peaks at $a = 4(\omega = \pi/2)$ and $8(\omega = \pi/4)$ can clearly be observed, and the strong periodic correlation at the two frequencies are well detected. However, two groups of periodic oscillations at $\omega = \pi$ and 2π, which exist respectively in two wavelet coefficients (or functions), are destroyed. This indicates no correlation at the two frequencies.

Experimental Apparatus and Procedure

A definition sketch of a plane jet is shown in Fig. 2, where x is the streamwise coordinate and y is the lateral coordinate. The jet was generated by a blower-type wind tunnel with flow-straightening elements, screens, settling length and a 24:1 contraction leading to a 350 mm × 25 mm nozzle. The nozzle width d is 25 mm and the aspect ratio of nozzle is 14. The measurements were performed at a Reynolds number (based upon exit mean velocity, U_a, and nozzle width, d) of Re = 3330 which corresponded to an exit velocity of U_a = 2 m/s. The measured exit turbulent intensity on the jet centerline is less than 0.04%. The velocity of the x-component was measured simultaneously using two standard hot wire probes located in the (x, y)-plane. In the present experiment, as shown in Fig. 2, the following two type measurements were carried out. (1) Type I measurements were performed with two probes for equal separations distances Δx centered at x on the jet centerline; and (2) type II measurements were performed with two probes at equal separate distances Δy from the jet centerline at various x locations. For the measurements with streamwise separation (type I), the present minimum value of $2\Delta x$ (= 25 mm) was such that the thermal wakes from the upstream hot wire did not interfere with the downstream probe. The statistics of velocity obtained from the downstream probe were unaffected by the presence of the upstream probe. The recording frequency of data is 2 kHz, and the recording length is 4 seconds.

The measurement errors due to the sensitivity of hot wire probe were the most dominant, other errors can be negligible. The uncertainty at 95 percent confidence for the wavelet correlation coefficient and its phase are approximately about 10 percent.

Application to a Plane Turbulent Jet

Wavelet Auto-Correlation Analysis of Flow Structure. In order to investigate self-similarity structures of the jet at various periods, the wavelet auto-correlation of the x-component of fluctuating velocities on the centerline at $x/d = 8.5$ are first analyzed. The modulus of the wavelet auto-correlation function $MWC(a, \tau)$ with its real part $RWC(a, \tau)$ is shown on the (a, τ) color plane (abscissa: time delay τ, ordinate: period a, rainbow colors for wavelet auto-correlation magnitudes) in Fig. 3. Below these color plates, the traditional auto-correlation coefficients $R(\tau)$ are also illustrated.

It is evident that $RWC(a, \tau)$ shows almost same distribution as $MWC(a, \tau)$. $RWC(a, \tau)$ not only gives exactly same the

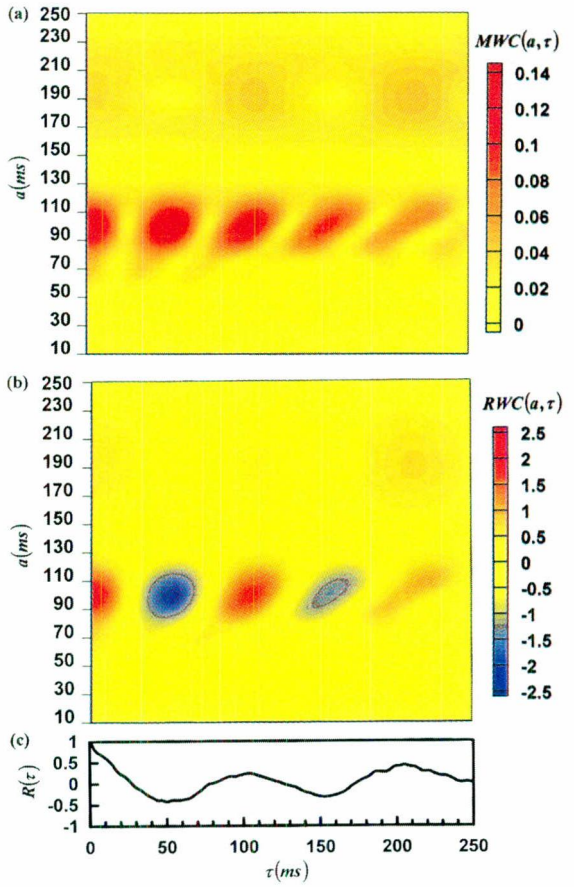

Fig. 3 Wavelet auto-correlation analysis of fluctuating velocity on the centerline at $x/d = 8.5$; (a) modulus of wavelet auto-correlation function; (b) real part of wavelet auto-correlation function; (c) traditional auto-correlation coefficients

information as $MWC(a, \tau)$, but also extracts local positive and negative correlation within the period a centered at τ. Therefore, it is proper that $RWC(a, \tau)$ replaces $MWC(a, \tau)$ to express the strength of the wavelet auto-correlation. In the following section, we utilize $RWC(a, \tau)$ to analyze the flow structure instead of $MWC(a, \tau)$. From the distribution of $RWC(a, \tau)$ in Fig. 3(a), the dominant distributions of two periodic oscillations at $a = 100$ and 195 ms are evident, and indicate that the periodic motions with two scales through the centerline. Making a comparison between $RWC(a, \tau)$ and $R(\tau)$, we find that the large positive and negative peaks in $R(\tau)$ correspond to the alternative strong positive and negative peaks of $RWC(a, \tau)$ at $a = 100-110$ ms. However, from $R(\tau)$ peaks and the information on auto-correlation appearing at $RWC(a, \tau)$ of $a = 195$ ms cannot be found. It is because its magnitude is smaller than that of $a = 100-110$ ms, and its effects are embedded due to the presence of the other scale. Although power spectrum may clearly describe peaks of auto-correlation in frequency space, it is impossible to provide information on the strength of auto-correlation responding to the changing the time delay.

Then, $RWR(a, \tau)$ and $\theta WC(a, \tau)$ for the x-component of the fluctuating velocity in the shear layer at $x/d = 10$ and $y/d = 2.5$ are shown in Fig. 4. $RWR(a, \tau)$ obviously gives a maximum (equal to the wavelet power spectrum density) at $\tau = 0$, i.e., $RWR(a, 0) = 1$. The traditional auto-correlation decreases to zero as τ increases, and does not provide any information of self-similar flow structure. However, From $RWR(a, \tau)$ the obvious periodic oscillations happen at $a = 15$, 40, 75, 100 and 150 ms, and imply strong periodic motions passing the shear layer. Among these periodic multi-scale motions, the stronger coherence appear at $a = 75$, 100 and 150 ms. The distribution of $RWR(a, \tau)$ also shows a map of apparent multi-scale similarity structure in the shear layer. From a positive peak at $a = 150$ ms, a large branching structure, which consists of two peaks at $a = 100$ ms, may be clearly observed around $\tau = 170$ ms. This indicates that a complex periodic larger-scale motion (or large eddy structure), which contains periodic smaller-scale motions (or small eddies), exists in the shear layer.

The values of $RWR(a, \tau)$ are larger than that of $R(\tau)$, because the traditional auto-correlation is the results of interference among auto-correlation magnitudes of all periods at a given time delay. Making a comparison between $RWR(a, \tau)$ and $R(\tau)$ it is found that the interference between the positive and negative magnitudes at various periods around τ may produce the zero value of $R(\tau)$. However, there must be existence of correlation at some period, and this means that $R(\tau)$ may hide some important coherent information. But the wavelet auto-correlation analysis can extract all information existing in the complex flow structure.

On the other hand, $\theta WC(a, \tau)$ expresses the distribution of phase difference between $\tau = 0$ and τ at any given period. The discontinue constant phase lines and the range of zero value in $\theta WC(a, \tau)$ correspond to the zero real part of auto-correlation lines and the region of the positive or negative peak in the map of $RWR(a, \tau)$, respectively. The cross-point of constant-phase lines equivalents to zero point of $MWC(a, \tau)$ which means noncorrelation. The distribution of the cross-point along the discontinue constant-phase lines decreases rapidly as the period increases, and this indicates that the periodic flow structure consists of many small-scale motions and few large-scale motion. From the distribution of the wavelet phase difference $\theta WC(a, \tau)$ between $\tau = 0$ and τ in Fig. 4(b), it is evident

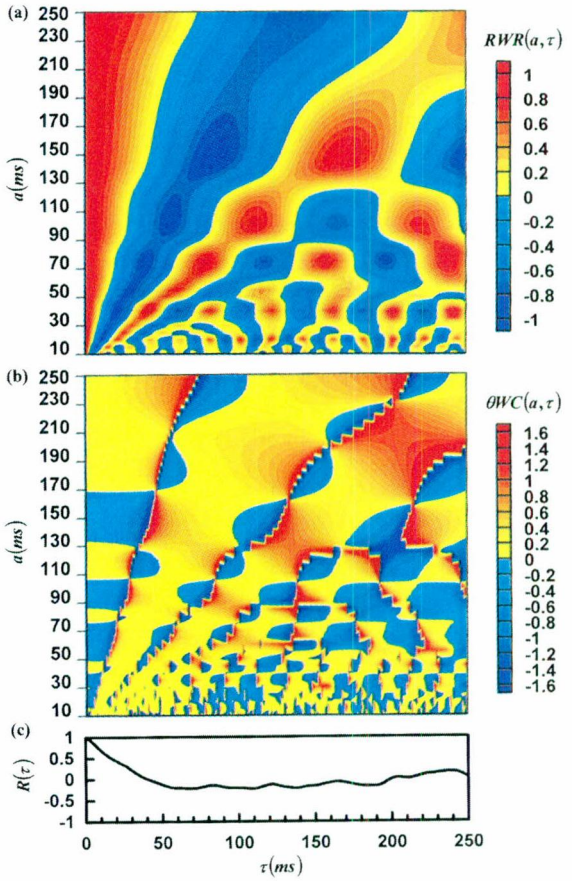

Fig. 4 Wavelet auto-correlation analysis of fluctuating velocity in the shear layer at $x/d = 10$ and $y/d = 2.5$; (a) wavelet auto-correlation coefficients; (b) phase of wavelet auto-correlation function; (c) traditional auto-correlation coefficients

that the interval of the discontinue constant-phase lines increases with the period. At any given period or scale, we can obtain an angular frequency $\omega(a, \tau)$ $(=\Delta\theta WC(a, \tau)/\Delta\tau)$ by differentiating the corresponding phase fields with respect to τ. In fact, $\omega(a, \tau)$ means the difference of the angular frequency between $\tau = 0$ and τ.

Wavelet Cross-Correlation Analysis of Coherent Structure (Type I Measurement). For identifying the organized structure in the turbulent plane jet, the wavelet cross-correlation coefficients $RWR_{xy}(a, \tau)$ and its phase $\theta WC_{xy}(a, \tau)$ between two x-components of fluctuating velocities are calculated for $2\Delta x/d = 2$ separation distances on the centerline at x/d ratios of 5, and are shown in Fig. 5 (abscissa: time delay τ, ordinate: period a, rainbow colors: amplitude of $RWR_{xy}(a, \tau)$ or $\theta WC_{xy}(a, \tau)$). Below the color plates, the result of the traditional cross-correlation coefficients $R_{xy}(\tau)$ is also plotted.

Making a comparison between $RWR_{xy}(a, \tau)$ and $R_{xy}(\tau)$, the large peaks of $R_{xy}(\tau)$ correspond to the nearly periodic correlation peaks at $a = 80$–105 ms, and the small peaks of $R_{xy}(\tau)$ equivalent to the nearly periodic peaks of $RWR_{xy}(a, \tau)$ below $a = 50$ ms. From the distributions of $RWR_{xy}(a, \tau)$, the branching structures can clearly be observed as follows. A strong positive correlation peak in high period range ($a = 145$ ms) at $\tau = 185$ ms is composed of two positive correlation peaks of medium period ($a = 105$ ms) at $\tau = 130$ and 230 ms. Furthermore, each of correlation peaks in medium period range consists of two correlation peaks in low period range. This implies that the periodic large-scale motion (or periodic large eddy) contains that of smaller scale (or periodic small eddies). With increasing τ, as shown in Fig. 5(a), the alternative positive and negative

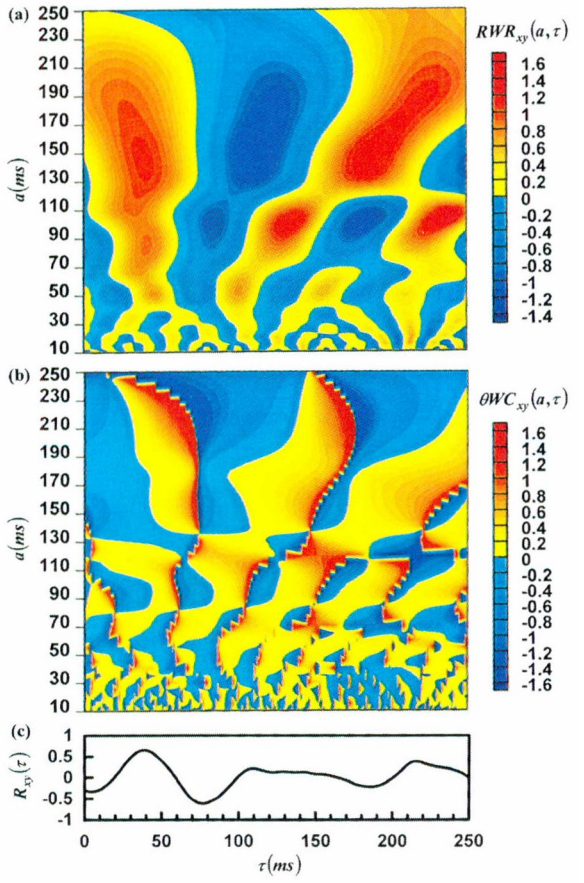

Fig. 5 Wavelet cross-correlation analysis of two velocity fluctuations at $x/d = 5$, $2\Delta x/d = 2$ (Type I); (a) wavelet cross-correlation coefficients; (b) phase of wavelet cross-correlation function; (c) traditional cross-correlation coefficients

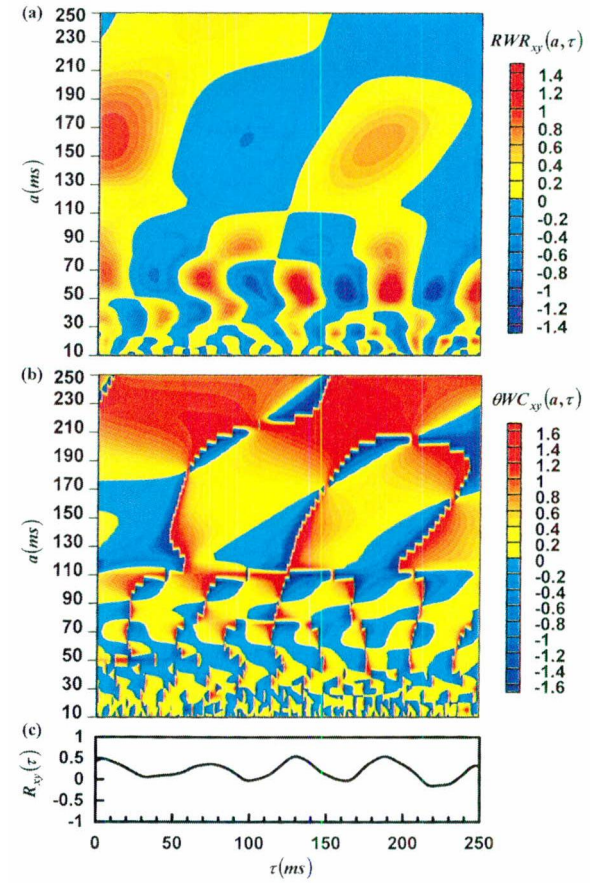

Fig. 6 Wavelet cross-correlation analysis of two velocity fluctuations at $x/d = 5$, $2\Delta y/d = 2$ (type II); (a) wavelet cross-correlation coefficients; (b) phase of wavelet cross-correlation function; (c) traditional cross-correlation coefficients

peaks at various periods are observed. The dominant feature of this figure is two periodic oscillation at $a = 145$ ms and at $a = 105$ ms after $\tau = 85$ ms, respectively. Four cycles of oscillations at $a = 50$ ms can also be observed. This indicates that the periodic eddies of $a = 50$, 105 and 145 ms pass through the shear layer, because the local potential core fluctuating ve-

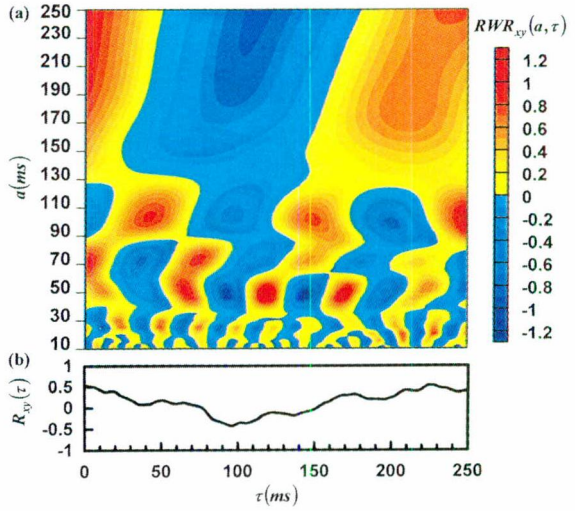

Fig. 7 Wavelet cross-correlation analysis of two velocity fluctuations at $x/d = 10$, $2\Delta y/d = 0.5$ (Type II) (a) wavelet cross-correlation coefficients; (b) traditional cross-correlation coefficients

locity has unusually large positive and negative peaks when an eddy moves close to the center line (Yule, 1978). There are weaker patterns in the range of $a = 20-30$ ms, and this indicates the existence of weaker periodic motions. The first positive peak of $R_{xy}(\tau)$ corresponds to two positive peaks of $RWR_{xy}(a, \tau)$ at $a = 85$ and 145 ms, which give the periods of eddy motion. Because $RWR_{xy}(a, \tau)$ has a strongly negative peak at period $a = 80$ ms at zero time delay, $R_{xy}(\tau)$ exhibits a negative value. However, this does not mean the negative correlation in all period range.

The second color graph of Fig. 5 shows a distribution of its $\theta WC_{xy}(a, \tau)$ using (a, τ) color plane representation. $\theta WC_{xy}(a, \tau)$ can describe the phase difference between two wavelet coefficients or two velocity fluctuations at two different locations for a time delay of τ at a given period a, and can help us identify the change of the phase difference from $-(\pi/2)$ to $\pi/2$. The discontinue isophase line between isophase line of $\pi/2$ and $-(\pi/2)$ corresponds to the zero value line of $RWR_{xy}(a, \tau)$, which means non-correlation. The zero isophase line of $\theta WC_{xy}(a, \tau)$ equivalents to the local maxima or minima of $RWR_{xy}(a, \tau)$ around τ at a given a, and this indicates that two signals at two points have a same phase value. Of course, positive or negative peaks in the map of $RWR_{xy}(a, \tau)$ exist on the zero isophase lines. A cross-point, which exists a cross between a zero isophase line and a discontinue isophase line, corresponds to the zero value of the modulus of wavelet cross-correlation coefficient $MWR_{xy}(a, \tau)$. The branching structures of the discontinue isophase line or the zero isophase line also indicate that the periodic flow structure consists of many periodic small-scale motions and few periodic large-scale motion. At a given period or scale, we can obtain an angular frequency $\omega_{xy}(a, \tau)$ $(=\Delta\theta WC_{xy}(a, \tau)/\Delta\tau)$ by differentiating the corresponding phase fields with respect to time delay. In fact, $\omega_{xy}(a, \tau)$ means the difference of the angular frequency between the two velocity fluctuations at two points for a time delay of τ.

It is well known that the traditional cross-correlation of velocity fluctuations has been used extensively to determine the convection velocity in various turbulent flows. Although Goldschmidt et al. (1981) considered both broadband and wavenumber-dependent convection velocities, and dominant convection velocities cannot be extracted. From the distribution of peaks in $RWR_{xy}(a, \tau)$, however, we can easily determine the convection velocities of various periods that dominate flow structures using the following method. The convection velocity for a given period is defined as the ratio of the longitudinal separation distance $2\Delta x$ between two probes and the time delay τ_{max} between local maxima or minima in $RWR_{xy}(a, \tau)$, or the ratio of the longitudinal separation distance $2\Delta x$ and the period a_{max} at which $RWR_{xy}(a, \tau)$ has the local maxima or minima. From the distribution of peaks in $RWR_{xy}(a, \tau)$ for various periods, it is obvious that the convection velocity is period dependent. The time delay between local maxima or local minima of $RWR_{xy}(a, \tau)$ clearly indicates that the large-scale motion moves slower than the small-scale motion.

Wavelet Cross-Correlation Analysis of Coherent Structure (Type II Measurement). Type II measurements were used to investigate the coherent structure of turbulent flow on opposite sides of the centerline in the shear layer. Color contour maps of $RWR_{xy}(a, \tau)$ and $\theta W C_{xy}(a, \tau)$ of the two fluctuating velocities with separations of $2\Delta y/d = 2$ at $x/d = 5$ in the shear layer are shown in Fig. 6. It exhibits positive values for $RWR_{xy}(a, \tau)$ at zero time delay and periodic oscillations for various periods with increasing the time delay. This indicates that symmetric and periodic motions with various scales exist in the shear layer. From Fig. 6(*a*), the obvious nearly periodic oscillations happen at $a = 65$, 90 ($\tau = 100-190$ ms), 160 ms, and several irregular weaker peaks at $a < 50$ ms range. This implies that the two-dimensionality of the periodic vortex street contains three periodic eddies and several irregular small eddies on opposite sides of the centerline. From the branching structures in $RWR_{xy}(a, \tau)$, the periodic eddy of $a = 90$ ms, which exists in the periodic large eddy of $a = 160$ ms, contains the periodic eddy of $a = 65$ ms. Above coherent structure is essentially coincident with what we find in Fig. 5. The distribution of $\theta WC_{xy}(a, \tau)$ is shown in Fig. 6(*b*). The cross-point and area of positive value of phase increase with increasing separation distance of $2\Delta y/d$. This implies that the periodic motions with various scales are much more active in the shear layer. The distribution of $\theta WC_{xy}(a, \tau)$ shows regular features in range of medium and high period, because periodic medium and large scale eddies appear in the shear layer. However, the distribution of $\theta WC_{xy}(a, \tau)$ becomes the most irregular features in low period range.

At a downstream distance of $x/d = 10$, the variation in $RWR_{xy}(a, \tau)$ for a separation of $2\Delta y/d = 0.5$ is shown in Fig. 7. It is apparent that the strong periodic correlation occurs at $a = 50$, 70, 105 ms, and high period range. There are also weaker periodic peaks appearing at $a < 30$ ms. Comparing with $RWR_{xy}(a, \tau)$ at $x/d = 5$ (Fig. 6(*a*)), the scale of dominant periodic eddy increases.

It is well-known fact that the turbulent plane jet exhibits an apparent sideways, flapping type motion (Goldschmidt and Bradshaw, 1973). The apparent flapping motion attributes either to the presence of organized coherent structures with lateral oscillations of finite extent or to an asymmetric coherent structure, which is hidden in the randomness of the turbulent field. This motion can be detected only by the distinctive negative correlation at zero time delay after long time averaged correlation of the longitudinal components of the velocity measured at two points, each one at opposite sides of the jet centerline (Gervantes and Goldschmidt, 1981). However, it is impossible to provide the information about the scale or period of this motion from the traditional correlation method. At $x/d = 10$, as shown in Fig. 7(*a*), the distinctive positive values appearing in $R_{xy}(\tau)$ at zero time delay. Usually this indicates the asymmetric organized motion and means no flapping motion at all. In this study we describe the flapping motion in the Fourier space using the wavelet cross-correlation analysis. From the distinctive positive values appearing in $RWR_{xy}(a, \tau)$ at zero time delay in Fig. 7(*a*), the symmetric organized structures can be detected at $a = 50$, 70 ms and high period range. However, $RWR_{xy}(a, \tau)$ at $a = 105$ ms and low period range exhibits the distinctive negative values at zero time delay. This implies that the apparent flapping behavior appears at these periods or scales, which is masked by the symmetric large-scale motions and cannot be detected by the traditional method. With increasing x/d, the disturbance due to the apparent flapping motion of the intermedium scale grows and ultimately results in the large-scale apparent flapping motion that can be observed by the traditional method. From above, it can say that the analysis of the apparent flapping motion should also carry out in the Fourier space.

Conclusions

The following main results are summarized.

(1) The wavelet correlation analysis can extract the information of coherent strength and phase in terms of period and time delay, which is lost if the data are analyzed only by the traditional correlation method.

(2) The peaks of wavelet correlation coefficients in the high period region correspond to large peaks in $R(\tau)$, and the peaks of wavelet correlation coefficients in the low period region are equivalent to small peaks in $R(\tau)$.

(3) In branching structures of wavelet correlation coefficients or phase, the correlation peak in the high period region consists of the correlation peaks in the low period region. That is, a periodic large-scale motion contains periodic smaller scale motions.

(4) From the time between local maxima or minima or the period of peaks in wavelet cross-correlation coefficients, the convective velocities of various scales that dominate the flow structure can easily be determined.

(5) From distribution of $RWR_{xy}(a, \tau)$ at $x/d = 5$, it is found that the two-dimensionality of the periodic vortex street contains three periodic eddies and several irregular small eddies on opposite sides of the centerline.

(6) In the shear layer of $x/d = 10$, any information of auto-correlation cannot be obtained from $R(\tau)$, but the strong periodic motions of eddy for $a = 75$, 100, and 150 ms are clearly observed in wavelet auto-correlation coefficients.

(7) The large-scale motions remain symmetric and periodic in the shear layer at $x/d = 10$. From distribution of $RWR_{xy}(a, \tau)$, however, it is evident that the apparent flapping motion appears in the region of intermedium scale.

Acknowledgment

This work was performed as part of research supported by a scientific research fund granted by Japanese Ministry of Education, Science and Culture (No. 07750202).

References

Antonia, R. A., Browne, L. W., Rajagopalan, S., and Chambers, A. J., 1983, "On the Organized Motion of a Turbulent Plane Jet," *Journal of Fluid Mechanics,* Vol. 134, pp. 49–66.

Argoul, F., Arneodo, A., Grasseau, G., Gagne, Y., Hopfinger, E. J., and Frisch, U., 1989, "Wavelet Analysis of Turbulence Reveals the Multifractal Nature of the Richardson Cascade," *Nature,* Vol. 338, No. 2, pp. 51–53.

Bacry, E., Arneodo, A., Frisch, U., Gagne, Y. and Hopfinger, E., 1991, "Wavelet Analysis of Fully Developed Turbulence Data and Measurement of Scaling Exponents," *Turbulence and Coherent Structures,* Kluwer Academic Publishers, pp. 203–215.

Benaissa A., Anselmet F., Moret-Bailly F. and Liandrat J., 1993, "Experimental Analysis of Coherent Motions in a Turbulent Boundary Layer," *Eddy Structure Identification in Free Turbulent Shear Flows,* J. P. Bonnet and M. N. Glauser, eds., Kluwer Academic Publishers, pp. 159–168.

Benzi, R., and Vergassola, M., 1991, "Optimal Wavelet Transform and its application to Two Dimensional Turbulence," *Fluid Dynamics Research,* Vol. 8, pp. 117–126.

Crow S. C., and Champagne, F. H., 1971, "Orderly Structure in Jet Turbulence," *Journal of Fluid Mechanics,* Vol. 48, 547–591.

Dallard, T., and Browand, F. K., 1993, "Scale Transitions at Defect Sites in the Mixing Layer: Application of the 2-D Arc Wavelet Transform," *Journal of Fluid Mechanics,* Vol. 247, pp. 339–368.

Dallard, T., and Spedding, G. R., 1993, "2-D Wavelet Transform: Generalisation of the Hardy Space and Application to Experimental Studies," *European Journal of Mechanics B/Fluids,* Vol. 12, pp. 107–134.

Everson, R., and Sirovich, L., 1990, "Wavelet Analysis of the Turbulent Jet," *Physics Letters,* Vol. 145, No. 6, pp. 314–322.

Farge, M., 1992, "Wavelet Transforms and Their Applications to Turbulence," *Annual Review of Fluid Mechanics,* Vol. 24, pp. 395–457.

Farge, M., Kevlahan, N., Perrier, V., and Goirand, E., 1996, "Wavelets and Turbulence," *Proceedings of the IEEE,* Vol. 84, No. 4, pp. 639–669.

Gervantes, de Gortari, J. G., and Goldschmidt, V. W., 1981, "The Apparent Flapping Motion of a Turbulent Plane Jet—Further Experimental Results," ASME JOURNAL OF FLUIDS ENGINEERING, Vol. 103, No. 1, pp. 119–126.

Goldschmidt, V. W., and Bradshaw, P., 1973, "Flapping of a Plane Jet," *Physics of Fluids,* Vol. 16, pp. 354–355.

Goldshmidt, V. W., Young, M. F., and Ott, E. S., 1981, "Turbulent Convective Velocities (Broadband and Wavenumber Dependent) in a Plane Jet," *Journal of Fluid Mechanics,* Vol. 105, pp. 327–345.

Gordeyev, S. V., and Thomas, F. O., 1995, "Measurement of Reynolds Stress Reversal in a Planar Jet by Means of a Wavelet Decomposition," *Turbulent Flows,* ASME, FED-Vol. 208, pp. 49–54.

Gordeyev, S. V., Thomas F. O., and Chu, H. C., 1995, "Experimental Investigation of Unsteady Jet Shear Layer Dynamics Using a Wavelet Decomposition," *Unsteady Flows,* ASME, FED-Vol. 216, pp. 167–172.

Goupillaud, P., Grossmann, A., and Morlet, J., 1984, "Cycle-Octave and Related Transforms in Seismic Signal Analysis," *Geoexploration,* Vol. 23, pp. 85–102.

Grossmann, A., and Morlet, J., 1984, "Decomposition of Hardy Functions ito Square Integrable Wavelets of Constant Shape," *SIAM J. Math. Anal.,* Vol. 15, pp. 723–736.

Gutmark, E., 1976, "The Planar Turbulent Jet," *Journal of Fluid Mechanics,* Vol. 73, Part 3, pp. 465–495.

Harr, A., 1910, "Zur Theorie der Orthogonalen Funktionen-Systeme," *Mathematische Annalen,* Vol. 69, pp. 331–371.

Higuchi, H., Lewalle J., and Crane P., 1994, "On the Structure of a Two-Dimension Wake Behind a Pair of Flat Plates," *Physics Fluids,* Vol. 6, No. 1, pp. 297–305.

Hsiao, F. B., and Huang, J. M., 1994, "On the Dynamics of Flow Structure Development in an Excited Plane Jet," ASME JOURNAL OF FLUIDS ENGINEERING, Vol. 116, No. 4, pp. 714–720.

Kaspersen, J. H., 1996, "A Study of Coherent Structures Using Wavelet Analysis," Ph.D. thesis.

Krothapalli, A., Baganoff, D., and Karamcheti, K., 1981, "On the Mixing of a Rectangular Jet," *Journal of Fluid Mechanics,* Vol. 107, pp. 201–220.

Lewalle, J., Petagna P. and Buresti G., 1994, "Wavelet Statistics of the Near-Field Structure of a Coaxial Jet," AIAA Paper 94-2323.

Liandrat, J., and Moret-Bailly, F., 1990, "The Wavelet Transform: Some Applications to Fluid Dynamics and Turbulence," *European Journal of Mechanics B/Fluids,* Vol. 9, No. 1, pp. 1–19.

Li H., 1997a, "Wavelet Analysis on Coherent Structure Dynamics in a Plane Turbulent Jet," *Experimental Heat Transfer, Fluid Mechanics and Thermodynamics 1997,* Edizioni ETS, PISA, pp. 1175–1782.

Li H., 1997b, "Wavelet Reynolds Stress Analysis of Two-Dimensional Vortex Flow," ASME FEDSM 97-3040.

Li, H., 1997c, "Wavelet Velocity Correlation Analysis in a Plane Turbulent Jet," *Proceedings of the 11th Symposium on Turbulent Shear Flows,* Vol. 3, P3-101–106.

Li, H., 1997d, "Turbulent Structure Analysis of a Two-Dimensional Jet Using Wavelets," *Proceedings of the 5th Triennial International Symposium on Fluid Control, Measurement and Visualization,* pp. 589–594.

Li, H., and Nozaki, T., 1995, "Wavelet Analysis for the Plane Turbulent Jet (Analysis of Large Eddy Structure)," *JSME International Journal, Fluids and Thermal Engineering,* Vol. 38, No. 4, pp. 525–531.

Li, H., Nozaki, T., Tabata T., and Oshige S., 1997, "Wavelet Analysis of Flow Structure in a Bounded Jet," *Proceedings of International Conference on Fluid Engineering,* Vol. 2, No. 97-107, pp. 589–594.

Li, H., Takei, M., Ochi, M., Saito, Y., and Horii, K., 1998a, "Velocity Correlation Analysis in the Near-Field of a Turbulent Jet With Help of Discrete Wavelet Transform," ASME FEDSM98-4823.

Li, H., Takei, M., Ochi, M., Saito, Y., and Horii, K., 1998b, "Multiresolution Visualization of the Turbulent Jet," *Album of Visualization,* No. 15, pp. 11–12.

Li, H., Takei, M., Ochi, M., Saito, Y., and Horii, K., 1998c, "Effect of Different Orthogonal Wavelet Basis on Multiresolution Image Analysis of a Turbulent Flow," *CD-ROM Proceedngs of International Conference on Optical Technology and Image.*

Li, H., and Tomita, Y., 1997, "Wavelet Statistical Analysis of Gas-Solid Flow in a Vertical Pipeline," *Experimental Heat Transfer, Fluid Mechanics and Thermodynamics 1997,* Edizioni ETS, PISA, pp. 1053–1060.

Li, H., and Tomita, Y., 1998, "Wavelet Analysis of Gas-Solid Two-Phase Flow in a Horizontal Pipe," *CD-ROM Proceedings of Third International Conference on Multiphase Flow.*

Morlet, J., Arens, G., Fourgeau, I., and Giard D., 1982, "Wave Propagation and Sampling Theory," *Geophysics,* Vol. 47, pp. 203–236.

Moum, J. N., Kawall, J. G., and Keffer, J. F., 1979, "Structure Features of the Plane Turbulent Jet," *Physics Fluids,* Vol. 22, No. 7, pp. 1240–1249.

Mumford, J. C., 1982, "The Structure of the Large Eddies in Fully Developed Turbulent Shear Flows. Part 1. The Plane Jet," *Journal of Fluid Mechanics,* Vol. 118, pp. 241–268.

Oler, J. W., and Goldschmidt, V. W., 1984, "Coherent Structures in the Similarity Region of Two-Dimensional Turbulent Jets," ASME JOURNAL OF FLUIDS ENGINEERING, Vol. 106, No. 2, pp. 187–192.

Quinn, W. R., 1994, "Development of a Large-Aspect-Ratio Rectangular Turbulent Free Jet," *AIAA Journal,* Vol. 32, No. 3, pp. 547–554.

Spedding, G. R., Browand, F. K., Huang N. E., and Long S. R., 1993, "A 2-D Complex Wavelet Analysis of an Unsteady Wind-Generated Surface Wave Field," *Dynamics of Atmospheres and Oceans,* Vol. 20, pp. 55–77.

Sullivan, P., and Pollard, A., 1996, "Coherent Structure Identification from the Analysis of Hot-Wire Data," *Measurement of Science Technology,* Vol. 7, pp. 1498–1516.

Thomas, F. O., and Chu, H. C., 1993, "Nonlinear Wave Coupling and Subharmonic Resonance in Planar Jet Shear Layer Transition," *Physics Fluids A,* Vol. 5, No. 3, pp. 630–646.

Walker, S. H., Gordeyev, S. V., and Thomas, F. O., 1995, "A Wavelet Transform Analysis Applied to Unsteady Jet Screech Resonance," *High Speed Jet Flows ASME,* FED-Vol. 214, pp. 103–108.

Weierstrass, K., 1895, "Mathematische Werke," Vol. 2, Mayer & Muller, Berlin.

Yamada, M. and Ohkitani, K., 1990, "Orthonormal Wavelet Expansion and Its Application to Turbulence," *Progress of Theoretical Physics,* Vol. 83, No. 5, pp. 819–823.

Yoda, M., Hesselink, L., and Mungal, M. G., 1992, "The Evolution and Nature of Large-Scale Structures in the Turbulent Jet," *Physics Fluids A,* Vol. 4, No. 4, pp. 803–811.

Yule, A. J., 1978, "Large-scale Structure in the Mixing Layer of a Round Jet," *Journal of Fluid Mechanics,* Vol. 89, pp. 413–432.

Turbulent Flow Through Spacer Grids in Rod Bundles

Sun Kyu Yang
Principal Researcher.

Moon Ki Chung
Principal Researcher.

Thermal Hydraulics Safety Research Team,
Korea Atomic Energy Research Institute,
Yusung, P.O. Box 105, Taejon,
305-600, Korea

The effects of the spacer grids with mixing vanes in rod bundles on the turbulent structure were investigated experimentally. The detailed hydraulic characteristics in subchannels of a 5 × 5 rod bundle with mixing spacer grids were measured upstream and downstream of the spacer grid by using a one component LDV (Laser Doppler Velocimetry). Axial velocity and turbulent intensity, skewness factor, and flatness factor were measured. The turbulence decay behind spacer grids was obtained from measured data. The trend of turbulence decay behaves in a similar way as turbulent flow through mesh grids or screens. Pressure drop measurements were also performed to evaluate the loss coefficient for the spacer grid and the friction factor for a rod bundle.

Introduction

Research on the turbulent flow characteristics of the fuel assembly with spacer grids is of importance for thermal hydraulic design and safety analysis in a nuclear reactor. This study is focused on turbulent structure modulation due to spacer grids in LWR (Light Water Reactor) rod bundles in normal operation. The coolant through the rods is single phase flow in LWR normal operation. The roles of the spacer grid are to support the rods regularly and to promote flow mixing which in turn enhances thermal mixing. The spacer grid tested in the present work is a spacer grid with mixing vanes.

Major features of turbulent phenomena in subchannels include cross-flow mixing between subchannels, anisotropy of turbulent diffusion, and secondary flow. They are illustrated in Fig. 1. In addition to these turbulent phenomena, there is drastic turbulence generation near spacer grid which is caused by the sharp edge and blockage of spacer grid. Generated turbulence due to spacer grid decreases rapidly as the flow develops. In this study, turbulence decay behind spacer grids was investigated more in detail.

Previous experimental studies on the flow characteristics near spacer grids in bare rod bundles include Rehme (1973), Rowe and Chapman (1973), Rehme and Trippe (1980), and Shen et al. (1991). Rehme (1973) measured the pressure drops for the various kinds of the spacer grids. An experimental study by Rowe and Chapman (1973) was carried out to evaluate the effect of spacer grids on the axial turbulent flow structure in rod bundles. Local axial velocity and turbulent intensity were measured upstream and downstream of spacer grids by using a LDV (Laser Doppler Velocimetry). The highest intensity was observed downstream near the spacer grid and decayed rapidly to stable level far downstream. However, they could not give information on the correlations for the turbulence behind spacer grids. And higher moments of turbulent fluctuations were not measured. Compared to Rowe and Chapman, in the present work, more detailed measurements for new turbulent parameters in axial locations were performed upstream and downstream of spacer grids, which gave information of the spacer grid effects on turbulent flow structure quantitatively. Rehme and Trippe measured, by using Pitot tubes, in detail the velocity distributions upstream and downstream of spacer grids. The mass flow separation and redistribution between the subchannels are discussed and compared with the prediction by a subchannel analysis code. Shen et al. performed detailed measurements using LDV in water to obtain information on the distribution of the transverse mean velocity and turbulent intensity for a flow through a sixteen-rod bundle with mixing blades on the spacer grid. They observed that the mixing rate varies largely with the angle of mixing blade on the spacer grid.

In this study, which was published earlier in a conference volume (Yang and Chung, 1995), detailed hydraulic characteristics of the turbulent flow through spacer grids with mixing vanes were measured by using a LDV. The measured parameters include pressure drops, axial velocity and turbulent intensity, skewness factor, and flatness factor. Loss coefficients for the spacer grid and friction factors for rod bundles were estimated from the measured pressure drops.

Experimental Method

Test Facility. The tested 5 × 5 spacer grid is shown in Fig. 2. The mixing vanes are attached with an angle of 22 deg on the spacer grid to enhance flow mixing. The test section, as shown in Fig. 3, of 68 mm square housing consists of 25 rods of 9.5 mm in diameter. The rod bundle forms in a square array with $P/D = 1.326$ and $W/D = 1.4263$. The hydraulic diameter (D_h) of the entire channel is 11.21 mm. Axial locations of spacer grids and pressure taps are shown in Fig. 4. The mixing spacer grids are positioned in the rod bundle with the span of 600 mm. Water is the working fluid. Fluid enters the bottom of the flow housing and flows upward. Test section is set up in test-loop shown schematically in Fig. 5, which includes variable speed pump, a storage tank, flow control values, and turbine flow meters etc. During the experiments, the water temperature in the test section was maintained at 25°C by adjusting the feed and drain of water in the storage tank. Pressure drops were measured by changing the mass flow rate controlled by variable pump speed and measured by the turbine flow meter. For the turbulent velocity measurement, the flow rate was 14.22 kg/s resulting in an average flow velocity of 5 m/s and a Reynolds number based on the hydraulic diameter of Re = 62500. The square housing is made of acrylic to allow access for laser beams to the location where the velocity measurement is to be performed.

LDV Measurements. The one-component He-Ne LDV system from TSI, which is used in the present work, was aligned by the dual-beam backward scattered mode. The dual beam spacing is 50 mm and the focal-length of the focusing lens is 250 mm. Silicon carbide particles, 1.5 μm in diameter, 3.2 g/cm^3 in density, 2.65 in refractive index, and 1.4 in geometrical standard deviation, were added into the fluid to obtain the scat-

Contributed by the Fluids Engineering Division for publication in the JOURNAL OF FLUIDS ENGINEERING. Manuscript received by the Fluids Engineering Division August 4, 1997; revised manuscript received July 8, 1998. Associate Technical Editor: S. Banerjee.

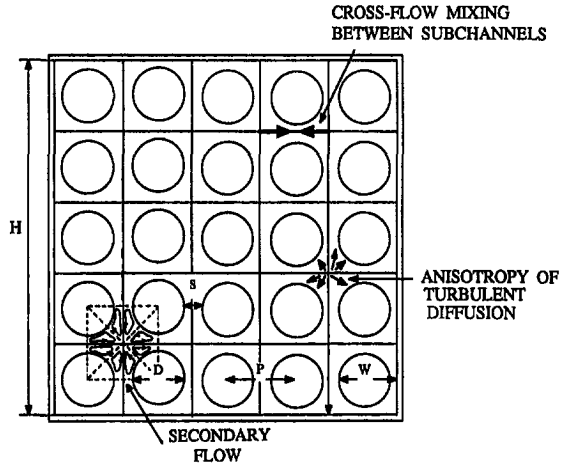

Fig. 1 Turbulent phenomena in subchannels

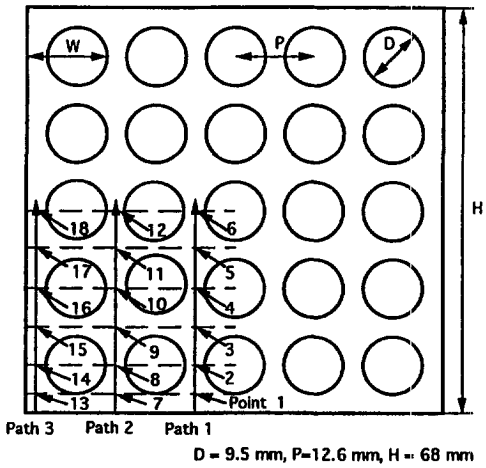

Fig. 3 Cross-section of 5 × 5 rod bundles and measuring location

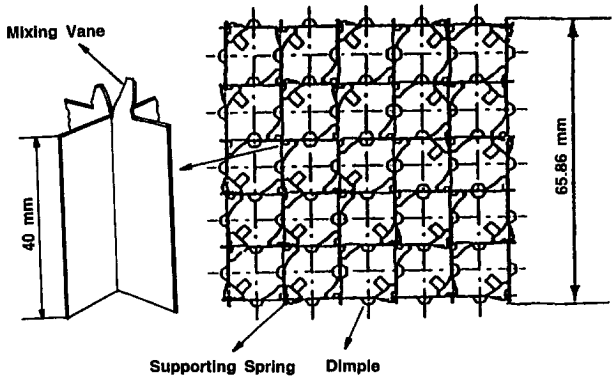

Fig. 2 5 × 5 spacer grid with mixing vanes

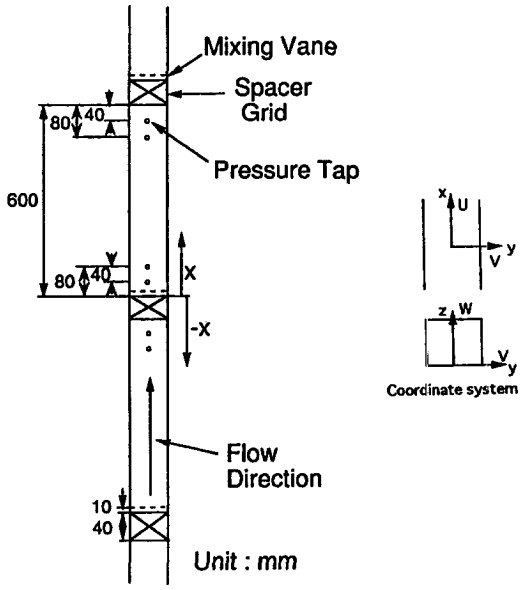

Fig. 4 Axial location of spacer grids and pressure taps

tered signal. The signals from the photomultiplier were processed using a counter type processor which consists of filters, an amplifier, a timer, a digital output, and a *D/A* (Digital to Analog) converter. The signals from the digital output of the signal processor were used to obtain the turbulent velocity and intensity by using data analysis program FIND from TSI installed in a personal computer. In this software, the correcting process for velocity bias is included.

Measuring Locations. Measuring paths and locations are shown in Fig. 3 and tabulated in Table 1 in accordance with the present coordinate system shown in Fig. 4. Turbulent velocities were measured at paths 1, 2, and 3 with varying the axial locations (x) in negative and positive direction covering the entire span between spacer grids. Paths are located at central region in gap between rods. At points on the paths more detailed flow measurements in axial direction were performed in particular near spacer grids. Pressure drops were measured at pressure taps shown in Fig. 4.

Experimental Results and Discussions

Pressure Drops. The pressure drop at the spacer grid (ΔP_G) is related to the bulk average fluid velocity, U_{av}, in the rod bundle (Rehme, 1973).

Nomenclature

D = rod diameter, m
D_h = hydraulic diameter, m
f = friction factor
P = pitch, m
p = pressure, Pa
Re = Reynolds number ($U_{av}D_h/\nu$), dimensionless
s = rod gap spacing, m
U = axial time mean velocity, m/s
U_{av} = entire subchannel average velocity, m/s
$\tilde{u}$ = instantaneous velocity, m/s
u = axial fluctuating velocity, m/s
u' = root mean square of u, m/s
V = radial time mean velocity, m/s
v = radial fluctuating velocity, m/s
W = wall distance, m
W = azimuthal time mean velocity, m/s
w = azimuthal fluctuating velocity, m/s
x = axial coordinate, m
y = traversing coordinate, m
z = traversing coordinate, m
κ = half angle of laser beam intersection, degree
λ = laser wavelength, m
ν = kinematic viscosity, m^2/s
ρ = fluid density, kg/m^3

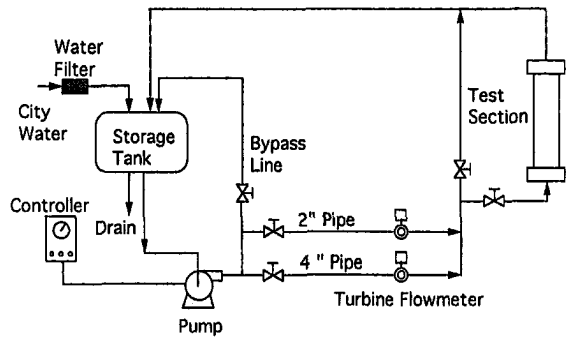

Fig. 5 Flow diagram of test loop

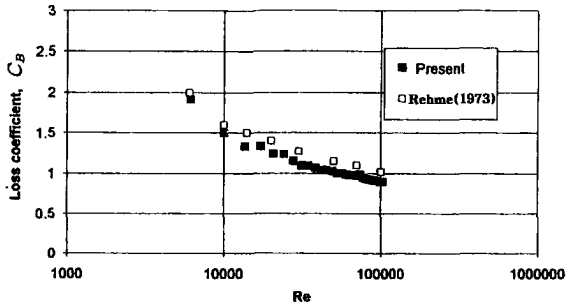

Fig. 6 Loss coefficients for 5 × 5 tests (Uncertainty in loss coefficient = ±2.8 percent)

$$\Delta P_G = C_B \rho \frac{U_{av}^2}{2} \tag{1}$$

where C_B is the loss coefficient of the spacer and ρ is the fluid density. Figure 6 shows the loss coefficient profile with variation of Reynolds number based on hydraulic diameter and average velocity. Loss coefficients are compared with the reproduced Rehme (1973)'s data for the square array with the spacer grid of tube squares axially connected. The present data show lower values than those reported by Rehme.

The friction factors (f) in rod bundles were estimated as shown in Fig. 7 from measured pressure drops and compared with the Blasius (1913) correlation given by $f = 0.316/\mathrm{Re}^{0.25}$, where f is Darcy friction factor. The friction factors were estimated as

$$f = -\frac{dP}{dx}\frac{2D_h}{\rho U_{av}^2} \tag{2}$$

The results show that those of the present work are a little higher, about 2.5 percent, than the values given by the Blasius curve.

Axial Velocity. Figure 8 shows the axially developing velocity profiles at paths 1–3. The velocity profiles at paths 1 and 2 are similar each other, however, different from that at path 3 which is in the wall and corner subchannels. The lower spacer grids disturb the local velocity field, which causes a change in mass flow within each subchannel through the spacer grids. Near the upstream spacer grid, at $x/D_h = 2$, the flow fluctuates drastically due to the flow blockage and turbulence generation induced by the sharp edge of the spacer grid. At $x/D_h = 32$ and 50, the flow is nearly developed. Figure 9 shows the axial velocity distribution at points at different axial locations downstream of spacer grid. At points on path 1 the velocities at points 1, 3, and 5 decrease and those at points 2, 4, and 6 increase through spacer grids. It is observed that flow mixing occurs intensively after passing through spacer grids up to about $x/D_h = 20$. As the flow develops, the flow distribution becomes recovered to the original one just before the lower spacer grid.

Table 1 Measuring locations for 5 × 5 rod bundle test

Point \ coord.	x/D_h	y/H	z/H
1	−11 ~ 53	0.097	0.06
2	−11 ~ 53	0.097	0.13
3	−11 ~ 53	0.097	0.22
4	−11 ~ 53	0.097	0.31
5	−11 ~ 53	0.097	0.41
6	−11 ~ 53	0.097	0.50
7	−11 ~ 53	0.28	0.06
8	−11 ~ 53	0.28	0.13
9	−11 ~ 53	0.28	0.22
10	−11 ~ 53	0.28	0.31
11	−11 ~ 53	0.28	0.41
12	−11 ~ 53	0.28	0.50
13	−11 ~ 53	0.47	0.06
14	−11 ~ 53	0.47	0.13
15	−11 ~ 53	0.47	0.22
16	−11 ~ 53	0.47	0.31
17	−11 ~ 53	0.47	0.41
18	−11 ~ 53	0.47	0.50
Path \ Coord.	**x/D_h**	**y/H**	**z/H**
1	2, 4, 8, 16, 32, 50	0.097	0.019 ~ 0.54
2	2, 4, 8, 16, 32, 50	0.28	0.019 ~ 0.54
3	2, 4, 8, 16, 32, 50	0.47	0.019 ~ 0.54

Axial Turbulent Intensity. Figure 10 represents the axial turbulent intensities at points. The highest intensity is distributed just behind the lower spacer grid. The intensity decreases to the lowest value at above $x/D_h = 30$. The turbulent intensity increases drastically through spacer grids, and decreases rapidly to the stable level as the flow develops. It is observed that the intensities far downstream in the upper grid span coincide excellently with the values far downstream in the lower grid span. This implies that the intensity distributions are repeatable with the grid spans. The turbulent intensity decay behind the spacer grid can be explained by turbulence decay in turbulent flows through mesh grids (Comte-Bellot and Corrsin, 1966 and Sreenivasan et al., 1980) or screens (Laws and Liversey, 1978). Usually the relation of the turbulence decay rate is expressed as

$$\frac{\overline{u^2}}{U^2} = \alpha\left(\frac{x}{M} - \frac{x_0}{M}\right)^{-n} \tag{3}$$

where α, M, x_0, and n are fitting constant, grid mesh size, virtual origin, and decay rate, respectively. Grid mesh size, M is assumed to be pitch length, P in the present study. The axial turbulent intensities at points 1–6 behind spacer grid are plotted in Fig. 11, and compared with the Sreenivasan et al.'s data. For

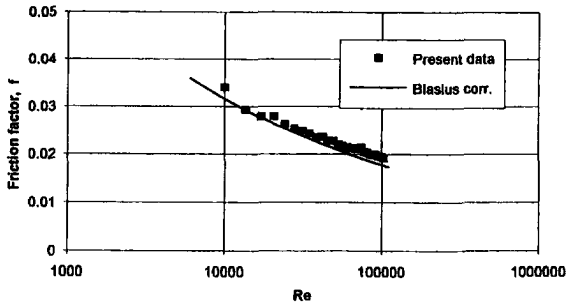

Fig. 7 Friction factors for 5 × 5 tests (Uncertainty in friction factor = ±2.79 percent)

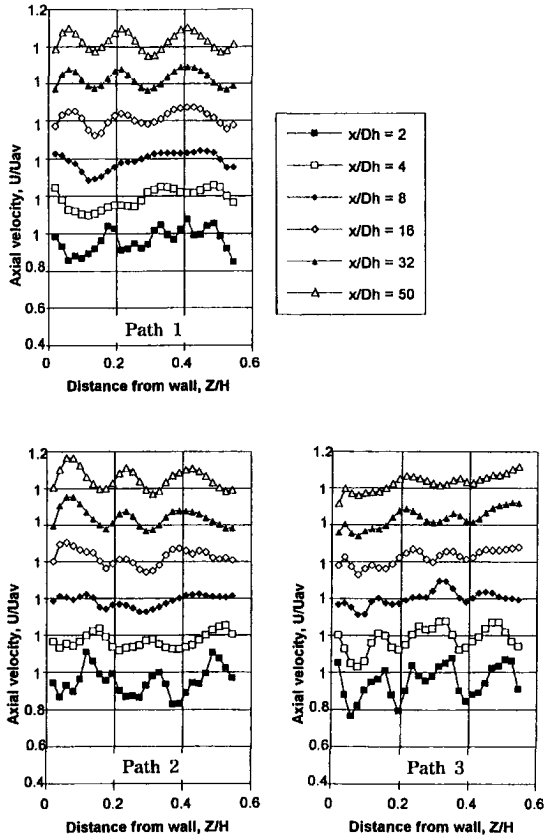

Fig. 8 Developing axial velocity at paths (Uncertainty in axial velocity = ±2.9 percent)

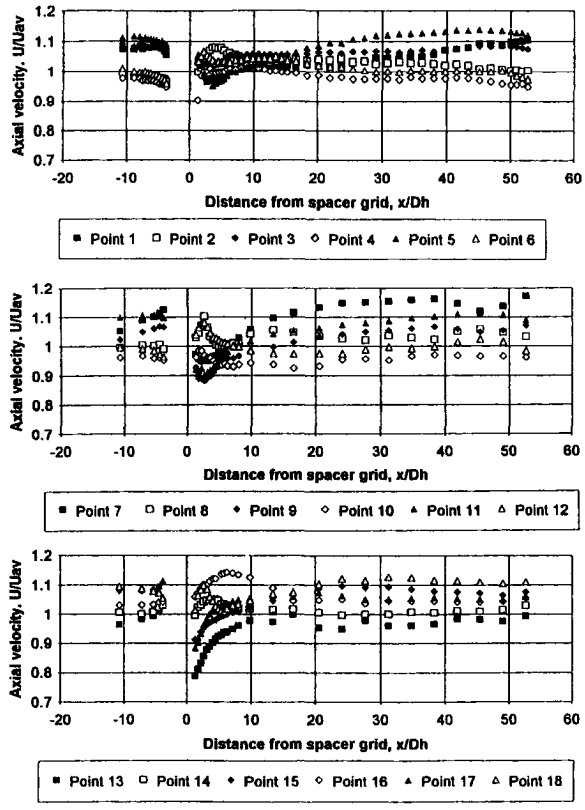

Fig. 9 Axial velocity distribution at points (Uncertainty in axial velocity = ±2.9 percent)

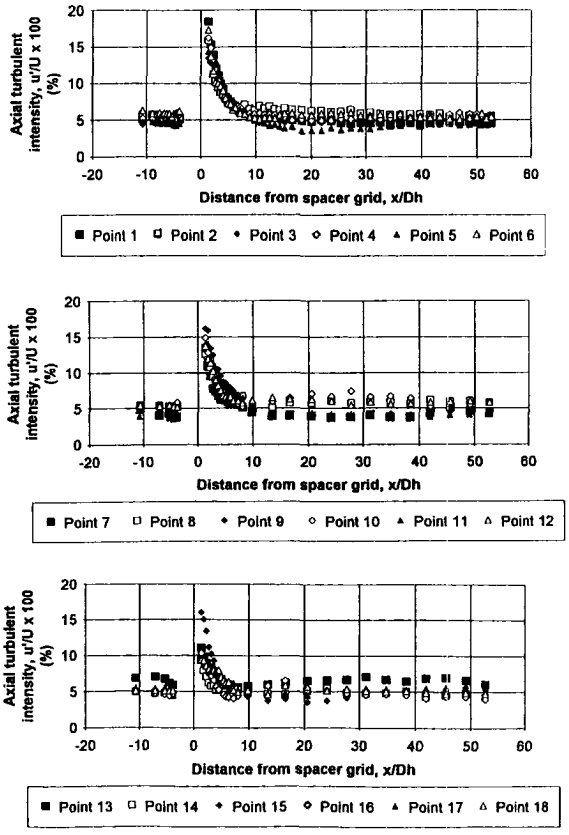

Fig. 10 Axial turbulent intensity distribution at points (Uncertainty in axial turbulent intensity = ±7.7 percent)

the case of Sreenivasan et al., the values of α, x_0/M, n are 0.04, 3 and 1.2, respectively. However, the virtual origin, x_0/M, of the present correlation in Fig. 11 was shifted from 3 to 0. The present correlation is obtained as

$$\frac{\overline{u^2}}{U^2} = 0.04\left(\frac{x}{P}\right)^{-1.2} \tag{4}$$

It is generally observed that the turbulent intensity decay at points inner region behaves as that of the mesh grid.

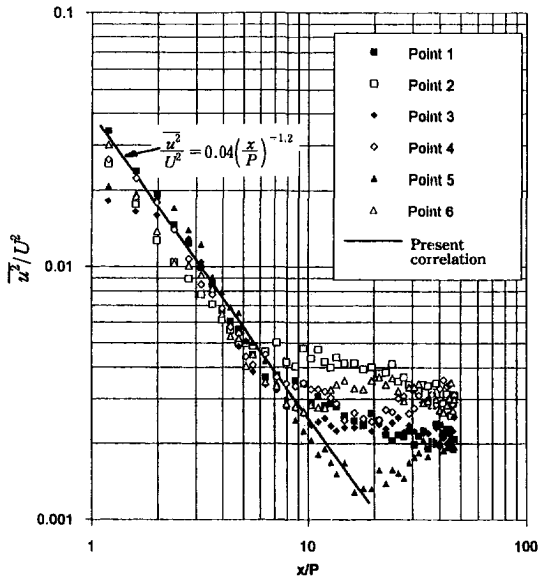

Fig. 11 Axial turbulent intensity decay behind spacer grid at points 1–6 (Uncertainty in axial turbulent intensity = ±7.7 percent)

Some observations from the results of axial turbulence decay can be deduced by referring to conservation equation of axial turbulent intensity in steady state, constant density and three-dimensional condition.

$$U\frac{\partial\overline{u^2}}{\partial x}+V\frac{\partial\overline{u^2}}{\partial y}+W\frac{\partial\overline{u^2}}{\partial z}=\underbrace{-2\overline{u^2}\frac{\partial U}{\partial x}}_{\text{I}}\underbrace{-2\overline{uv}\frac{\partial U}{\partial y}}_{\text{II}}-2\overline{uw}\frac{\partial U}{\partial z}$$

$$\underbrace{-\frac{\partial\overline{u^3}}{\partial x}-\frac{\partial\overline{u^2v}}{\partial y}-\frac{\partial\overline{u^2w}}{\partial z}}_{\text{III}}\underbrace{-\frac{2}{\rho}\frac{\partial\overline{pu}}{\partial x}}_{\text{III}}+\nu\left(\frac{\partial^2\overline{u^2}}{\partial x^2}+\frac{\partial^2\overline{u^2}}{\partial y^2}+\frac{\partial^2\overline{u^2}}{\partial z^2}\right)$$

$$\underbrace{+\frac{2}{\rho}\overline{p\frac{\partial u}{\partial x}}}_{\text{IV}}\underbrace{-2\nu\left\{\overline{\left(\frac{\partial u}{\partial x}\right)^2}+\overline{\left(\frac{\partial u}{\partial y}\right)^2}+\overline{\left(\frac{\partial u}{\partial z}\right)^2}\right\}}_{\text{V}} \quad (5)$$

where the designated terms I, II, III, IV, and V represent convection, production, diffusion, pressure redistribution, and dissipation terms, respectively. For the case of developing region, particularly immediately behind spacer grid, it is hard to explain the turbulence increase and decay. In developing region, all terms in Eq. (5) are contributing to axial turbulent intensity. Regarding the sharp increasing of the turbulence through spacer grids, notice the first term in Production in Eq. (5). As can be seen in Fig. 9, the axial velocities at points 1, 3, and 5 decrease rapidly through spacer grid up to nearly $x/D_h = 4$, which causes the first term of the Production to generate higher turbulence production. The axial velocities at points 2, 4, and 6 increase through spacer grid, which means that the first term of the production generates the negative-production. This fact is indicating that at points 2, 4, and 6, V, W, velocities as well as pressure redistribution are dominantly contributing to axial turbulent intensity. Considering the fully developed flow, x-derivatives, V and W become 0. In this case, the second and third terms in Production and Dissipation are dominant.

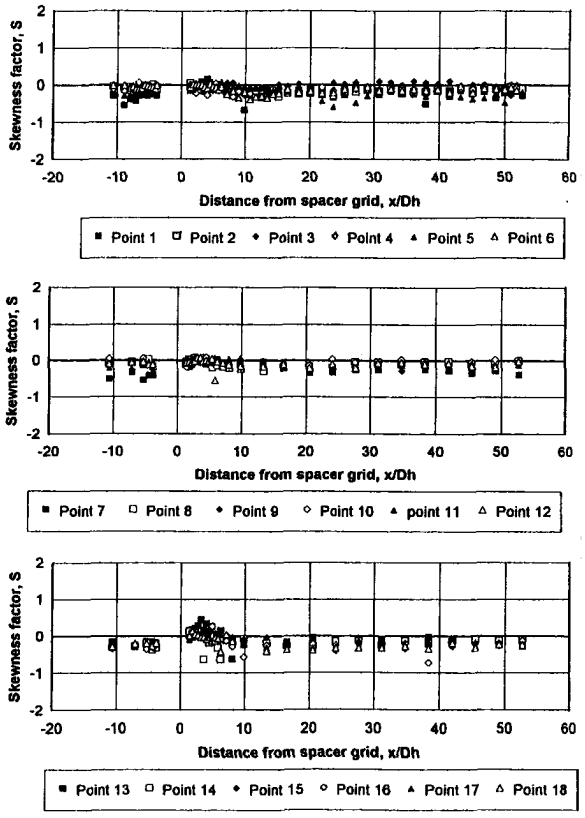

Fig. 12 Skewness factor at points 1–18 (Uncertainty in skewness factor = ±9.8 percent)

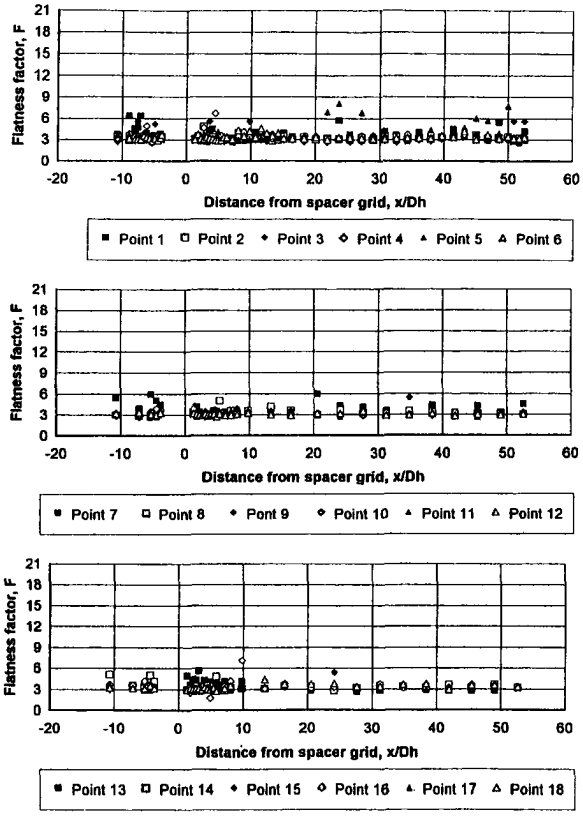

Fig. 13 Flatness factor at points 1–18 (Uncertainty in flatness factor = ±11 percent)

An interesting trend is found in the downstream region. The intensities in some Points increase after $x/D_h = 10 \sim 20$, where the turbulence level is even lower than that in the far-downstream region. This can be explained as the "energy reversal" of Rowe and Chapman (1973). As the flow develops, the turbulence scales grow gradually to the diffusive large scales by which the diffusion terms are governed. The increase of diffusion from the rod surface increases the turbulent kinetic energy. The intensities increase to the relatively higher value at about $x/D_h = 30$, which is called "saddle points" in Rehme (1992). The "energy reversal" and "saddle points" are caused by the large scale flow pulsation between the subchannels through gaps.

Higher Moments of Velocity Fluctuation. The skewness factor, S, and flatness factor, F, which are third and fourth moment of turbulent fluctuation, are defined as (Tennekes and Lumley, 1972):

$$S = \frac{\overline{u^3}}{(u')^3} \quad (6)$$

$$F = \frac{\overline{u^4}}{(u')^4} \quad (7)$$

S and F at points 1–18 are shown in Figs. 12 and 13. The reference values, S, and F for the Gaussian normal distribution are 0 and 3, respectively. For skewness factor, the fluctuation distribution is skewed upstream of the spacer grid, however just behind the spacer grid after passing through spacer grids, skewness factors are tended to be normal values. This implies that the turbulent flow becomes more isotropic through spacer grids. By Townsend (1976), the skewness factor is related to the turbulent energy convection from larger turbulent intensity

to smaller turbulent intensity. The flow far downstream region is strongly non-isotropic due to complex flow passage, which causes the flow region to be non-homogeneous in turbulent energy and to be deviated from normal values of skewness factor. By Townsend (1976), the flatness factor is related to intermittency. The effects relating to flatness factor are more pronounced the greater the difference in sizes between the energy containing eddies and the viscous eddies that dissipate the turbulent energy. In the present flow, because of non-isotropic and complex flow behavior such as inter-mixing between subchannels, the flatness factors show higher values than the normal value of 3. The effects of the spacer grid on the flatness factor are not so pronounced in the results.

Uncertainty Analysis. Experimental uncertainties in the experimental data were evaluated according to the ANSI/ASME PTC 19.1 Code (1985). Uncertainties of loss coefficient and friction factor factor are 2.8 and 2.79 percent, respectively. And the uncertainties of axial velocity, turbulent intensity, skewness factor, and flatness factor are 2.9, 7.7, 9.8, 11 percent, respectively.

Concluding Remarks

In order to investigate the effects on turbulence due to the mixing spacer grid in rod bundles, the detailed hydraulic characteristics in subchannels of a 5 × 5 rod bundle with mixing spacer grids were measured by using a LDV (laser Doppler Velocimetry). The experimental results led to the following conclusions.

It was generally observed that the turbulent intensity decay rates observed behind the spacer grid can be explained by turbulence decay in turbulent flow through mesh grids or screens, and show similar trends as mesh grid or screen flows. The flow immediately downstream of the spacer grid is intensively fluctuating with a higher turbulence energy and more isotropic than just before the spacer grid.

For skewness factor, the fluctuation distribution is skewed upstream of the spacer grid, however just behind the spacer grid after passing through spacer grids, skewness factors are tended to be normal values. The effects of the spacer grid on the flatness factor are not so pronounced in the results.

References

Measurement Uncertainty, Part-1, ANSI/ASME PTC 19.1, 1985, *ASME Performance Test Codes: Supplement on Instruments and Apparatus.*

Blasius, H., 1913, "The Law of Similarity for Frictional Processes in Fluids" (originally in German), *Forsch Arbeit Ingenieur-Wesen,* Berlin, p. 131.

Comte-Bellot, G., and Corrsin, S., 1966, "The Use of a Contraction to Improve the Isotropy of Grid-generated Turbulence," *Journal of Fluid Mechanics,* Vol. 25, part 4, pp. 657–682.

Laws, E. M., and Livesey, J. L., 1978, "Flow through Screens," *Annual Review of Fluid Mechanics,* Vol. 10.

Rehme, K., 1973, "Pressure Drop Correlations for Fuel Element Spacers," *Nuclear Technology,* Vol. 17, pp. 15–23.

Rehme, K., 1992, "The Structure of Turbulence in Rod Bundles and the Implications on Natural Mixing between the Subchannels," *International Journal of Heat and Mass Transfer,* Vol. 35, No. 2, pp. 567–581.

Rehme, K., and Trippe, G., 1980, "Pressure Drop and Velocity Distribution in Rod Bundles with Spacer Grids," *Nuclear Engineering and Design,* Vol. 62, pp. 349–359.

Rowe, D. S., and Chapman, C. C., 1973, "Measurement of Turbulent Velocity, Intensity and Scale in Rod Bundle Flow Channels Containing a Grid Spacer," BNWL-1757.

Shen, Y. F., Cao, Z. D., and Lu, Q. G., 1991, "An Investigation of Cross-flow Mixing Effect Caused by Grid Spacer with Mixing Blades in a Rod Bundle," *Nuclear Engineering and Design,* Vol. 125, pp. 111–119.

Sreenivasan, K. R., Tavoularis, S., Henry, R., and Corrsin, S., 1980, "Temperature Fluctuations and Scales in Grid-generated Turbulence," *Journal of Fluid Mechanics,* Vol. 100, Part 3, pp. 597–621.

Tennekes, H., and J. L. Lumley, J. L., 1972, *The First Course in Turbulence,* MIT Press, Cambridge, MA.

Townsend, A. A., 1976, *The Structure of Turbulent Shear Flow,* Cambridge University Press.

Yang, S. K., and Chung, M. K., 1995, "Turbulent Flow through Mixing Spacer Grids in Rod Bundles," HTD-Vol. 316, *National Heat Transfer Conference,* Vol. 14, pp. 33–40.

Analysis of Fluid-Structure Interaction by Means of Dynamic Unstructured Meshes

F. J. Blom
Ph.D. Student.

P. Leyland
Researcher.

IMHEF—DGM, Ecole Polytechnique Fédérale de Lausanne, CH-1015, Lausanne, Switzerland

This paper presents a computational analysis on forced vibration and fluid-structure interaction in compressible flow regimes. A so-called staggered approach is pursued where the fluid and structure are integrated in time by distinct solvers. Their interaction is then taken into account by a coupling algorithm. The unsteady fluid motion is simulated by means of an explicit time-accurate solver. For the fluid-structure interaction problems which are considered here the effects due to the viscosity can be neglected. The fluid is hence modeled by the Euler equations for compressible inviscid flow. Unstructured grids are used to discretise the fluid domain. These grids are particularly suited to simulate unsteady flows over complex geometries by their capacity of being dynamically refined and unrefined. Dynamic mesh adaptation is used to enhance the computational precision with minimal CPU and memory constraints. Fluid-structure interaction involves moving boundaries. Therefore the Arbitrary Lagrange Euler method (ALE-method) is adopted to solve the Euler equations on a moving domain. The deformation of the mesh is controlled by means of a spring analogy in conjunction with a boundary correction to circumvent the principle of Saint Venant. To take advantage of the differences between fluid and structure time scales, the fluid calculation is subcycled within the structural time step. Numerical results are presented for large rotation, pitching oscillation and aeroelastic motion of the NACA0012 airfoil. The boundary deformation is validated by comparing the numerical solution for a flat plate under supersonic flow with the analytical solution.

Introduction

The current trend in aeronautics is to diminish the weight of the structural components. As a consequence the structure is more susceptible to external forces and dynamic interaction between fluid and structure is more likely to occur. To calculate this interaction the fluid solvers have to be coupled to structural solvers.

The main interest of this research lies in the transonic flow regime where the nonlinearity of the fluid equations requires a time-accurate approach for the interaction between fluid and structure. To achieve this, the fluid and the structure are integrated in time by separate solvers and their interaction is taken into account by a coupling algorithm. The fluid is assumed to be compressible and inviscid so that it can be described by the Euler equations.

In the next section the numerical method is described. Thereafter the numerical results for several two dimensional test cases are discussed and finally, the conclusions are presented.

Numerical Method

This section describes the numerical method which is used to calculate fluid-structure interaction. The character of the subject is multi disciplinary, therefore the section is divided into five parts which discuss the numerical methods for the fluid, mesh adaptation, mesh deformation, structure and coupling respectively.

Euler Equations on a Deforming Domain. Fluid-structure interaction deals with a moving fluid domain. Consequently the governing equations have to be described in a moving coordinate system. Here the Arbitrary Lagrange Euler method (ALE-method, Donea et al., 1982) is adopted. For the ALE method the coordinates are neither fixed (Euler) nor moving with the particles (Lagrange), but they can move in an arbitrary way. For moving boundary problems the domain is deformed around this boundary. This method is well suited for fluid-structure interaction problems.

When the domain is fixed the inviscid fluid flow is described by the unsteady Euler equations. On a two-dimensional domain Ω and boundary Γ, the conservative integral form of these equations reads,

$$\iint_\Omega \frac{\partial \mathbf{W}}{\partial t}\, d\Omega + \int_\Gamma (\mathbf{F}n_x + \mathbf{G}n_y) d\Gamma = 0 \qquad (1)$$

where,

$$\mathbf{W} = \begin{pmatrix} \rho \\ \rho u \\ \rho v \\ \rho E \end{pmatrix} \qquad (2)$$

$$\mathbf{F} = \begin{pmatrix} \rho u \\ \rho u^2 + p \\ \rho uv \\ u(\rho E + p) \end{pmatrix} \quad \mathbf{G} = \begin{pmatrix} \rho v \\ \rho uv \\ \rho v^2 + p \\ v(\rho E + p) \end{pmatrix} \qquad (3)$$

ρ, u, v, E, and p denote the density, velocity in the x and y direction, total energy and pressure respectively. $\bar{n} = (n_x, n_y)$ denotes the outward normal to the boundary. Equation (1) is closed by the equation of state for a perfect gas,

$$p = (\gamma - 1)\rho[\tfrac{1}{2}(u^2 + v^2)] \qquad (4)$$

where γ is the ratio of the specific heats.

When the coordinates are moving, the metric of the system changes according to this movement. The Euler equations are hence modified. The integration volume becomes time depen-

Contributed by the Fluids Engineering Division for publication in the JOURNAL OF FLUIDS ENGINEERING. Manuscript received by the Fluids Engineering Division December 29, 1997; revised manuscript received August 6, 1998. Associate Technical Editor: J. A. C. Humphrey.

dent and in order to compensate for this change, the so-called transpiration fluxes (6) are added. On a moving domain the conservative integral form yields,

$$\frac{\partial}{\partial t}\iint_{\Omega(t)} \mathbf{W}\,d\Omega + \int_{\Gamma(t)} ((\mathbf{F} - x_t\mathbf{W})n_x + (\mathbf{G} - y_t\mathbf{W})n_y)d\Gamma = 0 \quad (5)$$

The domain is denoted by $\Omega(t)$ and $\Gamma(t)$ denotes the boundary of the domain which are both time dependent. x_t and y_t are the coordinate velocities in x and y direction respectively.

The difference between the Euler equations on a fixed domain (1) and those on a moving domain (5) is twofold. First, the integration volume $\Omega(t)$ changes in time, therefore the time derivative has moved out of the volume integral. Second, transpiration fluxes are added to calculate the conservative quantities which are transpired through the moving boundary $\Gamma(t)$. This transpiration flux is defined by,

$$F_{\text{trans}} = -\int_{\Gamma(t)} ((x_t\mathbf{W})n_x + (y_t\mathbf{W})n_y)d\Gamma \quad (6)$$

In order to retain a conservative numerical scheme it must at least be possible to calculate steady state flow on a moving mesh. Consequently the time integration of the transpiration fluxes has to be performed by the same integration algorithm as for the mesh. In the case of fluid-structure interaction this corresponds to the time integration of the structure. This condition is called the Geometrical Conservation Law (GCL, Farhat, 1995, Thomas and Lombard, 1979). For example, when the trapezoidal rule is used for the integration of the mesh from t^n to t^{n+1} the transpiration fluxes have to be calculated at time $t^n + (1/2)\Delta t$, where Δt is the time step $t^{n+1} - t^n$.

The Euler equations are solved on an unstructured moving grid which consists of triangles. The equations are spatially discretised by a Jameson like scheme on dual control volumes (Richter and Leyland, 1993). This scheme is of a central difference type with second and fourth order dissipation terms. These terms are added to avoid oscillations near shocks and for the solution to remain smooth far from the shock regions. This scheme is second order accurate in space and is integrated in time by an explicit fourth order Runge-Kutta scheme.

Dynamic Mesh Adaptation. The use of an unstructured mesh has particular advantages when the mesh is to be adapted to the solution. The mesh can be locally refined by adding nodes to the mesh or unrefined by suppressing nodes. This process is of high interest when transient phenomena have to be calculated. The zones of interest can be followed by a fine mesh while the mesh can be locally unrefined when a low gradient zone passes by to save CPU time and memory space.

Richter and Leyland (1993) have presented a nonhierarchical refinement/unrefinement algorithm which is combined with fluid-structure interaction in this paper. The mesh is refined or unrefined when the gradient of a chosen physical quantity exceeds a reference value.

When the refinement/unrefinement operation is carried out the mesh is further optimised by smoothing, diagonal swapping and node suppression procedures. For more details the reader is referred to Richter and Leyland (1993).

Mesh Deformation. The computational mesh has to be moved or deformed to solve the fluid equations on a moving domain. The method which is adopted to deform the mesh is called the spring analogy (Batina, 1990). This method is very general because it can handle moving boundaries as well as deforming boundaries which are needed for general fluid-structure interaction problems.

When the boundary is displaced the mesh is deformed and mesh cells are squeezed and stretched or maybe even inverted. The spring analogy is then used to restore the mesh to a more regular state. The spring analogy replaces the segments in the mesh by fictitious springs. When the boundary is deforming, the mesh is restored by means of these springs.

The displacements of the nodes are determined by calculating the elastic equilibrium using the generalised Hook's law, $\vec{F} = \alpha\vec{x}$. Where $\vec{F}$, α and $\vec{x}$ are the force vector, spring stiffness and displacement vector respectively. There are two different spring analogies which are distinguished by the equilibrium position of the springs.

The vertex method considers the springs to have their equilibrium position at zero length. Then the springs inside a mesh are always under tension unless their length is zero. When this method is used an initial mesh is not necessary in equilibrium. The method is used by Richter and Leyland (1993) to smooth the mesh after the refinement/unrefinement procedure.

The segment method considers the springs to have their equilibrium length at the length of the segment before mesh deformation. Accordingly, every mesh is initially in equilibrium and is not deformed unless the boundary is moved or deformed. This method is used by Batina (1990) to calculate forced vibration of an airfoil.

First the vertex method is discussed. The deformation of the mesh by the elastic springs is calculated by performing Jacobi iterations on Hook's law. The iterative equation to be solved is given by,

$$\vec{x}_i^{n+1} = \frac{\sum_{j=1}^{\eta_i} \alpha_{ij}\vec{x}_j^n}{\sum_{j=1}^{\eta_i} \alpha_{ij}} \quad (7)$$

where α_{ij} is the spring stiffness of the spring between node i and j. $\vec{x}_i$ is the position vector of node i. η_i denotes the number of neighbours of node i. The stiffness is taken as a power of the length of the segment multiplied by a scaling factor,

$$\alpha_{ij} = \phi((x_i - x_j)^2 + (y_i - y_j)^2)^{\psi} \quad (8)$$

where ϕ and ψ are adaptive parameters to be chosen by the user, in order to obtain a regular mesh deformation. The second method, the segment method also uses Jacobi iterations to solve the elastic equations. The iterative equation reads in this case,

$$\vec{\delta}_i^{n+1} = \frac{\sum_{j=1}^{\eta_i} \alpha_{ij}\vec{\delta}_j^n}{\sum_{j=1}^{\eta_i} \alpha_{ij}} \quad (9)$$

where $\vec{\delta}_i$ is the displacement vector of node i. The stiffness of the springs α_{ij} is again calculated by equation (8). The parameters correspond to $\phi = 1$ and $\psi = -(1/2)$ in the original method of Batina (1990).

For the present study the spring analogy is further improved. Since the nature of the elastic equations for the mesh is elliptic, the principle of Saint Venant holds for the deformation of the mesh. This principle states that local perturbations of the solution only have local consequences. Therefore the mesh is only deformed close to the deforming boundary. In order to circumvent this property the stiffness near the boundary is increased so that the deformation is spread out further into the mesh. To achieve this local stiffening of the system the factor ϕ in Eq. (8) is increased for a number of element layers adjacent to the boundary (Blom, 1996).

The spring analogy and the ALE-method are compared to a simple technique on a model problem for validation purposes. When the movement of the boundary is restricted to a rigid body movement of an isolated object, the whole mesh can be moved with the boundary (Richter and Leyland, 1993). In this way the mesh remains rigid and no integration volume changes have to be calculated. Hence, the addition of the transpiration

flux (6), to the Euler equations (1) is sufficient. The advantage of the rigid moving mesh is that there is no need for an algorithm to deform the mesh. However, the rigid moving mesh approach is less general than the spring analogy and it only serves for comparison here.

Structural System. To describe the structural system the equations of motion for an undamped mechanical system is chosen as a point of departure. The strains and deformations in the structure are supposed to remain small so that the linear theory can be applied. The equations are then written as,

$$[\mathbf{M}]\{\ddot{u}(t)\} + [\mathbf{K}]\{u(t)\} = \{\mathbf{F}(t)\} \tag{10}$$

where $[\mathbf{M}]$ is the mass matrix, $[\mathbf{K}]$ is the stiffness matrix, $\{u(t)\}$ is the vector of degrees of freedom, $\{\ddot{u}(t)\}$ denotes the double time derivative of this vector and $\{\mathbf{F}(t)\}$ is the external force vector. The matrix equation (10) can for example result from a finite element or finite difference approach of a continuous structure. In fluid-structure interaction problems the external force is provided by the fluid pressure on the interface.

The structure has to be integrated in time simultaneously with the fluid. Therefore (10) has to be solved by means of a direct integration method. Several integration methods for the structure are investigated. First the central difference method (Bathe, 1982) is considered. This method assumes the displacements to be parabolic in time. The second order function is interpolated among three time levels of the structure. The central difference method is an explicit method with the stability restriction on the time step, $\Delta t \leq (2/\omega_n)$. Here ω_n is the highest eigenfrequency of the structural system (10).

Next, the Newmark method (Bathe, 1982) is adopted. The Newmark method is an implicit integration method. The general Newmark method contains two variables δ and β which are chosen as: $\delta = 1/2$ and $\beta = 1/4$. These values lie within the stability limit, which is given by, $\beta \geq (1/4)(\delta + (1/2))^2$. When these values are taken the acceleration is constant in the time interval Δt and equal to $(\ddot{u}(t^{n+1}) + \ddot{u}(t^n))/2$. The velocity is then linear and integrated by means of the trapezoidal rule.

Finally, the Runge-Kutta method is taken. This method is chosen since the time integration in the fluid solver is of the same type. The method was proposed by Bendiksen (1991) in order to improve the energy transfer between fluid and structure. The Runge-Kutta method is an explicit method which is conditionally stable. Here the fourth-order Runge-Kutta scheme with standard coefficients is chosen so that the order is the same as for the fluid solver. The time step of this method is restricted to $\Delta t \leq (2\sqrt{2}/\omega_n)$ where ω_n is the highest eigenfrequency of the structural system.

The explicit integration methods will only be applied to the aeroelastic motion of a two degree of freedom airfoil because of their conditional stability.

Fluid—Structure Coupling. Now that the individual numerical methods for the fluid, mesh and structure have been described they have to be coupled. The coupling of the systems takes place at the fluid-structure interface. On the one hand, the structural displacements on the interface are transferred to the fluid. On the other the fluid pressures are transferred as an external force vector to the structure solver.

First the fluid and the structure integrators are supposed to have the same time step. This time step is determined by the smallest time step which is needed for stability of the fluid and structure solver. At time t^n the state of the fluid, structure and mesh is known. To advance the system to the next time level the following procedure is followed:

1. Predict the state of the structure at the end of the current time step ($t = t^{n+1}$).
2. Calculate the mesh movement during the current time step.
3. Integrate the fluid to the next time level.
4. Update the structure to the next time level using the fluid pressures on the boundary.

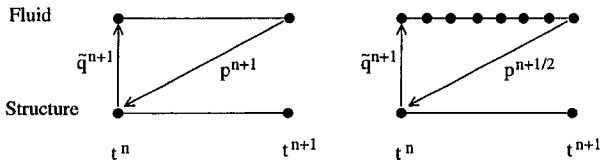

Fig. 1 Original (left) and subcycled (right) algorithm

Remarks

1. The structure is predicted by a linear predictor according to,

$$\{u^{n+1}\} = \{u^n\} + \Delta t\{\dot{u}^n\} \tag{11}$$

2. The mesh is updated by the improved spring analogy.
3. The fluid is integrated using the ALE-method.
4. The structure is integrated in time by the methods discussed in the previous section.

The coupling algorithm is schematically shown in Fig. 1. Since the structural movement is predicted to the next time level, the domains of the fluid and structure are not matching during the time step. This so-called volume-discontinuous method conserves the energy better than the volume-continuous method where the interfaces are matching. Piperno (1995) has shown that calculation with a prediction of the velocity at the correct time (volume-discontinuous) is more accurate than calculation with the right velocity at the incorrect time (volume-continuous). The time step Δt is limited by the stability limit of the time integration algorithms. Generally this is dominated by the fluid solver, which is restricted by the CFL condition.

For sufficiently fine meshes the explicit fluid solver requires small time steps in order to maintain stability whereas the structure solver often allows for larger time steps. To make use of this property, the fluid can be subcycled. The procedure to advance the system from t^n to t^{n+1} is described the following algorithm (see also Fig. 1),

1. Predict the state of the structure at the end of the current time step ($t = t^{n+1}$).
2. Calculate the mesh movement during the current time step.
3. Integrate the fluid to the next structure time level with as many fluid time steps as needed.
4. Update the structure to the next time level using the fluid pressure on the boundary.

Remarks

1. The time step $\Delta t = t^{n+1} - t^n$ is determined by the accuracy requirements for the structure.
2. The mesh velocity is constant during the time step Δt.
3. The fluid is integrated with time steps which are needed for stability of the fluid solver.
4. The external force vector for the structure is calculated from the mean of the pressures ($p^{n+1/2}$) during the time step Δt. In this way the optimal energy conservation properties are achieved as noted by Piperno (1995).

Numerical Results

The numerical methods are now validated by several test cases. First the improvements on the spring analogy are shown by a large rotation of the NACA0012 airfoil. Then a forced vibration problem on the airfoil is calculated. Aeroelasticity is

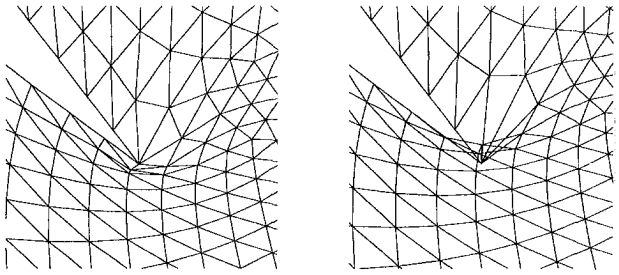

Fig. 2 Zoom at trailing edge of deformed meshes with (left) and without (right) boundary correction

then introduced by supporting the airfoil by two elastic springs. Finally, a boundary deformation is included for the flutter of a plate under supersonic flow.

Large Rotation of an Airfoil. To show the capabilities of the improved spring analogy the NACA0012 airfoil is rotated 45° around the quarter chord. The circular mesh consists of 3693 nodes and 7266 elements and has a radius of ten times the chord of the airfoil. After the deformation the mesh is heavily distorted. The mesh is recovered by the segment method which is most suitable for a moving boundary problem as will be shown in the next section. The parameters in Eq. (8) are taken as $\psi = -1$ and $\phi = 1$. The boundary correction is applied to one layer of elements near the boundary and there the multiplication factor is taken as $\phi = 3$. The Jacobi algorithm (9) converges in 3000 iterations. Figure 2 shows that in this case the boundary correction is imperative for the mesh to remain valid, i.e., to avoid inverted cells.

Forced Pitching Vibration of an Airfoil. In this section the moving mesh scheme is applied to a pitching NACA0012 airfoil which has been elaborately treated in the literature. Batina (1990) also used the segment spring method to move the mesh. Farhat and Lin (1990) used a multiple moving frame of reference approach which is more suitable for structured meshes. Richter and Leyland (1993) calculated the problem with a rotating frame of reference.

The airfoil is forced into a pitching oscillation around the quarter chord. The variation of the angle is given by,

$$\alpha(t) = 0.016° + 2.51° \sin\left[2\sqrt{\gamma}\, M_\infty k t\right] \qquad (12)$$

where k is the reduced frequency defined by $k = \omega d/(2U_\infty)$. M_∞ is the Mach number at infinity, d is the chord, U_∞ is the velocity at infinity, and ω is the frequency in radians per second. The reduced frequency is taken as $k = 0.0814$ and the Mach number at infinity as $M_\infty = 0.755$. The ratio of specific heats is taken as $\gamma = 1.4$. The initial solution is taken as a uniform Mach 0.775 flow with an incidence angle of 0.016°.

The mesh is the same as the one which is used in the previous section. The spring analogy is performed with the vertex and segment method. The parameters in Eq. (8) for the vertex method are taken as $\psi = 0.1$ and $\phi = 1$. The value of ϕ is changed in the first layer close to the boundary to $\phi = 2$. For the segment method the parameters are taken as $\psi = -1$ and $\phi = 1$. Close to the boundary the same $\phi = 2$ is taken as for the vertex method. Two Jacobi iterations per time step are performed on the spring system which shows to be sufficient.

The lift coefficients as function of the angle are compared for the different methods and to the experiment of Landon (1982). The result is depicted in Fig. 3. It can be seen that the lift coefficient of the vertex method performs oscillations in the beginning of the cycle. This is caused by the initialisation process of the mesh. The vertex method deforms the initial mesh due to the initial non-equilibrium of the system. The curve calculated with the segment spring method shows less oscillations. The maximum deviation of the lift coefficients at convergence is 5.18 percent for the segment method and 9.18 percent for the vertex method. The difference with the experimental results is also found in all other numerical simulation previously mentioned. The difference are probably due to an offset of the angle of attack in the experiment.

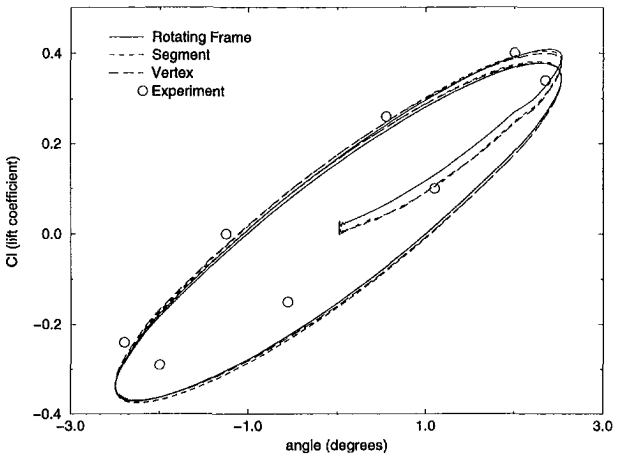

Fig. 3 Comparison of lift coefficients

Aeroelastic Motion of an Airfoil. The fluid-structure interaction algorithms are validated by the flutter simulation of the NACA0012 airfoil which is supported by two springs. Two springs are attached to the quarter chord, a torsion spring reacting to the pitching motion and a linear spring reacting to the plunging motion. This test case is also studied numerically by Rausch et al. (1989), Farhat and Lin (1990), and Piperno (1995).

The construction can be described by a system of two degrees of freedom. The nondimensional governing equation for the elastic system is given by,

$$\begin{bmatrix} 1 & \dfrac{S_\alpha}{2mb} \\ \dfrac{S_\alpha}{2mb} & \dfrac{I_\alpha}{4mb^2} \end{bmatrix} \begin{Bmatrix} \ddot{\bar{h}} \\ \ddot{\alpha} \end{Bmatrix} + \begin{bmatrix} \dfrac{4\omega_h^2 M_\infty^2}{U^{*2}\omega_\alpha^2} & 0 \\ 0 & \dfrac{I_\alpha M_\infty^2}{U^{*2} mb^2} \end{bmatrix} \begin{Bmatrix} \bar{h} \\ \alpha \end{Bmatrix} = \begin{Bmatrix} -\dfrac{M_\infty^2 C_l}{\pi\mu} \\ \dfrac{M_\infty^2 C_m}{\pi\mu} \end{Bmatrix} \qquad (13)$$

where h and α are the plunging and pitching displacements, $\bar{h} = h/2b$, b is the half-chord, m is the mass of the airfoil per unit span, S_α is the static moment around the elastic center, I_α is the rotational moment of inertia, ω_h, ω_α are the decoupled natural frequencies of the plunging and pitching moment respectively, M_∞ is the far field Mach number, $\mu = m/\pi b^2 \rho_\infty$ is the mass parameter, $U^* = U_\infty/b\omega_\alpha$ is the velocity parameter, ρ_∞ is the fluid density at infinity, U_∞ is the fluid velocity in the far field and C_l, C_m are the lift and moment coefficient, respectively.

The coefficients for the flutter analysis are listed in Table 1. The fluid mesh is the same as in the previous section. The initial conditions for the flow are taken as the steady flow over the

Table 1 Parameters for the elastically suspended NACA0012

ω_h	100 rad/s	b	0.5 m
ω_α	100 rad/s	I_α	0.8695 kg m
S_α	0.9 kg m	μ	60
m	1 kg		

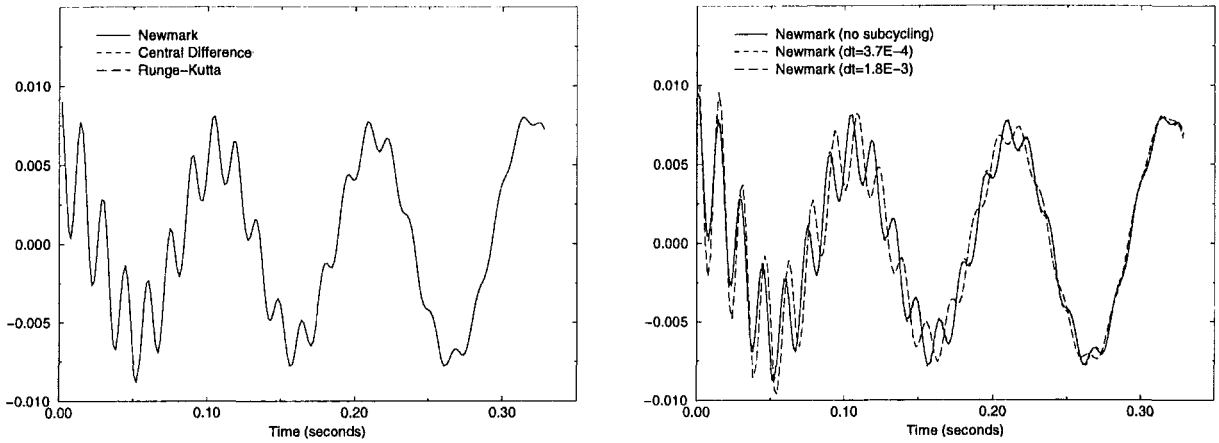

Fig. 4 Evolution of the angle without (left) and with (right) subcycling

airfoil at zero angle of attack. The angle of attack is then changed by 0.01 radians in order to introduce an initial perturbation into the system. The fluid-structure interaction problem is solved at a Mach number $M_\infty = 0.8$.

First the fluid-structure interaction is calculated with the original coupling algorithm where no subcycling is applied. The segment spring analogy is chosen for the mesh deformation because of its superior performance on the pitching problem. The calculations show an unstable motion for $U^* = 6.928$, nearly stable motion for $U^* = 5.477$ and stable motion for $U^* = 3.464$ which is also found by Farhat and Lin (1990) and Rausch et al. (1989). The results of the evolution of the angle calculated with the different structure integrators are shown in Fig. 4 for $U^* = 5.477$. The agreement among the different time integrators is very well, the curves are indistinguishable in the figure.

Next, the fluid is subcycled within the structural time step. The structural time step is fixed and the fluid is iterated in between as often as is needed for the stability of the fluid solver. The Newmark scheme is used to integrate the structure since its stability is unconditional. The evolution of the angle is depicted in Fig. 4. The low frequency at which instability arises is well captured by all of the simulations. However, when the structural time step is $1.8*10^{-3}$, the high frequency component can no longer be captured accurately. Nevertheless the overall numerical stability of the solution method is not affected.

The numerical data for the subcycling computations are listed in Table 2. The computation is performed on a Silicon Graphics R4400 processor. The table shows that the calculation with 24 subcycles does not benefit from subcycling. It can be seen that the number of iterations in the fluid solver increases when subcycling is introduced. This is caused by the fitting of the fluid time steps into the structural time step which bring about overhead costs. These overhead costs are larger for the second case than the gain in CPU time for less structural time steps. The structural problem has only two degrees of freedom, which is insufficient to account for subcycling benefits. In the third case the number of extra fluid iterations is much less which leeds to a slightly smaller CPU time. Clearly, there is nothing to be gained from subcycling with such a simple structural system. Substantial gains are only expected when the structure consists of a much more complex system.

Table 2 Comparison of CPU time for different subcycles

Str. time step	no subcycling	$3.7*10^{-4}$	$1.8*10^{-3}$
Fl. Iterations	20770	21294	20878
Str. Iterations	20770	900	180
Subcycles	0	24	116
CPU	41161.86	42754.27	40346.02

Supersonic Flow Over a Flat Plate. In this section the domain of the fluid is not only moved but also deformed. The problem which is solved is the flutter of a plate with infinite aspect ratio under supersonic flow. Bisplinghoff and Ashley (1962) and Houbolt (1958) calculated the analytical solution for this problem by means of the shallow shell theory and a first order approximation for the aerodynamics. The problem has been solved numerically by Piperno (1995) and also by Farhat et al. (1994).

To find the analytical solution the flat plate is described by the shallow shell theory. The plate has an infinite aspect ratio for which the governing equation yields,

$$m \frac{\partial^2 Y(x,t)}{\partial t^2} + D \frac{\partial^4 Y(x,t)}{\partial x^4} = P(x,t) \tag{14}$$

where $Y(x, t)$ is the vertical deflection of the plate and $P(x, t)$ the pressure per unit length, which are both a function of distance (x) and time (t). The m and D coefficients are given by,

$$m = \rho_s h$$

$$D = \frac{Eh^3}{12(1-\nu^2)} \tag{15}$$

where h is the thickness of the plate, ρ_s is the structural density, E is Young's modulus and ν is the Poisson ratio. The plate is clamped at both sides. In the first-order approximation for the aerodynamics the pressure on the plate is given by,

$$P(x,t) = -\frac{\rho_\infty U_\infty}{\sqrt{M_\infty^2 - 1}} \times \left(U_\infty \frac{\partial Y(x,t)}{\partial x} + \frac{M_\infty^2 - 2}{M_\infty^2 - 1} \frac{\partial Y(x,t)}{\partial t} \right) \tag{16}$$

where ρ_∞ is the far field density, U_∞ is the far field velocity and M_∞ the far field Mach number. Equation (16) can now be substituted into Eq. (14) which is solved in the frequency domain by the method of Houbolt (1958). For the parameters in Table 3 the stability limit is reached at Mach number $M_\infty =$

Table 3 Parameters for the flat plate flutter computation

L	0.5m	γ	1.4
h	1.35×10^{-3} m	P_∞	25714 N/m
ρ_s	2710 kg/m^3	ρ_∞	0.4 kg/m^2
E	7.728×10^{10} N/m^2	ν	0.3

Table 4 First two eigenfrequencies (rad/s) of a flat plate with the Finite Difference (FD), Finite Element (FE) and Exact (Ex.) method

N. of nds	1 FD	1 FE	1 Ex.	2 FD	2 FE	2 Ex.
50	205	197	197	564	544	544
100	201	197	197	554	544	544
200	199	197	197	549	544	544
300	198	197	197	547	544	544

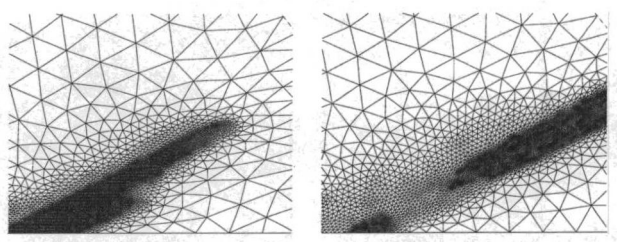

Fig. 6 Initial mesh, (3387 nodes, left) and adapted mesh, (4253 nodes, right) for the flow domain above the plate

2.2686 and a frequency of $\omega = 462.2$ rad/s. Piperno (1995) found numerically a stability limit of $M_\infty = 2.23$.

Next, this problem is also solved by the present numerical method. Two different numerical approaches for the plate are followed. First a Finite Difference (FD) method is used. The deflection of the plate is approximated by piecewise linear functions between the nodes. The method is hence non-conforming. The eigenfrequencies of the flat plate are calculated and compared to the exact solution (Weaver et al., 1990). The results are shown in Table 4 as a function of the number of nodes on the plate.

Since the finite difference approach gives rather poor results, a Finite Element (FE) method is used. The deflection is approximated by third order polynomials between the nodes. Now every node has two degrees of freedom, deflection and rotation. The mass matrix is calculated consistently (no lumping). The eigenvalues of the plate are also calculated with this method and the results are more accurate than these of the finite difference approach as seen in Table 4.

The supersonic flow is calculated in a semi-circular domain with a radius of 10 times the plate chord. The initial solution is given by the steady state flow above the plate which is deflected in its second eigenmode. The mesh is conforming on the fluid-structure interface, meaning that every mesh point on the structure coincides with a mesh point on the boundary of the fluid. Therefore there is no need for interpolation of the solutions on the interface. The fluid mesh consists of 10513 nodes and 20809 elements.

Starting from this steady state the flexibility of the plate is restored and the simulation is started. The maximum amplitude of the plate at flutter is situated at $x = 0.35$. The motion of this point in time is depicted in Fig. (5) for the finite difference method as well as for the finite element method.

For the finite difference method the flutter limit is found at $M_\infty = 2.9$, which is too high in comparison to the analytical value and the numerical value of Piperno (1995). This overestimation of the stability limit is caused by the small number of nodes on the plate for the finite difference approach. For the flutter calculation the plate is modeled by 125 nodes. The eigenfrequencies are overestimated for such a small number of nodes, as can be seen in Table 4. The stiffness of the plate is overpredicted by the finite difference model, therefore a higher flow rate is needed for the plate to reach the flutter limit. This explanation is reinforced by the frequency of 486 radians/s found at the flutter limit which is also an overestimation of the analytical value.

For the finite element simulation the same number of 125 nodes on the plate is sufficient as can be seen in Table 4. Here the stability limit is found at a Mach number of 2.24 which is closer to the analytical value than the finite difference approach. The result is also in good agreement with Piperno (1995) who has found a stability limit of $M_\infty = 2.23$. The agreement is also good for the flutter onset frequency which is found to be 467 radians/s.

Next, mesh adaptation is applied to this problem. The gradient of the density is taken as an adaptation criterion. The plate is modeled by 50 third order finite elements, which is sufficient according to Table 4. Since the number of mesh points in the fluid is changing, the transfer solutions of the structure/fluid on the interface are linearly interpolated onto their fluid/structure counterparts. The mesh is adapted 129 times over about 6.5 periods. This gives a mean value of 20 adaptations per period. The initial mesh and an intermediate mesh are depicted in Fig. 6. These meshes are adapted to the solutions which are depicted in Fig. 7. When the plate passes through zero (flat position) the pressure gradients on the plate are very small. This low pressure gradient is convected with the flow. In Fig. 7 this zone is clearly visible and it can be seen in Fig. 6 that the mesh is unrefined in this zone and remains fine in the zones of interest. With this method the stability limit is also predicted at $M_\infty = 2.24$.

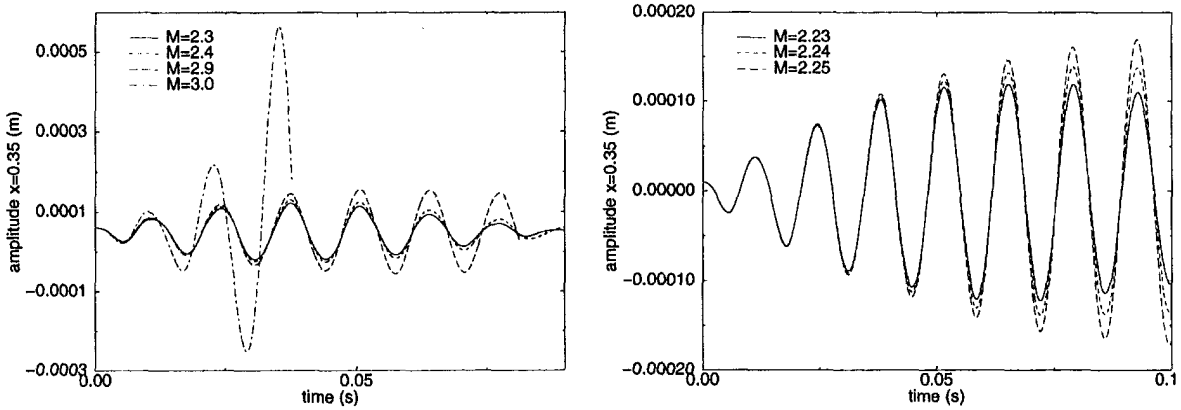

Fig. 5 Amplitudes of the clamped supersonic plate at $x = 0.35$, using a linear finite difference method (left) and a third order finite element one (right) for the structure

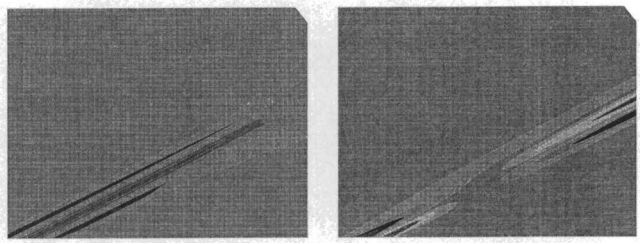

Fig. 7 Initial pressure (left) and pressure at $2.93*10^{-2}$ seconds (right)

Conclusions

The ALE-method has been shown to be well adapted to the calculation of unsteady aerodynamics. The improvement on the spring analogy enables very large deformations of the boundary which are not possible without boundary correction. With this new improved spring analogy and the ALE method good results for the rigid pitching airfoil problem have been obtained. This combination of methods is also suited for fluid-structure interaction calculations involving deforming boundaries. This was demonstrated with the supersonic plate flutter problem.

For the fluid-structure interaction, interesting results are obtained. The structural time integrator has a minor influence on the results, as might be expected while the time steps are very small. When subcycling is introduced the CPU time does not necessarily decrease for the aeroelastic airfoil problem. The overhead caused by the subcycling can be larger than the gain in CPU time. So the gain (or loss) from subcycling in the fluid will be examined for problems with more complex structural systems.

Finally, mesh adaptivity is applied to the flat plate problem. This method makes an efficient use of CPU and memory resources. The results are promising especially when unsteady transonic flows are to be examined, where high flow gradients appear in small, rapidly changing zones.

Acknowledgments

Financial support for this project was provided by the Leonhard Euler Center, the Swiss Pilot Center of the European Research Community On Flow Turbulence And Combustion (ERCOFTAC).

References

Bathe K. J., 1982, *Finite Element Procedures in Engineering Analysis,* Prentice-Hall, NJ.

Batina J. T., 1990, "Unsteady Euler Airfoil Solutions Using Unstructured Dynamic Meshes," *AIAA Journal,* Vol. 28, No. 8, pp. 1381–1388.

Bendiksen O. O., 1991, "A New Approach to Computational Aeroelasticity," AIAA Paper 91-0939-CP.

Bisplinghoff R. L., Ashley H., 1962, *Principles of Aeroelasticity,* Dover Publications, New York, NY.

Blom F. J., 1996, "Comparison of Different Mesh Displacement Algorithms on Unstructured Meshes," IMHEF Report T-96-13, EPF-Lausanne.

Donea J., Guiliani S., Halleux J. P., 1982, "An Arbitrary Lagrangian-Eulerian Finite Element Method for Transient Dynamic Fluid-Structure Interactions," *Computer Methods in Applied Mechanics and Engineering,* Vol. 33, pp. 689–723.

Farhat C., 1995, "High Performance Simulation of Coupled Nonlinear Transient Aeroelastic Problems," Cosmase Course, EPF-Lausanne.

Farhat C., Lin T. Y., 1990, "Transient Aeroelastic Computations Using Multiple Moving Frames of Reference," AIAA paper, 90-3053-CP.

Farhat C., Maman N., Lesoinne M., 1994, "Mixed Explicit/Implicit Time Integration of Coupled Aeroelastic Problems: Three-Field Formulation, Geometric Conservation Law and Distributed Solution," Center for Aerospace Structures 94-17, University of Colorado.

Houbolt J. C., 1958, "A Study of Several Aerothermoelastic Problems of Aircraft Structures in High-Speed Flight," Ph.D. thesis, ETH-Zurich.

Landon R. H., 1982, "NACA0012 Oscillatory and Transient Pitching," Compendium of Unsteady Aerodynamic Measurements, Dataset 3, AGARD-R-702.

Piperno S., 1995, "Simulation numérique de phénomenes d'interaction fluide-structure," PhD. thesis, Ecole Nationale Des Ponts et Chaussées, France.

Rausch R. D., Batina J. T., Yang H. T. Y., 1989, "Euler Flutter Analysis of Airfoils Using Unstructured Dynamic Meshes," AIAA Paper 89-1384-CP.

Richter R., Leyland P., 1993, "Precise Pitching Airfoil Computations by Use of Dynamic Unstructured Meshes," AIAA Paper 93-2971.

Thomas P. D., Lombard C. K., 1997, "Geometric Conservation Law and its Application to Flow Computations on Moving Grids," *AIAA Journal,* Vol. 17, No. 10, pp. 1030–1037.

Weaver W., Timoshenko S. P., Young D. H., 1990, *Vibration Problems in Engineering,* 5th edition, Wiley.

A Time-Marching Method for the Calculation of Nonsimilar 3D Boundary Layers on Turbomachinery Blades

W. Asvapoositkul
Lecturer,
Department of Mechanical Engineering,
King Mongkut's University of Technology
Thonburi, Bangkok 10140, Thailand

M. Zangeneh
Lecturer,
Department of Mechanical Engineering,
University College London,
London WC1E 7JE, United Kingdom

A method is presented for the computation of three-dimensional boundary layers on turbomachinery blades. The method is based on a finite difference approach on a body-fitted curvilinear coordinate system, in which the time-dependent 3D boundary layer equations are marched in time until the steady-state solution is found. The method does not employ a similarity law and can therefore be applied to nonsimilar boundary layers. The method not only enables one to compute the skin friction and displacement of the boundary, but also provides information on the sources of entropy generation on the blades. The entropy generation is in fact split into three main components, which correspond to heat conduction, streamwise shear stress, and cross-flow shear stress. By considering each of the components of shear stress, at the design stage considerable insight can be found on the best way of modifying the blade geometry in order to reduce blade losses. The method is validated by comparison with analytical data for a laminar flat plate, experimental results for a helical blade in turbulent flow, and an axial compressor blade. Finally, the method is applied to the prediction of boundary layers on a subsonic centrifugal compressor impeller blade.

Introduction

The flow through turbomachinery vanes and blades is dominated by three-dimensional viscous effects. As a result, an essential step in the aerodynamic design of turbomachines is the prediction of the 3D viscous flow in the designed blade channels. For this purpose, it is now quite common to use a 3D Navier-Stokes solver such as that of Dawes (1987) or Liu and Jameson (1993) for the computation of the flow through the blade channels in the final stages of the design process. Due to computer resource limitations, these Navier-Stokes solvers tend to employ some form of law-of-the-wall in order to model the inner sublayer. Since most of the entropy generation in the boundary layer is concentrated in the inner sublayer, see Denton (1993), the accuracy of the predicted loss is directly dependent on the law of the wall employed as well as the turbulence model. In fact the result of a recent survey, see Olcemen and Simpson (1992), shows that there is no strong evidence of law-of-the-wall similarity profile for 3D turbulent boundary layers. This could be one reason for the poor predictions of loss by most Navier-Stokes solvers even though they can predict the overall blockage effects in the flow channels quite accurately.

One way of obtaining accurate and yet computationally inexpensive predictions of the near wall flow is to solve the 3D boundary layer equations. The finite difference technique for the solution of the boundary-layer equations in turbomachinery application is well established. The conventional approach for the solution of the boundary layer equations is the so-called space-marching method, in which the solution is marched away from specified conditions on an initial line. Notable example of techniques based on this approach are the work of Vatsa (1985) and Oshima (1994). One limitation of the space marching is that due to the zone of dependence condition (see Wang, 1971), which is a result of the parabolic/hyperbolic nature of the boundary layer equations in three-dimensions, extra care should be taken in the discretization of the boundary-layer equations. Furthermore, the space-marching approach leads to complications in the specification of the boundary conditions especially at the side walls.

Another approach, which was first proposed by Steger and Van Dalsem (1985), is based upon a time-like algorithm in which the time-dependent three-dimensional boundary-layer equations are marched in time until the steady solution is found. This approach enables the use of flow dependent difference operators. Furthermore, the method can be used in the solution of time-dependent problems by using second-order accurate time-integration methods.

In the method to be presented in this paper the time-dependent boundary-layer equation is solved by using a relaxation method to drive the solution to steady-state conditions. The equations are solved without the use of similarity transformation as used by Vatsa (1985). All convective transport terms both in streamwise and cross-flow directions are discretized by using local upwind differences. The boundary-layer equations are solved in the direct mode, with the velocity or pressure at the edge of the boundary layer specified, while the FLARE approximation (appeared in Rehyner and Flugge-Lotz, 1968) is used to take account of small regions of flow separation.

Governing Equations

For flexibility and ease of use the boundary-layer equations are solved on a nonorthogonal coordinate system $(\bar{\xi}, \bar{\eta})$ in the plane parallel to the wall with an angle α between the two surface coordinates. The third coordinate $\bar{\zeta}$ is the actual distance measured normal to the surface. The relation between the curvilinear system $(\bar{\xi}, \bar{\eta}, \bar{\zeta})$ and a cylindrical coordinate system (x, r, θ) is shown in Fig. 1. The system $\bar{\xi}, \bar{\eta}, \bar{\zeta}$ is rotating around the x-axis with the constant angular velocity Ω. Using such a coordinate system the three-dimensional unsteady boundary-layer equations can be written as:

Contributed by the Fluids Engineering Division for publication in the JOURNAL OF FLUIDS ENGINEERING. Manuscript received by the Fluids Engineering Division July 10, 1997; revised manuscript received July 6, 1998. Associate Technical Editor: P. M. Sockol.

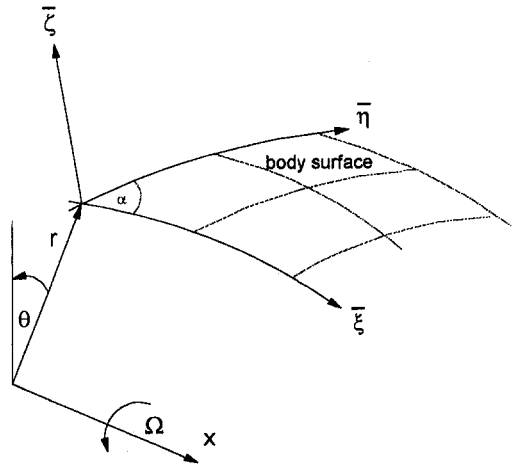

Fig. 1 Nonorthogonal curvilinear coordinate system on the body surface with angular velocity Ω

continuity:

$$\frac{\partial \rho}{\partial t} + \frac{1}{h_1 h_2 \sin \alpha}\left[\frac{\partial (h_2 \sin \alpha \rho u)}{\partial \bar{\xi}} + \frac{\partial (h_1 \sin \alpha \rho v)}{\partial \bar{\eta}} + \frac{\partial (h_1 h_2 \sin \alpha \rho w)}{\partial \bar{\zeta}}\right] = 0 \quad (1)$$

$\bar{\xi}$-momentum:

$$\rho \frac{\partial u}{\partial t} + \frac{\rho u}{h_1}\frac{\partial u}{\partial \bar{\xi}} + \frac{\rho v}{h_2}\frac{\partial u}{\partial \bar{\eta}} + \rho w \frac{\partial u}{\partial \bar{\zeta}} + K_{11}\rho u^2 + K_{12}\rho uv + K_{13}\rho v^2 + A_1 = K_{14}\frac{\partial p}{\partial \bar{\xi}} + K_{15}\frac{\partial p}{\partial \bar{\eta}} + \frac{\partial}{\partial \bar{\zeta}}\left([\mu + \mu_t]\frac{\partial u}{\partial \bar{\zeta}}\right) \quad (2)$$

$\bar{\eta}$-momentum:

$$\rho \frac{\partial v}{\partial t} + \frac{\rho u}{h_1}\frac{\partial v}{\partial \bar{\xi}} + \frac{\rho v}{h_2}\frac{\partial v}{\partial \bar{\eta}} + \rho w \frac{\partial v}{\partial \bar{\zeta}} + K_{21}\rho u^2 + K_{22}\rho uv + K_{23}\rho v^2 + A_2 = K_{24}\frac{\partial p}{\partial \bar{\xi}} + K_{25}\frac{\partial p}{\partial \bar{\eta}} + \frac{\partial}{\partial \bar{\zeta}}\left([\mu + \mu_t]\frac{\partial v}{\partial \bar{\zeta}}\right) \quad (3)$$

energy:

$$\rho \frac{\partial H}{\partial t} + \frac{\rho u}{h_1}\frac{\partial H}{\partial \bar{\xi}} + \frac{\rho v}{h_2}\frac{\partial H}{\partial \bar{\eta}} + \rho w \frac{\partial H}{\partial \bar{\zeta}} = \frac{\partial}{\partial \bar{\zeta}}\left[\left(\frac{\mu}{\mathrm{Pr}} + \frac{\mu_t}{\mathrm{Pr}_t}\right)\frac{\partial H}{\partial \bar{\zeta}}\right] + \frac{\partial}{\partial \bar{\zeta}}\left[\frac{1}{2}\left(\mu - \frac{\mu}{\mathrm{Pr}} + \mu_t - \frac{\mu_t}{\mathrm{Pr}_t}\right)\frac{\partial U_T^2}{\partial \bar{\zeta}}\right] + \frac{\rho u \Omega^2}{h_1 2}\frac{\partial r^2}{\partial \bar{\xi}} + \frac{\rho v \Omega^2}{h_2 2}\frac{\partial r^2}{\partial \bar{\eta}} + \rho \Omega^2 r[A_{02}u + A_{03}v] \quad (4)$$

where

$$K_{11} = \frac{\cos \alpha}{h_1 h_2 \sin^2 \alpha}\left[\frac{\partial h_1}{\partial \bar{\eta}} - \frac{\partial h_2 \cos \alpha}{\partial \bar{\xi}}\right]$$

$$K_{12} = \frac{1}{h_1 h_2 \sin^2 \alpha}\left[(1 + \cos^2 \alpha)\frac{\partial h_1}{\partial \bar{\eta}} - 2 \cos \alpha \frac{\partial h_2}{\partial \bar{\xi}}\right]$$

$$K_{13} = \frac{1}{h_1 h_2 \sin^2 \alpha}\left[\frac{\partial h_1 \cos \alpha}{\partial \bar{\eta}} - \frac{\partial h_2}{\partial \bar{\xi}}\right]$$

$$K_{14} = -\frac{1}{h_1 \sin^2 \alpha}$$

$$K_{15} = \frac{\cos \alpha}{h_2 \sin^2 \alpha}$$

$$K_{21} = -\frac{K_{11}}{\cos \alpha}$$

$$K_{22} = -\frac{1}{h_1 h_2 \sin^2 \alpha}\left[(1 + \cos^2 \alpha)\frac{\partial h_2}{\partial \bar{\xi}} - 2 \cos \alpha \frac{\partial h_1}{\partial \bar{\eta}}\right]$$

$$K_{23} = -K_{13} \cos \alpha$$

$$K_{24} = -K_{14} \cos \alpha$$

$$K_{25} = -K_{15} \cos \alpha$$

$$A_{02} = \mathbf{e}_1 \cdot \mathbf{e}_r = \frac{1}{h_1}\frac{\partial r_b}{\partial \bar{\xi}}$$

$$A_{03} = \mathbf{e}_2 \cdot \mathbf{e}_r = \frac{1}{h_2}\frac{\partial r_b}{\partial \bar{\eta}}$$

Nomenclature

h_1, h_2 = metric coefficients
H = total enthalpy
i, j, k = index of the grid point system
k = thermal conductivity
n = iteration level, time step, index of time
p = static pressure
Pr = Prandtl number ($c_p \mu / k$)
T = temperature
t = time
u, v, w = velocity components
α = angle between the lines on the body surface
δ^* = displacement thickness
$\Delta n, \Delta\xi, \Delta\eta, \Delta\zeta$ = grid spacing in time, ξ, η, and ζ coordinates
$\Delta x, \Delta y, \Delta z$ = grid spacing in x, y, z coordinates
ϵ = convergence criteria
Θ = momentum thickness
μ = dynamic viscosity of fluid
ν = kinematics viscosity
ξ = entropy production
ρ = density
τ = shear stress
ω = relaxation factor, safety factor
Ω = angular velocity

Subscript

b = at the blade surface
c = cross-flow direction
e = outer edge of the boundary layer
i, j, k = denoting coordinate direction
s = outer streamline direction
t = turbulent

$$A_1 = -2\rho\Omega(u\cos\alpha + v)\frac{1}{\sin\alpha}\frac{1}{h_1h_2\sin\alpha}\left(\frac{\partial r_b}{\partial\bar{\xi}}\frac{r_b\partial\theta_b}{\partial\bar{\eta}} - \frac{r_b\partial\theta_b}{\partial\bar{\xi}}\frac{\partial r_b}{\partial\bar{\eta}}\right) - \rho\Omega^2 r\frac{1}{\sin^2\alpha}\left(\frac{1}{h_1}\frac{\partial r_b}{\partial\bar{\xi}} - \frac{\cos\alpha}{h_2}\frac{\partial r_b}{\partial\bar{\eta}}\right)$$

$$A_2 = 2\rho\Omega(u + v\cos\alpha)\frac{1}{\sin\alpha}\frac{1}{h_1h_2\sin\alpha}\left(\frac{\partial r_b}{\partial\bar{\xi}}\frac{r_b\partial\theta_b}{\partial\bar{\eta}} - \frac{r_b\partial\theta_b}{\partial\bar{\xi}}\frac{\partial r_b}{\partial\bar{\eta}}\right) - \rho\Omega^2 r\frac{1}{\sin^2\alpha}\left(\frac{1}{h_2}\frac{\partial r_b}{\partial\bar{\eta}} - \frac{\cos\alpha}{h_1}\frac{\partial r_b}{\partial\bar{\xi}}\right)$$

The boundary conditions for the governing equations are given below.

at the wall $\bar{\zeta} = 0$: the no-slip condition, $u = v = w = 0$

either a specified temperature, $T = T_b$

or heat-transfer condition, $\dfrac{\partial T}{\partial\zeta} = q$ or $H = H_b$

at the edge of the boundary layer $\bar{\zeta} \to \infty$:

a specified free-stream conditions,

$u = u_e$, $v = v_e$, $T = T_e$ or $H = H_e$

More details of the transformation can be found in Yamazaki (1981) or Oshima (1994). In the above set of equations, all scale factors are calculated at the body surface $\bar{\zeta} = 0$ (i.e., x_b, r_b, θ_b). It should be noted that the distance r_b is a function of the surface coordinate $\bar{\xi}$, $\bar{\eta}$ only while r is the perpendicular distance of a point from the axis of rotation. In the above equations μ_t represents the turbulent eddy viscosity which in this method is evaluated by using the algebraic turbulence model of Baldwin-Lomax (1978).

Numerical Method

As boundary-layer flows contain severe velocity gradients in the direction normal to the wall and the boundary layer undergoes considerable growth depending on the severity of the pressure gradients, it is customary to use some form of similarity transformation (such as Lee-Levy) to stretch the coordinate normal to the surface in order to account for boundary-layer growth, see Vatsa (1985). Such transformations, although convenient to use, are of limited generality. So in the current method no similarity transformation was used.

In order to resolve the severe velocity gradients near the walls, the mesh points need to be clustered in the wall region. For this purpose, a variable grid spacing is formed by using a geometric series such that the quotient of two consecutive terms is constant. Therefore, the distance to the kth grid line is given by

$$\bar{\zeta}_k = \Delta\bar{\zeta}_1\frac{(RY^{k-1} - 1)}{(RY - 1)} \tag{5}$$

where $\Delta\bar{\zeta}_1$ is the distance from the solid wall to the first grid line.

If turbulent flow is computed, $\Delta\bar{\zeta}_1$ is chosen so that the first grid point is placed at approximately $\Delta\bar{\zeta}^+ \approx 1.5$ (defined as $\Delta\bar{\zeta}(\rho_b\tau_b)^{1/2}/\mu_b$) in order to resolve the thin laminar sublayer. While $\Delta\bar{\zeta}^+$ is constant for the whole calculation, the grid growth ratio (RY) is varied at different grid points in the flow direction since the boundary-layer edge is a function of the distance measured from the leading edge. Typically in laminar flow RY is set to 1.07 and then $\Delta\bar{\zeta}^+$ is varied.

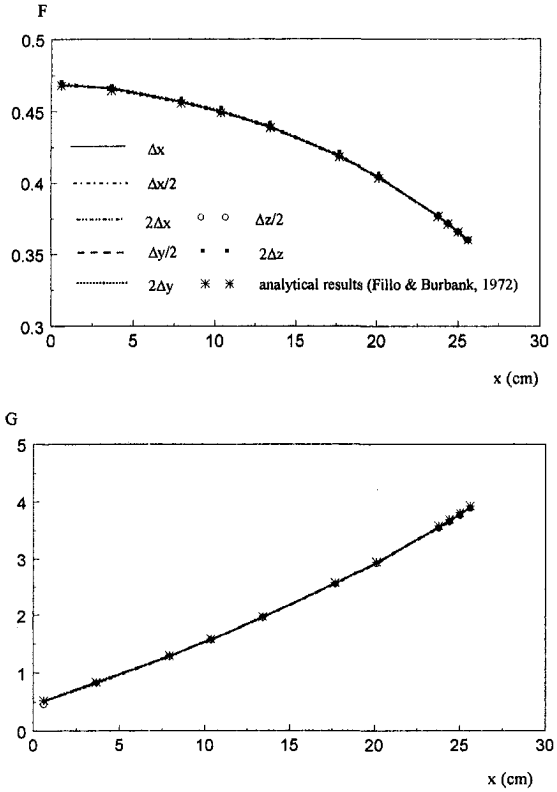

Fig. 2 The value of F and G at y = 9.15 cm for the x-, y- and z-spacing on the results

Since the mesh normal to the surface is nonuniformly spaced, an appropriate transformation has to be employed so that the boundary-layer equations are solved on a uniform computational domain. We can relate the non-uniformly grid system $(\bar{\xi}, \bar{\eta}, \bar{\zeta})$ to the uniform grid system (ξ, η, ζ) by setting

$$\xi = \xi(\bar{\xi}) = \bar{\xi}$$
$$\eta = \eta(\bar{\eta}) = \bar{\eta}$$
$$\zeta = \zeta(\bar{\xi}, \bar{\eta}, \bar{\zeta}) \tag{6}$$

Before we further discuss the discrete forms, one should bear in mind that only the derivatives in ζ are added to the governing equations after the transformation has been applied.

Discretization

The momentum and energy equations are solved by using an explicit second-order accurate upwind difference operator for spatial derivatives parallel to the body surface (ξ-, ζ-directions). For spatial derivatives normal to the solid surface (ζ-direction) an implicit second-order accurate central difference operator is used. The time derivative in the governing equations is approximated for an expansion level $n + 1$ with forward differencing. The resulting equations for quantities unknown at time $n + 1$ level are in a set of tridiagonal matrix system. For instance, the u^{n+1} values across the boundary layer are obtained from ξ-momentum. The tridiagonal matrix is given by Eq. (7)

$$au_{k-1}^{n+1} + bu^{n+1} + cu_{k+1}^{n+1} = \text{RHS} \tag{7}$$

where

$$a = -\frac{\rho u}{h_1}\zeta_{\bar{\xi}}\frac{1}{2\Delta\zeta} - \frac{\rho v}{h_2}\zeta_\eta\frac{1}{2\Delta\zeta} - \rho w\zeta_{\bar{\zeta}}\frac{1}{2\Delta\zeta} - \frac{\zeta_{\bar{\zeta}}}{2\Delta\zeta\Delta\zeta}(\mu\zeta_{\bar{\zeta}} + \langle\mu\zeta_{\bar{\zeta}}\rangle_{k-1})$$

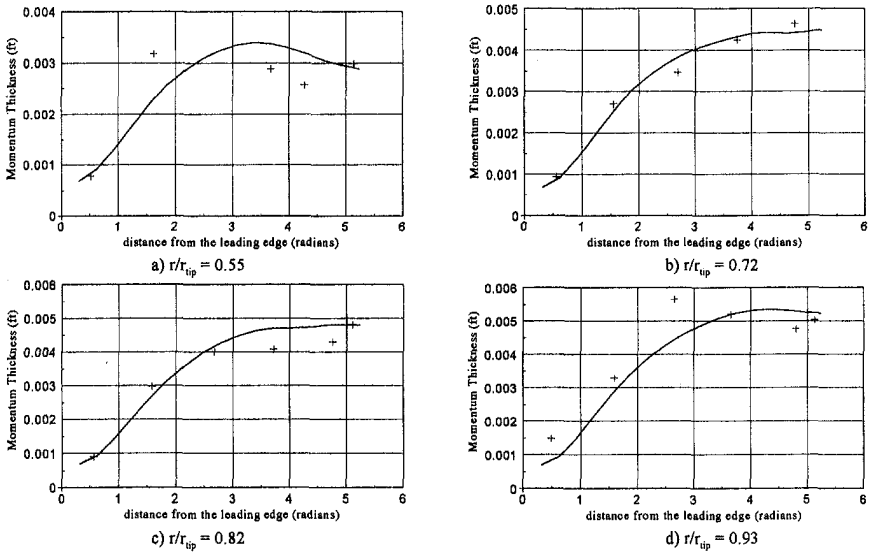

Fig. 3 Variation of momentum thickness on rotating helical blade, + measured (Lakshminarayana *et al.*, 1972) —— *present method*

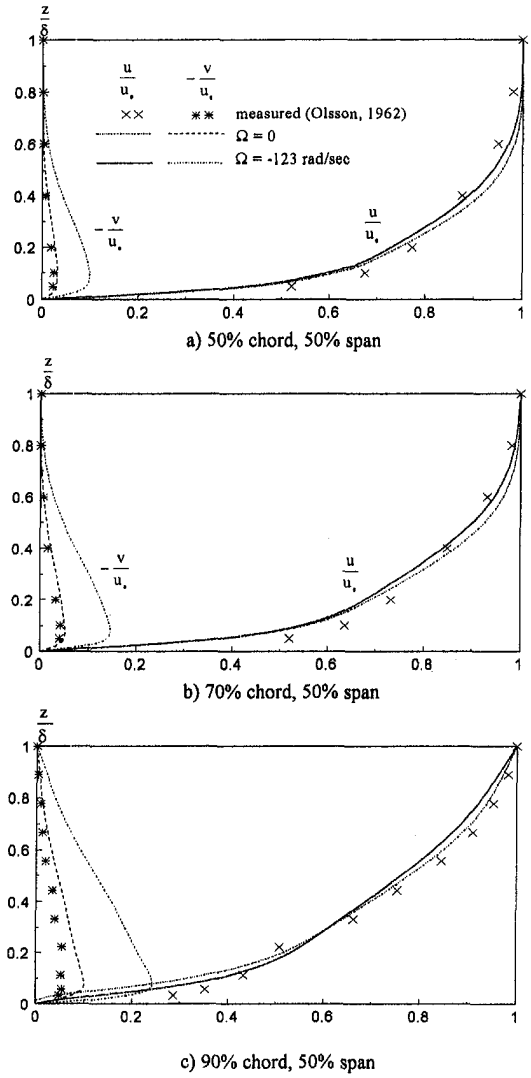

Fig. 4 Mean velocity *u* and *v* profiles of three-dimensional boundary layer 50 percent span for NACA Blade (suction side)

$$b = \rho \frac{1}{\Delta t} + \frac{\zeta_{\bar{\xi}}}{2\Delta\zeta\Delta\zeta}\left(\langle\mu\zeta_{\bar{\xi}}\rangle_{k-1} + 2\mu\zeta_{\bar{\xi}} + \langle\mu\zeta_{\bar{\xi}}\rangle_{k+1}\right)$$

$$c = \frac{\rho u}{h_1}\zeta_{\bar{\xi}}\frac{1}{2\Delta\zeta} + \frac{\rho v}{h_2}\zeta_{\eta}\frac{1}{2\Delta\zeta} + \rho w\zeta_{\xi}\frac{1}{2\Delta\zeta} - \frac{\zeta_{\bar{\xi}}}{2\Delta\zeta\Delta\zeta}\left(\mu\zeta_{\bar{\xi}} + \langle\mu\zeta_{\bar{\xi}}\rangle_{k+1}\right)$$

$$\mathrm{RHS} = \rho\frac{u}{\Delta t} - \frac{\rho}{h_1}\left[\frac{(u+|u|)}{2}\nabla_{\xi}u\right] - \frac{\rho}{h_1}\left[\frac{(u-|u|)}{2}\Delta_{\xi}u\right] - \frac{\rho}{h_2}\left[\frac{(v+|v|)}{2}\nabla_{\eta}u\right] - \frac{\rho}{h_2}\left[\frac{(v-|v|)}{2}\Delta_{\eta}u\right] + \frac{\rho_e}{h_1}\left[\frac{(u_e+|u_e|)}{2}\nabla_{\xi}u_e\right] + \frac{\rho_e}{h_1}\left[\frac{(u_e-|u_e|)}{2}\Delta_{\xi}u_e\right] + \frac{\rho_e}{h_1}\left[\frac{(v_e+|v_e|)}{2}\nabla_{\eta}u_e\right] + \frac{\rho_e}{h_1}\left[\frac{(v_e-|v_e|)}{2}\Delta_{\eta}u_e\right] + K_{11}(\rho_e u_e^2 - \rho u^2) + K_{12}(\rho_e u_e v_e - \rho u v) + K_{13}(\rho_e v_e^2 - \rho v^2) + A_{11}2\Omega(\{\rho u - \rho_e u_e\}\cos\alpha + \{\rho v - \rho_e v_e\}) + A_{12}\Omega^2 r(\rho - \rho_e)$$

$$A_{11} = \frac{1}{\sin\alpha}\frac{1}{h_1 h_2 \sin\alpha}\left(\frac{\partial r_b}{\partial\bar{\xi}}\frac{r_b\partial\theta_b}{\partial\bar{\eta}} - \frac{r_b\partial\theta_b}{\partial\bar{\xi}}\frac{\partial r_b}{\partial\bar{\eta}}\right)$$

$$A_{12} = \frac{1}{\sin^2\alpha}\left(\frac{1}{h_1}\frac{\partial r_b}{\partial\bar{\xi}} - \frac{\cos\alpha}{h_2}\frac{\partial r_b}{\partial\bar{\eta}}\right)$$

The operator notations used here are:

$$\nabla_{\xi}u = \frac{1}{2\Delta\xi}(3u - 4u_{i-1} + u_{i-2}),$$

$$\Delta_{\xi}u = \frac{1}{2\Delta\xi}(-3u + 4u_{i+1} - u_{i+2})$$

$$\nabla_\eta u = \frac{1}{2\Delta\eta}(3u - 4u_{j-1} + u_{j-2}),$$

$$\Delta_\eta u = \frac{1}{2\Delta\eta}(-3u + 4u_{j+1} - u_{j+2})$$

The subscripts by ξ, η, and ζ in the equations mean differentiation with respect to ξ, η, and ζ, respectively. The barred terms correspond to the nonuniformly spaced computational mesh.

The η-momentum and energy equations are discretized in a similar form. The discrete form of the continuity equation is centered at $(i, j, k + (1/2), n + 1)$. The ξ and η derivatives are approximated with a backward difference second-order accurate formula, except at the lateral boundaries. For spatial derivatives normal to a solid surface (ζ-direction) an implicit central difference operator is used.

$$w_{k+1}^{n+1} = \frac{\text{RHS}}{\text{Coeff}} \tag{8}$$

where

$$\text{Coeff} = -\frac{(\langle\zeta_{\bar{\zeta}}\rangle_{k+1} + \zeta_{\bar{\zeta}})}{2}\frac{1}{\Delta\zeta}\rho_{k+1}^{n+1}$$

$$\text{RHS} = -\frac{(\langle\zeta_{\bar{\zeta}}\rangle_{k+1} + \zeta_{\bar{\zeta}})}{2}\frac{1}{\Delta\zeta}\langle\rho w\rangle^{n+1} + \frac{(\rho_{k+1} + \rho)^{n+1} - (\rho_{k+1} + \rho)}{2\Delta t} + \frac{1}{h_1 h_2 \sin\alpha}\left\langle\frac{1}{2}\nabla_\xi(h_2 \sin\alpha\rho u)\right\rangle_{k+1}^{n+1}$$

$$+ \frac{1}{h_1 h_2 \sin\alpha}\left\langle\frac{1}{2}\nabla_\xi(h_2 \sin\alpha\rho u)\right\rangle^{n+1} + \frac{1}{h_1}\frac{(\langle\zeta_{\bar{\xi}}\rangle_{k+1} + \zeta_{\bar{\xi}})}{2}\frac{1}{\Delta\zeta}(\langle\rho u\rangle_{k+1} - \rho u)^{n+1} + \frac{1}{h_1 h_2 \sin\alpha}\left\langle\frac{1}{2}\nabla_\eta(h_1 \sin\alpha\rho v)\right\rangle_{k+1}^{n+1}$$

$$+ \frac{1}{h_1 h_2 \sin\alpha}\left\langle\frac{1}{2}\nabla_\eta(h_1 \sin\alpha\rho v)\right\rangle^{n+1} + \frac{1}{h_2}\frac{(\langle\zeta_{\bar{\eta}}\rangle_{k+1} + \zeta_{\bar{\eta}})}{2}\frac{1}{\Delta\zeta}(\langle\rho v\rangle_{k+1} - \rho v)^{n+1}$$

For spatial derivatives parallel to the body surface (ξ-, η-direction), a second-order accurate difference operator is used except at lateral boundaries where the derivative is approximated with a backward or a forward difference first order accurate formula.

Since our solutions are obtained from a tridiagonal matrix, we can analyze the stability concept of the equations with a tridiagonal constraint. To make a rough estimate of this, we might assume that $\Delta t \gg \Delta\bar{\zeta}$ (approximately true in our case) and $\langle\mu\zeta_{\bar{\zeta}}\rangle_{k+1} \approx \langle\mu\zeta_{\bar{\zeta}}\rangle_{k-1} \approx \langle\mu\zeta_{\bar{\zeta}}\rangle$. Then the stability of the equation requires that

$$\left|\frac{u\zeta_{\bar{\xi}}}{h_1} + \frac{v\zeta_{\bar{\eta}}}{h_2} + w\zeta_\zeta\right|\frac{\rho\Delta\zeta}{\mu\zeta_\zeta^2} < 2 \tag{9}$$

Computational Procedure

The solution method is based on time-marching; however, the method is applied for steady flow. The time integration is in a form of a tridiagonal system of equations that are solved in an uncoupled manner. The momentum equations can be solved for u^{n+1} and v^{n+1}, the energy equation for H^{n+1}, the equations of state for T^{n+1}, ρ^{n+1} and the viscosity law for μ^{n+1}. The next step is to solve the continuity equation for w^{n+1}. Finally, μ_t is updated at time $n + 1$ by employing the Baldwin-Lomax model. This sequence represents one cycle of an iteration procedure. For steady flow solutions, the process is repeated until the difference between two successive values of u, v and w, for ζ-η plane, be less than a specified tolerance. A suitable convergent criterion can be defined in terms of u. The equation is given as

$$\text{MAX}|u^{n+1} - u| \le \epsilon \quad \text{for all} \quad j, k \tag{10}$$

where ϵ is the convergence criterion (usually $\approx 1 \times 10^{-4}$).

We use u as a convergence criterion because it is a base parameter in the governing equations. If the convergence criterion (10) is not satisfied, all the parameters are updated and the process repeats.

$$u_{\text{new}} = \omega u^{n+1} + (1 - \omega)u_{\text{old}} \tag{11}$$

For this calculation the relaxation factor (ω) is ranging between 0.50 and 1.50 according to the convergence of the solution (i.e., over-relaxation when the convergence rate is fast and under-relation when the convergence is slow).

Results

To validate the method it is here applied to a number of test cases. The calculations were started from the leading edge to the trailing edge using only the free-stream values of all parameters and the specified body geometry.

Three-Dimensional Flow Over a Flat Plate With an Attached Cylinder. A study of three-dimensional boundary layers approaching a cylinder with its axis normal to a plate was discussed in detail by Fillo and Burbank (1972). A circular cylinder of radius "a" is mounted at distance x_0 downstream from the leading edge of the plate. The calculation domain is limited only up to $x/a = 4.2$ on the symmetry plane, and $y/a = 1.5$ on the y-axis before separation occurred.

This test case is used as a test for the accuracy and the suitability of the method. A $43 \times 16 \times 51$ grid point of x, y and z-direction was used in the calculation. This set of grid point represents $\Delta x = \Delta y = 0.61$. The convergence criterion was taken as 1×10^{-5} and it was needed about 39 iterations to pass this criterion. The results are shown in Fig. 2. As can be seen from the comparisons, our calculated results are in good agreement with those computed by Fillo and Burbank (1972).

Functions F and G are related to the wall shear stress as follows:

$$\tau_{xz} = \mu\left.\frac{\partial u}{\partial z}\right|_{z=0} = \mu u_e\left(\frac{u_e}{2\nu x}\right)^{1/2} F|_{z=0}$$

$$\tau_{yz} = \mu\left.\frac{\partial v}{\partial z}\right|_{z=0} = \mu v_e\left(\frac{u_e}{2\nu x}\right)^{1/2} G|_{z=0}$$

To investigate the mesh dependence of the method the solution was computed with different mesh sizes. The effect of Δx-spacing on the calculated $F|_{z=0}$ and $G|_{z=0}$ for a fixed Δy and Δz-spacing is also shown in Fig. 2. For these set of calculations the $\Delta x = 0.61$ was doubled by using half the number of mesh points (case $2\Delta x$) and double the number of mesh points (case

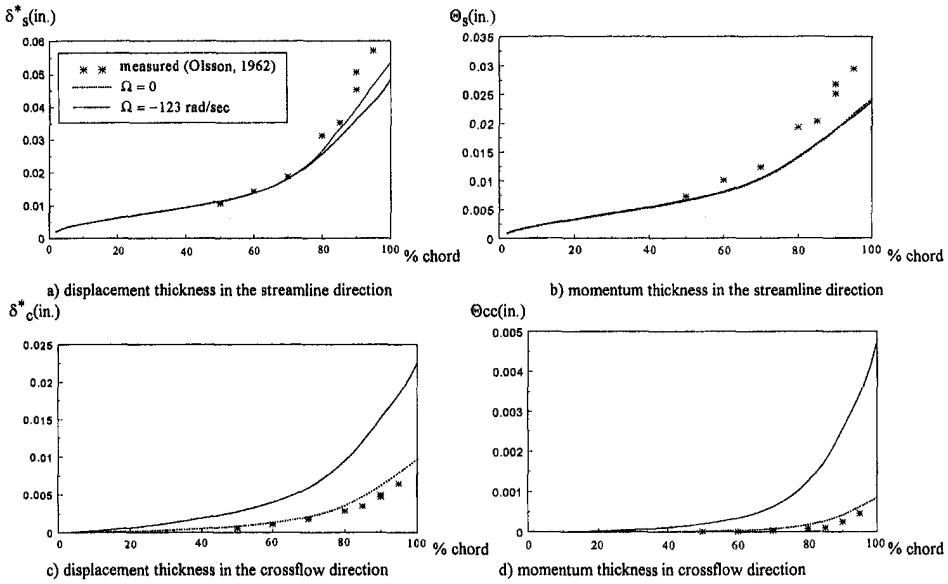

Fig. 5 Comparison of calculated and measured quantities for suction surface of NACA Blade, 50 percent span

$\Delta x/2$). The predicted results show only a very slight change between cases $2\Delta x$, Δx, and $\Delta x/2$, thereby confirming the mesh independence of the solution. Similarly, the effect of Δy-spacing and Δz-spacing on the calculated $F|_{z=0}$ and $G|_{z=0}$ for a fixed Δx is shown in Fig. 2. Again the mesh spacing was changed by increasing or decreasing the number of mesh points. For example in the case of Δz-spacing the set of grid points Δz, $2\Delta z$ and $\Delta z/2$ was corresponding to 51, 26 and 71 points across the boundary layer, respectively. The average number of iterations was slightly changed for the same convergence criterion in the case of a fixed Δx but the number of iterations was decreased when the number of mesh points in the x-axis was increased (Δx decreased). Again, the results confirm mesh independence of the solution.

Turbulent Flow on a Rotating Helical Blade. The second test case to be considered is the boundary-layer development in incompressible turbulent flow on a rotating helical blade, which was measured by Lakshminarayana et al. (1972). The hub radius of the blade is 9 in. and the tip radius is 18.30 in. The maximum angle θ measured from the leading edge is 300 deg, with blade pitch of 10 in. The blade rotates with an angular velocity of 57 rad/s (450 rev/min) corresponding to a Reynolds number of 7×10^5 based on the tip radius and kinematic viscosity of 160×10^{-6} ft^2/s. For this computation a $18 \times 18 \times 31$ mesh was used. The computation was started with a Blasius solution at the leading edge and transition from laminar to turbulent flow was set to occur at $\theta = 0.73$, based on the experimental evidence. The predicted momentum thickness, Θ_{ss} at various distances from the leading edge at $r/r_{tip} = 0.55$, 0.72, 0.82, and 0.93 is presented in Fig. 3. The prediction is excellent away from the endwalls (i.e., at $r/r_{tip} = 0.72$ and 0.82). Near the endwalls, however, the agreement is less close, although the general trend in momentum thickness growth agrees well with the measurements. The errors at the endwalls are due to the fact that the effect of annulus wall and hub are neglected in the

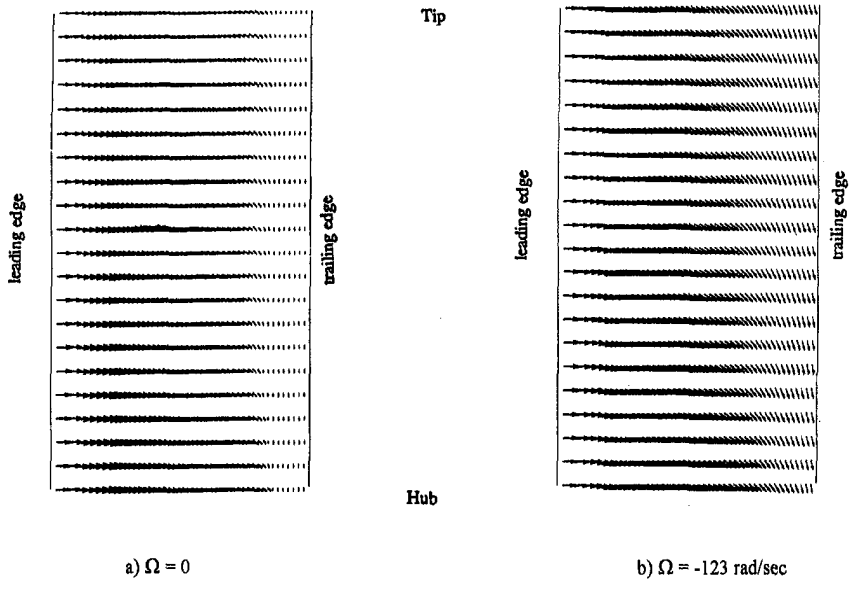

Fig. 6 Flow on NACA blade (suction surface)

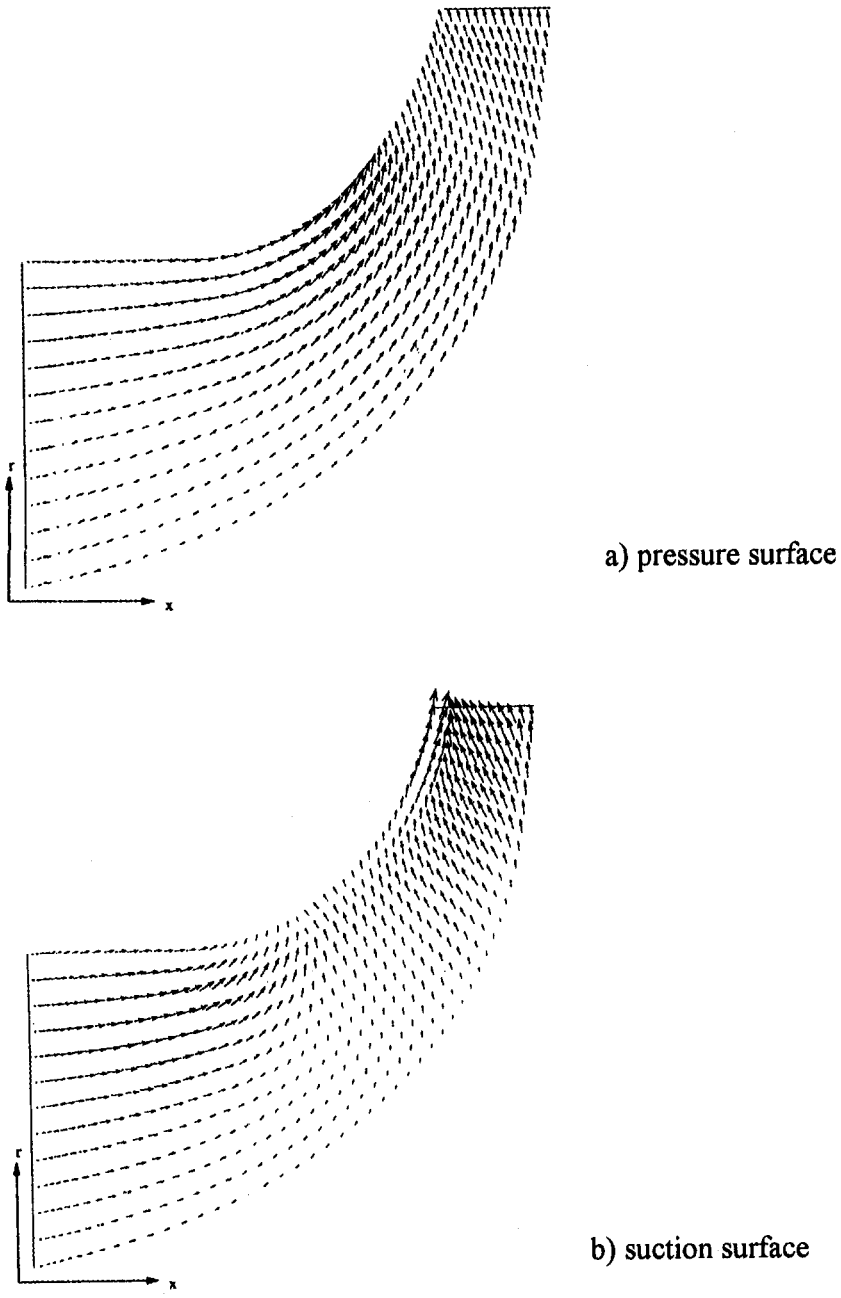

Fig. 7 Predicted velocity vectors (near the blade surface) on Eckardt's impeller

boundary-layer analysis. The computing time required per grid point was 0.087 seconds on a VAX Workstation. The average number of iterations was 78 to pass the convergence criterion of 2.5×10^{-5}.

Axial Compressor Blade. The third data used for validation of the method is the very comprehensive set of experimental results for an incompressible axial compressor, which was measured in details by Olsson (1962). The experiments were conducted in a stationary annular cascade. The measured free-stream velocity on the blade was specified for the boundary-layer calculation. The computational grid used for the calculation of the flow on the blade surfaces consisted of a $51 \times 21 \times 31$ mesh. To obtain the intermediate values of free-stream velocity from the measured data two-dimensional spline interpolation was used.

To demonstrate the effect of rotation on boundary-layer development in a similar manner to Karimpanah and Olsson (1992), the stator blades were used with the appropriate angular velocity which made the relative inlet flow angle to the rotor the same as the absolute inlet flow angle to the stator. This rotational speed was found to be 123 rad/s. The velocity profile predicted by the boundary layer code both on the stator and the rotor at 50 percent span on the suction surface are presented in Fig. 4 at different chordwise positions. The predicted streamwise velocity u/u_e for the stator correlates quite well with the experimental measurements, while the correlation for the cross-flow velocities is not as good. One reason for this could be due to the experimental errors which are estimated to be of the order ± 1.5 percent for the streamwise velocity and ± 10 percent for the cross-flow velocity. The results also indicate clearly that the presence of rotation has little effect on the streamwise velocity but results in substantial change in the cross-flow velocity due to the spanwise pressure gradients setup by the Corriolis acceleration.

Comparison between the corresponding predicted and measured integrated quantities such as displacement thickness and

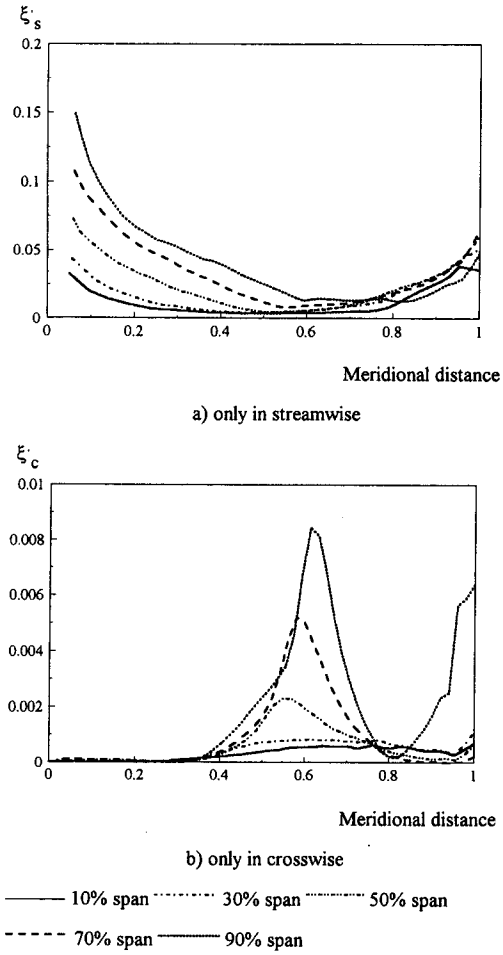

Fig. 8 Contours of the predicted entropy generation on the suction surface

momentum thickness are presented in Fig. 5. In case of the integrated quantities the measurement error for streamwise variables such as δ_s^* and Θ_s^* is ±4 percent, while the corresponding errors in the cross-flow variables is ±10–15 percent. There is again good correlation between the prediction and measurements for streamwise and cross-flow quantities. The predictions show that as a result of rotational effects the cross-flow displacement thickness at the mid-span location has increased considerably. This could be due to the secondary flows set up by the spanwise pressure gradient moving the low momentum fluids toward the mid-span location. This can be clearly seen in Fig. 6 which shows the predicted velocity vectors near the wall on the suction surface of the blade with and without rotation. The above computations were carried out using a VAX AXP computer. The convergence criterion used in the computation was 1×10^{-4}. It took about 25 iterations except in the case of suction surface with zero angular velocity which took about 56 iterations. This is because the flow is separated and the FLARE approximation is employed.

Centrifugal Compressor Impeller. The flow in centrifugal compressor impellers is dominated by endwall effects as a result of the strong interaction between the blade-blade and meridional secondary flows, see Zangeneh et al. (1997). As a result this type of flow is generally better predicted by Navier-Stokes solvers as opposed to boundary-layer methods. However, boundary-layer methods can be used as a computationally cheap means of obtaining information on the intensity of meridional secondary flows, which have an important effect on the flow field at the exit of the impeller, see Zangeneh et al. (1997).

To demonstrate this, the final test case used is a subsonic compressor blade, which was the subject of LDV measurements in the flow channel and away from the wall by Eckardt (1976). In order to compute the boundary-layer development on the suction and pressure surface of this impeller, it is important to know the free-stream velocity. In this case, the free-stream velocity was obtained by using Denton's (1983) three-dimensional Euler solver. Using this free-stream velocity and a $51 \times 13 \times 31$ computational mesh the boundary layer on the suction and pressure surface was computed. The convergence criterion of the solution was 1×10^{-4}. The computing time required was 1 minute and 2 seconds for the pressure surface and was 1 minute and 40 seconds (or about 58 iterations) for the suction surface. The resulting velocity vectors on the suction and pressure surface, presented in Fig. 7, show secondary flows both on the pressure and suction surfaces. Although as expected the secondary flows are more prominent on the suction surface.

The main aim of a designer in the aerodynamic or hydrodynamic design of turbo/hydraulic machinery is to minimize loss. It is usually possible to use Navier-Stokes solvers to predict loss in different designs at different locations such as the trailing edge or the exit of the computational domain. However, it is more instructive to consider local entropy generation, which is the source of loss on the blades. Asvapoositkul (1995), has used the energy equation for a boundary layer to derive the following expression for the rate of entropy production per unit surface area (ξ^*)

$$\xi^* = -\frac{k}{T}\frac{\partial T}{\partial \zeta}\bigg|_{\zeta=0} + \int_0^\delta \frac{\tau_s}{T}\,du + \int_0^\delta \frac{\tau_c}{T}\,dv + \int_0^\delta \frac{k}{T^2}\frac{\partial T}{\partial \zeta}\,dT \quad (12)$$

where

τ_s is streamwise shear stress $= \mu(\partial u/\partial \zeta)$
τ_c is crossflow shear stress $= \mu(\partial v/\partial \zeta)$

From the above equations, we can expect that the entropy generation near the wall is higher than that near the boundary-layer edge because velocities change rapidly near the wall. In the case of adiabatic wall temperature the heat transfer at the wall is zero ($(\partial T/\partial \zeta)|_{\zeta=0} = 0$). One interesting feature of Eq. (12) is that the total entropy production can be split into streamwise and crossflow components and so it enable one to quantify the contribution of each term on the total entropy production on the blade surfaces. An example of this is shown in Fig. 8, where the streamwise and cross-flow contributions to the entropy production on the suction surface are presented. The results confirm clearly that most of the entropy production is due to streamwise component particularly in the inducer region.

Conclusions

A method was presented for the solution of time-dependent three-dimensional boundary-layer equations in a rotating system and by employing a simple algebraic turbulence model. The method was validated using both analytic and experimental data using a variety of blade configurations. The results show that:

- The method can accurately predict the streamwise and cross-flow velocity profiles as well as skin friction and integrated quantities such as displacement and momentum thickness with a high degree of accuracy, both in laminar and turbulent flow.
- The method can model for the effect of rotation on the boundary-layer development on the blades.
- The boundary-layer method developed can be used as a rapid and accurate means of estimating the profile losses and state of boundary layers especially for axial compressor blades, axial pumps, marine propellers etc. It can also be used to obtain

some qualitative picture of the intensity of meridional secondary flows on blade surfaces of radial and mixed flow impellers.

Currently work is underway to develop the necessary interface between this three-dimensional boundary layer code and a 3D inverse design method developed by the second author for design of turbo/hydraulic machinery, see Zangeneh (1997). Furthermore, work is in progress to use higher-order turbulence models.

References

Asvapoositkul, W., 1995, "Calculation of Three-Dimensional Boundary Layers on Turbomachinery Blades," Ph.D. thesis, University of London.

Dawes, W. N., 1987, "Application of a Three-Dimensional Viscous Compressible Flow Solver to a High-Speed Centrifugal Compressor Rotor-Secondary Flow and Loss Generation," *Proceedings of the Institution of Mechanical Engineers International Conference: Turbomachinery-Efficiency Prediction and Improvement.*

Denton, J. D., 1983, "An improved time marching method for Turbomachinery flow calculations," ASME *Journal of Engineering for Power,* Vol. 105, No. 3, pp. 514.

Denton, J. D., 1993, "Loss Mechanisms in Turbomachines," ASME paper No. 93-GT-435.

Eckardt, D., 1976, "Detail Flow Investigation Within a High-Speed Centrifugal Compressor Impeller," ASME JOURNAL OF FLUIDS ENGINEERING, pp. 390–402.

Fillo, J. A., and Burbank, R., 1972, "Calculation of 3D Laminar Boundary Layer Flows," *AIAA Journal,* Vol. 10, No. 3, pp. 353–355.

Karimpanah, M. T., and Olsson, E., 1992, "Calculation Of Three-Dimensional Boundary Layers In Rotor Blades Using Integral Methods," ASME Paper 92-GT-210.

Lakshminarayana, B., Jabbari, A., and Yamaoka H., 1972, "Turbulent Boundary Layer on a Rotating Helical Blade," *Journal of Fluid Mechanics,* Vol. 51, Part 3, pp. 545–569.

Liu, Feng, and Jameson, Antony, 1993, "Multigrid Navier-Stokes calculations for Three-Dimensional Cascades," *AIAA Journal,* Vol. 31, No. 10, Oct.

Olceman, M. S., and Simpson, R. L., 1992, "Perspective: On the Near Wall Similarity of Three-Dimensional Turbulent Boundary Layers," ASME JOURNAL OF FLUIDS ENGINEERING, Vol. 114, pp. 487–495.

Olsson, E. K. A., 1962, "Centrifugal Effect on the Boundary Layer on a Blade of an Axial Turbomachine," Gas Turbine Laboratory, MIT., Report No. 66, Apr.

Oshima, A., 1994, "Analysis of Three-Dimensional Boundary-Layer on Propeller Blade," *Propellers/Shafting '94 Symposium,* Sept. 20–21.

Rehyner, T. A., and Flugge-Lotz, I., 1968, "The Interaction of a Shock Wave with a Laminar Boundary Layer," *International Journal of Non-Linear Mechanics,* Vol. 3, pp. 173–199.

Steger, J. L., and Van Dalsem, W. R., 1985, "Development in the Simulation of Separated Flows using Finite Difference Methods," *Proceedings of the Third Symposium on Numerical and Physical Aspects of Aerodynamic Flows,* California State University, Long Beach, Ca. Jan.

Vatsa, V. N., 1985, "A Three-Dimensional Boundary-Layer Analysis Including Heat-Transfer and Blade-Rotation Effects," *Third Symposium on Numerical and Physical Aspects of Aerodynamic Flows,* Long Beach, CA.

Wang, K. C., 1971, "On the Determination of the Zone of Influence and Dependence for Three-Dimensional Boundary Layer Equations," *Journal of Fluid Mechanics,* Vol. 48, pp. 397–404.

Yamazaki, R., 1981, "On the Theory of Marine Propellers in Non-uniform Flow," Memoirs of the Faculty of Engineering, Kyushu University, Vol. 41, No. 3, Sept.

Zangeneh, M., Goto, A., and Harada, H., 1997, "On the Design Criteria for Suppression of Secondary Flows in Centrifugal and Mixed Flow Impellers," Presented at the 42nd ASME/IGTI International Gas Turbine Conference, Orlando, FL, 2–5 June 1997. ASME Paper No. 97-GT-393. To be published in ASME *Journal of Turbomachinery.*

Zangeneh, M., 1997, "Development of a 3D Inverse Design Code for Application to Different Turbo and Hydraulic Machinery Components," Presented at the JSME International Conference on Fluids Engineering, Tokyo, Japan, July 13–16, JSME ICFE-97-701, pp. 195–200.

Sea Trials of the Ducted Tip Propeller

Ivar Hordnes[1]
Graduate Student.

Sheldon I. Green
Associate Professor.

Department of Mechanical Engineering,
University of British Columbia,
2324 Main Mall,
Vancouver, British Columbia
V6T 1Z4 Canada

Sea trials of a 45 ft seine boat, fitted first with a conventional tip, and subsequently with a ducted tip, 36 in. diameter propeller have been conducted. The trials consisted of careful propeller efficiency measurements at a number of advance ratios, and underwater video imaging of the different propellers under Bollard pull conditions. The trials have shown that flow-through ducts installed at the blade tips suppress the tip vortex roll-up, thus resulting in a substantial delay in the onset of tip vortex cavitation. The cavitation inception index for the ducted tip propeller is 50 percent lower than for the conventional propeller. This cavitation improvement comes without any efficiency penalty. In fact, the efficiency of the ducted tip propeller is up to 6 percent higher (at high advance ratios) than the efficiency of the same propeller fitted with conventional tips. The ducted tip propeller was originally thought to be useful only for boats with heavily loaded propellers, such as tug boats and trawlers. The current research has shown that the ducted tips may have much broader application.

1 Introduction

1.1 Marine Propeller Tip Vortices. All lifting surfaces (e.g., the wings of an airplane or the blades of a propeller) that terminate in a moving fluid create tip vortices. Tip vortices on marine propellers have two undesirable effects: they reduce the efficiency of the blade as a lifting surface by creating the equivalent of the downwash that affects aircraft wings (Fig. 10), and they may cause tip vortex cavitation. This cavitation typically occurs well before blade and hub cavitation on the same propeller. Cavitation is in general undesirable because of its detrimental effects both on equipment and on the comfort of boat passengers (Weitendorf, 1993). Cavitation is a major source of corrosion on the propeller and on the hull (above and aft of the propeller), and vibration associated with the cavitation can damage the propeller itself, the rudder, the shaft, the bearings and the engine (English et al., 1992). The cavitation noise may frighten fish away from fishing boats (Smith, 1996).

1.2 Previous Efforts to Alleviate the Effects of Tip Vortices. The most commonly used means of reducing the effects of tip vortices is to install a Kort nozzle around the propeller. The nozzle has the form of a shaped duct that fits with a fairly small clearance around the propeller. Kort nozzles can improve the efficiency of highly loaded propellers (e.g., as would be the case for a tug boat pulling a large barge) by up to 10 percent. However, nozzles have some negative attributes: the added wetted surface creates extra drag (which implies a reduction in efficiency when the propeller is less heavily loaded), and there are installation limitations related to the available space and the strength of the hull.

Other devices have also been proposed to alleviate the effects of tip vortices. Platzer and Souders (1979) is a comprehensive survey of the literature prior to 1980. Among the most promising concepts discussed in that report was the installation of bulbous tips on propeller blades (Crump, 1948). More recently, the concept has been tested on a hydrofoil by Johnsson and Rutgersson (1991); their results were not as encouraging.

There has been significant research since the Platzer and Souders report. Mani et al. (1988) have found that replacement of a conventional propeller tip by a porous tip can substantially delay inception, particularly at low advance ratios, without affecting the hydrodynamic performance of the propeller. Fruman and Aflalo (1989) were able to reduce the tip vortex cavitation inception index by 60 percent when a dilute polymer solution was ejected from an orifice at the tip of a hydrofoil. Simultaneous lift and drag measurements were carried out and showed that the hydrodynamic performance was unaffected by the polymer ejection. More recent experiments on a model propeller by Chahine et al. (1993) confirm the results of Fruman and Aflalo.

Several other methods to inhibit tip vortex cavitation have been tried. Two papers, by Itoh et al. (1987) and Itoh (1987), indicate that a model propeller fitted with small bladelets, equivalent to the Whitcomb winglets used on some aircraft, delayed the inception of tip cavitation, and increased the propeller efficiency by 1 to 4 percent. These results contradicted the findings of Goodman and Breslin (1980), who focused solely on the effects on the efficiency when bladelets are attached to a conventional outboard propeller. The differences between the findings of the different researchers is thought to be due to differences in the bladelet geometries tested.

1.3 The Ducted Tip Geometry. The propeller tip geometry that was investigated in this study—the ducted tip—was first proposed by Green et al. (1988). The ducted tip geometry is created by cutting off a small radial fraction of each propeller blade tip, and replacing it with a flow-through duct of diameter equal to the radius of the removed blade section. The axis of the duct is aligned with the local blade chord at the propeller tip. Green et al. found that installation of the ducted tip was very effective in reducing the hydrofoil tip vortex inception index. This improvement was attributed to the substantially larger tip vortex core generated by a ducted tip relative to a conventional tip. Green and Duan (1995) demonstrated an improved Lift/Drag (L/D) ratio, at high angles of attack, for an airfoil with the ducted tip. They also showed by means of flow visualization that there is a redistribution of the shed vorticity in the Trefftz plane when the ducted tips are installed. They ascribe the improvement of the L/D ratio to this vorticity redistribution.

The action of a duct is significantly different from that of a tip bulb of the same diameter. The duct modifies substantially the distribution of shed vorticity in the Trefftz plane, whereas a properly tapered bulb (i.e., one without significant flow separation) does not. The duct will also be likely to interrupt more

[1] Current address: Engineering Analysis Consultants AS, P.O. Box 1014, 3600 Kongsberg, Norway.

Contributed by the Fluids Engineering Division for publication in the JOURNAL OF FLUIDS ENGINEERING. Manuscript received by the Fluids Engineering Division July 15, 1997; revised manuscript received June 11, 1998. Associate Technical Editor: J. Katz.

effectively the roll up process due to the flow through the duct, and therefore better reduce the strength of the tip vortex.

1.4 Scope of Work. In this paper we describe sea trials of conventional and ducted tip propellers installed on a fishing boat. These trials were conducted in order to investigate the difference in propeller efficiency and tip vortex cavitation inception between a conventional propeller and a ducted tip propeller. We opted to perform sea trials, rather than the less difficult water tunnel testing, for several reasons. A propeller operating behind a boat of reasonable size operates at significantly higher Reynolds numbers than can be obtained in most propeller test facilities. There are known to be salient Reynolds number effects (both for cavitation inception testing and efficiency measurement) that might bias the results of model testing. In addition, real propellers operate in the wake of a boat, not in the essentially open-water conditions of most propeller testing. Finally, we chose to do sea trials because we wanted to know how a propeller really behaves at sea, not how it responds in an idealized laboratory environment.

Section 2 of this paper describes the preparations and the experimental equipment as well as the procedure employed during the sea trials. Section 3 presents the results, Section 4 is an analysis and a discussion, while a summary of this research is outlined as a conclusion and a set of recommendations in Section 5.

2 Experimental Equipment and Techniques

2.1 The Boat, the Propeller, and the Ducted Tips

2.1.1 The Boat. A 45 ft wooden seine boat (Pearl Sea) has been used for the sea trials. This boat is typical of a substantial number of seine boats that are operating in the coastal waters of British Columbia. At the time of the sea trials the stern roller, the net drum and the hydraulics associated with it were removed from the boat, making it substantially lighter than an operating seine boat. The width (beam) of the boat is 13 ft and it drafts 6 ft. The geometry of the hull can be described as having a very deep forebody with steep angles from the skegg and out towards the sides, changing sternwards into an afterbody that is fairly shallow and flat. A keel extends all the way sternwards to the single screw propeller, and the rudder is an extension of the keel immediately aft of the propeller.

Pearl Sea is powered by a General Motors V6-71 diesel engine, rated to 200 hp at 2100 rpm at maximum engine output, and 180 hp at 1800 rpm at cruising speed. The propeller shaft has a diameter, $D_s = 2.0$ in. It sits horizontally between the transmission and the stern bearing, and the axis of the propeller is therefore essentially aligned with the incoming flow.

2.1.2 The Propeller and Ducted Tips. To propel Pearl Sea, a bronze-manganese, 4 bladed, right-hand screw propeller was chosen (Fig. 1), with diameter, $D = 36$ in., and pitch, $P = 29$ in. The *expanded area ratio,* i.e., the total expanded area of the blades divided by the disk area, $A_E/A_0 = 0.5$. The area of the hub, which has a 5.5 in. diameter, is not regarded as a part of the expanded area. The propeller blades had a slight skewed-back contour, which often is employed in order to reduce the impact from any leading edge cavitation (Bjørheden, 1981). The profiles of the blade sections were shaped according to equations and tables given for the Wageningen B-Screw Series (Manen and Oossanen, 1988), to have an airfoil shape from the hub to $r = 0.8R$, and an ogival shape from $r = 0.8R$ to the tip of the blades. The propeller chord distribution is parabolic near the tip (i.e., the tip chord length is zero).

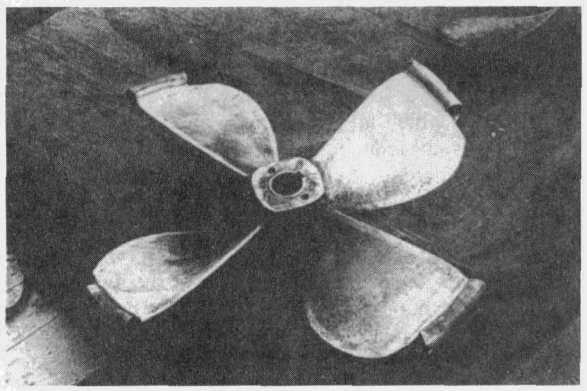

Fig. 1 The ducted tip propeller

After testing of this original propeller, the propeller diameter was reduced by 3 in. by removing a 1.5 in. (3.8 cm) radial section of each blade tip. Flow-through ducts of 1.5 in. diameter were silver soldered to the blades and aligned with the blade chords. The solder seams were covered with body filler and faired into a smooth transition between the ducts and the blades. The duct shape is geometrically similar to that used in the airfoil tests by Green and Duan (1995): duct-diameter/span, $d/b = 0.05$, and duct-length/chord, $l/c = 0.65$. The final dimensions are: $d = 1.5$ in. and $l = 5.5$ in. Each duct is built from a copper tube with wall thickness $t = 0.06$ in. that was bent into an arc with outer radius equal to the tip radius of the original propeller. The ducts have a completely circular cross section. The leading edge of the ducts have been formed into a spiral, or a lip, with the suction side of the duct extending farthest towards the blade leading edge. The thickness of the duct leading edge was increased with epoxy body filler and rounded to delay leading edge cavitation, while the thickness of the duct trailing edge was reduced by filing to minimize its wake (Fig. 1).

2.2 Instrumentation

2.2.1 The Torque and Thrust Transducer. In order to determine the efficiency of the propeller it is necessary to measure the torque and the thrust generated by the propeller, for example by measuring the stresses in the propeller shaft. Owing to the difficulty of such measurements at sea, surprisingly few sea trials of propeller efficiency have been done (Manen and Oossanen, 1988). The conventional method of measuring torque and thrust on any kind of a shaft is to cement strain gauges directly onto the shaft. However, on a propeller shaft there will always be a combination of axial and torsional forces, which complicates the measurements; the torque required to turn the propeller produces stresses that are an order of magnitude larger than the stresses produced by the thrust from the propeller. Many problems arise due to this large difference in strains.

A better technique of stress measurements involves mechanical decoupling and amplification of the strains. For the sea trials described in this paper, a torque and thrust transducer (Hordnes et al., 1995), hereafter referred to as the TTT, was built that consists of a set of links that decouple torque and thrust. The transducer (Fig. 2) fits into the shaft line between the flanges of a previously existing coupling that connects the propeller shaft with the drive shaft, and hence slightly extends the shaft line. The axial length of the transducer had to be less than the maximum distance the coupling could be split apart, which was in turn limited by the distance between the propeller and the rudder.

The transducer consists of two flanges, the same size as the coupling flanges, connected by means of three flat bars located circumferentially, at a radius of 5 cm (2 in.), around the centerline of the shaft axis. Each bar has one end connected to a support on the engine-side flange, while the other end is connected to a support on the propeller-side flange. Because both ends of each bar are free to rotate around an axis parallel with the shaft, through the support, all of the bars will experience only pure tension when the propeller imposes a torque on the shaft during forward motion of the boat. During backwards motion the force will be purely compressive. One of the bars

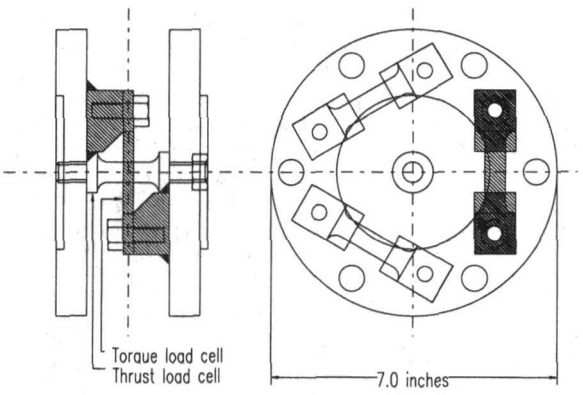

Fig. 2 The Torque and Thrust Transducer (TTT)

is equipped with strain gauges to form a load cell that measures the torque in terms of pure tensile or compressive strain.

The thrust is carried by a column located at the centerline between the two flanges. The diameter of the column has been reduced from a shaft size D_s = 2 in. (5 cm) to d_s = 0.5 in. (1.25 cm), thus increasing the strain by a factor of 16. The central column is equipped with strain gauges connected in a Wheatstone bridge to form a thrust load cell. The column is free to rotate around its own axis. In this way it experiences no torque, and as a load cell it will measure pure compressive or tensile strain. Because the compression of the column is small, the thrust imposes almost no bending on the flat bars, and conversely, the flat bars carry no thrust.

Laboratory testing of the TTT has confirmed that the transducer responds linearly to both torque and thrust, with no discernible cross-talk; the torque cell responds linearly when a pure torsional force is applied, while the thrust remains constant at a preset magnitude. Following the same trend, when a pure axial force is applied, the thrust varies linearly while the torque remains constant at a preset magnitude.

The signals produced by the torque and thrust load cells are conditioned separately by two printed circuit boards that each have an amplifier, an analog-to-digital (A/D) converter and a radio transmitter. Both boards are installed and sealed together with two 9V batteries for power supply, in a plastic box that is mounted on, and turns with, the shaft. After being conditioned, the signals from the torque and thrust load cell are transmitted simultaneously, at a rate of one signal a second, on two separate channels to a stationary receiver. The receiver is connected directly to a computer, which can log the data for any length of the sampling period.

2.2.2 Other Instrumentation. Drogues of varying drag were constructed of bundled car tires. These drogues were towed several boat lengths behind the boat, and were presumed not to interact hydrodynamically with the propeller. The drogue drag was monitored by a 5000 lb ring load cell. In this way any variation in the thrust from the propeller could be correlated to variations of the drag force on the drogue.

An industrial turbine flow meter for recording mass flow in pipes was adapted to measure the velocity of the boat. Compared to a standard velocity meter of the paddle wheel type, the turbine flow meter can measure lower velocities, although at low velocities it is non-linear due to bearing friction in the turbine. The lowest velocity it is capable of measuring is approximately V = 0.5 m/s. In order to measure the true velocity of the boat relative to the water, the flow meter had to be located away from the flow field induced around the hull. This was done by attaching the flow meter to one of the stabilizer poles, extending 17 ft. out to the side of the boat.

The propeller shaft rotation rate was measured by a MAXI-MAG magnetic sensor. The sensor counts the passage frequency of gear teeth on a gear (4 in. in diameter, with 60 teeth) connected to the propeller shaft.

Visual recordings of the tip cavitation were obtained with a Sony Hi8 CCD-V99 video camera with a maximum shutter speed of 1/10000 s. The video camera is mounted in a water tight, cast aluminum housing, and powered by either a 9 volt battery or 110 volts from the surface. Light was supplied by two 650 watt underwater lights.

2.3 Procedure for Sea Trials. The sea trials consisted of two sets of experiments; the first for the conventional propeller, and the second for the ducted tip propeller. Each set was divided into sub-experiments: first efficiency measurements at five different advance ratios, followed by cavitation observations at zero velocity.

The efficiency measurements involved sampling of torque, thrust, velocity, shaft rotation, and tow load data for five different drogue sizes:

1. Free running—no tow load
2. Light drogue—14 tires in one bundle
3. Medium drogue—30 tires in two bundles (14 + 16)
4. Heavy drogue—48 tires in two bundles (37 + 11)
5. Bollard pull—pulling against dock, zero velocity

For each drogue size data were collected from approximately 180 rpm up to the maximum shaft rotation rate, in small increments of rpm. For each increment, conditions were stabilized before data were acquired over a period of 30 seconds. Every data point presented in this report is an average of the data sampled over 30 seconds, unless otherwise stated. At maximum shaft rotation the boat was turned 180 deg and the measurements were retaken. In this way the effect of the tide, wind, and waves could be determined.

Cavitation observations were carried out by a diver taking video recordings of the turning propeller while the boat was tied to the dock. The diver was harnessed to the dock, filming from a 30–60 deg angle, approximately 10 feet aft of the propeller. Before the filming was started, the shaft rotation rate at cavitation inception was determined by increasing the shaft rotation in small increments until the diver could see the first white bubble of the tip vortex cavitation on the tips of the propeller. The shaft rotation was then reduced and video recordings were carried out for small increments of rpm from below the tip vortex inception shaft rpm to the maximum shaft rpm (the propeller shaft rpm is denoted by N). Diver determinations of σ_i were in excellent agreement with observations from the video recordings.

3 Results

3.1 General Observations About the Sea Trials. The sea trials went surprisingly well; we were able to complete all the trials with a particular propeller geometry in three days at sea. We attribute our success to careful "shakedowns" of the equipment prior to actual experimentation, and the very able guidance of our research engineer.

Upon installation of the ducted tips, the maximum propeller rotation rate, N, was reduced by less than 2 percent at free running speeds, which is very encouraging. Installation of the ducted tips does not reduce the shaft rotation rate and therefore does not cause the engine to run at off-peak efficiency, i.e., a boat retrofitted with a ducted tip propeller would not require installation of a new transmission.

During the sea trials a number of other factors caught our attention with respect to the performance of the ducted tip propeller: there were no noticeable changes to the maneuverability of the boat, a factor that was put to the test every time the boat was maneuvered in and out from the dock. According to the skipper the propeller still had good *bite,* i.e., high acceleration in either direction, when needed. The owner also commented

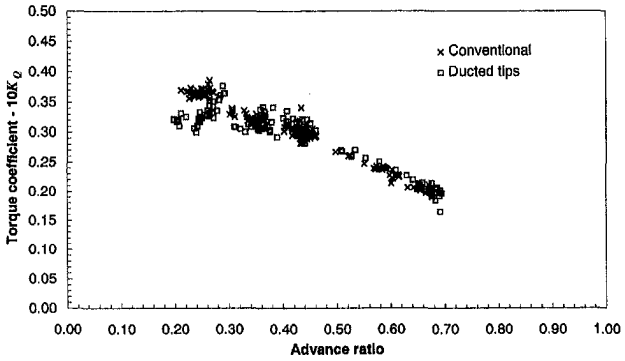

Fig. 3 Torque coefficients of the conventional and ducted tip propellers. The uncertainty in K_Q varies from ±9 percent for small J to ±5 percent at higher J. The error in the advance ratio is ±5 percent at the lowest J and ±2 percent for higher J, all at the 95 percent confidence level.

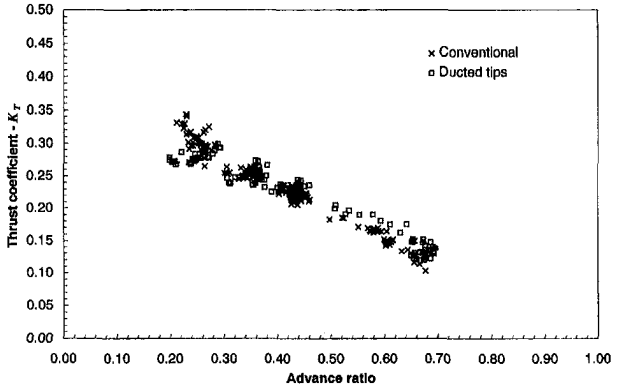

Fig. 4 Thrust coefficients of the conventional and ducted tip propellers. The uncertainty in K_T is ±3 percent and the uncertainty in J is as for Fig. 3.

on how the wake was different at low and moderate velocities. With the ducted tip propeller, the tip vortices were visible in the surface wake substantially further behind the transom than is the case with the conventional propeller. Although this does not prove that the propeller performance is improved, it should be regarded as an indication that the tip vortices have been suppressed.

Finally, the addition of the ducts did not seem to intensify the vibration onboard the boat. This implies that the ducted tips were installed with more or less identical orientation, resulting in an even loading on the four propeller blades. In addition, any weakening of the tip vortices as a result of installing the ducted tips will also contribute to reduce the vibration.

Variation of the data introduced by the external conditions (such as the aerodynamic drag) seemed to have had no effect on the efficiency measurements, other than resulting in a wider spread of the points, particularly the points recorded at low velocities at free running speeds. Thus, the test conditions can be assumed not to have affected the outcome of the sea trials.[2]

Prior to installing the propeller on the boat, the blade surfaces were sanded to a finish equivalent to that delivered by propeller manufacturers. Because of delays between installation and the first test runs of the conventional propeller, a certain degradation of the surface due to growth of marine micro organisms might have influenced the efficiency measurements, although frequent use and visual inspections suggest otherwise. At the time of installation of the conventional propeller, the hull of Pearl Sea was sanded down and given a new coat of bottom paint. During the nine months it took to complete the test program, the hull stayed essentially free of barnacles and other marine growth. We have therefore assumed that the marine environment had only a negligible effect on the measurements.

3.2 Efficiency Measurements. The torque and thrust measurements are compiled into K_Q and K_T curves, plotted as functions of the measured advance ratio, J (Figs. 3 and 4). In the normal fashion, K_Q, K_T, and J are defined as:

$$K_Q = Q/\rho n^2 D^5$$

$$K_T = T/\rho n^2 D^4$$

$$J = V/nD$$

where Q is the torque, T is the thrust, V is the boat velocity through the water, ρ is the water density, D is the propeller diameter, and n is the propeller rotation rate in revolutions per second ($n = N/60$).

[2] The ducted tip propeller was tested under similar, but slightly less rough, sea conditions than was the conventional propeller.

Figure 3 shows that installation of the ducted tips causes a slight reduction in the torque coefficient at low advance ratios, and a very slight K_Q increase at high advance ratios. The thrust coefficient shows similar trends with the addition of the ducted tips, although the percentage increase in K_T is greater at high advance ratios than is that of K_Q.

The torque and thrust measurements may be combined in the form of a propulsive efficiency, $\eta = VT/2\pi nQ$. The propulsive efficiency of both propellers is plotted against the advance ratio in Fig. 5. Several features of this graph warrant mention. There is increased scatter of the efficiency data at high advance ratios for both propellers owing to the increasing effect of hull waves at high J. At low advance ratios the decreased torque coefficient of the ducted tip propeller almost precisely offsets its decreased thrust coefficient, causing the propulsive efficiency measured before and after addition of the ducted tips to be the same to within experimental error. In contrast, at high advance ratio the higher thrust coefficient of the ducted tip geometry more than offsets its higher torque coefficient, thus producing a higher efficiency than the conventional propeller geometry.

Due to the significant experimental error combined with a large spread of the data that results from other sources (aerodynamic drag, wave loads, etc.), the exact trend of the efficiency is not readily observed. In order to better visualize this trend, the efficiency has been plotted as a function of the advance ratio, where, instead of using the measured values for Q, T, and V, the regression lines $Q = f(n)$, $T = f(n)$ and $V = f(n)$ have been used as input in the efficiency and advance ratio definitions, giving $J = f(n)$ and $\eta = f(n)$.

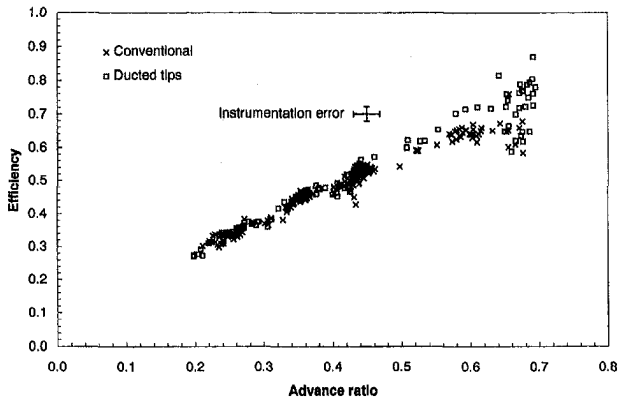

Fig. 5 All efficiency versus advance ratio measurements for both propellers. Owing to the varying V and n at which each of the measurements was taken, each measurement has different error bounds. A typical error bar is shown in the figure.

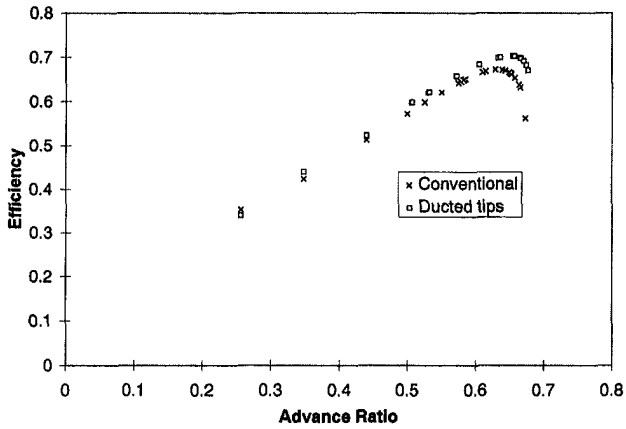

Fig. 6 The efficiency of the conventional and ducted tip propellers. The measured values of Q, T, and V were replaced by their regression lines in the efficiency equation. The points at J = 0.26, 0.35 and 0.44 describe the tests with heavy, medium, and light drogues, respectively, while all the remaining points describe the free running speeds. Owing to the averaging of data, all efficiency points are ±2 percent and all advance ratio points are ±3 percent at the 95 percent confidence limit.

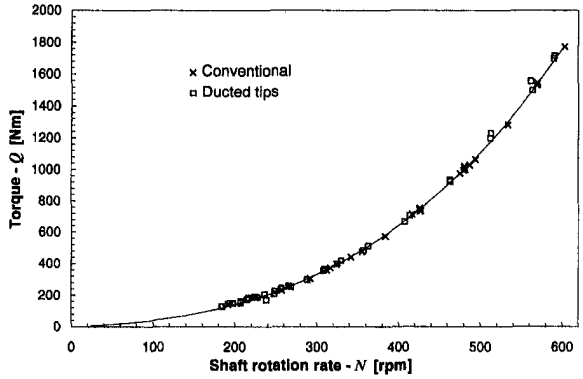

Fig. 7 The propeller shaft torque versus rotation rate for the conventional and ducted tip propellers at free running conditions. For shaft rotation rates of between 200 and 400 rpm, the torque required to drive the conventional and ducted propellers is identical to within experimental error. (The error in N is less than 1 percent and the torque error is about 5 percent at the 95 percent confidence level.)

The efficiency based on the regression lines for both propeller tip geometries is shown in Fig. 6.[3] At low and moderate advance ratios there is little or no change in the propeller efficiency. At high advance ratios, near the propeller maximum efficiency point, there is as much as a 6 percent improvement in the propeller efficiency with the addition of the ducted tip.

As one reviewer observed, it is possible that the ducted tip propeller might actually be less fuel efficient than the conventional propeller (based solely on Fig. 6), if at the same value of J the boat operated at a different speeds (i.e., one could effectively move off the design point, into a less efficient regime).

The ducted tip propeller was most efficient for $J \approx 0.65$, which occurs when the propeller spins fairly slowly ($N \approx 300$ rpm) under free running conditions. Figure 7 shows the torque required to drive the two propeller geometries as a function of N. For N near the optimum efficiency point ($250 < N < 350$), the torque required to drive each propeller is the same to within experimental error, and thus for these values of N the power consumed by the two propellers was the same. Figure 8 shows, for example, that for N = 320 rpm the boat speed was 3.4 m/s when fitted with the ducted propeller and 3.3 m/s when fitted with a conventional propeller, or roughly 3 percent higher with the ducted tip propeller. This is consistent with the claim that under these conditions the ducted propeller is approximately 9 percent more fuel efficient ($\eta = 0.72$ versus $\eta = 0.66$) than the conventional propeller.

At full throttle, under free running conditions, the advance ratio of the propeller is only 0.49. For this value of J the ducted tip propeller is only 2 percent more efficient than the conventional propeller, and hence the peak boat velocity should have been less than 1 percent greater (i.e., within experimental error) when it was driven by the ducted tip propeller. Our measurements of boat top speed confirmed this.

3.3 Cavitation Observations. Observing cavitation with a steady illumination source, as we have, is more difficult than with stroboscopic illumination. Nonetheless, the excellent agreement between the observations of the diver and the video recordings of the cavitation lends substantial credence to the results reported in Table 3.1. The video recordings made at Bollard pull conditions showed irrefutable indications of tip vortex cavitation from the conventional propeller at a propeller shaft rotation rate of N = 285 rpm, whereas there is no sign of any cavitation from the ducted tip propeller until 405 rpm $< N <$ 457 rpm. The large spread in the range of N at which tip vortex cavitation inception occurs from the ducted tip geometry is a result of the comparatively diffuse appearance of this cavitation. This diffuseness of the cavitation makes the accurate determination of N even more difficult for the ducted tip propeller than for the conventional propeller.

3.4 Instrumentation Error. The torque and thrust transducer measurements have errors due to shaft misalignment and instrument drift. The sum of these errors varies between 11 percent at N = 180 rpm, and less than 2 percent for $N > 500$ rpm. The turbine flowmeter has an error of 5 percent when the boat headway is small (<2 m/s), but is significantly more accurate at higher boat velocities through the water. The shaft rpm transducer has an error of less than 1 percent for all N.

The efficiency is a product of four parameters (velocity, shaft rotation, torque and thrust) that all have their individual errors. A method described by Bevington (1969) has been used to determine the square of the deviation for every efficiency point,

$$\frac{S_\eta^2}{\eta_j^2} = \frac{S_V^2}{V_j^2} + \frac{S_T^2}{T_j^2} + \frac{S_N^2}{N_j^2} + \frac{S_Q^2}{Q_j^2} + \frac{2S_VS_T}{V_jT_j} - \frac{2S_VS_N}{V_jN_j} - \frac{2S_VS_Q}{V_jQ_j} - \frac{2S_TS_N}{T_jN_j} - \frac{2S_TS_Q}{T_jQ_j} + \frac{2S_NS_Q}{N_jQ_j}$$

from which the standard deviation can be determined,

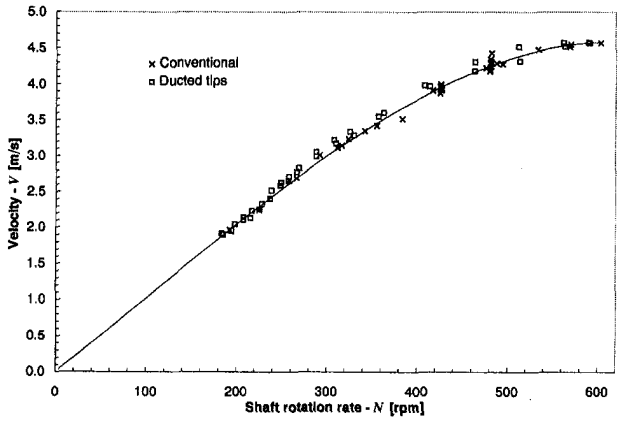

Fig. 8 Boat velocity as a function of shaft rotation rate, under free running conditions. The error in N is less than 1 percent and the error in boat velocity is under 2 percent, at the 95 percent confidence level.

[3] Virtually identical curves result from drawing regression lines directly through the η vs. J data.

Table 3.1 Summary of video recordings of cavitation

N (rpm)	Conventional Propeller	N (rpm)	Ducted Tip Propeller
252	No cavitation.	252	No cavitation.
266	A few infrequent bubbles.	259	No cavitation.
274	Intermittent cavitation (two blades only)	274	No cavitation.
285	Continuous cavitation from two blades, intermittent cavitation from two.	283	No cavitation.
301	Continuous cavitation from all blades.	305	No cavitation.
329	Propeller wake visible. Strong sternwards race aft of the propeller.	314, 335	No cavitation.
354	Well-defined tip cavitation helices.	355	No cavitation.
377	Extension of the helices.	365	No cavitation.
405	Extension of the helices.	404	Leading edge cavitation emerging from the duct entrances.
452	Extension of the helices.	457	Vapor cloud trails from the duct exits, forming very diffuse cavitation helices.
491	Maximum *N*. Strongly cavitating helices trailing behind the blade tips.	463	Maximum *N*. As for N = 457.

$$S_\eta = \sqrt{\frac{1}{M-1}\sum_{j=1}^{j=M} S_{\eta j}^2}$$

and, as for the individual instruments, the error is set to $2S_\eta$ in order to stay within a 95 percent confidence interval. There is of course an additional error caused by the varying sea conditions encountered in these trials. No attempt has been made to estimate this error.

4 Discussion

4.1 Comparison to the Open-Water Efficiency. Figure 9 shows the efficiency, torque and thrust coefficients for the conventional propeller plotted together with the corresponding open-water curves of the Wageningen B4-50 propeller, with $P/D = 0.8$. The digits in the B-series designation represent the number of blades and the expanded area ratio, respectively.

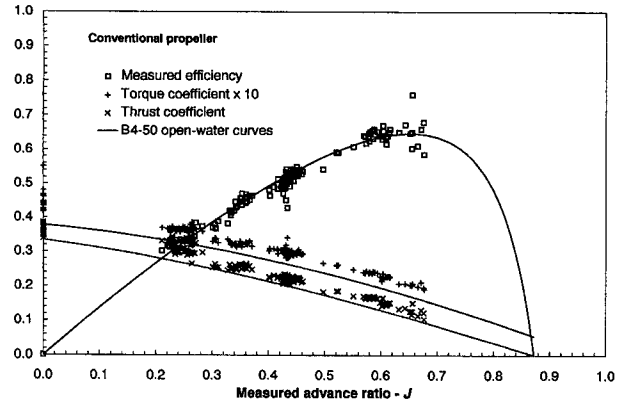

Fig. 9 Comparison of the measured propeller performance of the conventional propeller and the open-water curves of the B4-50 propeller. The error in the measurements is documented in the captions to Figs. 3, 4, and 5.

The open-water curves are based on the experiments of Troost (1937) on the 4-bladed B-screw propeller series, to which a polynomial, which is a function of A_E/A_0, P/D and J, was fitted by Lammeren et al. (1969).

Figure 9 shows that the conventional propeller has high efficiency, although the measured and open-water performance can not be compared directly. The measured efficiency is based on the boat velocity, V, while the open-water efficiency is based on the speed of advance, V_A. Because a propeller operating in the wake of a boat sees a different water approach velocity than an open water propeller, it can operate at the same shaft rotation rate and yet measure a different η and J. If the Taylor wake fraction, $w = 1 - V_A/V$, and hull efficiency of Pearl Sea were known, η and J could be adjusted to obtain a true comparison. By assuming $T/T_o = Q_o/Q = 1$, η could be adjusted down by ηw and in by Jw to give η_o and J_A for the conventional propeller. Such an analysis of the data of Fig. 9 indicates that all the measured efficiency points will remain on top of, or close to, the B4-50 curve even after such an adjustment. Transforming the torque and thrust coefficient measurements to "open water" conditions yields fairly good agreement with the B4-50 curves, but not as good as for the efficiency measurements.

In summary, the propeller studied here was well represented by the B4-50, with its similar geometry, diameter, pitch and area ratio. The excellent agreement between our measured efficiencies and those of the similar B4-50 also confirmed that our measurements were reliable. Any small differences in geometry between our propeller and the Wageningen series should be of no significance in the comparison between the ducted and conventional tip geometries.

4.2 Hydrodynamic Performance of the Ducted Tip Propeller. Green and Duan (1995) showed that the L/D ratio of a *ducted tip airfoil* is superior to that of a conventional airfoil for angles of attack larger than 8 deg. Consequently, it was expected that any efficiency improvement of a ducted tip propeller would occur when the blades operate at high angles of attack, i.e., at low advance ratios. At higher advance ratios, toward maximum efficiency, a loss of efficiency was expected, or at best no change at all. The results from the sea trials of the ducted tip propeller are therefore somewhat surprising; there is only a marginal efficiency improvement at low and moderate advance ratios, with increasing improvement towards higher advance ratios.

In order to understand these surprising results, we need to consider the forces acting on the propeller. According to blade element theory, the torque and thrust experienced by a radial section of a propeller blade located at radius r and dr wide (Fig. 10) can be expressed as:

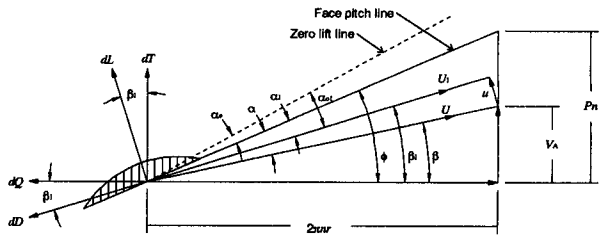

Fig. 10 Force and velocity diagram for a blade element, u is the induced velocity, P is the blade pitch. All other symbols are self-evident or are defined in this section.

$$dT = dL \cos \beta_I - dD \sin \beta_I$$

$$dQ = (dL \sin \beta_I + dD \cos \beta_I) r$$

Furthermore, the blade element efficiency can be written (analogously to the overall propulsive efficiency) as:

$$\eta = \frac{dTV_A}{2\pi n dQ}$$

By substituting for dT and dQ, it can be shown (Manen and Oossanen, 1988) that the element efficiency becomes a function of the Lift/Drag ratio:

$$\eta = \frac{\tan \beta}{\tan (\beta_I + \gamma)} \quad \text{and} \quad \tan \gamma = \frac{D}{L}$$

Hence, an increase in the L/D ratio of the blades of a propeller should result in an improved propeller efficiency. In addition, and more significantly, any reduction of the induced velocity, u, will reduce β_I and therefore improve the efficiency.

In view of this analysis, the efficiency will be related to the radial variation of the lift and drag coefficients (i.e., the angle of attack, α) as a function of the propeller radius and the advance ratio. Blade element theory tells us that the appropriate expression for α is:

$$\alpha = \arctan \frac{(P/D)}{\pi(r/R)} - \arctan \frac{J(1-w)}{\pi(r/R)} \qquad (4.1)$$

The wake fraction, w, could not be determined for Pearl Sea. Single screw ships with moderate blockage coefficients have Taylor wake fractions between 0.2 and 0.3 (Manen and Oossanen, 1988); $w = 0.2$ was chosen to plot Eq. (4.1) as Fig. 11.

Two extra lines have been plotted in the figure to indicate the upper and lower boundary of the region of possible improvement of the L/D ratio, hereafter referred to as the *improvement*

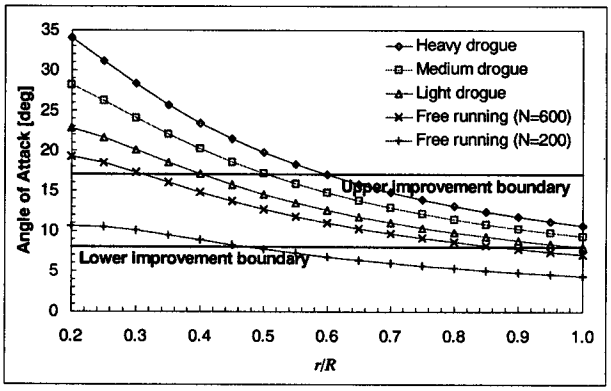

Fig. 11 The angle of attack, α, as a function of the propeller radius for different J, ranging from $J = 0.20$ (heavy drogue) to $J = 0.55$ (free running, $N = 200$), for a Taylor wake fraction $w = 0.20$. The induced velocity has been neglected.

envelope. The upper and lower boundaries for the improvement envelope were chosen to coincide with the lowest and highest angles of attack at which an improvement of the L/D ratio for the NACA 66-209 airfoil was measured by Green and Duan (1995). The airfoil they tested had a rectangular, untwisted, constant NACA 66-209 profile. The flow across a propeller blade is considerably more complex than the flow around such an airfoil. Nonetheless, the improvement boundaries from the work of Green and Duan are a starting point for our explanation of the propeller behaviour. Figure 11 indicates that the propeller should experience an increased L/D ratio over a large radial fraction of the blades when pulling the light drogue and at free running speed, $N = 600$ rpm. The figure also indicates that an improvement would not necessarily occur at high advance ratios, as a large radial section of the blades would be operating at conditions beyond stall. We emphasize that the improvement envelope shown in Fig. 11 is not truly representative of what one would expect for the propeller blades, owing to the higher tip loading of propeller blades relative to airfoils, and the radial variation of both the induced velocity and the blade profile. The effects of the last two factors are examined below.

In plotting Fig. 11, the velocity induced by the propeller rotation was neglected. We may estimate this induced velocity by a non-linear actuator disk calculation (Breslin and Andersen, 1994). For free running conditions at $N = 200$ rpm, the induced flow angle varies form about 2 deg for $r/R = 0.7$ to 5 deg for $r/R = 0.3$. While pulling the light drogue, the induced flow angle is about 10 deg at $r/R = 0.7$ and almost 18 deg at $r/R = 0.3$. For the medium and heavy drogues the induced flow angles are even larger.

The "upper improvement boundary" is determined by stall of the blade. Allowing for the induced velocity calculated above, and for the different stall angles of the propeller blade sections compared to the airfoil section, causes all angle of attack curves in Fig. 11 to be brought below the "upper improvement boundary."

The lower improvement boundary is determined by the lift coefficient at which the ducted tip reduces the induced drag to the extent that it compensates for both the extra parasite drag (associated with the large wetted area of the duct) and any loss of lift. This lift coefficient is a function of the absolute angle of attack, $\alpha - \alpha_0$. Because the propeller blade sections are substantially more cambered than was the airfoil tested by Green and Duan, those sections have larger values of α_0 and therefore should see performance improvements at smaller geometric angles of attack of the blade sections. Based on the known camber distribution of the propeller, we estimate that the lower improvement boundary will be modified from $\alpha = 8$ to $\alpha = 5.5$ deg at the hub and $\alpha = 7.5$ deg near the blade tip.

Typical values of $Re_{0.7}$ during the efficiency measurements are 1.0×10^6 to 3.5×10^6, respectively at minimum shaft rotation with the heavy drogue and maximum shaft rotation at free running speeds. The airfoil tests (Green and Duan, 1995) were conducted at $Re = 0.6 \times 10^6$. All other things being equal, higher Re is associated with less parasite drag. At high Re the reduction of induced drag, produced by addition of the ducted tips, will have a greater impact on the total drag of the blades than at low Re. Consequently, the ducted tips will start to be effective at smaller lift coefficients (smaller α) on the propeller geometry than on the airfoil, lowering further the "lower improvement boundary."

As a result of the blade camber and $Re_{0.7}$ effects, the lower improvement boundary is believed to shift below virtually all of the curves in Fig. 11. Consequently, for all testing conditions, the ducted tip geometry should have improved the propeller performance. We do not understand why the ducted tip did not measurably improve the propeller efficiency at low values of J. Planned future water tunnel tests may provide additional insight.

4.3 Cavitation Characteristics of the Propellers. For the discussion that follows, we use two different definitions of the cavitation inception index; one, for comparison with other propellers, is based on the boat velocity, V, and a second, for comparison with hydrofoils in a uniform flow, is based on the relative blade velocity, $U = (V_A^2 + U_\theta^2)^{0.5}$:

1. Propeller cavitation inception index,

$$\sigma_i = \frac{p_\infty - p_v}{\frac{1}{2}\rho V^2}$$

2. Blade cavitation inception index,

$$\sigma_{ir} = \frac{p_\infty - p_v}{\frac{1}{2}\rho U^2}$$

In the expression for U, V_A is the speed of advance of the boat ($V_A = V[1 - w]$), and U_θ is the tangential velocity of the blade at a radius r of 70 percent of the blade radius ($U_\theta = 2\pi n r$). p_v is the vapour pressure of the water, and p_∞ is the freestream pressure at the 5 ft depth of submergence of the propeller hub.

4.3.1 Conventional Propeller. When moored to the dock, the inception of tip vortex cavitation on the conventional propeller was determined to occur at shaft rotation rates between 266 and 274 rpm. $N_i = 274$ rpm will be referred to as the inception rotation rate in the subsequent discussion. It is also worth noting that the video recordings reveal that cavitation did not occur simultaneously on the four propeller blades. At $N = 274$ rpm cavitation occurs on only two of the four blades. This variation was caused by slightly different geometric characteristics of the blades, i.e., either slight blade-to-blade variations in pitch or tip roughness. Continuous cavities could, for the first time, clearly be seen emerging from all four tips at 301 rpm (Table 3.1).

In order to determine the propeller cavitation inception index, σ_i, it is necessary to define a boat velocity $V > 0$. It is reasonable to assume such a V exists during Bollard pulls; the thrust measured on the shaft is larger than the load on the tow line, indicating that the propeller induces a flow that creates an extra drag on the boat. By plotting V at $N = 274$ as a function of T for the different drogue sizes, a linear relationship between V and T was obtained. This line can be extrapolated to give $V = 0.55$ m/s at Bollard pull conditions. For the purpose of determining the blade cavitation inception index, σ_{ri}, it can be assumed that $V_A = V$. The cavitation inception index σ_i and σ_{ri} as well as the associated $Re_{0.7}$, J and α are listed in Table 4.1.

Now that σ_i and σ_{ir} have been established for the conventional propeller, it is of interest to compare them to values given in the literature. In order to avoid all the uncertainties associated with the flow relative to the propeller blades, the inception index for propellers, σ_i, is usually related to the freestream velocity, which in the case of sea trials is the forward velocity of the boat relative to the water. However, basing the analysis on σ_i as opposed to σ_{ir} is not free of complications. Due to the limited amount of information that exists on inception on propellers, it is difficult to compare propellers with different geometries, operating at different Reynolds numbers and advance ratios. This is demonstrated in Table 4.2, which shows the vastly different σ_i for model propellers operating at different advance ratios. There is a trend of increasing σ_i with decreasing J, which is what one would expect because reducing the advance ratio increases the angle of attack.

Table 4.1 Conditions at inception of tip vortex cavitation (conventional propeller)

N	$V_A = V$	U	$Re_{0.7}$	$J_A = J$	α	σ_i	σ_{ir}
274 rpm	0.55 m/s	9.20 m/s	$1.6 \cdot 10^6$	0.14	16°	745	2.7

Table 4.2 Comparing σ_i with values from previous research on propellers

Author	Re	$P/D_{0.7R}$	J	σ_i
Lodha and Arakeri (1984)				
* model propeller	1.1×10^6	0.83	0.50	33
* Strasberg's equation		1.15	0.14	626
Chahine et al. (1993)				
* model propeller	6.6×10^5		0.86	19.5
Jessup et al. (1993)				
* model propeller	4.0×10^6		1.26	2.3
* full scale propeller			1.26	1.7
	5.0×10^7			
This report	1.6×10^6	1.15	0.14	745

The large σ_i found for the sea trials can therefore be attributed to the extremely low J, which is confirmed by a scaling equation, suggested by Strasberg (Lodha and Arakeri, 1984), relating σ_i to the slip ratio, S:

$$\sigma_i = 1.9e^{6.6S} \text{ where}$$

$$S = 1 - \frac{J_A}{(P/D)_{0.7R}}$$

Strasberg's equation predicts that $\sigma_i \approx 605$ for $V_A = V = 0.61$ m/s, suggesting that the previous estimate giving $V = 0.55$ m/s is a little low. Nevertheless, together with the trend in Table 4.2, Strasberg's equation indicates that the conventional propeller had cavitation characteristics representative of propellers of similar size and geometry.

With respect to studies on hydrofoils, the σ_{ir} we measured, 2.7, is similar to that of previous research. At comparable angles of attack, McCormick (1962), Green (1991), Arndt et al. (1991), and Fruman et al. (1995) have measured inception indices ranging between 2 and 6 for different hydrofoils, although one would expect a higher value for the propeller than for the hydrofoils due to the stronger tip vortices generated by the propeller blades. The discrepancy between hydrofoil results and these propeller tests is most likely caused by the different flow conditions (tip vortex interaction, boat wake, freestream nuclei, etc.) of the propeller tests.

4.3.2 Ducted Tip Propeller. The video recordings of the ducted tip propeller speak for themselves: *the ducted tips substantially delay inception of tip vortex cavitation on marine propellers.* An inception point can not be determined for the ducted tip propeller, owing to the diffuse appearance of the cavitation. However, we are certain that tip cavitation did not occur for any shaft rotation rates up to and including $N = 404$ rpm. This N corresponds to a 47 percent cavitation improvement relative to the shaft rotation rate at inception on the conventional propeller. The delay, or absence, of tip vortex cavitation also confirms the encouraging results of the efficiency measurements. In addition to this most important observation, there are additional observations that warrant mention.

At N between 400 and 450 rpm a vapor cloud emerges from the exit of the ducts. Exactly what happens can not be deduced from the video owing to limitations of underwater filming (diver safety, lighting, and the like). The vapor clouds are most likely the tip vortices that at this point are starting to cavitate, which are being diffused by the flow exiting through the ducts, but some internal duct surface cavitation may also be present. To determine what the flow looks like at the exit of the ducts will require a flow visualization experiment set up in a cavitation tunnel. The very different appearance of tip vortex cavitation with the ducted tips installed implies that the substantial modification to the tip geometry—not the small modification to the loading distribution that results from installation of the ducted tips—is the cause of the large reduction in cavitation inception index.

Cavitation from the leading edge of the ducts was not observed until the shaft rotation rate was close to 400 rpm. At advance ratios higher than those during Bollard pulls, the ducts will have lower angles of attack relative to the incoming flow, and therefore duct leading edge cavitation likely will not occur at all once the boat is given a forward velocity. These observations suggest that the orientation of the ducts, aligned with the chord of the blade where the tips were cut, is correct. The video does not offer much information about the effect of the duct geometry. The near absence of duct leading edge cavitation may be a result of our efforts to round the leading edges, or it could be a result of the receding duct leading edge as it extends from the suction surface to the pressure surface.

At all shaft rotation rates there was substantially less radial spread of the race aft of the ducted tip propeller, which is in accordance with the observations of the boat owner, who commented on how the wake of the boat was different after the ducts had been installed.

5 Conclusion and Recommendations

5.1 Conclusion. The sea trials of the ducted tip propeller culminated in the following results:

1. The ducted tips substantially delayed tip vortex cavitation inception on a propeller that is representative of a large number of propellers installed on smaller commercial vessels, such as tug boats and fishing boats. For this particular propeller, the cavitation inception index was reduced by at least 47 percent, based on the shaft rotation rate at inception.
2. The ducted tip propeller did not suffer from efficiency losses due to the extra wetted surface of the ducts. On the contrary, the measurements indicate that up to a 6 percent improvement in the efficiency is possible.

The success of the sea trials can largely be attributed to the size and geometry of the ducted tips: the partial chord duct length offers a limited drag penalty, but remains very effective as a tip vortex suppressing device, both by obstructing the roll-up process itself, and by further retarding it as the internal and external flows mix at the exit of the ducts.

Obviously, the ducted tip propeller has a large commercial potential as it offers both an increased efficiency and improved cavitation performance. For most applications one of these factors, alone, would be sufficient to warrant installation of ducted tips, provided the installation costs can be kept at a reasonable level. For the propeller described in this report, the installation costs amounted to approximately $300, which is very modest. Discussions are presently underway with propeller manufacturers concerning commercialization of the ducted tip concept.

5.2 Recommendations for Future Work. In order to develop the ducted tip propeller into a commercial product, the following research should be carried out:

1. Optimization of the ducted tip design, including flow visualization to determine which type of cavitation appears at the exit of the ducts at high N. This work should involve studies to determine the best combination of duct length and duct diameter relative to the average chord and propeller radius, respectively.
2. Systematic experiments with ducted tips installed on model propellers with different P/D and A_E/A_0 ratios. This information should be compiled and expressed as a *ducted tip efficiency improvement* as a function of K_Q or K_T of the conventional propeller. From such diagrams the feasibility of installation of ducted tips could readily be assessed without knowing the details of the inflow.
3. A study of the effects of ducted tips installed on *controllable pitch* propellers and propellers with a highly skewed leading edge.
4. Evaluation of propeller strength and identification of good manufacturing procedures.

Acknowledgments

The authors are most appreciative of the aid provided by Doug and Al Leslie, the owners of Pearl Sea. Without their help this research could not have been completed. The assistance of our research engineer, Andre Bidaud, was invaluable. Andre's knowledge of both mechanical engineering design and electronics helped us overcome many difficulties. The authors also appreciate the assistance provided by the technicians of the Mechanical Engineering shop and the thoughtful comments of Professors Calisal and Rogak at UBC. This research was sponsored by the Natural Sciences and Engineering Research Council of Canada (NSERC).

References

Arndt, R. E. A., Arakeri, V. H., and Higuchi, H., 1991, "Some Observations of Tip Vortex Cavitation," *Journal of Fluid Mechanics,* Vol. 229, pp. 269–289.

Bjørheden, O., 1981, "Highly-Skewed Propellers—4 Years' Experience," *Canadian Shipping and Marine Engineering,* Sept., pp. 28–33.

Breslin, J. P., and Andersen, P., 1994, *Hydrodynamics of Ship Propellers,* Cambridge University Press.

Chahine, G. L., Frederick, G. F., and Bateman, R. D., 1993, "Propeller Tip Vortex Cavitation Suppression Using Selective Polymer Injection," ASME JOURNAL OF FLUIDS ENGINEERING, Vol. 115, pp. 497–503.

Crump, S. F., 1948, "The Effects of Bulbous Blade Tips on the Development of Tip Vortex Cavitation on Model Marine Propellers," report C-99, David Taylor Naval Ship Research and Development Center.

English, J. W., Suhrbier, K. R., and Stringer, P., 1992, "Propeller-Hull Vortex Cavitation on a Dynamically Positioned Support Vessel. A Comparative Study with Conventional And Ducted Propellers," *IMechE International Conference on Cavitation,* paper C453/001, pp. 223–230.

Fruman, D. H., and Aflalo, S. S., 1989, "Tip Vortex Cavitation Inhibition by Drag Reducing Polymer Solutions," ASME JOURNAL OF FLUIDS ENGINEERING, Vol. 111, pp. 211–216.

Fruman, D. H., Cerrutti, P., Pichon, T., and Dupont, P., 1995, "Effect of Hydrofoil Planform on Tip Vortex Rollup and Cavitation," ASME JOURNAL OF FLUIDS ENGINEERING, Vol. 117, pp. 162–169.

Goodman, T. R., and Breslin, J. P., 1980, "Feasibility Study of the Effectiveness of Tip Sails on Propeller Performance," report no. MA-RD-940-81006, Department of Ocean Engineering, Stevens Institute of Technology.

Green, S. I., 1991, "Correlating Single Phase Flow Measurements with Observations of Trailing Vortex Cavitation," ASME JOURNAL OF FLUIDS ENGINEERING, Vol. 113, pp. 125–129.

Green, S. I., Acosta, A. J., and Akbar, R., 1988, "The Influence on Tip Geometry on Trailing Vortex Rollup and Cavitation," ASME *Cavitation and Multiphase Flow Forum,* pp. 76–80.

Green, S. I., and Duan, S. Z., 1995, "The Ducted Tip—A Hydrofoil Tip Geometry with Superior Cavitation Performance," ASME JOURNAL OF FLUIDS ENGINEERING, Vol. 117, pp. 665–672.

Hordnes, I., Bidaud, A., and Green, S. I., 1995, "Torque Sensor," U.S. Patent 5,445,036.

Itoh, S., 1987, "Study of the Propeller with Small Blades on the Blade Tips (2nd Report: Cavitation Characteristics)," *Journal of the Society of Naval Architects of Japan,* Vol. 161, pp. 82–91. Published in Japanese with English abstract.

Itoh, S., Ishii, N., Tagori, T., and Ide, T., 1987, "Study of the Propeller with Small Blades on the Blade Tips (1st Report)," *Journal of the Society of Naval Architects of Japan,* Vol. 159, pp. 82–90. Published in Japanese with English abstract.

Jessup, S. D., Remmers, K. D., and Berberich, W. G., 1993, "Comparative cavitation performance evaluation of a naval surface ship propeller," ASME FED-Vol. 177, pp. 51–62.

Johnsson, C. A., and Rutgersson, O., 1991, "Leading Edge Roughness—A Way to Improve Propeller Tip Vortex Cavitation," *Propellers and Shafting Symposium,* paper no. 12.

Kuiper, G., 1978, "Scale Effects on Propeller Cavitation," *12th Symposium on Naval Hydrodynamics,* Vol. 12.

Lammeren, W. P. A. van, Manen, J. D. van, and Oosterveld, M. W. C., 1969, "The Wageningen B-screw series," *SNAME Transactions,* Vol. 77.

Lodha, R. K., and Arakeri, V. H., 1984, "Observations of Tip Vortex Cavitation Inception from a Model Marine Propeller," *Journal of the Indian Institute of Science,* Vol. 65(a), pp. 11–20.

Manen, J. D. van, and Oossanen, P. van, 1988, "Propulsion," *SNAME Principles of Naval Architecture,* Vol. 2, Chapter 6.

Mani, K., Sharma, S. D., and Arakeri, V. H., 1988, "Effect on Propeller Blade Modification on Cavitation Induced Noise," ASME FED, Vol. 64, pp. 64–67.

McCormick, B. W., 1962, "On Cavitation Produced by a Vortex Trailing from a Lifting Surface," ASME *Journal of Basic Engineering,* pp. 369–379.

Platzer, G. P., and Souders, W. G., 1979, "Tip Vortex Cavitation Delay with Application to Marine Lifting Surfaces. A Literature Survey," report no. 79/051, David Taylor Naval Ship Research and Development Center.

Smith, L., 1996, The Faeroe Fisheries Laboratories, personal communication.

Troost, L., 1937, "Open Water Test Series with Modern Propeller Forms," *North East Coast Institution of Engineers and Shipbuilders Transactions,* Newcastle-Upon-Tyne, Vol. 54, pp. 321–326.

Weitendorf, E. A., 1993, "On Propeller Vortex Cavitation as a Source of Ship Hull Vibration," ASME FED, Vol. 176, pp. 1–2.

Klaus W. Hoyer
Engineering Specialist,
Eidetics Corporation,
3425 Lomita Blvd.,
Torrance, CA 90505

Albert Gyr
Head of Research,
Institute of Hydromechanics and Water Resources Management,
Swiss Federal Institute of Technology,
Zurich, Switzerland

Heterogeneous Drag Reduction Concepts and Consequences

This paper deals with the nature of the heterogeneous drag reduction which occurs in turbulent pipe flows when a concentrated polymer solution is injected into the pipe center. According to earlier concepts, the achieved drag reduction is due to a direct, large-scale interaction of the viscoelastic polymer thread with the turbulent flow field. The authors prove that the heterogeneous drag reduction originates exclusively from agglomerates of dissolved polymer molecules present in the flow.

I Introduction

The reduction of drag in turbulent flow due to the addition of long-chain polymer molecules to a Newtonian solvent is known as the Tom's effect in honor of B. A. Toms (1948). He found that the addition of polymethylacrylate to monochlorobenzene reduced the frictional drag of the solution compared to the solvent alone. Since then, a variety of drag reducing agents have been found to reduce the turbulent frictional drag. They range from asbestos fiber suspensions to polymer and surfactant solutions—an overview is given in Gyr and Bewersdorff (1995). The drag reduction of a dilute homogeneous polymer solution of a few PPM concentration in weight is mainly characterized by two phenomena. 1. Drag reduction occurs at a certain onset value, usually given by the onset shear stress. 2. The velocity profile of a turbulent flow of a Newtonian liquid over flat walls is logarithmic (the Prandtl-von Kármán profile). For the drag reduced case, also logarithmic profiles are present; for maximum drag reduction they are bounded by the so-called Virk's asymptotic profile. This asymptotic profile is independent of the kind of polymer used. Extensive research has been carried out in this field, resulting in a thorough insight into the governing phenomena. Regarding the gross flow behavior, the drag reduction (DR) is defined as:

$$DR = (f_w - f_{DR})/f_w \quad \text{at constant flow rate} \qquad (1)$$

where f_w and f_{DR} are the friction factors for water and the drag reduced case, respectively. In the case of the heterogeneous drag reduction, which is achieved by injecting a concentrated polymer solution into the core of a turbulent pipe flow (see Smith and Tiedermann, 1991, Fig. 1), we are faced with a unusual drag reducing system which appears to be uniquely different from the ones previously described. This system is remarkable because the polymer solution emerging from the injection nozzle forms a thread which flows with the stream and stays as a second phase for very long times. The achieved drag reduction is of a considerable amount, although the mixed concentration—if the material would be immediately dissolved and homogenized—would be O (10 PPM). However, since the material seems to remain in the thread, we are confronted with the fact that either the thread itself is drag reducing or dissolved material at a much lower concentration than in the usual cases for homogeneous solutions are responsible for the effect. This type of drag reduction has, just as the ones previously described, certain similarities in the way it affects the flow field, but exhibits a mean velocity profile which cannot be explained if one assumes hydrodynamic interaction of single polymer molecules with the flow field. The main difference to the observations of the dilute polymer solutions is that the flow field is influenced out to the pipe center even at low drag reduction levels, whereas, in the homogeneous drag reduction, the polymer molecules affect only the near wall region of the flow and leave the core region (Newtonian core) unaffected. The onset of the heterogeneous drag reduction cannot be correlated in the same way as for the homogeneous solutions since it shows a strong dependency upon the master concentration C_o of the injected solution and on the injection parameters. In summarizing, we conclude that the different types of drag reduction achieved with different additive techniques show many common features. But they also have several major differences which need to be explained to present a complete picture of the governing phenomena.

It is the aim of this paper to show that the heterogeneous drag reduction is purely an effect of dissolved material. Since we propose a new concept of how heterogeneous drag reduction should be interpreted, a conceptual discussion is placed in front of the main text in Section II. In Section III the experimental proofs of our concepts will be given. The consequences are discussed and followed by the conclusions in Section IV.

II History and Conceptual Models of the Heterogeneous Drag Reduction

This type of drag reduction was first observed by Vleggaar and Tels (1973). They injected a 0.5 percent in weight solution of Polyacrylamide (Separan AP 30) into the core region of a turbulent pipe flow. They showed that a larger drag reduction occurred when the polymer is injected instead of being premixed, especially at lower Reynolds numbers. Since then, numerous researchers have worked in this special field of drag reduction. Bewersdorff (1984) reported drag reduction in his injection experiments, although the injected polymers were not diffused to the wall region (which is commonly accepted as crucial for drag reduction). Additionally, his measured velocity profiles at Re = 15,000 and 20,000 showed a significantly higher dimensionless velocity in the core region, and practically an unaffected velocity profile closer to the wall. At higher Reynolds numbers, he found that the slope of the velocity profile is increased throughout his covered profile. Because of the high Reynolds number and the dimension of his measurement volume, he did not approach the wall closer than 100 viscous units which he thought to be legitimate due to the work of Berman (1986). Usui et al. (1988) studied the velocity profile of the injected polymer phase and the surrounding water phase separately by seeding both liquids with tracer particles. They monitored the flow using a video camera which was moved with the flow at the average flow velocity. Hoyt and Sellin (1991) studied the thread injection technique using a variety of different viscoelastic solutions, ranging from water soluble Polyacrylamide (PAM), Polyethyleneoxide (PEO) and the surfactants Tetradecyltrimethylammonium bromide + 2 percent sodium salycilate (C_{14}TASal) and Hexadecyltrimethylammonium bro-

Contributed by the Fluids Engineering Division for publication in the JOURNAL OF FLUIDS ENGINEERING. Manuscript received by the Fluids Engineering Division January 21, 1997; revised manuscript received June 15, 1998. Associate Technical Editor: P. R. Bandyopadhyay.

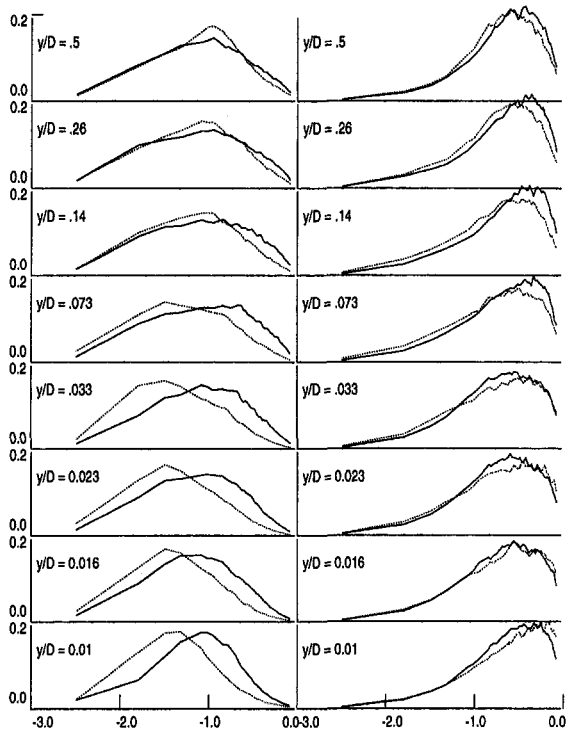

Fig. 1 Discrete frequency analysis of the velocity fluctuations in axial (left side) and wall normal (right side) direction. · · · · · *DR* = 40 percent, —— equal wall stress water flow, abscissa: log ω^+, ordinate: $\omega^+\phi$

mide + 2 percent sodium salycilate (C_{16}TASal), as well as water nonsoluble FLO (commercial pipe line drag reducer), Polyisobutene, and PEO dissolved in dichloromethane. For high Reynolds numbers they found that only the polymers showing drag reduction when they were premixed also reduced drag in a heterogeneous injection. At lower Reynolds numbers they found that the injected PEO solution showed drag reduction when the premixed solution did not (onset of drag reduction at lower Reynolds number). Believing that the thread was directly interacting with the flow as a drag reducer, they came to the conclusion that a new type of thread drag reduction existed at low Reynolds numbers, and that the thread properties had to be properly tuned so that significant oscillations of the thread were possible. They assumed a new type of drag reduction, originating from the viscoelastic properties of the concentrated polymer or surfactant solution thread present in the flow.

An explanation for the heterogeneous drag reduction was thought to lie in the ability of the thread to store and release strain energy, thus forcing the outer flow field over a certain frequency range similar to a forced mixing layer flow. This forcing of the outer flow field was assumed to interfere with the inertial energy cascade, which transfers turbulent kinetic energy to the dissipative eddies, and therefore decreases the overall dissipation. Regarding the findings, however, there were also doubtful voices stating that the heterogeneous drag reduction is not a new drag reduction effect, but is merely due to dissolved polymer material coming from the thread and acting in a very similar fashion to the premixed solutions (Virk, 1989). They argued that only very minute amounts of polymer must be present in the flow when the molecular weight is very large. Consequently, they reasoned that clusters of polymer molecules, so-called agglomerates which act like huge molecules, were present in the flow. Stenberg et al. (1977) reported an injection experiment where they mixed the injected polymer thread using a variable speed mixer. They found that an increase in the rate of mixing shifted the onset of drag reduction to higher Reynolds numbers and observed that the polymer thread split up into finer and finer strands according to the conditions, i.e., by increasing the mixer speed or Reynolds number. McComb and Rabie (1982a) investigated the radial dispersion of a 0.1 to 0.3 percent in weight solution of PEO and the corresponding drag reduction. In their experiments a polymer thread was not likely to remain stable because of the relative low concentration. They found that the effective annulus, where polymer has to be present in order to be drag reducing, lies between 15 and 100 viscous units. Also (McComb and Rabie, 1982b) their measured velocity profiles were similar to the ones obtained by the thread injection technique, that is they had an increased slope in the core region compared to Newtonian flow. Berman (1989) investigated the Reynolds stress signals of a turbulent flow field depending on whether a cluster of fine threads or a single polymer thread was present close to the LDV measuring volume. He achieved this by marking the polymer solution with a fluorescent dye, thus being able to do conditional sampling of the velocity signals. He found that the Reynolds stress signal was not altered by the presence of the singular thread, but that it was significantly reduced when a cluster of fine threads passed by. In addition, Smith and Tiederman (1991) found that the thread never comes closer to the wall than 100 viscous units. Wells and Spangler (1967) noticed immediate drag reduction after the polymer was injected into the wall region, and a delayed effect when introduced in the center of the flow. Analogous findings were reported by Luchik and Tiederman (1988) who found in their injection experiments that there exists an effective annulus $10 < y^+ < 100$ in which the polymer has to be present in order to be drag reducing.

As it has been shown in the preceding section, there exist two conceptually different types of explanations how the injected polymer solution is drag reducing. One explanation is based on an interaction of a viscoelastic thread with the turbulence, the other one assumes that the drag reducing effect is due to dissolved material and therefore the drag reducing mechanism is very similar to the one acting in homogeneous polymer solutions. Both mechanisms, however, could also act in an combined form. *Our goal is to show that the heterogeneous drag reduction is only due to dissolved material.* Therefore it has to be shown that the thread interactions are not drag reducing, and second, that dissolved material is present in the drag reduced case. To do so we have to summarize the possible interaction mechanisms which one has to disprove. 1) Due to its capabilities of storing and releasing strain energy the thread should alter the turbulent flow field in its immediate vicinity thus leading to an altered correlation of the turbulent fluctuations with respect to the distance of the thread leading to an overall drag reduction. 2) The thread forces the flow field in a certain frequency band thus being able to interfere with the turbulent kinetic energy transport from large to small scales. 3) The thread leads to a low dissipative Beltrami-like flow field via azimutal oscillations. In this flow field, the helicity density $h = \vec{\omega}\vec{u}$ was supposed to be increased leading to a smaller enstrophy production and therefore to a smaller overall dissipation. In a series of papers some aspects of this controversy have been treated, but to prove our statement, it needs an overview of all aspects, which will be given here.

III The Active Thread Versus Dissolved Molecules—An Experimental Investigation

First we have to disprove the concepts assuming that the heterogeneous drag reduction is the result of a direct interaction of the thread motions with the turbulent flow. We do this by showing that all mentioned mechanisms can be disproved experimentally.

1. Is an elastic thread centrally fed into a Newtonian fluid drag reducing?

The answer is no. An elastic rubber band, produced by Huber and Suhner CH-8330 Pfaffikon, of extremely low elastic modu-

lus and diameter 1.2 mm was continuously fed to the flow, or was held fixed shortly after the pipe entrance. In neither case did drag reduction occur (Hoyer et al., 1994). In this paper it is also theoretically shown, that the heterogeneous drag reduction cannot originate from an additional length scale introduced by the thread oscillations. If the thread had an effect, this would have to be a result of its viscoelasticity.

2. Is the thread acting as a forcing system amplifying certain frequencies in a resonance mode?

No, this is not the case, see also Hoyer and Gyr (1996). No narrow band augmentation in the discrete frequency spectra could be detected (which would have been observed when a forcing or resonance effect was responsible for the achieved drag reduction). On the contrary, the power spectra of the velocity fluctuations show the same changes from the Newtonian case as they are known for homogeneous dilute polymer solutions. No resonance mode what so ever could be detected, see Fig. 1. The discrete power spectrum of the velocity fluctuations in Fig. 1 is presented according to Perry and Abell (1975). The frequency ω is scaled with the viscous frequency so that $\omega^+ = \omega\nu/u_\tau^2$. The Fourier coefficients have been scaled with the variance of the corresponding velocity fluctuation so that $\phi_{kk} = \Phi_{kk}\sqrt{u'^2}$. Figure 1 shows the discrete power spectrum in axial (left) and wall normal (right) direction at various distances to the wall in the case of 40 percent drag reduction (dotted line) and water flow of equal wall stress (solid line). The abscissa scale is log ω^+ and the ordinate scale is $\omega^+\phi$.

3. Is there an energy storage-relaxation process responsible for drag reduction due to the viscoelasticity of the thread?

Since the thread is viscoelastic and deforming, a storage and perhaps also a relaxation process is present, but to be drag reducing, the thread had to interact preferentially with the turbulent structure. For example, by storing the energy of the high frequencies and relaxing it into the low ones. But this is hardly the case, since the inertia of the thread is rather responsible for an interaction only in a frequency range smaller than a critical value. In any case, if a mechanism of this kind would act, the altered turbulent structure measured close to the wall then should depend on the distance of the thread. This is not the case as shown in Hoyer and Gyr, 1995.

The suspected effect of a localized alteration of the phase relation between the turbulent velocity fluctuations in the vicinity of the thread proved to be incorrect, since the conditional sampling of the velocity records showed no dependency on the thread distance, see Fig. 2. Results presented in Fig. 2 show that the axial and wall normal velocity fluctuations as well as the major part of the Reynolds stress tensor are independent on the thread distance.

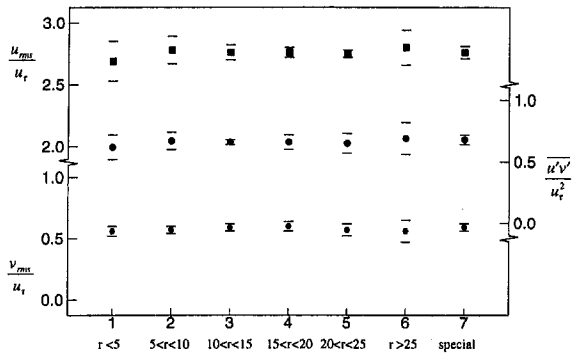

Fig. 2 Conditionally sampled velocity fluctuations and turbulent Reynolds stress as function of the distance to the thread. LDV measuring volume at $y^+ = 40$ for the case $DR = 25$ percent. The special class No. 7 consists of all the samples when the thread location was not uniquely identifiable (e.g., cluster of threads). For more details see Hoyer and Gyr (1995). For comparison, the integral scale at the chosen location is of the order of 1.25 mm.

4. Is the thread producing low dissipative effects interacting with the large structures of the turbulence?

It is known that two-dimensional or helical structures are low dissipative. It is therefore feasible that the thread is interacting with the turbulent flow field so that such structures are preferably enhanced. Large structures are dominated by the geometry of the flow system. By varying the channel geometry this hypothesis can be tested. Bewersdorff et al. (1993), investigated the drag reduction in channels of different cross sections, but with fixed hydraulic radius, see Fig. 3. Three different pipe cross sections (circular, square, and rectangular with aspect ratio 10:1) of the same hydraulic diameter $D_h = 30$ mm were investigated.

The onset of drag reduction[1] was independent of the cross section. In the rectangular channel, the slope increment δ (which, in Prandtl-von Kármán coordinates, is the difference in the slope of the friction factor-Reynolds number relation compared to the Newtonian value, Virk 1975) after onset was equal to the one obtained in the circular and the square pipe, when three injectors (equally spaced along the larger side) were used. When only one central injector was used, the slope increment was lower compared to the other two pipes. Flow visualization showed that centrally injected, colored water had only diffused over approximately half of the cross section along the pipe length of 10 m. The different pipe geometries showed no effect on the drag reduction in the injection experiments. If an increase in the helicity of the outer flow field caused the effect, there should have been less drag reduction in the square and even less drag reduction in the rectangular pipe than in the circular one.

All four investigations proved that the thread itself is not contributing to the reduction in turbulent drag.

To prove that the thread and its motions are not the reason for the drag reduction is one part of the problem, to prove that dissolved material is responsible is the other. This will be done in the following paragraphs. First of all, the onset of the heterogeneous drag reduction system has to be explained. In the gross flow measurements (friction factor versus Reynolds number) we discern two drag reduction characteristics: the so called type "A" and type "B" drag reduction. Type A occurs if a critical wall stress is exceeded and the friction factor starts to deviate at the onset point from the Prandtl-von Kármán law. In type B drag reduction, asymptotic drag reduction is achieved, following directly after the laminar regime. The asymptotic behavior is, as Virk (1975) showed, universal for all polymer additives. Virk (1975) proposed that the onset of drag reduction, in the case of dilute polymer solutions, occurs after a certain stress level of the flow is exceeded. This critical value is related to the stretching of the polymer molecules from their relaxed state and correlated to the radius of gyration of the polymer molecule in the following form:

$$R_G^3 \tau_{w0} = \Omega_T \qquad (2)$$

where the onset constant Ω_T, depends on the polymer type and on the solvent being of the order of 10^7 (R_G, in nm and τ_w in Pa), see also Lumley (1969). On the other hand, polymer drag reduction can occur without any discernible onset effect. Virk calls this a type B drag reduction, where the macromolecules causing the effect are already in an extended state and do not need to be stretched by a strong flow.

[1] After calibrating the hydraulic diameter (systematic error) and fitting it with a least square error to the Prandtl-von Kármán law, the relative error of the friction factor measurements (Figs. 3, 4, 6, and 7) due to uncertainties in flow rate and pressure drop measurement is estimated to be less than 2 percent and less than 1 percent for the velocity. The high friction factors found for the square channel at low Reynolds numbers in Fig. 3 are due to the polymer solution sinking to the bottom wall in this particular experiment due to slightly higher specific weight and the low velocity.

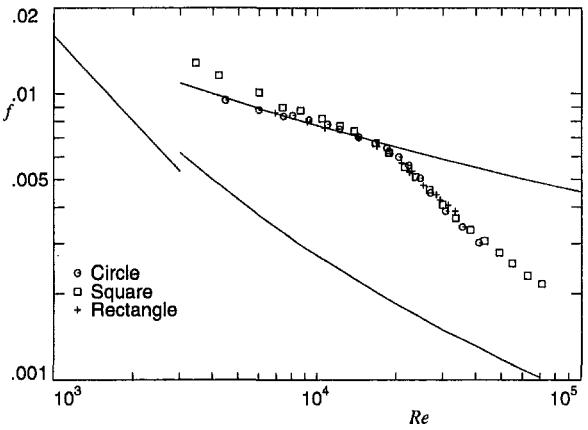

Fig. 3 Drag reduction in pipes with different cross sections but same hydraulic diameter D_h = 30 mm, injected master concentration C_0 = 1.0 wt percent

This, however, is contradictory to the onset behavior in the heterogeneous drag reduction system, since the system would have to exhibit type B behavior if one assumes large extended agglomerates of molecules to be present in the flow. Now the question arises how this onset behavior in the heterogeneous case can be explained. As it will be shown in the following CCD frames (Fig. 5 together with the measurements in Fig. 4), the onset and thereafter the drag reduction in the heterogeneous case is correlated to the deterioration of the polymer thread caused by the turbulent flow field—an interaction which introduces the polymer in a drag reducing configuration. In this investigation, gross flow measurements of the friction factor have been made simultaneously with a visualization of the thread condition. Figure 4 shows the obtained friction factors in the rectangular pipe with the use of two injectors mounted at $\frac{1}{4}$ and $\frac{3}{4}$ height of the channel. The corresponding numbers are referred to the CCD scans in Fig. 5, which are typical pictures of the thread condition. As can be seen from Fig. 4 the onset of drag reduction occurs after point no. 4 with increasing drag reduction levels at no. 5 to no. 7.

As seen from Fig. 5, point no. 4, the large scale interaction between the flow and the thread is present as soon as the flow is turbulent, but without any drag reduction. The drag reduction develops when the polymer thread starts to disintegrate and release polymer to the surrounding fluid (marked with ellipses in Fig. 5, no. 5 to no. 7).

The hypothesis remains a hypothesis as long as it cannot be proved that in the case of the heterogeneous drag reduction

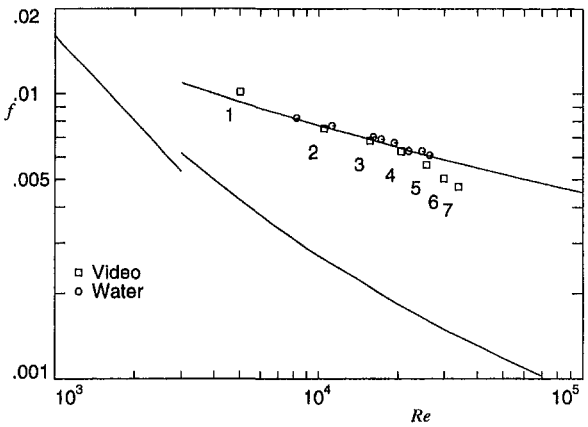

Fig. 4 Friction factor in the rectangular pipe for comparison with the CCD scans in Fig. 5

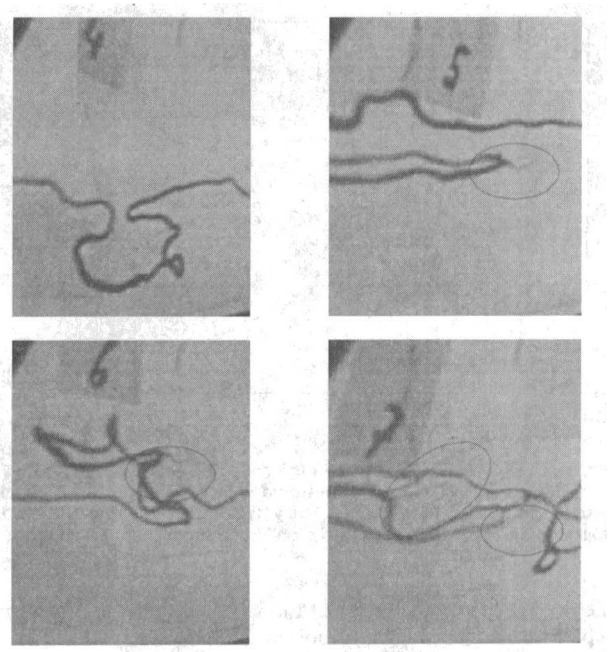

Fig. 5 Typical examples of the thread condition with increasing drag reduction. Flow direction is from right to left, field of view is approximately 8 cm (h) and 10 cm (w) (Only the bottom half of the rectangular pipe is shown). Note the deterioration in no. 5 to no. 7 (marked).

polymer is present in the near wall region. This was the main reason why it was thought for a long time that the thread is actively contributing to the effect, because no polymer could be identified with the available methods.

Hoyer (1994) and Hoyer et al. (1992) gave a direct proof by using the drag reducing effect itself as a test method. In a set of experiments, near wall fluid from the 30 mm inner diameter circular (D_i) pipe was collected using a slit suction device of height 0.25 mm, and investigated in a 4 mm Di pipe for drag reduction capability. The average thickness of the collected wall layer never exceeded 22 viscous units. This insured that no part of the concentrated polymer thread was sampled, since the probability that the thread approaches the wall closer than 100 viscous units tends to zero. Figure 6 shows the drag reduction behavior in the circular 30 mm Di pipe with variation of Reynolds number. The dotted vertical lines represent the Reynolds numbers at which near wall fluid was collected. Figure 7 shows

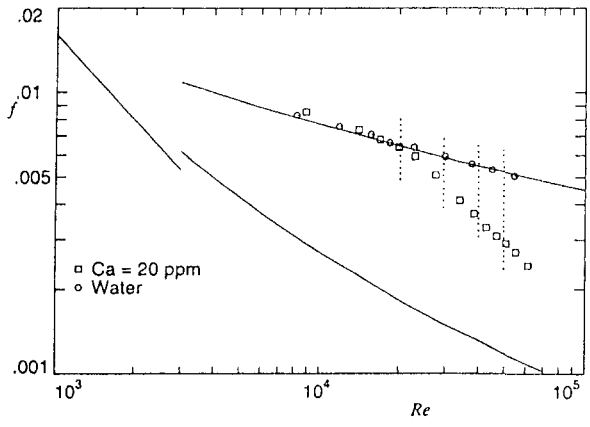

Fig. 6 Drag reduction in the D_i = 30 mm circular pipe with "average" concentration C_a = 20 PPM, injected master concentration C_o = 0.75 percent, dotted lines represent Reynolds numbers at which near wall fluid samples were taken and investigated in the D_i = 4 mm pipe (see Fig. 7).

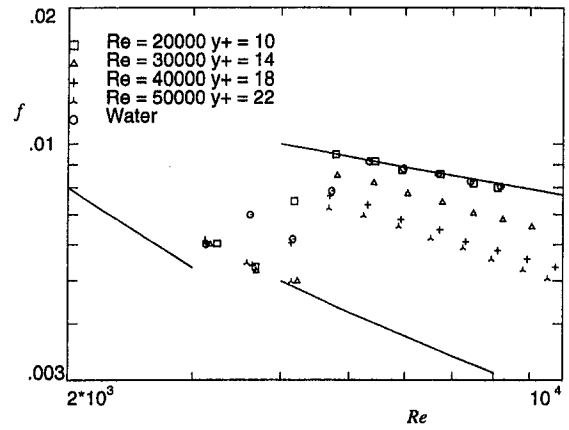

Fig. 7 Drag reduction behavior of the collected near wall fluid from Fig. 6 as measured in the D_i = 4 mm pipe with variation of the Reynolds number in the D_i = 30 mm pipe. The y^+ values given in the plot are the approximate layer thickness of the collected fluids.

the drag reduction behavior of the sampled fluids in a Di 4 mm pipe as test for presence of polymer molecules.

Comparing the Figs. 6 and 7 we see the following:

(*i*) Near wall fluid collected just before onset in the main pipe showed no drag reduction in the small pipe.

(*ii*) Fluid collected with increasing levels of drag reduction in the main pipe showed increasing drag reduction capabilities in the small pipe.

The results show clearly that the drag reducing capability of the near wall fluid is directly correlated to the drag reduction achieved in the D_i = 30 mm pipe. Comparison of drag reduction levels in the small pipe using premixed solutions showed that the collected samples behaved like the homogeneous solutions of concentrations 0.1–1 PPM, depending on the achieved drag reduction in the main pipe.

In addition to the presented results of how the onset in the heterogeneous system can be explained and the direct proof that there is polymer present in the near wall region, we would like to mention several characteristics regarding the turbulent flow field, which the heterogeneous and the homogeneous drag reduction systems have in common (Wei and Willmarth, 1992; Gampert and Yong, 1989; Berner and Scrivener, 1980; Hoyer and Gyr, 1996; Achia and Thompson, 1977). These common—or better similar—features include the changes in the rms velocity fluctuations, their correlation, their power spectra as well as the average time between bursts, the main Reynolds stress generating event. Heterogeneous drag reduction differs from the homogeneous drag reduction in the following aspects: The velocity profiles obtained in type A drag reduction at non-asymptotic drag reduction show a parallel shift of the central part of the flow field (Newtonian core) by an amount called the effective slip velocity S'. This shift increases with increasing drag reduction. At higher drag reduction levels the Newtonian core is still present, but the wall region shows a slope significantly larger than the Newtonian (three layer model of Virk et al., 1970). At maximum drag reduction the entire outer flow field shows an increased slope of about 12, about five times the Newtonian value. For the heterogeneous drag reduction system, the slope of the velocity profile in the inertial region is increased throughout the pipe compared to the Newtonian value by an amount equal to $1/(1 - DR)$. Whereas, for homogeneous drag reduction, it is commonly accepted that the flow has to be strong in order to interact with the molecules (Hinch, 1977), and therefore the region of the polymer interference is close to the wall extending outwards as the drag reduction increases, this is not the case in the injection type drag reduction. This phenomenon will be addressed in the next section.

IV Discussion

The present investigation is very general in its principal aspects, restricted by the used setup, material and flow parameters. One cannot expect that the results are universal, however heterogeneous drag reduction manifests itself mainly in the different mean velocity profiles (Hoyer and Gyr, 1996). This is the remaining problem which needs to be discussed, since the form of the mean velocity profile was often used as a proof that only dissolved material cannot be responsible for the effect. In this context, we would like to put our emphasis on the nonuniversality encountered by the injection type drag reduction. It is very important in which form and in which concentration the dissolved material is present at any location in the flow. By varying the injection concentration, or the relative velocity at the nozzle, or introducing some outer disturbance like nozzle geometry (diameter, length) etc. practically every anisotropic and inhomogeneous distribution can be achieved. Reference to Saadeh & Strehlow 1997 and Hoyer & Gyr 1996. For example, the increase in injector length from 15 mm to 200 mm shifted the onset Reynolds number from 18,000 to 35,000 with otherwise identical flow conditions. Similarly, using the longer injector, the decrease of the injection concentration from 1 to 0.75 percent shifted the onset Reynolds number from 35,000 to 20,000. In the present investigation, however, the dissolving was able to give, on the one hand, a complete picture of the process, and on the other, to elucidate the critical remarks. The polymers are torn off in form of tiny filaments and therefore the dissolving process is not a diffusive but a discontinuous one. By every such event another amount of polymer is released and further dissolution is a function of the now altered flow field and its structures. By light scattering analysis (Bewersdorff et al., 1993), it was found that the mean agglomerate in the wall layer fluid consisted of two molecules. It is therefore feasible to assume that the central part of the flow field contains larger agglomerates which are able to interfere with the dissipative scales of the outer flow field as discussed in Hoyer and Gyr (1996).

For a complete picture of the heterogeneous drag reduction system we would like to comment on some of the earlier published work. The turbulent velocity fluctuations $\underline{u'}$, v' and the main contribution to the Reynolds stress tensor $\rho\overline{u'v'}$ are altered mainly in the buffer layer between $10 < y^+ < 100$. On the other hand, the polymer thread stays outside $y^+ > 100$ almost all the time, since it feels the high mean shear rate at the wall. So the Reynolds stress deficit, which is present at the near wall region, has to be compensated by a molecular stress, since the thread is not present there. The increased slope of the velocity profile throughout the log law region can be explained with a concept based on agglomerates instead of single molecules. Simple analysis shows that agglomerates of only a few molecules are able to interfere with the dissipative scales throughout the pipe diameter (Hoyer, 1994; Hoyer and Gyr, 1996). Hinch and Elata (1979) showed that a heterogeneous network of concentrated polymer solution can interact with weak flows. Oliver and Bakhtiyarov (1983) showed that considerable amounts of drag reduction are possible with concentrations below 1 PPM when the molecular weight is very large. So it seems reasonable to say that the heterogeneous drag reduction is due to dissolved polymer material. The heterogeneous drag reduction is believed to be so effective due to the larger molecular weight and the corresponding broader molecular weight distribution of the agglomerates. The effective relaxation time scales, therefore, are spread wider, and that is why the area of interference extends out to the pipe center, even at nonasymptotic drag reduction levels. The onset correlation known from homogeneous drag reduction is not applicable to the heterogeneous drag reduction. Only when the nozzle design ensures relatively undisturbed outflow, the onset of heterogeneous drag reduction will be correlated to the turbulence intensity of the pipe flow. In this case, the

onset wall shear stress will depend on the master concentration because the interlocking of the polymer solution network increases with concentration, and a mechanical deterioration of the polymer phase becomes more difficult. The diffusion of polymer molecules from the polymer phase is negligible. The further mechanical dissociation of polymer molecules from the polymer phase at a constant Reynolds number is inhibited by the development of drag reduction, since there is a restraining feedback of the molecules on the high intensity turbulence which is suppressed.

V Conclusion

The heterogeneous drag reduction is discernible from the homogeneous drag reduction by an inhomogeneous distribution of the polymer concentration and a very broad molecular weight distribution of the agglomerates. The heterogeneous drag reduction has an onset after a certain stress level in the thread, produced by the flow field, is reached. It occurs when large agglomerates of polymer molecules are torn off the thread and subsequently downsized and mixed with the Newtonian fluid. Nevertheless, the heterogeneous drag reduction is the most efficient technique of adding polymer to the flow. This is because the polymer in the "thread" does not degrade, and the thread, therefore, is a source of very effective drag reducing material. Research in the heterogeneous drag reduction field should therefore be focused on practical aspects such as the concentration of the injected solution, the turbulence level at the nozzle exit, and injector design in order to optimize the injection process. Heterogeneous drag reduction is a very practical topic of research, but the difficulties in the control of the additive state render it ineffectual in the basic research in the field of turbulence and its manipulations.

References

Achia, B. U., and Thompson, D. W., 1977, "Structure of the Turbulent Boundary Layer in Drag-Reducing Pipe Flow," Journal of Fluid Mechanics, 13 July, Vol. 81, part 3, pp. 439–64.

Berman, N. S., 1989, *Large Eddies and Polymer Strings, Structure of Turbulence and Drag Reduction,* Gyr A., ed., Springer-Verlag, Berlin, pp. 275–88.

Berman, N. S., 1986, "Velocity Fluctuations in Non-Homogeneous Drag Reduction," *Chem. Eng. Commun.,* Vol. 42, pp. 37–51.

Berner, C., Scrivener, O., 1980, "Drag Reduction and Structure of Turbulence in Dilute Polymer Solutions," *Viscous Flow Drag Reduction,* Hough G. R., ed., Dallas, Texas, AIAA Inc. pp. 290–9.

Bewersdorff, H.-W., 1984, "Heterogeneous Drag Reduction in Turbulent Pipe Flow," *Rheologica Acta,* Sept.-Oct., Vol. 23, No. 5, pp. 522–43.

Bewersdorff, H.-W., Gyr, A., Hoyer, K., and Tsinober, A., 1993, "An Investigation of Possible Mechanisms of Heterogeneous Drag Reduction in Pipe and Channel Flows. *Rheologica Acta,* March-April, Vol. 32, No. 2, pp. 140–9.

Gampert, B., Yong, C. K., 1989, "Turbulent Viscoelastic Flow in a Square Channel," *Zeitschrift fur Angewandte Mathematik und Mechanik,* Vol. 69, No. 6, pp. 622–4.

Gyr, A., Bewersdorff, H.-W., 1995, *Drag Reduction of Turbulent Flows by Additives,* Kluwer Acad. Publ., Dortrecht, Boston, London.

Hinch, E. J., 1977, "Mechanical models of dilute polymer solutions in strong flows," (Structure of Turbulence and Drag Reduction, Washington, DC, USA, 7–12 June 1976)., *Physics of Fluids,* Oct., Vol. 20, no. 10, pt. 2, pp. S22–30.

Hinch, E. J., Elata, C., 1979, "Heterogeneity of dilute polymer solutions," *Proceedings of the IUTAM Symposium on Non-Newtonian Fluid Mechanics,* Louvain-la-Neuve, Belgium, 28 Aug.–1 Sept. 1978, *Journal of Non-Newtonian Fluid Mechanics,* April, Vol. 5, pp. 411–25.

Hoyer, K., Gyr, A., 1995, "Heterogeneous Drag Reduction," Actes du 12e Congres Français de Mechanique, Strassbourg, Vol. 3, pp. 313–316.

Hoyer, K., Gyr, A., 1996, "Turbulent Velocity Field in Heterogeneously Drag Reduced Pipe Flow," *Journal of Non-Newtonian Fluid Mechanics,* Vol. 65, pp. 221–40.

Hoyer, K., 1994, "Heterogene Widerstandsverminderung in turbulenten Rohrstromungen," PhD thesis No. 10525, ETH Zurich, Switzerland.

Hoyer, K., Bewersdorff, H.-W., Gyr, A., 1994, "Drag reduction by an elastic rubber band?," *Applied Scientific Research,* March, Vol. 52, no. 2, pp. 161–8.

Hoyer, K., Bewersdorff, H.-W., Gyr, A., Tsinober, A., 1992, "Studies on the Mechanism of Heterogeneous Drag Reduction," *Theor. and Applied Rheology,* Moldenaers P., Keunings R., eds., Elsevier Science Publ., pp. 183–5.

Hoyer, K., 1992, Presented at the XI International Congress of Rheology, Brussels, Belgium.

Hoyt, J. W., Sellin, R. H. J., 1991, "Polymer 'threads' and drag reduction," *Rheologica Acta,* July–Aug., Vol. 30, No. 4, pp. 307–15.

Luchik, T. S., Tiederman, W. G., 1988, "Turbulent structure in low-concentration drag-reducing channel flows," *Journal of Fluid Mechanics,* May, Vol. 190, pp. 241–63.

Lumley, J. L., 1969, "Drag Reduction by Additives," *Ann. Rev. Fluid Mech. 1,* pp. 367–84.

McComb, W. D., Rabie, L. H., 1982, "Local Drag Reduction Due to Injection of Polymer Solutions into Turbulent Flow of a Pipe, Part 1: Dependence on local Polymer Concentration," *AIChE Journal,* 28(4), pp. 547–57.

McComb, W. D., and Rabie, L. H., 1982, "Part 2: Laser Doppler Measurements of Turbulent Structure," *AIChE Journal,* Vol. 28, No. 4, pp. 558–565.

Oliver, D. R., Bakhtiyarov, S. I., 1983, "Drag reduction in exceptionally dilute polymer solutions," *Journal of Non-Newtonian Fluid Mechanics,* Jan., Vol. 12, No. 1, pp. 113–8.

Perry, A. E., Abell, C. A., 1975, "Scaling laws for pipe flow turbulence," *J. Fluid Mech.,* 67, pp. 257–71.

Saadeh, M., Strehlow, A., 1997, "The influence of the injection system on drag reduction," *Rheologica Acta,* July–Aug., Vol. 32, no. 4, pp. 398–404.

Smith, R. E., Tiederman, W. G., 1991, "The mechanism of polymer thread drag reduction," *Rheologica Acta,* March–April, Vol. 30, no. 2, pp. 103–13.

Stenberg, L. G., Lagerstedt, T., Sehlen, O., Rune Lindgren, E., 1977, "Mechanical mixing of polymer additive in turbulent drag reduction," Physics of Fluids, May, Vol. 20, No. 5, pp. 858–9.

Toms, B. A., 1948, "Some Observations on the Flow of Linear Polymer Solutions through straight Tubes at large Reynolds numbers., *Proceedings of the First international Conference on Rheology,* Vol. 2, pp. 135–41, North Holland, Amsterdam.

Usui, H., Maeguchi, K., Sano, Y., 1988, "Drag reduction caused by the injection of polymer thread into a turbulent pipe flow," Physics of Fluids, Sept., Vol. 31, No. 9, pp. 2518–23.

Virk, P. S., 1989, *Discussion in Structure of Turbulence and Drag Reduction,* Ed. Gyr A., Springer-Verlag, Berlin, pp. 591–3.

Virk, P. S., 1975, "Drag Reduction Fundamentals," *AIChE Journal,* July, Vol. 21, No. 4, pp. 625–56.

Virk, P. S., Mickley, H. S., Smith, K. A., 1970, "The ultimate Asymptote and Mean Flow Structure in Toms' Phenomenon," ASME *Journal of Applied Mechanics,* Paper No.: 70-APM-HH.

Vleggaar, J., Tels, M., 1973, "Drag reduction by polymer threads," *Chemical Engineering Science,* March, Vol. 28, No. 3, pp. 965–8.

Wei, T., Willmarth, W. W., 1992, "Modifying turbulent structure with drag-reducing polymer additives in turbulent channel flows," *Journal of Fluid Mechanics,* Dec., Vol. 245, pp. 619–41.

Wells, C. S., Spangler, J. G., 1967, Ling-Temco-Vought Research Center, Report No. 0-71000/TR-4.

Numerical Simulation of Concentrated Emulsion Flows

Michael Loewenberg
Assistant Professor,
Department of Chemical Engineering,
Yale University,
New Haven, CT 06520-8286

The macroscopic flow and detailed microphysics of a concentrated emulsion are described with three-dimensional numerical simulations. Numerical predictions for deformable drop interactions in shear-flow are in very close agreement to direct microscopic measurements. The results illustrate that drop deformation stabilizes drops against coalescence. Numerical simulations are used to describe an emulsion in shear flow at dispersed-phase volume fractions up to 30 percent. Shear-thinning viscosities and large normal stresses are found. The results are used to describe pressure-driven flow of a concentrated emulsion in a cylindrical tube. Blunted macroscopic velocity profiles and shear-thinning apparent viscosities are predicted. Our results suggest that some features of moderately concentrated emulsion flows can be predicted by an effective mean-field model.

1 Introduction

Emulsions are important in a wide range of industrial applications. Often it is desirable to predict or manipulate the rheology of an emulsion or its microstructure. Due to the complexity of the problem, however, there has been limited progress towards numerical simulations that can reliably predict the rheology and microstructure of emulsion flows. Instead, unreliable empirical correlations and ad hoc models have been used to predict emulsion flows.

Early descriptions of emulsion flow were restricted to dilute systems and undeformed spherical drops. Recently, there has been considerable progress with the development of numerical simulations of concentrated emulsion flows. Two-dimensional computer simulations have been developed to explore qualitative features of concentrated emulsion flows (e.g., Zhou and Pozrikidis, 1993, 1994; Li et al., 1995). By considering a cubic lattice of deformable drops Pozrikidis (1993) developed the first three dimensional description of a concentrated emulsion in shear flow.

Loewenberg and Hinch (1996) developed a many-drop three dimensional computer simulation for a dynamically-changing disordered microstructure of deformable emulsion drops in shear flow. With only modest computational resources, Loewenberg and Hinch were able to extract the steady-state rheology from long-time simulations. Dispersed-phase volume fractions up to 30 percent were explored. Their results reveal a complex non-Newtonian rheology with large normal stresses and pronounced shear thinning viscosities that are associated with an anisotropic microstructure of deformed drops. Under conditions that lead to significant drop deformation, the simulations of Loewenberg and Hinch (1996) show that the viscosity of an emulsion is only a moderately increasing function of the dispersed-phase volume fraction; in contrast to rigid particle suspensions, deformable drops do not form large clusters at volume fractions of 30 percent.

The foregoing numerical studies provide rheological information that may be applied to a wide range of practical emulsion flows. Moreover, numerical simulations provide a tool for exploring the detailed microstructure in an emulsion flow. These features have not been widely exploited. The aim of this article is to demonstrate the application of generic numerical simulations to a particular macroscopic flow of practical interest and to propose a simplified model for predicting the microstructure and rheology of an emulsion.

The problem formulation and assumptions are discussed in Section 2. In Section 3, we present simulations that illustrate the stability of deformable drops against coalescence; a scaling argument to explain these predictions is provided. Our numerical predictions are shown to be in very close agreement with the experimental measurements of Guido and Simeone (1998). In Section 4 we present results for the rheology of a concentrated emulsion in shear flow using our previously-developed computer simulation (Loewenberg and Hinch, 1996). The results are used to simulate pressure-driven flow of a concentrated emulsion. Numerical predictions of emulsion microstructure are presented in Section 5. An effective mean-field model is proposed in Section 6. Concluding remarks are made in Section 7.

2 Numerical Formulation

2.1 Macroscopic Flow. We assume that the macroscopic length scale L is much larger than the drop size a thus, a continuum description is appropriate. Accordingly, the macroscopic flow field is governed by

$$\mathrm{Re}\left(\frac{\partial \mathbf{u}}{\partial t} + \mathbf{u}\cdot\nabla\mathbf{u}\right) = \nabla\cdot\boldsymbol{\Sigma}; \quad \nabla\cdot\mathbf{u} = 0, \tag{2.1}$$

where Re is the macroscopic Reynolds number and $\boldsymbol{\Sigma}$ is the volume-averaged stress tensor which is computed by numerical simulation of the detailed microstructure as described in Section 2.2. The dispersed- and continuous-phase fluids are assumed to be Newtonian; however, $\boldsymbol{\Sigma}$ is generally non-Newtonian as a result of drop deformation.

2.2 Emulsion Microstructure. We assume that the local Reynolds number based on the drop size and local shear-rate is small:

$$\mathrm{Re}_{\mathrm{loc}} = \mathrm{Re}(a/L)^2 \ll 1, \tag{2.2}$$

where Re is the macroscopic Reynolds number. Thus, on the microscale, fluid motion in the dispersed and continuous phases is described by the quasisteady Stokes equations

$$\mu_0\nabla^2\mathbf{u} - \nabla p + \rho\mathbf{g} = 0, \nabla\cdot\mathbf{u} = 0;$$

continuous phase, (2.3)

$$\lambda\mu_0\nabla^2\mathbf{u} - \nabla p + (\Delta\rho + \rho)\mathbf{g} = 0, \quad \nabla\cdot\mathbf{u} = 0;$$

dispersed phase, (2.4)

Contributed by the Fluids Engineering Division for publication in the JOURNAL OF FLUIDS ENGINEERING. Manuscript received by the Fluids Engineering Division October 29, 1997; revised manuscript received August 10, 1998. Associate Technical Editor: M. Sommerfeld.

where μ_0, ρ and $\lambda\mu_0$, $\Delta\rho + \rho$ are the viscosities and densities of the continuous and dispersed phases. The volume-averaged velocity field

$$\langle \mathbf{u} \rangle = \mathbf{u}^\infty, \tag{2.5}$$

is imposed. On the deformable drop interfaces, the fluid velocity is continuous across the deformable drop interfaces but the normal traction $\mathbf{t}_n = \boldsymbol{\Sigma}:\mathbf{nn}$ suffers the jump

$$\mathbf{t}_n - \hat{\mathbf{t}}_n = \Delta\rho(\mathbf{g}\cdot\mathbf{x}) - 2\kappa\sigma \tag{2.6}$$

where σ is the surface tension, $\mathbf{n}$ is the outward normal vector, and κ is the mean curvature. Tangential tractions are continuous across the interface unless surface tension gradients (Marangoni stresses) arising from adsorbed surfactant or temperature gradients are important; Herein, Marangoni stresses are neglected. The initial drop shapes are given (e.g., spherical drops).

2.2.1 Boundary Integral Formulation. The foregoing initial-value problem is nonlinear (unless drop deformation is negligible). However, for a given instantaneous configuration of the drop interfaces, Equations (2.3)–(2.6) form a well-posed linear boundary-value problem for the fluid velocity. Thus, the problem can be conveniently recast as a boundary integral equation on the drop interfaces S (Pozrikidis, 1992):

$$\mathbf{u}(\mathbf{x}_i) = \frac{2}{\lambda+1} Ca\, \mathbf{u}^\infty(\mathbf{x}_i) - \frac{2}{\lambda+1}\frac{1}{8\pi}\int_S \mathbf{G}\cdot\mathbf{f}\, dS_x + \frac{\lambda-1}{\lambda+1}\frac{3}{2\pi}\int_S [\mathbf{T}\cdot\mathbf{u}]\cdot\mathbf{n}\, dS_x, \tag{2.7}$$

which has been made dimensionless using the drop size a (e.g., average undeformed drop radius) for characteristic length and the capillary relaxation velocity σ/μ_0 for the characteristic velocity. The $\mathbf{x}_i$ $(i = 1, N)$ are a set of marker points on the drop interfaces and $\mathbf{u}(\mathbf{x}_i)$ is the associated fluid velocity. If needed, the fluid velocity elsewhere in the domain (outside or inside the drops) can be obtained from a slightly modified form of Eq. (2.7) (Pozrikidis 1992); however, this was unnecessary for the results presented here.

The capillary number

$$Ca = \frac{\mu_0\dot{\gamma}a}{\sigma} \tag{2.8}$$

is the ratio of viscous stresses to surface tension (i.e., dimensionless shear-rate), where $\dot{\gamma}$ is the shear-rate. The (dimensionless) surface traction is

$$\mathbf{f} = [\mathrm{Bo}(\mathbf{e}\cdot\mathbf{x}) - 2\kappa a]\mathbf{n}, \tag{2.9}$$

where the Bond number is

$$\mathrm{Bo} = \frac{\Delta\rho g a^2}{\sigma}, \tag{2.10}$$

and $\mathbf{e}$ is a unit vector parallel to $\mathbf{g}$. Herein, neutral buoyancy is assumed thus, Bo = 0.

For isolated drops in Stokes flow, the kernel functions in Eq. (2.7)

$$\mathbf{G} = \frac{\mathbf{I}}{r} + \frac{\hat{x}\hat{x}}{r^3}, \quad \mathbf{T} = \frac{\hat{x}\hat{x}\hat{x}}{r^5}, \tag{2.11}$$

are the free-space Stokeslet and stresslet kernel functions, where $\mathbf{x} \in S$ is an integration point, $\hat{\mathbf{x}} = \mathbf{x} - \mathbf{x}_i$, and $r = |\hat{\mathbf{x}}|$. For concentrated emulsions, periodic boundary conditions are imposed by summing the free-space kernel functions on a lattice using Ewald summation (Beenaker, 1986); the resulting periodic kernel functions are given by Loewenberg and Hinch (1996). A strained cubic lattice is used to describe shear flow; by symmetry only strains $-(1/2) < \gamma \leq (1/2)$ are needed.

Evolution of the deformable drop microstructure and associated stresses is obtained by time-integrating the fluid velocity on the interfacial marker points

$$\frac{d\mathbf{x}_i}{dt} = u(\mathbf{x}_i), \quad i = 1, N. \tag{2.12}$$

A detailed description of our numerical method is described elsewhere (Loewenberg and Hinch, 1996, 1997). Using our numerical method, many-drop (e.g., twelve drop) computer simulations (with periodic boundary conditions) require a few hours on a workstation. Numerical convergence of our simulations is $1/N$.

2.3 Calculation of Macroscopic Stress. The volume-averaged stress tensor in an emulsion requires only the shape and velocity distribution on the drop interfaces which is directly obtained by solution of (2.7) from the boundary integral formulation described in Section 2.2.1. According to Batchelor (1970),

$$\boldsymbol{\Sigma} = \boldsymbol{\Sigma}^0 + \phi\boldsymbol{\Sigma}^P, \tag{2.13}$$

where $\boldsymbol{\Sigma}^0 = 2\mu_0\langle\mathbf{E}\rangle - \langle p\rangle\mathbf{I}$ is the stress contribution from the pure continuous-phase fluid (with volume-averaged rate-of-strain $\langle\mathbf{E}\rangle$ and pressure $\langle p\rangle$), ϕ is the dispersed-phase volume fraction, and

$$\Sigma^P_{ij} = \int_S [\kappa n_i x_j + (\lambda - 1)(u_i n_j + n_i u_j)]\, dS_x, \tag{2.14}$$

is the stress contribution of the drops. Locally small Reynolds numbers (2.2), neutral buoyancy (Bo = 0), and negligible Marangoni stresses are assumed. As a result of our nondimensionalization, $\boldsymbol{\Sigma}$ is normalized by the capillary pressure σ/a.

In shear-flow,

$$\mathbf{u}^\infty = (\dot{\gamma}x_2, 0, 0), \tag{2.15}$$

the continuous phase fluid contributes to the (dimensionless) total shear stress:

$$\bar{Ca} = Ca + \phi\Sigma^P_{12}. \tag{2.16}$$

which defines an effective capillary number. An effective shear viscosity is defined:

$$\frac{\bar{\mu}}{\mu_0} = \frac{\bar{Ca}}{Ca}. \tag{2.17}$$

The other off-diagonal stresses Σ_{13} and Σ_{23} vanish by symmetry.

Nonzero first- and second-normal stress differences result entirely from the dispersed-phase contributions

$$N_1 = \phi N_1^P = \phi(\Sigma^P_{11} - \Sigma^P_{22}), \tag{2.18}$$

$$N_2 = \phi N_2^P = \phi(\Sigma^P_{22} - \Sigma^P_{33}). \tag{2.19}$$

Herein, steady-state stresses are used to describe macroscopic emulsion flows. In our simulations, steady-state was reached after $5-10\tau$, where

$$\tau = \mu_0(1 + \lambda)a/\sigma \tag{2.20}$$

is the drop relaxation time. Thus, macroscopic time scales much larger than τ are assumed. Fortunately, this assumption usually holds in practice because τ is typically 1 millisecond.

Herein, the effects of polydispersity and phase segregation are ignored. A monodisperse drop size distribution and uniform dispersed-phase volume fraction are assumed. In general, dispersed-phase segregation occurs in a thin $O(a)$ region near macroscopic boundaries as a result of drop migration (Kennedy et al., 1994, Uijttewaal and Nijhof, 1995). In highly concentrated emulsions and foams this thin low-viscosity layer of continuous-phase fluid can have a pervasive macroscopic effect

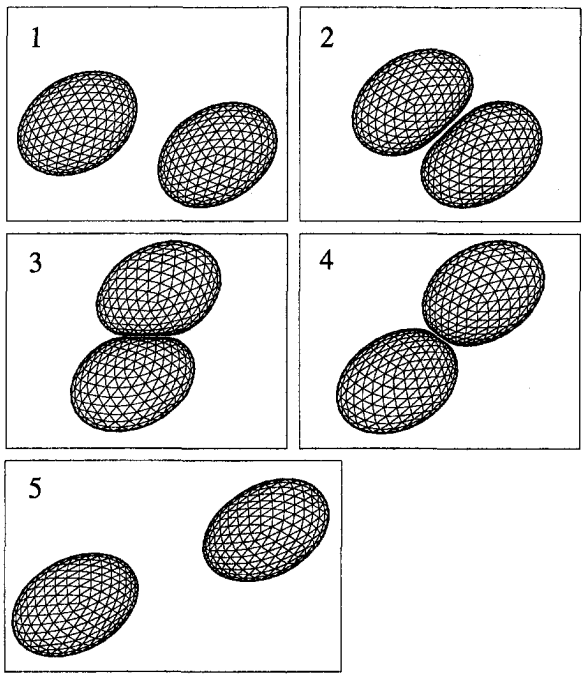

Fig. 1 Sequence (1–5) showing the interaction between equal-size drops in shear flow with $Ca = .135$, $\lambda = 1.37$; drops are in the shear plane ($x_1 - x_2$ plane). Initially, each drop is spherical with one drop centered at origin and the other at (−10.85, .5138, 0).

(e.g., apparent slip). However, for the moderately concentrated emulsions ($\phi \leq 30$ percent) considered herein, this thin phase-segregated layer has a negligible effect on the macroscopic flow because the effective viscosity of the emulsion is comparable to the viscosity of the continuous-phase fluid.

Under the conditions described above, the macroscopic stress tensor is fully characterized by the local capillary number (Ca), viscosity ratio (λ), and volume fraction (ϕ).

3 Interactions Between Deformable Drops

Figures 1 and 2 illustrate a pair interaction between deformable neutrally-buoyant drops in shear flow. The cross-flow component of the center-to-center drop separation is depicted in Fig. 2(a) and drop deformation

$$D = \frac{L - W}{L + W} \tag{3.1}$$

is depicted in Fig. 2(b), where L is the maximum and W is the minimum drop dimension.

The results illustrate that deformable drops are stabilized against coalescence. In the Appendix, this observation is explained by a scaling argument based on the lubrication flow between closely-spaced deformable drop interfaces. By symmetry, interactions between spherical particles/drops in shear flow do not produce a net cross-flow displacement. By contrast, interactions between deformable drops produce $O(a)$ net cross-flow displacements, as illustrated in Fig. 2(a). As a result, deformable drops undergo hydrodynamic diffusion (Loewenberg and Hinch, 1997).

Also shown in Fig. 2 are digitized experimental measurements of interacting 50 μm drops obtained by Guido and Simeone (1998). The parameters values ($Ca = .135$, $\lambda = 1.37$) and initial conditions used for our numerical simulations match the experimental conditions. As the results show, our predictions are in close agreement to the experiment.

4 Emulsion Flows

4.1 Concentrated Emulsion in Shear Flow. The steady-state rheology predicted by our numerical simulations is depicted in Figs. 3–5; non-Newtonian behavior is evident. Shear- and normal-stress contributions of the drops, given by Eq. (2.14) are shown in Figs. 3 and 5; the total shear- and normal-stresses are obtained using (2.16) and (2.18)–(2.19). The effective shear viscosity, defined by (2.17), is shown in Fig. 4.

The results depicted in Fig. 3(a) reveal strongly shear-thinning viscosities, particularly at larger volume fractions. Shear stresses are sensitive to λ as shown in Fig. 3(b): shear-thinning is considerably diminished for $\lambda > 1$. For low shear rates at 30 percent dispersed-phase volume fraction, the emulsion viscosity is nearly twice that of the continuous-phase fluid, according to the results shown in Fig. 4. Shear thinning increases sharply with the dispersed-phase volume fraction. As a result, the effective viscosity depends weakly on volume fraction at high shear rates.

Normal stresses result from drop deformation and alignment in the flow direction. Figure 5 shows that the first normal stress difference is large and positive whereas the second normal stress difference is small and negative, which is typical of polymeric fluids. At the highest volume fractions and shear-rates (capillary numbers) shown, the first normal stress difference is comparable to shear stresses in the emulsion. Our results show that normal stresses are $O(Ca^2)$ for $Ca \ll 1$, consistent with the predictions of small deformation theory (Choi and Schowalter, 1975). Normal stresses depend weakly on the viscosity ratio, as seen in Fig. 5(b).

Figure 6 shows the anisotropic microstructure predicted by our numerical simulations for a concentrated emulsion with 30

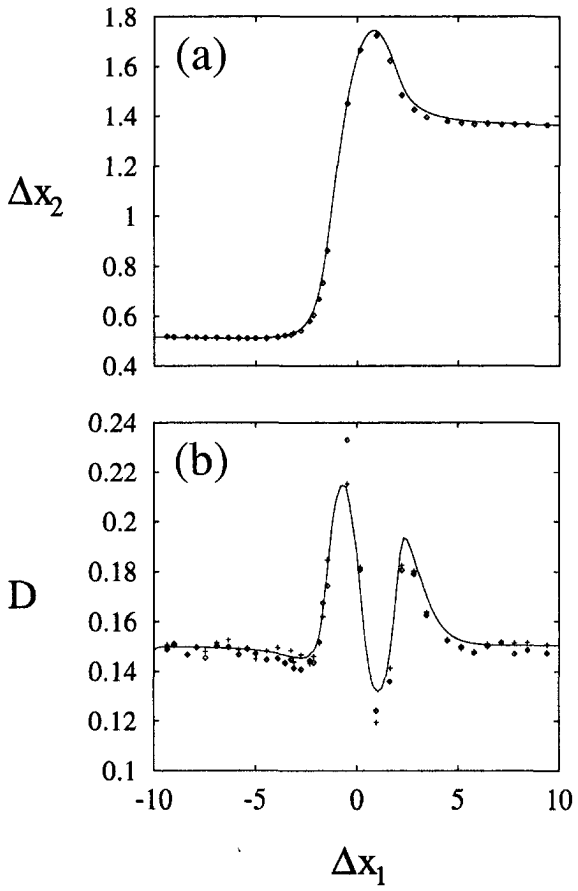

Fig. 2 Relative trajectory and deformation of drops depicted in 1. (a) Cross-flow displacement, (b) drop deformation. Symbols depict experimental measurements of Guido and Simeone (1998).

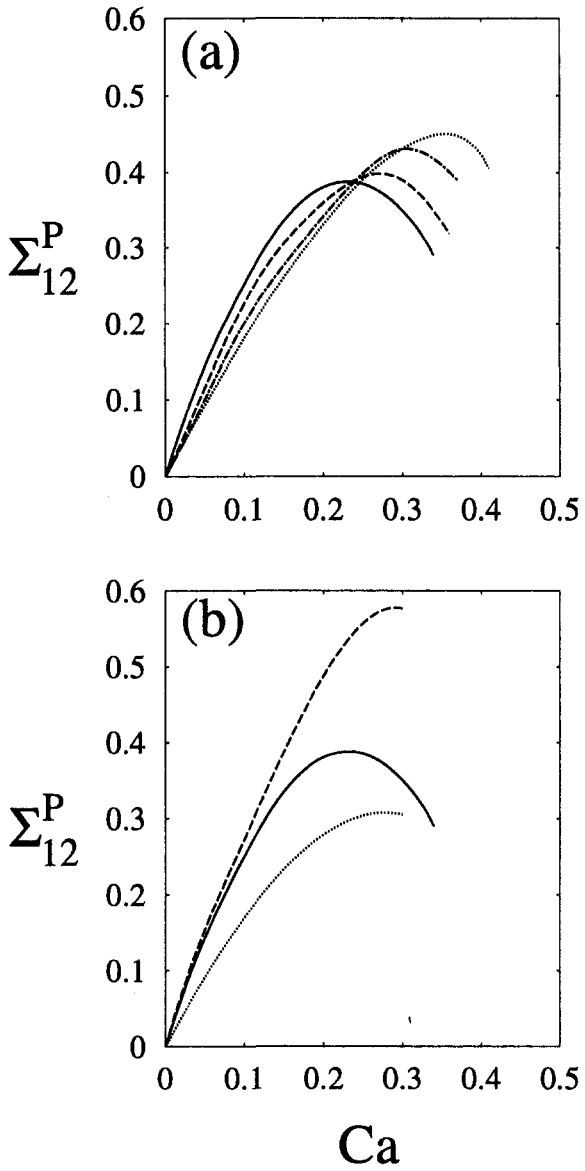

Fig. 3 Shear-stress contribution of drops. (*a*) $\lambda = 1$; $\phi = 0$ (dotted curve), $\phi = 10$ percent (dashed-dotted curve), $\phi = 20$ percent (dashed curve), $\phi = 30$ percent (solid curve). (*b*) $\phi = 30$ percent; $\lambda = 0.2$ (dotted curve), $\lambda = 1$ (solid curve), $\lambda = 2$ (dashed curve).

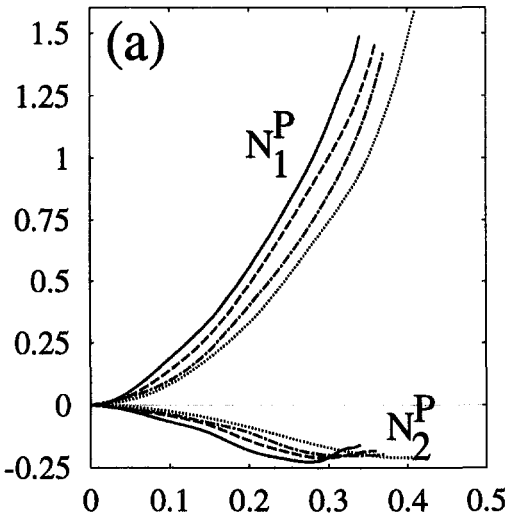

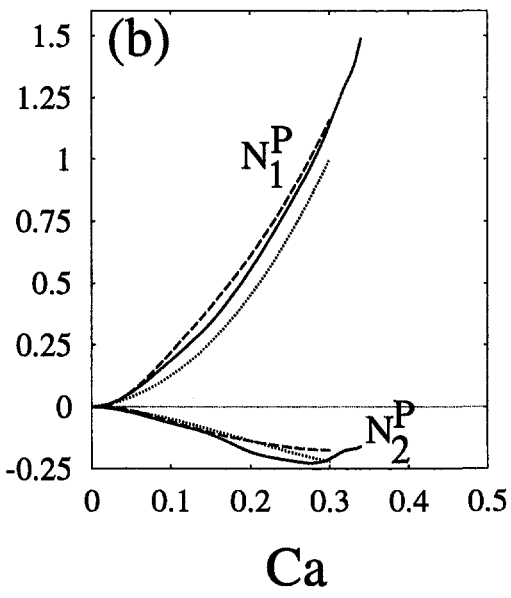

Fig. 5 Normal-stress contributions of drops. (*a*) $\lambda = 1$; $\phi = 0$ (dotted curve), $\phi = 10$ percent (dashed-dotted curve), $\phi = 20$ percent (dashed curve), $\phi = 30$ percent (solid curve). (*b*) $\phi = 30$ percent; $\lambda = 0.2$ (dotted curve), $\lambda = 1$ (solid curve), $\lambda = 2$ (dashed curve).

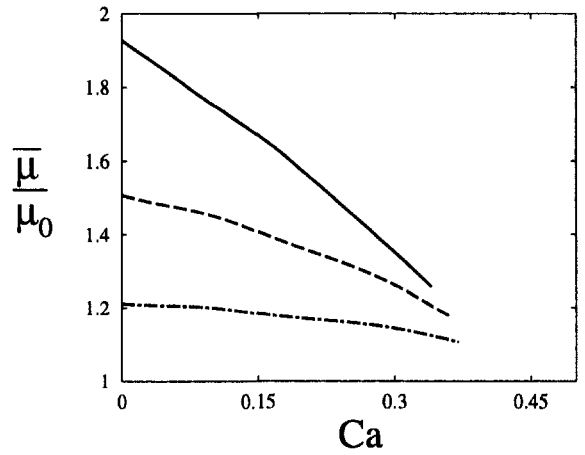

Fig. 4 Effective shear viscosity of a concentrated emulsion, $\lambda = 1$; $\phi = 30$ percent (solid curve), $\phi = 20$ percent (dashed curve), $\phi = 10$ percent (dashed-dotted curve)

percent dispersed-phase volume fraction. Viewed in the vorticity direction (6*a*), the microstructure reveals closely-spaced drops elongated in the flow direction; in the flow direction (6*b*) the microstructure is comparatively open and the cross-section for collisions thereby reduced. The microstructure shown in Fig. 6 helps to explain why emulsions are strongly shear thinning and have large normal stresses: the reduced collision cross-section of the drops allows them to glide past each other with less resistance; elongation of drops in the flow direction produces large first normal stress differences. Normal stresses and shear thinning increase with ϕ, as shown in Figs. 3–5, because of enhanced drop deformation and drop alignment at higher volume fractions.

4.2 Pressure-Driven Flow of a Concentrated Emulsion. Here, we describe pressure-driven flow of a monodisperse emulsion in a cylindrical tube with radius $R \gg a$ using the results of numerical simulations for shear flow. For laminar unidirectional flow, (2.1) reduces to:

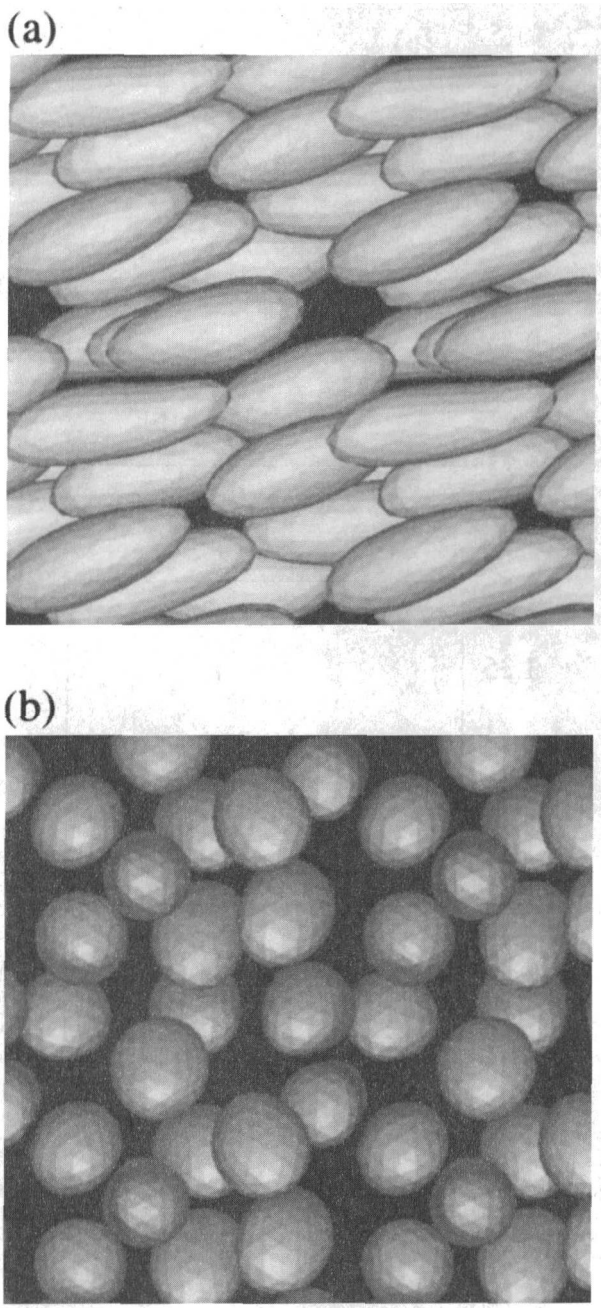

Fig. 6 Numerical simulation of an emulsion in shear-flow using 12 equal drops; ϕ = 30 percent, Ca = 0.3, λ = 1; initially drops are randomly located and spherical. (*a*) View of shear-plane (vorticity direction), (*b*) view in flow direction.

$$\frac{1}{r}\frac{d}{dr}(r\bar{C}a) = 2\bar{C}a_w, \tag{4.1}$$

where the radial coordinate r is nondimensionalized by R, $\bar{C}a$ is the dimensionless shear stress (2.16), and

$$\bar{C}a_w = \frac{aT_w}{\sigma} \tag{4.2}$$

is a wall-stress capillary number (dimensionless wall stress) based on the wall shear stress T_w which is associated with the applied pressure gradient G:

$$T_w = \tfrac{1}{2}RG. \tag{4.3}$$

Integrating (4.1) once (imposing smoothness at $r = 0$) yields

$$\bar{C}a(r) = r\bar{C}a_w. \tag{4.4}$$

Using $\bar{C}a$ from the numerical simulations presented in Section 4.1, this result provides an equation for the dimensionless shear-rate (Ca) which is numerically integrated (enforcing the no-slip boundary condition at $r = 1$) to obtain the velocity profile:

$$u(r) = 2\bar{u}(1 - r^2) + u'(r), \tag{4.5}$$

where $\bar{u}$ is the area-averaged velocity and u' is the deviation from a parabolic velocity profile; by definition $\bar{u}' = 0$. The deviation velocity is depicted in Fig. 7. Blunted velocity profiles are clearly seen which is a direct consequence of the shear thinning. The results indicate that shear-thinning effects increase with volume fraction, consistent with the results for shear flow (cf. Fig. 3(*a*)). As a consequence of nonuniform shear within the tube, the local shear viscosity varies nonlinearly from the maximum zero shear-rate limiting value at the tube centerline to a minimum value at the wall. Shear-thinning effects are more pronounced at high shear-rates because a wider range of viscosity occurs within the tube.

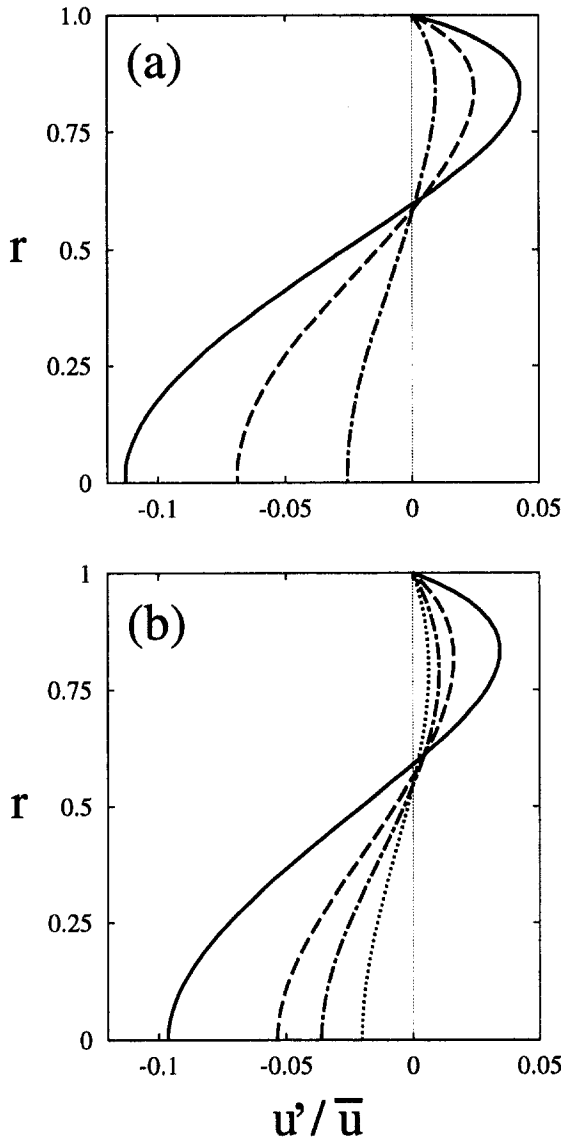

Fig. 7 Velocity profiles for pressure-driven flow of a concentrated emulsion in a tube, λ = 1 (deviation from parabolic velocity profile is shown). (*a*) $\bar{C}a$ = 0.425; ϕ = 10 percent (dashed-dotted curve), ϕ = 20 percent (dashed curve), ϕ = 30 percent (solid curve). (*b*) ϕ = 30 percent; $\bar{C}a_w$ = 0.1 (dotted curve), $\bar{C}a_w$ = 0.2 (dashed-dotted curve), $\bar{C}a_w$ = 0.3 (dashed curve), $\bar{C}a_w$ = 0.4 (solid curve).

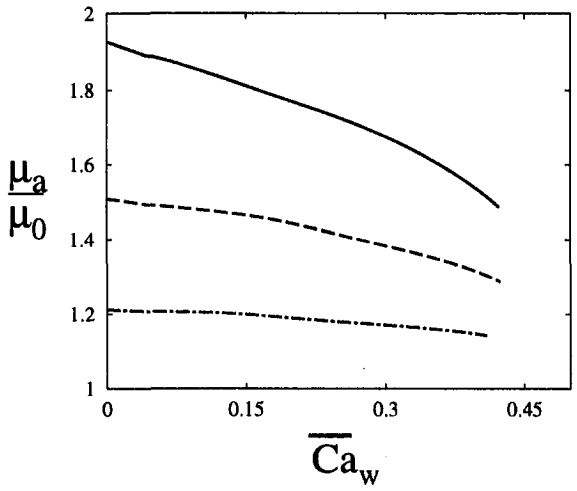

Fig. 8 Apparent viscosity for pressure-driven flow of a concentrated emulsion in a tube, $\lambda = 1$. $\phi = 10$ percent (dashed-dotted curve), $\phi = 20$ percent (dashed curve), $\phi = 30$ percent (solid curve).

An apparent viscosity is defined:

$$\frac{\mu_a}{\mu_0} = \frac{\bar{u}_0}{\bar{u}}, \tag{4.6}$$

where

$$\bar{u}_0 = \frac{RT_w}{4\mu_0} \tag{4.7}$$

is corresponding average velocity for the pure continuous-phase fluid.

Shear-thinning apparent viscosities are shown in Fig. 8. Comparing Figs. 4 and 8, we observe $\mu_a = \bar{\mu}$ for $\bar{Ca}_w$, $Ca \to 0$, as expected. However, shear thinning effects are reduced in pressure-driven flow as a result of nonuniform shear within the tube. The apparent viscosity is an average of the local viscosity in the tube; thus, $\mu_a > \bar{\mu}$ at finite shear rates.

5 Emulsion Microstructure

Average drop deformation and orientation are shown in Fig. 9. As the volume fraction increases, drops deform more and align more with the flow as the result of direct drop interactions as seen in Fig. 6. Drop deformation and orientation are presented in Fig. 10 as functions of the effective capillary number $\bar{Ca}$. The results show that the dependence of emulsion microstructure on volume fraction is approximately correlated by the effective capillary number. This finding indicates that normal stress differences do not significantly promote drop stretching and alignment.

Our simulations predict drop breakup for $Ca > Ca_c$, where Ca_c is the critical capillary number, given by the terminal values shown in Figs. 9–10. The correlation of emulsion microstructure by $\bar{Ca}$ seen in Fig. 10 suggests that drop breakup may correlate with the critical effective capillary number $\bar{Ca}_c$, defined by (2.16). As anticipated, the results depicted in Fig. 11 indicate that $\bar{Ca}_c$ is approximately independent of the dispersed-phase volume fraction in the range $\phi \leq 30$ percent.

For pressure-driven emulsion flow, drop breakup first occurs adjacent to the tube wall at $r = 1$, where the shear rate (shear stress) is highest. Drop breakup in pressure-driven flow occurs for $\bar{Ca}_w > \bar{Ca}_c$. The critical pressure gradient is given by (4.2)–(4.3) and the results in Fig. 11.

5.1 Effective Mean-Field Model. The results shown in Figs. 10–11 suggest an effective mean-field model of microstructural drop dynamics in terms of isolated drops embedded in a Newtonian fluid with viscosity $\bar{\mu}$.

The shear and normal stress contributions of the drops are shown as functions of the effective capillary number in Fig. 12 for $\lambda = 1$. The results indicate that $\Sigma^P(\bar{Ca}) \simeq \Sigma^{P,0}(\bar{Ca})$, where $\Sigma^{P,0}$ are the stress contributions for an isolated drop. This observation suggests the following approximation of (2.16), (2.18)–(2.19):

$$\bar{Ca} = Ca + \phi\Sigma_{12}^{P,0}(\bar{Ca}). \tag{5.1}$$

$$N_1 = \phi N_1^{P,0}(\bar{Ca}), \tag{5.2}$$

$$N_2 = \phi N_2^{P,0}(\bar{Ca}), \tag{5.3}$$

where $\Sigma_{12}^{P,0}$, $N_1^{P,0}$, and $N_2^{P,0}$ are calculated once from a single-drop calculation.

Shear stresses predicted by the effective mean-field model are compared to the results from numerical simulations in Fig. 13 for $\phi = 10$ percent. Worse agreement is obtained at larger volume fractions. Evidently, the mean-field model predicts drop deformation and breakup (Figs. 10–11) more accurately than the stress contributions of the drops.

The mean-field model reliably predicts drop deformation and breakup for volume fractions up to 30 percent provided that the shear stress is obtained from experiment (or numerical simulation) rather than the model. The mean-field model provides only an estimate of the rheology. The failure of the mean-field model to accurately predict emulsion rheology is partly explained by the observation that Σ depends on interface curvature according to (2.14), which is a more sensitive measure of drop shape than length and orientation angle.

The results shown in Fig. 11 indicate that the critical effective capillary number depends only weakly on viscosity ratio for

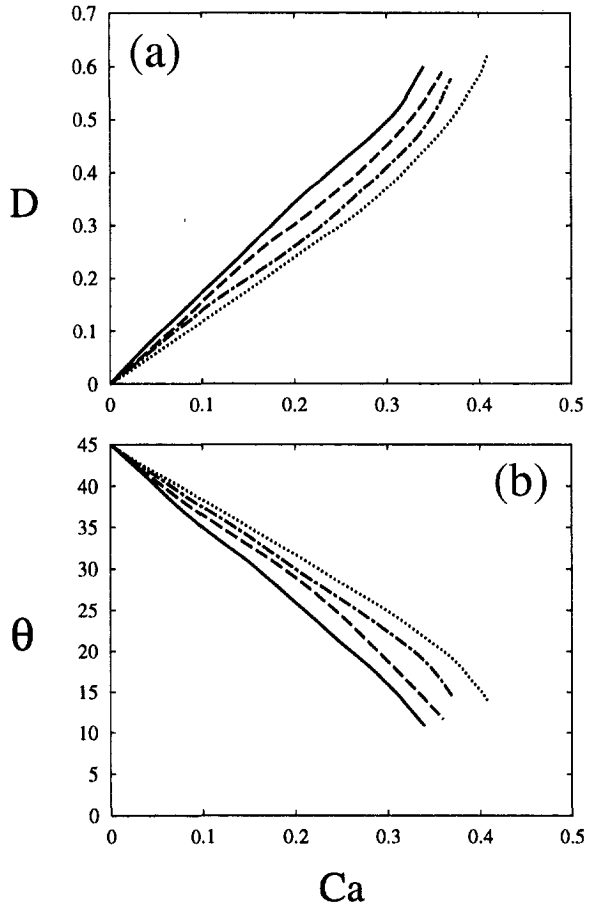

Fig. 9 Drop deformation (*a*), drop orientation (with respect to average flow) (*b*) versus capillary number. $\lambda = 1$; $\phi = 0$ (dotted curves), $\phi = 10$ (dashed-dotted curves), $\phi = 20$ (dashed curves), $\phi = 30$ (solid curves).

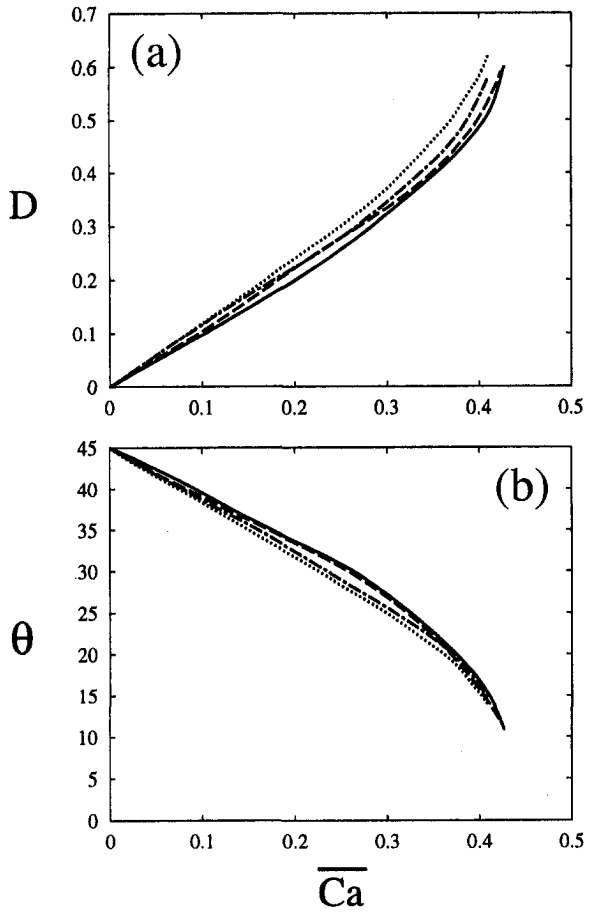

Fig. 10 Same as Fig. 9 but shown as functions of effective capillary number

$0.2 \leq \lambda \leq 2$. Drop dynamics in shear flow are expected to be sensitive to viscosity ratio for $\lambda \approx \lambda_c(\phi)$, where $\lambda_c(\phi)$ is the critical viscosity ratio for which $Ca_c \to \infty$. For an isolated drop, $\lambda_c(0) \approx 3 - 4$ (Grace, 1982, Kennedy et al., 1994). Critical

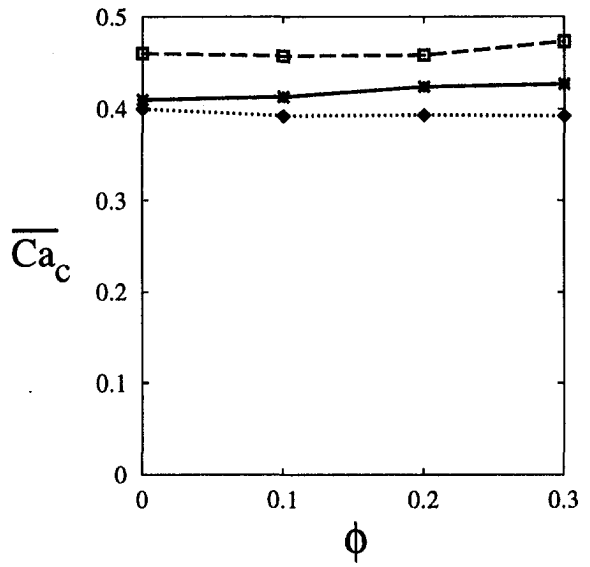

Fig. 11 Critical effective capillary number for drop breakup versus dispersed-phase volume fraction; $\lambda = 0.2$ (dotted curve), $\lambda = 1$ (solid curve), $\lambda = 2$ (dashed curve)

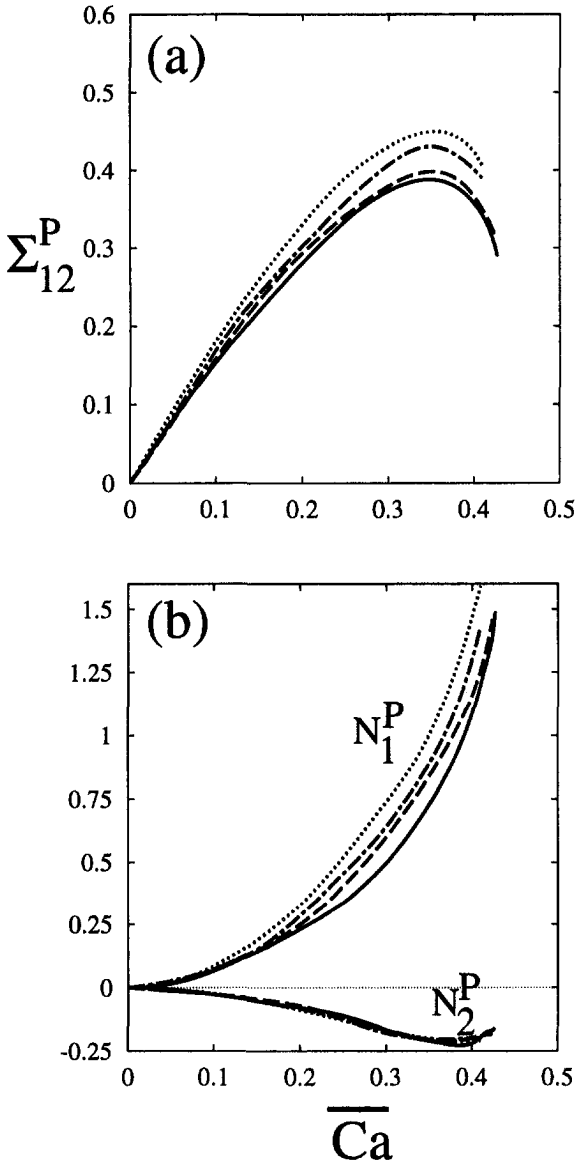

Fig. 12 Stress contributions of drops versus effective capillary number: (*a*) shear stress, (*b*) normal stresses; $\lambda = 1$; $\phi = 0$ (dotted curve), $\phi = 10$ percent (dashed-dotted curve), $\phi = 20$ percent (dashed curve), $\phi = 30$ percent (solid curve).

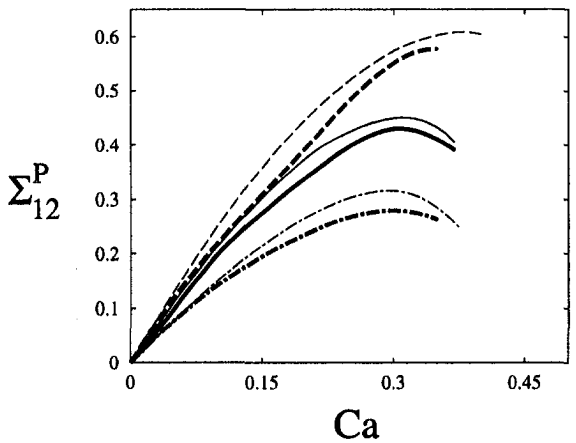

Fig. 13 Shear-stress contribution of drops, $\phi = 10$ percent; $\lambda = 0.2$ (dotted curves), $\lambda = 1$ (solid curves), $\lambda = 2$ (dashed curves). Numerical simulation (thick curves), model predictions (thin curves).

viscosities for concentrated emulsions are unknown; most likely λ_c increases with volume fraction.

For $\lambda \approx \lambda_c(\phi)$, the foregoing mean-field model can be extended by using an effective viscosity ratio $\bar{\lambda}$:

$$\bar{\lambda}\bar{\mu} = \lambda\mu_0, \tag{5.4}$$

where $\bar{\mu}$ is defined by (2.17). Accordingly, $\bar{\lambda}$ decreases with ϕ and the critical viscosity ratio

$$\lambda_c(\phi) = \lambda_c(0)\,\frac{\bar{\mu}}{\mu_0}. \tag{5.5}$$

increases with ϕ, as anticipated.

6 Concluding Remarks

Numerical simulations, based on the boundary integral method, have been used to describe shear- and pressure-driven emulsion flows. Numerical predictions for deformable drops interacting in shear flow are in close agreement with experimental measurements. Scaling arguments and numerical calculations show that the lubrication resistance between deformable drops prevents coalescence in the absence of van der Waals attraction.

Numerical results for concentrated emulsions in shear flow reveal non-Newtonian features including shear-thinning and nonzero normal stress differences. Pressure-driven flow of a concentrated emulsion in a tube was described using the effective stress tensor computed from simulations of shear flow. Shear-thinning emulsion viscosities are manifest by blunted velocity profiles and shear-thinning apparent viscosities. Beyond a critical pressure gradient, drop breakup is predicted to occur adjacent to the tube wall. The critical pressure gradient is approximately independent of the dispersed-phase volume fraction.

For dispersed-phase volume fractions up to 30 percent, the effective mean-field model provides predictions of drop breakup using single-drop calculations and shear viscosities obtained by experiment. Using only single-drop calculations, the mean-field model provides an estimate of emulsion rheology. An extension of the model for near-critical drop viscosities has been proposed but not tested.

Acknowledgments

This work was supported by grants from the National Science Foundation NSF grant CTS-9624615 and the National Aeronautics and Space Administration NASA grant NAG3-1935. The author wishes to thank Dr. Guido for supplying the experimental measurements shown in Fig. 2.

References

Beenaker, C. W. J., 1986, "Ewald Sum of the Rotne-Prager Tensor," *Journal of Chemical Physics,* Vol. 85, pp. 1581–1582.

Batchelor, G. K., 1970, "The Stress System in a Suspension of Force-free particles," *Journal of Fluid Mechanics,* Vol. 41, pp. 545–570.

Choi, S. J., and Schowalter, W. R., 1975, "Rheological Properties of Nondilute Suspensions of Deformable Particles," *Physics of Fluids,* Vol. 18, pp. 420–427.

Davis, R. H., Schonberg, J. A., and Rallison, J. M., 1989, "The Lubrication Force Between Two Viscous Drops," *Physics of Fluids A,* Vol. 1, pp. 77–81.

Grace, H. P., 1982, "Dispersion Phenomena in High Viscosity Immiscible Fluid Systems and Application of Static Mixers as Dispersion Devices in Such Systems," *Chemical Engineering Communications,* Vol. 14, pp. 225–277.

Guido, S., and Simeone, M., 1998, "Binary Collision of Drops in Simple Shear Flow by Computer-Assisted Video Optical Microscopy," *Journal of Fluid Mechanics,* Vol. 357, pp. 1–20.

Kennedy, M. R., Pozrikidis, C., and Skalak, R., 1994, "Motion and Deformation of Liquid Drops, and the Rheology of Dilute Emulsions in Simple Shear Flow," *Computers and Fluids,* Vol. 23, pp. 251–278.

Li, X., Zhou, H., and Pozrikidis, C., 1995, "A Numerical Study of the Shearing Motion of Emulsions and Foams," *Journal of Fluid Mechanics,* Vol. 286, pp. 379–404.

Loewenberg, M., and Hinch, E. J., 1996, "Numerical Simulation of a Concentrated Emulsion in Shear Flow," *Journal of Fluid Mechanics,* Vol. 321, pp. 395–419.

Loewenberg, M., and Hinch, E. J., 1997, "Collision of Two Deformable Drops in Shear Flow," *Journal of Fluid Mechanics,* Vol. 338, pp. 299–315.

Papadopoulos, D. P., Blawzdziewicz, J., and Loewenberg, M., 1996, "Near-Contact Motion of Surfactant-Covered Deformable Drops," Annual Meeting AIChE, Chicago.

Pozrikidis, C., 1992, *Boundary Integral and Singularity Methods for Linearized Viscous Flow,* Cambridge University Press.

Pozrikidis, C., 1993, "On the Transient Motion of Ordered Suspensions of Liquid Drops," *Journal of Fluid Mechanics,* Vol. 246, pp. 301–320.

Rallison, J. M., 1981, "A Numerical Study of the Deformation and Burst of a Drop in General Shear Flows," *Journal of Fluid Mechanics,* Vol. 109, pp. 465–482.

Uijttewaal, W. S. J., and Nijhof, E. J., 1995, "The Motion of a Droplet Subjected to Linear Shear Flow Including the Presence of a Plane Wall," *Journal of Fluid Mechanics,* Vol. 302, pp. 45–63.

Zhou, H., and Pozrikidis, C., 1993, "The Flow of Ordered and Random Suspensions of Two-Dimensional Drops in a Channel," *Journal of Fluid Mechanics,* Vol. 255, pp. 103–127.

Zhou, H., and Pozrikidis, C., 1994, "Pressure-Driven Flow of Suspensions of Liquid Drops," *Physics of Fluids,* Vol. 6, pp. 80–94.

APPENDIX A

Stability Against Coalescence

A thin film with thickness h and lateral extent $d \gg h$ forms between drops that are pressed together in the compressional quadrant of a shear-flow by a viscous force

$$F_v \sim \mu_0\dot{\gamma}a^2. \tag{A.1}$$

For spherical drops, the lubrication resistance scales as (Davis et al., 1989):

$$F_L \sim \lambda\mu_0\dot{h}a\sqrt{a/h}, \tag{A.2}$$

where $\sqrt{h/a} < \lambda < \sqrt{a/h}$. By integrating the force balance $F_v \sim F_L$, we find

$$\frac{h}{h_0} \sim \left(1 - \frac{\dot{\gamma}t}{\lambda}\sqrt{a/h_0}\right)^2, \tag{A.3}$$

where h_0 is the initial gap width. The result indicates that spherical drops undergo coalescence on the time scale $\dot{\gamma}t \sim \lambda\sqrt{h_0/a}$ without the help of van der Waals attraction.

A scaling argument helps to explain why drop deformation inhibits coalescence. For $Ca = O(1)$, the lateral extent of the near-contact region is

$$d \sim a. \tag{A.4}$$

In the following, we shall assume

$$(h/a)^2 < \lambda < a/h. \tag{A.5}$$

For finite λ this condition is satisfied for $h/a \to 0$.

The local velocity in the near-contact region between two deformable drops is

$$u = u_p + u_t, \tag{A.6}$$

where u_t is the tangential velocity on the drop interfaces associated with a plug-flow velocity profile and

$$u_p \sim \frac{\Delta p}{\mu_0}\frac{h^2}{d}, \tag{A.7}$$

is the parabolic pressure-driven flow, where the lubrication pressure balances the viscous force (9.1) thus,

$$\Delta p \sim \mu_0\dot{\gamma}(a/d)^2. \tag{A.8}$$

In the absence of Marangoni stresses, the tangential stress is continuous across the drop interface thus,

$$\mu_0 u_p/h \sim \mu_0\lambda u_t/d. \tag{A.9}$$

By continuity,

$$\frac{\dot{h}}{h} \sim -(u_p + u_t)/d, \tag{A.10}$$

which, with Eqs. (9.5) and (9.9), reduces to

$$\frac{\dot{h}}{h} \sim -\frac{u_p}{\lambda h}. \tag{A.11}$$

Then by inserting Eqs. (9.7)–(9.8) and (9.4) yields

$$\frac{\dot{h}}{h} \sim -\frac{\dot{\gamma} h}{\lambda a}. \tag{A.12}$$

For λ in the range given by (9.5), flow in the near-contact region is dominated by the plug-flow velocity u_t; the lubrication resistance is dominated by the flow inside the drops and is therefore proportional to the drop viscosity $\lambda\mu_0$. (The lubrication resistance is proportional to μ_0 for $\lambda > a/h$.)

Upon integration, Eq. (9.12) predicts slow algebraic film drainage:

$$\frac{h}{a} \sim \frac{\lambda}{\dot{\gamma} t}. \tag{A.13}$$

In contrast to spherical drops, van der Waals attraction is required for coalescence. Drop deformation stabilizes drops against coalescence.

The foregoing scaling analysis assumes $\dot{\gamma} t = O(1)$, which is the time scale for drop interactions in shear flow. At long-times $\dot{\gamma} t \gg 1$, internal circulation arrests the near-contact motion between drops with clean interfaces and prevents coalescence (Papadopoulos, Blawzdziewicz and Loewenberg, 1996).

Pipeline Leak Detection by Impulse Response Extraction

Chyr Pyng Liou
Professor,
Department of Civil Engineering,
University of Idaho,
Moscow, ID 83843

A system's response to an impulse can be used to detect and diagnose abnormalities. The impulse response can be extracted by using cross-correlations between a low amplitude pseudo random binary disturbance input and the system's output. This fact is applied to pipeline hydraulics as a means of real-time non-interruptive integrity monitoring. A method of generating the pseudo random binary disturbance is proposed. The extraction of a pipeline's impulse response with the presence of noise is investigated. The features of the response of an intact pipeline and characteristic changes in the impulse response as a result of a leak are established. The feasibility of using impulse response to detect and to locate a leak in real-time is demonstrated.

1 Introduction

Many cross-country pipelines are monitored remotely by interfacing monitoring logics with real-time data through a supervisory control and data acquisition system (SCADA). The effectiveness of such technology is hampered by data noise (Liou, 1993, 1995). Reliable software-based leak detection methodology is vital to the oil and petroleum product transportation industry (Mears, 1993).

The dynamic characteristics of a mechanical system may be evaluated by examining the system's response to an impulse. The response characterized with a system known to be normal can be compared with the system's response obtained later on. A departure signifies abnormality.

The direct implementation is to impose an impulse and then monitor the system's response. However, such an approach is seldom used because the amplitude of the imposed pulse must be small to avoid overloading and interference. As a result, the system's response function is masked by noise. Noise-level pseudo random binary signals can be used to extract a system's impulse response by a cross-correlation method. This method eliminates the concerns stated above, and has been used to test many systems (Balcomb et al., 1961; Li et al., 1994; Dellabetta, 1995). However, this method has not been used for monitoring pipeline integrity. This paper explores the feasibility of such an approach for real-time pipeline leak detection.

2 Pseudo-Random Binary Signals

A pseudo random binary signal (p.r.b.s) sequence can be generated from a shift register. A n-stage shift register is a device consisting of n consecutive binary memories, a clock, and a Boolean feedback logic. Initially, the 1st to the nth stage memories are filled with 0's and 1's in an arbitrary order except that not all of them are zero. The content of the first stage is the desired signal at the current time. The contents of some of the memories are used by the feedback loop to compute a value (1 or 0). At the beat of the clock, this value enters the n-th stage memory and pushes the content of each of the remaining memories down by one stage. This process is repeated indefinitely. The feedback logic can be chosen such that the pattern of 0's and 1's repeats itself after $p = 2^n - 1$ digits, where p is the period of the sequence. All the zeros in the sequence are then replaced by -1. Columb (1964) gives a general description about p.r.b.s sequences. Specific feedback logic for one to twenty-stage shift registers can be found in Baumert (1964).

As an example, consider a signal sequence generated by a 4-stage shift register. The feedback logic is a parity check on the contents of the first and second stage memories (1 when the sum is odd and 0 when the sum is even). The starting values from stage 4 to stage 1 are (1, 0, 0, 0). The resulting sequence for one period is (0, 0, 0, 1, 0, 0, 1, 1, 0, 1, 0, 1, 1, 1, 1). Replacing 0 by $-\alpha$ and 1 by α, a binary sequence Z with a half amplitude of α is established. Since the sequence repeats itself, it can be regarded as infinitely long. Figure 1 shows this binary sequence and its autocorrelation computed from

$$R_{zz_i} = \frac{1}{p}\sum_{j=1}^{p} Z_j Z_{j+i} \tag{1}$$

where Z is the p.r.b.s. sequence and R_{ZZ} is its autocorrelation. It is seen that the autocorrelation is a train of triangular pluses with a peak value of α^2, an offset of $-\alpha^2/p$, and a period of p. For a fixed α, a fixed time period, and a large n (equivalent to a small time step between clock beats), the offset and the base of the triangular pluses diminish, thus each period of the autocorrelation function of a p.r.b.s sequence approximates a Dirac delta function $\delta(\zeta - \theta)$ which is zero everywhere except at $\zeta = \theta$, where it is undefined, and yet

$$\int_{-\infty}^{\infty} F(\zeta)\delta(\zeta - \theta)d\zeta = F(\theta) \tag{2}$$

for any continuous function $F(\theta)$. Further discussions on this important property of the autocorrelation function of p.r.b.s sequences can be found in Eykhoff (1974). In this paper, Z is a sequence of random pressure head noise imposed at one end of a pipe. The function F is the pressure head impulse response at a given point along the pipe.

3 Impulse Response and Cross-Correlation

A well-known theory of linear systems states that when a wide-band signal is applied to the system input, the cross-correlation of this signal with the output is proportional to the impulse response of the system (Beauchamp and Yuan, 1979; Newland, 1975; Takahashi et al., 1972). This theory is briefly reviewed herein in the context of p.r.b.s. and the present application.

Let t be time. Suppose a linear system is excited by two inputs: a normal system input $f_i(t)$ and a disturbance or noise $f_d(t)$. Let the system output be $f_o(t)$ and the response of the system to a unit impulse at time zero be $G(t)$. It can be shown (Newland, 1975) that

$$f_o(t) = \int_{-\infty}^{\infty} G(\theta)[f_i(t - \theta) + f_d(t - \theta)]d\theta \tag{3}$$

where θ is the elapse time between the imposition of the impulse

Contributed by the Fluids Engineering Division for publication in the JOURNAL OF FLUIDS ENGINEERING. Manuscript received by the Fluids Engineering Division September 30, 1997; revised manuscript received April 21, 1998. Associate Technical Editor: D. P. Telionis.

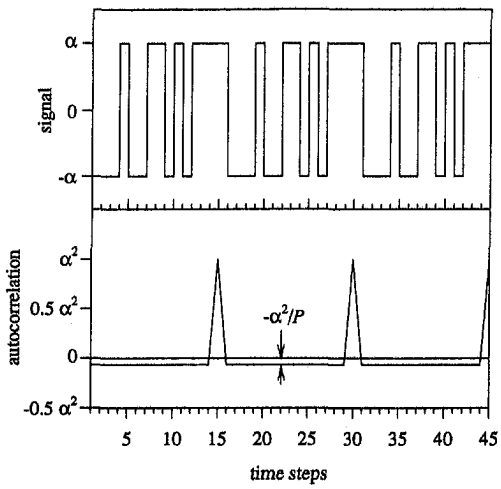

Fig. 1 Example binary signal and its autocorrelation ($n = 4$ and $p = 15$)

and the instant its result is being calculated. In the present application, the system is a pipeline, $f_i(t)$ is the head at one end or the boundary of the pipe, $f_d(t)$ is a noise imposed on $f_i(t)$, and $f_o(t)$ is the head at an interior point of the pipe. $G(t)$ is the impulse response function of the pipe at the interior point. $f_i(t)$, $f_d(t)$, and $f_o(t)$ have a dimension of length. $G(t)$ is dimensionless. The interior head (the output) responds to changes in the boundary head (the input) as the changes at the boundary propagate toward the pipe interior.

Let $R_{do}(\zeta)$ be the cross-correlation between the noise $f_d(t)$ and the interior head $f_o(t)$ so that

$$R_{do}(\zeta) = \lim_{T\to\infty} \frac{1}{T}\int_0^T f_d(t) f_o(t+\zeta)\,dt \qquad (4)$$

$$= E[f_d(t) f_o(t+\zeta)]$$

where $E[\ ]$ denotes the expected averaged value of the quantity in the square brackets. Substituting Eq. (3) into Eq. (4) and rearranging,

$$R_{do}(\zeta) = \int_{-\infty}^{\infty} G(\theta) E[f_d(t) f_d(t+\zeta-\theta)]\,d\theta + \int_{-\infty}^{\infty} G(\theta) E[f_d(t) f_i(t+\zeta-\theta)\,d\theta \qquad (5)$$

or

$$R_{do}(\zeta) = \int_{-\infty}^{\infty} G(\theta) R_{dd}(\zeta-\theta)\,d\theta + \int_{-\infty}^{\infty} G(\theta) R_{di}(\zeta-\theta)\,d\theta \qquad (6)$$

Thus the cross-correlation between the noise and the interior head depends on the autocorrelation of the noise and the cross-correlation between the noise and the boundary head.

When noise is generated from a p.r.b.s sequence with its autocorrelation $R_{dd}(\zeta-\theta)$ approaching a delta function, Eq. (2) is applied to Eq. (6) to obtain

$$R_{do}(\zeta) = \alpha^2 G(\zeta) + \int_{-\infty}^{\infty} G(\theta) R_{di}(\zeta-\theta)\,d\theta \qquad (7)$$

Furthermore, since the boundary head $f_i(t)$ and its noise $f_d(t)$ are independent and uncorrelated,

$$R_{di}(\zeta-\theta) = 0 \qquad (8)$$

thus the second term on the right side of Eq. (7) is zero. Therefore, the cross-correlation between the noise and the interior head equals the product of the square of the half-amplitude of the p.r.b.s. noise sequence and the impulse response function of the pipe at the interior point.

Let Z_j be the p.r.b.s noise sequence with $j = 1$ to p, and Y_j the time series of the interior head with $j = 1$ to N. The digital approximation of the first $m + 1$ cross-correlation between Z and Y is (Beauchamp and Yuan, 1979; Diggle, 1990)

$$R_{do_i} = \frac{1}{N}\sum_{j=1}^{N-i} Z_j Y_{j+i} \quad i = 0, 1, \ldots m \qquad (9)$$

N is related to the time period T in Eq. 4 and the time step dt of the shift register clock by $T = Ndt$. As explained later, dt is also the time step used in simulating the transient hydraulics in the pipe. The size of T varies. If one is interested in the impulse response of a portion of a very long pipeline where reflections need not be considered, then a small T is sufficient. When a dead-ended pipe is considered where reflections are dominant, then T needs to cover the time span over which the response to an impulse is sufficiently damped out.

4 Modeling of Small-Amplitude Transient Pipe Flows

The state of flow in a pipeline segment is governed by a pair of simplified equations of motion and continuity (Wylie and Streeter, 1993):

$$\frac{\partial H}{\partial x} + \frac{1}{gA}\frac{\partial Q}{\partial t} + \frac{fQ|Q|}{2gDA^2} = 0 \qquad (10)$$

$$\frac{\partial H}{\partial t} + \frac{a^2}{gA}\frac{\partial Q}{\partial x} = 0 \qquad (11)$$

where H = head, Q = flow, g = gravitational acceleration, A = pipe cross-sectional area, a = water hammer wave speed, f = Darcy-Weisbach friction factor, x = distance, and t = time.

Equations (10) and (11) are linearized around a mean state for small head and flow disturbances as

$$\frac{\partial h}{\partial x} + \frac{1}{gA}\frac{\partial q}{\partial t} + Rq = 0 \qquad (12)$$

$$\frac{\partial q}{\partial x} + \frac{gA}{a^2}\frac{\partial h}{\partial t} = 0 \qquad (13)$$

where h = head disturbance from a local mean head $\bar{H}$, q = flow disturbance from a local mean flow $\bar{Q}$

$$h = H - \bar{H}, \quad q = Q - \bar{Q} \qquad (14)$$

and R = linearized resistance per unit length of pipe,

$$R = \frac{f\bar{Q}}{gDA^2} \qquad (15)$$

Equations (12) and (13) can be transformed into a pair of ordinary differential equations in the distance-time plane ($x - t$ plane) by the method of characteristics,

$$\frac{dh}{dt} + \frac{a}{gA}\frac{dq}{dt} + aRq = 0 \quad \text{along} \quad \frac{dx}{dt} = a \qquad (16)$$

$$\frac{dh}{dt} - \frac{a}{gA}\frac{dq}{dt} - aRq = 0 \quad \text{along} \quad \frac{dx}{dt} = -a \qquad (17)$$

The pipeline segment can be a portion of a larger pipeline network with its ends connected to pumps, valves, pipe junctions, or reservoirs. All these boundary conditions can be readily modeled (see Wylie and Streeter, 1993). For the purpose of demonstrating the concept of using impulse response extraction for leak detection, it is sufficient to consider a constant head reservoir at the inlet and a valve at the outlet. For such a system, the upstream boundary condition is

$$h = 0 \tag{18}$$

At the downstream boundary, small excursions of the valve opening around a mean position are modeled by a linearized valve equation

$$q = \frac{\tau \bar{Q}_L}{2\bar{H}_L} h - (1 - \tau)\bar{Q}_L \tag{19}$$

where τ indicates valve opening and has a value of unity at the mean position. $\bar{Q}_L$ and $\bar{H}_L$ are the mean flow and head at the valve when $\tau = 1$. The excursions generate a sequence of pseudo-random head disturbances which are discussed later.

A leak flowing through an opening in the pipe wall can be simulated as an orifice flow with

$$\bar{Q}_l = (C_d A)_l \sqrt{2g\bar{H}_l} \tag{20}$$

where $(C_d A)_l$ is the product of the discharge coefficient and the area of the opening. After linearizing,

$$q_l = \frac{\bar{Q}_l}{2\bar{H}_l} h \tag{21}$$

where q_l = fluctuation in the leak flow, $\bar{Q}_l$ = mean leak flow rate, and $\bar{H}_l$ = mean head inside the pipe at the leak location.

The governing equations and the boundary conditions form the basis of a numerical model. The pipeline is divided into a number of equal-length computational sections. Head and flow disturbances are computed at the nodes between sections. The computed head disturbances at the nodes are treated as the "measured" head disturbances along the pipeline.

5 Impulse Response of Pipelines

As a distributed mass system, a pipeline's response to a head impulse is location dependent. At a given location, the response is a series of head and flow pulses with diminishing peaks over time. The magnitude and the sign of the pulses depend on how and to what extent the pulses are reflected from the ends, and on the attenuation due to frictional resistance to flow. Example responses of capped and, separately, infinitely long pipes can be found in Liou (1996).

Two features of the head response are useful for leak detection. First, as a head pulse propagates toward a leak, the transmitted pulse beyond the leak location has a reduced amplitude. This fact can be established by applying Eq. (16) along characteristics 1 and 3 and Eq. (17) along the characteristic 2 in Fig. 2, assuming no friction. In this figure dx and dt are the length of a computational section and the size of a time step, respectively. The result is

$$\frac{h}{\Delta h} = \frac{1}{1 + \dfrac{a\bar{Q}_l}{4gA\bar{H}_l}} \tag{22}$$

where Δh is the amplitude of the pulse approaching the leak and h is the head disturbance at and beyond the leak location. It is seen that the pulse is diminished more significantly when the leak is large or when the head is low. The sensitivity of pulse attenuation due to a leak is discussed later.

Secondly, the resistance term Rq in Eq. (12) resembles viscous damping in the sense that resistance is proportional to velocity (flow disturbance in this case). As a result, the peaks decay exponentially over time and distance. When a leak exists, the rate of decay will be different between pipe segments upstream and downstream of the leak. This difference is discernable by the slope change of the peak envelope in the natural log of the head pulse ln (h) versus distance plot.

The friction-caused attenuation can be separated from the leak-caused attenuation by plotting the ln (h) against distance. Any leak will cause a discontinuous downward shift of the peak envelope for the portion of the pipeline that "felt" the attenuated pulse. Knowing the location (needed to determine $\bar{H}_l$) and the magnitude of $h/\Delta h$ from the peak versus distance plot, the size of the leak $\bar{Q}_l$ can be estimated from Eq. (22). Should multiple leaks exist, the attenuation of each one can be calculated from Eq. (22). Associated with each leak is a discontinuity in the ln (h) versus distance plot.

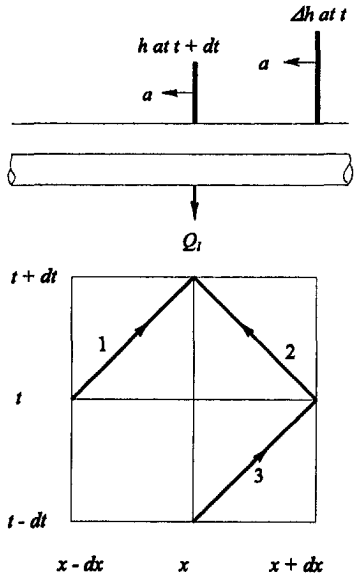

Fig. 2 Propagation and leak-induced attenuation of a head disturbance Δh. The x-t plane shows the characteristics along which Eq. (21) is applied.

6 Generation of Pseudo-Random Binary Head Disturbances

For a pipeline segment upstream from a valve, a sequence of desired pseudo random pressure head pulses at the valve can be generated by modulating the valve. Suppose that the flow, fed by a constant head reservoir, is at a steady state and no leak exists. The normal and thus anticipated conditions are a uniform flow $\bar{Q}$ and a head profile that varies linearly from $\bar{H}_r$ at the reservoir to $\bar{H}_L$ at the outlet. $\bar{H}_L$ equals $\bar{H}_r$ less the frictional head loss along the pipeline. Consider a succession of time steps over which a head disturbance is added to $\bar{H}_L$. This head disturbance comes from a p.r.b.s sequence. Responding to the imposed head disturbance, flow disturbance at the valve can be computed from Eq. (16). The valve τ that corresponds to the imposed head disturbance and the computed flow disturbance at the valve is solved from Eq. (19). At the next step, Eq. (16) is used again with the head disturbance next in the binary queue to find a new flow disturbance at the valve. A new valve τ can then be computed. By repeating this process, a sequence of τ values is established that defines the valve modulation.

Note that the pipeline's reaction to the imposed head disturbance influences the determination of τ. Therefore, the valve modulation is specific to the boundary and the flow conditions. When any of these change, the valve modulation must be reestablished.

7 Noise Added by the SCADA System

There are two kinds of noise: noise in the boundary head $f_i(t)$ and noise $n(t)$ added to the interior head $f_a(t)$. For the former, Eq. (8) applies.

The second kind of noise comes from the SCADA system where local pressures are measured and digitized by remote terminal units. The data are usually sent to the control center on a report-by-exception basis where new data is sent only

when it differs from the previous value by a specified dead band. At the control center, past data is assumed current unless new data is received. Because of the dead band and rounding used in data communication, the pressure traces at the control center resemble the kind of multi-level random sequence that can be generated by the procedure given in Newland (1975).

The noise $n(t)$ is added so that at each pressure measurement location

$$f_o(t) = \int_{-\infty}^{\infty} G(\theta)[f_i(t-\theta) + f_d(t-\theta)]d\theta + n(t) \quad (23)$$

The cross-correlation between $f_d(t)$ and $f_o(t)$ now becomes

$$R_{do}(\zeta) = \alpha^2 G(\zeta) + E[f_d(t)n(t+\zeta)] \quad (24)$$

Thus, the cross-correlation of the boundary head noise with the interior head may no longer be proportional to the pipeline's impulse response. However, since $f_d(t)$ and $n(t)$ are independent random processes, the expected value of the cross-correlation between them (i.e., $E[f_d(t)n(t+\zeta)]$ for all ζ is zero.

Therefore, with the added noise, $R_{do}(\zeta)$ is still expected to be proportional to the pipeline's impulse response but only in a statistical sense. In practice, only samples of $E[f_d(t)f_i(t+\zeta)]$ and $E[f_d(t)n(t+\zeta)]$ can be obtained. Individual samples of these cross-correlations may not be zero. Consequently, the impulse response needs to be extracted many times and averaged to minimize the effect of noise.

8 Advantage of the Cross-Correlation Approach

In theory, one can impose a noise-level head pulse at the valve end and monitor its propagation. The measured head traces are the pipeline's impulse response. When data noise is present, one can simply repeat this process many times and average out the noise. So, what is the advantage of the cross-correlation approach over this straightforward approach?

The advantage is that the effect of noise is smaller and can be controlled in the cross-correlation approach. As a result, far fewer number of impulse responses are needed. This is demonstrated by an example. Suppose the data noise is a random five-level signal sequence generated by averaging the current and the previous three consecutive random numbers in a queue of random numbers with values of 1 or -1 m. The resulting five levels are -1, -0.5, 0, 0.5, and 1 m. Also suppose that the 8-stage p.r.b.s sequence with $\alpha = 1$ m is used to extract the impulse response of the system. Since the "signal" to be extracted is the impulse response with $h(0) = 1$, the magnitude of the "noise" relative to the signal strength is simply $E[f_d(t)n(t+\zeta)]/\alpha^2$ according to Eq. (24). Regard this quantity as a scaled noise, which is plotted together with the 5-level noise sequence in the top portion of Fig. 3. Their cumulative averages are shown in the bottom portion of Fig. 3. It is seen that, by cross-correlating the p.r.b.s sequence with the noise, the effect of the noise is significantly reduced. Furthermore, Eq. (24) indicates that the impulse response is magnified by α^2 while $E[f_d(t)n(t+\zeta)]$ is only proportional to α. Thus when the system can tolerate a stronger p.r.b.s, the effect of the additive data noise can be reduced further by using a greater α.

9 Leak Detection Rationale

In leak detection, it is only necessary to extract the impulse response for the time span during which the "imaginary" unit head pulse propagates from the valve toward the reservoir. Hence only a small number (m in Eq. (9)) of cross-correlations need to be computed. If the boundary conditions and the flow conditions are the same as those expected (i.e., the same as those used in establishing the valve modulation) and if no leak exists, then the envelope of the peaks of the extracted impulse response should be a straight line on the ln (h) versus distance plot. If the envelope of the peaks is not as expected (i.e., not a straight line), then a leak or leaks may be suspected. Furthermore, if a discontinuous downward shift in h appears in the plot, and the line segments exhibit different slopes, then a leak must exist. Statistical methods can be applied to discern the discontinuity and the slope change and the results will be the basis for leak alarm.

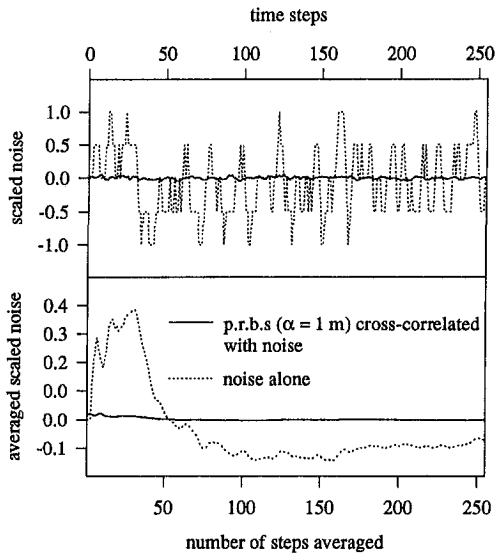

Fig. 3 A sample showing the reduced noise effect and faster convergence to zero when correlated with a p.r.b.s

10 Application Example

Consider a 30 cm inside diameter pipeline with a length of 20,000 m. Let $\bar{Q} = 0.1$ m^3/s, $\bar{H}_r = 200$ m, and $a = 1070$ m/s. The pipe has a relative roughness of 0.00017, from which $f = 0.022$ and $\bar{H}_L = 49.3$ m. The pipeline is divided into 10 computational sections resulting in a computational time step size of 1.869 s.

Numerical experimentations were carried out to determine the needed period of the p.r.b.s sequence p and the time period T (or N in Eq. (9)) over which cross-correlations should be carried out. A 4-stage shift register with a parity check on the first and second stages, a 6-stage shift register with a parity check on the first and second stages, and an 8-stage shift register with parity checks on the first, second, sixth, and seventh stages were used. The half amplitude of the imposed head disturbance, used in establishing the valve modulation, is 1 m. An N equaling to $2p$ was used for all cases. The results in terms of the envelope of the natural log of the peaks of the head disturbance propagating from the valve (node 11) to the reservoir (node 1) are shown in Fig. 4. Progressively better results were obtained with more stages. The result of the 8-stage register was compared with head disturbance propagation calculated directly and the discrepancies were less than 0.5 percent. Thus, the 8-stage p.r.b.s sequence was chosen.

A portion of the p.r.b.s sequence and the corresponding valve modulation are shown in Fig. 5. Note that there are no large valve excursions and the head disturbances at the valve always switches between 1 and -1 m. Therefore, there is no significant interference to the flow condition, a feature important in real-time leak detection.

The time histories of the extracted head disturbances when there is no leak are shown in Fig. 6 as dotted lines. The response at each node is a series of pulses with an alternating sign and diminishing amplitude. Right at the valve (node 11), the extracted peak response is 1 m, equaling the peak of the imaginary impulse imposed there. Collectively, the local responses indicate the propagation of a pulse from the valve toward the reser-

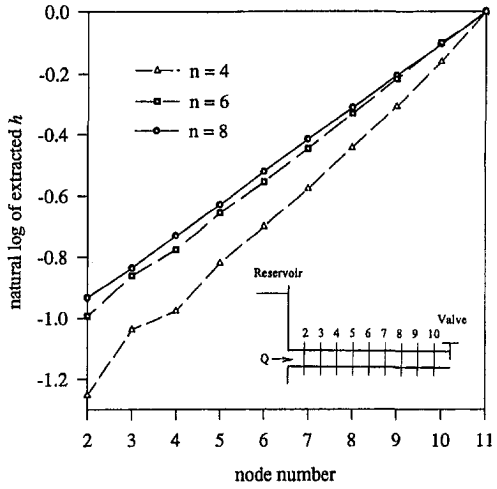

Fig. 4 Extracted head response with 4-, 6-, and 8-stage shift registers

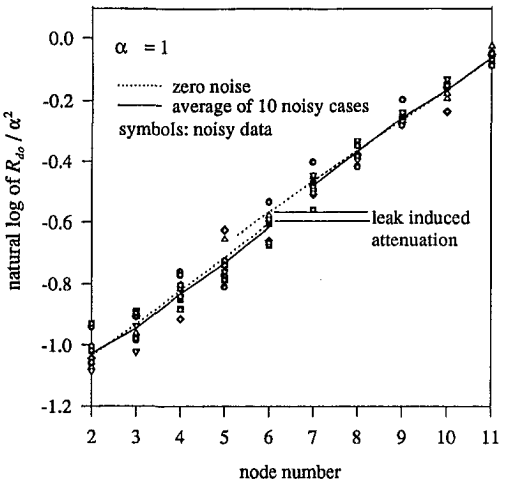

Fig. 7 Extracted head disturbances with and without data noise (p.r.b.s half amplitude α = 1 m)

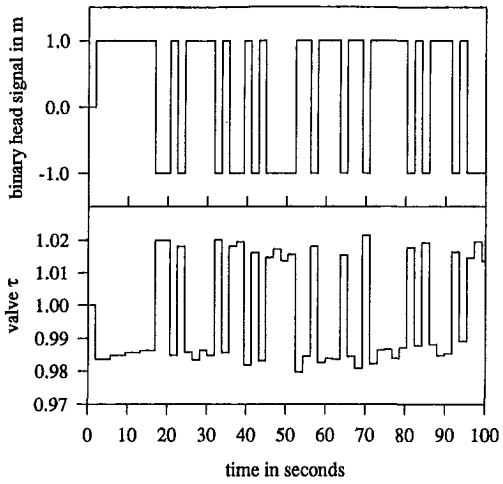

Fig. 5 The beginning portion of the 8-stage binary head signal and the corresponding valve modulation

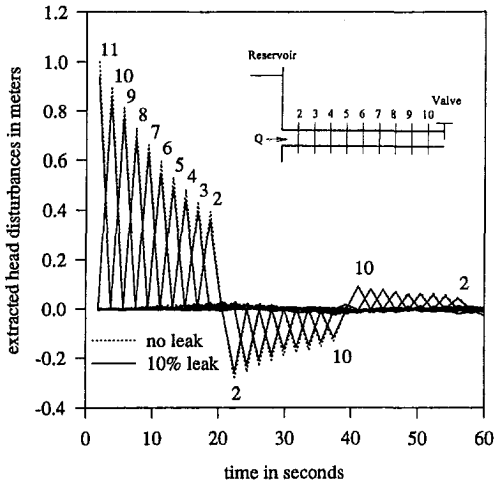

Fig. 6 Extracted head response to an imaginary 1 meter pulse imposed at the valve at time zero

voir and the reflection from the reservoir toward the valve. Frictional resistance and the associated line pack cause the peaks to attenuate over distance and time. The exponential decay of the peaks is evident.

Suppose that, unknown to the pipeline operator, a 10 percent leak (i.e., 0.01 m^3/s) has developed at the mid-length of the pipeline (node 6). With the same boundary conditions, the flow leaving the reservoir is now greater (0.1062 versus 0.1000 m^3/s) and the flow exiting the valve is now less (0.0962 versus 0.1000 m^3/s). The head at the valve is slightly reduced (45.7 versus 49.3 m). The extracted response using the valve modulation established previously will be different from the expected or no-leak response. In fact, the extracted response is only an approximation. This is because prior knowledge of the leak location and the leak flow rate are required to establish the correct impulse response. However, such prior knowledge is impossible to obtain. The extracted response when the leak is present is shown as solid lines in Fig. 6. It is seen that the peaks are lower than those associated with the intact pipeline. The exponential decay of the peaks is still evident.

The effect of the leak stands out better when the envelope of the natural log of the peak head disturbances is plotted against distance as dotted lines in Fig. 7. The line segment from node 11 to node 7 is extended beyond node 6 to demonstrate the discontinuous downward shift caused by the leak at node 6. Also noticeable is that the slope for the peak envelope from node 2 to node 6 is greater than that from node 7 to node 11. The greater mean flow upstream from the leak caused greater attenuation (see Eq. (12)) and hence the greater slope.

The effect of noise is investigated by adding a 5-level random noise sequence (described above) to each of the ten "measured" head disturbances. Ten sets of noise sequences were used and the results are shown by the symbols in Fig. 7. The average of the noisy results is indicated by the two solid line segments. There is considerable scatter in the noisy results and their average does not quite follow the dotted lines of the zero-noise case. Clearly, more impulse responses need to be extracted and averaged. Alternatively, a larger α can be used to reduce the effect of noise. This is demonstrated in Fig. 8 where α was increased from 1 to 2 m while the remaining data remained the same. As a result, the scatters were reduced by half and the averages closely followed the dotted lines associated with the zero-noise case.

11 Discussion

As long as it is not interfering with a pipeline's normal operation, the half amplitude α of the p.r.b.s sequence can be increased to minimize the effect of additive data noise. In the above example, α = 1 m corresponds to a noise-level p.r.b.s sequence. Since the level of head noise is usually much smaller than the head in a typical pipeline, a α many times greater than

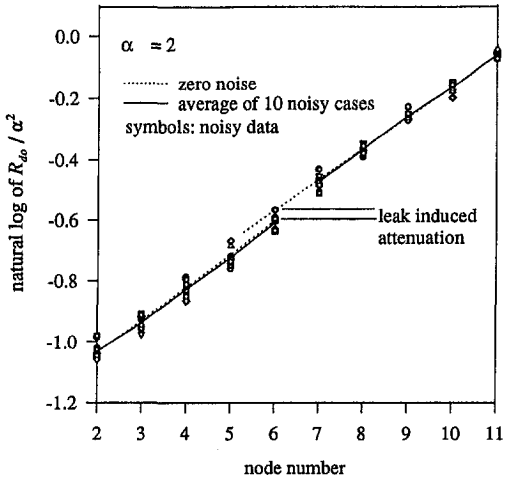

Fig. 8 Extracted head disturbances with and without data noise (p.r.b.s half amplitude α = 2 m)

the noise amplitude may be used. Hence the effect of additive data noise can be controlled to an acceptable level.

How sensitive is the leak induced attenuation of a head pulse? From Eqs. (20) and (22), it can be shown that

$$1 - \frac{h}{\Delta h} = \frac{1}{\frac{2\sqrt{2gH_l}}{a}\frac{A}{(C_dA)_l} + 1} \tag{25}$$

This equation is graphed in Fig. 9. The fractional attenuation of a head pulse due to a leak is indicated by $1 - h/\Delta h$. The size of the leak opening relative to the cross-sectional area of the pipe and the leak opening's resistance to flow are represented by the $(C_dA)_l/A$ along the abscissa. The fractional attenuation is more sensitive to the size of the leak opening when the mean head at the leak is smaller. For a fixed leak opening, the fractional attenuation becomes progressively greater as the mean head at the leak becomes smaller. To give a perspective, the point representing the conditions of the previous example is indicated in the figure.

Since the fractional attenuation approaches zero for a leak through a very small opening in a high head system, such a leak may not be detectable by the proposed method. However, different methodologies may be used for different size leaks (Mear, 1993). For detecting moderate-sized leaks, the proposed method offers two advantages over the common mass balance method (Liou, 1993). First, this new method does not require mass flow measurements at both ends of the pipeline. Such measurements are very expensive and can be physically difficult to implement on existing pipelines. Secondly, the proposed method can detect and locate one or more leaks. The method uses a logic different and independent from those currently in use. When used in conjunction with an existing leak detection system, the frequency of false alarms can be reduced.

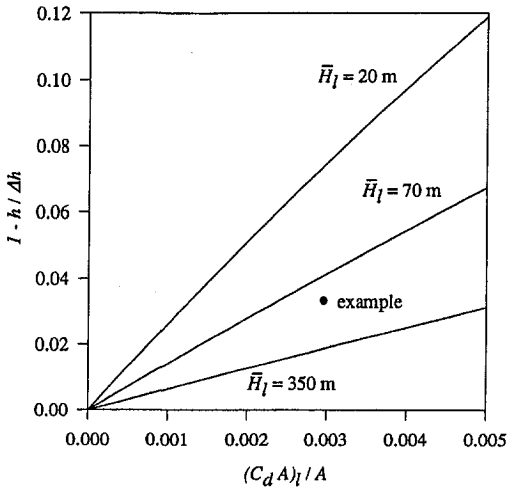

Fig. 9 Sensitivity of fractional attenuation of a head pulse caused by a leak (wave speed a = 1070 m/s)

12 Summary and Conclusion

When a wide-band disturbance signal is applied to the input of a linear system, the cross-correlation of this signal with the system's output is proportional to the impulse response of the system. Based on this fact and using a pseudo random binary signal to approximate the wide-band noise, a method to extract the impulse response of a pipeline under steady state conditions is proposed. Because the amplitude of the signal can be at the noise level, the impulse response can be extracted in real time without interfering pipeline operation. Since the impulse response is characteristic of the hydraulics of the pipeline, it provides a basis for real-time pipeline leak detection.

A method for generating pseudo random binary head signals, an explanation of their usefulness in impulse response extraction, and the theory on impulse response extraction by cross-correlation are briefly discussed. Small-amplitude transient pipe flows are then modeled numerically to generate surrogate "measured" head data. The impulse response to a unit head pulse, with and without a leak, is explained and the leak detection rationale established. Using valve modulation to generate the pseudo random binary head disturbances is proposed. The adverse effect of additive data noise and how to minimize it are investigated. An application example is given to show how the proposed approach can work.

References

Balcomb, J. D., Demuth, H. B., and Gyftopoulos, E. P., "A Cross-correlation Method for Measuring the Impulse Response of Reactor Systems," *Nuclear Science and Engineering,* Vol. 11, No. 2, Oct., pp. 159–166, 187–188.

Baumert, L. D., 1964, "Generation of Specified Sequences," *Digital Communications with Space Applications,* Golomb, S. W., ed., Prentice-Hall, pp. 17–26.

Beauchamp, K., and Yuan, C., 1979, *Digital Methods for Signal Analysis,* George Allen & Unwin, London, pp. 203–207.

Dallabetta, M. J., 1996, "Using Cross-correlation Techniques to Determine the Impulse Response Characteristics of Linear Systems," MS thesis, University of Idaho, Moscow, Idaho.

Diggle, P. J., 1990, *Time Series: A Biostatistical Introduction,* Clarendon Press, Oxford, p. 204.

Eykhoff, P., 1874, *System Identification—Parameter and State Estimation,* Wiley, pp. 386–394.

Golomb, S. W., 1964, "Introduction to Digital Communication," *Digital Communications with Space Applications,* Golomb, S. W., ed., Prentice Hall, pp. 7–15.

Li, H. W., Dallabetta, M. J., and Demuth, H. B., 1994, "Measuring the Impulse Response of Linear Systems using an Analog Correlator," *Proceedings of 1994 IEEE International Symposium on Circuits and Systems,* Vol. 5, London, England, pp. 65–68.

Liou, C. P., 1993, *Pipeline Variable Uncertainties and Their Effects on Leak Detectability,* API Publication 1149, American Petroleum Institute, Washington, D.C.

Liou, C. P., and Tian, J., 1995, "Leak Detection—Transient Flow Simulation Approaches," ASME *Journal of Energy Resources Technology,* Vol. 117, No. 3, pp. 243–248.

Liou, C. P., 1996, "Pipeline Integrity Monitoring Using System Impulse Response," *Proceedings of the 1st International Pipeline Conference, American Society of Mechanical Engineers,* Vol. 2, pp. 1137–1142.

Newland, D. E., 1975, *An Introduction to Random Vibrations and Spectral Analysis,* Longman Group Limited, London, pp. 62–66, 77–78, 175–181.

Takahashi, Y., Rabins, M. J., and Auslander, D. M., 1972, *Control and Dynamic Systems,* Addison-Wesley, Reading, MA, pp. 581–582.

Wylie, E. B., and Streeter, S. L., 1993, *Fluid Transients in Systems,* Prentice Hall, Englewood Cliffs, N.J., pp. 215–243, 289–290.

Thermoelectrically Driven Melt Motion During Floating Zone Crystal Growth With an Axial Magnetic Field

Y. Y. Khine
Graduate Research Assistant.

J. S. Walker
Professor. Fellow ASME

Department of Mechanical and Industrial Engineering, University of Illinois, Urbana, Il 61801

During semiconductor crystal growth with an externally applied magnetic field, thermoelectric currents may drive a melt circulation which affects the properties of the crystal. This paper treats a model problem for a floating zone process with a uniform axial magnetic field, with planar solid-liquid interfaces, with a cylindrical free surface, with a parabolic temperature variation along the crystal-melt interface, and with an isothermal feed rod-melt interface. The ratio of the electrical conductivities of the liquid and solid is a key parameter. The azimuthal velocity is much larger than the radial or axial velocity. There is radially outward flow near the crystal-melt interface which should be beneficial for the mass transport of dopants and species.

Introduction

In the floating zone process, a small zone of liquid is held by surface tension between the melting end of a cylindrical feed rod and the growing end of a coaxial cylindrical single crystal. An advantage of this process is that there is no contamination from a crucible or ampoule. A disadvantage is that the temperature variation along the free surface drives a thermocapillary convection which is almost always unsteady without a magnetic field. Unsteady melt motions produce fluctuations in the crystal growth rate which result in undesirable dislocations and striations in the crystal. Striations are spatial oscillations in the crystal's concentration of elements or dopants which are added to give the crystal the desired electrical or optical properties.

Most molten semiconductors are good electrical conductors, so that the application of a magnetic field with a magnetic flux density, B_o, as low as 0.5 T can reduce the magnitude and radial extent of the unsteady thermocapillary convection. Thus, the residual striations are weaker and are confined to a peripheral part of the crystal (Robertson and O'Connor, 1986; Cröll et al., 1994). Morthland and Walker (1998) have shown that a stronger magnetic field should eliminate all unsteadiness in the thermocapillary convection. Recently, Cröll et al. (1998) found a band of regularly spaced striations in the crystals grown in a strong magnetic field with $B_o = 3.0$ T. Cröll et al. speculate that these unexpected striations might be associated with the azimuthal melt motion driven by thermoelectric currents.

Since the values of the absolute thermoelectric power for the solid and liquid, S_s and S, respectively, are quite different for most semiconductors, a radial temperature variation along the crystal-melt interface would drive a meridional (radial and axial) circulation of thermoelectric currents through the crystal, melt and the feed rod. For example, pure silicon may have a temperature variation of several degrees along the crystal-melt interface due to the differences between the faceted growth near the centerline and the atomically rough growth near the periphery (Cröll et al., 1998). Thermoelectric effects may even play a more important role in the growth of alloyed semiconductors, such as five percent silicon and ninety-five percent germanium, because a larger temperature variation occurs at the crystal-melt interface due to the compositional dependence of the solidification temperature. The radial thermoelectric current interacts with the externally applied axial magnetic field to drive an important melt motion, which is known as the thermoelectric magnetohydrodynamic (TEMHD) flow.

Shercliff (1979) presented the first and most complete discussion of TEMHD flows for the liquid-metal coolants in fusion reactors. The TEMHD effects during bulk crystal growth with an applied magnetic field were first studied by Gorbunov (1987) and Gel'fgat and Gorbunov (1989). Moreau et al. (1993) showed that the application of a magnetic field results in strong TEMHD flows around the dendrites during the dendritic solidification of metallic alloys. Khine and Walker (1997, 1998) presented numerical and asymptotic results for the TEMHD flow in a vertical Bridgman crystal growth process with an applied axial magnetic field. The TEMHD flows for the Bridgman and floating-zone processes are different. In the Bridgman process, the melt boundary which is parallel to the crystal-melt interface is an ampoule surface or a free surface, both of which are electrical insulators which limit the thermoelectric currents and the resultant melt circulation, particularly for a strong magnetic field. In the floating zone process, the feed rod has the same electrical conductivity as the crystal and provides an important part of the electrical circuit. Khine et al. (1998) presented a strong-field asymptotic solution for TEMHD flows in floating zone crystal growth process with an applied axial magnetic field. Unfortunately, the asymptotic solution predicts an infinite velocity in the inviscid core region which is clearly unrealistic for any real situation. This paper presents numerical results for a floating zone process, and the difference between the asymptotic and numerical solutions is discussed.

A complete model of the TEMHD flows for alloyed semiconductor crystal growth would require treating the complex interactions among the thermal field, the thermally and compositionally driven buoyant convection, and the compositional dependence of the solidification temperature in order to determine the actual shape of the crystal-melt interface and the temperature variation along this interface. However, in our analysis, we assume a planar crystal-melt interface with a parabolic radial temperature variation in order to examine the basic physical phenomena in TEMHD. We also assume (1) that the feed rod-melt interface is planar and isothermal, (2) that the free surface is cylindrical, and (3) that the magnetic field is sufficiently strong that the meridional convection of linear momentum is negligible.

Contributed by the Fluids Engineering Division for publication in the JOURNAL OF FLUIDS ENGINEERING. Manuscript received by the Fluids Engineering Division January 27, 1998; revised manuscript received August 18, 1998. Associate Technical Editor: M. S. Cramer.

Problem Formulation and Solution

The thermoelectric currents in the crystal, melt and feed rod produce an induced magnetic field, which is superimposed on the applied axial magnetic field produced by a solenoid around the crystal growth furnace. The characteristic ratio of the induced magnetic field strength to the applied one is the magnetic Reynolds number, $R_m = \mu_p j_{ac} R/B_o$, where μ_p is the melt's magnetic permeability, j_{ac} is the characteristic magnitude of the thermoelectric current density, and R is the radius of the liquid zone. Since this ratio is very small for all crystal growth processes, so that the induced magnetic field is negligible, the dimensional magnetic field is $\mathbf{B}^* = B_o\hat{z}$, where $\hat{r}$, $\hat{\theta}$ and $\hat{z}$ are unit vectors for the cylindrical coordinates with the z axis along the common centerline of the crystal, melt and feed rod. We treat a melt zone whose length and diameter are equal. With r and z normalized by R, the liquid occupies the cylinder bounded by a free surface at $r = 1$, by the crystal-melt interface at $z = -1$, and by the feed rod-melt interface at $z = 1$. The crystal and feed rod have outside surfaces at $r = 1$ and extend to $z = -\infty$ and $z = \infty$, respectively.

For an axisymmetric flow, the characteristic ratio of the electromagnetic (EM) body force to the meridional convection of linear momentum is the interaction parameter, $N = \sigma B_o^2 R/\rho V_m$, where σ and ρ are the melt's electrical conductivity and density, while V_m is the characteristic value for the meridional (radial and axial) velocities. We assume that the magnetic field is sufficiently strong that $N \gg 1$, and that the meridional convection of linear momentum is negligible. The governing equations become linear with these assumptions, so that the TEMHD flow is decoupled from other melt motions, such as the thermocapillary convection or the thermally and compositionally driven buoyant convections. This paper focuses only on the TEMHD flow.

Further, the TEMHD problem splits into two sequential problems. The first problem governs the azimuthal melt motion which is driven by the meridional thermoelectric currents, and this is decoupled from the meridional motion. Khine and Walker (1998) showed that the appropriate characteristic azimuthal velocity and the characteristic meridional electric current density are $V_\theta = (S - S_s)(\Delta T)/B_o R$, and $j_{ac} = \sigma(S - S_s)(\Delta T)/R$, respectively, for $Ha \geq 1$, when the EM body forces are at least as strong as the viscous forces. Here, (ΔT) is the dimensional temperature difference between the center and periphery of the crystal-melt interface, and $Ha = B_o R(\sigma/\mu)^{1/2}$ is the Hartmann number while μ is the melt's viscosity.

For the melt, we introduce the electric stream function $h(r, z)$, which satisfies the continuity of meridional electric current density, where

$$j_r = \frac{1}{r}\frac{\partial h}{\partial z}, \quad j_z = -\frac{1}{r}\frac{\partial h}{\partial r}, \tag{1a, b}$$

and the same expressions for the crystal and feed rod with the subscripts s and f, respectively. The dimensionless governing equations of the azimuthal melt problem are

$$\frac{1}{r}\frac{\partial h}{\partial z} = Ha^{-2}\left(\frac{\partial^2 \nu_\theta}{\partial r^2} + \frac{1}{r}\frac{\partial \nu_\theta}{\partial r} + \frac{\partial^2 \nu_\theta}{\partial z^2} - \frac{\nu_\theta}{r^2}\right), \tag{2a}$$

$$r\frac{\partial \nu_\theta}{\partial z} = \frac{\partial^2 h}{\partial r^2} - \frac{1}{r}\frac{\partial h}{\partial r} + \frac{\partial^2 h}{\partial z^2}, \tag{2b}$$

$$0 = \frac{\partial^2 h_s}{\partial r^2} - \frac{1}{r}\frac{\partial h_s}{\partial r} + \frac{\partial^2 h_s}{\partial z^2}, \tag{2c}$$

$$0 = \frac{\partial^2 h_f}{\partial r^2} - \frac{1}{r}\frac{\partial h_f}{\partial r} + \frac{\partial^2 h_f}{\partial z^2}. \tag{2d}$$

Here, Eq. $(2a)$ is the azimuthal component of the linear momentum equation without the meridional convection of azimuthal velocity, without θ derivatives due to axisymmetry, and with the azimuthal component of EM body force due to the interaction of radial thermoelectric current and the axial magnetic field. Equations $(2b) - (2d)$ are the results of cross-differentiating the r and z components of the Ohm's law for the melt, crystal and feed rod in order to eliminate the static electric field $-\nabla\phi$ and the Seebeck EM force $-S\nabla T$ or $-S_s\nabla T$, where ϕ is the electric potential function (voltage) and T is the temperature.

The boundary conditions for the azimuthal motion are

$$\nu_\theta = 0, \quad h = h_s, \quad \left(\frac{\sigma}{\sigma_s}\right)\frac{\partial h_s}{\partial z} - \frac{\partial h}{\partial z} = r\frac{\partial T_i}{\partial r}, \quad \text{at } z = -1; \tag{3a–c}$$

$$\nu_\theta = 0, \quad h = h_f, \quad \left(\frac{\sigma}{\sigma_s}\right)\frac{\partial h_f}{\partial z} - \frac{\partial h}{\partial z} = 0, \quad \text{at } z = 1; \tag{3d–f}$$

$$\frac{\partial \nu_\theta}{\partial r} - \frac{\nu_\theta}{r} = 0, \quad h = 0, \quad \text{at } r = 1, \text{ for } -1 \leq z \leq 1; \tag{3g–h}$$

$$h_f = 0, \quad \text{at } r = 1, \text{ for } z \geq 1; \tag{3i}$$

$$h_s = 0, \quad \text{at } r = 1, \text{ for } z \leq -1; \tag{3j}$$

$$h_f \to 0, \text{ as } z \to \infty, \quad h_s \to 0, \text{ as } z \to -\infty, \tag{3k, l}$$

where σ_s is the electrical conductivity for both the crystal and feed rod, while T_i is the deviation of the temperature along the crystal-melt interface from its value at $r = 0$ and is normalized by (ΔT), so that $T_i = r^2$ with our assumed parabolic temperature variation along the crystal-melt interface. Equations $(3b)$ and $(3e)$ result from the continuity of the axial electric current density at each solid-liquid interface, while Eqs. $(3c)$ and $(3f)$ come from the continuity of ϕ at these interfaces. The only inhomogeneous term in this boundary value problem appears in Eq. $(3c)$ and comes from the jump in the radial Seebeck electromotive force across the crystal-melt interface associated with the difference between the absolute thermoelectric powers, S and S_s, in the melt and crystal. Since the feed rod-melt interface is assumed to be isothermal, there is no inhomogeneous term in Eq. $(3f)$.

The separation of variables solution of Eqs. $(2c)$ and $(2d)$ with Eqs. $(3i) - (3l)$ for the electric stream functions in the feed rod and crystal are

$$h_f = r\sum_{j=1}^{\infty} D_j J_1(\lambda_j r)\exp(-\lambda_j(z-1)), \tag{4a}$$

$$h_s = r\sum_{j=1}^{\infty} C_j J_1(\lambda_j r)\exp(\lambda_j(z+1)), \tag{4b}$$

respectively, where C_j and D_j are sets of unknown coefficients, J_k is the Bessel function of the first kind and of order k, and λ_j are the roots of $J_1(\lambda_j) = 0$.

The characteristic meridional velocity is determined by the balance between the driving radial centrifugal force due to the azimuthal melt velocity and the opposing radial EM body force, so that $V_m = \rho V_\theta^2/R\sigma B_0^2 = \rho(S - S_s)^2(\Delta T)^2/R^3\sigma B_0^4$ (Khine and Walker, 1998). For the dimensionless meridional velocities, we introduce a stream function $\psi(r, z)$ which satisfies the continuity of velocity, where

$$\nu_r = \frac{1}{r}\frac{\partial \psi}{\partial z}, \quad \nu_z = -\frac{1}{r}\frac{\partial \psi}{\partial r}. \tag{5a, b}$$

With the azimuthal component of Ohm's law, cross-differentiating the radial and axial components of the linear momentum

equation in order to eliminate the pressure terms and using Eqs. (5*a*) and (5*b*), we obtain the equation governing ψ,

$$\frac{\partial^2\psi}{\partial z^2} - Ha^{-2}\left(\frac{\partial^4\psi}{\partial r^4} - \frac{2}{r}\frac{\partial^3\psi}{\partial r^3} + \frac{3}{r^2}\frac{\partial^2\psi}{\partial r^2} - \frac{3}{r^3}\frac{\partial\psi}{\partial r} + 2\frac{\partial^4\psi}{\partial r^2\partial z^2} - \frac{2}{r}\frac{\partial^3\psi}{\partial r\partial z^2} + \frac{\partial^4\psi}{\partial z^4}\right) = 2\nu_\theta\frac{\partial\nu_\theta}{\partial z}. \quad (6)$$

The right-hand side of Eq. (6) is the only inhomogeneous term which drives the meridional melt motion in the boundary value problem governing ψ and is known from the solution for the azimuthal motion. The boundary conditions are

$$\psi = 0, \quad \frac{\partial\psi}{\partial z} = 0, \quad \text{at} \quad z = -1 \quad \text{and at} \quad z = 1; \quad (7a, b)$$

$$\psi = 0, \quad \frac{\partial^2\psi}{\partial r^2} - \frac{\partial\psi}{\partial r} = 0, \quad \text{at} \quad r = 1. \quad (7c, d)$$

We used a Chebyshev spectral collocation method to solve Eqs. (2*a*) and (2*b*) with Eqs. (3*a*) – (3*i*). We applied a Galerkin method for the conditions at the solid-liquid interfaces in order to get better results at the interfaces since the Gauss-Lobatto collocation points are optimal for the Chebyshev polynomials, but are not for the Bessel functions. With this approach, the number of terms in the series in Eqs. (4) can be larger than the number of radial collocation points. Therefore, we used the orthogonality of the Chebyshev polynomials for Eqs. (3*a*), (3*b*), (3*d*), and (3*e*) and we used the orthogonality of the Bessel functions for Eqs. (3*c*) and (3*f*). The integrals of the Chebyshev polynomials times the Bessel functions with their weighting functions were evaluated numerically using a trapezoidal-rule quadrature. Similarly, for the meridional motion, we solved Eqs. (6) and (7) using the same spectral collocation method. For all of the Hartmann numbers considered here, the Chebyshev polynomial representations gave excellent results with twenty polynomials in the radial direction, thirty polynomials in the axial direction and one hundred terms in the separation-of-variables solution for h_f or h_s.

Results and Discussion

The parameters in this problem are (σ/σ_s) and Ha. For (σ/σ_s), we used the value for silicon, namely $(\sigma/\sigma_s) = 20$. The contours of h, h_f and h_s for $Ha = 100$ are presented in Fig. 1. All of the thermoelectric currents flow through the crystal with a maximum value of $h_s = 0.0089$. Part of the current entering the melt returns directly to the crystal by completing its circuit through the Hartmann layer with $O(Ha^{-1})$ thickness adjacent to the crystal-melt interface. The rest of the current flows axially across the inviscid central melt region, and splits to complete its circuit through the feed rod and adjacent Hartmann layers which act as resistors in parallel. The maximum amount of current in the feed rod is 0.00245 which is about 28 percent of the total current produced in the crystal. Therefore, 72 percent of the total current completes its circuit through the two Hartmann layers in the melt.

The contours of ν_θ for $Ha = 100$ are presented in Fig. 2. The contours begin and end at the free surface. They are almost vertical for $0 < r < 0.6$, and they are concentrated near the liquid-solid interfaces in the Hartmann layers which match the values of ν_θ in the inviscid region and satisfy the no-slip condition at each solid surface. The contours of ν_θ are not straight and vertical for $0.6 < r < 1$ and this region is the parallel layer with $O(Ha^{-1/2})$ thickness adjacent to the free surface. The unrealistic results in the large Hartmann-number asymptotic solution (Khine et al., 1998) result from the assumption that the free-surface parallel layer has effectively zero thickness while it actually occupies $0.6 < r < 1$ for $Ha = 100$. The

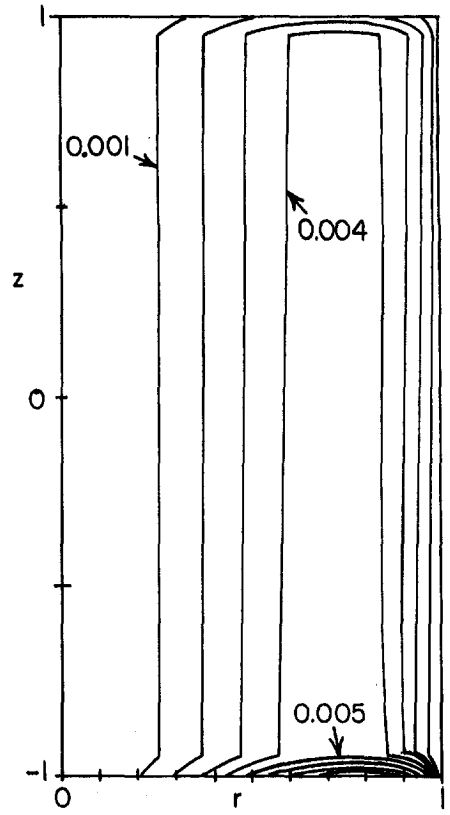

Fig. 1(*a*)

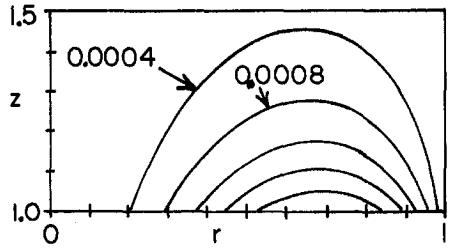

Fig. 1(*b*)

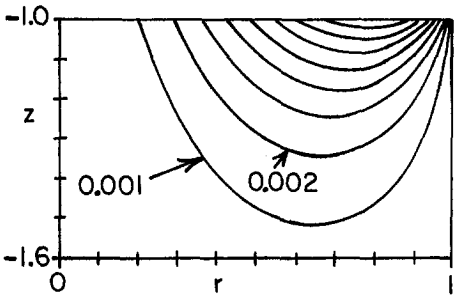

Fig. 1 Streamlines for the meridional thermoelectric currents with $Ha = 100$. (*a*) In the melt, $h = 0.001k$ for $k = 1$ to 8; (*b*) in the feed rod, $h_f = 0.0004k$ for $k = 1$ to 5; (*c*) in the crystal, $h_s = 0.001k$ for $k = 1$ to 8.

maximum ν_θ in this case is 0.522. The maximum ν_θ for $Ha = 50$, 200 and 300 are 0.357, 0.692 and 0.808, respectively, and these contours are similar to those in Fig. 2. The dimensional maximum azimuthal velocity decreases as B_0^{-p} as B_0 is increased. The asymptotic solution for $Ha \gg 1$ indicates that $p = 1$. The numerical results for arbitrary Ha and $(\sigma/\sigma_s) = 20$ indicate that p increases smoothly from 0.45 for $Ha = 50$ to 0.72 for $Ha = 300$, but p is still significantly below the $p = 1$ for $Ha \gg 1$. In order to validate our numerical approach, we compared predictions from an asymptotic solution for $Ha \ll 1$

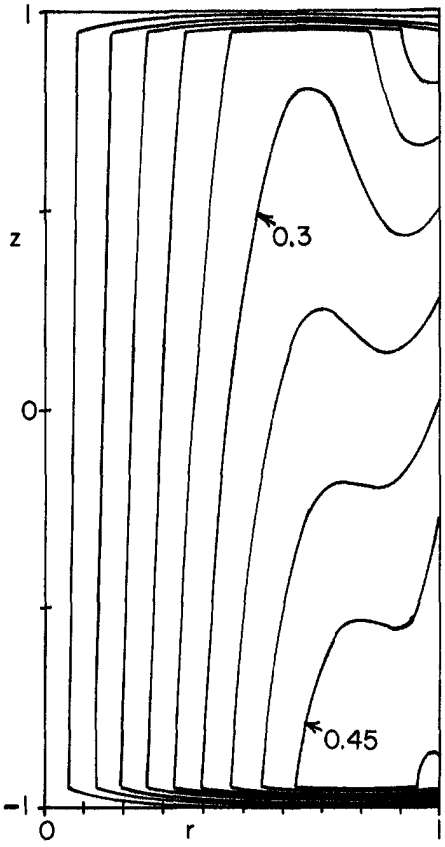

Fig. 2 Contours of ν_θ for $Ha = 100$: $\nu_\theta = 0.05k$ for $k = 1$ to 9

to the numerical results for $Ha = 0.1$ and found agreement to five significant figures.

Figure 3 presents the stream lines for the meridional motion in the melt for $Ha = 100$. The stream lines are concentrated near the free surface, producing an upward motion along the free surface, and circulate downward through the melt and radially outward near the crystal-melt interface in order to complete a loop. The radially outward flow near the crystal-melt interface is desirable for mass transport of dopants and species. The stream function value ranges from -0.00034 to 0.0423 in this case. The maximum values of the stream function for $Ha = 50$, 200, and 300 are 0.0228, 0.0815, and 0.115, respectively. The pattern of stream lines in each case is similar to each other, except that the stream lines become more concentrated near the free surface as the Ha becomes larger.

The maximum value of ν_θ in Fig. 2 is 0.522, while the maximum value of ν_z for the vertically upward flow near the free surface in Fig. 3 is 0.04, but these velocities are normalized by very different characteristic velocities, namely V_θ and V_m. In order to illustrate the extreme difference between the magnitudes of the azimuthal and meridional velocities, we compute the values of V_θ and V_m for molten silicon with $R = 4$ mm, $(S - S_s) = 10$ μV/mK, $(\Delta T) = 3$ K, and $B_o = 2$ T, obtaining $V_\theta = 3.8$ mm/s and $V_m = 1.8$ μm/s.

Only results for $(\sigma/\sigma_s) = 20$ are presented here, but it is easy to obtain results for other values of (σ/σ_s) from these results. For the thermoelectric (TE) current, the feed rod and two Hartmann layers are three electrical resistors in parallel, which are collectively in series with the crystal representing a fourth resistor and the electromotive force provided by the jump in Seebeck voltage at the crystal-melt interface. The division of the TE current between the three parallel resistors only depends on the ratio of the resistance of the feed rod to that of either Hartmann layer, namely $\gamma = Ha^{-1}(\sigma/\sigma_s)$. The results for $Ha = 100$ and $(\sigma/\sigma_s) = 20$ in Figs. 1 and 2 also apply to other combinations of Ha and (σ/σ_s) which give $\gamma = 0.2$. For example, we might double B_o and cut σ_s in half, so that $Ha = 200$ and $(\sigma/\sigma_s) = 40$, but γ is still 0.2. The electrical resistance of every important resistor has been doubled, so that the division of the TE current remains unchanged but the magnitude of every current is cut in half. The half current inside each Hartmann layer interacts with the double field strength to produce the same jump in ν_θ across each Hartmann layer, so that the values of ν_θ in Fig. 2 are the same.

When we plot the maximum values of the stream function versus Ha, $Ha = 50$ seems to be the separator between the small Ha solution, where the viscous effects are dominant, from the large Ha solution where the increase in stream function is proportional to Ha. Figure 4 presents the comparison of numerical solution and large Hartmann-number asymptotic solution for the stream function in the inviscid core region (Khine et al., 1998) of stream function distribution with r at $z = 0$ for $Ha = 100$ and 200. In both cases, the numerical solution starts at zero at centerline and increases to a maximum at a particular r, and then decreases to approach zero at the free surface. However, in the asymptotic solution for the inviscid core, the stream function starts at zero at the centerline and increases to infinity as r approaches one. In the asymptotic solution, all the upward flow is inside the free-surface parallel layer whose thickness is neglected. Therefore, the asymptotic solution gives unrealistic predictions for a relatively thick region near the free surface, even for $Ha = 200$. The difference between the two solutions for $Ha = 100$ is about 15 percent for $r < 0.6$, while for $Ha = 200$ the difference is less than 10 percent for $r < 0.7$.

Conclusions

Although we have ignored some important aspects, such as the concavity of the crystal-melt interface, this model pro-

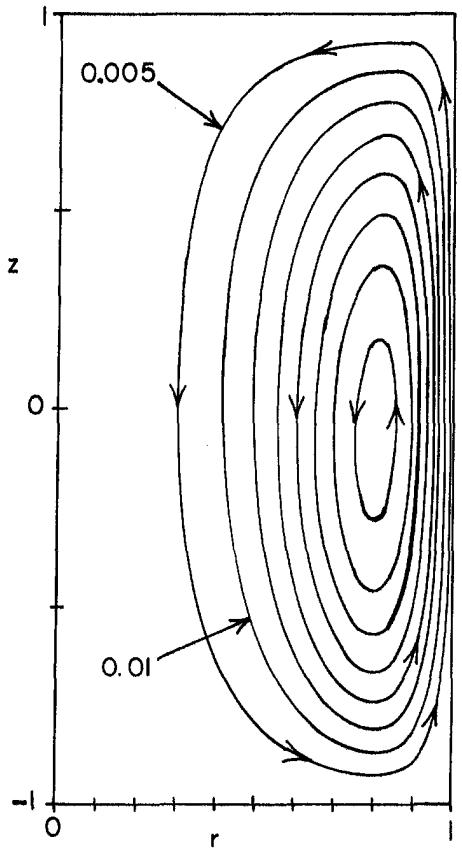

Fig. 3 Streamlines for the meridional melt motion for $Ha = 100$: $\psi = 0.005k$ for $k = 1$ to 8

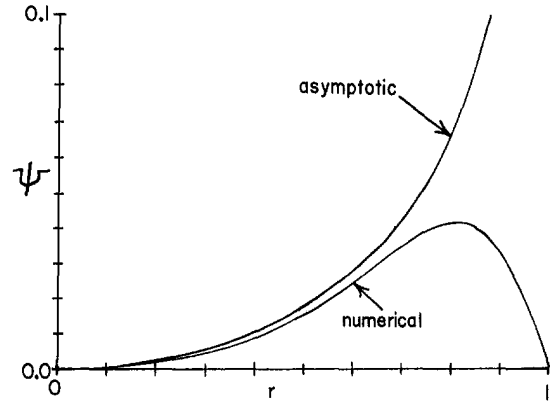

Fig. 4(*a*)

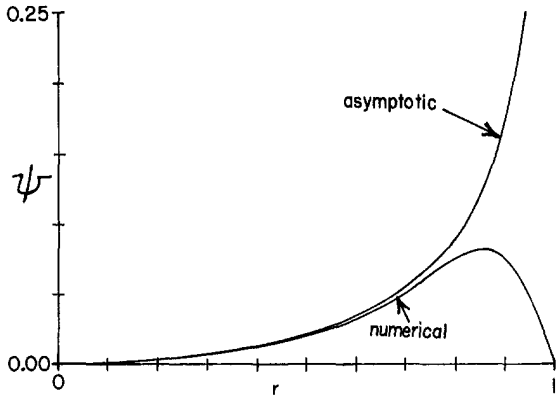

Fig. 4(*b*)

Fig. 4 Comparison of the values of the stream function at $z = 0$ from the numerical solution for arbitrary *Ha* and from the inviscid core solution in a large-*Ha* asymptotic analysis. (*a*) *Ha* = 100; (*b*) *Ha* = 200

vides physical insights into thermoelectric effects during the floating zone semiconductor crystal growth with an externally applied magnetic field. The numerical results are much more realistic than the large Hartmann-number asymptotic results.

A key result is that the TEMHD flows in our model only involves radially outward flows near the crystal-melt interface. If this is true for a complete model including other complex interactions, there will be positive implications for the mass transport of dopants and species. The thermocapillary convection produces radially inward flows near the crystal-melt interface. For alloyed crystal growth, the compositionally driven buoyant convection generally involves radially inward flow near the crystal-melt interface. Therefore, there may be a magnetic field strength where the outward TEMHD flow would cancel the inward flow from the thermocapillary and buoyant convections, so that the TEMHD may then eliminate radial macrosegregation in the crystal.

Another important aspect of the TEMHD flows is the difference between the order of magnitudes of the azimuthal and meridional velocities. According to our numerical results, the azimuthal velocity is much larger than the meridional velocities for typical values of Ha. Unfortunately, the present solution for steady axisymmetric case does not explain the striations observed experimentally by Cröll et al. (1998). However, we noticed that the experimentally observed striations occur in an annular band which is close to the radius where the maximum v_θ occurs. A magnetically damped Taylor-Couette instability in the strong azimuthal flow might produce axial vortices which are convected azimuthally and which might produce the observed striations.

Acknowledgments

This research was supported by the National Aeronautics and Space Administration under Cooperative Research Agreement NCC8-90 and by the National Science Foundation under Grant CTS 94-19484.

References

Cröll, A., Dold, P., and Benz, K. W., 1994, "Segregation in Si Floating Zone Crystals Grown Under Microgravity and in a Magnetic Field," *Journal of Crystal Growth,* Vol. 137, pp. 95–101.

Cröll, A., Szofran, F. R., Dold, P., Benz, K. W., and Lehoczky, S. L., 1998, "Floating-Zone Growth of Silicon in Magnetic Fields: Part II: Strong Static Axial Fields," *Journal of Crystal Growth,* Vol. 183, pp. 554–563.

Gel'fgat, Y. M., and Gorbunov, L. A., 1989, "An Additional Source of Forced Convection in Semiconductor Melts during Single-Crystal Growth in Magnetic Fields," *Soviet Physics Dokl.,* Vol. 34, pp. 470–473.

Gorbunov, L. A., 1987, "Effect of Thermoelectromagnetic Convection on the Production of Bulk Single-Crystals Consisting of Semiconductor Melts in a Constant Magnetic Field," *Magnetohydrodynamics,* Vol. 23, pp. 404–408.

Khine, Y. Y., and Walker, J. S., 1997, "Thermoelectric Magnetohydrodynamic Effects during Bridgman Semiconductor Crystal Growth with a Uniform Axial Magnetic Field: Large Hartmann-Number Solution," *Proceedings of Third International Conference on Transfer Phenomena in Magnetohydrodynamic and Electroconducting Flows,* Aussois, France.

Khine, Y. Y., and Walker, J. S., 1998, "Thermoelectric Magnetohydrodynamic Effects during Bridgman Semiconductor Crystal Growth with a Uniform Axial Magnetic Field," accepted by the *Journal of Crystal Growth,* Vol. 183, pp. 150–158.

Khine, Y. Y., Ma, N., and Walker, J. S., 1998, "Thermoelectrically Driven Melt Motion During Floating Zone Crystal Growth with a Strong Axial Magnetic Field," *Proceedings of the Seventh AIAA/ASME Joint Thermophysics and Heat Transfer Conference,* Albuquerque, NM.

Moreau, R., Laskar, O., and Tanaka, M., 1993, "Thermoelectric Magnetohydrodynamic Effects on Solidification of Metallic Alloys in the Dendritic Regime," *Materials Science and Engineering,* Vol. A173, pp. 93–100.

Morthland, T. E., and Walker, J. S., 1998, "Instabilities of Dynamic Thermocapillary Liquid Layers with Magnetic Fields," *Journal of Fluid Mechanics.*

Robertson, G. D., and O'Connor, D., 1986, "Magnetic Field Effects in Float-Zone Si Crystal Growth. III. Strong Axial Fields," *Journal of Crystal Growth,* Vol. 76, pp. 111–122.

Shercliff, J. A., 1979, "Thermoelectric Magnetohydrodynamics," *Journal of Fluid Mechanics,* Vol. 91, pp. 231–251.

Nancy Ma
Assistant Professor,
Department of Mechanical & Aerospace Engineering & Engineering Mechanics,
University of Missouri, Rolla, MO 65409

John Walker
Professor,
Department of Mechanical & Industrial Engineering,
University of Illinois, Urbana, IL 61801

David Bliss
Physicist.

George Bryant
Ceramic Engineer.

Rome Laboratory,
Hanscom Air Force Base,
MA 01731

Forced Convection During Liquid Encapsulated Crystal Growth With an Axial Magnetic Field

This paper treats the forced convection, which is produced by the rotation of the crystal about its vertical centerline during the liquid-encapsulated Czochralski or Kyropoulos growth of compound semiconductor crystals, with a uniform vertical magnetic field. The model assumes that the magnetic field strength is sufficiently large that convective heat transfer and all inertial effects except the centripetal acceleration are negligible. With the liquid encapsulant in the radial gap between the outside surface of the crystal and the vertical wall of the crucible, the forced convection is fundamentally different from that with a free surface between the crystal and crucible for the Czochralski growth of silicon crystals. Again unlike the case for silicon growth, the forced convection for the actual nonzero electrical conductivity of an indium-phosphide crystal is virtually identical to that for an electrically insulating crystal. The electromagnetic damping of the forced convection is stronger than that of the buoyant convection. In order to maintain a given balance between the forced and buoyant convections, the angular velocity of the crystal must be increased as the magnetic field strength is increased.

Introduction

In the Czochralski (CZ) process, a cylindrical semiconductor crystal is grown from a body of liquid (melt) contained in a cylindrical crucible whose radius is larger than that of the crystal. For silicon, the melt has a free surface between the bottom circumference of the crystal and the vertical wall of the crucible. For compound semiconductors, such as gallium-arsenide (GaAs) or indium-phosphide (InP), the radial gap above the melt between the crystal periphery and the vertical crucible wall is filled with a liquid encapsulant, which is usually boron oxide. The encapsulant prevents the evaporation of the volatile element, i.e., the arsenic or phosphorus. Since boron oxide blocks part of the thermal radiation spectrum, the encapsulant also reduces the axial temperature gradient in the crystal, so that fewer dislocations develop after crystallization due to thermal stresses. Very small amounts of other elements or dopants are added to the melt to give the crystal the desired electrical or optical properties. Recent advances in integrated circuits and in optical devices have produced a demand for much smaller dislocation densities and for much more uniform dopant distributions in compound semiconductor crystals.

Without a magnetic field, the melt motion is often unsteady, and the resultant fluctuations in the heat transfer and dopant transport from the melt to the crystal produce dislocations in the crystal and spatial oscillations of the dopant concentration in the crystal, called striations. Since molten semiconductors are excellent electrical conductors, a uniform, vertical (axial) magnetic field produced by a solenoid around the CZ furnace can be used to eliminated the unsteadiness in the melt motion and to control the remaining steady flow. For both GaAs (Carlson and Witt, 1992; Kimura et al., 1986) and InP (Bliss et al., 1991 and 1993; Miyairi et al., 1986), the application of a uniform axial magnetic field with a magnetic flux density B between $0.1T$ and $0.4T$ reduces the dislocation density, produces a more radially uniform dislocation density and produces a more radially uniform dopant concentration. The Kyropoulos process is a variation of the CZ process in which the crystal is allowed to grow into the melt before the crystal's vertical motion or "pulling" is begun. Using a magnetically stabilized, liquid-encapsulated Kyropoulos (MLEK) process, large twin-free InP crystals have been growth with $B = 0.2T - 0.4T$ (Bliss et al., 1991 and 1993). While a magnetic field with $B = 0.1T - 0.4T$ does not eliminate the striations, it does lead to smaller dislocation densities and to weaker striations whose spacing is related to the angular velocity of the crystal about its vertical centerline. The crystal is almost always rotated with at least a small angular velocity in order to insure that the crystal remains cylindrical in spite of the inevitable small deviations from axisymmetry in the temperature distribution. The crystal is often rotated at a larger angular velocity, so that the axial variation of the azimuthal velocity drives a radially outward melt motion adjacent to the crystal-melt interface. The crystal's angular velocity must be sufficiently large that the resultant centrifugal pumping or forced convection is larger than the radially inward motion near the crystal-melt interface due to buoyant convection. The convective heat and mass transfer associated with a radially outward flow adjacent to the crystal-melt interface generally produce a more desirable crystal-melt interface shape and a more radially uniform dopant distribution in the crystal (Lee et al., 1984).

The regularly spaced striations with a magnetic field are directly associated with the rotation of the crystal and with the resultant forced convection near the crystal-melt interface. This paper presents a model of the forced convection due to crystal rotation. This model reveals that there are several fundamental differences between the forced convection during silicon growth with a free surface and that during compound semiconductor growth with a liquid encapsulant. The balance between the forced and buoyant convections as a function of the crystal's angular velocity Ω changes as B is increased. This paper only presents solutions for steady, axisymmetric melt motions, while the regularly spaced striations must arise either from an intrinsic deviation from axisymmetry or from a flow instability leading to periodic or nonaxisymmetric melt motions. While the present model cannot directly predict the striations, it does provide the basis for future studies of the coupling between forced convection and a three-dimensional buoyant convection due to nonaxi-

Contributed by the Fluids Engineering Division for publication in the JOURNAL OF FLUIDS ENGINEERING. Manuscript received by the Fluids Engineering Division October 8, 1997; revised manuscript received August 17, 1998. Associate Technical Editor: M. S. Cramer.

symmetric heating (Ma and Walker, 1995 and 1996) and for future studies of magnetically damped Taylor instabilities in the rotationally driven melt motions.

Problem Formulation

A sketch of the liquid-encapsulated CZ process is presented in Fig. 1. With an axial magnetic field, there are different characteristic values for the azimuthal velocity v_θ and for the radial and axial velocities v_r and v_z in each θ = constant or meridional plane (Hjellming and Walker, 1986). The azimuthal melt motion is driven by the rotation of the crystal, so that the characteristic azimuthal velocity $U_a = \Omega R$, where the characteristic length R is the inside radius of the crucible. The meridional motion is driven by the axial variation of the radial centrifugal force, $\rho v_\theta^{*2}/r^*$, and is opposed by the radial electromagnetic (EM) body force, $\sigma B_{v_r}^2$, where ρ and σ are the melt's density and electrical conductivity, while an asterisk denotes a dimensional variable. Therefore the characteristic meridional velocity $U_m = \rho\Omega^2 R/\sigma B^2$. For a typical InP process with $B = 0.2T - 0.4T$, U_a is much larger than U_m, but the azimuthal motion does not produce any convection of momentum or heat as long as the velocity and temperature are axisymmetric. In addition, the characteristic velocity for the purely meridional buoyant convection $U_b = \rho g\beta(\Delta T)/\sigma B^2$, where $g = 9.81$ m/s^2, β is the melt's volumetric expansion coefficient, and (ΔT) is the characteristic temperature difference in the melt (Hjellming and Walker, 1987).

In addition to the applied magnetic field produced by a solenoid around the CZ furnace, there is an induced magnetic field produced by the electric currents in the melt and crystal. The characteristic ratio of the induced to applied magnetic field strengths is the magnetic Reynolds number, $R_m = \mu_p\sigma UR$, where μ_p is the melt's magnetic permeability, and the U here is the largest value among U_a, U_m, and U_b. Since R_m is extremely small for all crystal-growth processes, the induced magnetic field is negligible, and the dimensionless magnetic field is $\hat{z}$, which is the unit vector in the z direction.

In the Navier-Stokes equation, the characteristic ratio of the EM body force to the meridional convection of momentum is the interaction parameter, $N = \sigma B^2 R/\rho U$, where this U is the larger value between U_m and U_b, both of which vary as B^{-2}. In the internal energy equation, the characteristic ratio of convective heat transfer to heat conduction is the thermal Peclet number, $\mathrm{Pe} = UR/\kappa$, where κ is the melt's thermal diffusivity. For sufficiently large values of B, N is so large that the meridional convection of momentum is negligible, and Pe is so small that convective heat transfer is negligible. Langlois et al. (1987) presented numerical solutions of the full equations, including convective heat transfer and all inertial terms, for a typical silicon process with $B = 0.2T$. They found that setting $\mathrm{Pe} = 0$ or quadrupling the value of N produced negligible changes in the results, indicating that the convective heat transfer and inertial effects are indeed negligible for a silicon process with $B \geq 0.2T$. The parameter values for typical GaAs and InP processes with $B = 0.2T - 0.4T$ are comparable.

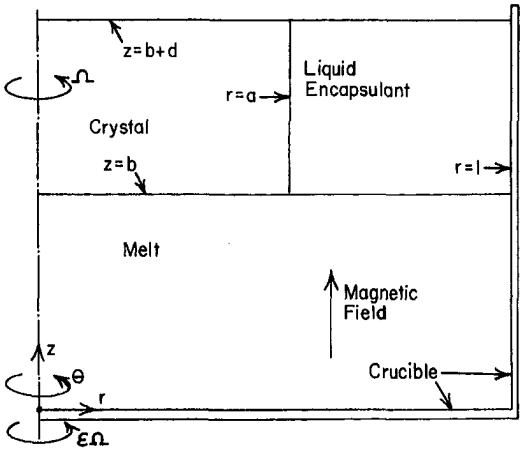

Fig. 1 Liquid-encapsulated Czochralski process with a uniform axial magnetic field. For the cylindrical coordinates (r, θ, z), r and z, as well as all lengths, are normalized by R, the inside radius of the crucible. The angular velocities of the crystal and crucible about their common vertical centerline are Ω and $\epsilon\Omega$, respectively.

With the assumptions that $N \gg 1$ and $\mathrm{Pe} \ll 1$, (1) the governing equations are linear, (2) the buoyant convection and the rotationally driven forced convection are decoupled from each other, and (3) the azimuthal motion is decoupled from the meridional motion in the forced convection. The dimensionless equations governing the azimuthal motion are

$$0 = -j_r + Ha^{-2}\left(\nabla^2 v_\theta - \frac{v_\theta}{r^2}\right), \quad j_r = -\frac{\partial\phi}{\partial r} + v_\theta, \qquad (1a, b)$$

$$j_z = -\frac{\partial\phi}{\partial z}, \quad \frac{1}{r}\frac{\partial}{\partial r}(rj_r) + \frac{\partial j_z}{\partial z} = 0, \qquad (1c, d)$$

in the melt, and

$$j_{rs} = \left(\frac{\sigma_s}{\sigma}\right)\left(-\frac{\partial\phi_s}{\partial r} + r\right), \quad j_{zs} = -\left(\frac{\sigma_s}{\sigma}\right)\frac{\partial\phi_s}{\partial z}, \qquad (1e, f)$$

$$\frac{1}{r}\frac{\partial}{\partial r}(rj_{rs}) + \frac{\partial j_{zs}}{\partial z} = 0, \qquad (1g)$$

in the crystal, where

$$\nabla^2 = \frac{\partial^2}{\partial r^2} + \frac{1}{r}\frac{\partial}{\partial r} + \frac{\partial^2}{\partial z^2}, \qquad (1h)$$

j_r and j_z are the radial and axial components of the electric current density normalized by $\sigma U_a B$, ϕ is the electric potential function normalized by $U_a BR$, the subscript s denotes a variable in the crystal, σ_s is the crystal's electrical conductivity, $\mathrm{Ha} = BR(\sigma/\mu)^{1/2}$ is the Hartmann number, and μ is the melt's viscosity. Equation $(1a)$ is the θ component of the Navier-Stokes equation without the meridional convection of azimuthal momentum, without a θ derivative of the pressure because of axisymmetry, and with the azimuthal EM body force due to the radial electric current and the axial magnetic field. Equations $(1b)$, $(1c)$, $(1e)$, and $(1f)$ are the r and z components of Ohm's law for a moving continuum in the melt and crystal, and Eqs. $(1d)$ and $(1g)$ are a solubility condition which guarantees that there is a solution of Maxwell's equations for the neglected $O(R_m)$ induced magnetic field.

Neglecting any gradients of the interfacial tension, the velocities and shear stresses in the encapsulant and in the melt are equal at their interface. For the temperatures in a typical process, the viscosity of liquid boron oxide is two thousand times that of molten InP, so that the shear stresses in the melt are negligible compared to those in the encapsulant. The encapsulant sees a stress-free boundary at its interface with the melt, so that its motion consists of a simple Couette flow with

$$v_{\theta e} = \frac{a^2(1-\epsilon) - (a^2-\epsilon)r^2}{(1-a^2)r}, \quad v_{re} = v_{ze} = 0, \qquad (2a, b)$$

where the radius of the crystal is aR and the angular velocity of the crucible is $\epsilon\Omega$ (Hjellming and Walker, 1988). If there are gradients of the interfacial tension due to gradients of temperature or of dopant concentration along the encapsulant-melt interface, shear stresses in the enormously viscous boron oxide balance the interfacial-tension gradients with very small encapsulant velocities, so that there are no thermocapillary or soluto-

capillary melt convections in liquid-encapsulated crystal growth. In other words, the Marangoni number for the encapsulant, $\mathrm{Ma}_e = \rho_e(-d\Gamma/dT)(\Delta T)R/\mu_e^2$, is small. Here ρ_e and μ_e are the density and viscosity of the encapsulant, while Γ is the interfacial tension of the encapsulant-melt interface. There is no published data on the tension of an interface between a liquid semiconductor and boron oxide. If we use the values of Γ for a liquid-silicon free surface, which are certainly much larger than those for an encapsulant-melt interface, we find that $\mathrm{Ma}_e = 0.037$ for our typical process with $(\Delta T) = 41$ K. Equations (2*a, b*) also assume that the buoyant convection in the encapsulant is negligible. The Boussinesq number for the encapsulant, $B_{oe} = \rho_e^2 g\beta_e(\Delta T)R^3/\mu_e^2$, has the value of 0.00423 for our typical process, where β_e is the volumetric expansion coefficient for the encapsulant.

The boundary conditions for the azimuthal motion are

$$v_\theta = \epsilon r, \quad j_z = 0, \quad \text{at} \quad z = 0, \tag{3a, b}$$

$$v_\theta = \epsilon, \quad j_r = 0, \quad \text{at} \quad r = 1, \tag{3c, d}$$

$$v_\theta = \frac{a^2(1-\epsilon) - (a^2-\epsilon)r^2}{(1-a^2)r}, \quad j_z = 0, \quad \text{at}$$

$$z = b \quad \text{for} \quad a \le r \le 1, \tag{3e, f}$$

$$v_\theta = r, \quad j_z = j_{zs}, \quad \phi = \phi_s, \quad \text{at}$$

$$z = b \quad \text{for} \quad 0 \le r \le a, \tag{3g–i}$$

$$j_{rs} = 0, \quad \text{at} \quad r = a, \quad \text{and} \quad j_{zs} = 0, \quad \text{at}$$

$$z = b + d, \tag{3j, k}$$

where the instantaneous melt depth is bR and the axial length of the crystal is dR.

The parameter ϵ can be eliminated from the linear boundary value problem for the azimuthal motion by introducing

$$v_\theta = r + (\epsilon - 1)V_\theta, \quad \phi = \frac{r^2}{2} + (\epsilon - 1)\Phi, \tag{4a, b}$$

$$j_r = (\epsilon - 1)J_r, \quad j_z = (\epsilon - 1)J_z, \tag{4c, d}$$

and the same expressions for ϕ_s, j_{rs} and j_{zs}. The only parameters in the problem governing V_θ, J_r, J_z, Φ, J_{rs}, J_{zs} and Φ_s are a, b, d, Ha, and (σ_s/σ).

The dimensionless equations governing the meridional motion in the rotationally driven forced convection are

$$-\frac{v_\theta^2}{r} = -\frac{\partial p}{\partial r} + j_\theta + \mathrm{Ha}^{-2}\left(\nabla^2 v_r - \frac{v_r}{r^2}\right), \tag{5a}$$

$$0 = -\frac{\partial p}{\partial z} + \mathrm{Ha}^{-2}\nabla^2 v_z, \quad j_\theta = -v_r, \tag{5b, c}$$

$$\frac{1}{r}\frac{\partial}{\partial r}(rv_r) + \frac{\partial v_z}{\partial z} = 0, \tag{5d}$$

where v_r and v_z are normalized by U_m, j_θ is the θ component of the electric current density normalized by $\sigma U_m B$, and p is the forced convection part of the deviation of the pressure from the hydrostatic pressure, normalized by $\sigma U_m B^2 R$. Equation (5*a*) is the radial component of the Navier-Stokes equation without the meridional convection of radial momentum, with the centrifugal force due to the azimuthal melt motion, and with the radial EM body force due to the azimuthal electric current and the axial magnetic field, while Eq. (5*b*) is the axial component of the Navier-Stokes equation without the meridional convection of axial momentum. Equation (5*c*) is the θ component of Ohm's law for a moving continuum without a θ derivative of ϕ due to axisymmetry, while Eq. (5*d*) is the continuity equation.

Equation (5*d*) leads to a stream function $\psi(r, z)$ for the meridional flow,

$$v_r = \frac{1}{r}\frac{\partial \psi}{\partial z}, \quad v_z = -\frac{1}{r}\frac{\partial \psi}{\partial r}. \tag{6a, b}$$

The parameter ϵ can be eliminated from the linear boundary value problem for the meridional motion by introducing

$$\psi = (\epsilon - 1)\psi_1 + (\epsilon - 1)^2\psi_2, \tag{7}$$

where ψ_1 and ψ_2 depend only on the parameters a, b, d, Ha, and (σ_s/σ). We cross-differentiate Eqs. (5*a*) and (5*b*) to eliminate p and to obtain the equations governing ψ_i for $i = 1$ or 2,

$$\frac{\partial^4\psi_i}{\partial r^4} - \frac{2}{r}\frac{\partial^3\psi_i}{\partial r^3} + \frac{3}{r^2}\frac{\partial^2\psi_i}{\partial r^2} - \frac{3}{r^3}\frac{\partial\psi_i}{\partial r} + 2\frac{\partial^4\psi_i}{\partial r^2\partial z^2}$$

$$-\frac{2}{r}\frac{\partial^3\psi_i}{\partial r\partial z^2} + \frac{\partial^4\psi_i}{\partial z^4} - \mathrm{Ha}^2\frac{\partial^2\psi_i}{\partial z^2} = \mathrm{Ha}^2 f_i, \tag{8a}$$

$$f_1 = -2r\frac{\partial V_\theta}{\partial z}, \quad f_2 = -2V_\theta\frac{\partial V_\theta}{\partial z}. \tag{8b, c}$$

The boundary conditions are

$$\psi_i = \frac{\partial\psi_i}{\partial z} = 0, \quad \text{at} \quad z = 0 \quad \text{and at} \quad z = b, \tag{9a}$$

$$\psi_i = \frac{\partial\psi_i}{\partial r} = 0, \quad \text{at} \quad r = 1. \tag{9b}$$

The only difference between the present boundary value problems for the liquid-encapsulated crystal growth and those for silicon growth with a free surface is that the boundary conditions for a free surface at $z = b$ for $a \le r \le 1$ are

$$\frac{\partial v_\theta}{\partial z} = 0, \quad j_z = 0, \quad \psi_i = 0, \quad \frac{\partial^2\psi_i}{\partial z^2} = 0, \tag{10a–d}$$

instead of Eqs. (3*e*), (3*f*), and (9*a*).

Asymptotic Solutions for Ha ≫ 1

Numerical solutions for Ha = 50, 100, 200 and 400 are presented in the next section. The large-Hartmann number asymptotic solutions, which are presented in this section, provide valuable insights into the numerical solutions and into the differences between the forced convections for liquid-encapsulated crystal growth and for silicon growth with a free surface. For Ha ≫ 1, the melt can be divided into the subregions shown in Fig. 2. Here i and o denote the inner and outer inviscid core regions where both the radial and axial derivatives are $O(1)$, h denotes the Hartmann layers with an $O(\mathrm{Ha}^{-1})$ axial thickness adjacent to the crucible bottom, crystal-melt interface and encapsulant-melt interface or free surface, w denotes the wall

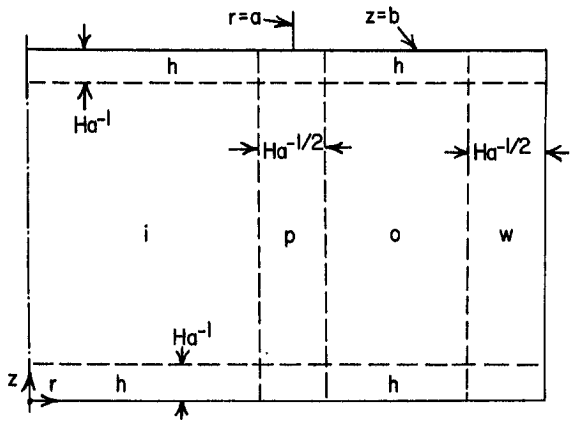

Fig. 2 Subregions of the melt for Ha ≫ 1

layer with an $O(\mathrm{Ha}^{-1/2})$ radial thickness adjacent to the vertical crucible wall, and p denotes the parallel interior layer with an $O(\mathrm{Ha}^{-1/2})$ radial thickness which lies along the magnetic field lines which intersect the outer circumference of the crystal at $r = a$. The wall and parallel layers are thicker than the Hartmann layers because they are parallel to the magnetic field. First we will summarize the key features of the asymptotic solution presented by Hjellming and Walker (1986) for the forced convection during silicon growth with a free surface, and then we will present the extension of the asymptotic analysis to liquid-encapsulated crystal growth.

For the azimuthal motion, the key features of either core region are (1) that the $O(1)$ v_θ is independent of z, (2) that the $O(\mathrm{Ha}^{-1})$ v_θ is a linear function of z, and (3) that $j_r = O(\mathrm{Ha}^{-2})$ so that the $O(\mathrm{Ha}^{-1})j_z$ is independent of z. The key feature of a Hartmann layer is that the jump in the $O(1)$ v_θ across the layer equals the total $O(\mathrm{Ha}^{-1})$ radial electric current inside the layer, i.e., the integral of the $O(1)j_r$ across the layer. If $\sigma_s = 0$, then the total $O(\mathrm{Ha}^{-1})$ radial electric current inside the Hartmann layer adjacent to the crystal-melt interface at some value of r must be equal and opposite to the $O(\mathrm{Ha}^{-1})$ radial electric current inside the bottom Hartmann layer at the same r. Therefore the jumps in v_θ across the top and bottom Hartmann layers for $0 \le r \le a$ must be equal, so that the $O(1)$ azimuthal motion in the inner core is a rigid-body rotation with an average of the angular velocities of the crystal and crucible,

$$v_{\theta i} = \tfrac{1}{2}(1 + \epsilon)r + O(\mathrm{Ha}^{-1}). \tag{11}$$

The $O(1)v_\theta$ changes from this value to r or ϵr across the top or bottom Hartmann layer, respectively. For the actual value $(\sigma_s/\sigma) = 0.05$ for silicon, the crystal and top Hartmann layer represent parallel resistors for the radial electric current. Some of the radial current which would be inside the top Hartmann layer for $\sigma_s = 0$ actually flows through the crystal, decreasing the jump in v_θ across the top Hartmann layer. As a consequence, the $O(1)v_\theta$ in the inner core lies between $(1 + \epsilon)r/2$ and r, where the relative deviation from these two values depends on the ratio of the total radial current in the crystal to that inside the top Hartmann layer at each value of r.

In the outer core with a free surface at $z = b$ for $a \le r \le 1$, the stress-free condition given by Eq. (10a) does not produce a jump in v_θ across the top Hartmann layer. Without a radial electric current inside the top layer, there cannot be one inside the bottom Hartmann layer, so that there is no jump in v_θ across the bottom Hartmann layer either. The outer core, the wall layer and the Hartmann layers for $a \le r \le 1$ rotate as a rigid body with the crucible, i.e., $v_\theta = \epsilon r$, to all orders in Ha^{-1}. Therefore for the azimuthal motion with a free surface, there is a jump in the $O(1)v_\theta$ across the parallel interior layer from $(1 + \epsilon)a/2$ in the inner core at $r = a$ to ϵa in the outer core at $r = a$. There are radially inward and outward electric currents in the Hartmann layers for $0 \le r \le a$, but none in the Hartmann layers for $a \le r \le 1$. Therefore there must be a concentrated axial electric current inside the parallel interior layer in order to complete the electrical circuit for the radial currents inside the Hartmann layers for $r \le a$. Numerical solutions of the full equations clearly show the jump in v_θ and the concentrated axial electric current for a radially thin parallel interior layer near $r = a$ for silicon growth with a free surface (Sabhapathy and Salcudean, 1991).

If v_θ is independent of z, then the associated centrifugal force, v_θ^2/r, is exactly balanced by a radial pressure gradient, and there is no meridional circulation. For the rigid-body rotation with the crucible for $r > a$, there is no meridional circulation in the outer core, the adjacent Hartmann layers or the wall layer, i.e., $\psi = 0$ to all orders in Ha^{-1} in these regions. The z-independent $O(1)v_\theta$ in the inner core does not produce any meridional circulation, but the linear z-variation of the $O(\mathrm{Ha}^{-1})v_\theta$ produces an $O(\mathrm{Ha}^{-1})\psi$ in the inner core. The jumps in the $O(1)v_\theta$ across the Hartmann layers for $r < a$ also produce $O(\mathrm{Ha}^{-1})$ meridional circulations which are completed through the inner core. Therefore ψ is $O(\mathrm{Ha}^{-1})$ in the inner core and adjacent Hartmann layers. The jump in the $O(1)v_\theta$ across the parallel interior layer is matched by a layer solution which varies as erf $[\mathrm{Ha}^{1/2}(r - a)/(b - z)^{1/2}]$. The axial variation of v_θ inside this layer drives an $O(1)$ meridional circulation which is entirely inside the parallel interior layer. Therefore the meridional melt motion consists of (1) a concentrated $O(1)$ circulation which is elongated over the entire depth of the melt inside the parallel interior layer and which involves large $O(\mathrm{Ha}^{1/2})$ values of v_z, (2) a much smaller $O(\mathrm{Ha}^{-1})$ circulation in the inner core and its Hartmann layers, and (3) no circulation at all in the outer core and its Hartmann layers. An axially elongated, radially thin circulation near $r = a$ is evident in the streamlines produced by the numerical solution of the full equations for silicon growth with a free surface (Kim and Langlois, 1991; Lee et al., 1984; Sabhapathy and Salcudean, 1991).

For liquid-encapsulated crystal growth, the stress-free condition is replaced by the prescribed value of v_θ given by Eq. (3e) at $z = b$ for $a \le r \le 1$. Therefore there are now equal jumps in v_θ across the Hartmann layers for $r > a$, and equal but opposite radial electric currents inside these layers. The $O(1)$ outer-core v_θ is the average of the azimuthal velocities of the encapsulant and crucible at each radius,

$$v_{\theta o} = \frac{a^2(1 - \epsilon) - (a^2 + \epsilon a^2 - 2\epsilon)r^2}{2(1 - a^2)r}, \tag{12}$$

neglecting the $O(\mathrm{Ha}^{-1})v_\theta$, which is again a linear function of z. Since $v_\theta = (1 + \epsilon)a/2$ in both the inner and outer cores at $r = a$, there is no jump in the $O(1)v_\theta$ across the parallel interior layer. Similarly, since the radial electric currents inside the Hartmann layers are continuous at $r = a$, there is no concentrated axial electric current inside the parallel interior layer. This layer now plays a very minor role, since it need only match the discontinuity of the radial gradient of v_θ. There is no $O(1)$ meridional circulation inside the parallel interior layer.

There is an $O(\mathrm{Ha}^{-1})$ meridional circulation in each core, which is driven by (1) the linear z variation of the $O(\mathrm{Ha}^{-1})v_\theta$ in each core, and (2) the jumps in the $O(1)v_\theta$ across the Hartmann layers. This $O(\mathrm{Ha}^{-1})\psi$ is continuous across the parallel interior layer, so that again this layer plays an insignificant role.

We have assumed a planar, horizontal crystal-melt interface. In the Kyropoulos process, this interface is initially convex into the melt and becomes more planar as growth continues. If we consider a convex or concave crystal-melt interface, the jump in the $O(1)v_\theta$ across the adjacent Hartmann layer still equals the total $O(\mathrm{Ha}^{-1})$ electric current inside this layer. Therefore the values of v_θ in the inner core are the same for a planar or convex crystal-melt interface, and the convex interface does not have any significant effect on the forced convection. On the other hand, the temperature distribution and the buoyant convection in the melt are affected by the shape of the crystal-melt interface, and we will treat this effect in a future paper.

The purposes of the large-Hartmann number asymptotic solutions which are described in this section are (1) to help understand the numerical results for liquid-encapsulated crystal growth with Ha = 50, 100, 200, and 400, which are presented in the next section, and (2) to emphasize the fundamental differences between the forced convections for liquid-encapsulated growth and for silicon growth with a free surface.

Forced Convection for Arbitrary Ha

In this section, we present numerical solutions of the inertialess equations for the rotationally driven forced convection or centrifugal pumping for arbitrary values of the Hartmann number. For the azimuthal motion, which is governed by Eqs. (1) with the boundary conditions given by Eqs. (3) and with the

substitution given by Eq. (4) to eliminate ϵ, we used: (1) a separation-of-variables solution for the crystal variables J_{rs}, J_{zs} and Φ_s, (2) a Chebyshev spectral collocation method for the melt variables V_θ, J_r, J_z and Φ, and (3) a Galerkin method to match the two solutions through the Eqs. (3*h*) and (3*i*). For the meridional motion, which is governed by Eqs. (8) with the boundary conditions given by Eqs. (9), we used a Chebyshev spectral collocation method. The same Chebyshev polynomials and the same Gauss-Lobatto collocation points were used for the azimuthal motion, the meridional forced convection, and the meridional buoyant convection. We found that each series could be truncated after the 14th polynomial in the axial direction and the 40th polynomial in the radial direction. A larger number of polynomials was needed in the radial direction because of the discontinuity between the boundary conditions at $z = b$ for $r < a$ and $r > a$. For Eqs. (3*f*) and (3*h*), we defined a weighted residual with the weighting function, $(1 - r^2)^{-1/2}$, for the radial Chebyshev polynomials, and we minimized this residual with respect to certain linear combinations of the coefficients in the Chebyshev polynomial representation of j_z. For Eq. (3*i*), we defined a weighted residual with the weighting function, r, for the Bessel functions in the separation-of-variables solution for ϕ_s, and we minimized this residual with respect to the coefficients in the solution for ϕ_s. Here we only present results for $a = 0.65$ and $b = d = 0.4$, which corresponds to a time during a typical liquid-encapsulated growth of an InP crystal when roughly 30 percent of the original melt has been crystalized. While V_θ, ψ_1, and ψ_2 are independent of ϵ, it is easier to understand the values of v_θ and ψ for a particular value of ϵ, so that we only present results for $\epsilon = 0$, corresponding to no rotation of the crucible.

For InP, $(\sigma_s/\sigma) = 0.0154$ (Glazov et al., 1976). We obtained results for v_θ and ψ for $(\sigma_s/\sigma) = 0.0154$ or 0.0 and for Ha = 50, 100, 200, and 400. As Ha is increased, the Hartmann layer adjacent to the crystal-melt interface becomes thinner, so that more electrical current flows through the actual crystal with non-zero electrical conductivity. Therefore we expected the largest differences between the results for the actual σ_s and for $\sigma_s = 0$ to occur for the largest value of Ha, and indeed our largest differences did occur for Ha = 400. However, the differences for Ha = 400 were all less than 3 percent and were much smaller for smaller values of Ha. We had expected larger differences because Hjellming and Walker (1986) and Langlois et al. (1987) found larger differences for a typical silicon process with $(\sigma_s/\sigma) = 0.05$ or 0.0. We now realize that the correct parameter to characterize the role of the crystal's non-zero electrical conductivity is b Ha (σ_s/σ), or the product of the Hartmann number based on the instantaneous melt depth and the conductivity ratio. For our InP case with Ha = 400, b Ha $(\sigma_s/\sigma) = 2.46$. Hjellming and Walker (1986) and Langlois et al. (1987) consider a smaller value of Ha, but their value of b Ha $(\sigma_s/\sigma) = 8.125$ because both (σ_s/σ) and b are larger. Silicon is often grown with a large initial melt depth in order to grow meter-long crystals. With compound semiconductors, the initial melt depth is always much smaller in order to control the buoyant convection (Koai et al., 1994), and the final crystal length is generally less than 10 cm. For compound semiconductors with values of (σ_s/σ) much larger than 0.0154, the non-zero crystal conductivity may play an important role, but for InP with $B = 0.2T - 0.4T$, the crystal's non-zero electrical conductivity is not significant. All results presented here are for $(\sigma_s/\sigma) = 0.0154$.

The contours of v_θ and ψ for Ha = 200 are presented in Fig. 3. For v_θ: (1) there are clearly Hartmann layers at $z = 0$ and at $z = b$, (2) the v_θ in the inner or outer core is nearly independent of z, while the $O(\text{Ha}^{-1})$ linear variation with z is largest near $r = a$, (3) the v_θ in the inner core increases with r to a maximum value near $r = a$, (4) the v_θ in the outer core decreases from this maximum as roughly half the $v_{\theta e}$ for the Couette flow in the encapsulant for no crucible rotation, and (5) there is no

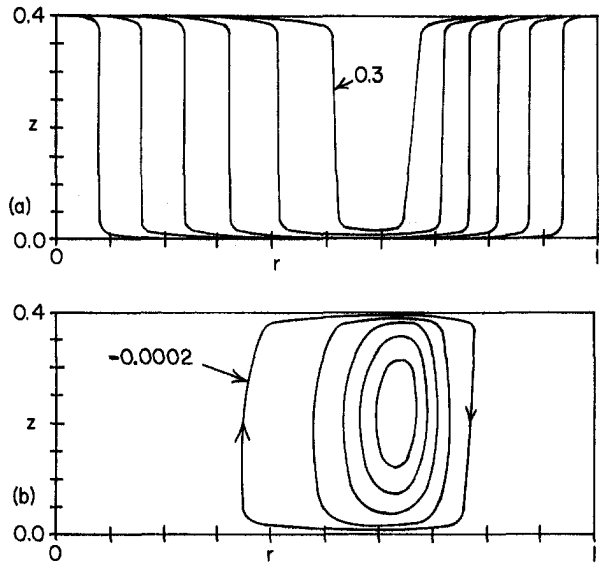

Fig. 3 Contours of v_θ and ψ for the forced convection produced by crystal rotation with Ha = 200. (*a*) $v_\theta = 0.05n$, for $n = 1$ to 6. (*b*) $\psi = -0.0002n$, for $n = 1$ to 5.

discontinuity in v_θ at $r = a$. The only differences between these contours of v_θ and those for Ha = 50, 100 and 400 are that the Hartmann-layer thickness decreases and the core contours become more vertical as Ha is increased.

The meridional motion is driven by the $O(\text{Ha}^{-1})$ linear variation of v_θ with z and by the jumps in v_θ across the Hartmann layers, and both of these driving forces increase from zero as r changes from either 0 or 1 to a. Therefore the meridional circulation is centered near $r = a$, but there is no axially elongated circulation inside the parallel interior layer at $r = a$. Without the $O(1)$ ψ inside the parallel interior layer for silicon growth with a free surface, we expect the minimum value of ψ to vary as Ha^{-1}, once Ha is large enough for the asymptotic solution to be valid. In a plot of ln $|\psi|$ versus ln (Ha) using results for Ha = 1, 10, 25, 50, 75, 100, 150, 200, 300, and 400, the slope changes smoothly from about -0.5 at Ha = 50 to about -0.7 at Ha = 400. Clearly Ha must be much larger than 400 for the slope of -1.0 predicted by the asymptotic solution. The asymptotic solution for the liquid encapsulated growth predicts a discontinuity between the positive and negative radial derivatives of v_θ at $r = a$ in the inner and outer cores and predicts that this discontinuity is matched by the parallel interior layer with essentially zero thickness. Since the Δr of the parallel interior layer is roughly 3 $\text{Ha}^{-1/2}$ or 0.15 for Ha = 400, the parallel layer is not actually thin for Ha = 400. Thus the plot of v_θ versus r at a given value of z is dramatically smoothed near $r = a$ from the discontinuous plot predicted by the asymptotic analysis. Since the $O(\text{Ha}^{-1})$ linear z variation of v_θ is largest in both cores near $r = a$, this smoothing eliminates some of the strongest centrifugal pumping for finite values of Ha. Therefore, as Ha is increased, the radial shrinkage of the actual interior layer near $r = a$ creates more local core and core pumping, so that the magnitude of the minimum ψ does not decrease as fast as Ha^{-1}. The asymptotic solution provides good physical insights, but it does not provide quantitatively accurate predictions until the value of $\text{Ha}^{-1/2}$ is very small.

Balance Between Buoyant and Forced Convections

In this section we use an approximate temperature distribution in the melt in order to study the balance between the buoyant and forced convections as a function of the crystal's angular velocity for various values of Ha. For Pe $\ll 1$, the dimensionless temperature $T(r, z)$ is governed by $\nabla^2 T = 0$, where T is the

deviation of the dimensional melt temperature from the solidification temperature, normalized by (ΔT). In our approximate model: (1) we continue to assume that the crystal-melt and encapsulant-melt interfaces lie in the horizontal $z = b$ plane, (2) we assume that there is no heat flux through the crucible bottom, (3) we assume that there is a uniform heat flux q through the vertical crucible wall to the melt, (4) we estimate the radiative and conductive heat transfer through the liquid encapsulant from measured temperatures for a typical InP process (Bachowski et al., 1990; Prasad et al., 1994), (5) we use a heat balance for the entire melt to estimate the value of q, and (6) we linearize the equation for the radiative heat transfer because the temperature variations in the melt are much smaller than those in the furnace. With $(\Delta T) = qR/k$, where k is the melt's thermal conductivity, the boundary conditions on T are

$$\frac{\partial T}{\partial z} = 0, \quad \text{at} \quad z = 0, \quad \frac{\partial T}{\partial r} = 1, \quad \text{at} \quad r = 1, \quad T = 0, \quad \text{at}$$

$$z = b \quad \text{for} \quad 0 \le r \le a, \quad (13a\text{–}c)$$

$$\frac{\partial T}{\partial z} = -C_0 - C_1 T, \quad \text{at} \quad z = b \quad \text{for} \quad a \le r \le 1, \quad (13d)$$

where our estimated values $C_0 = 0.709$ and $C_1 = 0.347$. This thermal model is qualitatively correct, but it misses some important aspects of the actual process for growing compound semiconductors, namely, (1) there is heat transfer through the crucible bottom, (2) the heat flux to the melt is not uniform, and the ability to tailor the distribution of the heat flux into the melt in order to tailor the buoyant convection is very important (Ma et al., 1996), (3) the crystal-melt and encapsulant-melt interfaces are not planar, and their actual shapes can significantly affect the buoyant convection, and (4) an accurate radiative heat transfer model for an actual furnace is needed. Our approximate T does give the approximate magnitude and characteristics of the buoyant convection, and our current objective is to study the balance between the buoyant and forced convections.

We used a separation-of-variables solution for T. For the buoyant convection, the stream function ψ_b, normalized by $U_b R^2$, is governed by Eq. (8a) with $f_i = r\partial T/\partial r$ and with the boundary conditions given by Eqs. (9). The isotherms for $a = 0.65$ and $b = 0.4$ are presented in Fig. 4(a). The maximum

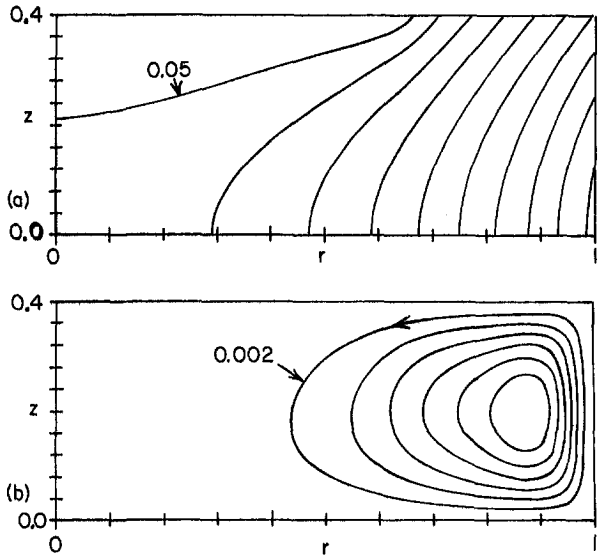

Fig. 4 Temperature and associated buoyant convection for Ha = 100. (a) Isotherms $T = 0.05n$, for $n = 1$ to 10. (b) Streamlines $\psi_b = 0.002n$, for $n = 1$ to 6.

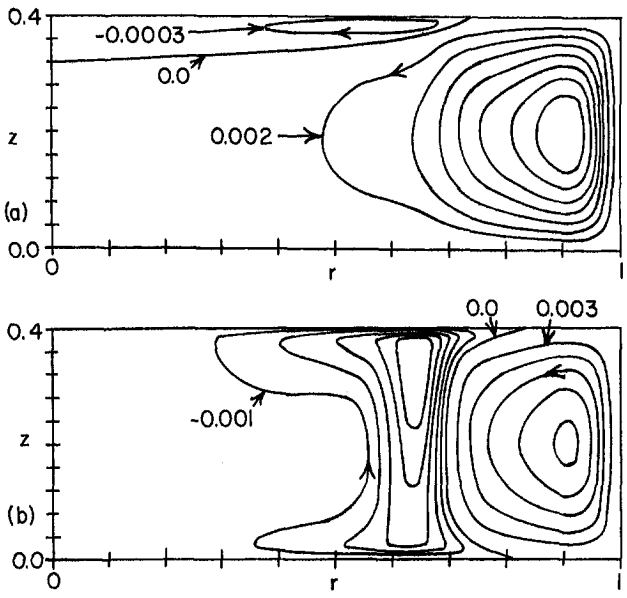

Fig. 5 Streamlines for both forced and buoyant convections for Ha = 200. (a) Crystal rotating at 40 rpm: $\psi = -0.0003$ and $\psi = 0.002n$, for $n = 0$ to 7. (b) Crystal rotating at 80 rpm: $\psi = -0.001n$, for $n = 1$ to 5 and $\psi = 0.003n$, for $n = 0$ to 5.

value of T is 0.516, and our approximate thermal model for a typical InP process indicates that this value corresponds to a maximum melt temperature which is 41 K above the solidification temperature. The streamlines for the buoyant convection with this temperature and for Ha = 100 are presented in Fig. 4(b). In the asymptotic solution for Ha $\gg$ 1, all the vertically upward flow is inside the wall layer with an $O(\mathrm{Ha}^{-1/2})$ radial thickness at $r = 1$, and there are no discontinuities at $r = a$ (Hjellming and Walker, 1987).

The stream functions for the forced and buoyant convections have been normalized with different characteristic velocities, namely U_m and U_b, respectively. We add the subscript f to the ψ for the forced convection for $\epsilon = 0$ and henceforth we use ψ to denote the total stream function normalized by $U_b R^2$, so that

$$\psi = \psi_b + \lambda\psi_f, \quad \lambda = \frac{U_m}{U_b} = \frac{\Omega^2 R}{g\beta(\Delta T)}. \quad (14a, b)$$

For a typical InP process with $R = 5$ cm, $\lambda = 0.143\Omega^2$, with Ω in radians/second.

The streamlines with both forced and buoyant convection for $a = 0.65$, $b = d = 0.4$, $(\sigma_s/\sigma) = 0.0154$, $\epsilon = 0$, Ha = 200 and $\Omega = 40$ rpm or 80 rpm are presented in Fig. 5. For 40 rpm, ψ varies from -0.000656 to 0.0159, where negative and positive values reflect the clockwise forced convection and the counterclockwise buoyant convection, respectively. Clearly the forced convection is very small and is confined to a very thin region directly below the crystal-melt interface. There is radially outward flow over the entire crystal-melt interface, but it is very weak and very local. For 80 rpm, ψ varies from -0.00613 to 0.0156, so that the forced convection is still smaller than the maximum buoyant convection. However, the forced convection is now strong enough to block the buoyant convection and to confine it to the region for $0.7 < r < 1$.

The asymptotic solutions predict that ψ_b is $O(1)$ and that ψ_f is $O(\mathrm{Ha}^{-1})$. This would mean that Ω must vary as $\mathrm{Ha}^{1/2}$ in order to maintain the same balance between the forced and buoyant convections as the magnetic field strength is increased. We have already seen that ψ_f does not decrease as fast as Ha^{-1} for Ha = 50 to 400. In addition, the maximum values of ψ_b are 0.01093, 0.01386, and 0.01595 for Ha = 50, 100, and 200, respectively, while the maximum value for Ha $\gg$ 1 is $b^2/8 =$

0.02 (Hjellming and Walker, 1987). The largest value of $r\partial T/\partial r = 1$ at $r = 1$. In the asymptotic solution, the wall layer has essentially zero thickness, so that there are no viscous forces opposing this large driving term at $r = 1$. In reality the wall-layer Δr is roughly 0.15 for Ha = 400, so that viscous effects greatly reduce the local maximum of the buoyant convection. Again, asymptotic predictions are only accurate when the value of $\mathrm{Ha}^{-1/2}$ is very small. For Ha = 50, the streamline patterns are very similar to those in Figs. 5(*a*) and 5(*b*) for $\Omega = 20$ rpm and 40 rpm, respectively. For Ha = 100, the patterns parallel Figs. 5(*a*) and 5(*b*) for $\Omega = 30$ rpm and 60 rpm, respectively. These are only rough equivalences because we only produced streamline plots at 10 rpm intervals, but they illustrate that Ω must be increased as Ha is increased in order to maintain the same balance between the forced and buoyant convections.

Concluding Remarks

With an axial magnetic field, the EM damping of the forced convection is stronger than that of the buoyant convection. This difference occurs because the magnetic field has no effect on the temperature gradient driving the buoyant convection, but the magnetic field reduces the axial variations of v_θ outside the Hartmann layers, thus reducing the part of the centrifugal force which cannot be balanced by a radial pressure gradient. The remaining large axial derivatives of v_θ are inside the Hartmann layers where the large viscous forces oppose the centrifugal force. Lee et al. (1984) describe a flow with the buoyant convection blocked by the forced convection and confined to an outer region as a favorable flow for crystal growth. To maintain this pattern for liquid-encapsulated crystal growth with a strong axial magnetic field would require large crystal rotation rates, e.g., 40 to 80 rpm. A typical crystal rotation rate for InP growth is 4 rpm, for which the forced convection would be negligible.

A crystal grown with a rotation rate of 80 rpm might not be better than one grown at 4 rpm. From Fig. 3(*a*), we see that

$$\frac{\partial}{\partial r}\left(\frac{v_\theta^2}{r}\right) < 0, \quad \text{for} \quad a \le r \le 1. \tag{15}$$

Therefore a Taylor-like instability will occur in the outer core at some crystal rotation rate. Such an instability would lead to an unsteady, nonaxisymmetric melt motion, and the purpose of the magnetic field is to eliminate unsteady, nonaxisymmetric motions. Because of the strong axial magnetic field, such an instability would be quite different from the classical Taylor-Couette instability leading to a steady axisymmetric flow with axially stacked azimuthal vortices. Azimithal vorticity is strongly damped by an axial magnetic field, but axial vorticity with an axial field has very weak electromagnetic damping. Therefore a magnetically damped Taylor-like instability would involve axial vortices which are convected with the azimuthal motion, so that the flow would be unsteady and nonaxisymmetric. We will investigate the stability of the azimuthal motion in a future paper.

Acknowledgments

This research was supported by the National Science Foundation under Grant CTS 94-19484, by the National Aeronautics and Space Administration under Cooperative Research Agreement NCC8-90, and by the University of Missouri Research Board. The calculations were performed on the Power Challenge Array at the National Center for Supercomputing Applications at the University of Illinois. The research at Rome Laboratory was supported by the Air Force Office of Scientific Research.

References

Bachowski, S., Bliss, D. F., Ahern, B., Hilton, R. M., Adamski, J., and Carlson, D. J., 1990, "Magnetically Stabilized Kyropoulos and Czochralski Growth of InP," *Proc. 2nd International Conference on InP and Related Materials,* pp. 30–34.

Bliss, D. F., Hilton, R. M., Bachowski, S., and Adamski, J. A., 1991, "MLEK Crystal Growth of (100) Indium Phosphide," *Journal of Electronic Materials,* Vol. 20, pp. 967–971.

Bliss, D. F., Hilton, R. M., and Adamski, J. A., 1993, "MLEK Crystal Growth of Large Diameter (100) Indium Phosphide," *Journal of Crystal Growth,* Vol. 128, pp. 451–456.

Carlson, D. J., and Witt, A. F., 1992, "Quantitative Analysis of the Effects of Vertical Magnetic Fields on Microsegregation in Te-Doped LEC GaAs," *Journal of Crystal Growth,* Vol. 116, pp. 461–472.

Glazov, V. M., Nashel'skii, A. Ya., Rzaev, F. R., and Mamedov, M. M., 1976, "Investigation of Electrical Properties of Indium Phosphide at High Temperatures Including Liquid Range," *Soviet Physics, Semiconductors,* Vol. 10, pp. 498–501.

Hjellming, L. N., and Walker, J. S., 1986, "Melt Motion in a Czochralski Crystal Puller with an Axial Magnetic Field: Isothermal Motion," *Journal of Fluid Mechanics,* Vol. 164, pp. 237–273.

Hjellming, L. N., and Walker, J. S., 1987, "Melt Motion in a Czochralski Crystal Puller with an Axial Magnetic Field: Motion Due to Buoyancy and Thermocapillarity," *Journal of Fluid Mechanics,* Vol. 182, pp. 335–368.

Hjellming, L. N., and Walker, J. S., 1988, "Isothermal Motion in a Liquid-Encapsulated Czochralski Crystal Puller with an Axial Magnetic Field," *Physico-Chemical Hydrodynamics,* Vol. 10, pp. 107–131.

Kim, K. M., and Langlois, W. E., 1991, "Computer Simulation of Oxygen Segregation in CZ/MCZ Silicon Crystals and Comparison with Experimental Results," *Journal of Electrochemical Society,* Vol. 138, pp. 1850–1855.

Kimura, T., Katsumata, T., Nakajima, M., and Fukuda, T., 1986, "The Effect of Strong Magnetic Field on Homogeneity in LEC GaAs Single Crystals," *Journal of Crystal Growth,* Vol. 79, pp. 264–270.

Koai, K., Seidl, A., Leister, H.-J., Muller, G., and Kohler, A., 1994, "Modelling of Thermal Fluid Flow in a Liquid Encapsulated Czochralski Process and Comparison with Experiments," *Journal of Crystal Growth,* Vol. 137, pp. 41–47.

Langlois, W. E., Hjellming, L. N., and Walker, J. S., 1987, "Effects of the Finite Electrical Conductivity of the Crystal on Hydromagnetic Czochralski Flow," *Journal of Crystal Growth,* Vol. 83, pp. 51–61.

Lee, K.-J., Langlois, W. E., and Kim, K. M., 1984, "Digital Simulation of Oxygen Transfer and Oxygen Segregation in Magnetic Czochralski Growth of Silicon," *PhysicoChemical Hydrodynamics,* Vol. 5, pp. 135–141.

Ma, N., and Walker, J. S., 1995, "Liquid Metal Buoyant Convection in a Vertical Cylinder with a Strong Vertical Magnetic Field and with a Nonaxisymmetric Temperature," *Physics of Fluids,* Vol. 7, pp. 2061–2071.

Ma, N., and Walker, J. S., 1996, "Buoyant Convection During the Growth of Compound Semiconductors by the Liquid-Encapsulated Czochralski Process with an Axial Magnetic Field and With a Nonaxisymmetric Temperature," ASME JOURNAL OF FLUIDS ENGINEERING, Vol. 118, pp. 155–159.

Ma, N., Bliss, D. F., Anselmo, A. P., and Walker, J. S., 1996, "Radio-Frequency Induction Heating for Semiconductor Crystal Growth from a Crucible," ASME *Proc. 31st National Heat Transfer Conference,* Vol. HTD-323, pp. 309–313.

Miyairi, H., Inada, T., Eguchi, M., and Fukuda, T., 1986, "Growth and Properties of InP Single Crystals Growth by the Magnetic Field Applied LEC Method," *Journal of Crystal Growth,* Vol. 79, pp. 291–295.

Prasad, V., Bliss, D. F., and Adamski, J. A., 1994, "Thermal Characterization of the High Pressure Crystal Growth System for In-Situ Synthesis and Growth of InP Crystals," *Journal of Crystal Growth,* Vol. 142, pp. 21–30.

Sabhapathy, P., and Salcudean, M. E., 1991, "Numerical Study of Czochralski Growth of Silicon in an Axisymmetric Magnetic Field," *Journal of Crystal Growth,* Vol. 113, pp. 164–180.

Journal of Fluids Engineering

Technical Brief

Fluid Dynamic Drag of an Axially Symmetrical Bluff Body Consisting of a Plane Surface and a Spherical Surface

S. Aiba[1]

Introduction

Bluff bodies have large dynamic drag resulting from separation of the flow over the body. A large number of studies on dynamic drag were concerned with bluff bodies placed transversely in a stream (e.g., Goldstein, 1965; Bearman, 1980). Numerous researchers have performed experiments on a circular cylinder in crossflow due to its importance from a practical viewpoint (e.g., Roshko, 1955; Bearman, 1965; Bearman, 1967; and Zdravkovich, 1981). In the case of a circular cylinder in crossflow, the drag coefficient C_D is almost 1.2 in the range of a Reynolds number, Re = $10^4 \sim 10^5$ (based on the cylinder diameter D, the uniform stream velocity U_∞ and the kinematic viscosity ν of air). The author and coworkers (Aiba and Watanabe, 1997; and Aiba and Hoshino, 1997) have reported a new method for the reduction of the fluid drag of a circular cylinder. In this case, the bluff body consisted of a flat surface and a circular surface. The flat surface was oriented transversly against the uniform flow. When the curvature of the shear flow from the normal surface equals that of the circular surface, a reduction of the fluid drag ($C_D = 0.6$) can be realized when the Reynolds number is larger than the critical Reynolds number Re > Re_c (critical Reynolds number = 2.5×10^4).

The main objective of this work is to show also that the drag of a sphere, which is very common axially symmetric bluff body, may be reduced by the same method used for a circular cylinder, although significant differences exist between the flow fields around a sphere and a circular cylinder (Bearman, 1980). As shown in Fig. 1, the test model consisted of a flat surface and a spherical surface. The body was placed with its flat surface normal to the stream. The height of the portion of body removed from the sphere is equal to $D/2(1 - \cos \theta_s)$, where θ_s is the angular position of cutting surface (in the case of a sphere, θ_s = 0 deg) and D the diameter of sphere. Here, θ_s ranged from 0 deg to 75 deg and Re from 4×10^4 to 5.75×10^4.

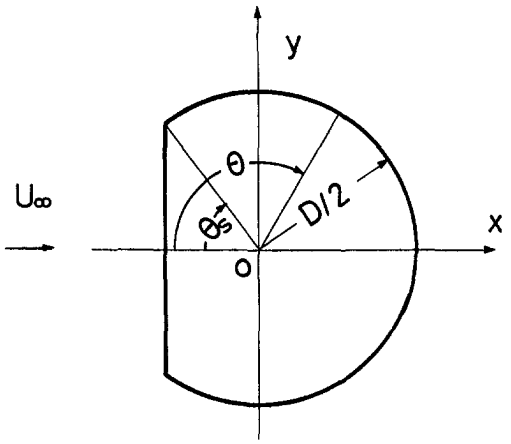

Fig. 1 Test section and coordinate system

Experimental Apparatus and Procedures

The blow-down tunnel used in the present experiments has a rectangular test section 325 mm high and 225 mm wide (Aiba and Watanabe, 1997). The free-stream turbulence intensity is kept under 0.003 throughout the experiments to avoid the effect of the free-stream turbulence on the bluff body flow (Sovran et al., 1978). The test models employed in this study were produced by cutting one side of a stainless steel sphere with a plane parallel to the y axis as shown in Fig. 1. A test model with D = 34.94 mm was used for the measurements of the drag coefficient and the flow visualization. The normal surface of the models was situated transversely to the direction of the x axis. The height of the portion of body removed from the sphere was equal to $D/2(1 - \cos \theta_s)$, where θ_s is the angular position (for the sphere, θ_s = 0 deg). Angles of θ_s = 0, 10, 20, 30, 40, 45, 48, 50, 51, 53, 55, 60, 70, and 75 deg were used. The test models were carefully polished, especially around the intersection between the normal surface and the curved one. For the drag tests, each model was attached to the wind tunnel balance with 0.2-mm-diameter piano wires. The total drag of the test body including the wires was measured by an electron balance (capacity of 0.1 ~ 2100 g). The calibration of the measuring system was also done according to the force in the direction of the y axis as shown in Fig. 1 by a wire balancing the standard weight. The corrections for the fluid drag coefficient C_{Dw} of the wires inclined against the uniform flow at the angle of α deg were made according to the following relation (Hoerner, 1958).

$$C_{Dw} = 1.1 \sin^3 \alpha + 0.02$$

The corrections for the wires were about 10 percent of the total drag throughout the experiments.

The oil flow pattern method was used for the flow visualization over the surface of the models.

[1] Professor, Department of Mechanical Engineering, Akita Technical College, Akita 011, Japan.

Contributed by the Fluids Engineering Division of THE AMERICAN SOCIETY OF MECHANICAL ENGINEERS. Manuscript received by the Fluids Engineering Division July 10, 1997; revised manuscript received May 4, 1998. Associate Technical Editor: P. W. Bearman.

Results and Discussions

The results for the drag coefficient C_D ($=D_r/0.5\rho U_\infty^2 \cdot S$, where D_r is drag, ρ density of air and S ($=\pi D^2/4$) cross-sectional area) are shown as a function of θ_s for Re = 5.75×10^4 in Fig. 2. For θ_s = 0 deg (sphere), C_D is almost identical with that value quoted by Schlichting (1968). C_D decreases gradually with increasing θ_s in the range 0 deg $\leqq \theta_s <$ 45 deg. At about $\theta_s \geqq$ 45 deg it drops sharply, and it takes a minimum value of 0.114 at around θ_s = 53 deg. At $\theta_s >$ 53 deg, C_D increases rapidly with increasing θ_s. A result (C_D = 1.17) of a hemisphere (Hoerner, 1958) is also shown. In the range Re = $4.0 \times 10^4 \sim 5.75 \times 10^4$, C_D does not depend on Re, although the results are not shown. Therefore, it is considered that the behavior of the flow around the test body does not change considerably with Re.

Figure 3 displays the variations of the separation point observed by the oil flow pattern method with θ_s for Re = 5.0×10^4. When θ_s = 0 deg, the separation point θ_p takes the value of 79 deg, which is 1 deg smaller than the result obtained by Taneda (1978). The boundary layer along the surface from θ_s to θ_p is laminar, in the range θ_s = 0 deg ~ 40 deg. However, θ_p increases slightly with increasing θ_s in the neighborhood of θ_s = 40 deg. In the range 45 deg $\leqq \theta_s \leqq$ 53 deg, the laminar boundary layer along the surface of the sphere becomes turbulent and the separation point θ_p moves rapidly with increasing θ_s in the downstream direction. The separated region behind the spherical region decreases, resulting in the decrease of C_D. The laminar boundary layer exists from the edge to the beginning of the turbulent boundary layer and the range of the laminar layer does not change significantly with θ_s, and is approximately 14 deg. On the other hand, the region of the turbulent boundary layer, which ranges almost from 26 deg to 30 deg, increases with increasing θ_s. When θ_s = 53 deg, the separation point θ_p of the turbulent boundary layer is located at about 98 deg. At θ_s = 55 deg, the laminar boundary layer from the edge mentioned above cannot be recognized. However, it can be observed that the shear layer separated from the edge reattaches at approximately θ = 68.6 deg and makes the transition to a turbulent boundary layer. The range of the turbulent layer is almost 18 deg and is narrower compared with those for θ_s = 45 deg ~ 53 deg. When $\theta_s >$ 55 deg, the shear layer shed from the edge does not reattach to the spherical surface and separation occurs at the edge of the flat surface. A stagnant flow region in the range of 25 deg from θ_s for the case θ_s = 70 deg is observed. The separation points from the edge of the flat surface are shown when $\theta_s >$ 55 deg in the figure.

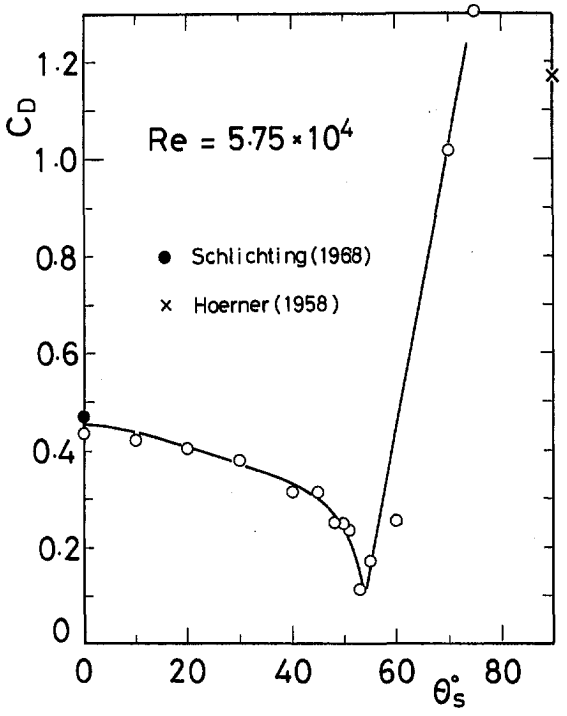

Fig. 2 Variations of C_D with θ_s at Re = 5.75×10^4 (statistical uncertainty: ±6 percent for the drag fluctuations)

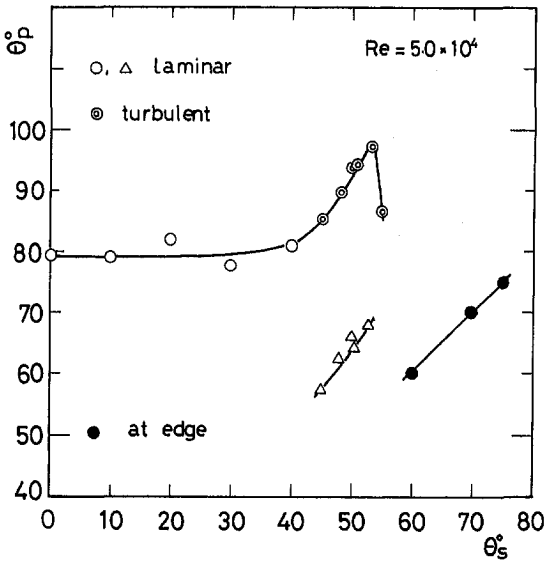

Fig. 3 Variations of separation point with θ_s for Re = 5.0×10^4 (uncertainty: ±3.5 percent for the mean values of θ_p)

The behavior of C_D in the range θ_s = 0 deg ~ 53 deg may be explained from the results of the visualization as follows. The tendency that C_D decreases gradually with increasing θ_s in the range 0 deg $\leqq \theta_s <$ 45 deg shows that the separation point θ_p moves in the downstream direction with the increase of θ_s, although the variation of the θ_p is very small throughout that range. The separation point of the turbulent boundary layer moves in the downstream direction and C_D decreases rapidly with increasing θ_s in the range 45 deg $\leqq \theta \leqq$ 53 deg. When θ_s = 53 deg, the separation point is located at about θ = 98 deg and C_D takes a minimum value of 0.114 (corresponding to about 25 percent of C_D for the sphere). In this case, the curvature of the shear flow from the normal surface equals that of the sphere. In the range $\theta_s >$ 55 deg, C_D increases sharply, caused by the direct separation from the edge of the normal surface, and by the increase of the area of the normal surface in proportion to $\sin^2 \theta_s$.

Conclusions

The drag coefficient C_D of models which consisted of a normal surface to the flow direction and a curved spherical surface have been measured and the following conclusions are drawn:

(1) A turbulent boundary layer exists on the spherical surface in the range 45 deg $\leqq \theta_s \leqq$ 55 deg. The separation point moves in the downstream direction with increasing θ_s in the range 45 deg $\leqq \theta_s \leqq$ 53 deg.

(2) C_D takes the minimum value (corresponding to approximately 25 percent of C_D for the sphere) when θ_s = 53 deg, independent of the Reynolds number in the analyzed range $4 \times 10^4 \sim 5.75 \times 10^4$.

Acknowledgments

The author would like to thank former students Messrs. Y. Funaki and C. Horii for their assistance in the experiments.

References

Aiba, S., and Watanabe, H., 1997, "Flow Characteristics of a Bluff Body Cut From a Circular Cylinder," ASME JOURNAL OF FLUIDS ENGINEERING, Vol. 119, pp. 453–454.

Aiba, S., and Hoshino, H., 1997, "Fluid Dynamic Drag of a Two-Dimensional Bluff Body Consisting of a Plane Surface and a Curved One," *JSME,* Vol. 63-615, pp. 3521–3526.

Bearman, P. W., 1965, "Investigation of the Flow behind a Two-Dimensional Model with a Blunt Trailing Edge and Fitted with a Splitter Plate," *Journal of Fluid Mechanics,* Vol. 21, pp. 241–255.

Bearman, P. W., 1967, "The Effect of Base Bleed on the Flow behind a Two-Dimensional Model with a Blunt Trailing Edge," *Aerospace Quarterly,* Vol. 18, pp. 207–224.

Bearman, P. W., 1980, "Bluff Body Flows Applicable to Vehicle Aerodynamics-Review," ASME JOURNAL OF FLUIDS ENGINEERING, Vol. 102, pp. 265–274.

Goldstein, S., ed., 1965, *Modern Developments in Fluid Dynamics,* Dover Publications, New York.

Hoerner, S. F., 1958, *Fluid-Dynamic Drag,* Published by the Author, pp. 3·11–3·17.

Roshko, A., 1955, "On the Wake and Drag of Bluff Bodies," *Journal of Aerospace Science,* Vol. 22, pp. 124–132.

Schlichting, H., 1968, *Boundary Layer Theory,* McGraw-Hill, New York, pp. 16–19.

Sovran, G., Morel, T., and Marson, Jr., W. T., ed., 1978, *Aerodynamic Drag Mechanisms of Bluff Bodies and Road Vehicles,* Plenum Press. New York, pp. 95–102.

Taneda, S., 1978, "Visual Observations of the Flow Past a Sphere at Reynolds Numbers between 10^4 and 10^6," *Journal of Fluid Mechanics,* Vol. 85-1, pp. 187–192.

Zdravkovich, M. M., 1981, "Review and Classification of Various Aerodynamic and Hydrodynamic Means for Suppressing Vortex Shedding," *Journal of Wind Engineering and Industrial Aerodynamics,* Vol. 7, pp. 145–189.